

M14




Knowledge Discovery in Big Data from Astronomy and Earth Observation

AstroGeoInformatics

EDITED BY
PETR ŠKODA
FATHALRAHMAN ADAM





Knowledge Discovery in Big Data from Astronomy and Earth Observation

AstroGeoInformatics

Edited by

Petr Škoda

Stellar Department

Astronomical Institute of the Czech Academy of Sciences

Ondřejov, Czech Republic

Fathalrahman Adam

Earth Observation Center

German Remote Sensing Data Center

DLR German Aerospace Center

Wessling, Germany



ELSEVIER

Elsevier
3251 Riverport Lane
St. Louis, Missouri 63043

Knowledge Discovery in Big Data from Astronomy and Earth Observation

ISBN: 978-0-12-819154-5

Copyright © 2020 Elsevier Inc. All rights reserved.

MATLAB® is a trademark of The MathWorks, Inc. and is used with permission.

The MathWorks does not warrant the accuracy of the text or exercises in this book.

This book's use or discussion of MATLAB® software or related products does not constitute endorsement or sponsorship by The MathWorks of a particular pedagogical approach or particular use of the MATLAB® software.

No part of this publication may be reproduced or transmitted in any form or by any means, electronic or mechanical, including photocopying, recording, or any information storage and retrieval system, without permission in writing from the publisher. Details on how to seek permission, further information about the Publisher's permissions policies and our arrangements with organizations such as the Copyright Clearance Center and the Copyright Licensing Agency, can be found at our website: www.elsevier.com/permissions.

This book and the individual contributions contained in it are protected under copyright by the Publisher (other than as may be noted herein).

Notices

Practitioners and researchers must always rely on their own experience and knowledge in evaluating and using any information, methods, compounds or experiments described herein. Because of rapid advances in the medical sciences, in particular, independent verification of diagnoses and drug dosages should be made. To the fullest extent of the law, no responsibility is assumed by Elsevier, authors, editors or contributors for any injury and/or damage to persons or property as a matter of products liability, negligence or otherwise, or from any use or operation of any methods, products, instructions, or ideas contained in the material herein.

Publisher: Candice Janco
Acquisitions Editor: Marisa LaFleur
Editorial Project Manager: Andrea Dulberger
Production Project Manager: Sreejith Viswanathan
Designer: Alan Studholme



Application of Databases Collected in Ionospheric Observations by VLF/LF Radio Signals

ALEKSANDRA NINA, PHD

23.1 INTRODUCTION

The ionosphere as a part of the terrestrial atmosphere is very sensitive to numerous external factors. Variable influences coming from both outer space and different domains of the Earth make the ionospheric plasma characteristics time-dependent. The most significant perturber from outer space originates in solar activity whose consequences can be either periodical due to the solar cycle, and seasonal and diurnal owing to the terrestrial motion (Lei et al., 2005; Pham Thi Thu et al., 2011), or transient like those arising from solar flares (McRae and Thomson, 2004; Nina et al., 2011, 2012a; Kolarski et al., 2011; Raulin et al., 2010) and coronal mass ejections (Balan et al., 2008; Bochev and Dimitrova, 2003) among others. Significant transient perturbations can also be induced by phenomena in deep outer space like gamma ray bursts (Fishman and Inan, 1988; Nina et al., 2015) and gamma ray flares (Inan et al., 2007b). In addition, there are some processes in the Earth lithosphere (like volcanic eruptions and earthquakes (Utada et al., 2011; Heki and Ping, 2005)) as well as in the atmosphere (like lightnings (Voss et al., 1998; Collier et al., 2011)) that cause nonperiodic, sporadic disturbances in the ionosphere. All of these events cause spatial and temporal changes in ionospheric plasma whose research requires data that can be obtained from databases collected by different types of observation.

Generally, the technique of atmospheric monitoring depends on the altitude of the considered medium. In this chapter our attention is paid to the low ionosphere, whose monitoring is based on rocket and radar measurements (Strelnikova and Rapp, 2010; Chau et al., 2014), and on technology involving the propagation of very low- and low-frequency (VLF/LF) radio waves. Here we discuss big databases and their applications obtained by the technique that uses data related to amplitude and phase of VLF/LF signals recorded at the

ground after the signal deflection from the ionosphere at heights below 90 km.

These databases have very important roles in both scientific and practical use. In the first case they are needed in detection of different astrophysical and geophysical events as well as for modeling plasma parameters under different conditions. In addition, there are indications of relationship between ionospheric perturbations and natural disasters like earthquakes. Some of these investigations show possible ionospheric variations before disasters which point out possible application of collected data in predictions of large catastrophes. Practical applications are primarily important in telecommunication. Namely, induced ionospheric disturbances may directly affect human activities on Earth that are related to radio communications, planned networks of mobile communications satellites, high-precision applications of global navigation satellite systems, etc.

The chapter is organized as follows. In Section 23.2 we describe observations of the low ionosphere and experimental setup used for this monitoring. Explanations of the collected big database applications in the detection of astrophysical and geophysical events, and in modeling plasma parameters are given in Sections 23.3 and 23.4, respectively, while practical applications are shown in Section 23.5. Finally, a short summary of this study is presented in Section 23.6.

23.2 EXPERIMENTAL SETUP AND OBSERVATIONS

The main way to analyze the low ionosphere is based on properties of propagating VLF/LF electromagnetic waves. Namely, during propagation from a transmitter to a receiver within the so-called Earth–ionosphere waveguide, these signals are reflected from the low ionosphere. The wave reflection height depends on the low ionospheric plasma properties (primarily the electron

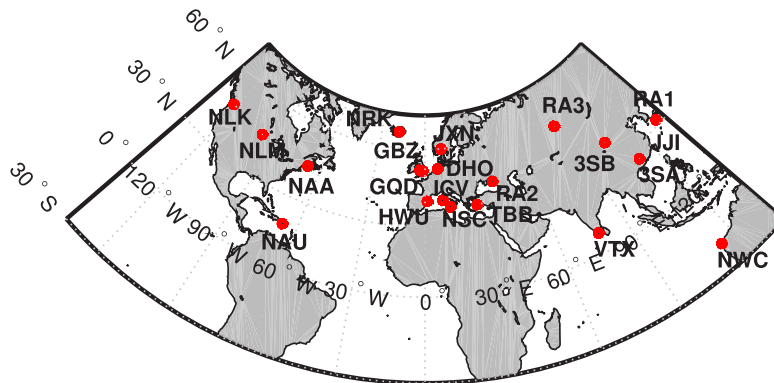


FIG. 23.1 Map of VLF and LF transmitters given in Table 23.1.

density space distribution) and its temporal variations induce changes in wave attenuation between a transmitter and receiver. Consequently, time variations of the recorded signal amplitude and phase visualize non-constant ionospheric characteristics and can be used in their analyses.

In the following text we describe a global experimental setup and present an example of a VLF/LF receiver and collected data.

23.2.1 Global Experimental Setups

The very important characteristics of this technique for the low ionospheric monitoring relevant to applications of the collected database relate to the observational space, and temporal resolution of the collected data. They can be given in the following two items:

- The global setup of this method consists of numerous worldwide located transmitters and receivers of VLF/LF radio waves.

In addition to power of an emitted electromagnetic wave, intensity and quality of received data depend on geographical locations of the considered transmitter and receiver. A map of geographical location and information on some VLF and LF transmitters are given in Fig. 23.1 and Table 23.1, respectively. On the other side, receivers are usually grouped in the global networks of radio receivers like Atmospheric Weather Electromagnetic System for Observation Modeling and Education (AWESOME) (Scherrer et al., 2008), South America VLF NETWORK (SAVNET) (Raulin et al., 2009), and Antarctic-Arctic Radiation-belt (Dynamic) Deposition – VLF Atmospheric Research Konsortium (AARDDVARK) (Clilverd et al., 2009), which are designed to make continuous long-range observations of the lower ionosphere.

Each transmitter emits energy into the entire surrounding space but attenuation of the waves near the Earth's surface is large and their intensities are weak at large distances. On the other side, sky waves which are reflected from the ionosphere propagate several thousand kilometers within the Earth–ionosphere waveguide with sufficient intensity, giving the most important contribution in the recorded signal at relevant frequencies and allowing us to use them in ionospheric observations. The fixed and unique frequency of a transmitter gives information about signal propagation path and space for which the collected data can be used in analyses, while the possibility of several detections by one receiver allows simultaneous monitoring of different regions of the low ionosphere from one position. In addition, numerous receivers provide the large number of databases with complementary information and their comparison practically cover whole latitude-longitude locations in the low ionosphere with high-quality data.

- Continuous emission and reception of radio signals with a very good time resolution (it can be 10 μ s) allow for the detection of sudden, and consequently not precisely predicted, events as well as the detection of short-term ionospheric reactions. This property of the obtained databases is very important because many phenomena cannot be predicted and consequently the monitoring of their detection and induced effects cannot be planned. Also, durations of many events and effects that they cause, like lightnings (Salut et al., 2013) and gamma ray bursts (Nina et al., 2015), are very short (they can take only several ms) and they can be detected only by measurements

TABLE 23.1
 Characteristics of some VLF and LF transmitters. The data for transmitters are found in the file
 AWESOME Transmitters.pdf on the web site http://nova.stanford.edu/~vlf/IHY_Test/TechDocs/.

Latitude (°)	Longitude (°)	Frequency (kHz)	Sign	Location
50.07	135.6	11.905	RA1	Komsomolsk-na-Amur, Russia
45.4	38.18	12.649	RA2	Krasnodar, Russia
55.76	84.45	14.881	RA3	Novosibirsk, Russia
59.91	10.52	16.4	JXN	Kolsas, Norway (NATO)
8.47	77.4	18.2	VTX	Katabomman, India
52.71	-3.07	19.6	GBZ	Anthorn, Great Britain (NATO)
-21.8	114.2	19.8	NWC	North West Cape, Australia (USA)
40.88	9.68	20.27	ICV	Isola di Tavolara, Italy (NATO)
25.03	111.67	20.6	3SA	Changde, China
39.6	103.33	20.6	3SB	Datong, China
40.7	1.25	20.9	HWU	Rosnay, France
20.4	-158.2	21.4	NPM	Lualualei, Hawaii, USA
40.7	1.25	21.75	HWV	Le Blanc, France (NATO)
52.4	-1.2	22.1	GQD	Anthorn, Great Britain (NATO)
32.04	130.81	22.2	JJI	Ebino, Japan
53.1	7.6	23.4	DHO	Rhauderfehn, Germany (DHO)
44.65	-67.3	24	NAA	Cutler, Maine, USA
48.2	-121.9	24.8	NLK	Jim Creek, Washington, USA
46.35	-98.33	25.2	NLM	LaMoure, North Dakota, USA
37.43	27.55	26.7	TBB	Bafa, Turkey
65	-18	37.5	NRK	Grindavik, Iceland (USA)
18	-67	40.75	NAU	Aguado, Puerto Rico (USA)
38	13.5	45.9	NSC	Sicily, Italy (USA)

with high time resolution like in the case of the considered setup.

These properties make the considered technique more suitable for monitoring local, short-term, and sudden events from techniques that are limited to localized observations and do not supply continuous measurements. However, unlike the rocket and radar measurements, propagation based on VLF/LF propagation techniques provides data that contain integral information along the entire waveguide between the transmitter and receiver. Due to the large distance between these devices and the atmospheric noise caused by various events, it is often not possible to isolate and analyze individually occurred phenomena. In some cases, this problem can be resolved by comparing multiple databases, as will be explained later.

23.2.2 Example of VLF/LF Receiver and Collected Data

Here, we present the AWESOME VLF/LF receiver and describe collected data at the Institute of Physics in Belgrade, Serbia, in the time period from 2008 to the present.

Receiver description. Collection of data by the AWESOME receiver is enabled by two wire-loop antennas, each sensitive to the component of the magnetic field in the direction orthogonal to the plane of the loop. They are set in North-South (NS) and East-West (EW) directions and connected to the computer through a preamplifier, long cable, GPS antenna (residing outdoors), and line receiver and ADC (residing indoors). The block diagram of the AWESOME receiver's main

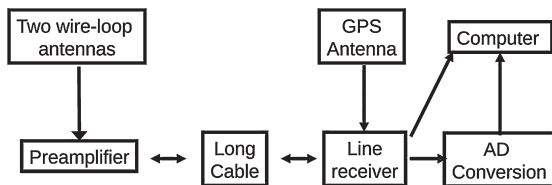


FIG. 23.2 Block diagram of the AWESOME receiver's components (a detailed description is given in Cohen et al., 2010).

components is shown in Fig. 23.2 while a detailed description is given in Cohen et al. (2010).

Collected data characteristics. This monitor provides two types of data: narrowband and broadband. The recorded data are separately systematized and their processing requires different techniques. The main characteristics of data collected by this receiver are:

- **Narrowband data.** This data type provides information about low ionospheric states. Namely, the relevant data relate to values of the amplitude and phase of the considered signals which are emitted by the VLF/LF transmitters a few hundred or thousand kilometers away from the receiver. As already said, the received signals are the so-called sky waves (waves closer to surfaces quickly attenuate) which are deflected from the low ionosphere and their variations in real-time primarily reflect the nonstationary physical and chemical conditions in the ionospheric plasma. The Belgrade AWESOME receiver can simultaneously record 15 signals emitted by different transmitters at fixed frequencies. This allows monitoring of the large area and detection of both local and global perturbations. The quality of the received data depends on the characteristics of the transmitter (the power of the emitted radiation) as well as the medium through which the signal propagates (the length of the route, the physical and chemical characteristics of the atmosphere, etc.). Thus, the signal noise increases with the length of the signal propagation path because of influences of more perturbations, while transmitted power affects the recorded amplitude level. In Table 23.2 properties of the most frequently considered signals in studies based on data collected by this VLF/LF receiver are presented. The optimal characteristics has the signal emitted from Germany (near Rhau-

TABLE 23.2 Transmitters characteristics and path length of the analyzed VLF/LF signals. The data for transmitters are found in the file AWESOME Transmitters.pdf on the web site http://nova.stanford.edu/~vli/IHY_Test/TechDocs/.

Sign	Location	Frequency (kHz)	Power (kW)	Length (km)
DHO	Rhauderfehn Germany	23.4	800	1304
GQD	Anthorn UK	22.1	200	1935
ICV	Isola di Tavolara Italy	20.27	20	976
NRK	Grindavik Island	37.5	800	3230
NAA	Cutler Maine, USA	24.0	1000	6548
NWC	North West Cape Australia	19.8	1000	11974

erfehn) due to a relatively short propagation path and large power of transmitted waves.

Time resolutions of the recorded data can range from 1 ms to 1 s, which is applicable for detection of very short-term perturbations lasting several ms.

By default, observations are divided into two time periods during the day. For each time period four files are generated for one particular transmitter: one file with a high and one file with a low time resolution for each of the two antennas (NS and EW). So, if we monitor all 15 signals, 120 files should be generated per day. They are sorted in a folder indicating the receiver station, subfolder indicating the year and, finally, subsubfolder indicating the day of the year. The file name gives information about the transmitter, date, and start time, as well as the antenna and data resolution, while the obtained database can reach several tens of gigabyte/day, i.e., several terabyte/year.

- **Broadband data.** Much better data time resolution is provided by the broadband measurements which, unlike those of the narrowband data, have data only for the amplitude and are related to the detection of both the natural and transmitter-emitted electromagnetic waves. The time resolution of the broadband

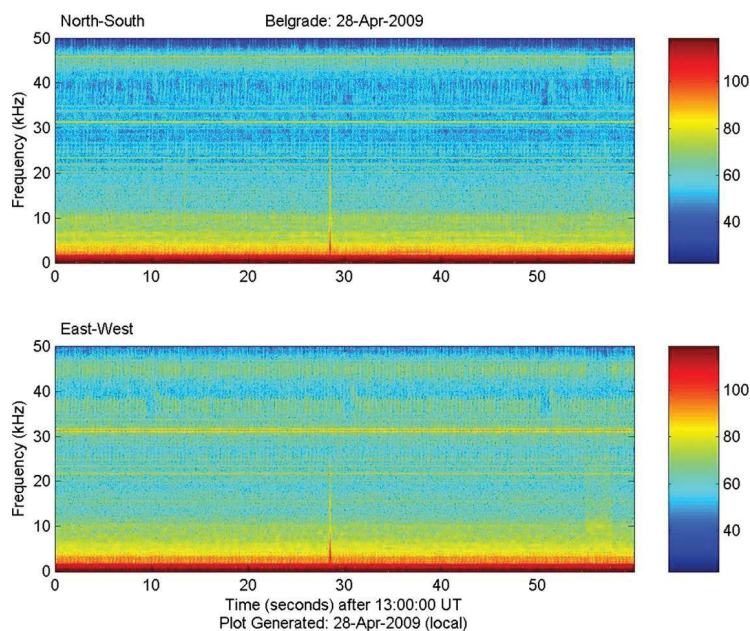


FIG. 23.3 FFT of broadband data collected by NS and EW antenna of the Belgrade AWESOME ELF/VLF/LF receiver.

data is $10 \mu\text{s}$ for waves in frequency domain from about 1 kHz to 47 kHz, i.e., in extremely low-, very low-, and low-frequency (ELF/VLF/LF) domains. The collected data reach about 32 gigabyte/day, or more than 10 terabyte/year.

The collected data show amplitude of the integral power of the electromagnetic waves in the indicated wave frequency domain. Extracting data for one particular frequency (e.g., very narrow frequency domain) can be done by using fast Fourier transform (FFT), which clearly shows significantly larger amplitudes at frequencies of the transmitter-emitted signals (see Fig. 23.3). For this reason we can connect the relevant data for the low ionospheric properties and use them in the analyses similarly as in the case of the narrowband data. However, there are two important differences in applications of these two types of data for ionospheric studies. First, the absence of information about phase in the broadband monitoring does not allow modeling of plasma parameters by methods based on both the amplitude and phase (Grubor et al., 2008) or only on phase values (Pacini et al., 2006). On

the other side, the second difference indicates a better applicability of the broadband data in detections of very short-term ionospheric disturbances induced by, for example, lightnings, whose durations can be significantly shorter than 1 ms.

23.3 APPLICATION OF DATABASES IN DETECTIONS OF ASTROPHYSICAL AND GEOPHYSICAL EVENTS

One of the most important applications of the considered databases is in the detection of different terrestrial and extraterrestrial events. In the following text we give a short review of phenomena that affect the low ionosphere and explain why a long-time monitoring of the low ionosphere with a good time resolution and different considered signals related to observations of various areas (and, consequently, big database) are necessary for detailed analyses of the mentioned detections. We will describe analyses of the signal perturbations in time and frequency domains, and their connection with a particular event or phenomenon. In addition, we will point out the importance of big databases in these investigations.

23.3.1 Sources of the Low Ionospheric Perturbations

As already said, the origins of events which disturb the low ionosphere are in the Earth's layers (atmosphere and lithosphere) as well as in outer space. Characteristics of their influence (intensity, durations, disturbed area) are dependent on the properties of radiation (radiation spectra, duration), medium of propagation (physical and chemical properties), and the low ionospheric plasma (physical and chemical properties) (Nina et al., 2018). All of these characteristics are space and time variables and can be used in different classifications in scientific studies (see, for example, Nina et al., 2017a and references therein).

There are several reviews on the phenomena that disturb the low ionosphere (Clilverd et al., 2009; Silber and Price, 2017). Here we give a classification of some of them according to induced variations important to detection and, consequently, data mining in the collected databases.

- **Extraterrestrial events.** The most important source of ionospheric perturbations is the Sun. However, some events that occurred in the deep universe can also significantly affect the upper atmosphere. Generally, these events can produce periodical and sudden ionospheric disturbances whose duration could range from 1 ms to several years.
 - Periodical perturbations. These perturbations are induced by variations in incoming solar radiation in the atmosphere due to:
 - Earth's rotation: daily variations which provide the most intensive signal changes reflected in larger amplitude during nighttime periods and increase and decrease going from sunrise to noon and from noon to sunset, respectively. Here it is important to point out excitation of acoustic and gravity waves induced by the solar terminator (Nina and Čadež, 2013).
 - Earth's revolution: seasonal variation which changes durations of daytime and nighttime signals as well as the amplitude intensity.
 - Solar cycle: the 11-year variations induced by changes in the number of sunspot during this period.
- In addition to the mentioned reviews, explanations of these perturbations are also given in Nina et al. (2017).
- Sudden perturbations. These perturbations can last from 1 ms to several hours or days. They are induced by both terrestrial and extraterrestrial phenomena.

- Solar X-ray flares. These events induce the most important variations in the ionospheric D-region, which last from a few tens of minutes to several hours. They can cause problems in communications by radio signals (so-called black-out) and additional deviations of satellite signals and variations of plasma parameters of several orders of magnitude. This influence is the subject of numerous scientific papers (Bajčetić et al., 2015; Nina et al., 2017; Schmitter, 2013; Srećković et al., 2017).
 - Coronal mass ejection (CME). Generally, impacts of relativistic charge particles (primarily electrons and protons) from outer space and upper atmosphere in the low ionosphere is significantly larger in the polar regions than in middle and especially equatorial areas due to properties of the geomagnetic field. These relativistic particles can induce disturbances in ionospheric plasma, lasting several minutes and more, which can be detected by the radio receiver considered in this chapter (Clilverd et al., 2007).
 - Gamma ray bursts and flares. This high-energy radiation with origin in the deep outer space arises during a supernova or hypernova as a rapidly rotating, high-mass star collapses to form a neutron star, quark star, or black hole, or appears to originate from a different process like the merger of binary neutron stars. The detected low ionospheric reactions range from a few tens of ms (Nina et al., 2015) to more than one hour (Inan et al., 2007b).
 - **Terrestrial events.** In addition to the mentioned extraterrestrial radiation, the low ionosphere can also be affected by volcanic eruptions, earthquake phenomena, and different meteorological conditions. These events provide aperiodic perturbations whose duration is usually shorter than in the cases of the influences from outer space.
 - Lightning-induced perturbations. They are the most frequently analyzed perturbations induced by processes in the Earth. Their duration is significantly shorter than in the previous case and a very high time resolution is usually required for their detection. These processes can be divided in
 - lightning-induced electron precipitation (LEP),
 - early VLF events, and
 - long recovery events,
- and their analyses are given in Silber and Price (2017) and references therein, where they are

connected by secondary events like sprites, elves, etc. In addition to narrowband monitoring, these perturbations are studied from the broadband observations (see Cheng and Cummer, 2005 and references therein).

Here it is also important to say that these phenomena can be associated with tropical cyclones and that lightning can be also generated during volcanic activities (see below). For these reasons their monitoring can be very important for investigations of natural disasters, especially because their intensification can be a precursor for the development of tropical depressions in hurricanes (Price et al., 2007).

- Earthquakes. There are many studies which point out to the ionospheric disturbance in periods around earthquake occurrences (Hayakawa, 2007; Pulnits and Boyarchuk, 2004). Their timescale is different and, in some cases, ionospheric variations are detected before the earthquake occurrences, which indicates a practical importance of relevant monitoring.
- Tropospheric not-short-term disturbances. These disturbances are not induced by lightnings and typical examples of them are periods around tropical depression beginnings (Nina et al., 2017b) and tropical cyclones (Kumar et al., 2017), lasting several hours. Like in the case of earthquakes and hurricanes there are some indications that these ionospheric disturbances can be precursors of intensive tropospheric motions.

23.3.2 Detections of the Low Ionospheric Perturbations

23.3.2.1 Time-Domain Analyses

To investigate signal variations and the ionospheric disturbances it is necessary to know answers to some of the following questions:

1. How do we know that the ionosphere is under the influence of an event?
2. Can we associate detected perturbations with the observed perturber?
3. How can we detect locations of local effects?
4. How can we connect perturbations with rare phenomena whose impact has not been sufficiently explored?

Descriptions of the importance of big databases in consideration of these items are explained in the text that follows where we present procedures related to (1) confirmation of an event occurrence, (2) association of detected perturbation with the considered event, (3) determinations of the local event location, and (4) detection of rare phenomena.

1. Confirmation of an event occurrence. As said in the introduction, the ionosphere is simultaneously exposed to influences of numerous natural and artificial events. Consequently, recorded signal characteristics which indirectly reflect ionospheric plasma properties are subject to noise and different tendencies which become of prime importance in the detection of particularly weak perturbations. Also, in addition to periodical and sudden variations in ionospheric plasma conditions, characteristics of signals like mutual locations of transmitter and receiver, power of transmitted signal, and geographical area of signal propagation affect the recorded signal properties. Namely, the intensity of the received signal amplitude depends on the emission power and on the distance between the transmitter and receiver. In the former case, a more intense emission induces a larger amplitude of the received signal than the emitted signal with lower power, but in the latter case the considered relationship is not so simple because the increase of the electron density in the low ionosphere does not necessarily induce amplitude rise. The numerical modeling of the signal propagation clearly indicates possibilities of the amplitude increase, decrease, and saturation, which is explained in detail in Nina et al. (2017a).

For these reasons, using a database or databases which indicate the event occurrence is necessary for the analysis of possible sudden ionospheric disturbance (SID) detections. As examples of used databases in the low ionospheric investigations are those collected by satellites like GOES¹ and Swift,² which provide information about solar events and the gamma ray bursts, respectively (see, for example, Selvakumaran et al., 2015; Nina et al., 2015). Even in the case of intensive SIDs and evident detection of their influences on the low ionosphere and signal propagation, these database are important for research of different influences (like, for example, periodical variations in the ionosphere due to daytime, season, and solar cycle changes) or radiation properties (Cresswell-Moorcock et al., 2015; Nina et al., 2018) on the considered detections.

Here it is important to say that inclusion of the other databases is not always easy and, in some cases, it is impossible. There are many reasons for

¹<https://satdat.ngdc.noaa.gov/sem/goes/data/>.

²https://gcn.gsfc.nasa.gov/swift_grbs.html.

that, like data availability, complicated administration to access information, long time to access data, and cost of data.

2. **Association of detected perturbation and considered event.** Despite the numerous impacts on the ionosphere, in some cases individual events can have a dominant influence on local plasma properties. Although signal time evolution can have different shapes (see the explanation in Nina et al., 2017a), in this case the relationship between a particular event and the corresponding SID detection is evident. Typical examples of the clear visible connections are sufficiently intensive solar X-ray flares, which are the most frequently studied influences from outer space on the daytime ionospheric D-region.

However, in some cases intensity of the SID is low and its effects on signal time evolution cannot be extracted from the noise in a particular case or the shape of the signal variation caused by the considered event is the same as or very similar to those induced by some other phenomena occurring in the same time period. Also, it is possible that the reaction is very short or that it does not induce clearly visible changes in recorded signal properties. In these cases, we cannot extract the low ionospheric reaction induced by some considered events but analyses of more events and applications of adequate statistical procedures can be used for confirmation of possible effects induced by the considered phenomena. There are different procedures for the detection of weak SIDs. Here we present three methods based on data processing from the VLF/LF database and a comparison with other relevant databases: the extraction of amplitude peaks, the comparison perturbed with relevant quiet period, and the superposed epoch technique.

- **Extraction of amplitude peaks.** This technique is used and described in Nina et al. (2015), where the short-lasting low ionospheric reaction on gamma ray bursts is confirmed in statistical analysis of 54 of these high-energy events.

The main goal of such a procedure is examination of changes in the peak numbers before and after registration of the considered event by some other relevant measurement. For example, in the mentioned study, the times of gamma ray burst occurrence are obtained from the database collected by the Burst Alert Telescope (BAT) on the Swift satellite.

In this method, a significant increase in the peak numbers after detection of the considered events indicates the existence of the low ionospheric reaction on this phenomenon. In addition to a pure confirmation of medium responses, variations of the width of time bins (used to divide the analyzed period) can be applied for analyses of time delay in the low ionospheric responses as well as confirmations of the secondary effects of the considered phenomenon in the ionospheric plasma.

This method is applicable to different datasets but it cannot be used for confirmation of the detectable variations induced by a particular event.

The existence of big databases in this type of analysis is important for the following four reasons: (1) the considered phenomena are generally unpredictable and measurements should be continuous; (2) the low ionospheric disturbances and, consequently, signal peaks are very short, and hence require high time resolution of data; (3) the frequency of studied phenomena is not necessarily high, and hence a long observation period is required to obtain an adequate number of samples for a quality statistical analysis; and (4) the same or very similar variations of signal characteristics can be induced by different phenomena and the sample used in a study should be formed from the events which occurred in time periods when the effects of the other phenomena are very low, which additionally reduces the sample and extends the observation time period.

- **Comparison of the perturbed with the related quiet period.** Information about the existence of sudden disturbances of the ionospheric plasma can be obtained using a comparison of signal characteristics from time periods with practically the same conditions, but in the absence of SIDs. This procedure is very useful in the cases without sudden strong variations in the signal-characteristic time evolutions. For this reason some large deviations of the signal time evolution from the expected values (estimated, for example, according to data relevant for the same time period but for the other, unperturbed, days) are not visible if someone analyzes only the considered time period.

There are several limitations and required confirmations that must be taken into account in applications of this method:

- For the consideration of signal deviations lasting up to a few hours it is very important to choose the relevant periods for several very close and quiet days. Namely, in some periods typical shapes of the signal amplitudes significantly vary from day to day (Cresswell-Moorcock et al., 2015) and it is necessary to find these tendencies and, according to them, to estimate the expected values for the considered time periods.
- Even if we can see unexpected time evolutions it is necessary that they stop for some time after the end of the perturbation source influence.
- In some cases, when it is necessary to analyze several days or months it is important to compare the obtained changes with possible variations during the same part of the previous or following years due to seasonal variations. Here we can have the influence of the solar cycle variations and this tendency should also be analyzed.

These limitations are a consequence of periodical variations in the low ionospheric characteristics.

For this model it is also important to perform a statistical analysis because similar effects on the signal propagation can be induced by some other phenomena too. Also, similarly to the previous method, this procedure is based on comparisons of datasets within the same database with additional use of the database of the other type for detection of the considered event.

As one can expect, it is very hard to make all these steps. The reasons are different: from technical (for example, a lack of data) to influences of many other phenomena. However, even if they can not be completely performed, it is very important to present parts that can be studied, first of all, because these analyses often refer to precursors of natural disasters.

As an example for this procedure we can quote the analyses of the periods around the solar terminator in search for a possible relationship between SIDs and tropical depressions (Nina et al., 2017b) and earthquakes (Molchanov et al., 1998). Similar changes are

recorded for more cases in a statistical analysis presented in Nina et al. (2017b) which indicates possibilities for the low ionospheric variations in the period around tropical depression beginnings and opens a need for more detailed analyses.

- **Superposed epoch technique.** This technique is applicable for a weak perturbation which is not clearly visible in one particular case but which is repeated under the same influence, like, for example, the transmitter-induced precipitation of inner radiation belt electrons in the low ionosphere (Inan et al., 2007a). It is based on averaged sums of data (representing time series of the signal amplitude relevant for many events) within the same database and their comparison for time periods of occurrence and absence of the considered influences (known from some other database). Here it is important to say that the perturbations are not short-term with respect to the considered time period. Namely, in the case when amplitude changes are short-term with respect to the considered time interval, and not frequent, this method cannot confirm them although their occurrences are in the same period after the influence of the perturber. This conclusion is obtained for short-term responses of the low ionosphere on gamma ray bursts (Nina et al., 2015) whose detection is confirmed using the procedure of extraction of amplitude peaks.

3. Determinations of local event location. In addition to the SID differences with respect to their intensity, they can be divided into global and local perturbations. Global SIDs result from extraterrestrial events which affect a large part of the Earth's atmosphere. Contrarily, the local ionospheric perturbations are induced by terrestrial phenomena such as lightnings and they are usually located within a relatively small area. Because of this spatial property, intensity and times of detected disturbances by various receivers are different and can be used for estimation or determination of the considered event locations and/or location of the perturbed low ionospheric part. Precision of the location determination primarily depends on the number of used receivers, i.e., collected databases. Also, the procedure to do that is different for one and several receivers. However, in both cases we can keep in mind that the signal propagates within the Earth-ionosphere wave-

uide and that some events which can significantly ionize the atmosphere, like lightnings, affect signal propagation not only in the ionosphere but also at lower altitudes. For this reason, when we speak about the perturbation location we think of longitude and latitude, and not altitude.

- **Detection by a single receiver.** These measurements can be applied only for estimation of perturbation locations. The procedure is based on analyses of several signals emitted by different transmitters located on various geographical locations which gives information about changes within different areas. Localization of event occurrences can be made by comparison of detected disturbances in the same (or very close) times by different signals which can be classified in two areas with respect to the receiver position and signal propagation paths:

- **Disturbances near a receiver.** In this case the signal perturbation is visible for all considered paths.

- **Disturbances far from a receiver.** In this case the absence of perturbations in the signal coming from one side indicates the SIDs above propagation paths of the perturbed signals.

- **Detection by at least three receivers.** The possibility to use several receivers allows us to find the perturbation location with high precision. There are several receiver networks whose databases are processed in the goal of detection of some events and their application is based on time differences in detected disturbances in different signals.

An example of these networks is the World Wide Lightning Location Network (WWLLN), which is used for lightning monitoring by more than 70 VLF receivers and produces regular maps of lightning activity over the entire Earth. This network is also used as the global volcanic lightning monitor, which provides databases containing information about activities of close to 2000 volcanos worldwide.

4. **Detection of rare phenomena.** In the case of rare, especially local and unpredictable phenomena, like earthquakes, big databases are required because a long time period is needed for the collection of information of enough events to perform statistical analyses. In addition, in these studies comparative analyses of the different databases

are important because more events can be included in the analyses.

23.3.2.2 Frequency-Domain Analyses

The frequency-domain analyses are primarily used for processing broadband data. However, in these analyses we can speak about integral information of the ionospheric variations and different excited electromagnetic waves because, as already said in Section 23.2.2, the broadband data provide information about both the natural (can be excited everywhere) and man-made (emitted by transmitters for the ionospheric monitoring) waves. There are numerous relevant studies which analyze the detection of different phenomena related to disturbances induced by lightnings, earthquakes (Cohen and Marshall, 2012), etc. They are based on application of FFT or wavelet transformations of data in time domain.

On the other side, processing of narrowband data and their analysis in frequency domain provides information on hydrodynamical waves excited in the low ionosphere by sufficient intensive events. As an example of a perturber we can give the solar terminator which generated acoustic and gravity waves in this ionospheric part (Nina and Čadež, 2013). In the presented procedure extraction of waves is based on the Fourier amplitude increase at some frequency in the time period after the event occurrence with respect to its value in the period before. In this type of investigations confirmation of induced waves by the considered phenomena is possible by using two criteria: the amplitude of the excited wave attenuates in time after the event influence, and the detected excitations and attenuations are repeating at many occurrences of the considered phenomenon.

23.4 APPLICATION OF DATABASES IN MODELING LOW IONOSPHERIC PLASMA PARAMETERS

As said in the introduction, the ionosphere is permanently exposed to influences of numerous events whose intensity is space- and time-dependent. Consequently, variations in the ionospheric plasma parameters can be very large. They can reach several orders of magnitude, which significantly changes conditions, and validity of approximations in different models becomes questionable. For this reason, the existence of different databases is of crucial importance in modeling the ionospheric parameters. In this sense, the VLF/LF databases are of great importance in modeling which can be used not only in scientific studies but also in practical applications (see Section 23.5). An advantages of the big

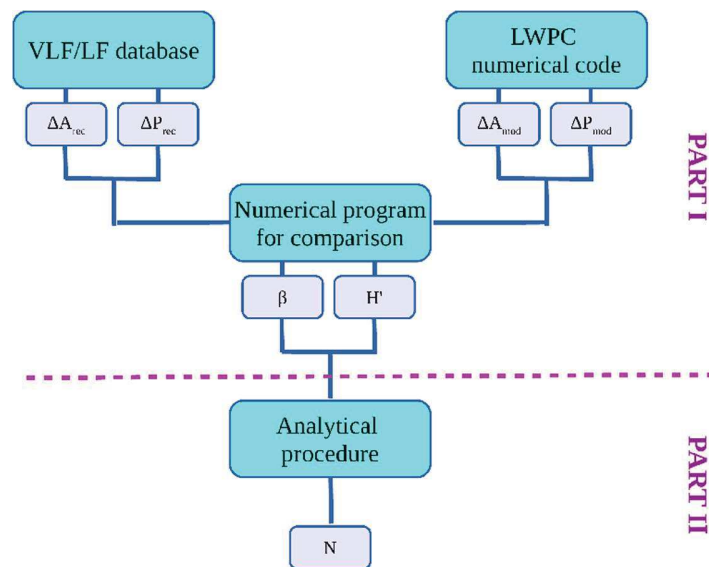


FIG. 23.4 Schematic representation of a database application in electron density modeling.

VLF/LF databases with respect to other similar databases is that they contain continual information about a very large part of the low ionosphere with a good time resolution in long time periods. These properties allow for the application of different numerical and analytical procedures in calculations of plasma parameters and their responses to numerous astro- and geophysical phenomena. The major disadvantage of these data is that they provide information about an entire area between a transmitter and receiver. However, using various procedures in modeling can reduce imprecisions caused by this characteristic.

23.4.1 Modeling of Low Ionospheric Plasma Parameters

Although one can find numerical and analytical procedures for a lot of parameters, the electron density determination is of primary importance because it is necessary for calculations of numerous other parameters. There are a few procedures for determination of the electron density from the data collected by the VLF/LF receiver. They are based on processing of values of amplitude values (Thomson, 1993), phase (Inan et al., 2007a), or both amplitude and phase (Grubor et al., 2008), and implementation of numerical models like LWPC (Ferguson, 1998) or Modfinder/Mode-search (Morfitt and Shellman, 1976). Finally, the parameters obtained from these numerical programs are

involved in analytical expressions for calculations of time and space electron density values.

The knowledge of $N_e(h, t)$ allows us to use different analytical expressions for calculations of plasma parameters like the effective recombination coefficients (Žigman et al., 2007; Nina et al., 2012b; Nina and Čadež, 2014), temperature (Bajčetić et al., 2015) and, total electron content in the D-region (Todorović Drakul et al., 2016), as well as comparisons of their properties with characteristics of other values such as, for example, variation in the X-ray radiation spectrum during a solar X-ray flare (Nina et al., 2018).

23.4.2 Example of VLF/LF Database Application in Modeling

Here we present a procedure for the calculation of the electron density time evolution for the D-region altitudes h within the range between 60 km and 90 km during disturbed periods. This procedure, shown schematically in Fig. 23.4, is based on Wait's model of the ionosphere (Wait and Spies, 1964) and can be divided in two parts: numerical determination of Wait's parameters and analytical calculation of the electron density.

23.4.2.1 Numerical Determination of Wait's Parameters

As one can see in Fig. 23.4, implementation of the collected VLF/LF database is required in this part of the

procedure for the electron density modeling. Namely, the input values in the numerical program for comparison of experimentally and numerically obtained values are data for the signal amplitude and phase deviations from values relevant to quiet ionospheric conditions (ΔA_{rec} and ΔP_{rec}) obtained from the considered database. This program is based on criteria given in Grubor et al. (2008), which allow for the determination of time evolutions of White's parameters "sharpness" β and reflection height H' . These criteria require the best fit of the recorded and modeled (by the LWPC model) amplitude (ΔA_{rec} and ΔA_{mod} , respectively) and phase (ΔP_{rec} and ΔP_{mod} , respectively) variations relative to their initial conditions, i.e.,

$$\Delta A_{\text{mod}}(\beta, H') \approx \Delta A_{\text{rec}}(t), \quad (23.1)$$

$$\Delta P_{\text{mod}}(\beta, H') \approx \Delta P_{\text{rec}}(t). \quad (23.2)$$

Time evolution of White's parameters can be obtained when we apply the presented procedure for a discrete set of recorded data within the considered time period.

23.4.2.2 Analytical Calculation of Electron Density

The electron density time evolution $N(t, h)$ at a fixed altitude h can be derived from time evolutions of White's parameters "sharpness" β and reflection height H' and the following expression (Thomson, 1993):

$$N_e(h, t) = 1.43 \cdot 10^{13} e^{-\beta(t)H'(t)} e^{(\beta(t)-\beta_0)h}, \quad (23.3)$$

where N_e is in m^{-3} , $H'(t)$ and h are in km, β is in km^{-1} , and $\beta_0 = 0.15 \text{ km}^{-1}$. One example of the obtained electron density time and altitude distribution is given in Fig. 23.5, where we visualize the presented procedure during the influence of the solar X-ray flare that occurred on 5 May 2010. The collected data relate to the 23.4 kHz signal emitted by the DHO transmitter and received by the AWESOME receiver station located in the Institute of Physics in Belgrade, Serbia.

The explained method is used in numerous studies (see for example references in the review paper Radovanović, 2018). The obtained values are generally in good agreement with those obtained from other models or in measurements by rockets (Schmitter, 2013) especially within altitude domains around the signal reflection height (H').

23.5 PRACTICAL APPLICATIONS

In addition to significance in scientific research, the collected databases can find their important role also

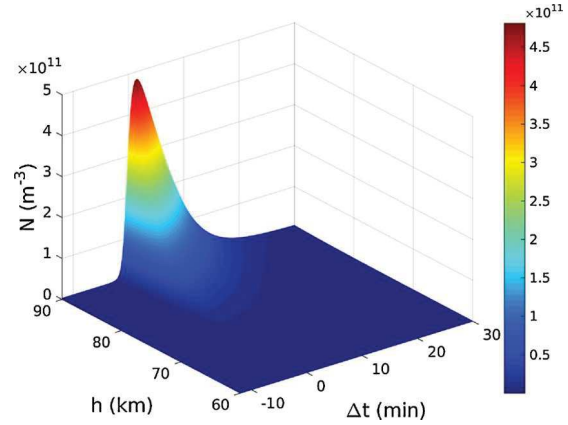


FIG. 23.5 Surface plot of the electron density time and space distribution during the analyzed solar X-ray flare. The Δt axis shows time with respect to its values for maximum X-ray intensity recorded by the GOES-14 satellite in the wavelength domain between 0.1 nm and 0.8 nm.

in practical applications. There are two major types of these applications: in research and possible prediction of natural disasters and in telecommunications.

23.5.1 Natural Disasters

Although solar activity has a dominant influence on the ionosphere, violent processes in the Earth's layers can be sufficiently intensive to significantly perturb the ionospheric plasma. For some phenomena, like for example lightnings, detection of these SIDs is confirmed and many studies describe their properties. However, there are numerous analyses which indicate the possibility of connections of SIDs with some events. The most important of these indications are related to natural disasters: earthquakes and cyclones.

23.5.1.1 Earthquakes

Investigation of the SID connections with large earthquakes started in the second half of the 20th century (see Hayakawa, 2007 and references therein). These studies present variations in signal characteristics for particular earthquake events as well as statistical analyses of more events.

In the literature, we can find a few possible hypotheses on the mechanism of coupling between the lithospheric activity and ionosphere. Primarily, they relate to geochemical processes and acoustic waves.

- Chemical processes can result in variation of parameters like temperature and radon concentration

near the Earth surface, which induce perturbations in the atmospheric conductivity and further, through the atmospheric electric field, the ionospheric disturbances (Pulinets and Boyarchuk, 2004; Sorokin et al., 2006).

- The perturbations of the parameters like temperature and pressure at the Earth's surface in a seismo-active region excites oscillations in the atmosphere which can move up to the ionospheric heights (Molchanov et al., 2001; Miyaki et al., 2002).

Here it is interesting to mention that heating and additional ionization can also be induced by radio waves generated in the lithosphere. However, the analysis given in Molchanov et al. (1995) indicates that this mechanism is not so important because the electromagnetic emission in the lithosphere is weak at all radio frequencies.

The most important conclusion of these studies is a possibility for earthquake prediction in the period of several days before the disasters. Significance of this possible practical application of the VLF/LF technology results in a big importance of relevant databases. Investigations are based on analyses of databases collected by a particular receiver as well as databases incorporated in networks of VLF and LF radio receivers. These networks are formed in the Pacific region and Europe, and their detailed descriptions are given in Hayakawa (2007) and Biagi et al. (2011), respectively. A global Pacific VLF/LF network consists of receivers in Japan, Russia, and Taiwan. Receivers in Italy, Greece, Turkey, Romania, and Portugal form the European VLF/LF radio network. All of them monitor several signals emitted by different transmitters and comparisons of the collected databases enable a better determination of perturbation location than in the case of a single receiver.

23.5.1.2 Cyclones

The most important atmospheric violent motions which induce natural disasters are tropical cyclones. Similarly to the case of earthquake events, electrical and electromagnetic effects (Isaev et al., 2002; Sorokin et al., 2005; Thomas et al., 2010) and the acoustics and gravity waves (Xiao et al., 2007) are considered as mechanisms of the troposphere-ionosphere links. The relevant low ionospheric perturbations are studied through analyses of the VLF/LF signals variations before (Price et al., 2007) and during (Nina et al., 2017b) a tropical depression and during tropical cyclones (Peter and Inan, 2005; Thomas et al., 2010; Kumar et al., 2017). So, for this phenomenon too, there are indications that the VLF/LF signals and, consequently, collected databases could be

used for the prediction of natural disasters of a tropical cyclone.

In the research of both the earthquake and cyclone events, data processing is based on different procedures, including statistical analysis, data mining, and wavelet transformations. The timescales of disturbances are different. Consequently, in some cases analyses require high time resolutions while some of them study long time periods. In addition, a continuous monitoring by different transmitters and comparisons of databases obtained by different receivers are necessary for these studies because of low frequencies of these events, unperiodical and still unpredictable occurrences, different locations, and a relatively small radius of possible SIDs. For all of these reasons it is clear why big databases are needed for application of this Earth observation technique.

23.5.2 Telecommunication

Generally speaking, the ionosphere is a medium which affects propagation of electromagnetic waves. This property is used in many practical applications, such as information transfers over thousands of kilometers by telecommunication signals in a waveguide bordered by the Earth's surface and the ionosphere, and detection of different events using telecommunication signals (see Section 23.3).

On the other side, changes of the signal propagation paths and its attenuation can cause different types of errors and problems in communications, including radio black-out. These influences are altitude- and time-dependent due to variations in electron density height distribution. In addition, the intensity of these influences depends on signal frequency. The role of the low ionosphere is more important for signals emitted from the ground at the VLF and LF domains than for satellite signals of GHz frequency which primarily deviate in the F-region. The E-region has a smaller but still nonnegligible role in signal propagation properties while the lowest D-region is usually ignored in corresponding modeling. However, during periods of intensive perturbation, the D-region electron density can be sufficiently increased so that its influence on signal deviations cannot be ignored in modeling of the Global Navigation Satellite System (GNSS) and synthetic-aperture radar (SAR).

For these reasons one can see that big VLF/LF databases are also important in applications in telecommunication and, consequently, in other areas of human activity, like geodesy and land surveying, emergency responses, precision agriculture, and all forms of transportation (space stations, aviation, maritime, railroad, and mass transit).

23.6 SUMMARY

This chapter presents an example of application of big databases obtained in the Earth observations. Our attention was focused on the low ionosphere, which is the medium containing a lot of information relevant to geo- and astrophysics as well as for different practical applications. Here we described databases which are obtained in the low ionospheric monitoring by VLF and LF radio waves and point out their importance for:

- detection of different astro- and geo-phenomena,
- modeling of the ionospheric plasma parameters, and
- practical application for possible natural disaster prediction and in telecommunication.

In this text we showed the major reasons why big databases obtained in observations by VLF/LF radio waves are required. Primarily, they relate to continuous observations of different geographical locations with good time resolutions. Also, various procedures for processing the observed bases and the necessity of their connection are explained.

Finally, we want to emphasize that each of these databases is unique in the sense that it refers to observation of certain areas. Bearing in mind the importance of the information they contain, it is very important to point out the need to increase the number of the related receivers (primarily on the Southern Earth hemisphere, where they are not too numerous), as well as the development of their mutual connection, in order to provide a wider and clearer picture of phenomena and processes they describe.

ACKNOWLEDGMENT

This work was supported by the COST project TD1403. Also, this study was carried out under the grants III 44002 and 176002 of the Ministry of Education, Science and Technological Development of the Republic of Serbia. The author is grateful to Vladimir M. Čadež for very useful suggestions and comments. Requests for the VLF data used for analysis can be directed to the corresponding author.

REFERENCES

- Bajčetić, J., et al., 2015. Ionospheric D-region temperature relaxation and its influences on radio signal propagation after solar X-flares occurrence. *Thermal Science* 19 (Suppl. 2), S299–S309. <https://doi.org/10.2298/TSCI141223084B>.
- Balan, N., et al., 2008. Magnetosphere-ionosphere coupling during the CME events of 07–12 November 2004. *Journal of Atmospheric and Solar-Terrestrial Physics* 70, 2101–2111. <https://doi.org/10.1016/j.jastp.2008.03.015>.
- Biagi, P.F., et al., 2011. The European VLF/LF radio network to search for earthquake precursors: setting up and natural/man-made disturbances. *Natural Hazards and Earth System Sciences* 11 (2), 333–341. <https://doi.org/10.5194/nhess-11-333-2011>.
- Bochev, A.Z., Dimitrova, I.I.A., 2003. Magnetic cloud and magnetosphere - ionosphere response to the 6 November 1997 CME. *Advances in Space Research* 32, 1981–1987. [https://doi.org/10.1016/S0273-1177\(03\)90636-3](https://doi.org/10.1016/S0273-1177(03)90636-3).
- Chau, J.L., Röttger, J., Rapp, M., 2014. PMSE strength during enhanced D region electron densities: Faraday rotation and absorption effects at VHF frequencies. *Journal of Atmospheric and Solar-Terrestrial Physics* 118, 113–118. <https://doi.org/10.1016/j.jastp.2013.06.015>.
- Cheng, Zhenggang, Cummer, Steven A., 2005. Broadband VLF measurements of lightning-induced ionospheric perturbations. *Geophysical Research Letters* 32 (8), L08804. <https://doi.org/10.1029/2004GL022187>.
- Clilverd, Mark A., et al., 2007. Energetic particle precipitation into the middle atmosphere triggered by a coronal mass ejection. *Journal of Geophysical Research: Space Physics* (ISSN 2156-2202) 112 (A12). <https://doi.org/10.1029/2007JA012395>.
- Clilverd, M.A., et al., 2009. Remote sensing space weather events: Antarctic-Arctic Radiation-belt (Dynamic) Deposition-VLF Atmospheric Research Consortium network. *Space Weather* 7, S04001. <https://doi.org/10.1029/2008SW000412>.
- Cohen, M.B., Inan, U.S., Paschal, E.W., 2010. Sensitive broadband ELF/VLF radio reception with the AWESOME instrument. *IEEE Transactions on Geoscience and Remote Sensing* 48, 3–17. <https://doi.org/10.1109/TGRS.2009.2028334>.
- Cohen, M.B., Marshall, R.A., 2012. ELF/VLF recordings during the 11 March 2011 Japanese Tohoku earthquake. *Geophysical Research Letters* 39 (11). <https://doi.org/10.1029/2012GL052123>.
- Collier, A.B., et al., 2011. Source region for whistlers detected at Rothera, Antarctica. *Journal of Geophysical Research* 116, A03219. <https://doi.org/10.1029/2010JA016197>.
- Cresswell-Moorcock, Kathy, et al., 2015. Techniques to determine the quiet day curve for a long period of subionospheric VLF observations. *Radio Science* (ISSN 1944-799X) 50 (5), 453–468. <https://doi.org/10.1002/2015RS005652>.
- Ferguson, J.A., 1998. Computer Programs for Assessment of Long-Wavelength Radio Communications, Version 2.0. Space and Naval Warfare Systems Center, San Diego, CA.
- Fishman, G.J., Inan, U.S., 1988. Observation of an ionospheric disturbance caused by a gamma-ray burst. *Nature* 331, 418–420. <https://doi.org/10.1038/331418a0>.
- Grubor, D.P., Šulić, D.M., Žigman, V., 2008. Classification of X-ray solar flares regarding their effects on the lower ionosphere electron density profile. *Annales Geophysicae* 26, 1731–1740. <https://doi.org/10.5194/angeo-26-1731-2008>.
- Hayakawa, Masashi, 2007. VLF/LF radio sounding of ionospheric perturbations associated with earthquakes. *Sensors* (ISSN 1424-8220) 7 (7), 1141–1158. <https://doi.org/10.3390/s7071141>.

- Heki, K., Ping, J., 2005. Directivity and apparent velocity of the coseismic ionospheric disturbances observed with a dense GPS array. *Earth and Planetary Science Letters* 236, 845–855. <https://doi.org/10.1016/j.epsl.2005.06.010>.
- Inan, U.S., Golkowski, M., et al., 2007a. Subionospheric VLF observations of transmitter-induced precipitation of inner radiation belt electrons. *Geophysical Research Letters* 34 (2), L02106. <https://doi.org/10.1029/2006GL028494>.
- Inan, U.S., Lehtinen, N.G., et al., 2007b. Massive disturbance of the daytime lower ionosphere by the giant γ -ray flare from magnetar SGR 1806-20. *Geophysical Research Letters* 34, L08103. <https://doi.org/10.1029/2006GL029145>.
- Isaev, N.V., et al., 2002. Electric field enhancement in the ionosphere above tropical storm region. In: *Seismo Electromagnetics: Lithosphere - Atmosphere - Ionosphere Coupling*. TERRAPUB, Tokyo, pp. 313–315.
- Kolarski, A., Grubor, D., Šulić, D., 2011. Diagnostics of the solar X-flare impact on lower ionosphere through seasons based on VLF-NAA signal recordings. *Baltic Astronomy* 20, 591–595. <https://doi.org/10.1515/astro-2017-0342>.
- Kumar, Sushil, et al., 2017. Perturbations to the lower ionosphere by tropical cyclone Evan in the South Pacific Region. *Journal of Geophysical Research: Space Physics* (ISSN 2169-9402) 122 (8), 8720–8732. <https://doi.org/10.1002/2017JA024023>.
- Lei, J., et al., 2005. Variations of electron density based on long-term incoherent scatter radar and ionosonde measurements over Millstone Hill. *Radio Science* 40, RS2008. <https://doi.org/10.1029/2004RS003106>.
- McRae, W.M., Thomson, N.R., 2004. Solar flare induced ionospheric D-region enhancements from VLF phase and amplitude observations. *Journal of Atmospheric and Solar-Terrestrial Physics* 66, 77–87. <https://doi.org/10.1016/j.jastp.2003.09.009>.
- Miyaki, K., Hayakawa, M., Molchanov, O.A., 2002. The role of gravity waves in the lithosphere - ionosphere coupling, as revealed from the subionospheric LF propagation data. In: *Seismo Electromagnetics: Lithosphere - Atmosphere - Ionosphere Coupling*. TERRAPUB, Tokyo, pp. 229–232.
- Molchanov, O.A., et al., 1998. Precursory effects in the subionospheric VLF signals for the Kobe earthquake. *Physics of the Earth and Planetary Interiors* (ISSN 0031-9201) 105 (3–4), 239–248. [https://doi.org/10.1016/S0031-9201\(97\)00095-2](https://doi.org/10.1016/S0031-9201(97)00095-2).
- Molchanov, O.A., Hayakawa, M., Miyaki, K., 2001. VLF/LF sounding of the lower ionosphere to study the role of atmospheric oscillations in the lithosphere-ionosphere coupling. *Advances in Polar Upper Atmosphere Research* (ISSN 1345-1065) 15, 146–158. <https://ci.nii.ac.jp/naid/110000037544/en/>.
- Molchanov, O.A., Hayakawa, M., Rafalsky, V.A., 1995. Penetration characteristics of electromagnetic emissions from an underground seismic source into the atmosphere, ionosphere, and magnetosphere. *Journal of Geophysical Research: Space Physics* 100 (A2), 1691–1712. <https://doi.org/10.1029/94JA02524>.
- Morfitt, D.G., Shellman, C.H., 1976. MODESRCH, an improved computer program for obtaining ELF/VLF mode constants in an Earth-ionosphere waveguide. Naval Electronics Laboratory Center, USA.
- Nina, A., Čadež, V.M., 2013. Detection of acoustic-gravity waves in lower ionosphere by VLF radio waves. *Geophysical Research Letters* (ISSN 1944-8007) 40 (18), 4803–4807. <https://doi.org/10.1002/grl.50931>.
- Nina, A., Čadež, V.M., 2014. Electron production by solar Ly- α line radiation in the ionospheric D-region. *Advances in Space Research* 54 (7), 1276–1284. <https://doi.org/10.1016/j.asr.2013.12.042>.
- Nina, Aleksandra, Čadež, Vladimir M., et al., 2017a. Diagnostics of plasma in the ionospheric D-region: detection and study of different ionospheric disturbance types. *The European Physical Journal D* (ISSN 1434-6079) 71 (7), 189. <https://doi.org/10.1140/epjd/e2017-70747-0>.
- Nina, A., Čadež, V.M., et al., 2018. Analysis of the relationship between the solar X-ray radiation intensity and the D-region electron density using satellite and ground-based radio data. *Solar Physics* 293, 64. <https://doi.org/10.1007/s11207-018-1279-4>.
- Nina, A., Čadež, V., Bajčetić, J., et al., 2017. Responses of the ionospheric D-region to periodic and transient variations of the ionizing solar Ly α radiation. *Journal of the Geographical Institute "Jovan Cvijic" SASA* 67 (3), 235–248. <https://doi.org/10.2298/IJG1703235N>.
- Nina, A., Čadež, V., Srećković, V.A., et al., 2011. The influence of solar spectral lines on electron concentration in terrestrial ionosphere. *Baltic Astronomy* 20, 609–612. <https://doi.org/10.1515/astro-2017-0346>.
- Nina, A., Čadež, V., Srećković, V., et al., 2012a. Altitude distribution of electron concentration in ionospheric D-region in presence of time-varying solar radiation flux. *Nuclear Instruments & Methods in Physics Research. Section B* 279, 110–113. <https://doi.org/10.1016/j.nimb.2011.10.019>.
- Nina, A., Čadež, V., Šulić, D., et al., 2012b. Effective electron recombination coefficient in ionospheric D-region during the relaxation regime after solar flare from February 18, 2011. *Nuclear Instruments & Methods in Physics Research. Section B* 279, 106–109. <https://doi.org/10.1016/j.nimb.2011.10.026>.
- Nina, Aleksandra, Radovanović, Milan, et al., 2017b. Low ionospheric reactions on tropical depressions prior hurricanes. *Advances in Space Research* (ISSN 0273-1177) 60 (8), 1866–1877. <https://doi.org/10.1016/j.asr.2017.05.024>.
- Nina, Aleksandra, Simić, Saša, et al., 2015. Detection of short-term response of the low ionosphere on gamma ray bursts. *Geophysical Research Letters* (ISSN 1944-8007) 42 (19), 8250–8261. <https://doi.org/10.1002/2015GL065726>.
- Pacini, Alessandra Abe, Raulin, Jean-Pierre, 2006. Solar X-ray flares and ionospheric sudden phase anomalies relationship: a solar cycle phase dependence. *Journal of Geophysical Research: Space Physics* 111 (A9). <https://doi.org/10.1029/2006JA011613>.
- Peter, W.B., Inan, U.S., 2005. Electron precipitation events driven by lightning in hurricanes. *Journal of Geophysical Research: Space Physics* 110, A05305. <https://doi.org/10.1029/2004JA010899>.

- Pham Thi Thu, H., Amory-Mazaudier, C., Le Huy, M., 2011. Time variations of the ionosphere at the northern tropical crest of ionization at Phu Thuy, Vietnam. *Annales Geophysicae* 29, 197–207. <https://doi.org/10.5194/angeo-29-197-2011>.
- Price, C., Yair, Y., Asfur, M., 2007. East African lightning as a precursor of Atlantic hurricane activity. *Geophysical Research Letters* 34, L09805. <https://doi.org/10.1029/2006GL028884>.
- Pulinets, S., Boyarchuk, K., 2004. *Ionospheric Precursors of Earthquakes*. Springer, Berlin.
- Radovanović, M., 2018. Investigation of solar influence on the terrestrial processes: activities in Serbia. *Journal of the Geographical Institute "Jovan Cvijic" SASA* 68 (1), 149–155. <https://doi.org/10.2298/IJGI1801149R>.
- Raulin, J.-P., Bertoni, F.C.P., et al., 2010. Solar flare detection sensitivity using the South America VLF Network (SAVNET). *Journal of Geophysical Research: Space Physics* 115, A07301. <https://doi.org/10.1029/2009JA015154>.
- Raulin, J.-P., Correia de Matos David, P., et al., 2009. The South America VLF NETWORK (SAVNET). *Earth, Moon, and Planets* 104, 247–261. <https://doi.org/10.1007/s11038-008-9269-4>.
- Salut, M.M., et al., 2013. On the relationship between lightning peak current and Early VLF perturbations. *Journal of Geophysical Research: Space Physics* 118 (11), 7272–7282. <https://doi.org/10.1002/2013JA019087>.
- Scherrer, D., et al., 2008. Distributing space weather monitoring instruments and educational materials worldwide for IHY 2007: the AWESOME and SID project. *Advances in Space Research* 42, 1777–1785. <https://doi.org/10.1016/j.asr.2007.12.013>.
- Schmitter, E.D., 2013. Modeling solar flare induced lower ionosphere changes using VLF/LF transmitter amplitude and phase observations at a midlatitude site. *Annales Geophysicae* 31 (4), 765–773. <https://doi.org/10.5194/angeo-31-765-2013>.
- Selvakumaran, R., et al., 2015. Solar flares induced D-region ionospheric and geomagnetic perturbations. *Journal of Atmospheric and Solar-Terrestrial Physics* (ISSN 1364-6826) 123, 102–112. <https://doi.org/10.1016/j.jastp.2014.12.009>.
- Silber, Israel, Price, Colin, 2017. On the use of VLF narrowband measurements to study the lower ionosphere and the mesosphere–lower thermosphere. *Surveys in Geophysics* 38 (2), 407–441. <https://doi.org/10.1007/s10712-016-9396-9>.
- Sorokin, V.M., Isaev, N.V., et al., 2005. Strong DC electric field formation in the low latitude ionosphere over typhoons. *Journal of Atmospheric and Solar-Terrestrial Physics* (ISSN 1364-6826) 67 (14), 1269–1279. <https://doi.org/10.1016/j.jastp.2005.06.014>.
- Sorokin, V.M., Yaschenko, A.K., et al., 2006. DC electric field formation in the mid-latitude ionosphere over typhoon and earthquake regions. In: *Recent Progress in Seismo Electromagnetics and Related Phenomena. Physics and Chemistry of the Earth. Parts A/B/C* (ISSN 1474-7065) 31 (4), 454–461. <https://doi.org/10.1016/j.pce.2005.09.001>.
- Srećković, V., et al., 2017. The effects of solar activity: electrons in the terrestrial lower ionosphere. *Journal of the Geographical Institute "Jovan Cvijic" SASA* 67 (3), 221–233. <https://doi.org/10.2298/IJGI1703221S>.
- Strelnikova, I., Rapp, M., 2010. Studies of polar mesosphere summer echoes with the EISCAT VHF and UHF radars: information contained in the spectral shape. *Advances in Space Research* 45, 247–259. <https://doi.org/10.1016/j.asr.2009.09.007>.
- Thomas, J.N., et al., 2010. Polarity and energetics of inner core lightning in three intense North Atlantic hurricanes. *Journal of Geophysical Research: Space Physics* 115, A00E15. <https://doi.org/10.1029/2009JA014777>.
- Thomson, N.R., 1993. Experimental daytime VLF ionospheric parameters. *Journal of Atmospheric and Terrestrial Physics* 55, 173–184. [https://doi.org/10.1016/0021-9169\(93\)90122-F](https://doi.org/10.1016/0021-9169(93)90122-F).
- Todorović Drakul, M., et al., 2016. Behaviour of electron content in the ionospheric D-region during solar X-ray flares. *Serbian Astronomical Journal* 193, 11–18. <https://doi.org/10.2298/SAJ160404006T>.
- Utada, H., et al., 2011. Geomagnetic field changes in response to the 2011 off the Pacific Coast of Tohoku Earthquake and Tsunami. *Earth and Planetary Science Letters* 311, 11–27. <https://doi.org/10.1016/j.epsl.2011.09.036>.
- Voss, H.D., et al., 1998. Satellite observations of lightning-induced electron precipitation. *Journal of Geophysical Research* 103, 11725–11744. <https://doi.org/10.1029/97JA02878>.
- Wait, J.R., Spies, K.P., 1964. Characteristics of the Earth-ionosphere waveguide for VLF radio waves. *NBS Technical Note 300*. National Bureau of Standards, Boulder, CO.
- Xiao, Zuo, et al., 2007. Morphological features of ionospheric response to typhoon. *Journal of Geophysical Research: Space Physics* (ISSN 2156-2202) 112 (A4), A04304. <https://doi.org/10.1029/2006JA011671>.
- Žigman, V., Grubor, D., Šulić, D., 2007. D-region electron density evaluated from VLF amplitude time delay during X-ray solar flares. *Journal of Atmospheric and Solar-Terrestrial Physics* 69, 775–792. <https://doi.org/10.1016/j.jastp.2007.01.012>.

M21a

Article

Two-Dimensional Correlation Analysis of Periodicity in Noisy Series: Case of VLF Signal Amplitude Variations in the Time Vicinity of an Earthquake

Andjelka B. Kovačević ^{1,2,*} , Aleksandra Nina ³ , Luka Č. Popović ^{1,2,4}  and Milan Radovanović ^{5,6} 

¹ Department of Astronomy, Faculty of Mathematics, University of Belgrade, Studentski trg 16, 11000 Belgrade, Serbia

² Key Laboratory for Particle Astrophysics, Institute of High Energy Physics, Chinese Academy of Sciences, 19B Yuquan Road, Beijing 100049, China

³ Institute of Physics Belgrade, University of Belgrade, Pregrevica 118, 11080 Belgrade, Serbia

⁴ Astronomical Observatory, Volgina 7, 11160 Belgrade, Serbia

⁵ Geographical Institute Jovan Cvijić SASA, 11000 Belgrade, Serbia

⁶ Institute of Sports, Tourism and Service, South Ural State University, 454080 Chelyabinsk, Russia

* Correspondence: andjelka@matf.bg.ac.rs

Abstract: Extraction of information in the form of oscillations from noisy data of natural phenomena such as sounds, earthquakes, ionospheric and brain activity, and various emissions from cosmic objects is extremely difficult. As a method for finding periodicity in such challenging data sets, the 2D Hybrid approach, which employs wavelets, is presented. Our technique produces a wavelet transform correlation intensity contour map for two (or one) time series on a period plane defined by two independent period axes. Notably, by spreading peaks across the second dimension, our method improves the apparent resolution of detected oscillations in the period plane and identifies the direction of signal changes using correlation coefficients. We demonstrate the performance of the 2D Hybrid technique on a very low frequency (VLF) signal emitted in Italy and recorded in Serbia in time vicinity of the occurrence of an earthquake on 3 November 2010, near Kraljevo, Serbia. We identified a distinct signal in the range of 120–130 s that appears only in association with the considered earthquake. Other wavelets, such as Superlets, which may detect fast transient oscillations, will be employed in future analysis.

Keywords: numerical method; periodicity detection; VLF signal amplitude; earthquake

MSC: 37M10; 62M15



Citation: Kovačević, A.B.; Nina, A.; Popović, L.Č.; Radovanović, M. Two-Dimensional Correlation Analysis of Periodicity in Noisy Series: Case of VLF Signal Amplitude Variations in the Time Vicinity of an Earthquake. *Mathematics* **2022**, *10*, 4278. <https://doi.org/10.3390/math10224278>

Academic Editor: Eugene Postnikov

Received: 20 October 2022

Accepted: 5 November 2022

Published: 15 November 2022

Publisher's Note: MDPI stays neutral with regard to jurisdictional claims in published maps and institutional affiliations.



Copyright: © 2022 by the authors. Licensee MDPI, Basel, Switzerland. This article is an open access article distributed under the terms and conditions of the Creative Commons Attribution (CC BY) license (<https://creativecommons.org/licenses/by/4.0/>).

1. Introduction

Monitoring of different parts of the Earth and space collect data whose analyses can provide numerous important pieces of information for both scientific research and practical applications. One of the most important applications of various forms of monitoring is in the field of natural disaster prediction. However, in many cases, the possibilities and reliability of the corresponding predictions are still in the research phase. One of these examples is the application of data obtained in the monitoring of the lower ionosphere with very low frequency (VLF) signals to the prediction of earthquakes. These signals are emitted by worldwide located transmitters and propagate in the so-called “Earth-ionosphere waveguide”, while numerous receivers record the signal amplitude and phase at their locations. Variations in the characteristics of the recorded signal enable the indirect detection of numerous phenomena, among which are those related to natural disasters. Among others, a large number of studies based on the analysis of VLF signals investigate the possibility of the existence of earthquake precursors in the form of ionospheric perturbations. Those precursors are primarily associated with changes in the VLF signal amplitude and/or

phase [1–5] and the amplitude minimum time shift during solar terminator periods (the so-called “terminator time”) [6–10]. In addition, the most recent research suggests that there are reductions in the noise of the VLF signal amplitude and phase a few tens of minutes before the observed type of disaster [11–13]. Although various data processing procedures have been applied in previous studies, there is still no way to reliably predict an earthquake. For this reason, the application of new models in VLF signal processing is essential.

Signals are similar to quantum systems due to wave-particle duality. The scientist who first noticed this and prove the uncertainty principle for signals was Gabor [14], who did so by applying to arbitrary signals the same mathematical apparatus that was employed in the Heisenberg-Weyl [15,16] derivation of the uncertainty principle in quantum mechanics.

As it is well known, according to Heisenberg’s uncertainty principle [15] the product of the standard deviations of position (σ_x) and momentum (σ_p) cannot be less than a non-zero constant $\sigma_x \sigma_p \geq \frac{h}{4\pi}$, involving Planck constant h . Similarly, the basic Gabor Uncertainty Principle [see 14] states that the product of the uncertainties in frequency (σ_f) and time (σ_t) must exceed a fixed constant $\sigma_f \sigma_t \geq \frac{1}{4\pi}$. As a direct consequence of this, it is impossible to know the exact time and frequency of a signal simultaneously; hence, it is impossible to describe a signal as a point on the time-frequency (TF) plane. TF analysis of time series is traditionally carried out by employing the Fourier spectra on successive sliding time windows (e.g., see [17], and references therein). Wide windows offer high-frequency resolution but low temporal resolution, and vice versa; this is where the Heisenberg–Gabor uncertainty principle starts to have an influence. The characterization of a time series in the frequency domain by means of the spectral density function $S(f)$, which establishes the distribution of the time series variance at specific frequencies f , is one of the most used diagnostic tools for the identification of quasiperiodic fluctuations in a time series across disciplines. The simplest estimator of the $S(f)$ is the periodogram defined as the product of the time series sampling rate divided by the number of points and the square modulus of the discrete Fourier transform. The major issues of the periodogram are well investigated (see [18], and references therein): (i) Because of the finite frequency resolution, power leakage into adjacent bins occurs (ii) a bias in the estimate that was not known a priori, and which was dependent on the time series itself and (iii) the associated variance, that is equal to the estimate itself.

To get around the above-mentioned problems, multiscale approaches, which are also known as multiresolution methods, have been developed. An example of one of these methods is the continuous wavelet transform (CWT, see [19]). The CWT provides a good relative temporal location of the signal, since it may either tighten or inflate a mother wavelet depending on the frequency of the signal [20].

The CWT is capable of pinpointing the location of the oscillation in time, but as the frequency increases, it sacrifices its frequency resolution [21]. However, in many instances, it is not possible to find the difference between frequency components that are immediately adjacent to one another. Because of this, analyses are frequently carried out making use of a dyadic representation. One example of this is the dyadic discrete wavelet transform (DWT), in which the $T/2^j$ wavelet amplitude coefficients arising from the j -th stage of the DWT, and $T = 2^n$ [22] are employed. On the other hand, this representation does not do a very good job of resolving the high frequencies.

Our hybrid method, which is based on two-dimensional (2D) correlation analysis, was created to solve the problems that have previously been encountered (see [23,24]). It has been validated by the utilization of optical and photometric data obtained from several studies of active galactic nuclei, which are fueled by supermassive black holes (see e.g., [23,25]). The fundamental feature of these data is that they have irregular sampling, with huge gaps, and signal with low amplitude, if it exists at all, is buried in the red noise.

The 2D Hybrid method can utilize various wavelets (e.g., CWT, DWT, Weighted wavelet transform, high-resolution Superlets) to localize oscillations in the period-period plane of the time series in question. The method produces a contour map of correlation

intensity on a period-period plane defined by two independent period axes corresponding to the two-time series (or one). The map is symmetric and able to be integrated along any of the axes, resulting in a depiction of the level of correlation among oscillations that is similar to a periodogram. Therefore our approach could be interpreted as the two-dimensional distributions of correlation of the variance of time series in the time domain, which could also be projected into the one-dimensional domain. Our goal is to further illustrate the performance of the 2D hybrid technique and its application on time series of highly sampled very low frequency (VLF) radio signal amplitude data. In this study, we present computations of 2D correlation maps of the VLF signal amplitude oscillations before, during, and after the earthquake nearby the city of Kraljevo in Serbia on 3 November 2010. As perturbation of VLF signal amplitude is associated with the occurrence of earthquakes, this application presents an opportunity for the acquisition of novel insights.

2. Materials

This study is based on the processing of data recorded in the low ionosphere monitoring by the 20.27 kHz VLF radio signal emitted by the VLF transmitter (whose name is ICV, see e.g., [26]) located in Italy (Isola di Tavolara, Sardinia, latitude 43.74° N, longitude 20.69° E) and recorded by the Absolute Phase and Amplitude Logger (AbsPAL) receiver in Belgrade, Serbia (latitude 44.8° N, longitude 20.4° E). The time intervals are determined in relation to the time of the earthquake that occurred near Kraljevo (Serbia) on 3 November 2010 at 00:56:54.4 Universal Time (UT). In Figure 1, we show the path of the observed VLF signal and the location of the Kraljevo earthquake epicenter [27] for which the data are given in <http://www.emsc-csem.org/Earthquake/> (accessed on 25 June 2018).

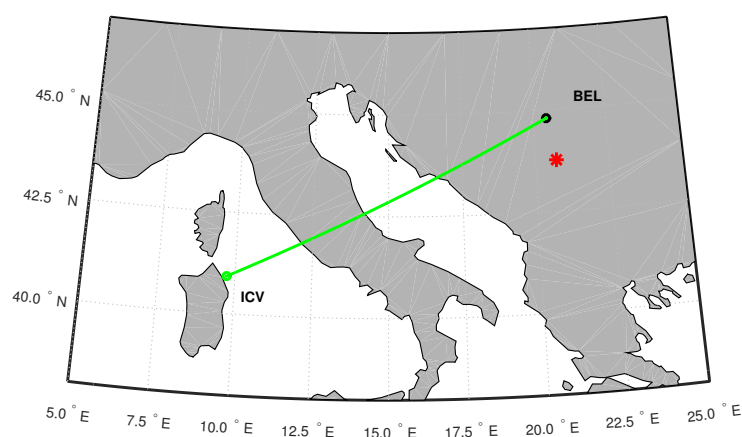


Figure 1. Propagation path of the VLF signal recorded by the Belgrade receiver station (BEL) in Serbia and emitted by the ICV transmitter in Isola di Tavolara, Sardinia, Italy (solid line). The location of the Kraljevo earthquake epicenter is shown as a star.

In this study, we consider data series showing VLF signal amplitude values recorded with a sampling of 0.1 s in five time intervals starting 2 h and 1 h before the Kraljevo earthquake, at the moment of its occurrence, and 1 h and 2 h after that time. To compare the obtained results with those relevant for periods without seismic activity, we additionally analyze the time intervals in the same season period but about one year earlier (1–2 November 2009). These periods are chosen to exclude the effects of daily and seasonal changes that are visible in the VLF signal amplitudes and that may affect the observed comparison. In addition, it was taken into account to eliminate the potential influences of other natural phenomena with origin in the atmosphere and from space as well as non-natural causes of variations in the emission and reception of the considered signal (these influences are described in detail in [11,13]). For this reason, the reference intervals are chosen in periods when no significant disturbances in meteorological, geomagnetic, and

space weather conditions were recorded, and when approximately the same values of the amplitude and its noise were recorded as in the quiet period before the Kraljevo earthquake.

3. Methods

Here, we are presenting a detailed view of the 2D Hybrid method, where the main steps of this process are depicted, while we provide excerpts of the algorithm in pseudocode for revealing additional important details (see Algorithm A1, in Appendix A). To start, we review some of the fundamental ideas and information associated with wavelet analysis (see Section 3.1). The overall concept of the 2D Hybrid method is presented in Section 3.2, along with a detailed description of the period’s uncertainty (Section 3.2.1) and significance (Section 3.2.2) estimate. In conclusion, Section 3.2.3 presents the wavelet that was implemented in our 2D Hybrid method.

3.1. Summary of Wavelet Concept

A wavelet function (abbreviated wavelet) is a function belonging to the space of all square-integrable functions $\psi \in L_2(\mathbb{R})$, averaged $\int_{\mathbb{R}} \psi = 0$, and normalized $\|\psi\| = 1$ (see more details in [19,28]). When we compare the wavelet approach to the Fourier method, we find that the Fourier analysis disassembles a signal into a set of sinusoids defined with distinct frequencies, but the wavelet method unwinds a signal into the shifted or scaled shapes that originate from a mother wavelet. Wavelet maps a signal into a time-scale plane which is the same as the time-frequency plane in the short-time Fourier transform, so that each scale represents a certain frequency range of the time-frequency plane [29]. Given the signal $f(t)$, its CWT at time u and scale s is defined as:

$$CWf(u, s) = \frac{1}{\sqrt{s}} \int_{-\infty}^{+\infty} f(t) \psi^* \left(\frac{t - u}{s} \right) dt \quad s \in \mathbb{R} - 0, u \in \mathbb{R} \tag{1}$$

The result of the CWT is a matrix (scalogram) filled with wavelet coefficients located by scale and position:

$$\mathcal{S}(s) = \|CWf(u, s)\| = \left(\int_{-\infty}^{+\infty} \|CWf(u, s)\|^2 du \right)^{1/2} . \tag{2}$$

The aforementioned equation could be interpreted as the amount of energy, denoted by CWf present at scale s , provided that the condition $\mathcal{S}(s) \geq 0$ holds. When seen in this context, the same equation enables us to determine the scales that contribute the most to the overall energy of the signal.

In most cases, we are only interested in searching for oscillations inside a predetermined time span such as $[t_{min}, t_{max}]$, and because of this, we can define the windowed scalogram that corresponds to this interval as follows:

$$\mathcal{S}_{[t_{min}, t_{max}]}(s) = \|CWf(u, s)\|_{t_{min}}^{t_{max}} = \left(\int_{t_{min}}^{t_{max}} \|CWf(u, s)\|^2 du \right)^{1/2} \tag{3}$$

In actuality, any time series f that is appropriate for wavelet analysis needs to be defined over a limited time interval $[t_{min}, t_{max}]$ and sampled with a specified resolution to obtain discrete data. In terms of sampling, any discrete signal can be studied in a discrete domain by utilizing discrete wavelets, or in a continuous manner by employing neural and Gaussian process models of discrete series with gaps.

If we are given two-time series, f and f' , we can examine their respective scalograms, \mathcal{S} and \mathcal{S}' , to determine whether or not they exhibit patterns that are comparable to one another. For instance, we can perform an absolute comparison of scalograms using the formula $\|\mathcal{S} - \mathcal{S}'\|$ [30].

3.2. General Description of 2D Hybrid Method

Now, we are ready to present our 2D Hybrid approach, which compares the scalograms of two different (or one) series by using correlation. Given a scalogram \mathcal{S} with dimensions $M \times N$ and another scalogram \mathcal{S}' with dimensions $P \times Q$, the two-dimensional cross-correlation (\star) of these scalograms is the matrix $\mathcal{C} = \mathcal{S} \star \mathcal{S}'$ with dimensions $[M + P - 1] \times [N + Q - 1]$, which has following elements:

$$\mathcal{C}_{(k,l)} = \sum_{m=0}^{M-1} \sum_{n=0}^{N-1} \mathcal{S}(m,n) \overline{\mathcal{S}'(m+k,n+l)} \tag{4}$$

where $\overline{\mathcal{S}'}$ stands for complex conjugate of \mathcal{S}' and $-(P - 1) \leq k \leq M - 1, -(Q - 1) \leq l \leq N - 1$.

As the cross-correlation of scalograms is defined on the field of complex numbers, both the real and imaginary components of the complex cross-correlation function are referred to as the synchronous and asynchronous 2D correlation spectra, respectively (see [31]). Since we are only interested in physical phenomena whose correlation can be tracked in the field of real numbers, we only supply the mathematical formulation of synchronous 2D correlation spectra [32]

$$\mathcal{M} = \frac{Cov(\tilde{\mathcal{S}}, \tilde{\mathcal{S}'})}{\sigma\sigma'} \tag{5}$$

where Cov stands for covariance and σ and σ' are standard deviations of scalograms $\tilde{\mathcal{S}}$ and $\tilde{\mathcal{S}'}$ of two time series, respectively.

Notably, in the discrete formulation of cross-correlation, a synchronous 2D correlation map is simply defined as the inner product of the $\tilde{\mathcal{S}}$ and $\tilde{\mathcal{S}'}$ [32]:

$$\mathcal{M} = \tilde{\mathcal{S}}^T \tilde{\mathcal{S}'} \tag{6}$$

The resemblance between oscillations in two different (or one) time series is measured via a 2D correlation map (which we will also refer to as a heatmap). A high positive correlation value shows that periodic signals vary in a coordinated manner, implying that the signals have a common or related origin [23].

The two-dimensional correlation map is presented as a contour map of correlation strength on a period plane that is defined by two axes that are independent of one another. When done in this fashion, plotting a synchronous spectrum results in a map that is symmetric in relation to the primary diagonal line of the map. The correlation of two (or one) time series at the same period refers to the intensity of the correlation that may be found at the main diagonal of the map. As a result, peaks that are located on the main diagonal line are referred to as auto-peaks. The intensities of auto-peaks are representative of the total extent of the signals' dynamic fluctuations [23]. It is important to note that a two-dimensional correlation map can be summed with the absolute value of $C(k, l)$ along any of the dimensions. This is because a negative correlation can also appear for some signals which should not be canceled in the summation. This integration provides an interpretation similar to a periodogram, with the horizontal axis counting periods and the vertical axis standing for the degree of correlation peaks.

3.2.1. Concept of Estimating Uncertainty of Detected Periods

To find the uncertainty of detected periods, we first calculate the full-width half maximum of the peak in a periodogram-like image, and then use the `mquantile` module in Python to estimate points that fall between the 25th and 75th quantiles. The upper and lower error estimates are represented by these points. The reason behind using quantiles is that peaks in periodogram-like structure do not conform to the theoretical normal distribution, actually they are skewed. In this particular situation, quantiles provide more suitable information than the standard deviation. The sample quantile is based on order statistics and calculated regardless of the underlying distribution. The p -th quantile of a set of values

represents a summarizing quantity having less than or equal to p , where, $0 \leq p \leq 1$. Similar to the median, which is the value below which 50% of all values in the sample lie, we might define that the first quartile (25th quantile) as the value below which 25% of all values in the sample lie and the third quartile (75th quantile) as the value below which 75% lie.

Our period error method is inspired by 'post mortem analysis' by [33], which requires the so-called Mean Noise Power Level (MNPL) in the vicinity of the detected period. The 1-sigma confidence interval on period then is equal to the width of the line at the period—MNPL level.

3.2.2. Concept of Estimating Significance of Detected Periods

The significance of detected period σ_p , we estimated following the approach outlined in [34]. After shuffling the dates of each and every observation and its magnitude, the period was recalculated across this newly updated data set, and the power of the highest peak in this uncorrelated data set was compared to that of the initial simulated data. After performing this procedure a total of one hundred times (presumably due to the large computing time needed for highly sampled VLF signals), the significance level was finally calculated as:

$$\sigma_p = \frac{x}{N} \quad (7)$$

where x represents the number of times that the peak power of the period in the original data was greater than that of the uncorrelated ensemble and N is the total number of shuffles (100). This formula, therefore, has a maximum of 1, corresponding to a 100 percent recovery rate. When multiple periods are found in an original curve, the significance of each peak is measured by comparing the power of peaks in shuffled curves found at the place of detected periods to the power of peaks in the original curve.

3.2.3. Wavelets Used in 2D Hybrid Method

The effective implementation of the 2D Hybrid approach is going to be demonstrated in the next Section by making use of Weighted Wavelet Z-transform (WWZ) wavelets [35]. This wavelet approach can be utilized on data that has been sampled both regularly and irregularly. The WWZ wavelets are defined on a basis that consists of functions: $\cos[\omega(t - \tau)]$, $\sin[\omega(t - \tau)]$, $I(t) = 1$. In addition, the projection of data via WWZ makes use of weights that take the form $\exp(-c\omega^2(t - \tau)^2)$, where c is a parameter that can be adjusted according to the data set.

The tuning constant c , whose value determines the window's width, can have a variety of choices. For instance, the value $c = 0.0125$ was initially suggested in [35], to improve the time resolution on shorter parts of the data. However, the value of c might go as high as 0.005, and it is used to improve frequency resolution.

In the former scenario, this translates to the wavelet decaying by e^{-1} in ~ 1.4 cycles, while, in the latter scenario, this translates to the wavelet deteriorating in ~ 2.4 cycles. In our study, we used $c \sim 0.003$. This value can be compared to e.g., $c = 0.001$ used in [36,37] for longer data sets than the one used here.

Because each of the analyzed time series has 36,000 points, the application of our 2D Hybrid method takes 45 min to complete on the `google.colab` computing platform, which has a CPU: $1 \times$ single core hyper threaded Xeon Processors 2.2 GHz (1 core, 2 threads) and RAM: ~ 13 GB. It takes about 70 h on the same platform to calculate the significance of a detected period using 100 artificial time series.

4. Results and Discussion

As the amplitude fluctuation of the VLF signal during the Kraljevo earthquake is known to be difficult to analyze using Fourier periodicity, we decided to demonstrate our method using this data. We computed 2D hybrid maps and their integrated versions for each segment of the time series for the date of the earthquake occurrence (see Figure 2) and for the same date but one year earlier as a control case (see Figure 3). For each time series segment, we kept the same parameters of WWZ wavelets: $c = 0.003$, range of frequencies

$[1/150, 1/30] s^{-1}$, and the number of points in the frequency grid (200). Table 1 provides a summary of the detected periods for the date of earthquake occurrence, whereas Table 2 provides the values for those detected periods for the control date one year earlier.

Table 1. Summary of detected periods on the date of the earthquake. Periods are measured from the integrated version of the 2D Hybrid map (bottom marginal panels) in Figure 2. Columns: series part with respect to earthquake beginning time, detected periods, lower and upper errors.

Series ID	Period [s]	−err [s]	+err [s]	Significance [%]
−2 h	147.06	56.8	60.0	99
	86.2	4.2	5.8	99
	80.6	15.5	18.8	99
	63.02	11.3	12.8	99
	50.33	9.7	10.7	99
−1 h	121.0	10.0	0.9	
	35.9	0.7	0.2	99
0 h	131.6	7.4	1.1	
	47.2	0.9	0.3	99
	35.5	0.5	0.2	99
+1 h	121.0	7.8	1.3	99
	69.4	2.5	1.7	
+2 h	85.2	3.9	1.0	99
	58.6	2.0	0.25	99
	38.9	0.8	0.2	99

The heatmaps show the prominent oscillations in time series segments which are plotted on the top of the heatmap. The frequencies are displayed in s^{-1} along both the x and y axes of the plot. The degree of correlation between the oscillations in the time series is represented by the color of the heatmap cell for each pair of values (x, y) . According to the color bar scale that can be seen to the right of each plot, the hues of the heatmap are related to the correlation coefficients. It is important to note that the topology of heatmaps varies across different time series segments.

Table 2. Summary of detected periods in control case corresponding to the same date as earthquake occurrence but one year earlier. Periods are measured from integrated versions of 2D Hybrid maps (bottom marginal panels) in Figure 3. Columns: series part with respect to nominal earthquake beginning time, detected periods, lower and upper errors.

Series ID	Period [s]	−err [s]	+err [s]	Significance [%]
−2 h	140.4	2.7	2.7	99
	47	0.07	0.07	99
−1 h	92.6	3.6	1.1	99
	60.5	1.5	0.5	99
0 h	83.3	2.9	0.9	99
	74.2	2.3	0.7	99
	56.4	1.3	0.4	99
	39.9	0.8	0.03	99
+1 h	101.3	5.2	0.3	99
	41.4	0.7	0.2	99
+2 h	111.9	6.5	0.1	99
	79	2.6	0.3	99
	57.7	1.5	0.2	99
	40.8	0.7	0.2	99
	33.8	0.5	0.2	99

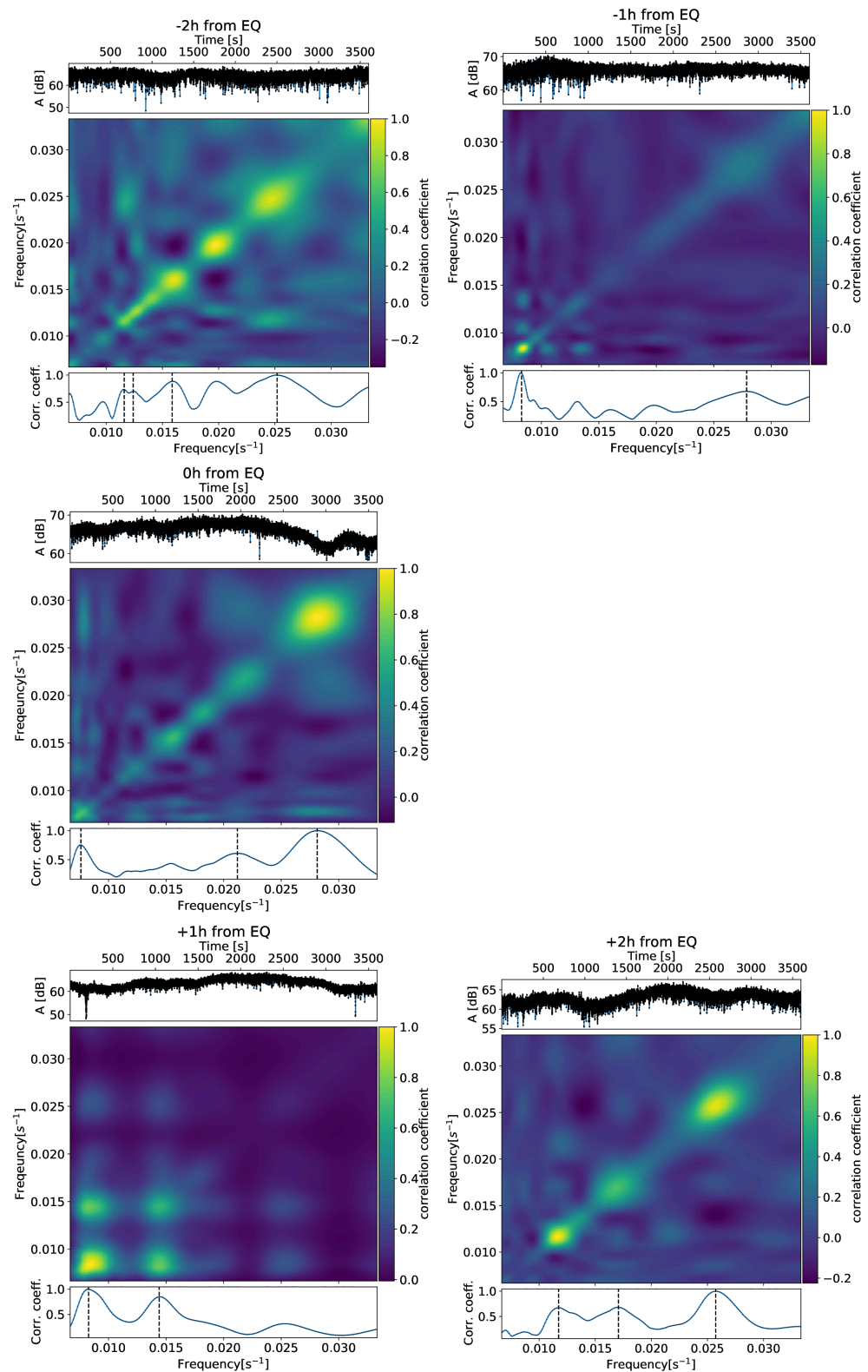


Figure 2. 2D Hybrid maps of oscillations in VLF signal amplitude data. Each plot shows a portion of the time series relative to the beginning of the earthquake (top marginal panel), a 2D Hybrid map (middle panel), and a projected 2D Hybrid map (bottom marginal plot), the color bar represents correlation coefficients on map. Top row: time series 2 h before earthquake (left) and 1 h before earthquake (right); middle row: 0 h from earthquake; bottom row: 1 h after earthquake (left) and 2 h after earthquake (right).

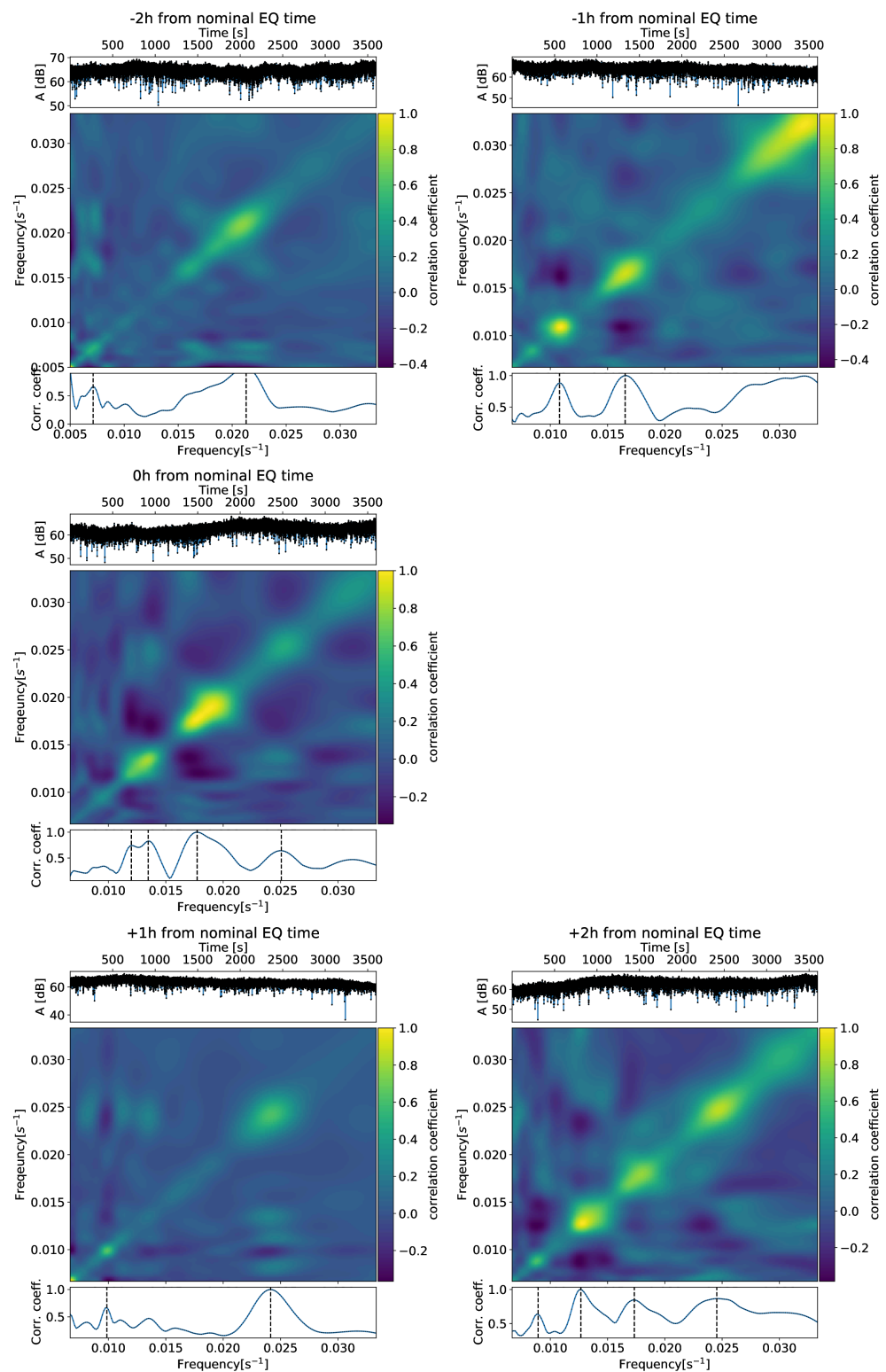


Figure 3. The same as Figure 2 but for date 1 year earlier.

At 2 h before the earthquake (shown in Figure 2 top row, left plot) we observe several signals of ≥ 80 s with correlation coefficients larger than 0.5 (shown in the bottom marginal plot of heatmap integrated projection), but there is only one peak above 100 s (located at 147 s, see also Table 1). All of the other oscillations have been muted by the passage of time, so that only the oscillation of 120 s that occurred 1 h before the earthquake is clearly visible in the top right panel of Figure 2.

During the earthquake, at 0 h from the event (middle plot), our approach records an oscillation at 131 s, with an amplitude that is approximately 20 percent lower than the peak that was recorded at 120 s during the hour-long interval preceding the earthquake (top right plot). In addition, there is one more signal at 35 s (middle plot).

After an hour has passed since the occurrence (bottom left plot), the oscillation at 121 s and 70 s once again appears. Finally, two hours after the earthquake (bottom right plot), the signals lasting longer than one hundred seconds vanished, and the graph once again began to show oscillations in the 80–90 s range, just as it had done in the period lasting two hours before the earthquake (top left plot).

One hour after the event, once again appears oscillation at 121 s, and 70 s. Finally, two hours after the earthquake the signals above 100 s disappeared, and once again comes to display oscillations around ~ 80 –90 s as in the period of two hours before the earthquake. Interestingly, only time series segments corresponding to -2 h (the top left panel) and $+2$ h (the bottom right panel) have a topology that is comparable to one another.

As it can be seen in Table 1, there are some ionospheric periodical oscillations of the order of one to two minutes. It is a question of this oscillation and its physical origin. One of the possibilities is that the electron density in the ionosphere is following periodical changes in the electromagnetic field which are registered close to the epicenters of earthquakes (see e.g., [38–41]), or that be generated by acoustic waves (see e.g., simulations in [38]). However, the true nature and physical background of the short-period oscillations given in Table 1 should be investigated in more detail, which is out of the scope of this paper.

In the scenario when there is no earthquake (the same date but one year earlier), the topology of the 2D hybrid maps Figure 3 looks very different from the topology of the maps corresponding to the record for earthquake date (Figure 2). The primary diagonal is where the majority of the correlation clusters are arranged. The VLF signal amplitude variation can be seen as switching between a dominated correlation cluster at -2 h (top row-left), $+1$ h (bottom row, left), and a more granular structure (at $+2$ h (bottom row-right), and -1 h (top row-right)). This variation in topology cannot be seen during earthquake occurrence (see Figure 2). On top of this, we observe a dominating core cluster present at 0 h (middle panel). On the other hand, the values of detected periods are less than 111 s (at $+2$ h, $+1$ h, 0 h, and -1 h, see Table 2). It is interesting to note that a period of 140 s is captured in the -2 h time series segment, which is comparable to a period of 147 s that was captured in the -2 h segment when the earthquake occurred (Table 1).

A comparison of the obtained results with those given in [11] (based on the application of the Fast Fourier transform (FFT) to the data in the relevant time intervals of 1 h) shows that the agreement is better before the earthquake. For the first observed interval starting 2 h before the earthquake, the agreement is good for the obtained values below 1.5 min, while, in both studies, these values decrease to similar values for the interval of the next hour. After an earthquake, the FFT method gives lower values of the period of excited waves than the method presented in this paper. Wave excitations with wave periods of about 2 min obtained in the first 4 observed intervals are also visible in the study presented in [11] for intervals starting about 2 h before the earthquake and in the first hour after it. The post-earthquake wave periods obtained in this study are also in agreement with those shown in [42] which indicate values from less than 10 s to a few hundred seconds.

As previously, mentioned notable characteristics of our two-dimensional hybrid method include the simplification of complex spectra of detected oscillations that are composed of many overlapping peaks in Fourier periodograms, the enhancement of apparent spectral resolution through the spreading of peaks over the second dimension, and the establishment of the direction of changes in signal through correlation coefficients. The normal VLF signal amplitude seen in the control case one year before the earthquake shows a more coherent topology of maps and oscillations below 111 s, whereas, during the event of an earthquake, perturbations occur so that maps have more features off-diagonal. This is in stark contrast to the observable oscillations of 120 and 130 s during the earthquake. Moreover, as oscillations of 140–147 s are documented in the earthquake and quiet

daytime series data occurring 2 h before the nominal earthquake occurrence, we predict this oscillation as usual behavior.

Finally, we will take a moment to reflect on the ways in which our study could be expanded. For the purpose of this investigation, we made use of the WWZ wavelet, which is defined in terms of trigonometric functions. However, to test for the presence of non-sinusoidal oscillations, it is essential to use wavelets on a base that does not involve trigonometry. In light of this, we believe that Superlets will prove to be the most suitable option for the continuation of our research. Superlet is a spectral estimator enabling time-frequency super-resolution which uses sets of wavelets with increasingly constrained bandwidth. These are combined geometrically to maintain the good temporal resolution of single wavelets and gain frequency resolution in upper bands. The normalization of wavelets in the set facilitates the exploration of data with scale-free, fractal nature, containing oscillation packets that are self-similar across frequencies. Importantly, they can reveal fast transient oscillation events in single trials that may be hidden in the averaged time-frequency spectrum by other methods.

5. Conclusions

In this work, we explored the use of our 2D Hybrid technique for detecting oscillations in VLF signal amplitude time series in the time vicinity of the Kraljevo earthquake in Serbia in 2010. Furthermore, we demonstrated how the approach captures the difference between time series in the time vicinity of an earthquake and a control day one year earlier, which can be utilized to establish topology differences between certain ionosphere occurrences.

The cross-correlation of scalograms of time series, which can be further integrated, is a crucial principle in our approach. This has two significant advantages. First, the method simplifies complex spectra with numerous overlapped peaks in periodograms, i.e., increasing apparent spectral resolution by spreading peaks over the second dimension. For example, we were able to detect various oscillation patterns at various time series segments.

The second advantage is the usage of correlation coefficients to determine the direction of signal changes. This enabled us to distinguish between the cohesive topology of 2D maps during a calm day and more dispersed correlation clusters during the Kraljevo earthquake. We discovered that oscillations in the 120–130 s range appear 1 h before the earthquake, continue to exist during the earthquake, and disappear 1 h after the earthquake. Fluctuations of the order 140–147 s occur 2 h before the nominal start of the earthquake during the calm day and can be interpreted as normal oscillations in the VLF signal amplitude. Finally, we briefly described how we could extend our research by using Superlets, which can reveal fast transient oscillation events that other types of wavelets may mask in averaged time-frequency scalograms.

Author Contributions: L.Č.P. conceptualized study; A.B.K. designed methodology, performed calculations, plotted figures, and wrote the whole manuscript; A.N. collected data and prepared parts related to VLF data and ionospheric observations; A.B.K., A.N., L.Č.P. and M.R. revised the manuscript. All authors have read and agreed to the published version of the manuscript.

Funding: A.B.K. and L.Č.P. acknowledge funding provided by the University of Belgrade-Faculty of Mathematics (the contract 451-03-68/2022-14/200104), through the grants by the Ministry of Education, Science, and Technological Development of the Republic of Serbia. A.B.K. and L.Č.P. thank the Chinese Academy of Sciences President's International Fellowship Initiative (PIFI) for visiting scientist support. A.N. acknowledges the funding provided by the Institute of Physics Belgrade through the grant by the Ministry of Education, Science, and Technological Development of the Republic of Serbia. L.Č.P. acknowledges the funding provided by the Astronomical Observatory (the contract 451-03-68/2022-14/ 200002), through the grants by the Ministry of Education, Science, and Technological Development of the Republic of Serbia. M.R. acknowledges the funding provided by the Geographical Institute "Jovan Cvijić" SASA through the grant by the Ministry of Education, Science, and Technological Development of the Republic of Serbia.

Data Availability Statement: Requests for the VLF data used for analysis can be directed to A.N.

Acknowledgments: The authors would like to express their gratitude to Reviewer 1 and Reviewer 2 for providing insightful comments that helped to strengthen the presentation of our work.

Conflicts of Interest: The authors declare no conflict of interest. The funders had no role in the design of the study; in the collection, analyses, or interpretation of data; in the writing of the manuscript; or in the decision to publish the results.

Appendix A. Pseudocode of 2D Hybrid Method

In case readers would like to implement the 2D Hybrid method, we have provided the implementation-agnostic pseudocode of our algorithm in Algorithm A1.

Algorithm A1 Pseudocode of 2D Hybrid method

```

Initialization:
import wavelet module
import Gaussian process module
import time series 1 – $y_1$ 
import time series 2 – $y_2$ 
Initialize parameters for Gaussian process modeling if needed, otherwise set parameters
as 0
Compute Gaussian process model of  $y_1$  and  $y_2$  if parameters for modelling are nonzero
procedure 2D HYBRID MAP( $y_{input1}, y_{input2}$ )
  compute scalogram  $\mathcal{S}_\infty$  of  $y_{input1}$ 
  compute scalogram  $\mathcal{S}_\epsilon$  of  $y_{input2}$ 
  compute 2D correlation map as  $M = \text{Cov}(\mathcal{S}_\infty, \mathcal{S}_\epsilon)$ 
  Integrate 2D map along axis 1  $I_1 = \sum_i M_{ij}$ 
  Integrate 2D map along axis 2  $I_2 = \sum_j M_{ij}$ 
  return ( $\mathcal{S}_\infty, \mathcal{S}_\epsilon, I_1, I_2$ )
end procedure
Calculate error of periods: determine FWHM of peaks in  $I_1$  and  $I_2$  with correlation larger
than 0.5, and determine 25th and 75th quantiles, so that array of lower errors are 25th
quantiles, and an array of upper errors are 75th quantiles
Calculate significance of period: set number of shuffling  $N = 100$ 
 $y_{new} = \text{zeros}(2,:)$ 
for  $j \in (1, 2)$  do
  for  $i \in (N)$  do
     $y_{new}[j,:,:] = \text{random.shuffle}(y_j)$ 
  end for
   $\mathcal{S}[1,:,:], \mathcal{S}[2,:,:], I[1,:,:], I[2,:,:] = \text{procedure 2D Hybrid map}(y_{new}[1,:,:], y_{new}[2,:,:])$ 
end for
 $\text{counter1} = 0, \text{counter2} = 0$ 
for  $P1, P11$  in  $\text{zip}(\text{Peak}(I_1), \text{Peak}(I[1,:,:]))$  do
  if  $P1 > P11$  then
     $\text{counter1} = \text{counter1} + 1$ 
  end if
end for
for  $P2, P22$  in  $\text{zip}(\text{Peak}(I_2), \text{Peak}(I[2,:,:]))$  do
  if  $P2 > P22$  then
     $\text{counter2} = \text{counter2} + 1$ 
  end if
end for
 $\text{significance1} = \text{counter1}/N, \text{significance2} = \text{counter2}/N$ 
print  $P1, P2, \text{lower error}, \text{upper error}, \text{significance1}, \text{significance2}$ 

```

References

1. Biagi, P.; Castellana, L.; Maggipinto, T.; Piccolo, R.; Minafra, A.; Ermini, A.; Martellucci, S.; Bellecci, C.; Perna, G.; Capozzi, V.; et al. LF radio anomalies revealed in Italy by the wavelet analysis: Possible preseismic effects during 1997–1998. *Phys. Chem. Earth Parts A/B/C* **2006**, *31*, 403–408. [[CrossRef](#)]
2. Biagi, P.F.; Piccolo, R.; Ermini, A.; Martellucci, S.; Bellecci, C.; Hayakawa, M.; Kingsley, S.P. Disturbances in LF radio-signals as seismic precursors. *Ann. Geophys.* **2001**, *44*, 1011–1019. [[CrossRef](#)]
3. Biagi, P.F.; Piccolo, R.; Ermini, A.; Martellucci, S.; Bellecci, C.; Hayakawa, M.; Capozzi, V.; Kingsley, S.P. Possible earthquake precursors revealed by LF radio signals. *Nat. Hazards Earth Syst. Sci.* **2001**, *1*, 99–104. [[CrossRef](#)]
4. Rozhnoi, A.; Solovieva, M.; Molchanov, O.; Hayakawa, M. Middle latitude LF (40 kHz) phase variations associated with earthquakes for quiet and disturbed geomagnetic conditions. *Phys. Chem. Earth Parts A/B/C* **2004**, *29*, 589–598. [[CrossRef](#)]
5. Zhao, S.; Shen, X.; Liao, L.; Zhima, Z.; Zhou, C.; Wang, Z.; Cui, J.; Lu, H. Investigation of Precursors in VLF Subionospheric Signals Related to Strong Earthquakes ($M > 7$) in Western China and Possible Explanations. *Remote Sens.* **2020**, *12*, 3563. [[CrossRef](#)]
6. Hayakawa, M. The precursory signature effect of the Kobe earthquake on VLF subionospheric signals. *J. Comm. Res. Lab.* **1996**, *43*, 169–180.
7. Maurya, A.K.; Venkatesham, K.; Tiwari, P.; Vijaykumar, K.; Singh, R.; Singh, A.K.; Ramesh, D.S. The 25 April 2015 Nepal Earthquake: Investigation of precursor in VLF subionospheric signal. *J. Geophys. Res. Space Phys.* **2016**, *121*, 10403–10416. [[CrossRef](#)]
8. Molchanov, O.; Hayakawa, M.; Oudoh, T.; Kawai, E. Precursory effects in the subionospheric VLF signals for the Kobe earthquake. *Phys. Earth Planet. Inter.* **1998**, *105*, 239–248. [[CrossRef](#)]
9. Yamauchi, T.; Maekawa, S.; Horie, T.; Hayakawa, M.; Soloviev, O. Subionospheric VLF/LF monitoring of ionospheric perturbations for the 2004 Mid-Niigata earthquake and their structure and dynamics. *J. Atmos. Sol.-Terr. Phys.* **2007**, *69*, 793–802. [[CrossRef](#)]
10. Yoshida, M.; Yamauchi, T.; Horie, T.; Hayakawa, M. On the generation mechanism of terminator times in subionospheric VLF/LF propagation and its possible application to seismogenic effects. *Nat. Hazards Earth Syst. Sci.* **2008**, *8*, 129–134. [[CrossRef](#)]
11. Nina, A.; Pulnits, S.; Biagi, P.; Nico, G.; Mitrović, S.; Radovanović, M.; Č. Popović, L. Variation in natural short-period ionospheric noise, and acoustic and gravity waves revealed by the amplitude analysis of a VLF radio signal on the occasion of the Kraljevo earthquake ($M_w = 5.4$). *Sci. Total. Environ.* **2020**, *710*, 136406. [[CrossRef](#)] [[PubMed](#)]
12. Nina, A.; Biagi, P.F.; Mitrović, S.T.; Pulnits, S.; Nico, G.; Radovanović, M.; Popović, L.Č. Reduction of the VLF Signal Phase Noise Before Earthquakes. *Atmosphere* **2021**, *12*, 444. [[CrossRef](#)]
13. Nina, A.; Biagi, P.F.; Pulnits, S.; Nico, G.; Mitrović, S.T.; Radovanović, M.; Urošev, M.; Popović, L.Č. Variation in the VLF signal noise amplitude during the period of intense seismic activity in Central Italy from 25 October to 3 November 2016. *Front. Environ. Sci.* **2022**, *10*, 1005575. [[CrossRef](#)]
14. Gabor, D. Theory of communication. *J. Inst. Electr. Eng.* **1946**, *93*, 429–457. [[CrossRef](#)]
15. Heisenberg, W. Über den anschaulichen Inhalt der quantentheoretischen Kinematik und Mechanik. *Z. Phys.* **1927**, *43*, 172–198. [[CrossRef](#)]
16. Weyl, H. *The Theory of Groups and Quantum Mechanics Paperback*, 2014 Reprint of 1931 ed.; Dover Publications Inc.: New York, NY, USA, 2014.
17. Moca, V.V.; Bârzan, H.; Nagy-Dabacan, A.; Mureșan, R.C. Time-frequency super-resolution with superlets. *Nat. Commun.* **2021**, *12*, 337. [[CrossRef](#)]
18. Di Matteo, S.; Viall, N.M.; Kepko, L. Power spectral density background estimate and signal detection via the multitaper method. *J. Geophys. Res. Space Phys.* **2021**, *126*, e2020JA028748. [[CrossRef](#)]
19. Daubechies, I. *Ten Lectures on Wavelets*; Society for Industrial and Applied Mathematics: Philadelphia, PA, USA, 1992.
20. Mallat, S.A. *Wavelet Tour of Signal Processing: The Sparse Way*; Academic Press, Elsevier: Cambridge, MA, USA, 2008.
21. Torrence, C.; Compo, G.P.A. Practical guide to wavelet analysis. *Bull. Am. Meteorol. Soc.* **1998**, *79*, 61–78. [[CrossRef](#)]
22. Subasi, A. *Practical Machine Learning for Data Analysis Using Python*; Academic Press, Elsevier: Cambridge, MA, USA, 2020.
23. Kovačević, A.B.; Pérez-Hernández, E.; Popović, L. Č.; Shapovalova, A. I.; Kollatschny, W.; Ilić, D. Oscillatory patterns in the light curves of five long-term monitored type 1 active galactic nuclei *Mon. Not. R. Astron. Soc.* **2018**, *471*, 2051–2066. [[CrossRef](#)]
24. Kovačević, A. B.; Popović, L. Č.; Ilić, D. Two-dimensional correlation analysis of periodicity in active galactic nuclei time series, *Open Astron.* **2020**, *29*, 51–55. [[CrossRef](#)]
25. Kovačević, A. B.; Popović, L. Č.; Simić, S.; Ilić, D. The Optical Variability of Supermassive Black Hole Binary Candidate PG 1302–102: Periodicity and Perturbation in the Light Curve. *Astrophys. J.* **2019**, *871*, 32. [[CrossRef](#)]
26. Zhao, S.; Zhou, C.; Shen, X.; Zhima, Z. Investigation of VLF Transmitter Signals in the Ionosphere by ZH-1 Observations and Full-Wave Simulation. *J. Geophys. Res. Space Phys.* **2019**, *124*, 4697–4709. [[CrossRef](#)]
27. Knezević Antonijević, S.; Arroucau, P.; Vlahović, G. Seismotectonic Model of the Kraljevo 3 November 2010 M_w 5.4 Earthquake Sequence. *Seismol. Res. Lett.* **2013**, *84*, 600–610. [[CrossRef](#)]
28. Vidaković, B. *Statistical Modeling by Wavelets*; John Wiley & Sons, Inc.: New York, NY, USA, 1999; pp. 43–117.
29. Byeon, Y.H.; Pan, S.B.; Kwak, K.C. Intelligent Deep Models Based on Scalograms of Electrocardiogram Signals for Biometrics. *Sensors* **2019**, *19*, 935. [[CrossRef](#)]

30. Bolós, V.J.; Benítez, R. The Wavelet Scalogram in the Study of Time Series. In *Advances in Differential Equations and Applications*; Casas, F., Martínez, V., Eds.; SEMA SIMAI Springer Series; Springer: Cham, Switzerland, 2014; pp. 147–154.
31. Noda, I. Techniques of two-dimensional (2D) correlation spectroscopy useful in life science research. *Biomed. Spectrosc. Imaging* **2015**, *4*, 109–127. [[CrossRef](#)]
32. Schulze, G.; Jirasek, A.; Blades, M.W.; Turner, R.F.B. Identification and Interpretation of Generalized Two-Dimensional Correlation Spectroscopy Features Through Decomposition of the Perturbation Domain. *Appl. Spectrosc.* **2004**, *57*, 1561–1574. [[CrossRef](#)]
33. Schwarzenberg-Czerny, A. Accuracy of period determination. *MNRAS* **1991**, *253*, 198–206. [[CrossRef](#)]
34. Johnson, M.A.C.; Gandhi, P.; Chapman, A.P.; Moreau, L.; Charles, P.A.; Clarkson, W. I.; Hill, A.B. Prospecting for periods with LSST—Low-mass X-ray binaries as a test case. *MNRAS* **2019**, *484*, 19–30. [[CrossRef](#)]
35. Foster, G. Wavelets for period analysis of unevenly sampled time series. *Astron. J.* **1996**, *112*, 1709–1729. [[CrossRef](#)]
36. Templeton, M.R.; Mattei, J.A.; Willson, L.A. Secular Evolution in Mira Variable Pulsations. *Astron. J.* **2005**, *130*, 776–788. [[CrossRef](#)]
37. Young, N.J.; Stappers, B.W.; Lyne, A.G.; Weltevrede, P.; Kramer, M.; Cognard, I. Long-term radio observations of the intermittent pulsar B1931+24. *MNRAS* **2013**, *429*, 2569–2580. [[CrossRef](#)]
38. Shinagawa, H.; Iyemori, T.; Saito, S.; Maruyama, T. A numerical simulation of ionospheric and atmospheric variations associated with the Sumatra earthquake on December 26, 2004. *Earth Planets Space* **2007**, *59*, 1015–1026. [[CrossRef](#)]
39. Otsuka, Y.; Kotake, N.; Tsugawa, T.; Shiokawa, K.; Ogawa, T.; Effendy; Saito, S.; Kawamura, M.; Maruyama, T.; Hemmakorn, N.; et al. GPS detection of total electron content variations over Indonesia and Thailand following the 26 December 2004 earthquake. *Earth Planets Space* **2006**, *58*, 159–165. [[CrossRef](#)]
40. Kherani, E.A.; Lognonné, P.; Kamath, N.; Crespon, F.; Garcia, R. Response of the ionosphere to the seismic triggered acoustic waves: Electron density and electromagnetic fluctuations. *Geophys. J. Int.* **2009**, *176*, 1–13. [[CrossRef](#)]
41. Heki, K., Ionospheric Disturbances Related to Earthquakes. In *Ionosphere Dynamics and Applications*; American Geophysical Union (AGU): Washington, DC, USA, 2021; Chapter 21, pp. 511–526. [[CrossRef](#)]
42. Ohya, H.; Tsuchiya, F.; Takishita, Y.; Shinagawa, H.; Nozaki, K.; Shiokawa, K. Periodic Oscillations in the D Region Ionosphere After the 2011 Tohoku Earthquake Using LF Standard Radio Waves. *J. Geophys. Res. Space Phys.* **2018**, *123*, 5261–5270. [[CrossRef](#)]



Variation in natural short-period ionospheric noise, and acoustic and gravity waves revealed by the amplitude analysis of a VLF radio signal on the occasion of the Kraljevo earthquake (Mw = 5.4)

Aleksandra Nina^{a,*}, Sergey Pulinetz^b, Pier Francesco Biagi^c, Giovanni Nico^{d,e}, Srđan T. Mitrović^f, Milan Radovanović^{g,h}, Luka Č. Popović^{i,j}

^aInstitute of Physics Belgrade, University of Belgrade, Belgrade, Serbia

^bSpace Research Institute, Russian Academy of Sciences, Moscow, Russia

^cUniversità di Bari, Physics Department, Bari, Italy

^dIstituto per le Applicazioni del Calcolo (IAC), Consiglio Nazionale delle Ricerche (CNR), Bari, Italy

^eDepartment of Cartography and Geoinformatics, Institute of Earth Sciences, Saint Petersburg State University (SPSU), 199034 Saint Petersburg, Russia

^fNovelic, Belgrade, Serbia

^gGeographical Institute Jovan Cvijić SASA, Belgrade 11000, Serbia

^hSouth Ural State University, Institute of Sports, Tourism and Service, 454080 Chelyabinsk, Russia

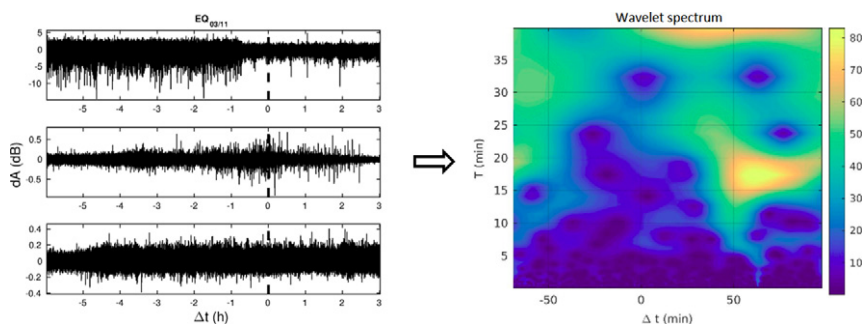
ⁱAstronomical Observatory, Belgrade, Serbia

^jFaculty of Science, University of Banja Luka, Banja Luka, R. Srpska, Bosnia and Herzegovina

HIGHLIGHTS

- Reduction in VLF signal amplitude noise is recorded before the earthquake.
- Count of short-term lower ionosphere disturbances increases prior the earthquake.
- Excitations/attenuations of acoustic and gravity waves are detected.

GRAPHICAL ABSTRACT



ARTICLE INFO

Article history:

Received 4 July 2019

Received in revised form 26 December 2019

Accepted 27 December 2019

Available online 30 December 2019

Guest Editor: Snezana Dragovic

Keywords:

Earthquake

Ionosphere

VLF signal

ABSTRACT

We analyse the lower ionosphere disturbances in the time period around the Mw 5.4 Kraljevo earthquake (EQ), which occurred on 3 November 2010 in Serbia. The results presented herein are based on analysis of the amplitudes of three VLF signals emitted in Italy, UK, and Germany and recorded in Serbia whose variations primarily result from changes in the electrical properties of the lower ionosphere at a distance more than 120 km from the epicentre of the EQ. The primary goals of this study are to reveal specific variations as possible EQ precursors as well as disturbances following the EQ event recorded by the observational equipment, and to investigate whether better time resolution data can affect the analysis of the lower ionosphere disturbances possibly connected to the EQ. We process two sets of data with sampling periods of 1 min and 0.1 s. As the first analysis indicates the absence of long-term disturbances, which can clearly be connected to the Kraljevo EQ, our attention is focused on the study of short-period noise amplitude and the excitation and attenuation of acoustic and gravity waves in the lower ionosphere. Processing of the amplitudes of three VLF signals during the nights of the four EQs with magnitude greater than 4 that occurred in Serbia,

* Corresponding author.

E-mail address: sandrast@ipb.ac.rs (A. Nina).

as well as EQs of all magnitudes during the three days of 3, 4, and 9 November, indicates that the detected ICV radio signal noise amplitude reduction starting before the Kraljevo EQ is also observed for 13 additional EQ events near the signal propagation path, and occurred during all three days (for all EQs with magnitude greater than 4 and several less intensive events). Excitation and attenuation of acoustic waves are also found for all these EQ events with a magnitude greater than 4.

© 2019 Elsevier B.V. All rights reserved.

1. Introduction

The complexity of processes on our planet is a consequence of both permanent and variable influences of outer space phenomena on the Earth system (Radovanović, 2018; Srećković et al., 2017; Šulić and Srećković, 2014; Šulić et al., 2016) and the coupling between different terrestrial layers (Dragović et al., 2014; Georgoulas et al., 2016; Kastelis and Kourtidis, 2016; Ke et al., 2018; Kumar et al., 2017; NaitAmor et al., 2018; Nina et al., 2017; Perrier et al., 2005; Petrović et al., 2018; Tanaka et al., 2010). Many investigations show connections in physical and chemical changes at locations separated by several thousands of kilometers. These connections can be induced by various mechanisms such as propagation of different types of radiation, electric or magnetic fields, and they are often a combination of several processes. For these reasons, research of possible connections of different disturbances is a very complex task, and, in many cases, it still requires proper theoretical explanations.

Phenomena, whose research is of crucial importance for practical applications, including the saving of human lives, are possible precursors of natural disasters. In this research, a very important role is played by the investigation of ionospheric disturbances that are connected with, for example, tropical cyclones (Ke et al., 2018; NaitAmor et al., 2018; Nina et al., 2017; Price et al. 2007), and earthquakes (Molchanov et al., 1998; Pulinets and Boyarchuk, 2004; Pulinets and Ouzounov, 2011).

Studies of ionospheric disturbances are based on observational data obtained by different methods tailored to different altitudes. For example, measurements by ionosondes are relevant for altitudes between approximately 110 km and the height of electron density maximum in the F-region; monitoring of very low frequency and low frequency (VLF/LF) radio signals is applicable for the lower ionosphere studies; and satellite signals (such as GPS - Global Positioning System) can provide integral information about propagation paths within the ionosphere.

When discussing ionospheric variability, we deal with different types of variability depending on the particular spatial (latitude, longitude, altitude) and temporal (daily, seasonal, solar cycle etc.) domains that are considered. There were several attempts to quantify the ionospheric variability (Bradley and Cander, 2002; Forbes et al., 2000; Rishbeth and Mendillo, 2001). Unfortunately, due to the predominance of publications focused on the GPS total electron content (TEC), the majority of attention is drawn to the positive and negative variations of TEC, which is an overall integrated view of the ionosphere. However, many details remain beyond the scope of consideration because of the lack of information about the vertical structure of the electron concentration profile. For example, during a geomagnetic storm, we deal with the plasmasphere inflation (positive TEC variation) while at the height maximum of the F2 (HmF2) layer, we may have negative variations (negative phases of the geomagnetic storm) (Balan et al., 2010). Under some special conditions, additional layers can be observed (Depuev and Pulinets, 2001). A redistribution of the vertical profile before EQs is observed in Hirooka et al. (2011). In this regard, the study of the variability of the D-region before the occurrence of earthquakes sensed by the VLF subionospheric propagation anomalies technique (but not sensed by GPS TEC) is of great importance.

To identify the pre-earthquake anomalies, it is important to use additional techniques and different types of precursor analyses such as terminator-time for the VLF propagation, and the acoustic and gravity wave (AGW) generation before and after earthquakes (Titova et al., 2019). Such types of analyses will be provided in this paper where attention will be focused on the comparison of anomalies in the lower ionosphere, which is recognized as the medium with possible precursor changes for large EQ events (Hayakawa, 2007), and the GPS TEC variations before and after an EQ.

There are many studies which indicate and model the time shift of the amplitude minimum during solar terminator periods (the so-called "terminator time") a few days before EQ events (Hayakawa, 1996; Molchanov et al., 1998; Yamauchi et al., 2007), signal amplitude variations (Biagi et al., 2001a,b; Rozhnoi et al., 2010), and periodic fluctuations (Biagi et al., 2006; Hayakawa et al., 2010; Miyaki et al., 2001; Molchanov et al., 2001; Ohya et al., 2018; Rozhnoi et al., 2004). The possible importance of the lower ionosphere monitoring in the EQ predictions was the motivation for the integration of several receivers in European (Biagi et al., 2011) and Pacific (Hayakawa et al., 2010) networks to search for earthquake precursors and to develop procedures for extracting anomalies in the VLF/LF signals as the precursors of an EQ (Popova et al., 2018).

Research studies of the lower ionosphere disturbances to establish their connection to EQ events are primarily based on the comparison of variations detected on different days, and they are based on VLF/LF data with sampling rates greater than 1 s (usually 1 min). However, research presented by Ohya et al. (2018) shows the excitation of waves with periods shorter than 30 s after the Mw9.0 Tokyo EQ. Although this EQ was very strong, these waves were recorded more than 400 km to 500 km away from the EQ epicentre; this opens the question: can such variations be detected earlier, i.e. should short-term variations of the lower ionosphere be considered as possible EQ precursors?

In this study, we analyse variations in the electrical properties of the atmosphere between altitudes of 60 km and 90 km (i.e. the lower ionospheric disturbances) before and after the earthquake EQ_{03/11} of magnitude 5.4, that occurred near Kraljevo, Serbia, on 3 November, 2010 (the seismotectonic model of this event is presented in Knezevic Antonijevic et al. (2013)) using data collected by the VLF radio signals emitted by transmitters located in Italy (ICV), the UK (GQD), and Germany (DHO), and received in Serbia by the Absolute Phase and Amplitude Logger (AbsPAL) receiver located at the Institute of Physics Belgrade. We use datasets of the recorded signal amplitudes with different time samplings to analyse the signal variations with the aim of exploring both long- and short-period perturbations of the lower ionosphere before and after the Kraljevo earthquake, and to determine whether better time sampling resolutions can provide more information about the relationship between the earthquake and disturbances in the considered atmospheric layer. To study the localisation of the lower ionospheric disturbances, the influence of periodic daily variations, and the EQ magnitude on the detected types of variations in the case of the Kraljevo EQ, we additionally study the signal amplitudes in periods around several other EQ events. These analyses are done to examine our research hypothesis that better time resolution of the collected VLF/LF amplitudes can provide new types of precursors and aftershocks of EQs.

The paper is organized as follows: In Sections 2 and 3, we describe the observations (study area and data) and the methodology of the study. Results are presented in Section 4. The conclusions of this study, including the description of analyses that need to follow the presented research, are given in Section 5.

2. Study area and data

2.1. Analysed EQ events

According to the database given in <http://www.emsc-csem.org/Earthquake/>, four earthquakes of magnitude greater than 4 occurred in Serbia between 7 October and 4 November 2010. As one can see in Table 1, these events were during night-time periods and, according to their locations (shown in Fig. 1), they can be divided into two groups: G1 (EQ_{03/11} and EQ_{04/11}) and G2 (EQ_{07/10} and EQ_{11/10}). These characteristics allow us to compare the lower ionosphere variations related to these events and to study the localisation of analysed disturbances.

In this work, we focus attention on the most intensive of these EQ events, which occurred on 3 November at 00:56.54 UT near Kraljevo, Serbia (EQ_{03/11}), while analyses of the other EQs are done in order to research the influence of EQ location on detection of specific variations registered in the case of EQ_{03/11}.

In addition, we analyse variations recorded during three days (3, 4, and 9 November 2010) when 46 EQs (excluding the 29 that occurred in the hours after EQ_{11/03} when extraction of their influence is not possible) were detected with epicentres not far from the ICV signal propagation path (see Section 2.2 and Fig. 1).

2.2. Monitoring of the lower ionosphere

One of the most important techniques for the lower ionosphere observation is based on the propagation of the VLF signals. Specifically, variations in the recorded amplitude and phase primarily reflect changes in the electric properties of the lower ionosphere. In this paper, the research of lower ionosphere disturbances is based on analysis of the amplitudes of three VLF signals detected by the AbsPAL receiver in Belgrade, Serbia (44.8 N, 20.4 E) which are emitted by transmitters ICV (Isola di Tavorara, Italy, 40.92 N, 9.73 E), GQD (Anthorn, the UK, 54.91 N, 3.28 W), and DHO (Rhauderföhn, Germany, 53.08 N, 7.61E). As one can see in Fig. 1, the VLF signal whose propagation path lies the closest to the EQ_{03/11} location (43.74 N, 20.69 E) is the 20.27 kHz signal emitted from Italy (see Fig. 1 and Table 1 where the shortest distances of all four EQ epicentres from the ICV signal path are given). For this reason, we focus our attention on research of its properties while the other two signals at 22.1 kHz and 23.4 kHz emitted from the UK and Germany, respectively, are analysed to research the influence of the distance between the EQ epicentre and signal path on recorded amplitude variations.

Time resolutions of data recorded by the Belgrade AbsPAL receiver are 1 min and 0.1 s. The former resolution is more appropriate for analysis of long-term periods lasting from several days to a few months, which, as mentioned in the Introduction, were the subject of previous investigations of the lower ionosphere disturbances possibly connected with EQ events. In this study, we use datasets with 1-min resolution to check the existence of amplitude profiles, which have already been noticed as possible EQ precursors. Here, we point out that the Kraljevo EQ is not a strong EQ like those usually analysed in earlier studies. Furthermore, the shortest distance between its epicentre and the ICV signal path is not very small (more than 120 km). The second time resolution is better for study of the short-term time variations during periods of several hours, which are still insufficiently investigated and which are the focus of this research.

3. Methodology

Because of the numerous influences on the considered area and the differences in the quality of information which can be provided by the 1-min and 0.1-s time resolution data collected by monitoring the VLF signals, analyses of new types of disturbances require study of these effects before proceeding with signal variation analyses. For this reason, the methodology of this study can be summarized as follows:

- Checking for the presence of non-ionospheric disturbances which can perturb the VLF signal;
- Preliminary analysis of different time sampling resolutions;
- Processing of selected datasets to investigate the disturbances in the time and frequency domains.

As will be shown in the text that follows, the study of the second item showed that the 0.1-s resolution dataset is more appropriate for analyses of recorded disturbances, and the third, the key part of study, is based on processing and analyses of this type of dataset. We present analyses in both the time and frequency domains. In the first case, we focus research on variations in the short-period noise amplitude, while in the second case, we provide a study of acoustic and gravity waves.

3.1. Non-ionospheric influences on signals

Before we give a detailed analysis of short-term variations of the VLF signal amplitudes, we want to emphasize that they represent short-term variations related to rapid variations of the medium in which these signals are propagating. As these signals propagate like channelled waves in a waveguide bounded by the troposphere-ground and lower ionosphere, the variations happen mainly in that region. In addition to the atmospheric influence, the noise intensity in the radio signals could be produced continuously or occasionally by sources such as electric or electronic devices operating nearby the receiver, electric cables without good shielding, amateur radios operating in the zone, an improperly grounded receiver, or natural electromagnetic emissions from nearby faults or micro-fractured zones, among others. To examine the possible influence of these sources on our research, we first consider the non-ionospheric sources that can cause signal instability and that are not connected with EQs: the transmitter, receiver, meteorological conditions, and geomagnetic conditions (Biagi et al., 2011).

- **Transmitter influence.** In the case that noise changes are due to variations in the signal emission, they should also be detected by other receivers. To check this, we analyse data with the same sampling of 0.1 s recorded by another receiver (Kilpisjärvi ULTRA Data, http://psddb.nerc-bas.ac.uk/data/access/download.php?menu=1,_7&bc=1,_4,_7,_8,_9&source=1&class=37,_110,_232&type=ULTRA&site=Kilpisjarvi&year=2010&day=307&month=11&graph=main) for which we can exclude the Kraljevo EQ influence due to the large distance between the EQ epicentre and the signal propagation path. Visualization of this amplitude time evolution confirms the absence of noise variations; this allows us to exclude the transmitter influence from our conclusions.
- **Receiver influence.** In the case that some other sources of electromagnetic waves affect the reception of the VLF signal or if some technical problem occurs in the receiver, it is reasonable to expect variations in other recorded signals at the same time interval due to their similar frequencies. This is not the case in our analysis, and, for this reason, we can assume that our receiver is not the source of the VLF signal changes.

Table 1
List of the earthquakes of magnitudes greater than 4 occurring near the Kraljevo EQ event location in the period of 1 October to 30 November, 2010. Data are given in <http://www.emsc-csem.org/Earthquake/>.

Date	Time (UTC)	Latitude (°)	Longitude (°)	d_{EQ-ICV} (km)	Magnitude
2010-10-07	20:23:10.9	42.4	21.62	290.1	4.3
2010-10-11	00:34:35.6	42.42	21.59	287.2	4.5
2010-11-03	00:56:54.4	43.74	20.69	126.0	5.4
2010-11-04	21:09:05.5	43.78	20.62	120.7	4.4

- **Influence of meteorological conditions.** Due to the absence of storm events over Europe (except for a heavy rain in Sardinia on 10–11 October when the ICV signal amplitude is not perturbed) during periods relevant for the principal conclusions of this study (according European Severe Weather Database (<https://www.eswd.eu/cgi-bin/eswd.cgi>)), we can conclude that meteorological conditions did not significantly affect changes in signal propagation and, consequently, we can neglect them in our analysis.
- **Influence of geomagnetic conditions.** Keeping in mind that variations in Earth's magnetic field are not recorded near the signal propagation path in the period around the Kraljevo EQ (the plot is available in Monthly magnetic bulletin of the Castello Tesino Observatory <http://roma2.rm.ingv.it/download/userfiles/public/datimagnetici/Bulletins/CTS/2010/November.pdf>), we exclude the possibility of a substantial geomagnetic influence on the recorded signal variations.

According to this analysis of possible influences of non-ionospheric sources on signal properties, and the fact that VLF signal variations due to natural properties of the propagation medium are primarily coming from the ionosphere, we assume that the analysed signal variations are probably a consequence of changes in the ionosphere.

3.2. Preliminary analysis of datasets with different time sampling

As indicated in Section 2.2, the AbsPAL receiver records data with two time sampling resolutions of 1 min and 0.1 s. The former dataset is more appropriate for long term analyses that have been the subject of most of the previous studies, while the latter dataset can provide more information related to the short-term disturbances. Here, we first give a short preliminary analysis of these data for the ICV signal in the period around the EQ_{03/11} event.

3.2.1. Time resolution of 1 min

Visualizations of the amplitude time evolution and the solar terminator shift (used in previous studies for detection of the ionospheric disturbances) in the period of two months around the EQ_{03/11} event show that the connection between the recorded variations and the EQ_{03/11} event are not clear. Namely, the recorded changes cannot relate to the EQ event because a very similar amplitude profile has also been recorded during the same period of the previous year.

The reduction of the short-period atmospheric noise after approximately 0.5 h before the EQ induces a smoother amplitude time evolution recorded with 1-min time sampling, as well as a wave-like profile in the ICV signal amplitude evolution after the EQ occurrence (see the white line in the upper panel of Fig. 2). In comparison with the bottom panel, which presents the amplitude evolution during the

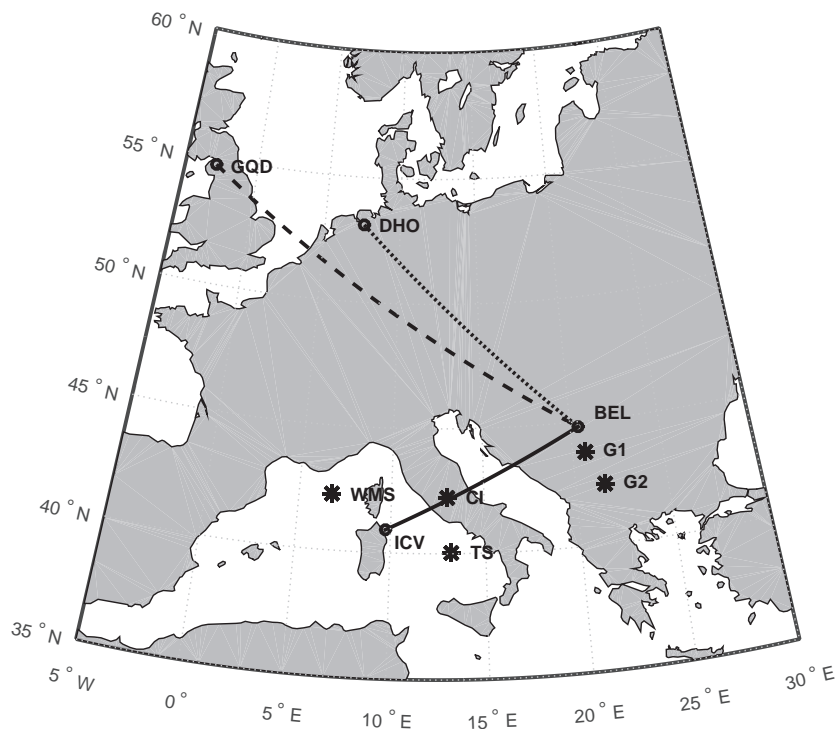


Fig. 1. Propagation paths of the VLF signals recorded by the Belgrade receiver station (BEL) in Serbia and emitted by the transmitters ICV in Italy (solid line), GQD in the UK (dashed line), and DHO in Germany (dotted line). Locations of the earthquakes are classified into groups G1 (EQ_{03/11} and EQ_{04/11}) and G2 (EQ_{07/10} and EQ_{11/10}). Locations of additional EQs considered in analysis of the short-period noise amplitude during whole days are shown as stars.

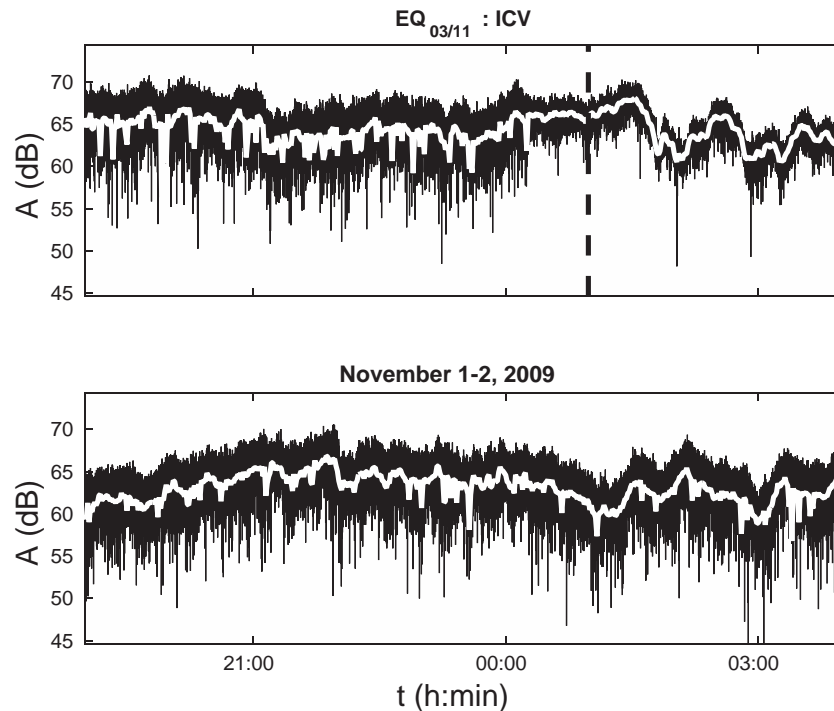


Fig. 2. Time evolutions of the ICV signal amplitude recorded in Belgrade, Serbia during night-time 2–3 November 2010 when EQ_{03/11} occurred (upper panel), and during the quiet night-time on 1–2 November 2009 (bottom panel). Time resolutions of the presented data are 1 min (white line) and 0.1 s (black line). The vertical dashed line indicates the time of occurrence of the EQ_{03/11} event.

period of one night one year ago, it can be seen that these changes are not expected under quiet conditions, i.e. that the 1-min resolution sampling data indicates the presence of an ionospheric disturbance before the EQ event. However, due to the relatively short time interval being considered, we process the 0.1-s resolution dataset to analyse these variations.

3.2.2. Time resolution of 0.1 s

Contrary to the absence of the recorded long-term signal amplitude variations in processing the dataset with a time resolution of 1 min presented above, the relevant dataset with the 0.1-s time resolution provides visible changes in its evolution. It is clearly visible in Fig. 2, where we show the time evolution of the ICV signal amplitude during the night-time period (2–3 November 2010) when the EQ_{03/11} event occurred (upper panel) and during the night-time period (1–2 November 2009) in the absence of EQ events (the bottom graph). Here, the following variations are clearly visible:

- A significant reduction of the signal's short-period noise amplitude which began more than half 0.5 h before the EQ event, and
- A wave-like temporal evolution of the amplitude immediately after the EQ event.

These variations are the major subjects of the analysis that follows, which can be divided in two parts:

1. Analysis of short-term variations which includes determinations of the short-period noise amplitude, and
2. Analysis of excitation and attenuation of acoustic and gravity waves within different wave period domains.

3.3. Analysis of the dataset with 0.1-s sampling time

According to the analyses given in Sections 3.2.1 and 3.2.2, we further continue to study the dataset of the 0.1-s sampling time. As

discussed at the beginning of Section 3, the analyses are performed in both the time and frequency domains where research is focused on short-term variations, and acoustic and gravity waves, respectively; these analyses are the primary subjects of this study.

3.3.1. Short-term variations: short-period noise amplitude

Determination of the short-period noise amplitude (A_{noise}) is done using the procedure which is explained in detail in Nina et al. (2015). This procedure is based on calculation of $dA(t) = A(t) - A_{base}(t)$ representing the deviation of the signal amplitude $A(t)$ from the basic amplitude A_{base} at time t . Here, $A_{base}(t)$ is obtained as the mean value of amplitudes in the defined time bins around time t . The short-period noise amplitude $A_{noise}(t)$ is determined as the maximum of $|dA|$ after elimination of the largest p percent of its values.

The explained procedure is first applied to amplitudes recorded during the night-time periods. In this way, we exclude the influence of the Sun's radiation, which significantly affects signal characteristics.

Keeping in mind that the medium through which a signal propagates is under the permanent influence of numerous phenomena, the observed variations cannot be a-priori connected to the Kraljevo EQ. For this reason, we consider the following two questions:

- Are these variations also visible in the cases of the three additional EQs that occurred at the very close location (EQ_{04/11}) and the relatively close locations (EQ_{07/10} and EQ_{11/10}) in the night-time periods?
- Are these variations typical for the night-time during the considered period?

To answer these questions, we applied the presented procedures in two analyses:

- First, we analyse night-time periods when all considered EQ events occurred. This research provides information about amplitude variations in the period around the considered EQ events and allows us to compare detected changes.

- Second, to compare the obtained values for the EQ nights with other days, we performed the same analyses for nights during a two month period between 1 October and 30 November 2010. In this way, we can compare the increases and decreases of the values obtained during the EQ nights with the variations for the other days.

Additionally, as shown in Section 3.1, significant non-ionospheric effects (induced by natural or artificial sources) on the signal were not present during the observed periods. Finally, we analyse the 24 h time evolution of the short-period noise amplitude to examine regular daily variations and solar radiation influences on the noise parameter. We chose three days when many EQ events occurred close to the ICV signal propagation path. This allows us to provide an additional brief statistical analysis to check the relevance of the presented procedure for detection of the noise amplitude changes during the entire day and for weak EQ events.

3.3.2. Acoustic and gravity waves: excitations and attenuations

In the analysis of oscillation characteristics, we assume the quasilinear approximation and a dominant influence of the lower ionosphere on signal oscillations (see explanation in Section 3.1). The study of AGWs in periods around an EQ event is based on the fast Fourier transform (FFT) applied to the recorded amplitude values in the time domain. Keeping in mind that the FFT provides information about frequencies of waves (i.e. wave periods) within the considered time interval, this procedure cannot be used for exact determination of the time when a wave is excited or attenuated. The decrease in the considered time interval requires a more precise analysis. On the other hand, this interval affects the maximum of observable wave period. For these reasons we present the Fourier amplitude (A_F) analysis for different window time intervals (WTIs). We consider only the night-time period, which restricts the number of WTIs depending on their duration and overlap.

The AGWs in the lower ionosphere are already studied in Nina and Čadež (2013), where the excitation of both acoustic and gravity waves was shown to be possible during solar terminator periods. To analyse their existence in periods around the EQ_{03/11} event, we first estimate τ_0 and τ_{BV} corresponding to the acoustic cut-off (periods when the acoustic waves have lower values) and the Brunt-Väisälä oscillation period (periods when the gravity waves have larger values), respectively:

$$\tau_0 = \frac{4\pi v_s}{\gamma g}, \quad \tau_{BV} = \frac{2\pi}{N_{BV}}, \quad (1)$$

where γ is the standard ratio of specific heats, g is gravitational acceleration, v_s^2 is the adiabatic sound speed squared, and N_{BV} is the Brunt-Väisälä frequency given as $N_{BV}^2 = (\gamma - 1)g^2/v_s^2$. The quantity v_s^2 can be calculated from $v_s^2 = \gamma k_B T_0 / m_a$, where m_a is mass of atoms and the Boltzmann constant $k_B = 1.3807 \cdot 10^{-23}$ J/K. For details of the derivations, see, for example, Yeh and Liu (1972) or Goedbloed and Poedts (2004). According to the International Reference Ionosphere - IRI-2012 ionospheric model (https://ccmc.gsfc.nasa.gov/modelweb/models/iri2012_vitmo.php), the gas temperature T_0 is between 238.0 K and 209.7 K for the area above the EQ epicentre at heights between 60 km and 85 km on 3 November 2010 at 01:00 UT. In our calculation, we use $T_0 = 220$ K. Mass m_a and γ are assumed to be 10^{-25} kg and 5/3, respectively. Keeping in mind that the expected reflection height of VLF waves is below approximately 85 km during the night, we assume that $g = 9.6$ m/s² (this is a valid value for the altitudes between approximately 52 km and 85 km; i.e. we can assume that the value used represents the entire lower ionosphere domain where the VLF waves propagate).

The obtained values indicate waves with periods $T < \tau_0 = 176.7$ s and $T > \tau_{BV} = 180.4$, representing acoustic and gravity modes, respectively.

4. Results and discussions

This study aims to research the disturbances of the ICV signal amplitude recorded by the Belgrade receiver AbsPAL before and after the Kraljevo earthquake (EQ_{03/11}).

Because the analysis given in Section 3 shows the absence of long-term variations of the ICV signal amplitude, but does indicate the detection of short-term variations in the signal amplitude, we focus our study on the short-term variations. The following analysis can be divided into two parts. Namely, as Fig. 2 shows, two types of visible variations in the ICV signal amplitude are recorded: (1) changes in the short-period noise amplitude and (2) excitation of AGWs. Analyses of these properties for the considered signals are given in Sections 4.1 and 4.2, respectively.

The study of the spatial characteristics of short-term variations in the time domain is done by (1) applying the related procedures on two additional signals emitted by the transmitters GQD and DHO located in the UK and Germany, respectively (see Fig. 1) and (2) examining if the recorded data to determine if variations are detected in the other three EQ events (EQ_{07/10}, EQ_{11/10} and EQ_{04/11}). In addition, the presence of regular daily variations in the short-period noise amplitude is checked in comparison with their time evolutions during three days.

4.1. Noise amplitude

Analysis of variations in the noise amplitude is performed in three steps:

1. We determine the expected values for the three signals under quiet conditions in the period of the EQ_{03/11} occurrence.
2. We analyse the time evolution of the short-period noise amplitude at night-times when the analysed EQ events occurred.
3. We check for periodic variations by comparing the time evolution of the signals during three days. As will be seen, this will also give information about additional EQ events, which were frequent in the considered time period.

In the following analyses, we use the procedure explained in Section 3 to calculate the deviation $dA = A(t) - A_{base}(t)$ of the recorded ICV signal amplitude (dA) from its baseline (A_{base}) values and short period noise amplitude A_{noise} .

4.1.1. Short-period noise amplitude under quiet conditions

To determine the expected values under quiet night-time conditions, we first analyse the short-period noise amplitude in time periods between 1 October and 30 November. We consider one-hour intervals (30 min before and after the time of EQ_{03/11} (00:56:54.4 UT)) for the considered days. Here we notice that some days with a lack of data are excluded from the analysis. In the cases of the ICV, DHO, and GQD signal recordings, the number of these days is 3, 6, and 2, respectively (out of total 61 considered days), and they do not significantly affect the study because of time differences between these days and the EQ day.

The results presented in Fig. 3 show the mean, maximum and minimum values of the short-period noise amplitude within the considered time period. The expected night-time values of A_{noise} are calculated as the median of the mean values; they are 2.5377 dB, 0.0827 dB and 0.0777 dB for the ICV, GQD and DHO signals, respectively.

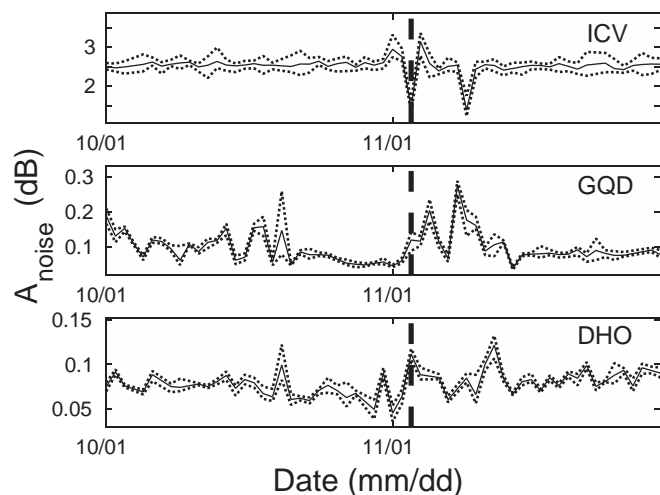


Fig. 3. The short-period noise amplitude within 10-min time windows for time periods of 1 h around 00:54 UT (the EQ_{03/11} time) in the period 1 October–30 November for the ICV (upper panel), GQD (middle panel) and DHO (bottom panel) signals. Mean values are denoted by the solid lines while the dotted lines represent maximum and minimum of the short-period noise amplitude. The vertical dashed line indicates the EQ_{03/11} day.

The complex shapes of the presented time evolutions indicate disturbances a few days before and after the day of EQ_{03/11}. We notice here that storm events over Europe during these nights are not reported in the European Severe Weather Database (<https://www.eswd.eu/cgi-bin/eswd.cgi>). Amplitude variations are the most pronounced for the ICV signal and can be categorized into two groups: (1) increased values in the short-period noise amplitude recorded two days before and one day after the day of the considered EQ, and (2) significantly lower values obtained on this EQ day and six days thereafter. Both of these two indicated variations are important. Namely, in the first case, the shown increase is recorded not only during the considered one-hour intervals but also during long night-time periods (see, for example, Fig. 6, the middle panel). Furthermore, we point out that the increase in night-time variations a few days before an EQ is also shown in previous analyses (Maekawa et al., 2006; Maurya et al., 2016). On the other hand, the additional analysis including EQ events of all magnitudes and areas around the entire signal propagation path from the ICV transmitter to Belgrade showed that two EQs occurred in the period of the second decrease of A_{noise} , first in Central Italy (01:32:14 UT; 42.23 N, 13.01 E; Mw 2.5) and then in Serbia (02:24:24 UT; 43.76 N, 20.69 E; Mw 3.2). More details about these EQ events are given in Section 4.1.2. Here we only point out that although the first EQ had small intensity, its epicentre was under the signal propagation path, which allows us to consider any connection between its occurrence and the recorded signal deviation.

The short-period noise amplitude values of the GQD and DHO signals are more than one order of magnitude lower than those of the ICV signal and their time evolutions are less stable. As we will see in the text below, these properties, together with those explained in Sections 4.1.2 and 4.1.3, indicate that there are no detected changes in the GQD and DHO signals that can be attributed to EQ events.

4.1.2. Short-period noise amplitude during night-time of the considered EQ events

Keeping in mind that the ionosphere is exposed to many influences, it is difficult to extract its response to a particular event of moderate intensity like those related to an earthquake occurrence. For this reason, it is very important to exclude the known effects, particularly solar radiation. Because all the considered EQ events occurred during

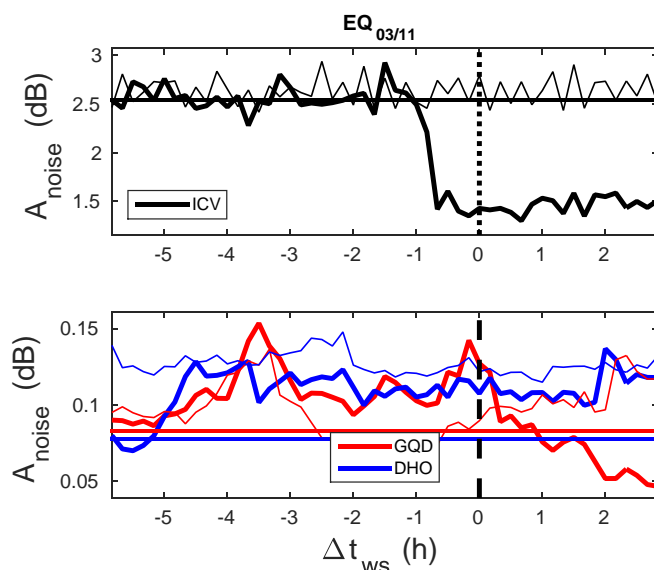


Fig. 4. The short-period noise amplitude A_{noise} within time windows lasting 10 min with time difference Δt_{ws} with respect to the EQ_{03/11} time for the ICV (upper panel), and the GQD and DHO (bottom panel) signals. The thicker lines indicate the EQ night, while thinner ones refer to the reference quiet night. Vertical lines represent the expected night-time values of A_{noise} under quiet conditions obtained by the procedure explained in Section 4.1.1.

the night-time period, we are able to focus on night-time conditions from approximately 6 h before to 3 h after the EQ_{03/11} occurrence.

The obtained time evolution of dA , shown in Supplementary Fig. 1 (upper panel), visualizes a rapid decrease of the recorded ICV amplitude deviation from its basic values starting before the EQ_{03/11} event with a tendency to slowly increase after the EQ_{03/11} occurrence. As seen in Fig. 2 (bottom panel) and as it will be shown in Section 4.1.3, these rapid decreases are not recorded at the beginning of the days with quiet conditions, while the analyses of periods around several EQ events during three days confirm the same trends. Observations of the other two considered areas (defined by the signal propagation paths) indicate that changes are also detected in the GQD (middle panel) and DHO (bottom panel) signals but with different characteristics: (1) a reduction of the GQD signal short-period noise amplitude is also detected but its minimal values are recorded at the end of the considered time interval with a tendency to further decrease; maximum values are recorded several minutes before the EQ occurrence, and (2) the increase of the DHO signal amplitude started approximately 5 h before the considered event and, for this signal, a decrease of the short-period noise amplitude is not visible before the end of the considered time interval, i.e. before the sunrise. Although variations of dA are also recorded in these two signals, detailed analyses show that very similar changes are recorded during two additional days, which indicates regular daily variations.

The presented changes in short-period noise amplitude, which are possibly related to EQ_{03/11} processes, are better visualized in Fig. 4. Here we present values obtained in calculations of the short-period noise amplitude A_{noise} within time windows of 10 min starting Δt_{ws} before and after the EQ_{03/11} occurrence for the ICV (upper panel), the GQD and the DHO (bottom panel) signals. We can see that values for the ICV signal at the beginning of the considered time period are similar to those during quiet days but that they differ from the expected values during periods of several hours starting before the EQ occurrence. On the other hand, the presented time evolutions are very similar in the EQ and referent quiet nights for the GQD and DHO signals (see bottom panel). Here we note that we additionally check the increase before and the decrease after the EQ event for the

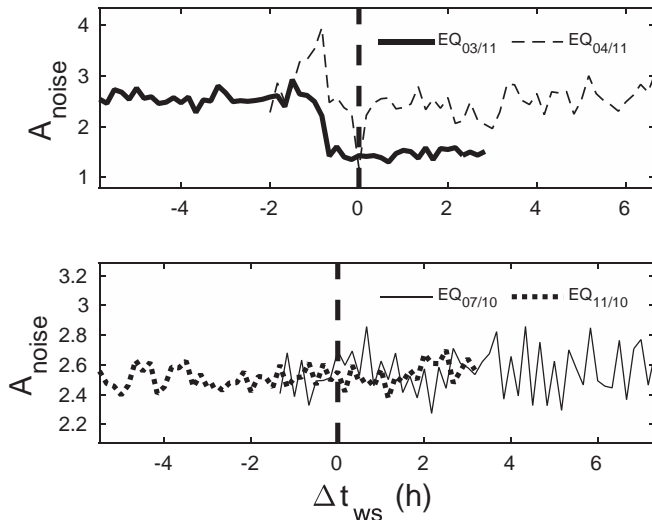


Fig. 5. The short-period noise amplitude A_{noise} within time windows lasting 10 min with time difference Δt_{ws} with respect to the EQ_{03/11} time for the ICV signal in night-times of the EQ_{03/11} and EQ_{04/11} (upper panel), and EQ_{07/10} and EQ_{11/10} (bottom panel) events.

GQD signal in the analysis for whole days. We found that a similar increase exists on 9 November, also before the EQ event, but because of a very small noise amplitude, we cannot connect them with the considered phenomenon without a detailed statistical analysis. On the other hand, a decrease is also recorded during 4 November in the absence of an EQ event in this period, which also does not allow us to confirm variations for periods around the earthquake.

As one can see in Fig. 5 (upper panel) and Supplementary Fig. 2 (upper panel), a significant reduction in the short-period noise amplitude is also recorded for the second EQ in group G1 (EQ_{04/11}). This reduction lasts approximately 0.5 h and begins approximately

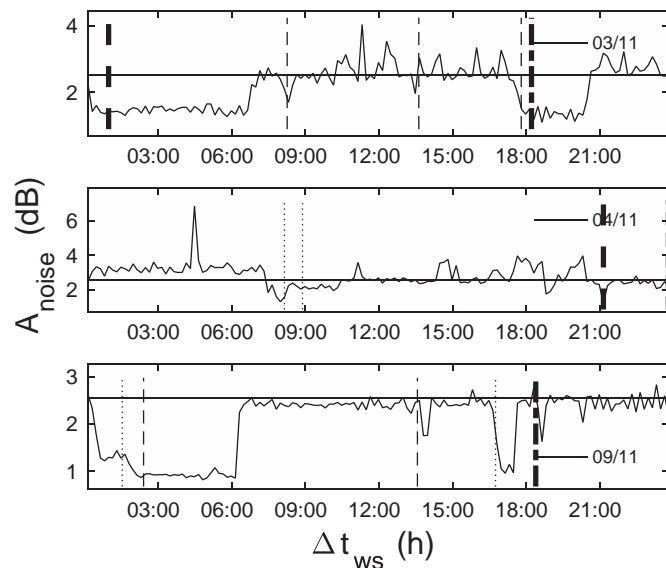


Fig. 6. Time evolutions of A_{noise} of the ICV signal for three days: 3 November (upper panel), 4 November (middle panel), and 9 November (bottom panel), 2010. Vertical lines indicate the time of recorded EQs that can be related to reduction of dA : the tick lines indicate EQ events with magnitudes larger than 4, dashed and dotted lines relate to EQ with the epicentres near Kraljevo and Central Italy, respectively, while dashed-dotted lines indicate EQs in Tyrrhenian Sea (3 November) and Western Mediterranean Sea (9 November).

10 min before the EQ event. Contrary to the events from group G1, these variations are not visible in Fig. 5 (bottom panel) and in the middle and bottom panels of Supplementary Fig. 2, which are related to the EQs from group G2 (at a greater distance from the signal propagation path). Although the calculation of the short-period noise amplitude A_{noise} shows an increase (40 min after the EQ event) followed by a decrease (2 h 10 min after the EQ event) for the EQ_{07/10} event and, although in the case of the EQ_{11/10} the maximum value of A_{noise} is recorded 2 h 20 min after the EQ event (analysis of later values is not possible because of the sunrise), these variations are very small, and we cannot say that they confirm signal reactions relevant to an EQ from group G1.

In addition, it is very important to pay attention to the differences due to EQ intensity. Comparison of EQ_{03/11} (Mw 5.4) with EQ_{04/11} (Mw 4.4) which occurred at practically same locations shows that the reduction of the noise amplitude lasts longer for the first, more intensive event.

4.1.3. Short-period noise amplitude during whole days

The third step in this study is related to the analysis of the short-period noise amplitude during whole days. This time extension from the night-time to 24 h allows us to examine the regular daily variations in the noise amplitude (important for the extraction of the sudden variations from periodic variations), the solar radiation influence on its values and, consequently, the possibility for applying the suggested procedure to the entire day. Keeping in mind that many EQ events occurred not far from the ICV signal propagation path during these time periods, we chose three days which provide us an additional brief statistical analysis that is important for detecting changes in the short-period noise amplitude during the whole days and for detecting EQ events of small intensity.

The daily evolutions of the short-period noise amplitude are compared for three days: 3, 4 and 9 November. These days are chosen because the analysed EQ events with detected noise amplitude reduction occurred in the first two days while the low values of A_{noise} in the upper panel in Fig. 3 are recorded on 9 November.

As one can see in Supplementary Fig. 3, the regular daily noise amplitude variations for the ICV signal are not recorded. However, the presence of many noise reductions in different day periods indicates the possibility for a brief additional analysis to examine similar detections in signal properties for several other EQ events. Namely, during the considered days, 46 EQs (excluding 29 that occurred in a few hours after EQ_{11/03} when extraction of their influence is not possible) were detected with epicentres not far from the ICV signal propagation path. This analysis which covers all EQ magnitudes and areas around the entire ICV signal propagation path, shows the occurrence of 13 EQ events (listed in Supplementary Table 1 and represented by vertical lines in Supplementary Fig. 2 and Fig. 6) which can be related to the recorded noise reductions. Keeping in mind that only 11 of these 46 EQs had magnitudes greater than 3 (two have Mw > 5, two events are between 4 and 5, and seven events are between 3 and 4) and that many epicentre locations are more than 150 km away from the signal propagation path, the number of 13 events is very important.

According to the recorded EQ events given in Supplementary Table 1 and their epicentres (see Fig. 1) and magnitudes, one can see:

- The short-period amplitude reduction starting before the EQ event is recorded for all 4 detected EQs with magnitude greater than 4.
- In addition to the considered two EQ events that occurred near Kraljevo, the noise reduction is recorded for the other 6 EQ events at practically the same epicentre locations and with a minimum magnitude of 2.5. Here we indicate that 8 of 10 EQs near Kraljevo (i.e. 80%) with magnitude greater than 2.5 are connected with the noise amplitude reduction.

- Very interesting are the detections of the short-period amplitude reductions connected with EQs of small magnitudes whose epicentres were in Central Italy. Namely, the signal propagation path passes above their epicentre locations, which indicates a possibility of occurrence of lower ionospheric disturbances related to very low EQ magnitudes. Here we point out that the results indicate the influence of other conditions for these detections. Namely, in addition to 4 EQs of magnitudes from 2.2 to 2.5 which are related to the noise reductions, there were two Mw 2.2 and one Mw 2.3 EQs which cannot be related to ionospheric perturbations.
- Thirteen out of a total of 15 (or 87%) decreases of the short-period noise amplitude can be related to EQ events.
- Reductions of the short-period noise amplitude are recorded in all day periods.

This brief analysis shows that the reduction of the short-period noise amplitude recorded in the case of EQ_{11/03} is also recorded in several other EQ events. The obtained results indicate the need for detailed analyses in longer time periods with larger sample sizes and sufficient events to allow the formation of different types of subsamples whose analyses will be statistically significant and which should analyse influences of different parameters on detections of the noise amplitude reductions that can be connected with EQ events.

On the other hand, applying the same analysis on the GQD and DHO signal amplitudes shows that the recorded variations in the case of the EQ_{11/03} event are similar to those recorded during other days. For this reason, and due to analyses given in Sections 4.1.1 and 4.1.2, which show very small noise amplitudes and their variations during the period of two analysed months, we can conclude that the types of changes considered in these two signals are not recorded.

4.2. Acoustic and gravity waves

To analyse the excitation of AGWs in periods around the EQ time we apply the fast Fourier transform (FFT) on the time series of the recorded ICV signal amplitude. As discussed in Section 3.3.2, the time interval over which the FFT is applied affects the precision of the analysis and the interval of the considered wave periods. For these reasons, we present analyses of the Fourier amplitude (A_f) for the time domain windows whose intervals (WTI) are 20 min, 1 h and 3 h. In this way, we focused separately on the short, middle and long periods ($T = 1/f$) of the waves with frequency f , allowing the analysis of the duration of excited waves with particular periods. The time step of the window's beginning is 10 min for all three cases, while Δt_{vs} indicates the time of the interval's start with respect to the EQ time. For better visibility of results, we divide the 3D graphs into two domains of period T with different scaling of A_f .

In these graphs, both the excitation and attenuation of the waves are visible, as well as their combinations within three specific domains of the wave periods T in time intervals around the EQ occurrence:

- **Wave excitations (WE)** are visible for very small wave periods (time period 1 - TP1) $0.03 < T < 0.08$ min. These waves are excited approximately 0.5 h before the EQ, which is visible in the left upper panel of Fig. 7 describing the WTI of 20 min. For all WTIs, it is found that the wave excitations do not attenuate before the end of the analysed time period. This indicates long-term oscillations on the considered frequencies whose attenuation cannot be visible because of the intensive influence of solar radiation at sunrise.
- **Wave attenuations (WA)** are detected for particular wave periods within the domain of TP2 (0.1–1.3 min). The visualization shows that these wave attenuations are completed before the EQ occurs.

- **Combinations of attenuations and excitations** of waves are detected for $T > 2$ min (TP3). Contrary to the previous two wave period domains, in this case, a more complex time evolution of waves is clearly visible at most of the relevant frequencies. Namely, for these wave periods, the attenuations are recognizable by the three properties of A_f behaviour: (1) attenuation of wave amplitude before the EQ, (2) their small values in the period around the EQ and (3) excitation with A_f larger than those before the indicated attenuation. In the upper and middle right panels we can see that for $T \leq 20$ min these excitations start after the EQ and their attenuations occur within the time period before the sunrise. These variations are clearly visible in Supplementary Fig. 4 where we present the wavelet transform for the time period from approximately 70 min before the EQ to approximately 100 min after the EQ. As one can see, the most important variations are detected during the time period between 40 min and 1 h after the EQ.

In the bottom right panel in Fig. 7 there are visible excitations of waves with time periods $T \approx 0.5$ h and ≥ 1 h. To find a more precise wave period, we additionally fitted the function $\Delta A(t)$ obtained as the deviation of the amplitude $A(t)$ from its mean value in the considered time period of 3 h after the EQ_{03/11} event. This is done using the following sine series:

$$A(t) = \sum_{i=1}^N a_i \sin(b_i t + c_i) \quad (2)$$

where $N = 8$. The obtained fitted curve is shown in Supplementary Fig. 5 (upper panel) while coefficients are given in Supplementary Table 2. Comparison of this curve with the fitted function of $\Delta A(t)$ in the period of 3 h before the EQ (middle panel) is presented in the bottom panel where one can see larger values of the amplitude a for periods after the EQ and a significant increase of waves with the period of 1 h.

As one can see in Supplementary Table 2, the obtained time periods $T_i = 2\pi/b_i \leq 1.5$ h are 59.9 min, 31.5 min, 18.5 min, 23.5 min, 26.7 min and 16.0 min (these periods are at least 2 times smaller than the considered time period and can be taken into consideration in the wave analyses).

According to the analysis of AGWs given in Section 3.3.2, where we determined that their wave periods are less than 2.9 min and more than 3 min, respectively, we can conclude that both types of these waves are excited during the EQ_{03/11} event.

To compare the obtained periods of excited/attenuated AGWs with other signals and cases, we applied the previously explained procedure to the GQD and DHO signal amplitudes for the EQ_{03/11} event and to the ICV amplitude for three EQ events given in Supplementary Table 1 with magnitude greater than 4. In the first case, similar excitations are recorded only for the wave period of approximately 1 s, but they are significantly less pronounced. On the other hand, the analyses of the other three EQs show very similar excitations and attenuations in TP1 and TP2, respectively, in all three cases. Keeping in mind that these properties are not visible under quiet conditions of the referent night, we can infer that these acoustic waves are probably attributed to the considered EQ events and that their appearance should be investigated in future statistical studies.

Although analyses of waves with larger wave periods cannot be useful for comparison because of different time intervals of the noise amplitude reduction, fitting of the recorded data gives very similar wave periods like those in the case of the EQ_{03/11} event (except for the largest one of approximately 1 h) for 2 of 3 cases. However, fitting of the amplitude time evolution during the referent quiet night (1–2 November 2009) shows the existence of waves with wave periods of 35.7 min, 60.1 min, 19.5 min, 19.4 min and 23.8 min. For this

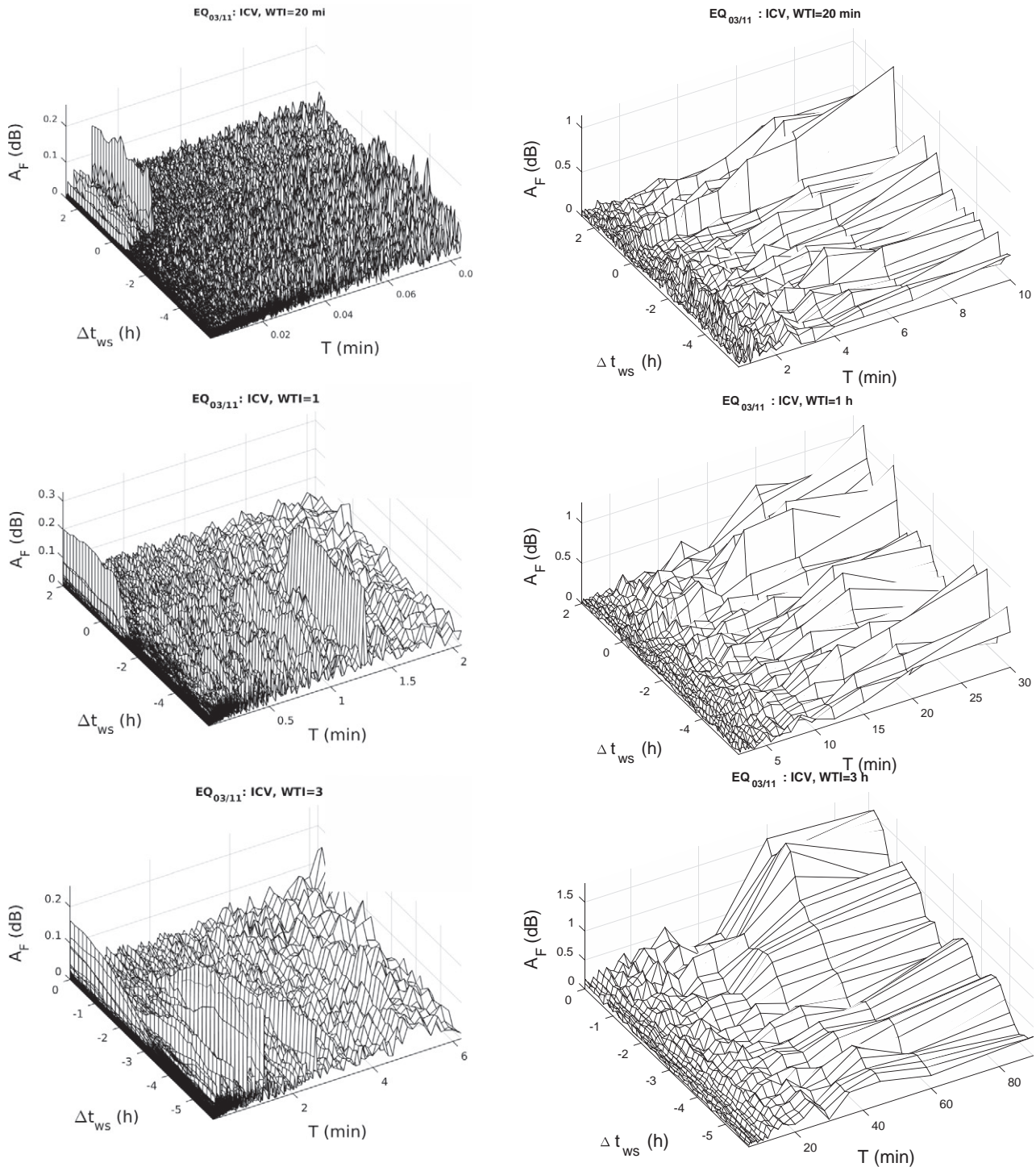


Fig. 7. Fourier amplitude of waves with period T obtained by applying FFT to the ICV signal amplitudes recorded in time with window time intervals (WTI) of 20 min (upper panels), 1 h (middle panels), and 3 h (bottom panels) which begin with a Δt_{ws} shift with respect to the EQ time. Due to a significantly large A_F at larger T , the graphics are divided into smaller (left panels) and greater (right panels) wave periods.

reason, we cannot be sure that the gravity waves with wave periods indicated in Supplementary Table 2 (lower than 1 h) are a consequence of the considered EQ events, and their relationship should be investigated in future studies.

4.3. Comparison with previous observations

As we indicated in the Introduction, there are many studies of the relationships between the earthquakes and ionospheric disturbances.

They are based on different measurement techniques (first, on GPS and VLF signals relevant for upper and lower ionosphere, respectively); they are usually based on datasets with time sampling larger than 1 s.

In this study, we analyse two sets of VLF data with time resolutions of 1 min and 0.1 s. Examination of the presence of changes indicated in Hayakawa (1996), Molchanov et al. (1998), and Yamauchi et al. (2007) (time shift of the “terminator time” a few days before the EQ events) and Biagi et al. (2007, 2001a), Hayakawa (2011), Rozhnoi et al. (2015),

and Solovieva et al. (2015) (signal amplitude variations) with the 1-min resolution dataset show that the changes cannot be confirmed in the case of EQ_{03/11} due to seasonal variations. This can be explained by the moderate EQ intensity and the greater distance between the EQ epicentre and the considered signal propagation path.

On the other hand, the primary subject of this study, related to the processing of the 0.1-s resolution datasets, indicates variations starting only a few minutes or a few tens of minutes before the EQ occurrence, contrary to most of the recorded disturbances in different ionospheric regions considered as EQ precursors recorded a few days earlier. As one can see in Section 4.1.3, the presented procedure also gives the noise amplitude reduction for several other EQ events, including those of magnitudes lower than 3. This result indicates a possible method for the earthquake prediction that is more sensitive than those that can be found in the literature. This is very important because the inclusion of EQ events with moderate to small magnitudes allows statistical analyses that are not possible in the case of very strong earthquakes whose statistical analyses require samples of events occurring within long time intervals and at different locations thereby not allowing examination of influences of different parameters on signal disturbance detection. In this sense, the present study can be considered as a pioneer study, which reveals the need for further statistical research.

It is important to say that some of the obtained wave periods of induced AGWs are lower than 30 s, which agrees with results presented in Ohya et al. (2018). Additionally, the short-period noise amplitude increase observed two days before the Kraljevo EQ agrees with the increases in night-time variations before the EQ presented in Maekawa et al. (2006) and Maurya et al. (2016).

5. Conclusions

In this paper, we presented an analysis of variations in the VLF signals, used for the lower ionosphere observations and detection of changes in the electrical properties of this atmospheric layer, in a period around the Mw 5.4 earthquake that occurred on 3 November 2010 near the town of Kraljevo in Serbia. We focused our attention on variations in the ICV signal amplitude whose propagation path is close to the EQ epicentre, and we analysed time evolutions of datasets with 1-min and 0.1-s resolution. To check the obtained conclusions and influence the localisation of recorded changes, presumably in the lower ionosphere, we applied the described procedures to the GQD and DHO signals and considered the properties of the ICV signal in night-time periods around three additional EQs. Moreover, to examine regular daily variations in the noise amplitude and solar radiation influence on its values to check the possibility of applying the suggested procedure during the entire day, we analysed cases of three whole days. The days were chosen within the period of frequent earthquake events occurrences, allowing us to conduct a brief statistical study, which indicated the need for more detailed analyses in future research.

The obtained conclusions are:

- Detection of signal variations, probably induced by the lower ionospheric disturbances, depends on the time resolution of recorded data. In the case of the 1-min sampling data, useful for analysis of long-term signal disturbances (daily variations) which can be attributed to an EQ event, we did not record changes in the global daily amplitude trends that are indicated as EQ precursors in previous studies; or their possible occurrences (terminator time shift) are masked by seasonal variations. A noise amplitude reduction is only visible after the earthquake. This reduction provides a clearer view of the wave-like time evolution of the amplitude than can be observed during quiet night. On the other hand, a better time resolution provides clearly visible short-term changes before and after the EQ.

- We detected short-term signal variations, which probably reflect the lower ionospheric disturbances. They are visualized as variations in the signals' short-period noise amplitude which starts before the EQ and can be considered as an EQ precursor. These changes are also detected for a few days before and after the EQ.
- These variations are recorded only for the ICV signal, which points to local ionospheric disturbances.
- Reductions of the short-period noise amplitude are recorded for all day periods during the three analysed days. In this analysis, which includes many EQ events occurring at moderate and small distances from the ICV propagation path, we find: (1) Thirteen out of a total of 15 (or 87%) decreases of the short-period noise amplitude can be attributed to EQ events; (2) The short-period noise amplitude reduction starting before the EQ event is recorded for all four detected EQs with magnitude larger than 4; (3) Eight of 10 analysed EQs near Kraljevo (i.e. 80%) with magnitudes larger than 2.5 are connected with the noise amplitude reduction; (4) Reductions of the short-period noise amplitude are recorded in several cases of weak EQ events in Central Italy which indicates a possible very large sensitivity of the proposed method in the case when the signal propagation path passes above the EQ epicentre.
- Acoustic wave excitations and attenuations at wave periods $0.03 < T < 0.08$ min and $0.1 < T < 1.3$ min, which are detected in the case of the Kraljevo EQ are also recorded in three other EQ events with magnitude larger than 4. The recorded gravity waves cannot be a-priori connected with the considered EQ events because of the excitation of waves with similar periods during quiet nights. Their relationship should be investigated in future studies.

To conclude, we point out that the fundamental question opened in this study is: Can improving the time resolution of the observed data provide us with a new technique for EQ forecasting? Keeping in mind that the obtained variations fall within one hour before the considered EQ and that the used observational method is based on continuous monitoring, the obtained indications are of great importance and should be investigated in the forthcoming research.

Declaration of competing interest

The authors declare that they have no known competing financial interests or personal relationships that could have appeared to influence the work reported in this paper.

Acknowledgments

This research is supported by the European Cooperation in Science and Technology (COST) Action CA15211. It is also supported by the Ministry of Education, Science and Technological Development of the Republic of Serbia, under the projects 176001, 176002, 176004, III44002, III47007 and COST Actions TD1403 and CA18109.

The authors are grateful to Vladimir M. Čadež for very useful suggestions and comments, and Robert Holzworth and Craig Rodger for help in preparation of this study. The authors also thank to the referees and editors for very useful comments.

Requests for the VLF data used for analysis can be directed to the corresponding author. The Kilpisjärvi VLF data were supplied by the Sodankylä Geophysical Observatory, University of Oulu, Finland. For checking of the meteorological conditions we used information given on the European Severe Weather Database website. For checking of the geomagnetic conditions we used information given in Monthly magnetic bulletin of Castello Tesino Observatory.

Appendix A. Supplementary data

Supplementary data to this article can be found online at <https://doi.org/10.1016/j.scitotenv.2019.136406>.

References

- Balan, N., Shiokawa, K., Otsuka, Y., Kikuchi, T., Vijaya-Lekshmi, D., Kawamura, S., Yamamoto, M., Bailey, G.J., 2010. A physical mechanism of positive ionospheric storms at low latitudes and mid latitudes. *J. Geophys. Res. - Space* 115, A2. <https://doi.org/10.1029/2009JA014515>.
- Biagi, P., Castellana, L., Maggipinto, T., Piccolo, R., Minafra, A., Ermini, A., Martellucci, S., Bellecci, C., Perna, G., Capozzi, V., Molchanov, O., Hayakawa, M., 2006. LF radio anomalies revealed in Italy by the wavelet analysis: possible preseismic effects during 1997–1998. *Phys. Chem. Earth* 31, 403–408. <https://doi.org/10.1016/j.pce.2005.10.001>.
- Biagi, P.F., Castellana, L., Maggipinto, T., Maggipinto, G., Minafra, A., Ermini, A., Capozzi, V., Perna, G., Solovieva, M., Rozhnoi, A., Molchanov, O.A., Hayakawa, M., 2007. Decrease in the electric intensity of VLF/LF radio signals and possible connections. *Nat. Hazards Earth Syst. Sci.* 7, 423–430. <https://doi.org/10.5194/nhess-7-423-2007>.
- Biagi, P.F., Maggipinto, T., Righetti, F., Loiacono, D., Schiavulli, L., Ligonzo, T., Ermini, A., Moldovan, I.A., Moldovan, A.S., Buyuksarac, A., Silva, H.G., Bezzeghoud, M., Contadakis, M.E., 2011. The European VLF/LF radio network to search for earthquake precursors: setting up and natural/man-made disturbances. *Nat. Hazards Earth Syst. Sci.* 11, 333–341. <https://doi.org/10.5194/nhess-11-333-2011>.
- Biagi, P.F., Piccolo, R., Ermini, A., Martellucci, S., Bellecci, C., Hayakawa, M., Capozzi, V., Kingsley, S.P., 2001a. Possible earthquake precursors revealed by LF radio signals. *Nat. Hazards Earth Syst. Sci.* 1, 99–104. <https://doi.org/10.5194/nhess-1-99-2001>.
- Biagi, P.F., Piccolo, R., Ermini, A., Martellucci, S., Bellecci, C., Hayakawa, M., Kingsley, S.P., 2001b. Disturbances in LF radio-signals as seismic precursors. *Ann. Geophys.* 44. <https://doi.org/10.4401/ag-3552>.
- Bradley, P.A., Cander, L.R., 2002. Proposed terminology for the classification and parameters for the quantification of variability in ionosphere morphology. *Ann. Geophys.* 45. <https://doi.org/10.4401/ag-3495>.
- Depuev, V., Pulinet, S., 2001. Intercosmos-19 observations of an additional topside ionization layer: the f3 layer. *Adv. Space Res.* 27, 1289–1292. [https://doi.org/10.1016/S0273-1177\(01\)00205-8](https://doi.org/10.1016/S0273-1177(01)00205-8).
- Dragović, R., Gajić, B., Dragović, S., Djordjević, M., Djordjević, M., Mihailović, N., Onjia, A., 2014. Assessment of the impact of geographical factors on the spatial distribution of heavy metals in soils around the steel production facility in Smederevo (Serbia). *J. Clean. Prod.* 84, 550–562. <https://doi.org/10.1016/j.jclepro.2014.03.060>.
- Forbes, J.M., Palo, S.E., Zhang, X., 2000. Variability of the ionosphere. *J. Atmos. Solar-Terr. Phys.* 62, 685–693. [https://doi.org/10.1016/S1364-6826\(00\)00029-8](https://doi.org/10.1016/S1364-6826(00)00029-8).
- Georgoulas, A.K., Alexandri, G., Kourtidis, K.A., Lelieveld, J., Zanis, P., Pöschl, U., Levy, R., Amiridis, V., Marinou, E., Tsikerdekes, A., 2016. Spatiotemporal variability and contribution of different aerosol types to the aerosol optical depth over the eastern Mediterranean. *Atmos. Chem. Phys.* 16, 13853–13884. <https://doi.org/10.5194/acp-16-13853-2016>.
- Goedbloed, H., Poedts, S., 2004. *Principles of Magnetohydrodynamics: With Applications to Laboratory and Astrophysical Plasmas*. Cambridge University Press, UK.
- Hayakawa, M., 1996. The precursory signature effect of the Kobe earthquake on VLF subionospheric signals. *J. Comm. Res. Lab.* 43, 169–180. <https://ci.nii.ac.jp/naid/80009515165/en/>.
- Hayakawa, M., 2007. VLF/LF radio sounding of ionospheric perturbations associated with earthquakes. *Sensors* 7, 1141–1158. <https://doi.org/10.3390/s7071141>.
- Hayakawa, M., Horie, T., Muto, F., Kasahara, Y., Ohta, K., Liu, J.Y., Hobara, Y., 2010. Subionospheric VLF/LF probing of ionospheric perturbations associated with earthquakes: a possibility of earthquake prediction. *SICE J. Control Meas. Syst. Integr.* 3, 10–14. <https://doi.org/10.9746/jcmsi.3.10>.
- Hayakawa, M., 2011. Probing the lower ionospheric perturbations associated with earthquakes by means of subionospheric VLF/LF propagation. *Earth. Sci.* 24, 609–637. <https://doi.org/10.1007/s11589-011-0823-1>.
- Kastelis, N., Kourtidis, K., 2016. Characteristics of the atmospheric electric field and correlation with CO₂ at a rural site in southern balkans. *Earth Planets Space* 68, 3. <https://doi.org/10.1186/s40623-016-0379-3>.
- Hirooka, S., Hattori, K., Nishihashi, M., Takeda, T., 2011. Neural network based tomographic approach to detect earthquake-related ionospheric anomalies. *Nat. Hazards Earth Syst. Sci.* 11, 2341–2353. <https://doi.org/10.5194/nhess-11-2341-2011>.
- Ke, F., Wang, J., Tu, M., Wang, X., Wang, X., Zhao, X., Deng, J., 2018. Morphological characteristics and coupling mechanism of the ionospheric disturbance caused by super typhoon Sarika in 2016. *Adv. Space Res.* 62, 1137–1145. <https://doi.org/10.1016/j.asr.2018.06.015>.
- Knezevic-Antonijević, S., Arroucau, P., Vlahovic, G., 2013. Seismotectonic model of the Kraljevo 3 November 2010 Mw 5.4 earthquake sequence. *Seismol. Res. Lett.* 84, 600–610. <https://doi.org/10.1785/0220120158>.
- Kumar, S., NaitAmor, S., Chanrion, O., Neubert, T., 2017. Perturbations to the lower ionosphere by tropical cyclone Evan in the south Pacific region. *J. Geophys. Res. - Space* 122, 8720–8732. <https://doi.org/10.1002/2017JA024023>.
- NaitAmor, S., Cohen, M.B., Kumar, S., Chanrion, O., Neubert, T., 2018. VLF signal anomalies during cyclone activity in the Atlantic Ocean. *Geophys. Res. Lett.* 45. <https://doi.org/10.1029/2018GL078988>. 10 185–10 192.
- Maekawa, S., Horie, T., Yamauchi, T., Sawaya, T., Ishikawa, M., Hayakawa, M., Sasaki, H., 2006. A statistical study on the effect of earthquakes on the ionosphere, based on the subionospheric LF propagation data in Japan. *Ann. Geophys.* 24, 2219–2225. <https://hal.archives-ouvertes.fr/hal-00318154>.
- Maurya, A.K., Venkatesham, K., Tiwari, P., Vijaykumar, K., Singh, R., Singh, A.K., Ramesh, D.S., 2016. The 25 April 2015 Nepal earthquake: investigation of precursor in VLF subionospheric signal. *J. Geophys. Res. - Space* 121. <https://doi.org/10.1002/2016JA022721>. 10,403–10,416.
- Miyaki, K., Hayakawa, M., Molchanov, O., 2001. The role of gravity waves in the lithosphere - ionosphere coupling, as revealed from the subionospheric LF propagation data. *Seismo Electromagnetics: Lithosphere - Atmosphere - Ionosphere Coupling*; TERRAPUB: Tokyo. pp. 229–232.
- Molchanov, O., Hayakawa, M., Miyaki, K., 2001. VLF/LF sounding of the lower ionosphere to study the role of atmospheric oscillations in the lithosphere-ionosphere coupling. *Adv. Polar Upper Atmos. Res.* 15, 146–159.
- Molchanov, O., Hayakawa, M., Oudoh, T., Kawai, E., 1998. Precursory effects in the subionospheric VLF signals for the Kobe earthquake. *Phys. Earth Planet. Inter.* 105, 239–248. [https://doi.org/10.1016/S0031-9201\(97\)00095-2](https://doi.org/10.1016/S0031-9201(97)00095-2).
- Nina, A., Radovanović, M., Milovanović, B., Kovačević, A., Bajčetić, J., Popović, L.Č., 2017. Low ionospheric reactions on tropical depressions prior hurricanes. *Adv. Space Res.* 60, 1866–1877. <https://doi.org/10.1016/j.asr.2017.05.024>.
- Nina, A., Simić, S., Srećković, V.A., Popović, L.Č., 2015. Detection of short-term response of the low ionosphere on gamma ray bursts. *Geophys. Res. Lett.* 42, 8250–8261. <https://doi.org/10.1002/2015GL065726>. 2015GL065726.
- Nina, A., Čadež, V.M., 2013. Detection of acoustic-gravity waves in lower ionosphere by VLF radio waves. *Geophys. Res. Lett.* 40, 4803–4807. <https://doi.org/10.1002/grl.50931>.
- Nina, A., Čadež, V.M., Popović, L.Č., Srećković, V.A., 2017. Diagnostics of plasma in the ionospheric D-region: detection and study of different ionospheric disturbance types. *Eur. Phys. J. D* 71, 189. <https://doi.org/10.1140/epjd/e2017-70747-0>.
- Ohya, H., Tsuchiya, F., Takishita, Y., Shinagawa, H., Nozaki, K., Shiokawa, K., 2018. Periodic oscillations in the D region ionosphere after the 2011 Tohoku earthquake using LF standard radio waves. *J. Geophys. Res. - Space* 123, 5261–5270. <https://doi.org/10.1029/2018JA025289>.
- Perrier, F., Richon, P., Sabroux, J.C., 2005. Modelling the effect of air exchange on 222rn and its progeny concentration in a tunnel atmosphere. *Sci. Total Environ.* 350, 136–150. <https://doi.org/10.1016/j.scitotenv.2004.12.060>.
- Petrović, J., Djordjević, M., Dragović, R., Gajić, B., Dragović, S., 2018. Assessment of radiation exposure to human and non-human biota due to natural radionuclides in terrestrial environment of Belgrade, the Capital of Serbia. *Environ. Earth Sci.* 77, 290. <https://doi.org/10.1007/s12665-018-7470-y>.
- Popova, I., Rozhnoi, A., Solovieva, M., Chebrov, D., Hayakawa, M., 2018. The behavior of VLF/LF variations associated with geomagnetic activity, earthquakes, and the quiet condition using a neural network approach. *Entropy* 20. <http://www.mdpi.com/1099-4300/20/9/691>. <https://doi.org/10.3390/e20090691>.
- Price, C., Yair, Y., Asfur, M., 2007. East African lightning as a precursor of Atlantic hurricane activity. *Geophys. Res. Lett.* 34, 9805. <https://doi.org/10.1029/2006GL028884>.
- Pulinet, S., Boyarchuk, K., 2004. *Ionospheric Precursor of Earthquakes*. Springer, Heidelberg, Germany.
- Pulinet, S., Ouzounov, D., 2011. Lithosphere – atmosphere – ionosphere coupling (LAIC) model – an unified concept for earthquake precursors validation. *J. Asian Earth Sci.* 41, 371–382. <https://doi.org/10.1016/j.jseas.2010.03.005>.
- Radovanović, M., 2018. Investigation of solar influence on the terrestrial processes: activities in Serbia. *J. Geogr. Inst. Cvijic* 68, 149–155. <https://doi.org/10.2298/IJG1801149R>.
- Rishbeth, H., Mendillo, M., 2001. Patterns of F2-layer variability. *J. Atmos. Solar-Terr. Phys.* 63, 1661–1680. [https://doi.org/10.1016/S1364-6826\(01\)00036-0](https://doi.org/10.1016/S1364-6826(01)00036-0).
- Rozhnoi, A., Solovieva, M., Molchanov, O., Biagi, P.F., Hayakawa, M., Schwingenschuh, K., Boudjada, M., Parrot, M., 2010. Variations of VLF/LF signals observed on the ground and satellite during a seismic activity in Japan region in May–June 2008. *Nat. Hazards Earth Syst. Sci.* 10, 529–534. <https://doi.org/10.5194/nhess-10-529-2010>.
- Rozhnoi, A., Solovieva, M., Molchanov, O., Hayakawa, M., 2004. Middle latitude LF (40 kHz) phase variations associated with earthquakes for quiet and disturbed geomagnetic conditions. *Phys. Chem. Earth* 29, 589–598. <https://doi.org/10.1016/j.pce.2003.08.061>.
- Rozhnoi, A., Solovieva, M., Parrot, M., Hayakawa, M., Biagi, P.F., Schwingenschuh, K., Fedun, V., 2015. VLF/LF signal studies of the ionospheric response to strong seismic activity in the far eastern region combining the DEMETER and ground-based observations. *Phys. Chem. Earth*, 85–86, 141–149. <https://doi.org/10.1016/j.pce.2015.02.005>.
- Solovieva, M., Rozhnoi, A., Fedun, V., Schwingenschuh, K., Hayakawa, M., 2015. Ionospheric perturbations related to the earthquake in Vrancea area on November 22, 2014, as detected by electromagnetic VLF/LF frequency signals. *Ann. Geophys.* 58, 0552. <https://doi.org/10.4401/ag-6827>.
- Srećković, V., Šulić, D., Vujičić, V., Jevremović, D., Vyklyuk, Y., 2017. The effects of solar activity: electrons in the terrestrial lower ionosphere. *J. Geogr. Inst. Cvijic* 67, 221–233. <https://doi.org/10.2298/IJG1703221S>.
- Šulić, D., Srećković, V.A., 2014. A comparative study of measured amplitude and phase perturbations of VLF and LF radio signals induced by solar flares. *Serb. Astron. J.* 148, 45–54. <https://doi.org/10.2298/SAJ148045S>.
- Šulić, D., Srećković, V., Mihajlov, A., 2016. A study of VLF signals variations associated with the changes of ionization level in the D-region in consequence of solar conditions. *Adv. Space Res.* 57, 1029–1043. <https://doi.org/10.1016/j.asr.2015.12.025>.

- Tanaka, Y.T., Raulin, J.P., Bertoni, F.C.P., Fagundes, P.R., Chau, J., Schuch, N.J., Hayakawa, M., Hobar, Y., Terasawa, T., Takahashi, T., 2010. First very low frequency detection of short repeated bursts from Magnetar SGR J1550-5418. *Astrophys. J. Lett.* 721, L24–L27. <https://doi.org/10.1088/2041-8205/721/1/L24>.
- Titova, M., Zakharov, V., Pulinets, S., 2019. Detection of ionospheric disturbances over the region of Haiti Island in the period of 01–15 January 2010 by GPS data in quiet geomagnetic conditions. *Geomagnet. Aeronomy* 59, in press.
- Yamauchi, T., Maekawa, S., Horie, T., Hayakawa, M., Soloviev, O., 2007. Subionospheric VLF/LF monitoring of ionospheric perturbations for the 2004 mid-Niigata earthquake and their structure and dynamics. *J. Atmos. Solar-Terr. Phys.* 69, 793–802. <https://doi.org/10.1016/j.jastp.2007.02.002>.
- Yeh, K.C., Liu, C.H., 1972. *Theory of ionospheric waves*. Academic Press, New York.

M21



Article

VLF Signal Noise Reduction during Intense Seismic Activity: First Study of Wave Excitations and Attenuations in the VLF Signal Amplitude

Aleksandra Nina

Institute of Physics Belgrade, University of Belgrade, Pregrevica 118, 11080 Belgrade, Serbia; sandrast@ipb.ac.rs

Abstract: This study is a continuation of pilot research on the relationships between seismic activity and changes in very low frequency (VLF) signals starting a few minutes or a few dozen minutes before an earthquake. These changes are recorded in the time and frequency domains and their duration can be influenced not only by the strongest earthquake but also by others that occur in a short time interval. This suggests that there are differences in these changes in cases of individual earthquakes and during the period of intense seismic activity (PISA). In a recent study, they were validated in the time domain by comparing the amplitude noise reductions during the PISA and before earthquakes that occurred in the analysed periods without intense seismic activity (PWISA). Here, we analyse the changes in the VLF signal amplitude in the frequency domain during the PISA and their differences are compared to the previously investigated relevant changes during PWISA. We observe the signal emitted by the ICV transmitter in Italy and received in Serbia from 26 October to 2 November 2016 when 907 earthquakes occurred in Central Italy. The study is based on analyses of the Fourier amplitude A_F obtained by applying the fast Fourier transform (FFT) to the values of the ICV signal amplitude sampled at 0.1 s. The obtained results confirm the existence of one of the potential earthquake precursors observed during PWISA: significantly smaller values of A_F for small wave periods (they can be smaller than 10^{-3} dB) than under quiet conditions (the expected values are larger than 10^{-2} dB). Exceptions were the values of A_F for wave periods between 1.4 s and 2 s from a few days before the observed PISA to almost the end of that period. They were similar or higher than the values expected under quiet conditions. The mentioned decrease lasted throughout the observed longer period from 10 October to 10 November, with occasional normalisation. It was many times longer than the decreases in A_F around the considered earthquakes during PWISA, which lasted up to several hours. In addition, no significant wave excitations were recorded at discrete small values of the wave periods during the PISA, as was the case for earthquakes during PWISA. These differences indicate the potential possibility of predicting the PISA if the corresponding earthquake precursors are recorded. Due to their importance for potential warning systems, they should be analysed in more detail in future statistical studies.



Citation: Nina, A. VLF Signal Noise Reduction during Intense Seismic Activity: First Study of Wave Excitations and Attenuations in the VLF Signal Amplitude. *Remote Sens.* **2024**, *16*, 1330. <https://doi.org/10.3390/rs16081330>

Academic Editors: Yuriy G. Rapoport, Volodymyr Grimalsky, Anatoly Kotsarenko and Gianfranco Cianchini

Received: 1 February 2024

Revised: 4 April 2024

Accepted: 5 April 2024

Published: 10 April 2024

Keywords: earthquake precursors; VLF signal; wave excitations/attenuations



Copyright: © 2024 by the authors. Licensee MDPI, Basel, Switzerland. This article is an open access article distributed under the terms and conditions of the Creative Commons Attribution (CC BY) license (<https://creativecommons.org/licenses/by/4.0/>).

1. Introduction

The decades-long efforts of researchers to find a mechanism for the detection of earthquake precursors have been focused on the investigation of numerous phenomena [1–3]. These include studies of changes in the ionosphere [4–14] and the electromagnetic signals used to monitor it [15–18].

This paper analyses the characteristics of a very low frequency (VLF) radio signal used to monitor the lower ionosphere. As numerous studies show, there are several different changes in the characteristics of VLF and low-frequency (LF) signals that can occur before an earthquake. They are mostly detected a few days or weeks before strong earthquakes [19–21], and are manifested in a significant increase/decrease in the

signal amplitude/phase [22,23], in the shift of the terminator time during sunrise and sunset [8,20,24,25] and in variations in the wavelet power spectrum [22,26]. These investigations are mainly based on amplitude/phase processing of VLF/LF signals sampled with a time interval of not less than 1 s.

In 2020, the first relevant research based on the analysis of VLF signal amplitudes recorded with a time resolution of 0.1 s was published [27]. This improvement in resolution led to the discovery of new potential earthquake precursors observed in the time and frequency domains. In the time domain, the corresponding changes are manifested by reductions in the amplitude and phase noises. In the frequency domain, the analysis of the Fourier amplitude obtained by applying the fast Fourier transform (FFT) to the time evolutions of the signal amplitude and phase shows its increases at discrete low values of wave periods and its decreases at other, also low-value, wave periods. The first investigations of these changes in signal characteristics have been published in several studies [27–31]. One of the basic conclusions is that it is possible to connect several earthquakes that occur in a short time interval in some localised area with one change in the signal, i.e., that several events occur during one continuous disturbance. This has led to the conclusion that the detection of the mentioned changes is influenced by the duration of seismic activity. This has been confirmed in the case of the amplitude noise reduction in the time domain in the analysis of the period of intense seismic activity (PISA) in Central Italy when almost 1000 earthquakes were registered in a period of 10 days. Namely, the results of the study presented in [29] show that one amplitude noise reduction that occurs before one earthquake can continue without normalisation and without additional reductions during the period of occurrence of other earthquakes.

The aim of this research is to examine the changes in the VLF signal amplitude during the seismically active period in the frequency domain, which is a continuation of the analysis of the corresponding changes in the time domain given in [29]. We observe the amplitude characteristics of the ICV signal emitted in Italy and received at the Institute of Physics Belgrade in Belgrade, Serbia. The focus of the analysis is on the eight-day period from 26 October to 2 November 2016. Here, we use the same methods as those described in the studies of earthquakes that occurred during periods without intense seismic activity (PWISA) [27,30]. In addition, the daily values of the parameters relevant to the study during a one-month interval (10 October–10 November 2016) are presented in order to determine the beginnings and endings of the observed changes. Detailed analyses are also conducted for 3 October 2010 and 25 October 2016, which are taken as reference days in the analyses of the considered changes.

This paper is organized as follows. Section 2 describes the events that took place in the observed period and the signal whose characteristics are analysed. The signal processing is explained in Section 3, and the obtained results and their discussion are presented in Section 4. The conclusions of this study are set out in Section 5.

2. Observations

According to the data provided on the Euro-Mediterranean Seismological Centre website [32], earthquakes in Central Italy were registered every day (except on 18 October 2016) during a one-month interval from 10 October to 10 November 2016. The total number of earthquakes and the number of earthquakes with a minimum magnitude of four (hereafter referred to as stronger earthquakes) that occurred in that time interval are given in the upper and lower panels of Figure 1, respectively. Here, we note that the magnitudes on the mentioned website are given in the moment magnitude [33], body-wave magnitude [34], and Richter [35] scales. As in the previous relevant studies, here, we considered earthquakes with a minimum magnitude of four on any of these scales and used M as a common term for all given magnitudes. The obtained time evolutions indicated that the total number of earthquakes increased sharply on 26 October. On that day, six earthquakes of minimum magnitude four were recorded, including earthquakes of magnitudes M_w 5.5 and M_w 6.1. For these reasons, 26 October was the beginning of the

period that was the focus of this study. The highest seismic activity was on 30 October with 268 earthquakes, including 14 stronger earthquakes with a maximum magnitude of Mw 6.5. The calming of the ground tremors in Central Italy after that maximum was slower than its intensification, but the recorded magnitudes were not large. It can be assumed that the series of earthquakes with $M \geq 4$ ended on 3 October. Namely, only one such earthquake occurred in the following week (on 7 November). Based on this and the fact that the analysed signal was bad during a significant part of 3 October, 2 November was set as the end of the period in which the data that were the focus of this study were recorded.

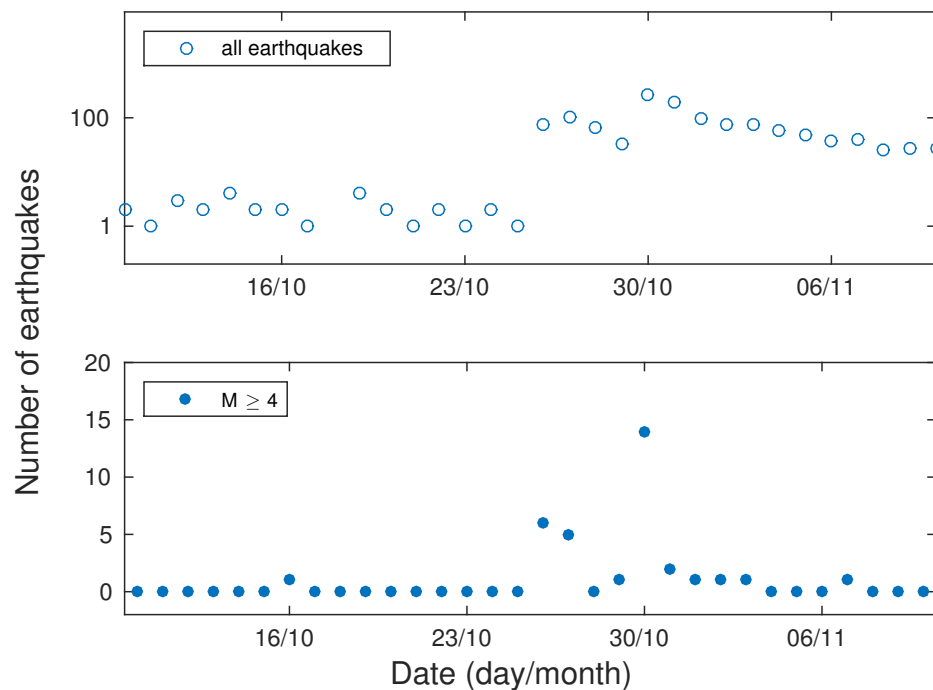


Figure 1. The total number of earthquakes (**upper panel**) and earthquakes with minimum magnitude of 4 (**bottom panel**) that occurred in the period from 10 October to 10 November 2016. The displayed data are taken from the Euro-Mediterranean Seismological Centre website [32]. The boxed part indicates the time period considered in detail in this study.

In this study, we used a VLF signal that monitors the low ionosphere to investigate earthquake precursors. The importance of this technique in research of sudden events such as earthquakes lies in the continuous observation of a large area. Namely, it is based on the operation of numerous transmitters and receivers of VLF signals that are distributed all over the world. In addition, the time resolution of the recorded data can be of the order of milliseconds. This ensures (a) the ability to detect short-term changes that last less than 1 s, and (b) the analysis of somewhat longer changes (lasting several seconds or minutes) that require a lot of data during the disturbance period. Otherwise, the receivers can record the electrical or magnetic component of VLF and LF signals, depending on whether the antenna is electrical or magnetic. Some of them record both the amplitude and the phase of the signal, while others record only one of these signal parameters.

As in previous analyses of excitations and attenuations of small-period waves in the time intervals around the considered earthquakes [27,29,30], we examined the changes in the amplitude characteristics of the VLF signal emitted by the ICV transmitter located in Isola di Tavolara, Sardinia, Italy (40.92 N, 9.73 E) and received by the Absolute Phase and Amplitude Logger (AbsPAL) receiver in Belgrade, Serbia (44.8 N, 20.4 E). The ICV transmitter emits at 20.27 kHz with a power of 20 kW. The used receiver (located at the Institute of Physics Belgrade) has an electrical antenna and records both the amplitude and the phase of VLF/LF signals. It can monitor five signals simultaneously and provides

two data sets with time sampling resolutions of 0.1 s and 1 min. In this study, we used the first data set. The route of this signal and the epicentres of all earthquakes that were recorded in its vicinity during the observed time interval are shown in Figure 2. The locations of the epicentres show that they were dominantly concentrated in a localized area in Central Italy. The classification of the considered earthquakes according to their magnitudes is visualised by the different colours of the dots representing the locations of their epicentres (see explanation in the caption of Figure 2). It indicates that only two stronger earthquakes did not occur in Central Italy (they were registered in Bosnia and Herzegovina and Southern Italy). The characteristics of all shown stronger earthquakes are given in Table 1, where the two highlighted in grey are mentioned.

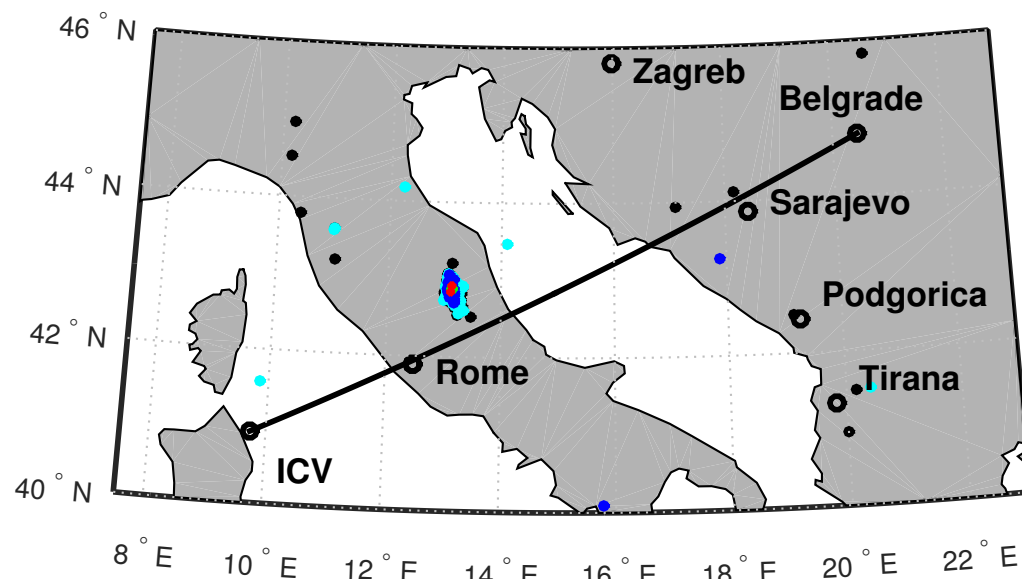


Figure 2. Map of the observed area around the path of the signal transmitted by the ICV transmitter located in Italy and received in Belgrade, Serbia. The epicentres of the earthquakes of magnitudes $M < 3$, $3 \leq M < 4$, $4 \leq M < 5$, $5 \leq M < 6$, and $M \geq 6$ that occurred in the period from 26 October to 2 November 2016 are represented by black, cyan, blue, green, and red dots, respectively.

Table 1. List of the considered earthquakes with magnitudes $M \geq 4$. Data for dates, times, epicentres (latitudes and longitudes), magnitudes, and the corresponding scale (the symbols Mw, mb, and ML denote the moment magnitude [33], body-wave magnitude [34] and Richter [35] scales, respectively) are given in [32].

No	Date	Time (UT)	Latitude (°)	Latitude (°)	Magnitude
DAY 1					
1	26 October 2016	17:10:36	42.88	13.13	Mw 5.5
2	26 October 2016	19:16:57	42.88	13.16	ML 4.3
3	26 October 2016	19:18:07	42.92	13.13	Mw 6.1
4	26 October 2016	21:24:51	42.87	13.08	mb 4.1
5	26 October 2016	21:42:02	42.86	13.13	Mw 4.7
6	26 October 2016	23:52:32	42.82	13.14	mb 4.0
DAY 2					
7	27 October 2016	00:21:32	42.96	13.06	mb 4.2
8	27 October 2016	03:19:27	42.84	13.15	mb 4.4
9	27 October 2016	03:50:24	42.99	13.13	Mw 4.2
10	27 October 2016	08:21:46	42.87	13.10	Mw 4.4
11	27 October 2016	17:22:23	42.84	13.10	ML 4.2

Table 1. Cont.

No	Date	Time (UT)	Latitude (°)	Latitude (°)	Magnitude
DAY 3					
-					
DAY 4					
12	29 October 2016	11:58:07	40.09	15.79	ML 4.3
13	29 October 2016	16:24:33	42.81	13.10	mb 4.4
DAY 5					
14	30 October 2016	06:40:18	42.84	13.11	Mw 6.5
15	30 October 2016	06:55:40	42.74	13.17	ML 4.1
16	30 October 2016	07:00:40	42.88	13.05	ML 4.1
17	30 October 2016	07:05:56	42.79	13.16	ML 4.1
18	30 October 2016	07:13:06	42.73	13.16	ML 4.5
19	30 October 2016	07:07:54	42.70	13.17	mb 4.2
20	30 October 2016	07:34:47	42.92	13.13	ML 4.0
21	30 October 2016	08:35:58	42.83	13.08	mb 4.6
22	30 October 2016	10:19:26	42.82	13.14	ML 4.1
23	30 October 2016	11:21:09	43.06	13.08	ML 4.1
24	30 October 2016	11:58:17	42.84	13.06	ML 4.0
25	30 October 2016	12:07:00	42.84	13.08	ML 4.6
26	30 October 2016	13:34:54	42.80	13.17	ML 4.6
27	30 October 2016	18:21:09	42.79	13.15	ML 4.2
DAY 6					
28	31 October 2016	03:27:40	42.77	13.09	mb 4.3
29	31 October 2016	07:05:45	42.83	13.17	Mw 4.2
30	31 October 2016	09:38:13	43.26	17.88	ML 4.2
DAY 7					
31	1 November 2016	07:56:39	43.00	13.16	Mw 4.9
DAY 8					
32	2 November 2016	19:37:52	42.89	13.11	ML 4.0

3. Data Processing

The investigation of the excitations and attenuations of small-period waves by processing the amplitude of the VLF signal in this study is based on the procedures applied in previous relevant studies [27,28,30]. For this reason, we only list the main features of these procedures in this section. In addition, Figure 3 provides a flowchart that visually explains the processing steps.

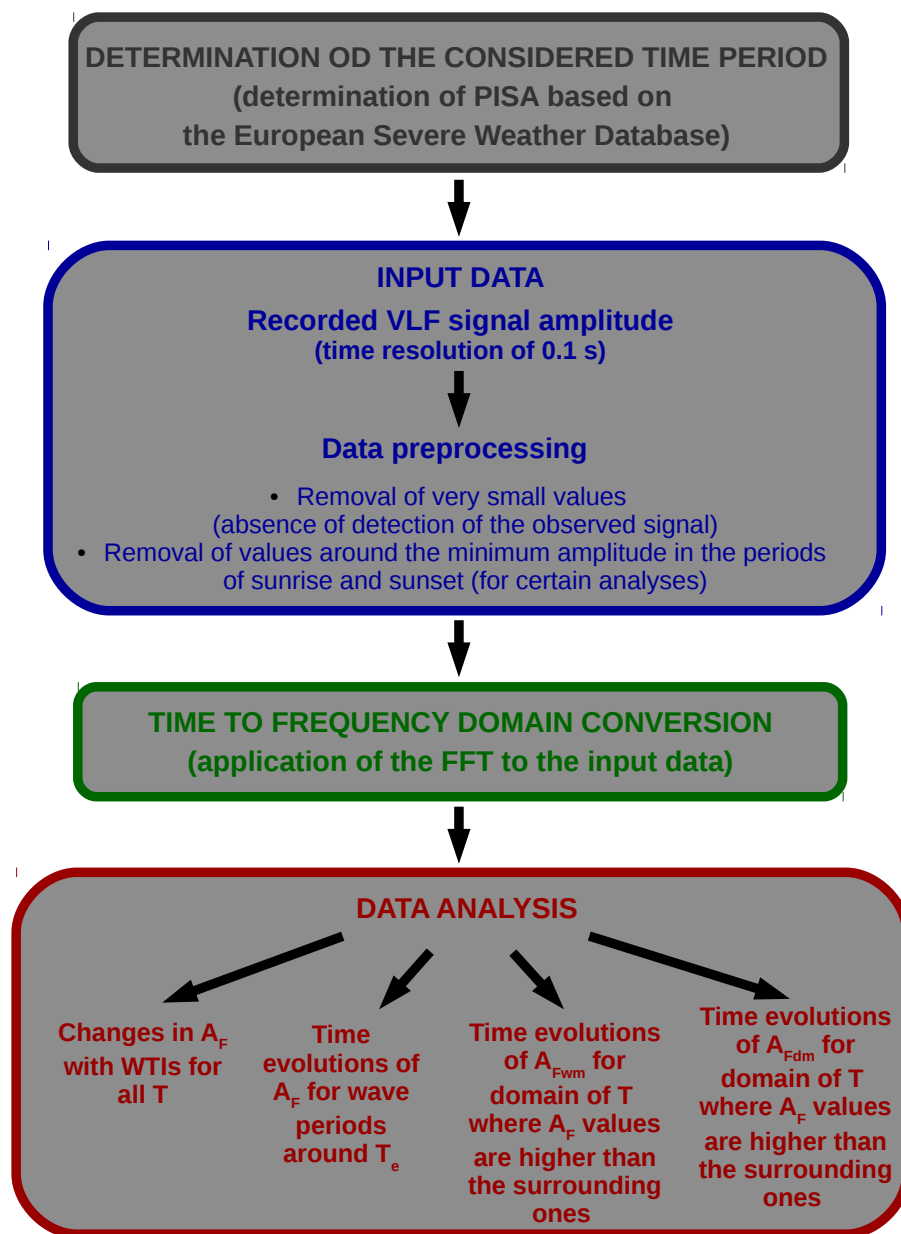


Figure 3. A flowchart explaining the processing steps in this study: (a) determination of the considered time period using the Euro-Mediterranean Seismological Centre [32], (b) determination of the input VLF data and corresponding data preprocessing, (c) time- to frequency-domain conversion using the fast Fourier transform (FFT), and (d) data analysis. Data analysis relates to time dependencies of (i) the Fourier amplitude A_F for all values of wave periods T , (ii) A_F for wave periods around values of T_e for which wave excitations are visible around the time of earthquakes that occurred during PWISA, (iii) mean values A_{Fwm} of A_F , and (iv) daily mean values A_{Fdm} of A_{Fwm} in the window time intervals (WTIs) in the domain of T for which higher values are observed compared to the surrounding ones.

3.1. Input Data

The input data were the values of the ICV signal amplitude recorded by the AbsPAL receiver in Belgrade, Serbia. The time resolution of these data was 0.1 s.

Bearing in mind that not all values of the input data are relevant due to artificial influences (e.g., the signal was not broadcast in certain periods) or due to the dominant influence of other natural phenomena such as sunrise and sunset on their variations,

the data were preprocessed before the analysis in the frequency domain. It consisted in eliminating the data (i.e., replacing them with NaN values) recorded in the periods:

- In which the amplitude values were too low (this indicated the absence of ICV signal detection). This process was carried out for all shown analyses.
- Around the amplitude minima that are characteristic during sunrise and sunset. These data were only eliminated in cases where the increase in A_F was significant and only in determining the mean daily values of the considered parameters.

3.2. Frequency Domain

The analysis in the frequency domain is made possible by applying the FFT to the input data recorded in the time domain. As in previous studies, the FFT was applied to window time intervals (WTIs) of 20 min, 1 h, and 3 h. In this study, the WTIs were shifted by steps of:

- Ten minutes in all three cases in 3D representations of the $A_F(T, t_{ws})$ dependence;
- Twenty minutes for analyses based on determining mean values in 20 min intervals (so all recorded data were included in the analysis, and due to the non-overlapping WTIs, a single value was included in the mean value representing only one WTI).

As in the mentioned earlier relevant studies, the Fourier amplitude A_F was represented as a function of the wave period T , which corresponds to the reciprocal value of the frequency f obtained directly by applying the FFT to the input data ($T = 1/f$). A minimum value of T of 0.2 s was determined as twice the time resolution of the recorded data, and its maximum values depended on the observed WTIs and were half of their values, i.e., 10 min, 30 min, and 90 min.

We emphasise at this point that although we observe dependencies on T , we use the term “frequency domain” in this, as well as in previous relevant studies, because it is the most common term found in the relevant literature and because of the very simple and well-known relationship between these two physical quantities.

3.3. Data Analysis

The data analysis in this study can be divided into four parts:

- **Visualisation of the changes in A_F with WTIs which are represented by the times of their beginnings t_{ws} for all values of T .** The error in the determination of t_{ws} is equal to the time resolution of the recorded data (0.1 s). Bearing in mind that it is significantly smaller than the value of t_{ws} , it can be considered approximately negligible. This also applies to other analyses in which this parameter is used. In the case of an error in the determination of T , there are two cases that depend on the values of T . This explanation is given in [30] and is based on the fact that by applying the FFT to data recorded at equidistant time intervals, equidistant values of f are obtained. Given that $T = 1/f$, the distance between neighbouring values of T increases with it. The distance for small values of T can be calculated as $\Delta T = \Delta f / f^2 = T^2 \Delta f$ where $\Delta f = 1/\text{WTI}$ and has values of 8.3333×10^{-4} Hz, 2.7778×10^{-4} Hz, and 9.2593×10^{-5} Hz for WTIs of 20 min, 1 h, and 3 h, respectively. The error for the higher periods is determined by the absolute difference between a certain value of T and the first larger discrete value of this parameter. In this study, only a visual analysis was performed for higher values of T , so that error was only determined in the first way.
- **Analysis of A_F in WTIs starting at t_{ws} for wave periods around values of T_e for which wave excitations are visible around the time of earthquakes that occurred during PWISA.** We performed analyses for all values of T_e that are specified in [30]: 0.2000 s, 0.2333 s, 0.3500 s, 0.4677 s, 0.7001 s, and 1.400 s. In order to take into account the possibility of more significant changes in very close periods, we considered the maximum value A_F^* of A_F values for the considered T_e and for 5 of its closest larger and smaller values in WTI starting at t_{ws} :

$$A_F^*(t_{ws}) = \max\{A_F^*(T_e(i_e - 5 : i_e + 5), t_{ws})\}, \quad (1)$$

where i_e is the ordinal position assigned to the element that represents T_e in the data array for T . Taking into account the analysis of the error in the determination of T in the previous point and the fact that this analysis is relevant for WTI = 20 min, it can be approximately assumed that in this case, $\Delta T_e = 5 \times 8.3333e^{-4} T_e^2$ s, where T_e is expressed in s.

- **Analysis of the mean values A_{Fwm} of A_F in WTIs starting at t_{ws} in the domain of T for which higher values are observed compared to the surrounding ones.** This parameter was calculated as follows:

$$A_{Fwm}(t_{ws}) = \frac{\sum_{i=1}^N A_F(i, t_{ws})}{N}, \quad (2)$$

where N is the total number of A_F values in the considered WTI for the chosen T domain, and i is the ordinal position of a particular value in this array.

- **Analysis of the time evolution of daily averaged values A_{Fdm} of A_{Fwm} in the domain of T for which higher values are observed compared to the surrounding ones.** This parameter was calculated by the following expression:

$$A_{Fdm} = \frac{\sum_{j=1}^D A_F(j)}{D}, \quad (3)$$

where D is the total number of relevant A_F values in the considered day, and j is the ordinal position of a particular value in this array. We emphasise here that incorrect data were not considered in the respective analyses, so that D was not the same for all days. The analyses were performed both for its absolute values in the considered T domain and for its corresponding relative values r in relation to the reference domain with Fourier amplitude A_{Fdm}^{ref} :

$$r = \frac{A_{Fdm}}{A_{Fdm}^{ref}}. \quad (4)$$

In this way, we analysed the localisation of the observed differences, which is significant because, as seen in Section 4, in some cases, it is clearly visible, while in others, it is not. From this, we can conclude that the corresponding changes in the value of A_F over time have different causes.

The time evolutions of the mentioned parameters related to A_F were also compared with the corresponding time evolutions of the relevant noise amplitude (denoted as A_{noise} when referring to a particular WTI, and $A_{noisedm} = \sum_{j=1}^D A_{noise}(j)/D$ when referring to a particular day). The determination of A_{noise} is explained in detail in [36] and used in [30] and the relevant references therein.

4. Results and Discussion

The investigation of the ICV signal amplitude changes in the frequency domain, which can possibly be linked to processes in the lithosphere during the PISA in Central Italy from 26 October to 2 November 2016, was carried out in two phases. To distinguish the periodic changes that occurred during the day, we first performed an analysis for a quiet period (Section 4.1). Then, we studied the results of the FFT application on the signal amplitude values recorded on the analysed days. In these analyses, A_F and the corresponding parameters are shown (a) for whole days, for all values of T (the dependences $A_F(T, t_{ws})$ are shown in 3D graphs), for the selected values around T_e for which wave excitations were observed in the periods around the considered earthquakes that occurred during PIWSA [30] (we present time evolutions of A_F^* and A_{Fwm}), and (b) for a one-month period that included the eight-day period as well as the periods before and after (we present time evolutions of A_{Fdm}).

In the presented analyses, we excluded the intervals in which the recorded amplitude values were visibly disturbed by unnatural influences (e.g., the time periods in which no signal was emitted). In the analyses covering a period of one month, we also omitted the intervals during sunrises and sunsets in which the amplitude noise was increased. In this way, the influence of these factors on the analyses in the frequency domain was avoided, which is important as they are not always clearly visible on the presented graphs.

4.1. Quiet Conditions

In this analysis, the determination of the characteristics of the considered VLF signal under quiet conditions was complex. Namely, the seismic activity in Central Italy was intensified over a long time period. Therefore, it was not possible to single out an entire day immediately before or after the eight-day interval analysed in this study during which there were no earthquakes. For this reason, the analysis of the reference periods which are intended to show the periodic changes in A_F was carried out for two days:

- On 3 October 2010, when the conditions were quiet and not a single earthquake was recorded.
- On 25 October 2016 (the day before the analysed period), during which the amplitude noise was stable with values around 2 dB except for a short period during the afternoon when an earthquake of magnitude ML 3.9 occurred in Central Italy [29].

It is important to emphasise here that both selected days were in October, as was the beginning of the observed eight-day period. In this way, possible seasonal variations in the amplitude characteristics in the frequency domain were avoided.

4.1.1. First Reference Day: 3 October 2010

The dependence $A_F(T, t_{ws})$ during 3 October 2010 is shown in Figure 4.

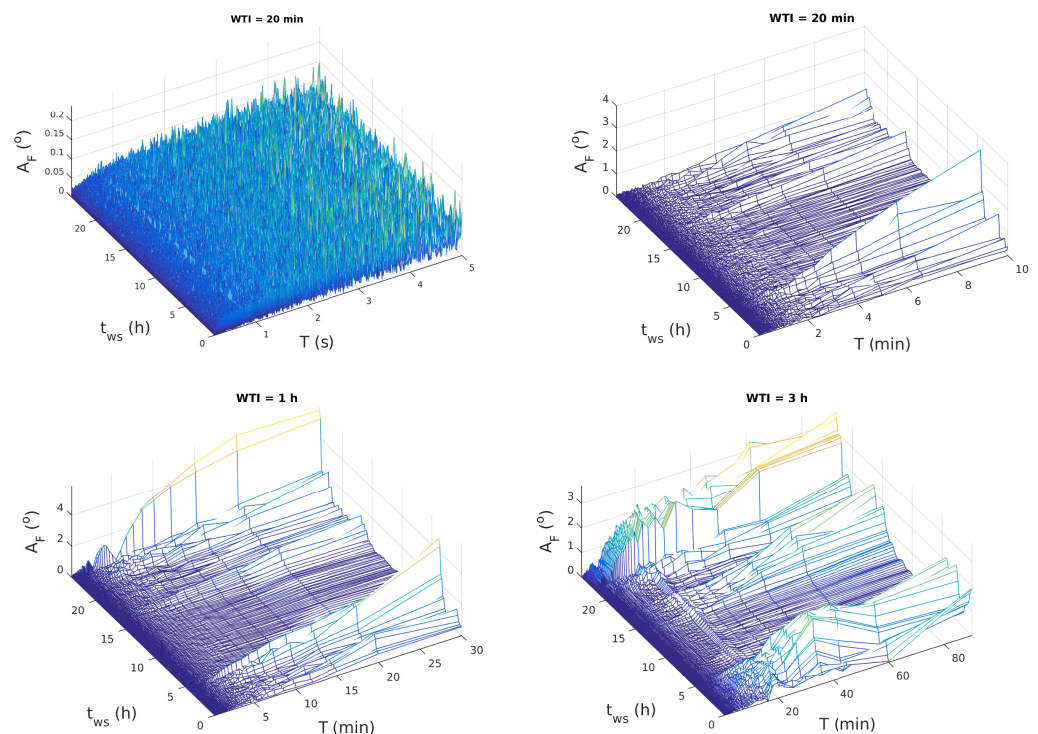


Figure 4. Fourier amplitude A_F of waves with period T obtained by applying the FFT to the ICV signal amplitude recorded on 3 October 2010 with window time intervals (WTIs) of 20 min (**upper panels**), 1 h (**bottom left panel**), and 3 h (**bottom right panel**) starting at t_{ws} .

In the upper left panel, which shows the time evolution of A_F (obtained by applying the FFT to data in WTIs of 20 min) up to $T = 5$ s, no significant changes can be seen. In other words, the potential changes in these domains cannot be periodic daily changes. In the other three panels (upper left panel for WTI = 20 min, and lower left (WTI = 1 h) and right (WTI = 3 h) panels), periodic changes are visible for T greater than about 2 min. They are manifested by increases in the A_F values during the sunrise and sunset periods with the highest values before 5 UT as well as after 15 UT and towards the end of a day.

The lack of changes for $T \leq 5$ s is consistent with the results in the quiet period from 19:00 UT on 3 November 2009 to 4:00 UT on 4 November 2009 [30]. Moreover, the mentioned variations for T longer than a few minutes are consistent with those obtained in the corresponding analyses related to the time periods around the analysed earthquake near Kraljevo (3 November 2010) [27] and the earthquakes near Kraljevo (4 November), in the Tyrrhenian Sea and in the Western Mediterranean Sea [30]. We emphasise here that although these are periods in which earthquakes with a magnitude greater than four occurred, no additional changes due to seismic activity were observed for the mentioned wave periods.

4.1.2. Second Reference Day: 25 October 2016

The dependencies of $A_F(T, t_{ws})$ during 25 October 2016 are shown in Figure 5. Comparing the obtained graphs with the corresponding ones from the previous figure, it can be noticed that the descriptions of the observed variations are very similar, except for the reduction in A_F in the afternoon, when the noise amplitude is also reduced (as already mentioned, this reduction can be associated with an earthquake in Central Italy). The only significant difference is the higher A_F values in the T domain between about 1.4 s and 2 s compared to the values for the other T values during the day.

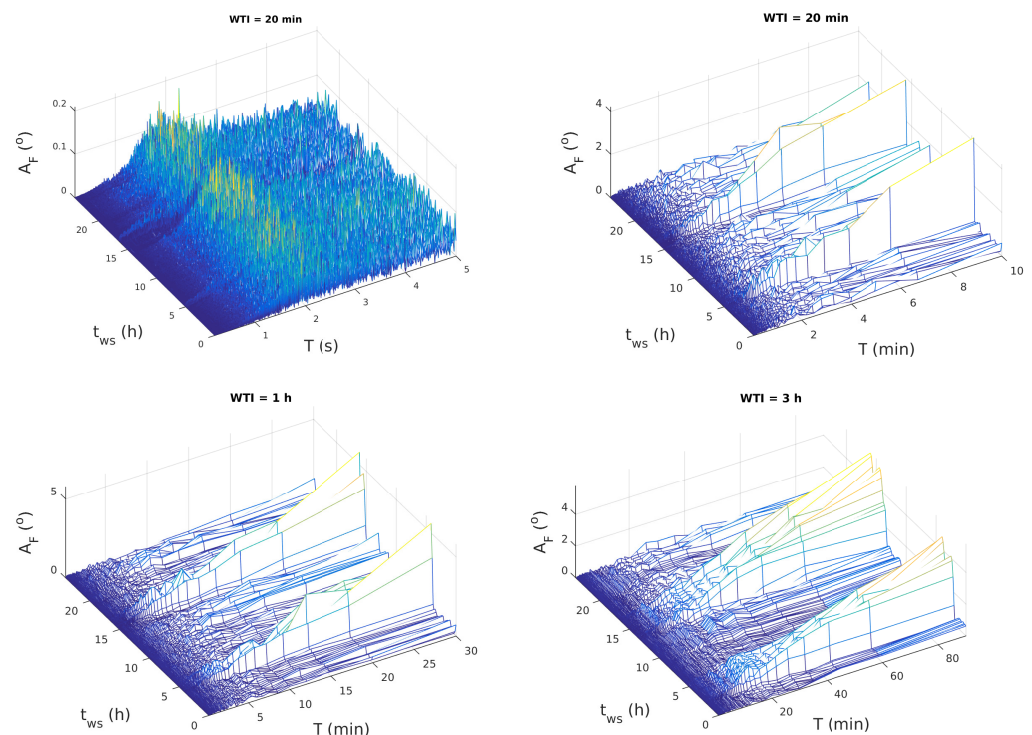


Figure 5. Fourier amplitude A_F of waves with period T obtained by applying the FFT to the ICV signal amplitude recorded on 25 November 2016 with window time intervals (WTIs) of 20 min (**upper panels**), 1 h (**bottom left panel**), and 3 h (**bottom right panel**) starting at t_{ws} .

4.1.3. Comparisons of the Time Evolutions of A_F for Narrow Domains of T during the Observed Reference Days

In previous analyses of earthquakes that occurred during PWISA, wave excitations were observed at discrete T_e values. In addition, higher values of A_F were observed in the domain of T values between 1.4 s and 2 s on the second reference day (Section 4.1.2). To analyse the expected values of A_F under quiet conditions for these specific T , we compared their time evolutions for the considered two days, and their shapes with those of the amplitude noise A_{noise} during the corresponding time periods. The following parameters are shown in Figure 6:

- Upper panels: Maximum A_F values for each t_{ws} for six sets of 11 discrete T values determined around the values 0.2000 s, 0.2333 s, 0.3500 s, 0.4677 s, 0.7001 s, and 1.400 s, respectively (these values and their five closest lower and higher values). Based on the explanation in Section 3, ΔT s for the given T in these analyses are 0.0002 s, 0.0003 s, 0.0006 s, 0.001 s, 0.003 s, and 0.009 s, respectively.
- Middle panels: mean A_F values for T between 1.4 s to 2 s for each t_{ws} .
- Bottom panels: the time evolutions of A_{noise} given in [29].

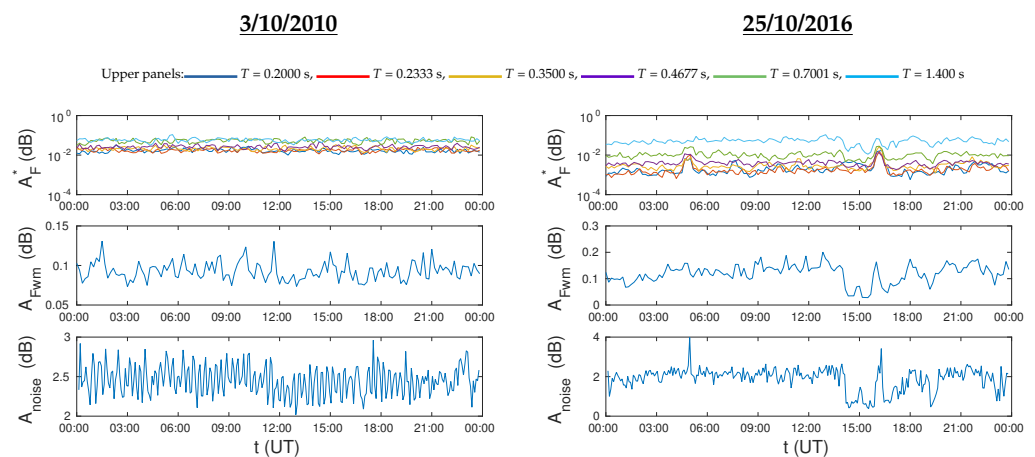


Figure 6. Time evolutions of the maximum values of the Fourier amplitude A_F^* for the observed wave periods T_e and the five closest high and low values (**upper panels**), the mean values of the Fourier amplitude A_{Fwm} for the wave periods T in the domain 1.4–2 s (**middle panels**), and the amplitude noise A_{noise} (**bottom panels**) in each window time interval (WTI) starting at t_{ws} for the reference days 3 October 2010 (**left panels**) and 25 October 2016 (**right panels**).

In the upper left panel, it can be seen that all displayed dependencies for the first reference day vary around very similar values throughout the day. This indicates that there is no significant influence of solar radiation and its changes on the observed values of A_F^* , A_{Fwm} and A_{noise} . In this case, all values of A_F^* are approximately within one order of magnitude. Comparing the values of A_{noise} in the lower panels shows that its value is slightly lower for the second reference day. A more significant difference for the two observed days is visible in the upper panels. Namely, during the second day, a decrease in A_F^* is visible for all T_e except for $T_e = 1.4$ s. This difference increases with a decrease in T_e and is more than 10 times greater for $T_e = 0.2$ s. In the case of A_{Fwm} , higher values are observed for the second reference day. In other words, these comparisons for a quiet day outside the PISA and quiet parts of a day just before the PISA show a decrease in A_F values for the considered $T < 1.4$ s and their increase for the T domain from 1.4 s to 2 s for the second considered day.

In the analysis of the second day, it is interesting to note that the reduction in A_{noise} in the afternoon is followed by a decrease in A_F^* for all observed values of T_e , except for its lowest value (0.2 s) where an increase in A_F^* is observed (this corresponds to the wave excitation at this wave period). This is important to emphasise because this reduction in

the amplitude noise can be related to the earthquake that occurred during its duration. However, the wave excitation at this T_e in periods around earthquakes that occurred during PWISA were only registered for one event in the amplitude and phase analyses, which is why they could not be associated with seismic activity based on previous analyses.

In addition, it can be seen that the effects of sunrise and sunset during the second reference day, which are seen as peaks in the time evolution of A_{noise} , cause increases in A_F^* for lower values of T_e , while no pronounced changes are seen for the highest observed T_e and for the domain of T from 1.4 s to 2 s.

4.2. Seismic Active Period

As in previous relevant studies [27,28,30] and in Section 4.1, the analysis of ICV signal amplitude characteristics in the frequency domain was performed by applying the FFT to data sets recorded with a time resolution of 0.1 s, and to WTIs of 20 min, 1 h, and 3 h. The time evolutions of the processed signal amplitude during the observed days (from 26 October to 2 November 2016) are given in [29].

Bearing in mind that each displayed data point refers to the entire considered WTI, the accuracy of determining the time of occurrence of changes depends on its duration, and it was the best for WTI = 20 min and worst for WTI = 3 h. For this reason and due to the fact that the maximum relevant values of T are equal to half of the time interval to which the FFT is applied, the analysis of the changes was performed separately for three domains of T . These domains were between 0.2 s and 10 min (small wave periods), 10 min and 30 min (medium wave periods), and 30 min and 90 min (large wave periods), where A_F was obtained by applying the FFT to WTIs of 20 min, 1 h, and 3 h, respectively.

In the following analyses, the incorrect values were discarded as follows:

- The data in the period 9:00 UT–12:20 UT on 31 October were not processed in all analyses, as no ICV signal was detected in that period. This can be seen from the time evolution of its amplitude which is shown in [29]. For the same reason, the data from parts of several days that were considered for examining the beginnings and ends of multi-day changes were removed.
- In the case of an increased A_F , the recorded data in the periods of sunrise and sunset were not taken into account in the analyses of the daily values of A_{Fwm} and A_{noise} .

In this way, the influence of changes in the signal characteristics due to clearly visible artificial influences and other phenomena that occurred at sunrise and sunset was avoided. In the time periods relevant to the second case, A_F was displayed in 3D graphics to visualise the effects of changes in incident radiation in the morning and evening. This is also interesting because in previous studies, no differences were visible for small values of T in these periods of the day compared to others.

4.2.1. Small Wave Periods

Based on the results of previous studies and the changes presented in Section 4.1, it can be concluded that analysing wave changes in the small-wave-period domain is the most important. In this domain, we analysed the following:

- The existence of wave excitations at T_e of 0.2333 s, 0.3500 s, 0.4677 s, 0.7001 s, and 1.400 s, which were visible in the cases of the previously analysed earthquakes that occurred during PWISA;
- Values of A_{Fwm} for the domain T from 1.4 s to 2 s, which were higher than other close values of T on almost all days from 26 October to 1 November;
- Attenuations of the waves at low wave periods.

Analyses of 3D graphs: The 3D graphs obtained by applying the FFT to the WTI of 20 min are shown in Figure 7 in two parts for each day, as the A_F values for lower and higher values of T were very different. The threshold value was $T = 5$ s. Low values are shown on the left, and higher values on the right.

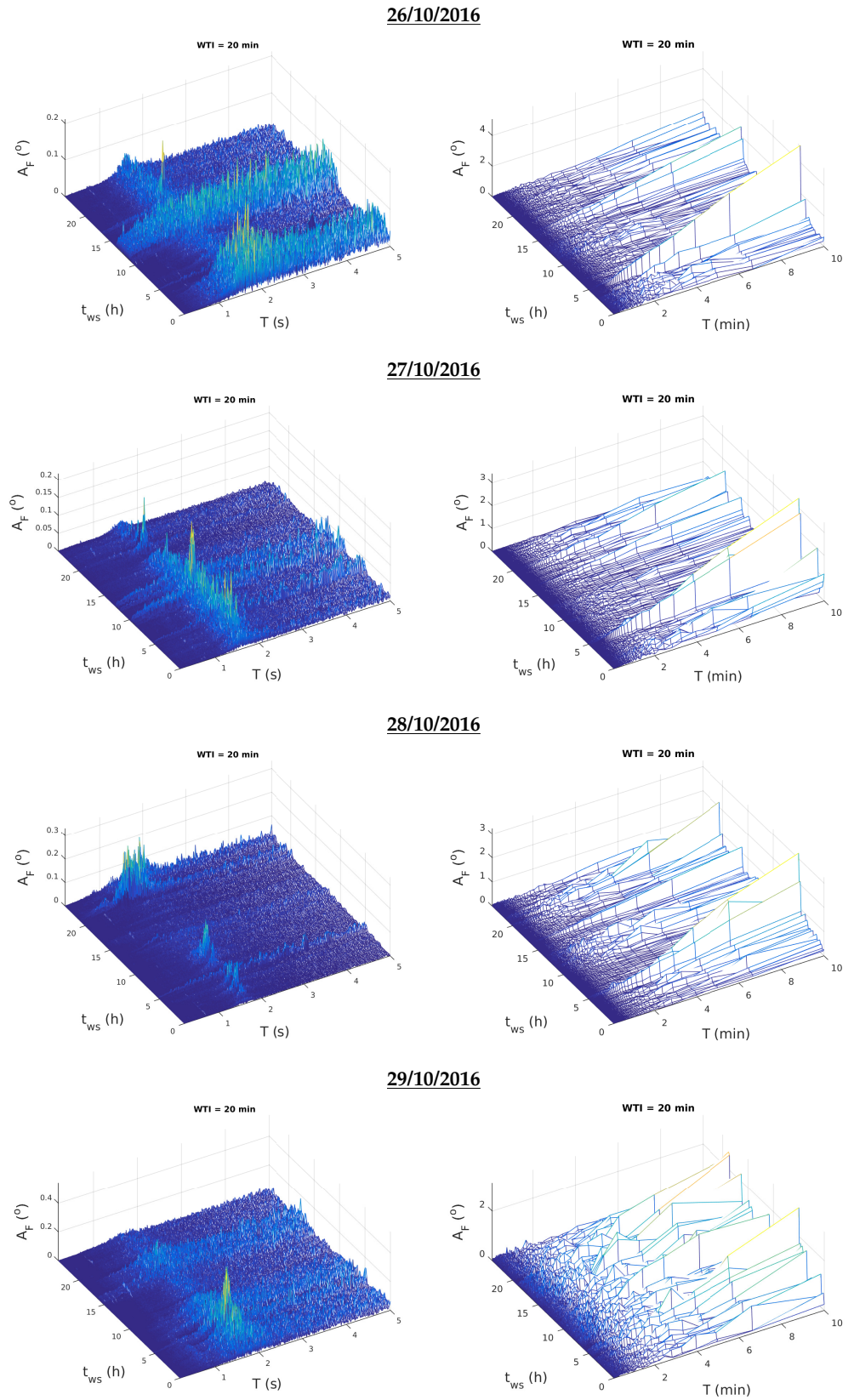


Figure 7. Cont.

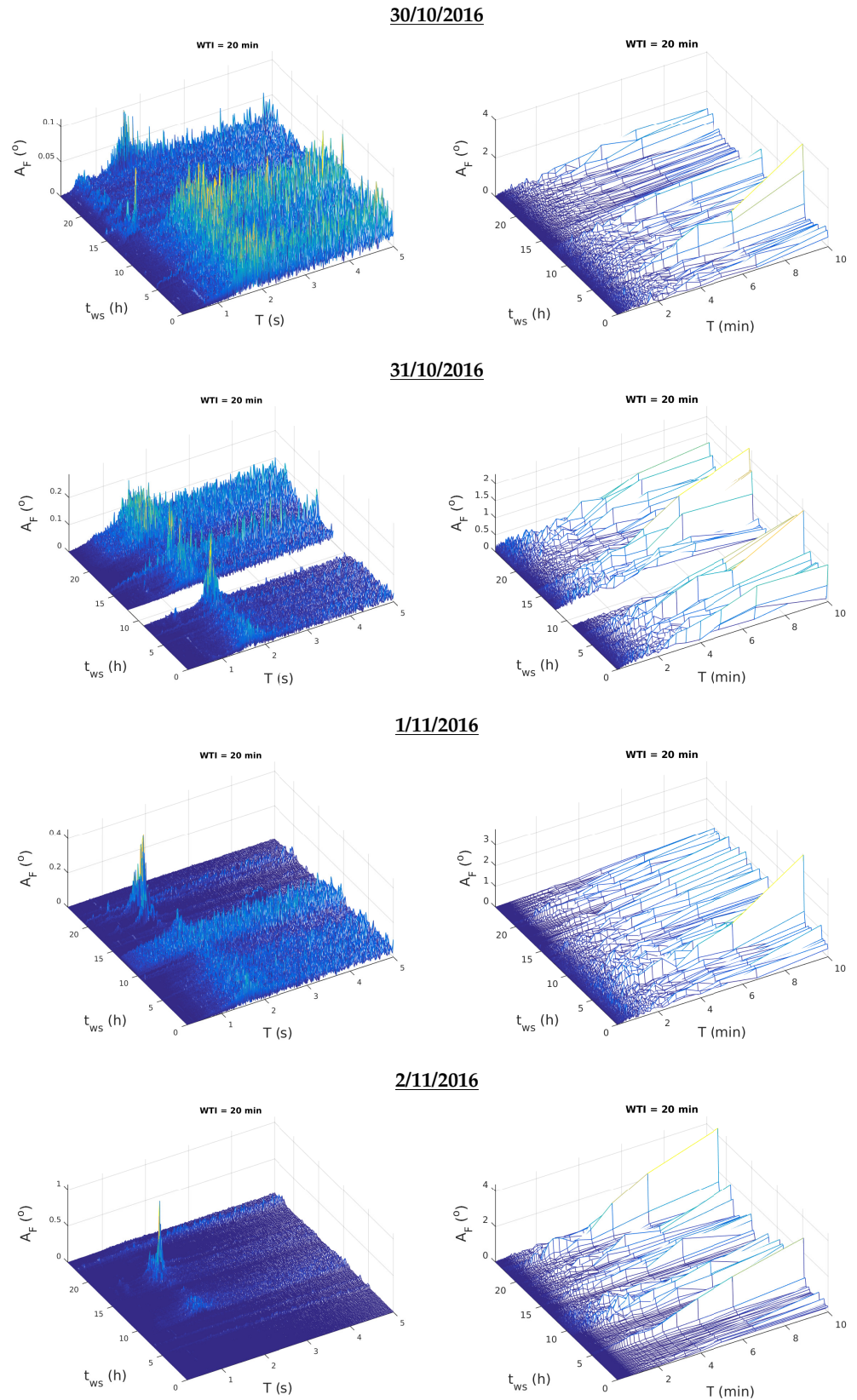


Figure 7. Dependencies of the Fourier amplitude A_F on the wave period T and the start time t_{ws} of the window time intervals (WTIs) from 26 October to 2 November 2016. The results of applying the fast Fourier transform to the WTI of 20 min for $T \leq 5$ s and $T > 5$ s are shown in the left and right panels, respectively.

Before analysing the wave excitations and attenuations, it is important to note the following changes compared to the results of the analyses of the reference days in Section 4.1 and the studies presented in [27,30]:

- With the exception of time intervals of a few hours on 26, 29, and 31 October and on 1 November, the A_F values for $2 \text{ s} < T \leq 5 \text{ s}$ were significantly lower than the values given for the reference days in Figures 4 and 5. During the isolated intervals, A_{noise} was approximately equal to the values recorded on quiet days (see [29] and Figure 8).
- Although it is not noticeable on the 3D graphs due to the significantly smaller values of A_F compared to their maximum, the values of this parameter for a small T were about an order of magnitude smaller than the values recorded on the first reference day (3 October 2010), which was also true for the values recorded on 25 October 2016 (the second reference day). This can be clearly seen in Figure 8.
- When the A_F values were small in the periods of sunrise and sunset, smaller increases in A_F were observed for $T \leq 5 \text{ s}$ in the short term.

From the 3D graphs presented in Figure 7, it can be seen that there are no long-term pronounced increases in A_F at discrete values of T , including those for which wave excitations with onset prior to the observed earthquakes were visible in previous studies. Although short increases in A_F compared to its surrounding values were observed on all days, the obtained values were lower than those observed on quiet days.

Higher values of A_F in the domain of T from 1.4 s to 2 s compared to the others for $T < 5 \text{ s}$ were observed on all days from 26 October to 1 November with shorter interruptions on 26, 27, and 30 October. However, these higher values were only approximately comparable to those obtained on quiet days, except in short-term periods when significant increases were visible. These increases were observed on all days except 30 October and are analysed in more detail in the description of Figure 8.

On the last observed day, the A_F values were very low throughout the day, with the exception of shorter intervals for the isolated domain T (around 9 UT and 17 UT). In the second case, A_F reached the highest values in the observed eight-day interval (about 1 dB).

In addition to the mentioned variations, a shift of higher A_F values from the mentioned domain to the domain of T values from about 0.4 s to about 1 s was observed. In the observed time interval, this change was only registered on 30 October. The largest number of earthquake occurred on that day (268, see Figure 1). However, they occurred throughout the day and it is not possible to establish a connection between the aforementioned changes and the occurrence of an earthquake. On the other hand, the time evolutions of the signal amplitude and its noise indicated a sharp decrease in the value of both these signal parameters (amplitude noise reduction of Type 3) in the period of the shift of higher A_F values to smaller wave periods. The ends of the mentioned changes in all three parameters were towards the end of that day when the higher values of A_F returned to the original domain of T with higher values.

The comparison of time evolutions of A_F for small wave periods for $T > 5 \text{ s}$ (right panels in Figure 7) with corresponding graphs for reference days (upper right panels in Figures 4 and 5) shows that there are no significant changes that can be associated with the PISA. Namely, the largest increases in A_F for these values of T were before 5 UT, after 15 UT, and toward the end of a day or around midnight, which was already registered during the two observed days in Section 4.1. The only changes could be observed on 1 November, when the latter two mentioned increases were not observed due to lower values of A_F in that period of the day than in other cases, but they could not be associated with seismic activity.

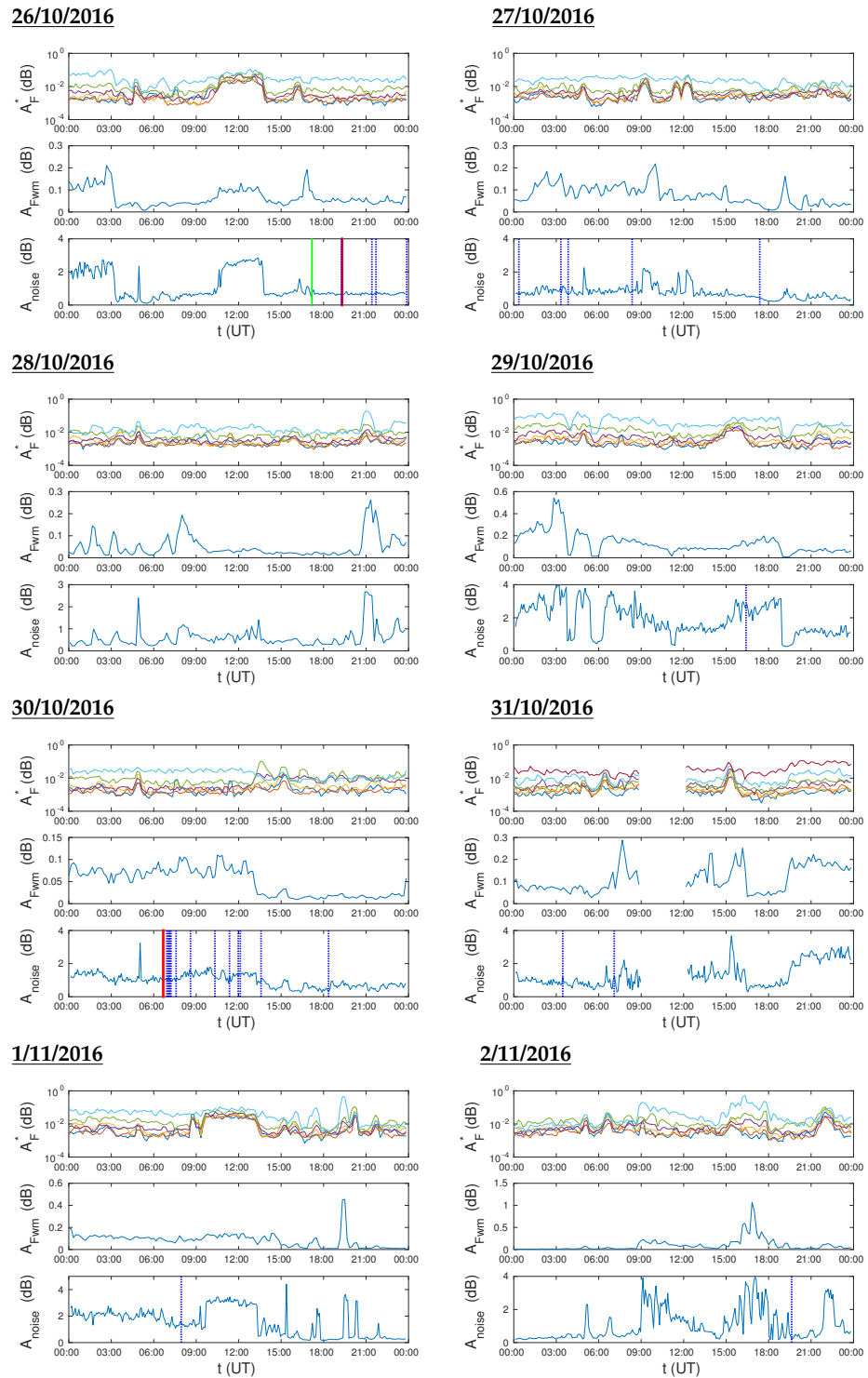


Figure 8. Time evolutions of the maximum values of the Fourier amplitude A_F^* for the observed wave periods T_e and the five closest higher and lower values (**upper panels**), the mean values of the Fourier amplitude A_{Fwm} for the wave periods T in the domain 1.4–2 s (**middle panels**), and the amplitude noise A_{noise} (**bottom panels**) in each window time interval (WTI) starting at t_{ws} for the period from 26 October to 3 November 2016. The shown blue, green, and red vertical lines indicate the times of the earthquakes with magnitudes between 4 and 5, between 5 and 6, and greater than 6, respectively.

Analyses of A_F^* for the wave periods T_e and $A_{F_{wm}}$ between 1.4 s and 2 s. To visualise and compare the described changes in the Fourier amplitude more clearly and to compare the changes in the frequency and time domains, we show the relevant dependencies in Figure 8. The time evolutions of A_F^* for T_e and the mean values $A_{F_{wm}}$ of A_F for T in the domain 1.4–2 s are presented in the upper and middle panels, respectively. The time evolution of A_{noise} is given in the lower panels, where the times of the earthquakes in Central Italy given in Table 1 are marked with vertical lines. The values for A_F^* and $A_{F_{wm}}$ are determined using the procedure explained in Section 3, while the procedure for the determination of A_{noise} is developed in [36] and explained in earlier studies (see [30] and references therein).

As one can see in the middle panels of Figure 8, significant short-term increases in the $A_{F_{wm}}$ values were observed on all days except 30 October. Their maxima were sometimes preceded by the maxima of A_F^* at all T_e (except in some cases for its maximum value). However, due to the occurrence during the larger values of A_{noise} and due to the end before the shown times of stronger earthquakes, these wave excitations had different characteristics than those recorded in previous studies at T_e (they lasted throughout the reduction in the signal amplitude noise and end after the considered earthquake). Moreover, there was no regularity in their occurrence with respect to the occurrence of stronger earthquakes, which is why they are probably the consequence of other phenomena.

The analysis of the shapes of the displayed dependencies indicated that there were no wave excitations at low periods T_e and in the observed domain T from 0.4 s to 2 s in the periods around the stronger shown earthquakes. At the same time, it can be seen that these shapes were more similar to the shape of the time evolution of A_{noise} . In addition, if we compare their values with the relevant values obtained for the reference days, we can conclude that they are more similar to the reference day that preceded the observed PISA. This is very important because it opens the question of whether the PISA can be predicted on the basis of these parameters (or whether long-term seismic activity can be expected after the first strong earthquake). This possibility should be examined in the analyses of the beginnings of a statistically significant number of PISAs.

Long-term analysis of $A_{F_{dm}}$ for T between 1.4 s and 2 s. As already mentioned, seismic activity was present in Central Italy before and after the observed PISA. In addition, the analysis of the amplitude noise in [29] in October 2016 (end of 24 October) showed that its values were below 2 dB, which differed from the expected state in quiet conditions. Only two multi-hour periods were observed in this interval (approximately from 3 UT to 8 UT on 13 October and from 6 UT to 11 UT on 15 October), which can be provisionally considered as quiet periods.

In this study, we investigated the daily mean values of $A_{F_{wm}}$ in the T domain from 1.4 s to 2 s, denoted as $A_{F_{dm}}$, in a one-month time interval from 10 October to 10 November 2016. In addition to analysing the absolute values of this parameter, we give their ratio ($r = A_{F_{dm}} / A_{F_{dm}}^{ref}$) to the corresponding values of $A_{F_{dm}}^{ref}$ in the reference domain T , which was taken from 2.4 s to 3 s (no deviations in A_F in this domain from the corresponding values for the surrounding values of T were recorded). The obtained results are shown in Figure 9, where the bottom panel shows the daily mean averaged values of the amplitude noise (this time evolution was added to compare the changes in the time and frequency domains). In contrast to the analysis in [29], all shown values were determined only for intervals in which their values were not influenced by other known factors (see Section 4).

In the upper panel of this figure, the variations in $A_{F_{dm}}$ with the maximum value of 0.4517 dB (17 October) can be seen. Bearing in mind that the corresponding value for 3 October 2010 and the first half of 25 October 2016 (when no earthquakes were recorded) were 0.0929 dB and 0.1236 dB, respectively, it can be concluded that $A_{F_{dm}}$ was smaller than the expected values during quiet conditions in the entire considered period. The smallest values were found at the beginning and at the end of the observed interval, when larger relevant values were obtained for the reference T domain (seen in the middle panel ($r < 1$)). The peak values were visible throughout the entire observed interval, so they could not

be associated with the PISA. On the other hand, higher values of A_{Fdm} were obtained in relation to A_{Fwm}^{ref} during the entire considered PISA (more significant deviations were obtained on 6 out of 8 days), which was not the case in the periods before and after. Namely, the relevant increase was only visible on 13 and 23 October, while the considered values were similar for other days (r was approximately one). If we compare the upper and middle panels with the bottom one where the values of $A_{noisedm}$ are given, we can see similar shapes of the changes in A_{Fdm} in the frequency domain with the specified parameter in the time domain. Looking at the variations in r , it can be concluded that the changes in the time domain are more visible at the lower observed values of T .

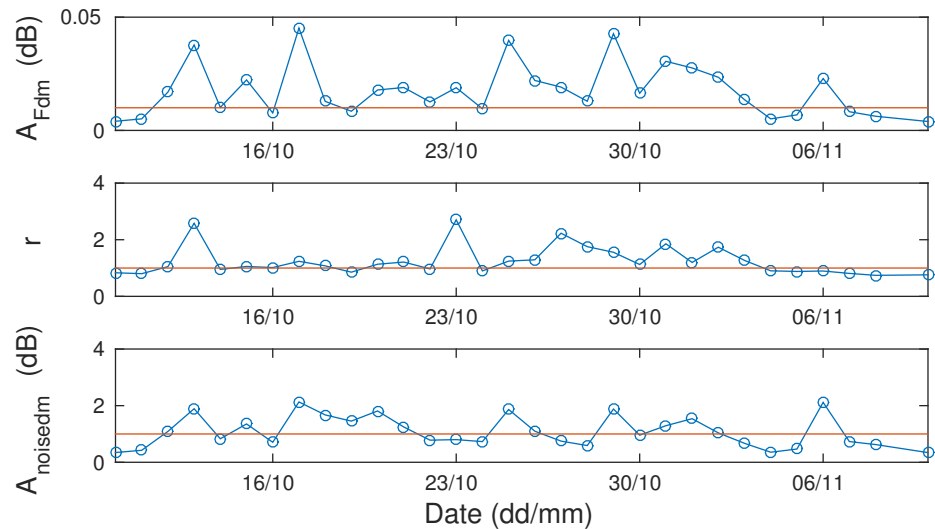


Figure 9. Time evolutions of the daily average values of A_{Fwm} in the T domain from 1.4 s to 2 s, denoted as A_{Fdm} (**upper panel**), its ratio (r) to the corresponding values of A_{Fwm}^{ref} in the reference domain T , ranging from 2.4 s to 3 s (**middle panel**), and the daily mean amplitude noise $A_{noisedm}$ (**bottom panel**) for the period from 10 October to 10 November 2016.

The mentioned changes before and during the PISA are potential precursors of this period in the frequency domain. Their differences from the changes recorded before the earthquake during PWISA are very significant as they can indicate long-term earthquake hazards. As in previous relevant studies, these assumptions should be tested in statistical analyses. Analysing other independent data is also necessary to explain the detected changes. Namely, VLF signals spread between transmitters and receivers located several hundred or thousand kilometres apart in the Earth-ionosphere waveguide, which is over 70 km high during the daytime and over 80 km high during the nighttime. As the amplitude and phase values recorded by a receiver provide information about the integral changes of a signal in this entire space, it is not possible to spatially localise the cause of the detected changes using these measurements alone.

4.2.2. Medium and Large Wave Periods

To analyse medium (10–30 min) and long (30–90 min) wave periods, we used the results of the FFT application on WTIs of 1 h and 3 h, which are shown in Figures 10 and 11. The conclusions from comparing these graphs with the corresponding graphs in Figures 4 and 5 are the same as those mentioned in Section 4.2.1 for $5\text{ s} < T \leq 10\text{ min}$. In other words, no changes that can be associated with seismic activity were observed in these T domains compared to the reference days.

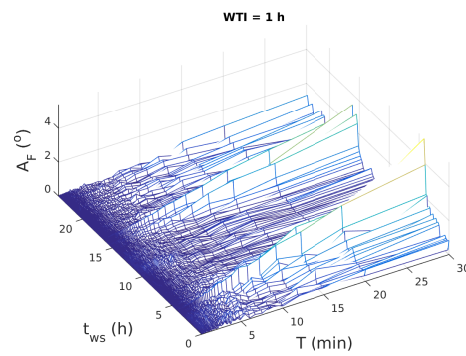
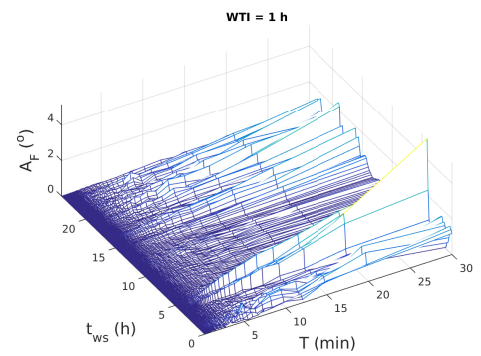
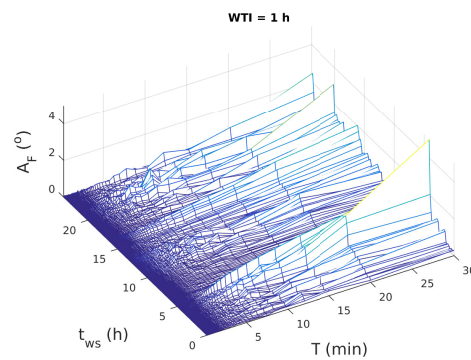
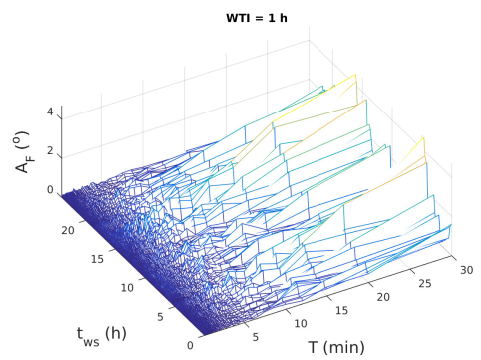
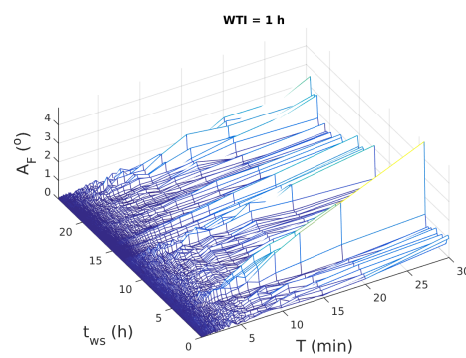
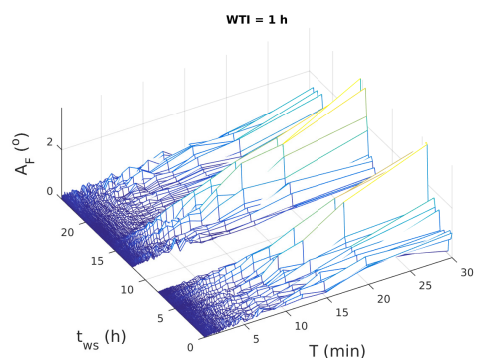
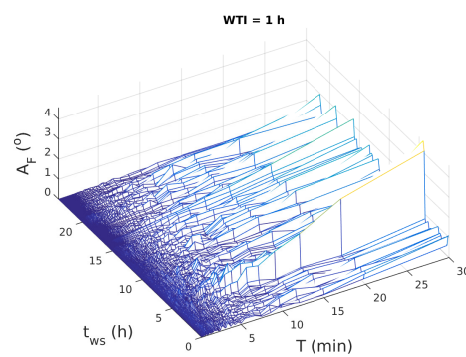
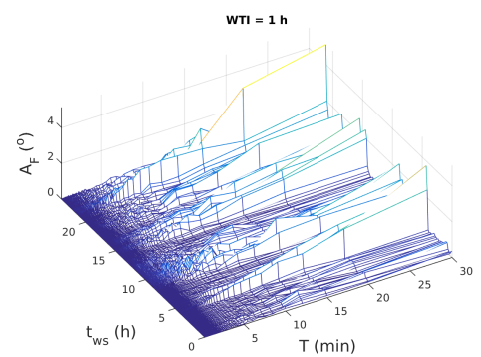
26/10/2016**27/10/2016****28/10/2016****29/10/2016****30/10/2016****31/10/2016****1/11/2016****2/11/2016**

Figure 10. Dependencies of the Fourier amplitude A_F on the wave period T and the start time t_{ws} of the window time intervals (WTIs) of 1 h from 26 October to 2 November 2016.

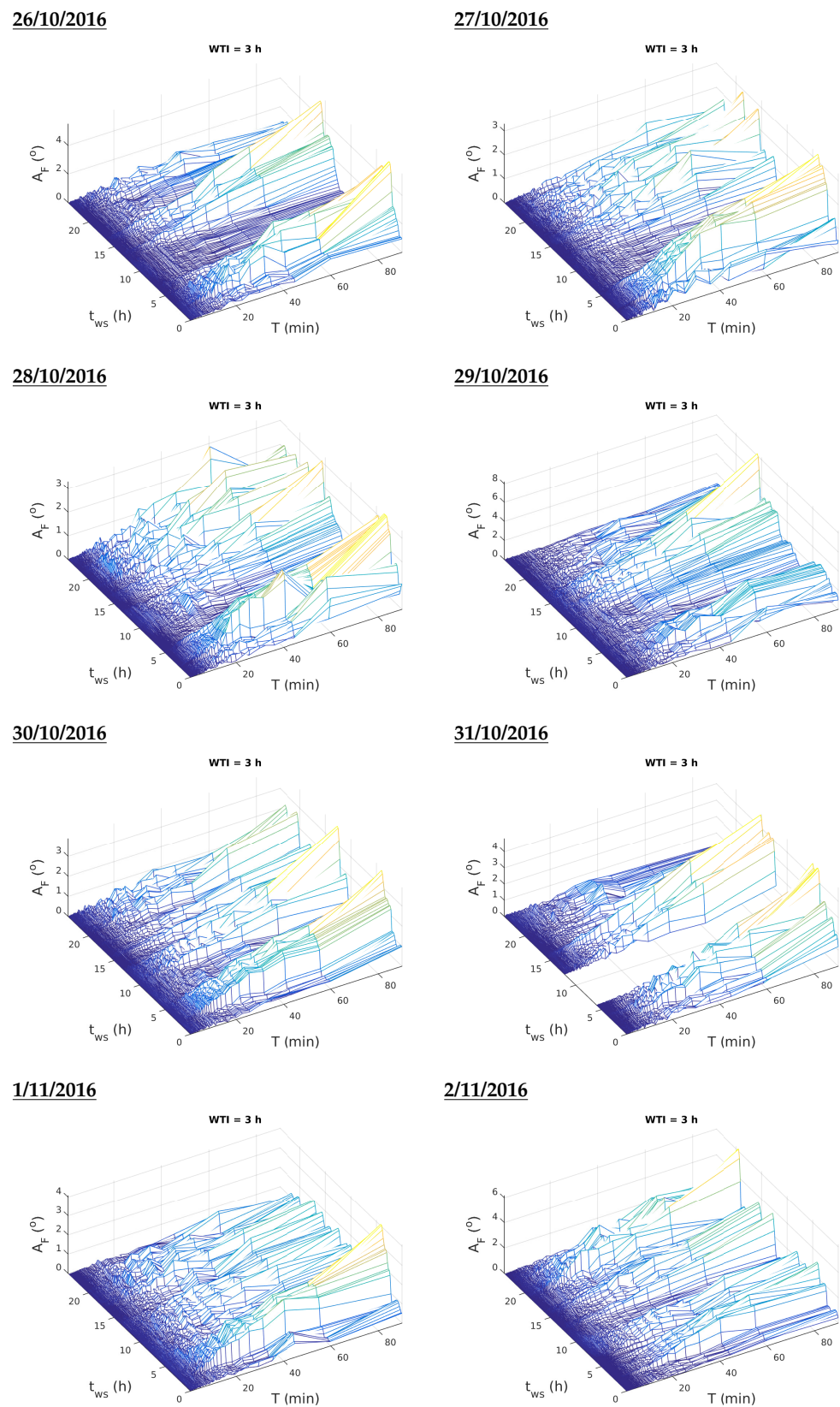


Figure 11. Dependencies of the Fourier amplitude A_F on the wave period T and the start time t_{ws} of the window time intervals (WTIs) of 3 h from 26 October to 2 November 2016.

We point out here that the upper limit of T of the domain in which A_F values are lower than expected in a quiet period is several minutes or in the domain of medium wave periods. Its exact determination is not possible due to the long time period of the aforementioned reduction and variability in A_F , and also due to the fact that the determination of this parameter is approximately possible even for short time intervals of a few dozens of minutes.

4.3. Analysis of the Reliability of the Relationship between Recorded Signal Changes and Seismic Activity and Possible Influences of Other Phenomena

Changes in VLF signals used to monitor the ionosphere can be the result of numerous influences from processes and phenomena both from space and from the Earth's layers. They relate to meteorological and geomagnetic conditions (influences of changes in the atmosphere on VLF signals are shown in numerous papers, see, e.g., [37] and references therein), as well as to extraterrestrial radiation (changes in the VLF signal are most strongly influenced by solar X-ray flares [38–43], and the possibility of a multi-hour influence of gamma ray bursts on these signals has also been confirmed [44]).

In some cases, changes in VLF signals caused by different phenomena have the same or very similar characteristics. In addition, the detection of some phenomena depends on a large number of parameters, leading to differences in their characteristics. Therefore, statistical studies are necessary to confirm certain correlations. In the case of earthquakes, this confirmation is very complex because the perturbations are local, and there are numerous parameters that can influence detection. They relate to:

- Earthquake characteristics (characteristics of the location where it occurred, the depth at which it occurred, its magnitude);
- The occurrence of other earthquakes (near the epicentre of the observed earthquake or at distant locations that are also near the propagation path of the observed signal) and their characteristics;
- The epicentre position in relation to the propagation path of the observed signal (their mutual distance, the epicentre position in relation to the considered transmitter and receiver);
- The state of the atmosphere during the analysed period;
- Characteristics of the observed signal, including parameters relevant to the observed transmitters and receivers.

For these reasons, research into the relationship between changes in the VLF signal and seismic activity should be divided into the following phases:

- Phase I: diagnostics of changes that can be regarded as potential precursor of an earthquake given the defined characteristics of the recorded parameters.
- Phase II: determining the parameters that characterise these changes based on the smaller number of earthquakes in the case of PWISA, or the smaller number of PISAs, and the appropriate criteria to distinguish them from other potentially similar changes caused by other phenomena.
- Phase III: analysis of these parameters and criteria using a statistically significant number of appropriate samples for one signal.
- Phase IV: appropriate statistical analyses for several transmitters and receivers, which should (a) verify the results obtained in the previous phase and reveal possible differences for different signals and receivers and (b) provide detailed analyses of the observed changes in space.

The development of suitable warning systems can begin only after the potential confirmation of the observed connections, the definition of relevant parameters and criteria for different conditions in the mentioned phases, and the development of software for the automatic detection of defined changes.

Relevant studies on VLF signal changes a few minutes or dozens of minutes before an earthquake are recent (the first paper was published in 2020) and can be considered as pilot studies. In the case of the earthquake precursor analyses during PWISA, there are studies relevant for Phase I and II, and investigations for Phase III are ongoing. In the case of the PISA,

the studies in Phase I are still ongoing. Our plan is to continue this research in all remaining phases, which includes not only analysing the data but also forming a new network of relevant receivers and involving other researchers and/or groups in further work.

It is important to emphasise that there were no significant impacts of other natural phenomena during the observed period. This analysis is given in [29] and refers to the influence of meteorological and geomagnetic conditions. These checks were carried out on the basis of the data presented in [45–47]. In addition, technical problems during reception were excluded in the aforementioned study.

5. Conclusions

This study presented an analysis of the VLF signal amplitude in the frequency domain during a period of intense seismic activity in Central Italy, where 907 earthquakes were registered from 26 October to 2 November 2016. The presented research was carried out within the framework of the investigation of new potential earthquake precursors, which manifest themselves in changes in VLF signal amplitude and phase characteristics in the time (reduction of amplitude/phase noise) and frequency (excitation and attenuation of waves at small periods) domains. In general, the contribution of this investigation to the relevant studies on earthquake precursors is the result of the improvement of the observed data time resolution from the usual several dozens of seconds or minutes to 0.1 s. This made it possible to see the following:

- A reduction in the VLF signal amplitude and phase noises;
- The detection of excitations and attenuations of waves at small wave periods, which can be less than 1 s.

These were not observed with the previously used data. These changes started only a few minutes or a few dozens of minutes before an earthquake, which is a significantly more accurate prediction than other methods that detect changes a few days before an earthquake. In addition, the existence of differences in the observed changes indicated the potential possibility of predicting long-term earthquake hazards.

In this study, relevant analyses in the frequency domain related to the seismically active period were presented for the first time. They represented a continuation of the research given for the time domain, in which the changes before earthquakes in that period were already shown in the form of long-term reductions in the amplitude noise.

The results presented in this study were obtained by processing the amplitude values of the signal emitted by the ICV transmitter in Italy and received in Belgrade, Serbia. They showed changes in the observed amplitude characteristics compared to quiet conditions and differences compared to changes observed in periods around earthquakes that did not occur during the period of intensive seismic activity in the localized area. The conclusions of the presented research are as follows:

- Changes in the observed period relative to quiet conditions were visible for small values of the considered wave periods. This is consistent with previous analyses of earthquakes that did not occur under the considered seismic conditions.
- Reduced values of the Fourier amplitude (indicating wave attenuation) were visible in a longer time interval (a longer time interval was observed from 10 October to 10 November). Therefore, it was not possible to determine whether this change was related to seismic activity or caused by some other influence.
- In the domain of wave periods from 1.4 s to 2 s, higher values of the Fourier amplitude (close to the values expected in quiet conditions) were observed compared to its values for near wave periods. This increase was evident during and just before the observed period, indicating the possibility of a link with seismic activity.
- Wave excitations at discrete values of wave periods below 1.5 s, found in previous studies associated with earthquakes that did not occur during intense seismic activity, were not registered.

Even if there is no correlation with seismic activity, it is interesting that the Fourier amplitude for wave periods of less than 5 s increased in the periods around the minimum signal amplitude during sunrise and sunset. These values were much smaller than those recorded during quiet days, which is why the corresponding changes were not observed under quiet conditions.

Since the changes compared to quiet conditions were noticeable and different from those observed in the analyses of earthquakes that did not occur during periods of intense seismic activity, this study indicates the possibility of predicting relevant hazardous periods.

The main limitation of this study is the fact that only one period of intense seismic activity was considered. For this reason, it is necessary to perform the presented analyses for a larger number of these periods in order to obtain statistically significant conclusions and to be able to make a more reliable comparison with changes in VLF signal amplitude characteristics before earthquakes that occur during and outside of these periods. To study the possibility of defining the relevant parameters related to the reduction in the Fourier amplitude and the occurrence of their higher values in certain domains of the wave periods is of utmost importance for the prediction of the duration of the earthquake hazard. For this reason, it is important to point out that it is necessary to include the relevant databases of as many groups as possible in this investigation in order to collect a statistically significant number of these periods.

Funding: The author acknowledges funding provided by the Institute of Physics Belgrade through the grants by the Ministry of Education, Science, and Technological Development of the Republic of Serbia.

Data Availability Statement: Publicly available datasets were analysed in this study. These data can be found at <http://www.emsc-csem.org/Earthquake/> (accessed on 8 April 2021). The VLF data used for analysis are available from the corresponding author.

Acknowledgments: The author is grateful to the editors and unknown reviewers for help in preparing the paper and very useful suggestions and comments.

Conflicts of Interest: The author declares no conflict of interest.

References

1. Boudriki Semlali, B.E.; Molina, C.; Park, H.; Camps, A. On the Correlation Between Earthquakes and Prior Ionospheric Scintillations Over the Ocean: A Study Using GNSS-R Data Between 2017 and 2021. *IEEE J. Sel. Top. Appl.* **2024**, *17*, 2640–2654. [[CrossRef](#)]
2. Huang, Y.; Zhu, P.; Li, S. Feasibility Study on Earthquake Prediction Based on Impending Geomagnetic Anomalies. *Appl. Sci.* **2024**, *14*, 263. [[CrossRef](#)]
3. Hayakawa, M.; Nickolaenko, A.P.; Galuk, Y.P.; Kudintseva, I.G. Manifestations of Nearby Moderate Earthquakes in Schumann Resonance Spectra. *Int. J. Electron. Appl. Res.* **2020**, *7*, 1–28. [[CrossRef](#)]
4. Davies, K.; Baker, D.M. Ionospheric effects observed around the time of the Alaskan earthquake of March 28, 1964. *J. Geophys. Res.* **1965**, *70*, 2251–2253. [[CrossRef](#)]
5. Yuen, P.C.; Weaver, P.F.; Suzuki, R.K.; Furumoto, A.S. Continuous, traveling coupling between seismic waves and the ionosphere evident in May 1968 Japan earthquake data. *J. Geophys. Res.* **1969**, *74*, 2256–2264. [[CrossRef](#)]
6. Calais, E.; Minster, J. GPS, earthquakes, the ionosphere, and the Space Shuttle. *Phys. Earth Planet. Interiors* **1998**, *105*, 167–181. [[CrossRef](#)]
7. Pulinets, S.; Boyarchuk, K. *Ionospheric Precursor of Earthquakes*; Springer: Berlin/Heidelberg, Germany, 2004.
8. Maekawa, S.; Horie, T.; Yamauchi, T.; Sawaya, T.; Ishikawa, M.; Hayakawa, M.; Sasaki, H. A statistical study on the effect of earthquakes on the ionosphere, based on the subionospheric LF propagation data in Japan. *Ann. Geophys.* **2006**, *24*, 2219–2225. [[CrossRef](#)]
9. Sasmal, S.; Chakrabarti, S.K. Ionospheric anomaly due to seismic activities; Part 1: Calibration of the VLF signal of VTX 18.2 KHz station from Kolkata and deviation during seismic events. *Nat. Hazards Earth Syst. Sci.* **2009**, *9*, 1403–1408. [[CrossRef](#)]
10. Chakrabarti, S.K.; Mandal, S.K.; Sasmal, S.; Bhowmick, D.; Choudhury, A.K.; Patra, N.N. First VLF detections of ionospheric disturbances due to Soft Gamma Ray Repeater SGR J1550-5418 and Gamma Ray Burst GRB 090424. *Indian J. Phys.* **2010**, *84*, 1461–1466. [[CrossRef](#)]
11. Oyama, K.I.; Devi, M.; Ryu, K.; Chen, C.H.; Liu, J.Y.; Liu, H.; Bankov, L.; Kodama, T. Modifications of the ionosphere prior to large earthquakes: Report from the Ionosphere Precursor Study Group. *Geosci. Lett.* **2016**, *3*, 6. [[CrossRef](#)]

12. Xiong, P.; Long, C.; Zhou, H.; Battiston, R.; De Santis, A.; Ouzounov, D.; Zhang, X.; Shen, X. Pre-Earthquake Ionospheric Perturbation Identification Using CSES Data via Transfer Learning. *Front. Environ. Sci.* **2021**, *9*, 779255. [[CrossRef](#)]
13. He, L.; Wu, L.; Heki, K.; Guo, C. The Conjugated Ionospheric Anomalies Preceding the 2011 Tohoku-Oki Earthquake. *Front. Earth Sci.* **2022**, *10*, 850078. [[CrossRef](#)]
14. Molina, C.; Boudriki Semlali, B.E.; Park, H.; Camps, A. A Preliminary Study on Ionospheric Scintillation Anomalies Detected Using GNSS-R Data from NASA CYGNSS Mission as Possible Earthquake Precursors. *Remote Sens.* **2022**, *14*, 2555. [[CrossRef](#)]
15. Biagi, P.F.; Piccolo, R.; Ermini, A.; Martellucci, S.; Bellecci, C.; Hayakawa, M.; Capozzi, V.; Kingsley, S.P. Possible earthquake precursors revealed by LF radio signals. *Nat. Hazards Earth Syst. Sci.* **2001**, *1*, 99–104. [[CrossRef](#)]
16. Biagi, P.F.; Maggipinto, T.; Righetti, F.; Loiacono, D.; Schiavulli, L.; Ligonzo, T.; Ermini, A.; Moldovan, I.A.; Moldovan, A.S.; Buyuksarac, A.; et al. The European VLF/LF radio network to search for earthquake precursors: Setting up and natural/man-made disturbances. *Nat. Hazards Earth Syst. Sci.* **2011**, *11*, 333–341. [[CrossRef](#)]
17. Hegai, V.; Kim, V.; Liu, J. The ionospheric effect of atmospheric gravity waves excited prior to strong earthquake. *Adv. Space Res.* **2006**, *37*, 653–659. [[CrossRef](#)]
18. Perrone, L.; De Santis, A.; Abbattista, C.; Alfonsi, L.; Amoruso, L.; Carbone, M.; Cesaroni, C.; Cianchini, G.; De Franceschi, G.; De Santis, A.; et al. Ionospheric anomalies detected by ionosonde and possibly related to crustal earthquakes in Greece. *Ann. Geophys.* **2018**, *36*, 361–371. [[CrossRef](#)]
19. Biagi, P.F.; Piccolo, R.; Ermini, A.; Martellucci, S.; Bellecci, C.; Hayakawa, M.; Kingsley, S.P. Disturbances in LF radio-signals as seismic precursors. *Ann. Geophys.* **2001**, *44*, 1011–1019. [[CrossRef](#)]
20. Molchanov, O.; Hayakawa, M.; Oudoh, T.; Kawai, E. Precursory effects in the subionospheric VLF signals for the Kobe earthquake. *Phys. Earth Planet. Interiors* **1998**, *105*, 239–248. [[CrossRef](#)]
21. Yamauchi, T.; Maekawa, S.; Horie, T.; Hayakawa, M.; Soloviev, O. Subionospheric VLF/LF monitoring of ionospheric perturbations for the 2004 Mid-Niigata earthquake and their structure and dynamics. *J. Atmos. Solar-Terr. Phys.* **2007**, *69*, 793–802. [[CrossRef](#)]
22. Rozhnoi, A.; Solovieva, M.; Molchanov, O.; Hayakawa, M. Middle latitude LF (40 kHz) phase variations associated with earthquakes for quiet and disturbed geomagnetic conditions. *Phys. Chem. Earth Parts A/B/C* **2004**, *29*, 589–598. [[CrossRef](#)]
23. Zhao, S.; Shen, X.; Liao, L.; Zhima, Z.; Zhou, C.; Wang, Z.; Cui, J.; Lu, H. Investigation of Precursors in VLF Subionospheric Signals Related to Strong Earthquakes ($M > 7$) in Western China and Possible Explanations. *Remote Sens.* **2020**, *12*, 3563. [[CrossRef](#)]
24. Maurya, A.K.; Venkatesham, K.; Tiwari, P.; Vijaykumar, K.; Singh, R.; Singh, A.K.; Ramesh, D.S. The 25 April 2015 Nepal Earthquake: Investigation of precursor in VLF subionospheric signal. *J. Geophys. Res. Space Phys.* **2016**, *121*, 10403–10416. [[CrossRef](#)]
25. Boudjada, M.Y.; Biagi, P.F.; Eichelberger, H.U.; Nico, G.; Galopeau, P.H.M.; Ermini, A.; Solovieva, M.; Hayakawa, M.; Lammer, H.; Voller, W.; et al. Analysis of Pre-Seismic Ionospheric Disturbances Prior to 2020 Croatian Earthquakes. *Remote Sens.* **2024**, *16*, 529. [[CrossRef](#)]
26. Biagi, P.; Castellana, L.; Maggipinto, T.; Maggipinto, G.; Minafra, A.; Ermini, A.; Molchanov, O.; Rozhnoi, A.; Solovieva, M.; Hayakawa, M. Anomalies in VLF radio signals related to the seismicity during November–December 2004: A comparison of ground and satellite results. *Phys. Chem. Earth Parts A/B/C* **2009**, *34*, 456–463. [[CrossRef](#)]
27. Nina, A.; Pulnests, S.; Biagi, P.; Nico, G.; Mitrović, S.; Radovanović, M.; Č. Popović, L. Variation in natural short-period ionospheric noise, and acoustic and gravity waves revealed by the amplitude analysis of a VLF radio signal on the occasion of the Kraljevo earthquake ($M_w = 5.4$). *Sci. Total Environ.* **2020**, *710*, 136406. [[CrossRef](#)] [[PubMed](#)]
28. Nina, A.; Nico, G.; Mitrović, S.T.; Čadež, V.M.; Milošević, I.R.; Radovanović, M.; Popović, L.Č. Quiet Ionospheric D-Region (QIonDR) Model Based on VLF/LF Observations. *Remote Sens.* **2021**, *13*, 483. [[CrossRef](#)]
29. Nina, A.; Biagi, P.F.; Pulnests, S.; Nico, G.; Mitrović, S.T.; Čadež, V.M.; Radovanović, M.; Urošev, M.; Popović, L.Č. Variation in the VLF signal noise amplitude during the period of intense seismic activity in Central Italy from 25 October to 3 November 2016. *Front. Environ. Sci.* **2022**, *10*, 1005575. [[CrossRef](#)]
30. Nina, A. Analysis of VLF Signal Noise Changes in the Time Domain and Excitations/Attenuations of Short-Period Waves in the Frequency Domain as Potential Earthquake Precursors. *Remote Sens.* **2024**, *16*, 397. [[CrossRef](#)]
31. Kovačević, A.B.; Nina, A.; Popović, L.Č.; Radovanović, M. Two-Dimensional Correlation Analysis of Periodicity in Noisy Series: Case of VLF Signal Amplitude Variations in the Time Vicinity of an Earthquake. *Mathematics* **2022**, *10*, 4278. [[CrossRef](#)]
32. The Euro-Mediterranean Seismological Centre. Available online: <https://www.emsc-csem.org/> (accessed on 8 April 2021).
33. Hanks, T.C.; Kanamori, H. A moment magnitude scale. *J. Geophys. Res. Solid Earth* **1979**, *84*, 2348–2350. [[CrossRef](#)]
34. Kanamori, H. Magnitude scale and quantification of earthquakes. *Tectonophysics* **1983**, *93*, 185–199. [[CrossRef](#)]
35. Richter, C.F. An instrumental earthquake magnitude scale. *Bull. Seismol. Soc. Am.* **1935**, *25*, 1–32. [[CrossRef](#)]
36. Nina, A.; Simić, S.; Srečković, V.A.; Popović, L.Č. Detection of short-term response of the low ionosphere on gamma ray bursts. *Geophys. Res. Lett.* **2015**, *42*, 8250–8261. [[CrossRef](#)]
37. Wang, J.; Huang, Q.; Ma, Q.; Chang, S.; He, J.; Wang, H.; Zhou, X.; Xiao, F.; Gao, C. Classification of VLF/LF Lightning Signals Using Sensors and Deep Learning Methods. *Sensors* **2020**, *20*, 1030. [[CrossRef](#)] [[PubMed](#)]
38. Thomson, N.R.; Rodger, C.J.; Clilverd, M.A. Large solar flares and their ionospheric D region enhancements. *J. Geophys. Res. Space Phys.* **2005**, *110*, A06306. [[CrossRef](#)]

39. Kolarski, A.; Grubor, D.; Šulić, D. Diagnostics of the Solar X-Flare Impact on Lower Ionosphere through Seasons Based on VLF-NAA Signal Recordings. *Balt. Astron.* **2011**, *20*, 591–595. [[CrossRef](#)]
40. Basak, T.; Chakrabarti, S.K. Effective recombination coefficient and solar zenith angle effects on low-latitude D-region ionosphere evaluated from VLF signal amplitude and its time delay during X-ray solar flares. *Astrophys. Space Sci.* **2013**, *348*, 315–326. [[CrossRef](#)]
41. Schmitter, E.D. Modeling solar flare induced lower ionosphere changes using VLF/LF transmitter amplitude and phase observations at a midlatitude site. *Ann. Geophys.* **2013**, *31*, 765–773. [[CrossRef](#)]
42. Ammar, A.; Ghalila, H. Ranking of Sudden Ionospheric Disturbances by Means of the Duration of VLF Perturbed Signal in Agreement with Satellite X-Ray Flux Classification. *Acta Geophys.* **2016**, *64*, 2794–2809. [[CrossRef](#)]
43. Chakraborty, S.; Basak, T. Numerical analysis of electron density and response time delay during solar flares in mid-litudinal lower ionosphere. *Astrophys. Space Sci.* **2020**, *365*, 1–9. [[CrossRef](#)]
44. Inan, U.S.; Lehtinen, N.G.; Moore, R.C.; Hurley, K.; Boggs, S.; Smith, D.M.; Fishman, G.J. Massive disturbance of the daytime lower ionosphere by the giant γ -ray flare from magnetar SGR 1806-20. *Geophys. Res. Lett.* **2007**, *34*, 8103. [[CrossRef](#)]
45. The European Severe Weather Database. Available online: <https://eswd.eu/cgi-bin/eswd.cgi> (accessed on 28 May 2022).
46. The Helmholtz Centre Potsdam—GFZ German Research Centre for Geosciences. Available online: https://www-app3.gfz-potsdam.de/kp_index/Kp_ap_Ap_SN_F107_since_1932.txt (accessed on 28 May 2022).
47. The National Aeronautics and Space Administration—NASA. Available online: https://hesperia.gsfc.nasa.gov/goes/goes_event_listings/ (accessed on 28 May 2022).

Disclaimer/Publisher’s Note: The statements, opinions and data contained in all publications are solely those of the individual author(s) and contributor(s) and not of MDPI and/or the editor(s). MDPI and/or the editor(s) disclaim responsibility for any injury to people or property resulting from any ideas, methods, instructions or products referred to in the content.



Article

Analysis of VLF Signal Noise Changes in the Time Domain and Excitations/Attenuations of Short-Period Waves in the Frequency Domain as Potential Earthquake Precursors

Aleksandra Nina

Institute of Physics Belgrade, University of Belgrade, Pregrevica 118, 11080 Belgrade, Serbia; sandrast@ipb.ac.rs

Abstract: In this paper, we complete pioneering research that indicates the very low frequency (VLF) signal amplitude and phase noise reductions, and short-period wave excitations and attenuations as new potential earthquake precursors. We consider changes in the VLF signal broadcast in Italy by the ICV transmitter and recorded in Serbia that start a few tens of minutes before earthquakes. The sampling interval of the analyzed data is 0.1 s. The main objectives of this study are (1) to complete this research in the time and frequency domains during the periods of the four earthquakes analyzed in the previous studies, and (2) to define the parameters of the VLF signal amplitude and phase in both domains that should be further examined in statistical analyses of the aforementioned potential earthquake precursors. In the first part of this study, we analyze the ICV signal amplitude in the frequency domain during the period around three earthquakes that occurred in November 2010 near the considered signal propagation path. Here, we apply the Fourier transform to the relevant recorded data. In the second part, we compare characteristics of the signal amplitude and phase noise reductions in the time domain, and wave excitations and attenuations in the frequency domain. The results of these comparisons indicate the parameters that should be analyzed in subsequent studies to confirm the connection of the considered VLF signal changes with seismic activity before earthquakes, and potentially establish procedures for their detection are: (a) the start and end times of the noise reductions in the time domain and the excited/attenuated waves in the frequency domain, (b) the differences in the corresponding times, and (c) the wave periods of wave excitations of both the signal amplitude and phase.

Keywords: earthquake; VLF signal; noise reduction; precursor; wave excitations/attenuations



Citation: Nina, A. Analysis of VLF Signal Noise Changes in the Time Domain and Excitations/Attenuations of Short-Period Waves in the Frequency Domain as Potential Earthquake Precursors. *Remote Sens.* **2024**, *16*, 397. <https://doi.org/10.3390/rs16020397>

Academic Editor: Alex Hay-Man Ng

Received: 24 September 2023

Revised: 28 December 2023

Accepted: 16 January 2024

Published: 19 January 2024



Copyright: © 2024 by the author. Licensee MDPI, Basel, Switzerland. This article is an open access article distributed under the terms and conditions of the Creative Commons Attribution (CC BY) license (<https://creativecommons.org/licenses/by/4.0/>).

1. Introduction

The application of electromagnetic signals in ionospheric observations allows obtaining sets of various types of data. Their processing produces results important to both research in several scientific disciplines and research that has practical applications. One of the directions in the analysis of these data refers to the examination of possible ionospheric disturbances that precede earthquakes. Although the first studies on this topic were published in the sixties of the last century [1,2], the most important goal of these studies, the establishment of a sufficiently reliable method for predicting this natural disaster, has not yet been achieved. The most important reasons for that are the complexity of the cause-and-effect relationships between processes in the lithosphere and atmosphere, the existence of numerous processes in the Earth's layers and outer space that simultaneously affect the area at ionospheric heights and also the lack of observational data with the necessary temporal and spatial resolutions. However, the importance of this goal makes these studies actual in all previous decades [3,4]. Moreover they have been intensified at the global level in recent years [5–7].

One of the techniques for monitoring the ionosphere is based on the propagation of very low frequency (VLF) radio signals. These signals propagate in the so-called Earth-ionosphere waveguide from transmitters to receivers that are distributed around the world.

The emission of these signals is continuous, and the data can be detected with a time resolution of several ms, which makes it possible to obtain information related to both short-term disturbances (e.g., caused by lightning [8]) and unpredictable phenomena, among which earthquakes are included [9–11].

In previous research, the variations in VLF signals before earthquakes indicate a time shift of the characteristic minima of their amplitudes in the periods of sunrise and sunset [4,12,13], and a significant increase or decrease in these values as well as their oscillatory temporal evolution in some periods [14–18]. These changes are generally noted a few days or weeks before strong earthquakes, and, as in the case of seismic process research in other scientific disciplines (see for example [19]), they can be detected in time and frequency domains.

In addition to analyses of the main tendencies of some physical quantities or characteristics of signals used for the corresponding observations, analyses of the noise of relevant parameters can also be used to investigate phenomena such as seismic processes [20,21]. The recent analyses of both VLF signal parameters (amplitude and phase) in the time and frequency domains indicate potentially new effects that occur a few minutes or tens of minutes before an earthquake: (a) the reductions in the amplitude and phase noises (visible in the time domain and defined as the maximum absolute values of the deviations of the recorded amplitude and phase values from the relevant smoothed curves obtained after elimination p percent of their largest and lowest values in the considered time intervals), and (b) the wave excitations and attenuations (visible in frequency domain) [11,22]. In these two studies, the ICV signal emitted in Italy and received in Serbia is analyzed in the periods around the four earthquakes of magnitude greater than 4 that occurred in Serbia near Kraljevo (K1) and in the Tyrrhenian Sea (TS) on 3 November 2010, near Kraljevo (K2) on 4 November 2010, and in the Western Mediterranean Sea (WMS) on 9 November 2010. The obtained results show the following:

- Time domain: the reductions in the amplitude and phase noises are visible before all four earthquakes ([11] and [22], respectively);
- Frequency domain: the excitations and attenuations of waves manifested as increases and decreases in the Fourier amplitude before the earthquake at different wave periods are recorded for
 - the amplitude in the case of the K1 earthquake [11], and
 - the phase for all four considered cases [22].

These two studies are the first studies that investigate the reductions in the VLF signal amplitude and phase noises, as well as the excitations and attenuations of waves with small periods in their time evolutions before earthquakes. In other words, we can consider them as pilot studies of these potential earthquake precursors. However, these studies do not provide a complete analysis of the VLF signal changes before the observed four earthquakes because the amplitude analysis in the frequency domain is given only for the period around the K1 earthquake. For this reason, we complete this research in the first part of this study giving analyses of the recorded wave extinctions and attenuations in the periods around the remaining three earthquakes.

Although these two studies are based on a small number of earthquakes, the obtained results clearly indicate specific types of changes which, bearing in mind the importance of earthquake prediction, should be statistically examined in future studies. For this reason, in the second part of this study, we define the parameters for determining the described changes in a VLF signal that should be analyzed in investigations of possible earthquake precursors in the following studies. Here, we used the results obtained in the first part of this study, and in [11,22]. In that way, this study concludes the described pilot investigation and provides guidance for appropriate further research.

This paper is organized as follows. The observations, and data processing are described in Section 2. The obtained results are presented in Section 3. In particular, the results related to the analysis of the amplitude in the frequency domain in the periods around

the TS, K2, and WMS earthquakes and their comparisons with previous results are given in Section 3.1, while the determination of the signal amplitude and phase parameters that should be analyzed in future statistical studies of the indicated possible earthquake precursors are shown in Section 3.2. Finally, the conclusions of this study and guidance for appropriate further statistical analyses are given in Section 4.

2. Observations and Data Processing

2.1. Observational Setup and Studied Earthquake Events

This paper provides an analysis of the amplitude of the 20.27 kHz VLF signal emitted by the ICV transmitter located in Isola di Tavolari, Sardinia, Italy (40.92°N, 9.73°E). The presented data are recorded at the Institute of Physics Belgrade in Belgrade, Serbia, (44.8°N, 20.4°E) by the Absolute Phase and Amplitude Logger (AbsPAL) VLF receiver with sampling periods of 0.1 s during 3, 4 and 9 November 2010. This receiving setup is developed by the Radio and Space Physics Group of Otago University, New Zealand, and consists of the electric VLF antenna, the GPS antenna, the VLF preamplifier, feed cables, the Service Unit, and the DSP (digital signal processor) card for the computer.

The map with the locations of the used transmitter and receiver and the signal propagation path is given in Figure 1. In this figure, stars represent the epicenters of the considered four earthquakes with magnitude:

- Mw 5.4 that occurred near Kraljevo (K1; 43.74°N, 20.69°E) on 3 November 2010;
- mb 5.1 that occurred in the Tyrrhenian Sea (TS; 40.03°N, 13.2°E) on 3 November 2010;
- ML 4.4 that occurred near Kraljevo (K2; 43.78°N, 20.62°E) on 4 November 2010 (since this location is very close to the location of the K1 earthquake epicentre, the same star refers to both these earthquakes);
- ML 4.3 that occurred in the Western Mediterranean Sea (WMS; 42.25°N, 6.77°E) on 9 November 2010

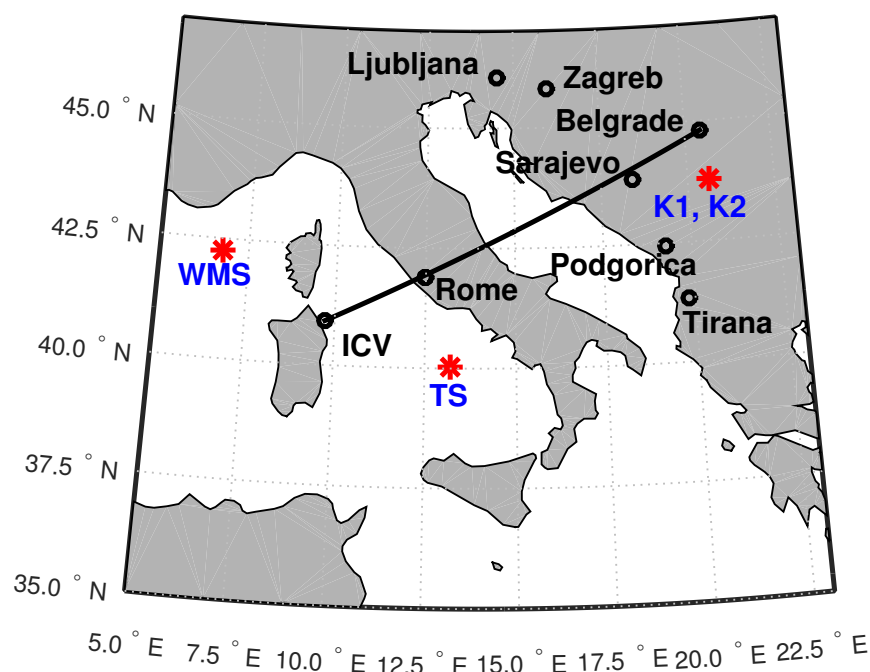


Figure 1. The VLF signal propagation path from the ICV transmitter to the Belgrade receiver station in Serbia. The red stars represent the epicenters of the considered earthquakes in the Tyrrhenian Sea (TS), Western Mediterranean Sea (WMS), and the two earthquakes near Kraljevo K1 and K2 (the same star shows them).

The above data are provided on the website of the Euro-Mediterranean Seismological Centre [23]. The symbols Mw, mb and ML denote the moment magnitude [24], body-wave magnitude [25] and Richter [26] scales, respectively. The relations between their values are complex [27], and some of them are shown in statistical studies (see, for example, [28,29]).

The shortest distances of the epicenters of the mentioned earthquakes from the observed VLF signal propagation path are 126 km, 219 km, 114 km and 287 km, respectively.

2.2. Data of the ICV Signal Amplitude Analyzed in Detail in This Study

The time evolutions of the ICV signal amplitude, A , recorded by the AbsPAL receiver during the periods around the TS, K2, and WMS earthquakes are shown in Figure 2. The vertical lines indicate the times of all earthquakes that occurred close to the observed signal path (data on these earthquakes and the distances of their epicenters from the path of the observed signal are given in [22,23]). The times of occurrences of the considered three events are indicated by the vertical red dash lines.

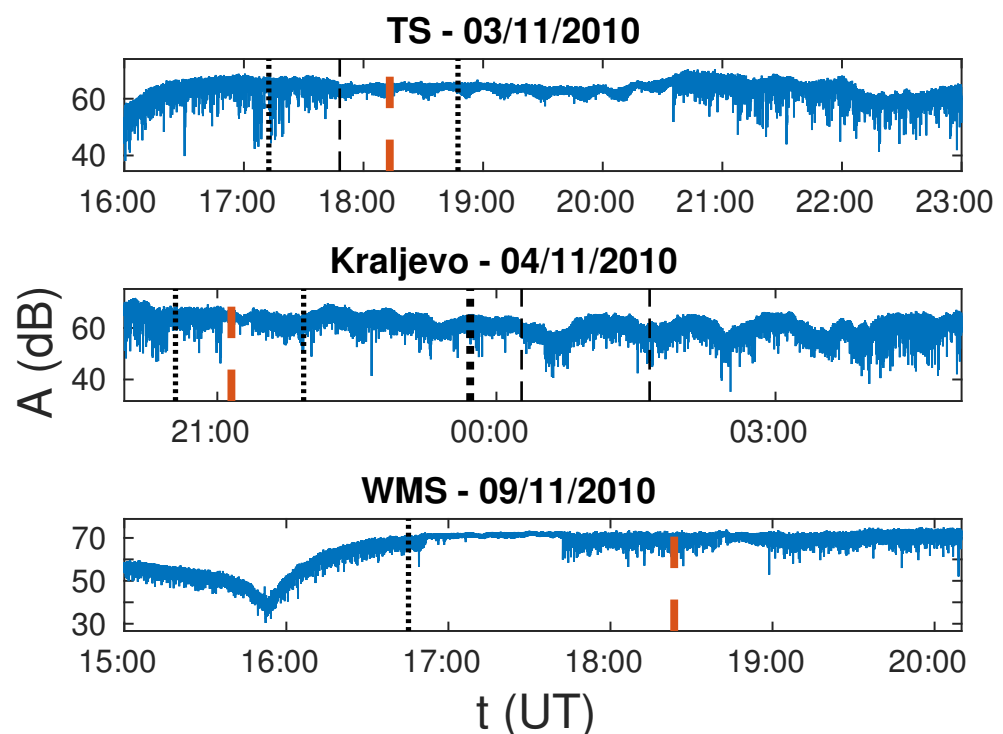


Figure 2. The ICV signal amplitude for time periods around the TS (upper panel), K2 (middle panel) and WMS (bottom panel) earthquakes. The vertical dashed red lines indicate these earthquakes, while the vertical black lines indicate additional earthquakes with magnitudes below 2.5 (thin dotted lines), between 2.5 and 3 (thin dashed lines), and between 3 and 4 (tick dotted line).

In Figure 2, it can be seen that the amplitude noise reduction is most pronounced before the strongest earthquakes in all three observed time intervals. Additional two, and four earthquakes during 3 and 4 November, respectively, occurred during the period of visible amplitude noise reduction in relation to its values at the beginnings and ends of the respective time intervals. In the third time interval, the amplitude noise reduction is visible only before the strongest earthquake, but it is interrupted during a shorter period (including the time of the earthquake). This interrupted part may indicate the existence of a short-term additional source of the noise, or that the corresponding connection should be established only with the second noise amplitude reduction. The delay of minutes of this amplitude noise reduction in relation to the time of the earthquake can potentially be explained by the greater distance of the epicenter from the signal path, and/or the fact that it is moved from that route in the sense that the shortest considered distance is the one to

the transmitter. The most pronounced amplitude noise reduction is visible in the case of the first observed earthquake with the strongest magnitude.

2.3. Data Processing

As stated in the Introduction, analyses of VLF and LF signals show changes in both their parameters (amplitude and phase) before the occurrence of an earthquake. In this paper, analyses of the characteristics of changes in both these parameters of the ICV signal are provided in the time and frequency domains. These procedures are described in detail in the first study of the appropriate amplitude noise reduction [11]. Here, we will only list their basic characteristics.

2.3.1. Data Analyses in the Time Domain

To determine changes in the time domain, the time evolutions of the amplitude $A(t)$ and the phase $P(t)$ are processed. Although the processing of these data for determining the amplitude noise A_{noise} using the method given in [11] consists of two phases (1. determining the deviation of the recorded values from the relevant smoothed curve dA , and 2. determining the A_{noise} defined in [30] as the maximum absolute values of dA after removing p percent of their highest values due to the elimination of potential short-term influences of other phenomena), only the first part is applied in this study. The reason is the better precision in the estimation of the time of the observed changes because A_{noise} is calculated for certain time intervals, and not for every time t . This is especially important in the cases where the intervals in which the amplitude and phase noise decrease are only a few minutes. Because the observed changes are not instantaneous, their times are set at 30 s. In other words, the error of determining the start and end times of the amplitude and phase noise reductions is 30 s. Bearing in mind that the critical values of the parameters characterizing the noise level reduction must be determined in analyses with a statistically significant sample, in this study the reduction in the amplitude and phase noises are determined visually.

2.3.2. Data Analyses in the Frequency Domain

As we said in the Introduction, in the first part of this study, we provide a detailed analysis of the ICV signal amplitude in the frequency domain for the time periods around the TS, K2, and WMS earthquakes. As in the relevant analyses given in [11,22], we apply the Fast Fourier Transform (FFT) to the data shown in Figure 2 (recorded in the time domain) in the windows time intervals (WTIs) of 20 min, 1 h, and 3 h. In all three cases, the steps between two neighboring WTIs are 10 min. The obtained results represent the Fourier amplitudes A_F that depend on the wave period $T = 1/f$, where f is frequency, while the increase and decrease in its values in time indicate the excitation or attenuation of the wave at the observed T , respectively. The analysis of these changes in the frequency domain is the focus of the first part of this study, while the obtained results are included in the second part, where the parameters relevant for statistical analyses of the amplitude and phase noise reductions and the obtained changes in A_F for all four events are compared to define parameters which should be analyzed as a possible earthquake precursor in the forthcoming statistical studies.

To obtain the considered times with the lowest error we determine them from the results for WTI = 20 min. In this case, errors in the determination of the time t , wave period T , and Fourier amplitude A_F are:

- The error in the time determinations is the step between two WTIs, e.g., 10 min.
- The error in the determination of T is not the same because these values are not equidistant (in FFT the values of frequency f are equidistant), and depends on its values. It can be determined in two ways:
 - In the case of high frequencies, e.g., low wave periods (here, we consider the maximum value for this case of 1 min) for which the differences of adjacent values are small, an approximate determination of the error ΔT is made from

the relationship between the wave period and frequency ($T = 1/f$), and the error of frequency Δf : $\Delta T = \Delta f/f^2 = T^2\Delta f$ where $\Delta f = 1/WTI$ (for WTI of 20 min, 1 h and 3 h, the values of Δf are 8.3333×10^{-4} Hz, 2.7778×10^{-4} Hz, and 9.2593×10^{-5} Hz, respectively).

- In the case of lower frequencies, i.e., the wave periods longer than 1 min, the error is determined by the absolute difference of a certain value of T and the first more discrete value of this parameter.
- For the same reason as in the case of determining the reduction of the amplitude and phase noise, the increasing and decreasing of A_F is determined visually.

2.4. Comparisons of the Parameters Relevant for the Statistical Analyses Related to the Considered Possible Earthquake Precursors

As stated in the Introduction, the determination of the parameters that are relevant for the statistical analyses of the amplitude and phase noise reductions, and the excitation and attenuation of short-period waves is based on the comparisons of the results presented in the first part of this study as well as in [11,22]. An overview of the data sources for the ICV signal amplitude and phase in the time and frequency domains in the periods around the considered K1, TS, K2, and WMS earthquakes is given in Table 1.

Table 1. Data sources for the ICV signal amplitude and phase for the analyses in the time and frequency domains in the periods around the considered K1, TS, K2, and WMS earthquake occurrences.

Earthquake	Time Domain	Frequency Domain
	Amplitude	
K1	[11]	[11]
TS	[11]	this study
K2	[11]	this study
WMS	[11]	this study
	Phase	
K1	[22]	[22]
TS	[22]	[22]
K2	[22]	[22]
WMS	[22]	[22]

Based on the previous two indicated studies, these changes are manifested as:

- The reductions in the VLF signal amplitude and phase noises in the time domain;
- The excitations of waves at discrete low values of wave periods (below 1.5 s) and the attenuations of waves at other wavelengths that may have upper limit values after which changes are not observed. These effects are visible in the frequency domain.

In order to determine the parameters that should be further analyzed in statistical studies (they are the main results of this overall pilot research), we compare the times of the beginnings and endings of the mentioned changes in both domains, and the characteristic values of the wave periods in which changes are observed in the frequency domain.

3. Results and Discussion

As we stated in the previous text, the results of this research and their analyses are presented in two parts. In the first part (Section 3.1), we present the investigation of the signal amplitude in the frequency domain during the periods around the earthquakes that occurred in the Tyrrhenian Sea (TS earthquake) on 3 November 2010, near Kraljevo (K2 earthquake) on 4 November 2010, and in the Western Mediterranean Sea (WMS earthquake) on 9 November 2010. Comparisons of the results given in [11,22], and Section 3.1 and

related to the ICV signal amplitude and phase in the time and frequency domains for all four considered earthquakes are presented in Section 3.2.

3.1. Analysis of the Signal Amplitude in the Frequency Domain

The dependences $A_F(T, \Delta t_{ws})$ obtained by applying the procedure described in Section 2 to the data recorded during a quiet period, and the periods around the TS, K2, and WMS earthquakes (presented in Figure 2) are shown in Figures 3, 4, 5 and 6, respectively. In these figures, we consider the window time intervals (WTIs) of 20 min, 1 h and 3 h. The x-axes show the times of the beginnings of those intervals in relation to the time when the main analyzed earthquake in the considered day is registered (Δt_{ws}). In the case of the shortest WTI of 20 min, the obtained dependencies are divided into two graphs in order to separate the dependencies for $T \leq 5$ s and $T > 5$ s due to the large difference in A_F values.

3.1.1. Analysis of the ICV Signal Amplitude in a Quiet Period

To rule out the influence of periodic variations on signal propagation characteristics, we apply the FFT to the time evolution of the ICV signal amplitude from 19:00 UT on 3 November 2009, to 4:00 UT on 4 November 2009, when there were no significant impacts of sudden events (including earthquakes) on the considered VLF signal [11]. The obtained results presented in Figure 3 show the following:

- Increases and decreases in A_F in time are not recorded in the upper panels showing the results for WTI = 20 min. In other words, excitations and attenuations of waves with a wave period below 10 min are not visible.
- A_F has higher values during the periods of sunset and sunrise, which is a consequence of intense variations in the signal amplitude time evolution, which include pronounced minima (see, for example, [31,32]). Here, we emphasize that the variations in A_F last for a long time because specific data provide integral information for the relevant time interval WTI to which the FFT is applied.

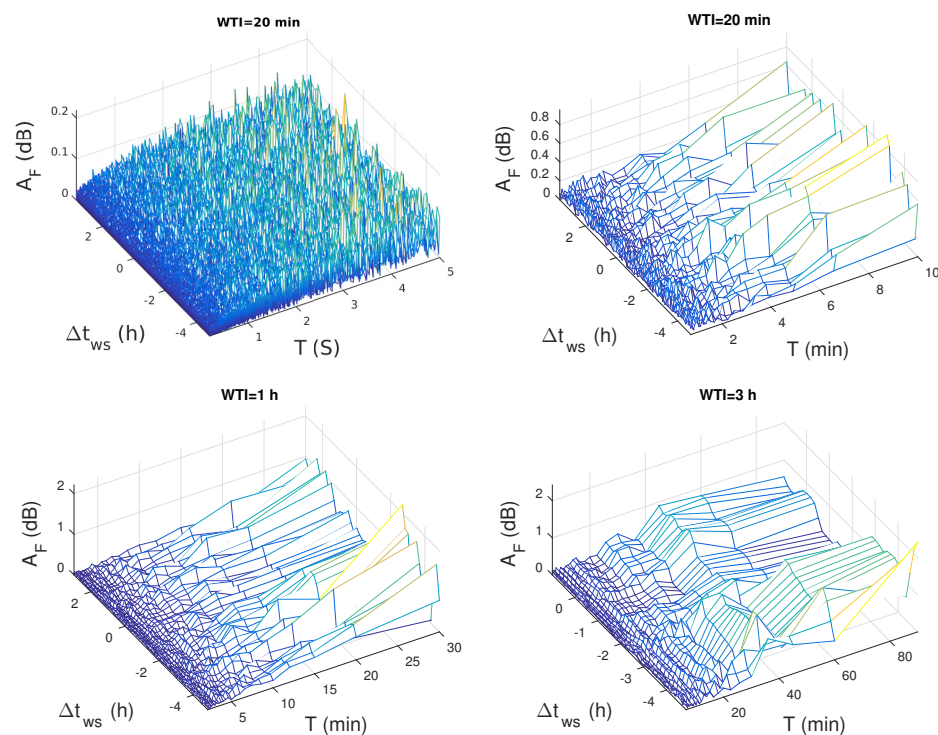


Figure 3. The Fourier amplitude of waves with the period T obtained by applying the FFT to the ICV signal amplitude recorded in the quiet period from 19:00 UT on 3 November 2009 to 4:00 UT on 4 November 2009, with the window time intervals (WTI) of 20 min (upper panels), 1 h (bottom left panel), and 3 h (bottom right panel) which begin with a Δt_{ws} shift with respect to the midnight.

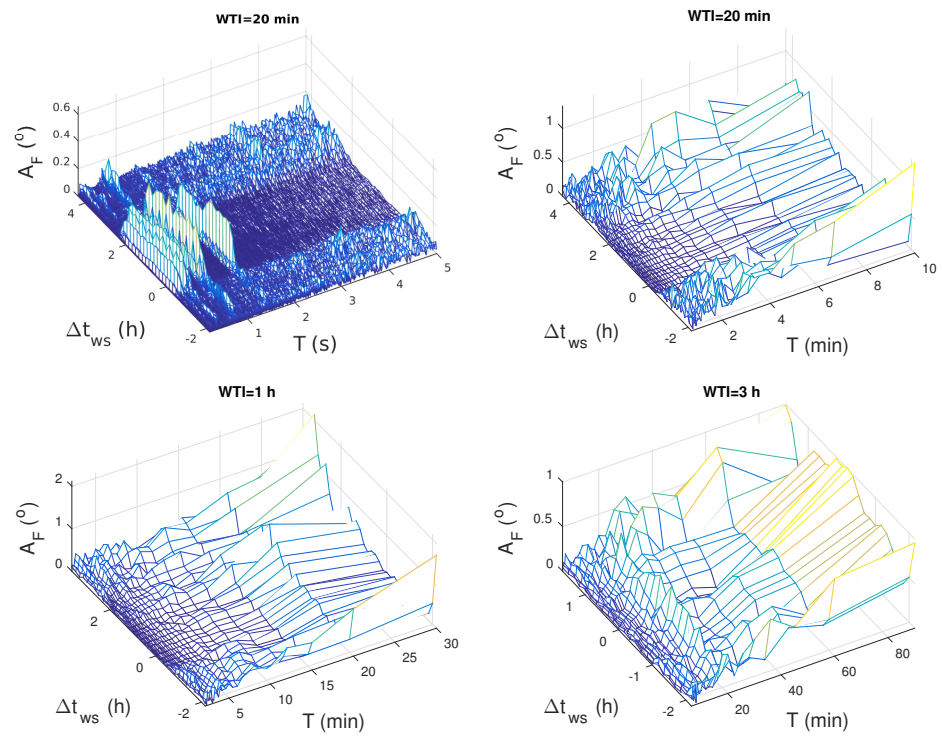


Figure 4. The Fourier amplitude of waves with the period T obtained by applying the FFT to the ICV signal amplitude recorded in time around the TS earthquake occurred on 3 November 2010, with the window time intervals (WTI) of 20 min (upper panels), 1 h (bottom left panel), and 3 h (bottom right panel) which begin with a Δt_{ws} shift with respect to the TS earthquake time.

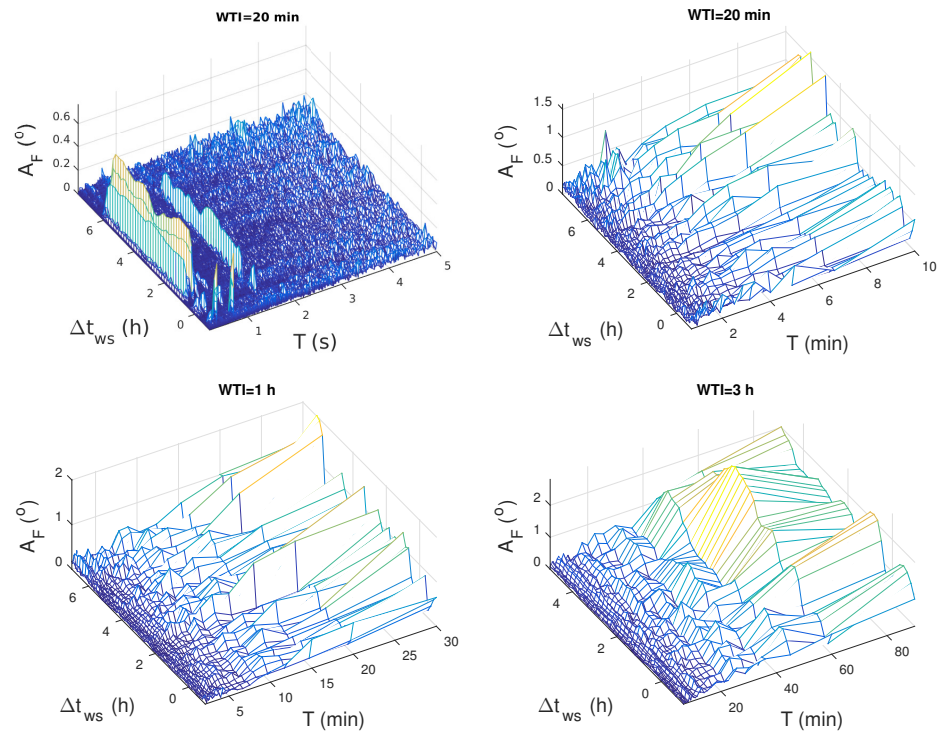


Figure 5. The Fourier amplitude of waves with the period T obtained by applying the FFT to the ICV signal amplitude recorded in time around the K2 earthquake occurred on 4 November 2010, with the window time intervals (WTI) of 20 min (upper panels), 1 h (bottom left panel), and 3 h (bottom right panel) which begin with a Δt_{ws} shift with respect to the K2 earthquake time.

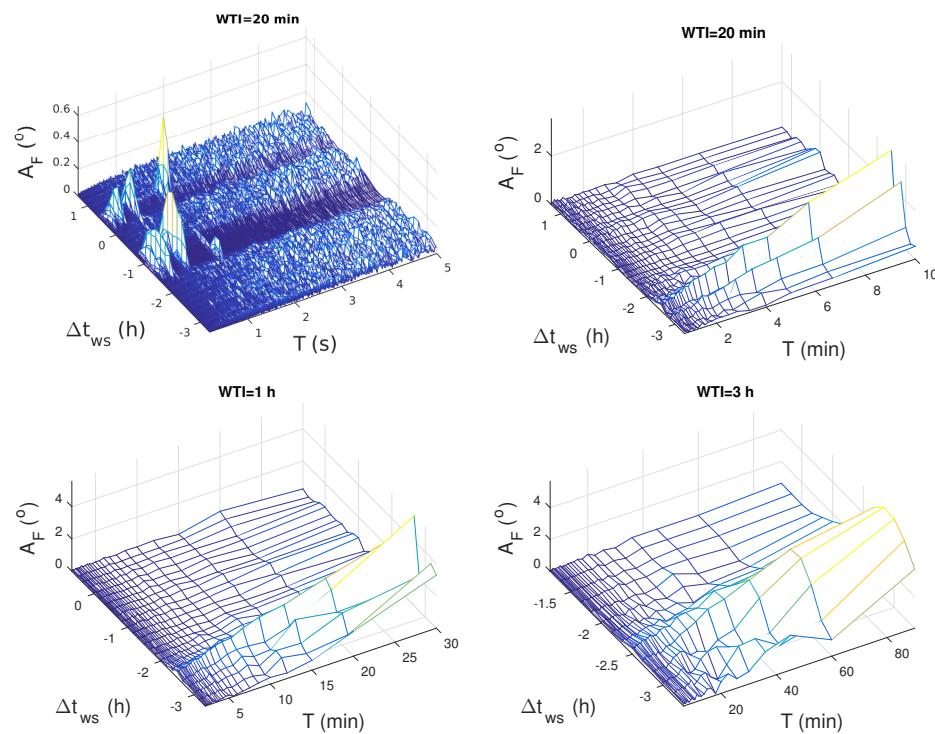


Figure 6. The Fourier amplitude of waves with the period T obtained by applying the FFT to the ICV signal amplitude recorded in time around the WMS earthquake occurred on 9 November 2010, with window time intervals (WTI) of 20 min (upper panels), 1 h (bottom left panel), and 3 h (bottom right panel) which begin with a Δt_{WS} shift with respect to the WMS earthquake time.

Bearing in mind these conclusions in the case of a quiet period, we will exclude the mentioned variations on larger wave periods for WTI of 1 h and 3 h from the following analyses related to the time periods around the considered three earthquakes.

3.1.2. Analysis of the ICV Signal Amplitude in the Period around the TS Earthquake

The TS earthquake occurred in the Tyrrhenian Sea at 18:13:10 UT on 3 November 2010. In the considered time period around this earthquake (16:00 UT–23:00 UT on 3 November 2010), the three smaller ones are recorded near the propagation path of the considered ICV signal (the two before and the one after the TS earthquake). Their characteristics are given in Table 2.

Table 2. Characteristics of the earthquakes that occurred in the considered period around the TS earthquake: the occurrence time t , the latitude (LAT) and longitude (LON) of the epicenter positions, the magnitude, and the locations. The shown data are given in [23] and used in [22].

t (UT)	Position (LAT/LON)	Magnitude	Location
17:12:30	(42.4°N, 13.35°E)	ML 2	Central Italy
17:48:04	(43.75°N, 20.7°E)	ML 2.5	near Kraljevo
18:13:10	(40.03°N, 13.2°E)	mb 5.1	TS
18:47:23	(43.73°N, 20.67°E)	ML 2.1	near Kraljevo

The visualization of wave excitations and attenuations in this time period is given in Figure 4 which shows the time evolutions of A_F at discrete values of T . The following characteristics of the most pronounced changes visible in this figure are:

- As in the studies presented in [11,22], the wave excitations are visible at small discrete values of the wave periods below 1.5 s. They can be seen in the upper left panel for

WTI = 20 min (for smaller values of T) in the time interval starting (40 ± 10) min before the TS earthquake and ending (130 ± 10) min after it. The specific values of the periods of the excited waves T_{exc} are (0.2333 ± 0.0001) s, (0.2800 ± 0.0001) s, (0.3500 ± 0.0002) s, (0.4667 ± 0.0002) s, (0.7001 ± 0.0005) s, and (1.400 ± 0.002) s. The stated errors are determined based on the explanation given in Section 2. A clearer representation of the A_F jumps representing the indicated wave excitations is shown in Figure 7 where the dependencies $A_F(T)$ (in moments when wave excitations are visible) are given for all four considered cases.

- The wave attenuations, manifested as decreases in A_F , are recorded for all values of T from its minimum value to 15 min except for those at which the indicated wave excitations are visible. They occur in similar time intervals as the mentioned excitations (determined on the panels for WTI = 20 for the best accuracy). The value of 15 min is determined in the graph for WTI = 1 h (lower left panel in Figure 4) because of better precision than in the case for WTI = 3 h (lower right panel). Here, we emphasize that this determination is not relevant for WTI = 20 min since the maximum value of T in that case is 10 min (half of WTI).

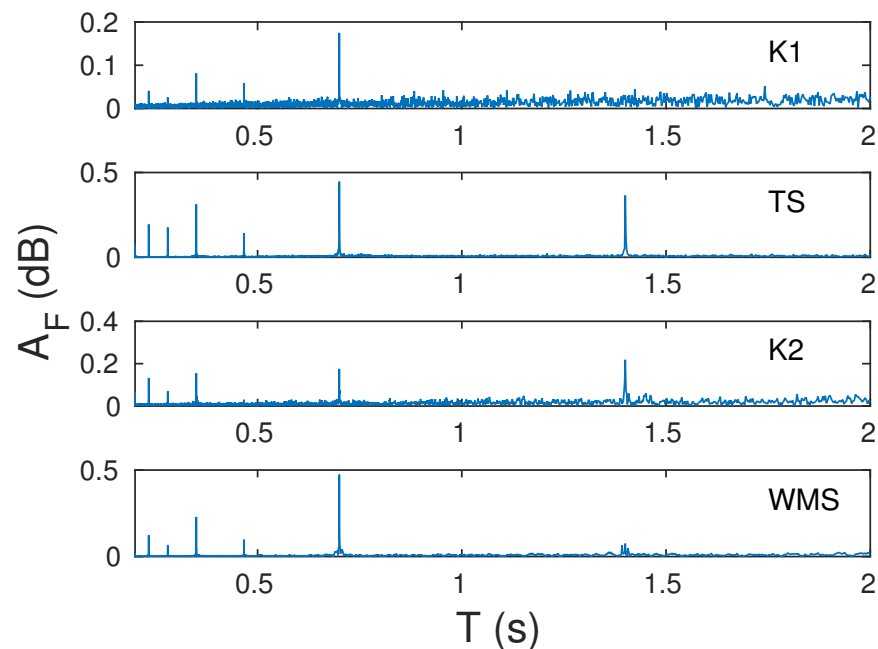


Figure 7. The Fourier amplitude A_F obtained by applying the FFT to the ICV signal amplitude during excitations of waves with periods less than 2 s in the time intervals around the K1, TS, K2, and WMS earthquake occurrences (panels are shown, respectively, from top to bottom) with period T .

The time period in which the mentioned wave excitations occur includes the times of the TS earthquake and the second and third earthquakes given in Table 2. In addition, the weaker increases in A_F are visible in the time interval when the first earthquake listed in the mentioned table occurred.

3.1.3. Analysis of the ICV Signal Amplitude in the Period around the K2 Earthquake

The K2 earthquake occurred near Kaljevo in Serbia at 21:09:05 UT on 4 November 2010. As can be seen in Table 3, the five smaller ones (the one before, and the four after the K2 earthquake) are recorded near the propagation path of the considered VLF signal during the considered time period (20:00 UT on 4 November–05:10 UT on 5 November 2010).

Table 3. Characteristics of the earthquakes that occurred in the considered period around the K2 earthquake: the occurrence time t , the latitude (LAT) and longitude (LON) of the epicenter positions, the magnitude, and the locations. The shown data are given in [23] and used in [22].

t (UT)	Position (LAT/LON)	Magnitude	Location
20:33:01	(43.75°N, 20.7°E)	ML 1.9	near Kraljevo
21:09:05	(43.78°N, 20.62°E)	ML 4.4	near Kraljevo
21:55:40	(45.81°N, 7.55°E)	ML 1.2	Northern Italy
23:43:05	(43.78°N, 20.62°E)	ML 3.3	near Kraljevo
00:16:14	(43.74°N, 20.64°E)	ML 2.8	near Kraljevo
01:38:48	(43.76°N, 20.69°E)	ML 2.5	near Kraljevo

The obtained values of A_F for the considered three WTIs are shown in Figure 5. As in the previous case, the excitations and attenuations of the waves, which can be considered as potential earthquake precursors, are visible in multiple time intervals: the first can be associated with the earliest earthquake, the second includes the time of the K2 earthquake and the longest third during which the remaining four earthquakes were recorded. This is very important to note because of two facts:

- By the analyses of the signal characteristics in the periods of other earthquakes, the lasting of the wave excitation/attenuation period can be related to the number of earthquakes that occur within a relatively short time period.
- The magnitudes of the additional earthquakes are below 3.5 because that indicates that the dependence of the earthquake intensity and the excited/attenuated waves characteristics are not simple and that their examinations require the analyses of statistically significant samples with the inclusion of additional parameters that characterize the considered earthquakes, positions of their epicenters relative to the considered signal propagation path, signal, and states of the atmosphere.

The characteristics of the excitations and attenuations of the waves that start before the K2 earthquake are:

- The wave excitations are visible in the time interval starting (20 ± 10) min before the K2 earthquake and ending (10 ± 10) min after it at the wave periods T_{exc} of (0.2333 ± 0.0001) s, (0.2000 ± 0.0001) s, (0.2800 ± 0.0001) s, (0.3500 ± 0.0002) s, (0.4667 ± 0.0002) s, (0.7001 ± 0.0005) s, and (1.400 ± 0.002) s. As in the first case, T_{exc} is determined from the upper left panel of the corresponding figure (WTI = 20 min), and the stated errors are determined based on the explanation given in Section 2. Also, a clearer representation of the A_F jumps representing the indicated wave excitations is shown in Figure 7.
- As in the first case, the wave attenuations, manifested as decreases in A_F , are visible in similar time intervals as the mentioned excitations for all values of T from its minimum value to 6.667 min except for those at which the indicated wave excitations are visible (see the both upper panels for WTI = 20 min, and the bottom left panel for WTI = 1 h).

3.1.4. Analysis of the ICV Signal Amplitude in the Period around the WMS Earthquake

The WMS earthquake occurred in the Western Mediterranean Sea at 18:23:36 UT on 9 November 2010. In this case, one additional earthquake occurred before it in the considered time period (15:00 UT–20:10 UT on 9 November 2010). Their corresponding characteristics are given in Table 4, while the obtained dependencies $A_F(T, \Delta t_{WS})$ are presented in Figure 6.

Table 4. Characteristics of the earthquakes that occurred in the considered period around the WMS earthquake: the occurrence time t , the latitude (LAT) and longitude (LON) of the epicenter positions, the magnitude, and the locations. The shown data are given in [23] and used in [22].

t (UT)	Position (LAT/LON)	Magnitude	Location
16:45:13	(43.59°N, 12.36°E)	ML 2.3	Central Italy
18:23:36	(42.25°N, 6.77°E)	ML 4.3	WMS

In this case, the two time periods when the already explained wave excitations and attenuations exist are visible. The first of them occurs before the WMS earthquake but also ends before it. The other typical changes occur soon after. A possible explanation for this interruption could be some source of noise in that period. In addition, the position of this earthquake with respect to the signal path differs from those in the previous two cases: (a) the distance of the location of its epicenter from the signal path is the greatest, (b) the closest part of the signal path to it is the ICV transmitter. Also, it should be emphasized that the WMS earthquake is preceded by a weak earthquake. However, although noise amplitude reductions are also recorded in cases of earthquakes of magnitude below 3 [11], in this case, the reduction is detected after that earthquake, which is why it cannot be considered as its precursor. Of course, this does not exclude the possibility of a subsequent change in the characteristics of the VLF signal, but connecting them requires better statistics. In the following analysis, we assume that both mentioned periods are associated with the WMS earthquake.

The characteristics of the explained excitations and attenuations (determined in the same way as in the previous two cases) are:

- The wave excitations are visible in the time interval starting (100 ± 10) min before the WMS earthquake and ending (30 ± 10) min after it at the wave periods T_{exc} of (0.2333 ± 0.0001) s, (0.2800 ± 0.0001) s, (0.3500 ± 0.0002) s, (0.4667 ± 0.0002) s, (0.7001 ± 0.0005) s, and (1.400 ± 0.002) s (see Figure 7).
- As in the first case, the wave attenuations manifested as decreases in A_F , are visible in similar time intervals as the mentioned excitations for all values of T from its minimum value to 5.455 min except for those at which the indicated wave excitations are visible (see both upper panels for WTI = 20 min, and the bottom left panel for WTI = 1 h).

3.1.5. Comparisons of the Obtained Results

The common characteristics of the observed changes in all three cases are:

- The beginnings of changes in A_F are recorded before the time of the earthquake;
- Wave excitations are most pronounced for discrete values of period T below 1.5 s;
- The best representation of wave excitations is obtained for minimum time intervals of 20 min;
- Wave attenuations during those time intervals are pronounced for other periods below several minutes.

The obtained conclusions are in accordance with those obtained in the analysis of the ICV signal amplitude in the period around the earthquake near Kraljevo of magnitude 5.4 that occurred on 3 November 2010 [11]. A comparison with the results of the Fourier transformation of the ICV signal phase in the periods around these four earthquakes presented in [22] show similar time periods when excitations/attenuations are visible, similar values of T for which wave excitations are recorded, but also significantly larger domains of T for which the attenuation in waves of phase is visible.

3.2. Defining of VLF Signal Amplitude and Phase Parameters in the Time and Frequency Domains as Potential Earthquake Precursors

Based on the results presented in Section 3.1, and the studies given in [11,22], the changes in the VLF signal amplitude and phase can be classified

- In the time domain according to:
 - Characteristics of the amplitude/phase noise reduction,
- In the frequency domain according to:
 - Characteristics of excited waves before an earthquake at discrete values of the wave periods lower than 1.5 s,
 - Characteristics of attenuated waves on other wave periods with or without visible limitations in the upper limit of the observed domain.

To determine directions in further research of possible earthquake precursors manifested in the reduction in the VLF signal amplitude and phase noises, and the wave excitations and attenuations at small wave periods, we provide the following comparisons and we analyse the effects of other earthquakes on the duration of the mentioned changes.

- In the time domain:
 - The start time Δt_{rs} of the amplitude/phase noise reduction in relation to the time of the considered earthquake,
 - The end time Δt_{re} of the amplitude/phase noise reduction in relation to the time of the considered earthquake;
- In the frequent domain:
 - The start time Δt_{es} of the wave excitation/attenuation in relation to the time of the considered earthquake,
 - The end time Δt_{ee} of the wave excitation/attenuation in relation to the time of the considered earthquake,
 - Discrete values of T_{exc} of the excited waves,
 - The upper limit of the wave period domain within the wave attenuation is visible;

Here, we emphasize once again that this analysis is a pilot study and that its goal is to determine the parameters that, based on the observed sample, indicate possible changes that are potential precursors of earthquakes, their relationship and comparison of the quality and clarity of their detection. In addition to these parameters, future statistical studies should also include additional ones whose analysis requires a larger number of events. Here, we primarily mean the influence of earthquake characteristics (magnitude, depth) and the relative position of the earthquake epicentre and the path of the observed signal, the state of the atmosphere (primarily daytime, nighttime and solar terminator periods) on the characteristics of signal disturbances.

3.2.1. Intervals of Changes in the Time and Frequency Domains

Comparisons of the considered start and end times of changes in the time (Δt_{rs} and Δt_{re} , respectively) and frequency (Δt_{es} and Δt_{ee} , respectively) domains for the amplitude and phase are shown in Table 5, where it is assumed that the time intervals of the wave excitation and attenuation are the same for an earthquake (based on the obtained dependences $A_F(\Delta t_{ws}, T)$). To obtain the most accurate results, the displayed times are determined from the analysis of the graphs obtained for the smallest considered WTI of 20 min. As we stated in Section 2.3, the errors of determining the analyzed times in the time and frequency domains are 30 s and 10 min, respectively.

The following can be concluded from this table:

- The times Δt_{rs} and Δt_{re} are the same (in three cases) and similar (in the last case) in the time evolutions of the amplitude and phase of the ICV signal, while the time intervals in which the increases in the Fourier amplitude A_F are observed are the same for both signal parameters. Discrepancies in Δt_{rs} and Δt_{re} for the amplitude and phase of 20 min and 2 min, respectively, are recorded in the case of an earthquake that differs from the others in the position of its epicenter in relation to the signal path (the distance is the greatest and it is located to the west of the transmitter), and in the type of the noise amplitude reduction which, according to the study given in [33], indicates the displacement of the amplitude values after the reduction of its noise

(it is a reduction in Type II in contrast to other cases where they are reductions in Type I). For this reason, the characteristics that should be the subject of analysis in statistical studies are the relationships between the times Δt_{rs} and Δt_{re} for the signal amplitude and phase, as well as the connection of the discrepancy of these times with the reduction type.

- The times Δt_{es} and Δt_{ee} are the same for the amplitude and phase for all cases.
- The times Δt_{rs} and Δt_{re} , and Δt_{es} and Δt_{ee} are not the same for different events. Although they depend on the occurrence of other earthquakes, the investigation of these parameters depending on the magnitude and depth of the earthquake, and the position of its epicentre in relation to the observed VLF signal propagation path is of essential importance for the analyses of the considered changes as possible precursors of earthquakes. Of course, a sample of a significantly larger number of events that can be observed independently is necessary for that and, as stated earlier, this issue will be the subject of future research.
- The start and end times of disturbances are not the same in the time and frequency domains. Here, it should be kept in mind that the resolution in the second case is worse due to the shift in the time intervals on which the Fourier transform is applied in steps of 10 min, and due to the fact that the results of transformation refer to the entire observed time intervals Δt_{ws} . Although the comparison of the mentioned times is not relevant due to the given reasons, it is noticeable that the obtained differences are different in different cases. This variation indicates the need for more detailed statistical analysis to determine the existence or non-existence of their dependence on the characteristics of earthquakes and signals.

Table 5. The start and end times (with respect to the times of the K1, TS, K2, and WMS earthquakes) of the noise reductions (NR) in the time (t) domain (Δt_{rs} and Δt_{re} , respectively), and excitations/attenuations in the frequency (f) domain (Δt_{es} and Δt_{ee} , respectively) of the ICV signal amplitude (A) and phase (P). The errors in determining the analyzed times in the time and frequency domains are 30 s and 10 min, respectively.

Earthquake	Domain	Parameter	Start		End	
			A	P	A	P
K1	t	$\Delta t_{rs}/\Delta t_{re}$	−45 min	−45 min	5 h 50 min	5 h 50 min
	f	$\Delta t_{es}/\Delta t_{ee}$	−50 min	−50 min	5 h 50 min	5 h 50 min
TS	t	$\Delta t_{rs}/\Delta t_{re}$	−25 min	−25 min	2 h 23 min	2 h 23 min
	f	$\Delta t_{es}/\Delta t_{ee}$	−40 min	−40 min	2 h 10 min	2 h 10 min
K2	t	$\Delta t_{rs}/\Delta t_{re}$	−6 min 30 s	−6 min 30 s	13 min 30 s	13 min 30 s
	f	$\Delta t_{es}/\Delta t_{ee}$	−20 min	−20 min	10 min	10 min
WMS	t	$\Delta t_{rs}/\Delta t_{re}$	−1 h 35 min	−1 h 15 min	35 min	33 min
	f	$\Delta t_{es}/\Delta t_{ee}$	−1 h 40 min	−1 h 40 min	30 min	30 min

3.2.2. Characteristics of the Wave Excitations and Attenuation Periods

In addition to the duration of observed disturbance time intervals, two more parameters relevant for the frequency domain can be analyzed as precursors of earthquakes: the periods of wave excitation T_{exc} , and the maximum period T_{max} at which wave attenuation is noticeable in the period around the considered earthquake occurrence.

The values of T_{exc} are the wave periods for which the A_F is increased in time intervals starting before the moment when the observed earthquake occurred. These increases are visible in the 3D graphics in Figures 4–6 in this study, and in the relevant figures shown in [11,22]. In order to more clearly show the values of T at which the peaks in A_F are observed, we give the dependences of $A_F(T)$ for the signal amplitude and phase (at the moments when wave excitations are present) in Figures 7 and 8, respectively.

These values are given in Table 6. In cases where excitations are present for several close periods, the values with the highest A_F are taken.

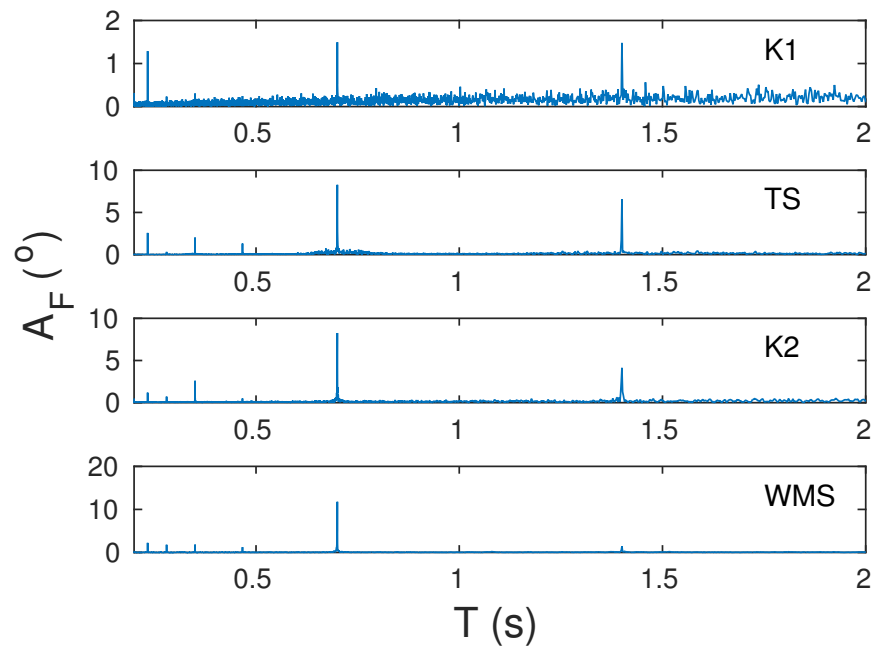


Figure 8. The Fourier amplitude A_F obtained by applying the FFT to the ICV signal phase during excitations of waves with periods less than 2 s in the time intervals around the K1, TS, K2, and WMS earthquake occurrences (panels are shown, respectively, from top to bottom) with period T .

Table 6. The wave periods of wave excitations T_{exc} obtained for the ICV signal amplitude A and phase P for the K1, TS, K2, and WMS earthquakes.

Earthquake	A/P	T_{exc} (s)						
		0.2000 ± 0.0001	0.2333 ± 0.0001	0.2800 ± 0.0001	0.3500 ± 0.0002	0.4667 ± 0.0002	0.7001 ± 0.0005	1.400 ± 0.002
K1	A		+	+	+	+	+	
	P	+	+	+	+	+ ¹	+	+
TS	A		+	+	+	+	+	+
	P		+	+	+	+	+	+
K2	A	+	+	+	+	+ ¹	+	+
	P		+	+	+	+	+	+
WMS	A		+	+	+	+	+	+
	P		+	+	+	+	+	+

¹ The peak is not significant, but it is visible and, given that it is detected in all other cases, it was included in the analysis.

Comparisons of T obtained by Fourier transformation of the A and P time evolutions show the following:

- The periods of the excited waves recorded in the analysis of both the signal amplitude and phase for all four earthquakes are (0.2333 ± 0.0001) s, (0.2800 ± 0.0001) s, (0.3500 ± 0.0002) s, (0.4667 ± 0.0002) s, and (0.7001 ± 0.0005) s. Waves with the period of (1.400 ± 0.002) s are excited in all cases except in the case of the amplitude during the period around the K1 earthquake. (Here, we observe all excitations in contrast to the study given in [22] where only the most significant ones are listed.)
- Wave excitations with $T = (0.2000 \pm 0.0001)$ s are recorded only in the phase analysis for the K1 earthquake, and in the amplitude analysis for the K2 earthquake.

The differences in the obtained characteristics of the Fourier amplitudes obtained from the A and P time evolutions are most noticeable in T_{\max} . In the case of amplitude, these values are significantly smaller and there are no clearly noticeable transitions in the T domains between parts where attenuations are clearly visible, and where they are not significant or do not exist (because of that the relevant values given in Table 7 are estimated). In contrast, reductions in A_F obtained by applying the FFT to $P(t)$ are clearly visible for all observed values of T for the K1, TS, and WMS earthquakes. Bearing in mind that the maximum value of WTI is 3 h, the maximum of T shown on the presented graphs is 90 min. For this reason, for these three earthquakes, we can only state that T_{\max} is at least 90 min, but that it most likely reaches higher values. In the case of the K2 earthquake no attenuation is visible for $T = 90$ min, which is a consequence of the short time interval within which noise reduction is visible. However, in this case, clear attenuations are also visible for periods of 90 min after this earthquake, when three weaker earthquakes are recorded at locations close to the K2 earthquake epicenter.

Table 7. The maximum wave periods at which wave attenuation obtained from the amplitude (T_{\max_A}) and phase (T_{\max_P}) time evolutions are noticeable in the period around the considered K1, TS, K2, and WMS earthquake occurrences.

Earthquake	T_{\max_A} (min)	T_{\max_P} (min)
K1	≈ 6.67	at least 90
TS	≈ 15	at least 90
K2	≈ 6.667	60–90
WMS	≈ 5.455	at least 90

4. Conclusions

In this paper, we complete the first investigation that indicates (a) the reductions in the VLF signal amplitude and phase noises, (b) the excitations of waves in the signal amplitude and phase time evolutions at discrete wave periods below 1.5 s, and (c) the attenuations of waves in the signal amplitude and phase time evolutions at small wave periods as new potential earthquake precursors. This investigation is based on processing the VLF signal amplitude and phase in the time periods around the four earthquakes with magnitudes greater than 4 when the observed signal is not already affected by intensive seismic activities connected with previous strong earthquakes.

In the previous two studies, changes are visible as the noise reduction in both the amplitude and phase in the time domain (analyses are given for all four cases), and as the wave excitations and attenuations in the frequency domain (amplitude analyses are given for the strongest earthquake, and phase analyses are provided for all four cases).

The presented study consists of two parts:

1. Completing the analysis of the 20.27 kHz ICV signal amplitude in the frequency domain for the time periods around the remaining three earthquakes (in the Tyrrhenian Sea on 3 November 2010, near Kraljevo on 4 November 2010, and in the Western Mediterranean Sea on 9 November 2010) that occurred near the path of the observed radio signal emitted by the ICV transmitter in Italy and recorded in Serbia.
2. Determination of VLF signal amplitude and phase parameters in the time and frequency domains that can be considered as potential earthquake precursors from comparisons of specific changes in the ICV signal amplitude and phase during the time period around the analyzed four earthquakes.

The obtained results in the first part indicate the same conclusions as in the corresponding analysis of the VLF signal amplitude for the Kraljevo earthquake that occurred on 3 November 2010:

- Excitation of waves with the wave periods below 1.5 s before the earthquake;

- Attenuation of waves for other periods below several minutes;
- The choice of the time interval on which the Fourier transformation is performed affects the clarity of the observed excitations and attenuations displayed. The best visibility is obtained for the shortest observed window time intervals of 20 min.

Comparisons of the ICV signal amplitude and phase characteristics in the time and frequency domains during the periods around the mentioned four earthquakes, which are presented in the second part of the study, indicate:

- The start and end times of the noise reduction in the time evolutions of the ICV signal amplitude and phase are the same in the three cases where the amplitude reduction is the reduction in Type I (the amplitude noise reduction is a consequence of increasing the minimum and decreasing the maximum values of the signal amplitude), and different in the case of the earthquake for which the noise reduction is the reduction in Type II (the amplitude noise reduction is a consequence of increasing the minimum values of the signal amplitude) and whose epicenter is farthest from the signal path and located west from the ICV transmitter;
- The time intervals in which the observed Fourier amplitude excitation is the same for both signal parameters;
- The start and end times of disturbances in relation to the time of the earthquake are various for different events;
- The start and end times of disturbances are not the same in the time and frequency domains and these differences are not the same for different events;
- The periods of the excited waves match for all considered earthquakes and both signal parameters for (0.2333 ± 0.0001) s, (0.2800 ± 0.0001) s, (0.3500 ± 0.0002) s, (0.4667 ± 0.0002) s, and (0.7001 ± 0.0005) s, while the wave excitations with the period of (1.400 ± 0.002) s are absent only in the case of the amplitude for the Kraljevo earthquake that occurred on 3 November 2010;
- The wave period domains of wave attenuations are much more pronounced for the Fast Fourier transform of the phase time evolution, where they are not limited in the observed ranges if the time period of the change is large enough. In the case of the Fast Fourier transform of the signal amplitude, the attenuation is present on smaller wave periods, and their upper limit of a few minutes is not clearly defined.

Bearing in mind that the obtained conclusions are based on a small sample, this study cannot confirm the connection between the analyzed changes in the characteristics of the VLF signal and the seismic activity. However, the goal of this study, based on pilot research on a smaller sample that is completed, determines significant parameters for statistical analyses that would potentially confirm the mentioned relationship is achieved. Based on the obtained conclusions, we propose statistical analyses of the dependencies of the following signal parameters on earthquake characteristics:

- The start and end times of the VLF signal amplitude and phase noise reductions in the time domain, their comparisons, and connecting the (non)existence of corresponding differences with the type of noise amplitude reduction;
- The start and end times of the excited/attenuated waves of the amplitude and phase in the frequency domain;
- Differences in the start and end times of corresponding disturbances in the time and frequency domains;
- The wave periods of the amplitude and phase wave excitations in the frequency domain.

All the above analyses will be the subjects of our next studies.

In the end, we would like to point out that the presented study refers to the VLF signal analysis in the periods around earthquakes when the seismic activity is not intense in the considered localized area. Bearing in mind the possibility of the influence of previous seismic activity on the detection of earthquake precursors due to the already present reduction in the signal amplitude/phase noise, the analyses shown in this study should also be performed for periods of intense seismic activity and, by comparing the obtained

conclusions, possible differences in the respective analyses should be established. This investigation will also be the focus of our research in the coming period.

Funding: The author acknowledges funding provided by the Institute of Physics Belgrade through grants by the Ministry of Education, Science, and Technological Development of the Republic of Serbia.

Data Availability Statement: Publicly available datasets were analyzed in this study. This data can be found here: <http://www.emsc-csem.org/Earthquake/> (accessed on 28 February 2021). The VLF data used for analysis is available from the corresponding author.

Acknowledgments: The author thanks Vladimir Čadež for his help in preparing this paper.

Conflicts of Interest: The author declares no conflicts of interest.

References

- Davies, K.; Baker, D.M. Ionospheric effects observed around the time of the Alaskan earthquake of March 28, 1964. *J. Geophys. Res.* **1965**, *70*, 2251–2253. [[CrossRef](#)]
- Leonard, R.S.; Barnes, R.A.J. Observations of Ionospheric Disturbances Following the Alaska Earthquake. *J. Geophys. Res.* **1965**, *70*, 1250–1253. [[CrossRef](#)]
- Yuen, P.C.; Weaver, P.F.; Suzuki, R.K.; Furumoto, A.S. Continuous, traveling coupling between seismic waves and the ionosphere evident in May 1968 Japan earthquake data. *J. Geophys. Res.* **1969**, *74*, 2256–2264. [[CrossRef](#)]
- Molchanov, O.; Hayakawa, M.; Oudoh, T.; Kawai, E. Precursory effects in the subionospheric VLF signals for the Kobe earthquake. *Phys. Earth Planet. Inter.* **1998**, *105*, 239–248. [[CrossRef](#)]
- Biagi, P.F.; Piccolo, R.; Ermini, A.; Martellucci, S.; Bellecci, C.; Hayakawa, M.; Kingsley, S.P. Disturbances in LF radio-signals as seismic precursors. *Ann. Geophys.* **2001**, *44*, 1011–1019. [[CrossRef](#)]
- Němec, F.; Santolík, O.; Parrot, M. Decrease of intensity of ELF/VLF waves observed in the upper ionosphere close to earthquakes: A statistical study. *J. Geophys. Res. Space Phys.* **2009**, *114*, A04303. [[CrossRef](#)]
- Maurya, A.K.; Venkatesham, K.; Tiwari, P.; Vijaykumar, K.; Singh, R.; Singh, A.K.; Ramesh, D.S. The 25 April 2015 Nepal Earthquake: Investigation of precursor in VLF subionospheric signal. *J. Geophys. Res. Space Phys.* **2016**, *121*, 10403–10416. [[CrossRef](#)]
- Price, C.; Yair, Y.; Asfur, M. East African lightning as a precursor of Atlantic hurricane activity. *Geophys. Res. Lett.* **2007**, *34*, 9805. [[CrossRef](#)]
- Biagi, P.F.; Maggipinto, T.; Righetti, F.; Loiacono, D.; Schiavulli, L.; Ligonzo, T.; Ermini, A.; Moldovan, I.A.; Moldovan, A.S.; Buyuksarac, A.; et al. The European VLF/LF radio network to search for earthquake precursors: Setting up and natural/man-made disturbances. *Nat. Hazards Earth Syst. Sci.* **2011**, *11*, 333–341. [[CrossRef](#)]
- Kumar, S.; NaitAmor, S.; Chanrion, O.; Neubert, T. Perturbations to the lower ionosphere by tropical cyclone Evan in the South Pacific Region. *J. Geophys. Res. Space Phys.* **2017**, *122*, 8720–8732. [[CrossRef](#)]
- Nina, A.; Pulinet, S.; Biagi, P.; Nico, G.; Mitrović, S.; Radovanović, M.; Č. Popović, L. Variation in natural short-period ionospheric noise, and acoustic and gravity waves revealed by the amplitude analysis of a VLF radio signal on the occasion of the Kraljevo earthquake (Mw = 5.4). *Sci. Total Environ.* **2020**, *710*, 136406. [[CrossRef](#)] [[PubMed](#)]
- Hayakawa, M. The precursory signature effect of the Kobe earthquake on VLF subionospheric signals. *J. Comm. Res. Lab.* **1996**, *43*, 169–180.
- Yamauchi, T.; Maekawa, S.; Horie, T.; Hayakawa, M.; Soloviev, O. Subionospheric VLF/LF monitoring of ionospheric perturbations for the 2004 Mid-Niigata earthquake and their structure and dynamics. *J. Atmos. Sol.-Terr. Phys.* **2007**, *69*, 793–802. [[CrossRef](#)]
- Biagi, P.; Castellana, L.; Maggipinto, T.; Piccolo, R.; Minafra, A.; Ermini, A.; Martellucci, S.; Bellecci, C.; Perna, G.; Capozzi, V.; et al. LF radio anomalies revealed in Italy by the wavelet analysis: Possible preseismic effects during 1997–1998. *Phys. Chem. Earth Parts A/B/C* **2006**, *31*, 403–408. [[CrossRef](#)]
- Hayakawa, M.; Horie, T.; Muto, F.; Kasahara, Y.; Ohta, K.; Liu, J.Y.; Hobar, Y. Subionospheric VLF/LF Probing of Ionospheric Perturbations Associated with Earthquakes: A Possibility of Earthquake Prediction. *SICE J. Control Meas. Syst. Integr.* **2010**, *3*, 10–14. [[CrossRef](#)]
- Molchanov, O.; Hayakawa, M.; Miyaki, K. VLF/LF sounding of the lower ionosphere to study the role of atmospheric oscillations in the lithosphere-ionosphere coupling. *Adv. Polar Up. Atmos. Res.* **2001**, *15*, 146–158.
- Ohya, H.; Tsuchiya, F.; Takishita, Y.; Shinagawa, H.; Nozaki, K.; Shiokawa, K. Periodic Oscillations in the D Region Ionosphere After the 2011 Tohoku Earthquake Using LF Standard Radio Waves. *J. Geophys. Res. Space Phys.* **2018**, *123*, 5261–5270. [[CrossRef](#)]
- Rozhnoi, A.; Solovieva, M.; Molchanov, O.; Hayakawa, M. Middle latitude LF (40 kHz) phase variations associated with earthquakes for quiet and disturbed geomagnetic conditions. *Phys. Chem. Earth Parts A/B/C* **2004**, *29*, 589–598. [[CrossRef](#)]
- Song, D.; Chen, Z.; Ke, Y.; Nie, W. Seismic response analysis of a bedding rock slope based on the time-frequency joint analysis method: A case study from the middle reach of the Jinsha River, China. *Eng. Geol.* **2020**, *274*, 105731. [[CrossRef](#)]

20. Madley, M.; Yates, A.; Savage, M.; Wang, W.; Okada, T.; Matsumoto, S.; Iio, Y.; Jacobs, K. Velocity changes around the Kaikōura earthquake ruptures from ambient noise cross-correlations. *Geophys. J. Int.* **2022**, *229*, 1357–1371. [[CrossRef](#)]
21. Bonilla, L.F.; Ben-Zion, Y. Detailed space–time variations of the seismic response of the shallow crust to small earthquakes from analysis of dense array data. *Geophys. J. Int.* **2021**, *225*, 298–310. [[CrossRef](#)]
22. Nina, A.; Biagi, P.F.; Mitrović, S.T.; Pulinets, S.; Nico, G.; Radovanović, M.; Popović, L.Č. Reduction of the VLF Signal Phase Noise Before Earthquakes. *Atmosphere* **2021**, *12*, 444. [[CrossRef](#)]
23. The Euro-Mediterranean Seismological Centre. Available online: <https://www.emsc-csem.org/> (accessed on 5 February 2021).
24. Hanks, T.C.; Kanamori, H. A moment magnitude scale. *J. Geophys. Res. Solid Earth* **1979**, *84*, 2348–2350. [[CrossRef](#)]
25. Kanamori, H. Magnitude scale and quantification of earthquakes. *Tectonophysics* **1983**, *93*, 185–199. [[CrossRef](#)]
26. Richter, C.F. An instrumental earthquake magnitude scale. *Bull. Seismol. Soc. Am.* **1935**, *25*, 1–32. [[CrossRef](#)]
27. Bormann, P.; Wendt, S.; DiGiacomo, D. Seismic sources and source parameters. In *New Manual of Seismological Observatory Practice 2 (NMSOP2)*; Deutsches GeoForschungsZentrum GFZ: Potsdam, Germany, 2013; Volume 25, pp. 1–259. [[CrossRef](#)]
28. Zare, M.; Amini, H.; Yazdi, P.; Sesetyan, K.; Demircioglu, M.B.; Kalafat, D.; Erdik, M.; Giardini, D.; Khan, M.A.; Tsereteli, N. Recent developments of the Middle East catalog. *J. Seismol.* **2014**, *18*, 749–772. [[CrossRef](#)]
29. Mereu, R.F. A study of the relations between ML, Me, Mw, apparent stress, and fault aspect ratio. *Phys. Earth Planet. Inter.* **2020**, *298*, 106278. [[CrossRef](#)]
30. Nina, A.; Simić, S.; Srećković, V.A.; Popović, L.Č. Detection of short-term response of the low ionosphere on gamma ray bursts. *Geophys. Res. Lett.* **2015**, *42*, 8250–8261. [[CrossRef](#)]
31. Nina, A.; Čadež, V.M.; Popović, L.Č.; Srećković, V.A. Diagnostics of plasma in the ionospheric D-region: Detection and study of different ionospheric disturbance types. *Eur. Phys. J. D* **2017**, *71*, 189. [[CrossRef](#)]
32. Kolarski, A.; Srećković, V.; Langović, M.; Arnaut, F. Energetic solar flare events in relation with subionospheric impact on 6–10 September 2017: Data and modeling. *Contrib. Astron. Obs. Skaln. Pleso* **2023**, *53*, 138–147. [[CrossRef](#)]
33. Nina, A.; Biagi, P.F.; Pulinets, S.; Nico, G.; Mitrović, S.T.; Čadež, V.M.; Radovanović, M.; Urošev, M.; Popović, L.Č. Variation in the VLF signal noise amplitude during the period of intense seismic activity in Central Italy from 25 October to 3 November 2016. *Front. Environ. Sci.* **2022**, *10*, 1005575. [[CrossRef](#)]

Disclaimer/Publisher’s Note: The statements, opinions and data contained in all publications are solely those of the individual author(s) and contributor(s) and not of MDPI and/or the editor(s). MDPI and/or the editor(s) disclaim responsibility for any injury to people or property resulting from any ideas, methods, instructions or products referred to in the content.



Article

Modelling of the Electron Density and Total Electron Content in the Quiet and Solar X-ray Flare Perturbed Ionospheric D-Region Based on Remote Sensing by VLF/LF Signals

Aleksandra Nina

Institute of Physics Belgrade, University of Belgrade, Pregrevica 118, 11080 Belgrade, Serbia; sandrast@ipb.ac.rs

Abstract: Many analyses of the perturbed ionospheric D-region and its influence on the propagation of ground-based and satellite signals are based on data obtained in ionospheric remote sensing by very low/low frequency (VLF/LF) signals. One of the most significant causes of errors in these analyses is the lack of data related to the analysed area and time period preceding the considered perturbation. In this paper, we examine the influence of the estimation of the quiet ionosphere parameters on the determination of the electron density (N_e) and total electron content in the D-region (TEC_D) during the influence of a solar X-ray flare. We present a new procedure in which parameters describing the quiet ionosphere are calculated based on observations of the analysed area by a VLF/LF signal at the observed time. The developed procedure is an upgrade of the quiet ionospheric D-region (QIonDR) model that allows for a more precise analysis of the D-region intensively perturbed by a solar X-ray flare. The presented procedure is applied to data obtained in ionospheric remote sensing by the DHO signal emitted in Germany and received in Serbia during 30 solar X-ray flares. We give analytical expressions for the dependencies of the analysed parameters on the X-ray flux maximum at the times of the X-ray flux maximum and the most intense D-region perturbation. The results show that the obtained N_e and TEC_D are larger than in the cases when the usual constant values of the quiet ionosphere parameters are used.

Keywords: VLF/LF signals; remote sensing; ionospheric D-region; electron density; total electron content; solar X-ray flares



Citation: Nina, A. Modelling of the Electron Density and Total Electron Content in the Quiet and Solar X-ray Flare Perturbed Ionospheric D-Region Based on Remote Sensing by VLF/LF Signals. *Remote Sens.*

2022, 14, 54. <https://doi.org/10.3390/rs14010054>

Academic Editor: Michael E. Gorbunov

Received: 23 November 2021

Accepted: 17 December 2021

Published: 23 December 2021

Publisher's Note: MDPI stays neutral with regard to jurisdictional claims in published maps and institutional affiliations.



Copyright: © 2021 by the authors. Licensee MDPI, Basel, Switzerland. This article is an open access article distributed under the terms and conditions of the Creative Commons Attribution (CC BY) license (<https://creativecommons.org/licenses/by/4.0/>).

1. Introduction

In addition to the importance of ionospheric D-region modelling in scientific studies (see, for example, [1–6]), knowledge of properties of this atmospheric layer is necessary for the analysis of the electromagnetic signal propagation. Consequently, this modelling can have practical application in technologies based on the propagation of satellite and ground-based signals, such as space geodesy and telecommunications. Namely, during intense perturbations of the D-region, its influence on the satellite signal delay is not negligible [7], which is consequently reflected in the determination of the ionospheric influence in many measurements (see, for example, [8]). Due to lower frequencies of ground based signals, the importance of D-region modelling is more pronounced in the determination of the characteristics of their propagation, which is significant in, for example, telecommunications.

Monitoring of the ionospheric D-region is based on three techniques: rocket measurements, radar sounding, and propagation of very low/low frequency (VLF/LF) signals in the Earth–ionosphere waveguide. The latter technique is most commonly used for the corresponding studies. The two main reasons for this are: (1) the global system for these observations consists of numerous worldwide distributed transmitters and receivers, thus ensuring good coverage of the lower ionosphere, and (2) data are recorded continuously with the possibility of time sampling of only a few milliseconds, which allows the detection of sudden and short-term variations. However, this technique requires a large distance between a transmitter and a receiver that is a minimum of several hundred kilometres. Due

to the spatial and time variations of this atmospheric layer caused by both periodic changes and unpredictable sudden effects of numerous terrestrial and extraterrestrial phenomena and processes, it is necessary that observational data relevant to the observed area and time period be included in modelling. Even in studies of perturbations affecting the entire signal propagation path (induced by some phenomena from the outer space such as solar X-ray flares), it is necessary to introduce several approximations. The most significant of them are the horizontal uniformity of the ionosphere (either along the entire signal propagation path or partially along its sections) and the estimation of the quiet ionosphere parameters in the time period preceding the considered perturbation. The first approximation is good for a not too long signal propagation path and for daytime periods of a few hours around midday in absence of intensive local disturbances. Estimations of the quiet ionosphere parameters are given in several studies [9–13]. However, there are no studies on the influence of the choice of the quiet ionosphere parameters on D-region modelling during disturbances. That analysis is in the focus of this study.

In this research, we present a new methodology for calculating the parameters of the perturbed D-region, which refers to the analysed time period and the observed area. We analyse the “sharpness” (β), the signal reflection height (H'), the D-region electron density (N_e), and the total electron content in the D-region (TEC_D). The first two parameters describe the so-called Wait model of the ionosphere, and their common name is Wait’s parameters. As a source of ionospheric perturbation, we observe solar X-ray flares. They can induce intense D-region perturbations which can last from several tenth of minutes to over one hour. This astrophysical phenomenon can induce an increase in the D-region electron density by more than one order of magnitude (see, for example, [14]). This analysis is a continuation of the research given in [13] in which the quiet ionospheric D-region (QIonDR) model is presented. The motivation to develop the presented procedure was the need for more precise determination of the initial state in both the considered time period and the observed area for modelling of the perturbed D-region. Namely, the QIonDR model provides a procedure for estimating the dependencies of ionospheric parameters on the solar cycle period and season, as well as the equations relevant to a part of Europe. That analysis is relevant for quiet conditions, but the equations obtained by fitting the estimated values in the analysed periods give the values with certain errors which, consequently, affects modelling of ionospheric parameters during perturbations. In the presented study, we give the following three analyses: first, we describe the influence of the choice of Wait’s parameters in the quiet state on the determination of their time evolutions during perturbations; second, we present a procedure for the determination of these parameters before perturbations caused by solar X-ray flares; and, third, we model the considered ionospheric parameters during perturbation using the Long-Wave Propagation Capability (LWPC) numerical model [15] and the initial values of Wait’s parameters estimated by the presented procedure. We apply the developed procedure to (1) the entire time period of a perturbation caused by a single flare and (2) the times of the X-ray flux maxima recorded by the geostationary operational environmental system (GOES) and the times of the D-region perturbation maxima determined by the times of the TEC_D maxima for 30 events. Here, it is important to emphasise that, although the D-region disturbance is most intense some time after the considered X-ray flux maximum, the previous statistical studies are primarily related to the values of ionospheric parameters at the time of the X-ray flux maximum. In other words, the maximum effects of X-ray flares on both the D-region parameters and the propagation of electromagnetic waves in this area have not been investigated from a statistical point of view.

We observe variations caused by solar X-ray flares that are sources of intense D-region disturbances. The impact of these events on the atmosphere is global and for several hours around noon it causes similar variations at the same altitude along relatively short VLF/LF signal paths that extend in the low and mid latitude areas. For this reason, we are able to apply an approximation of the horizontally uniform ionosphere. The presented analysis is based on the data recorded by the receiver station in Belgrade, Serbia, and refers to the DHO signal emitted in Rhaderfehn, Germany.

The paper is organised as follows. After describing the analyses of observations and events in Section 2, we present our proposed methodology in Section 3. Section 4 shows the results of the presented procedure applied to the considered class-C and -M solar X-ray flares at the times of the X-ray flux and the D-region perturbation maxima. The conclusions of this study are given in Section 5.

2. Observational Setups, Studied Area, and Considered Events

The procedure presented in this study is based on data collected by a VLF/LF receiver while the observed periods are selected based on GOES satellite measurements.

In this study, we use data recorded by the atmospheric weather electromagnetic system for observation modelling and education (AWESOME) receiver [16] located in Belgrade, Serbia, relating to the VLF signal emitted by the DHO transmitter in Germany. This receiver was a part of the Stanford/AWESOME Collaboration for Global VLF Research (<http://waldo.world/narrowband-data/>, accessed on 5 November 2021). As in many previous studies (see, for example, [7,8,17]), we analyse the DHO signal because of the best quality of the recorded data. Consequently, the analytical expressions obtained in this study refer to the D-region over the part of Europe included within the transmitter (Rhauderfehn, Lower Saxony, Germany) and receiver (Belgrade, Serbia) locations.

The observed time periods are selected based on X-ray flux data recorded by the GOES satellites. Datasets of the X-ray fluxes recorded by the GOES satellites are available on the National Oceanic and Atmospheric Administration's (NOAA's) National Centers for Environmental Information website (<http://satdat.ngdc.noaa.gov/sem/goes/data>, accessed on 7 September 2021). A GOES satellite provides data recorded by two detectors in the energy channels A (0.05 nm–0.4 nm) and B (0.1 nm–0.8 nm), which better describe the influence of an X-ray flare in the bottom and upper D-region, respectively [17]. Bearing in mind that the electron density increases with the D-region altitude, i.e., the upper D-region provides the dominant contribution to TEC_D , we assume that the flux representing the X-radiation (Φ) is the flux recorded by the GOES channel B. The data recorded through this channel are also used in many previous studies of the solar X-ray flare perturbed D-region (see, for example, [18–20]).

In this study, we consider the time period from 2010 to 2016 that includes both the minimum and maximum of the 24th solar cycle. We analyse 30 flares whose characteristics (dates, start times, and flare classes) are shown in Table 1. The last two columns list the daily smoothed sunspot number (σ) and season parameter ($\chi = DOY/365$, where DOY is the day of year). These two parameters show that the obtained numbers of sunspots are in a wide range and that the events took place throughout the year. This allows us to analyse the impact of variations during the solar cycle and seasonal changes on the observed parameters.

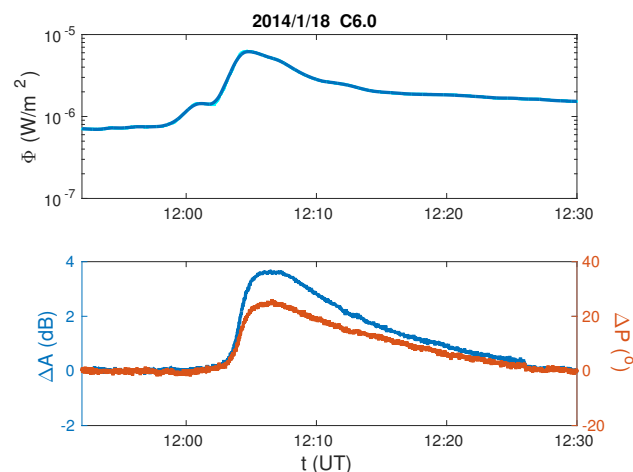
These flares are selected based on the following criteria:

- The DHO signal amplitude and phase are recorded by the AWESOME receiver in Belgrade during the period when the D-region is perturbed by a solar X-ray flare. Significant changes in amplitude and phase resulting from the influence of other phenomena or technical problems in signal emission/reception are not recorded during the period significant for the presented analysis;
- The impact of an X-ray flare is in the midday period. This condition makes it possible to avoid the effects of diurnal changes which are more pronounced during the morning and afternoon when an approximation of the horizontally uniform ionosphere cannot be taken during the whole period of perturbation;
- The X-ray flare class is from C1 to M5. The lower limit is set because weaker flares do not cause clear changes in the signal characteristics, while the upper limit is introduced because modelling of the electron density by the procedure given in [21] is more appropriate for not too intensive flares.

Table 1. Dates, times, and classes of the considered X-ray flares, the daily smoothed sunspot number (σ), and season parameter ($\chi = \text{DOY}/365$, where DOY is the day of year).

No	Date	Time (UT)	Flare Class	σ	χ
1	5 May 2010	11:37	C8.8	10.714	0.345
2	13 July 2010	10:43	C2.6	18.381	0.534
3	14 July 2010	12:11	C1.4	18.524	0.537
4	14 January 2012	12:00	C4.1	96.952	0.038
5	16 January 2012	10:31	C5.5	101.190	0.044
6	21 March 2012	12:38	C2.9	86.333	0.222
7	9 April 2012	12:12	C3.9	71.000	0.274
8	25 April 2012	12:07	C3.7	83.238	0.318
9	2 May 2012	11:32	C3.2	107.952	0.337
10	29 June 2012	09:13	M2.2	72.952	0.496
11	30 June 2012	10:48	C2.7	72.857	0.499
12	8 October 2012	11:05	M2.3	78.524	0.773
13	20 November 2012	12:36	M1.7	88.571	0.890
14	5 November 2013	11:51	C8.0	130.905	0.849
15	8 January 2014	11:56	C6.1	124.571	0.022
16	18 January 2014	11:57	C6.0	122.000	0.049
17	1 February 2014	10:43	C3.5	106.048	0.088
18	3 February 2014/2/3	10:58	C4.4	105.810	0.093
19	2 March 2014	11:55	C2.4	149.571	0.170
20	1 July 2014	11:05	M1.4	102.714	0.501
21	29 October 2014	11:02	C5.3	86.048	0.827
22	7 November 2014	10:13	M1.0	107.905	0.855
23	15 November 2014	11:40	M3.2	100.143	0.877
24	13 December 2014	10:49	C3.8	108.810	0.953
25	6 January 2015	11:40	C9.7	112.571	0.016
26	21 January 2015	11:32	C9.9	87.619	0.058
27	6 May 2015	11:45	M1.9	84.857	0.348
28	4 June 2015	09:36	C8.1	60.238	0.427
29	17 September 2015	09:34	M1.1	53.952	0.715
30	14 May 2016	11:28	C7.4	68.619	0.370

To show the influence of the choice of Wait's parameters in the quiet state (β_0 and H_0) on modelling of the considered parameters during the entire period of perturbation, we analyse the D-region perturbed by an X-ray flare that occurred on 18 January 2014. The time evolution of the solar X-ray flux Φ recorded by the GOES satellite is shown in Figure 1 (upper panel), while the time evolutions of the signal amplitude and phase changes with respect to their value in quiet conditions are presented in the bottom panel.

**Figure 1.** Time evolutions of the energy X-ray flux (Φ) (upper panel), and the recorded amplitude (ΔA) and phase (ΔP) changes with respect to quiet conditions (bottom panel) during a solar X-ray flare that occurred on 18 January 2014.

3. Methodology

In this section, we present a methodology for modelling β , H' , N_e , and TEC_D during the influence of a solar X-ray flare. It takes into account the different states of the quiet ionosphere before the observed perturbations and provides a new procedure for the determination of Wait's parameters β_0 and H'_0 .

3.1. Determination of Wait's Parameters

In this section, we (1) describe the procedure for the determination of the time evolutions of β and H' , (2) describe how the choice of β_0 and H'_0 affects the determination of Wait's parameters during a disturbance caused by a solar X-ray flare, and (3) give criteria for the estimation of β_0 and H'_0 before a particular X-ray flare event.

- Determination of the time evolutions of Wait's parameters. Modelling of these dependencies is based on observational data and the LWPC numerical model [15]. For the considered VLF/LF signal and receiver location, the input parameters in this numerical program are Wait's parameters, and its outputs are the modelled amplitude (A_{mod}) and phase (P_{mod}). The presented procedure for the determination of β and H' at time t is based on the comparison of the observed changes in the recorded signal amplitude (ΔA) and phase (ΔP) with respect to quiet conditions with the corresponding modelled changes:

$$\Delta A(t) = A_{\text{mod}}(\beta(t), H'(t)) - A_{\text{mod}}(\beta_0, H'_0) \quad (1)$$

and

$$\Delta P(t) = P_{\text{mod}}(\beta(t), H'(t)) - P_{\text{mod}}(\beta_0, H'_0). \quad (2)$$

In these expressions, β_0 and H'_0 are considered known, while $\beta(t)$ and $H'(t)$ are determined based on the best agreement of the left and right sides of Equations (1) and (2) at time t . This procedure is well known and used in many papers [19,22], but it differs according to the mentioned criteria and the taken values β_0 and H'_0 . In some studies, these criteria are not clearly defined, while β_0 and H'_0 are usually taken as constants. The consequence of the last approximation is the neglect of daily and seasonal variations, variations during a solar cycle, as well as variations due to various sudden influences.

In this paper, the criterion for the best agreement of the recorded and modelled changes in the signal characteristics (for pre-estimated values β_0 and H'_0) is the minimum value of the sum of the corresponding differences normalised to the corresponding maximum recorded values.

$$\beta(t) = \beta^*, \quad H'(t) = H'^* : \quad G(\beta(t), H'(t)) = \min\{G(\beta^*, H'^*)\}, \quad (3)$$

where

$$G(\beta^*, H'^*) = \frac{|A_{\text{mod}}(\beta^*, H'^*) - A_{\text{mod}}(\beta_0, H'_0) - \Delta A(t)|}{\Delta A_{\text{max}}} + \frac{|P_{\text{mod}}(\beta^*, H'^*) - P_{\text{mod}}(\beta_0, H'_0) - \Delta P(t)|}{\Delta P_{\text{max}}}. \quad (4)$$

Here, β^* and H'^* are all possible values of Wait's parameters.

In this paper, special attention is paid to the choice of parameters β_0 and H'_0 . We propose a new methodology for their determination that represents an upgrade of the QIonDR model. An explanation of the significance of this analysis and a description of the proposed methodology are given in the following text.

- Description of the influence of Wait's parameters describing quiet ionosphere before the considered solar X-ray flare on modelling of their values under the disturbed conditions.

As it can be seen from Equation (4), the pair (β_0, H'_0) affects the value of G and, consequently, the value of the pair (β, H') obtained by applying the criterion given by

Equation (3). To better explain this impact, we analyse the results of modelling by the LWPC numerical program for two pairs (β_0, H'_0) and for the given registered amplitude ΔA and phase ΔP changes of 3 dB and 30° , respectively. The surfaces presented in Figure 2 show A_{mod} and P_{mod} (left and right panel, respectively) corresponding to all combinations of the considered values of Wait's parameters. The isolated points (blue and red diamonds) correspond to the two combinations of β_0 and H'_0 : $(0.4 \text{ km}^{-1}, 72 \text{ km})$ and $(0.3 \text{ km}^{-1}, 74 \text{ km})$, respectively. The points that form the blue and red "lines" indicate the pairs of Wait's parameters for which the modelled amplitude (left panel) and phase (right panel) are approximate 3 dB and 30° larger than the corresponding values obtained for the two considered initial states, respectively. Although there are a number of pairs (β, H') for which one of the modelled changes is approximately equal to the corresponding given change, there are only a few combinations of Wait's parameters (for one observed initial state) that give approximate agreement of both signal characteristics changes. It can be seen in Figure 3, where the obtained modelled pairs are presented in the 2D Wait's parameter space. The estimated intersection points on the left and right panels $((0.48 \text{ km}^{-1}, 68.2 \text{ km})$ and $(0.38 \text{ km}^{-1}, 68.4 \text{ km})$, respectively) represent Wait's parameters obtained for their initial combinations $(0.4 \text{ km}^{-1}, 72 \text{ km})$ and $(0.3 \text{ km}^{-1}, 74 \text{ km})$, respectively. Based on the estimated pairs of Wait's parameters, the electron density values at 65 km, 75 km, and 85 km are $1.8 \times 10^8 \text{ m}^{-3}$, $4.9 \times 10^9 \text{ m}^{-3}$, and $1.3 \times 10^{11} \text{ m}^{-3}$, in the first case, and $2.3 \times 10^8 \text{ m}^{-3}$, $2.3 \times 10^9 \text{ m}^{-3}$, and $2.3 \times 10^{10} \text{ m}^{-3}$, in the second case, while the corresponding values of TEC_D are 0.2 TECU and 0.03 TECU, respectively (the procedures for modelling these parameters are given in Sections 3.2 and 3.3). A comparison of these values indicates a significant influence of the choice of β_0 and H'_0 on modelling of the perturbed D-region. In order to better understand its significance, it is necessary to emphasise that the given changes in the signal characteristics are not too large and that the selected pairs of initial Wait's parameters represent their real values that are not quiet close to the corresponding intervals limits. In other words, the obtained differences may be more pronounced in some other, also realistic, conditions.

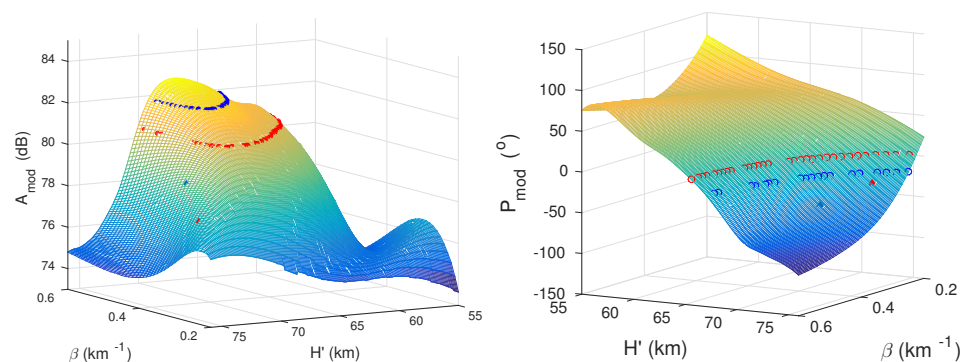


Figure 2. Surface plots of the modelled amplitude (A_{mod}) (left panel) and phase (P_{mod}) (right panel) on the Wait's parameters "sharpness" (β) and signal reflection height (H'). The isolated points (blue and red diamonds) correspond to the two combinations of β_0 and H'_0 : $(0.4 \text{ km}^{-1}, 72 \text{ km})$ and $(0.3 \text{ km}^{-1}, 74 \text{ km})$, respectively. Blue and red circles indicate the pairs of Wait's parameters for which the modelled amplitude (left panel) and phase (right panel) are approximate 3 dB and 30° larger than the corresponding values obtained for the two considered initial states, respectively.

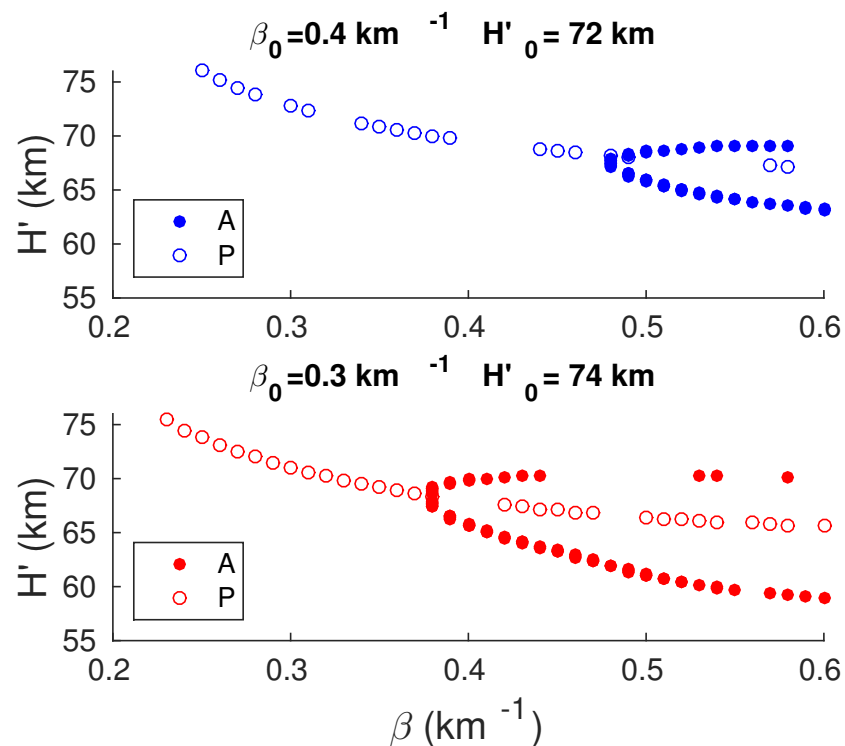


Figure 3. Pairs of the Wait's parameters, “sharpness” (β) and signal reflection height (H'), for which the modelled amplitude (left panel) and phase (right panel) are approximative 3 dB and 30° larger than the corresponding values obtained for the two initial combinations of Wait's parameters (0.4 km^{-1} , 72 km) (**upper panel**) and (0.3 km^{-1} , 74 km) (**bottom panel**). The filled and open circles relate to the modelled amplitude and phase, respectively. These scatters correspond to those shown in Figure 2.

- Criteria for estimation of Wait's parameters in the quiet state before the considered solar X-ray flare.

Intensification of a D-region disturbance causes an increase/decrease in β and H' , respectively, while the tendencies of these time evolutions are opposite during the return to the steady state of the ionosphere [2,13,17]. However, the choice of β_0 and H'_0 significantly influences the shapes of their time evolutions, which allows us to introduce criteria for choosing the combination that gives the best dependences $\beta(t)$ and $H'(t)$. To better explain the differences in the time evolutions of Wait's parameters, we present four different shapes for an X-ray flare that occurred on 18 January 2014 (see Figure 4). In the presented graphs, the points represent the corresponding values obtained at time t using the criterion given by Equation (3), while the lines show their smoothed values.

As it can be seen in the upper panels, there are values of pairs (β_0, H'_0) for which the time evolutions of β decrease (upper left panel) or reach the maximum possible value in a longer time period (right panel) which is not in accordance with the expected form. These discrepancies allow us to exclude all combinations (β_0, H'_0) for which the corresponding forms are similar to those shown on these two panels. In addition, many combinations (β_0, H'_0) give $\beta(t)$ dependences that fall very quickly to the initial values with respect to the time evolutions of H' , A , and P , which also excludes the corresponding pairs (β_0, H'_0) . One such example is given in the bottom left panel. An example of the shape of function $\beta(t)$ that can describe the time evolution of this Wait's parameter is given in the bottom right panel.

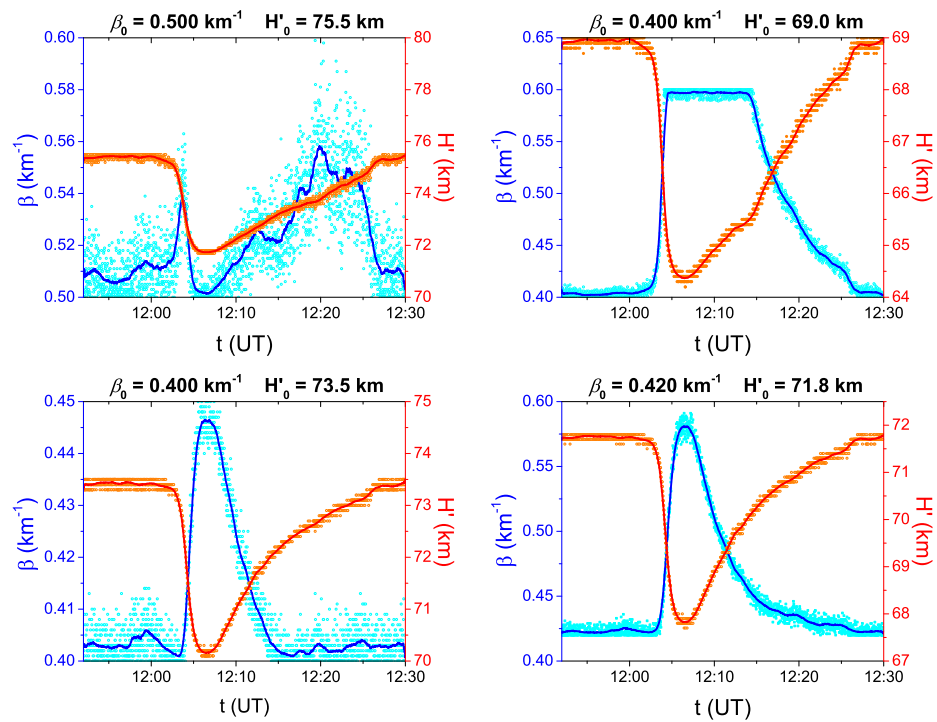


Figure 4. Examples of the four different shapes of the time evolutions of Wait's parameters for an X-ray flare that occurred on 18 January 2014.

To estimate the initial conditions and model the time evolutions of Wait's parameters we use the following criteria:

1. The obtained values of β cannot be greater than 0.6 km^{-1} . We take this value based on the studies presented in [10–13,21,23].
2. The shape of the smoothed time evolution of β is characterised by an increase to the maximum value (occurs after the maximum X-ray flux in the period, when H' reaches minimum value) followed by a decrease. Deviations from this shape are possible if the corresponding characteristics are observed in the signal amplitude/phase but, in that case, we consider only events in which these variations do not affect the analysis, i.e., when these variations occur after extreme values of Wait's parameters.
3. The relaxation of β to its value in the quiet state after the considered disturbance should be as similar as possible to the signal amplitude relaxation. For this reason, we introduce the condition that the time when β reaches values corresponding to quiet conditions should be after the time when ΔA falls to some given value. This value is not unique due to differences in the characteristics of various impacts on the observed area during the analysed time period. Based on the presented analysis, the estimated value of this parameter is between 0.5 dB and 1 dB.
4. Generally, there are several combinations of β_0 and H'_0 that meet criteria 1 and 2 and have a similar time when β reaches values corresponding to quiet conditions. Therefore, we introduce an additional criterion that allows us to determine the combination (β_0, H'_0) that deviates the least from Wait's parameters, β_0^{QIonDR} and H'_0^{QIonDR} , predicted by the QIonDR model. This deviation (δ) is calculated by the following expression:

$$\delta = \min \left\{ \frac{|\beta_0 - \beta_0^{\text{QIonDR}}|}{\varepsilon_{\beta_0}} + \frac{|H'_0 - H'_0^{\text{QIonDR}}|}{\varepsilon_{H'_0}} \right\}, \quad (5)$$

where dependencies of midday Wait's parameters on the daily smoothed sunspot number (σ) and the seasonal parameter (χ) estimated by the QIonDR model are given by following equations [13]:

$$\beta_0^{\text{QIonDR}} = 0.2635 + 0.002573 \cdot \sigma - 9.024 \cdot 10^{-6} \sigma^2 + 0.005351 \cdot \cos(2\pi(\chi - 0.4712)) \quad (6)$$

and

$$H_0^{\text{QIonDR}} = 74.74 - 0.02984 \cdot \sigma + 0.5705 \cdot \cos(2\pi(\chi - 0.4712) + \pi). \quad (7)$$

Here, $\varepsilon_{\beta_0} = 0.1 \text{ km}^{-1}$ and $\varepsilon_{H_0} = 4 \text{ km}$ are the estimated maximal absolute deviations of β_0 and H_0' from β_0^{QIonDR} and H_0^{QIonDR} , respectively. These values are estimated based on the maximum absolute deviations of Wait's parameters from their fitted values for data shown in [10] (0.03 km^{-1} and 1.5663 km), [19] (0.07 km^{-1} and 1.8 km), and [13] (0.08 km^{-1} and 3.6 km). We note that the fitted functions for the first two sets of data are given in [24].

Here, it is important to emphasise that the values of ε_{β_0} and ε_{H_0} are estimated and that they can influence the choice of pairs (β_0, H_0') if the analysed deviations are similar for multiple combinations of initial Wait's parameters. In this case, it is necessary to check which values of Wait's parameters at the time of the X-ray flux maximum fit best with those obtained in other cases. In our study, this correction procedure is applied in only three cases (10% of the total number of the analysed cases). The correction for these class-C4.1, -C6.1, and -C8.0 solar X-ray flares is made due to the excessive value of β (0.59 km^{-1} , 0.55 km^{-1} , and 0.57 km^{-1} , respectively) at the X-ray flux maximum obtained before correction.

3.2. Determination of the Electron Density

As in many previous papers (see, for example, [25–27]), we calculate the time evolution of the D-region electron density N_e at the altitude h using Equation [21]:

$$N_e(h, t) = 1.43 \cdot 10^{13} e^{-\beta(t)H'(t)} e^{(\beta(t)-0.15)h}, \quad (8)$$

where N_e , β , and H' and h are given in m^{-3} , km^{-1} , and km , respectively.

3.3. Determination of the D-Region Total Electron Content

The determination of TEC in the entire ionosphere has both practical and scientific significance. The contribution of the D-region to TEC is very often neglected in these calculations or the presence of its perturbations is not taken into account [28–32]. However, a recent study, presented in [7], shows that neglecting the impact of this ionospheric layer on satellite signals due to its low electron density is justified in quiet conditions, but it can result in significant errors in space geodesy during intensive ionospheric perturbations. For this reason, we further analyse TEC_D using the expression [24]:

$$\text{TEC}_D(t) = \int_{h_b}^{h_t} N_e(h, t) dh = 1000 \frac{N_e(h_t, t) - N_e(h_b, t)}{\beta(t) - \beta_0}, \quad (9)$$

where $h_b = 60 \text{ km}$ and $h_t = 90 \text{ km}$ are the bottom and upper D-region boundary, respectively. The factor 1000 is introduced because β and TEC_D are given in km^{-1} and m^{-3} , respectively.

4. Results and Discussions

The presented methodology for the estimation of β , H' , N_e , and TEC_D is applied to 30 flares of classes C and M. We present two analyses relating to: (1) the time evolutions of the considered ionospheric parameters during a solar X-ray flare which occurred on 18 January 2014 and (2) the statistical analysis of their dependencies on the maximum X-ray flux in the times of the radiation maximum and the most intense D-region disturbance. To show the importance of the choice of initial conditions, we compare the obtained

dependences with those obtained for the initial values of Wait's parameters which were commonly used in previous studies. In the second analysis, the comparisons with results presented in previous studies are also given.

4.1. Time Evolutions of the Considered Ionospheric Parameters during a Single Flare

In this section, we present the application of the procedure described in Section 3 to an individual event. We analyse the considered parameters during the perturbation induced by an X-ray flare that occurred on 18 January 2014. The time evolutions of the X-ray flux, and the DHO signal amplitude and phase registered by the AWESOME receiver in Serbia during this period are shown in Figure 1.

The first step in this analysis is to determine β_0 and H'_0 , using the following procedure:

- The time dependences $\beta(t)$ and $H'(t)$ are determined for all combinations of Wait's parameters in quiet conditions in the ranges 0.2 km^{-1} to 0.55 km^{-1} with a step of 0.01 km^{-1} for β and 65 km to 76 km with a step of 0.1 km for H' .
- Wait's parameters β_0 and H'_0 are determined by applying criteria 1–4 given in Section 3 to the obtained dependences $\beta(t)$ and $H'(t)$.

To obtain the time evolutions $\beta(t)$ and $H'(t)$, we include the obtained pair of initial values of Wait's parameters (0.43 km^{-1} , 71.8 km) in the LWPC numerical model and apply the criterion given by Equation (3) to the analysed datasets related to the changes in the registered signal amplitude and phase. These time evolutions are shown in Figure 5.

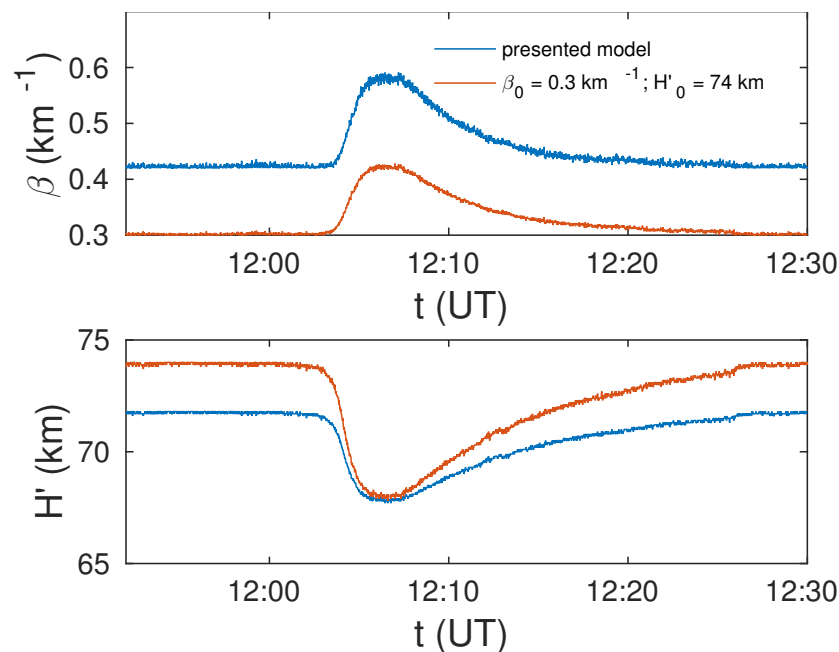


Figure 5. Time evolutions of the “sharpness” (β) (**upper panel**) and the signal reflection height (H') (**bottom panel**) obtained for the initial values of Wait's parameters determined by the procedure developed in this study (blue lines) and for commonly used $\beta_0 = 0.3 \text{ km}^{-1}$ and $H'_0 = 74 \text{ km}$.

In order to compare the obtained time evolutions of Wait's parameters (represented by blue lines in Figure 5) with those obtained for commonly used $\beta_0 = 0.3 \text{ km}^{-1}$ and $H'_0 = 74 \text{ km}$, we show the corresponding dependencies in the second case by red lines. In the top panel, it can be seen that $\beta(t)$ is higher for the initial parameters estimated in the procedure presented in this study and that the difference between the corresponding two presented time evolutions is very similar for the entire considered time period. In other words, this difference does not significantly vary during the perturbation with respect to the pre-disturbance value. On the other hand, $H'(t)$ is smaller in the first case during the entire time period. This difference decreases significantly with increasing perturbation intensity. After the minimum of $H'(t)$, the difference increases again and reaches the initial

value at the end of the considered perturbation. These conclusions are in line with the results obtained in the statistical analysis presented below (see Section 4.2).

The electron density time variations, obtained from Equation (8), and the calculated time evolutions of Wait's parameters for both considered pairs of β_0 and H'_0 are shown in Figure 6. In these two cases, the altitude-time dependencies look similar, but the obtained values are different. The values obtained in the procedure presented in this paper (upper left panel) are higher than those obtained for $\beta_0 = 0.3 \text{ km}^{-1}$ and $H'_0 = 74 \text{ km}$ (upper right panel) in the middle and upper part of the D-region, while this relationship is opposite in the bottom part of this ionospheric layer. Going to the lower boundary of the D-region, the considered difference decreases and, from some height, the values in the second case become larger than in the first case. The absolute values of this difference are shown in the bottom left panel where it can be seen that they increase with the perturbation intensity and with h above around 70 km. The obtained differences in the D-region bottom part are significantly smaller than at its highest altitudes, which is in line with the increase in N_e with h .

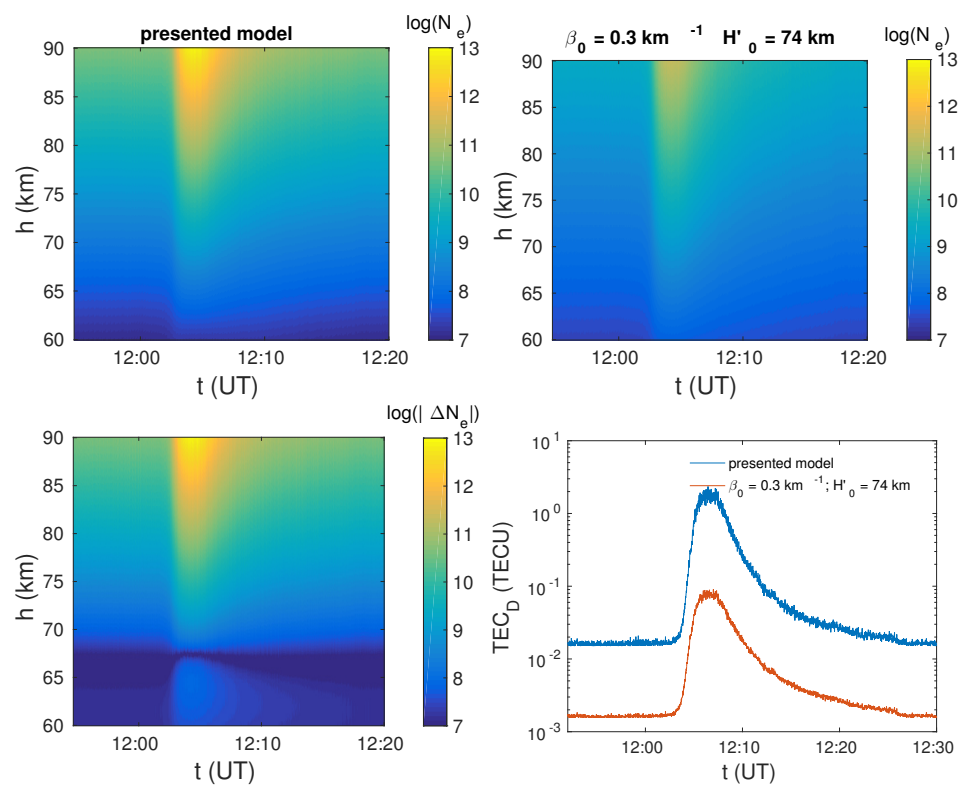


Figure 6. Surface plots of the logarithm of the electron density values given in m^{-3} obtained for the initial Wait's parameters determined by the procedure developed in this study (**upper left panel**) and for commonly used $\beta_0 = 0.3 \text{ km}^{-1}$ and $H'_0 = 74 \text{ km}$ (**upper right panel**). The absolute values of the corresponding differences are shown in the bottom left panel. The time evolutions of the total electron content in the D-region, TEC_D , obtained for the analysed initial Wait's parameters are shown in the bottom right panel.

The time evolutions of TEC_D for both cases are obtained from Equation (9). As can be seen in the bottom right panel, the values of TEC_D obtained by the procedure developed in this study are significantly higher (one order of magnitude) than the corresponding values obtained in the second case. Although the difference is similar throughout the observed time period, its increase with the perturbation intensity is noticeable.

4.2. Statistical Analysis

In this section, we study the influence of the X-ray flare class represented by the X-ray flux maximum in the wavelength domain $0.1 \text{ nm} - 0.8 \text{ nm}$, Φ_{max} , on β , H' , N_e , and TEC_D .

We study the 30 X-ray flares listed in Table 1, applying the procedure shown in Section 4.1 to each individual event, and analyse β_0 , H'_0 , and all observed parameters at the times of the X-ray flux maximum ($t_{\Phi_{\max}}$) and the TEC_D maximum ($t_{\text{TEC}_{D\max}}$).

The influence of the solar cycle period and season on the observed dependences is included via β_0 and H'_0 . Namely, these parameters are determined in a procedure based on the QIonDR model (see details in Section 3) which gives the dependences of Wait's parameters in the midday period on the day of year and sunspot number. To analyse the effects of these periodic changes in the times $t_{\Phi_{\max}}$ and $t_{\text{TEC}_{D\max}}$, different seasons are represented with blue squares (winter), green triangles (spring), red circles (summer), and yellow diamonds (autumn), while the increase in their size corresponds to the increase in parameter σ .

Wait's Parameters

The obtained values of β_0 and H'_0 , and their comparisons with the corresponding values modelled by the QIonR and International Reference Ionosphere (IRI)—2016 [9] (for the observed times and geographical coordinates of the DHO signal mid-path) models, are shown in Figure 7. In the latter case, we model Wait's parameters from electron density altitude distributions determined from both the IRI-95 [33] and Faraday-International Reference Ionosphere (FIRI) [34] D-region models, which are included in the IRI-2016 ionosphere model (https://ccmc.gsfc.nasa.gov/modelweb/models/iri2016_vitmo.php, accessed on 11 December 2021) and which are based on rocket data. As it can be seen in the upper panel, β_0 agrees well with the values obtained by the QIonDR model and the IRI-2016 model when the D-region electron density is calculated by the FIRI model. The values of β_0 that are obtained by the IRI-2016 model using the IRI-95 model of the D-region are approximatively constant which differs from the other three cases. The agreement of H'_0 obtained by the presented procedure with the values obtained using the other three considered models is good. The results obtained for both parameters are within the ranges expected from the results shown in [18,23,35].

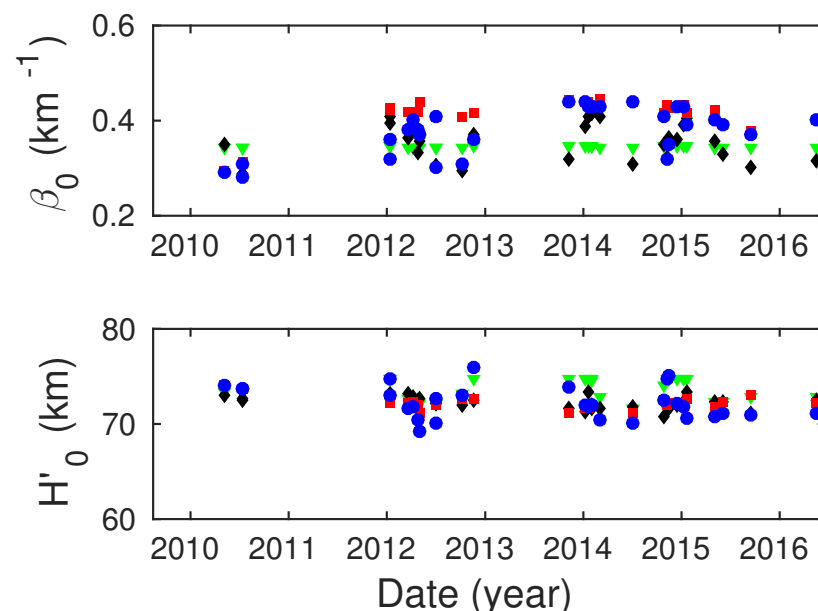


Figure 7. The “sharpness” (β_0 ; upper panel) and the signal reflection height (H'_0 ; bottom panel) describing the quiet ionosphere before the considered solar X-ray flares. The results obtained by the presented procedure, and the QIonDR and IRI-2016 (which includes modelling of the D-region by the IRI95 and FIRI models) models are represented by blue circles, red squares, green triangles, and black diamonds, respectively.

A detailed analysis of the differences in the results obtained by the procedure presented in this study and the QIonDR model is given in Supplementary Materials.

The dependences of Wait’s parameters on $\log_{10}(\Phi_{\max})$ at the time $t_{\Phi_{\max}}$ ($\beta_{t_{\Phi_{\max}}}$ and $H'_{t_{\Phi_{\max}}}$) and at the time $t_{\text{TEC}_{\text{Dmax}}}$ ($\beta_{t_{\text{TEC}_{\text{Dmax}}}}$ and $H'_{t_{\text{TEC}_{\text{Dmax}}}}$) are shown in Figures 8 and 9 (left panels). The values of Φ_{\max} are given in W/m^2 .

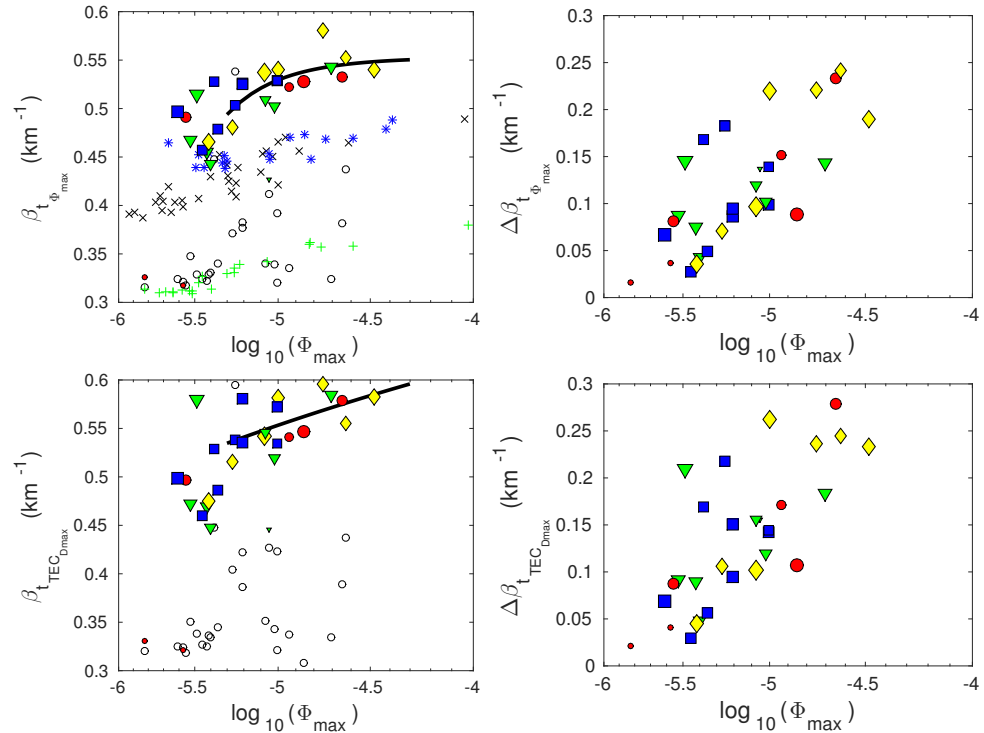


Figure 8. Dependencies of the “sharpness” (β) (left panels) and its changes with respect to the initial value ($\Delta\beta$) (right panels) on the logarithm of the X-ray flux maximum given in W/m^2 ($\log_{10}(\Phi_{\max})$) at the times of the X-ray flux maxima ($t_{\Phi_{\max}}$) (upper panels) and the D-region perturbation maxima ($t_{\text{TEC}_{\text{Dmax}}}$) (bottom panels). The values obtained in this study are presented by blue squares (X-ray flares occurred in winter), green triangles (X-ray flares occurred in spring), red circles (X-ray flares occurred in summer), and yellow diamonds (X-ray flares occurred in autumn). The results presented in [18,23,35] are represented by “x”, “+”, and “*”, respectively. The black lines show fitting of the obtained values for the X-ray flares whose flux maxima are greater than $5 \times 10^{-6} \text{ Wm}^{-2}$ and which occurred on days for which the daily smoothed sunspot number is greater than 50.

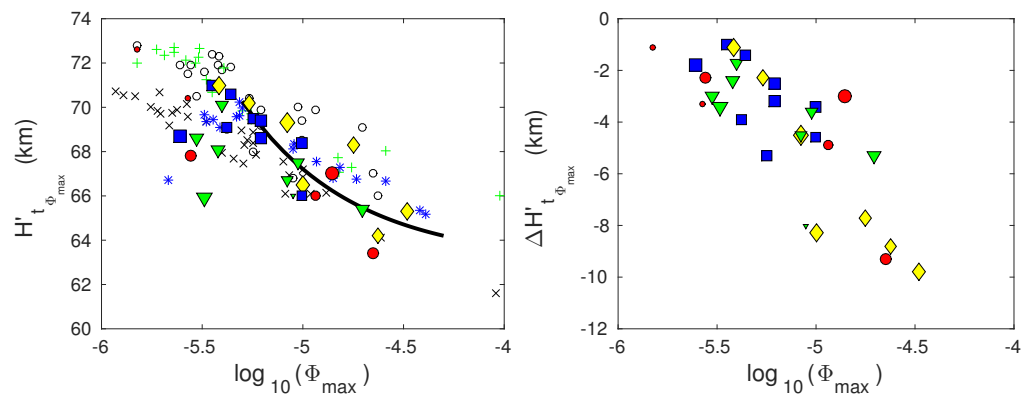


Figure 9. Cont.

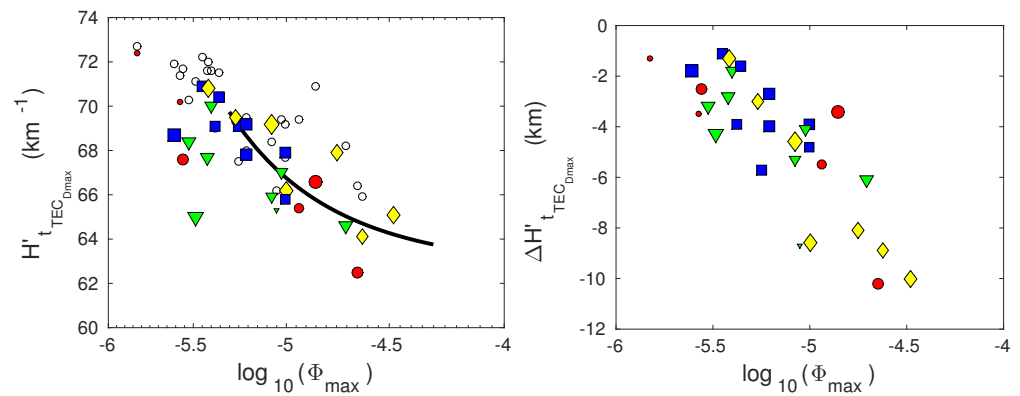


Figure 9. Dependencies of the signal reflection height (H') (**left panels**) and its changes with respect to the initial value ($\Delta H'$) (**right panels**) on the logarithm of the X-ray flux maximum given in W/m^2 , ($\log_{10}(\Phi_{\max})$) at the times of the X-ray flux maxima ($t_{\Phi_{\max}}$) (**upper panels**) and the D-region perturbation maxima ($t_{TEC_{Dmax}}$) (**bottom panels**). The values obtained in this study are presented by blue squares (X-ray flares occurred in winter), green triangles (X-ray flares occurred in spring), red circles (X-ray flares occurred in summer), and yellow diamonds (X-ray flares occurred in autumn). The results presented in [18,23,35] are represented by “x”, “+”, and “*”, respectively. The black lines represent fitting of the obtained values for the X-ray flares whose flux maxima are greater than $5 \times 10^{-6} Wm^{-2}$ and which occurred on days for which the daily smoothed sunspot number is greater than 50.

Based on the presented data, we can conclude the following:

- The dispersion of points on the graph $\beta(\log_{10}(\Phi_{\max}))$ is greater at the time $t_{TEC_{Dmax}}$, which can be explained by the additional influence of differences in the radiation characteristics after the maximum of its flux. This difference is not significant for H' .
- The dispersion of the obtained values decreases with $\log_{10}(\Phi_{\max})$, which indicates a decrease in the influence of the initial state of the ionosphere on the considered parameters during disturbance with the flare class. This can be explained by the fact that the solar X-radiation dominates the solar hydrogen Ly α and cosmic radiation (these two radiations are the most important sources of ionisation in the unperturbed D-region) in electron gain processes at the time of the X-ray flux maximum [36]. This dominance increases with Φ_{\max} and, consequently, the considered differences in Wait's parameters decrease with Φ_{\max} .
- The effect of variations in the radiation intensity during a solar cycle on β at times $t_{\Phi_{\max}}$ and $t_{TEC_{Dmax}}$ is significant in the period around the solar cycle minimum. In the cases of the two X-ray flares of classes C1.4 and C2.6, which occurred in this period, β has significantly less values than those estimated for the other analysed flares of the similar classes. This difference is reduced for the stronger flare of class-C8.8. The values of H' for all three events which occurred during this period are similar to the corresponding values for the other analysed events.
- The influence of seasonal changes on the observed parameters is not visible for less intense flares. In the case of more intense flares (starting with class-C5), there is indication that $\beta_{t_{\Phi_{\max}}}$ and $\beta_{t_{TEC_{Dmax}}}$ are slightly higher during the winter (blue squares) and autumn (yellow diamonds) periods than during the second part of year (green triangles and red circles). However, these differences are not significant which is why we analyse all these flares together (see the next item).
- The dispersion of the obtained values is significant for the considered weak X-ray flares of low intensity. Therefore, and due to the mentioned differences in $\beta_{t_{\Phi_{\max}}}$ and $\beta_{t_{TEC_{Dmax}}}$ for events which occurred in the period around the solar cycle minimum, we fit the obtained values for the X-ray flares whose maximum flux is greater than

$5 \times 10^{-6} \text{ Wm}^{-2}$ and which occurred on days for which $\sigma > 50$. The fitted functions have the form:

$$f = a\Phi_{\max}^b + c, \quad (10)$$

where f is the considered parameter. The corresponding values of a , b , and c are given in Supplementary Materials (Table S2).

To see the significance of the choice of parameters β_0 and H'_0 , we show the values of the corresponding parameters obtained for the commonly used values $\beta_0 = 0.3 \text{ km}^{-1}$ and $H'_0 = 74 \text{ km}$ [17–19,22] and applying the selection criteria given by Equation (3) (open circle in Figures 8 and 9). Comparing the results of these two analyses, it can be concluded that the differences are more pronounced for β , and at time $t_{\text{TEC}_{\text{Dmax}}}$. The values obtained in this study are larger for β and smaller for H' at both times. The differences are more noticeable for the first parameter. Contrary to the results of the presented model, the dispersion of the values of Wait's parameters for $\beta_0 = 0.3 \text{ km}^{-1}$ and $H'_0 = 74 \text{ km}$ are more pronounced for flares of higher intensities.

Bearing in mind that previous statistical studies primarily refer to the dependences of Wait's parameters on Φ_{\max} at the time of the X-ray flux maximum, we present comparisons of the values obtained in this study for the time $t_{\Phi_{\max}}$ with those given in previous studies [23,35] (also used in [10,18]). As in the previous comparison, the differences are more noticeable for $\beta_{t_{\Phi_{\max}}}$. They are similar in the entire observed X-ray flux domain in contrast to the differences in the dependences $H'_{t_{\Phi_{\max}}}$ which decrease with $\log_{10}(\Phi_{\max})$.

The choice of the initial values of Wait's parameters at the time $t_{\Phi_{\max}}$ has a dominant influence on the differences in the obtained values. This can be seen from the comparison of the results related to the same year and the same D-region area, as well as from the comparison of the results of studies based on data recorded in different periods of a solar cycle and in observations of different areas.

- In the first case, we compare studies presented in [18,35] that analyse solar X-ray flares that occurred in 2011 (medium solar cycle conditions) and the D-region area monitored by the NWC signal emitted in Australia and recorded in India. The pairs of Wait's parameters (β_0, H'_0) used in [18,35] are ($0.43 \text{ km}^{-1}, 71 \text{ km}$) and ($0.3 \text{ km}^{-1}, 74 \text{ km}$), respectively. A comparison of these values (presented in the upper left panels in Figures 8 and 9) shows that β_0 is higher and H'_0 is less in the first case.
- In the second case, we compare Wait's parameters in the time $t_{\Phi_{\max}}$ obtained in [23] with those shown in [18,35]. The study presented in [23] analyses perturbations caused by X-ray flares which occurred during the solar cycle minimum and medium (1994–1998). It is based on data related to the NPM and NLK signals from USA recorded in New Zealand. The values shown in [23] are between the values given in [18,35]. They are very similar to those given in [35] which corresponds to similar values of β_0 (this value is 0.39 km^{-1}) and the same value of H'_0 .

Finally, the agreement of the results obtained in this study with those given in the previous three can be explained in the same way as in the previous analysis: agreement is best with the results of analyses in which the pair (β_0, H'_0) has similar values to those estimated for a single observed event analysed in this research. The values of $\beta_{t_{\Phi_{\max}}}$ shown in [35] are greater than the corresponding values shown in [18,23]. Consequently, they are in the best agreement with the results obtained in this study for events that occurred since 2012, i.e., for events for which the values of β_0 are higher and the values of H'_0 are less than the corresponding values during the minimum of the solar cycle. The agreement of the results of this study is better with those given in [18] in the cases of weak flares that occurred in 2010, i.e., in the period around the solar cycle minimum. In these cases, the initial values of Wait's parameters are similar in both studies.

In all three analyses in which the pair (β_0, H') is the same for all cases, the dependences of Wait's parameters on $\log_{10}(\Phi_{max})$ are linear in the observed domain of X-ray flux. In this analysis, it is shown that the variations of this pair induce the deviations of the considered dependences from the corresponding linear functions. Moreover, the influence of the pair (β_0, H') on Wait's parameters at the time $t_{\Phi_{max}}$ is so pronounced in cases of weak flares that fitting is not relevant for the analysis of the dependences of Wait's parameters on the X-ray flux maximum. Fitting of the obtained values that describe the considered flares for which $\Phi_{max} > 5 \times 10^{-6} \text{ Wm}^{-2}$ and $\sigma > 50$ indicates a decrease in changes of Wait's parameters with $\log_{10}(\Phi_{max})$. The tendency towards saturation is more pronounced for $\beta_{t_{\Phi_{max}}}$ in the observed X-ray flux domain.

4.3. Determination of the Electron Density

Knowledge of Wait's parameters allows us to calculate the D-region electron density at the times $t_{\Phi_{max}}$ and $t_{TEC_{Dmax}}$ using Equation (8). The corresponding values at 65 km, 75 km, and 85 km are shown in Figure 10, where the left and right panels refer to the times $t_{\Phi_{max}}$ and $t_{TEC_{Dmax}}$, respectively.

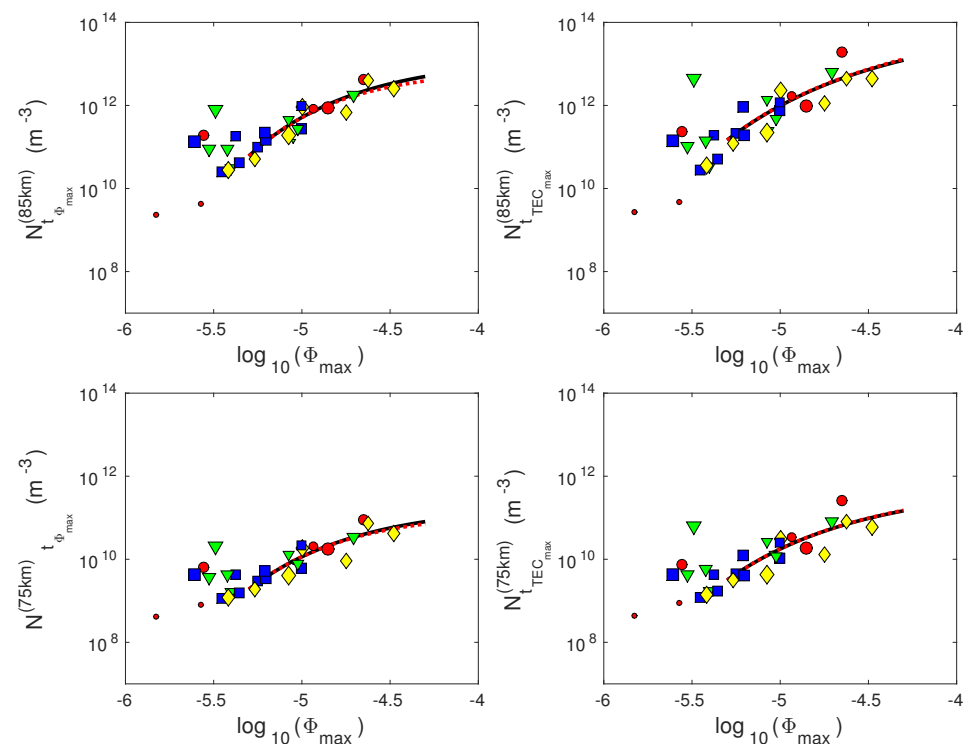


Figure 10. Cont.

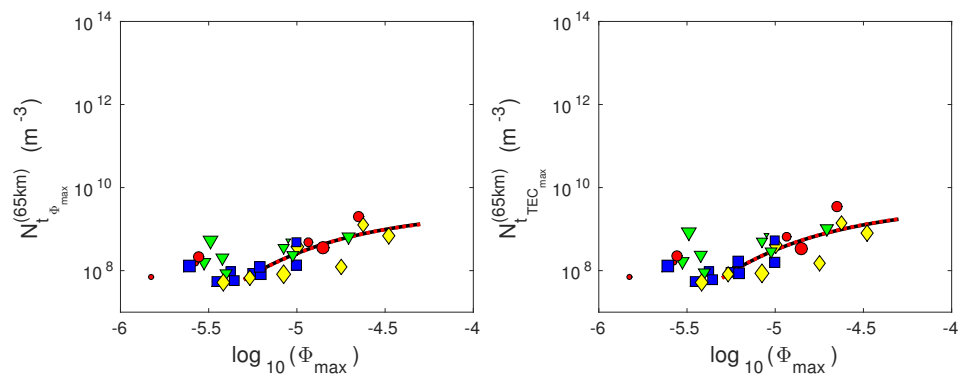


Figure 10. Dependencies of the electron density (N_e) at 85 km (**upper panels**), 75 km (**middle panels**), and 65 km (**bottom panels**) on the logarithm of the X-ray flux given in W/m^2 ($\log_{10}(\Phi_{\max})$) at the times of the X-ray flux maxima ($t_{\Phi_{\max}}$) (**left panels**) and the D-region perturbation maxima ($t_{TEC_{D\max}}$) (**right panels**). The values obtained in this study are presented by blue squares (X-ray flares occurred in winter), green triangles (X-ray flares occurred in spring), red circles (X-ray flares occurred in summer), and yellow diamonds (X-ray flares occurred in autumn). The black lines represent fitting of the obtained values for the X-ray flares whose flux maxima are greater than $5 \times 10^{-6} Wm^{-2}$ and which occurred on days for which the daily smoothed sunspot number is greater than 50. The red lines indicate the corresponding values obtained by applying Equation (8) to the fitted Wait's parameters.

The obtained graphs show the following:

- As in the case of Wait's parameter β , the dispersion of the obtained values of N_e is greater at the time $t_{TEC_{D\max}}$.
- The influence of the ionospheric initial state is more manifested in the cases of weak flares, which is reflected in more pronounced dispersion of the obtained values at all heights for the corresponding part of the observed flux domain.
- Deviations of points representing weak flares that occurred during periods near the solar cycle minimum are visible at 85 km for both the considered times.
- Fitting of the modelled values refers to the considered flares for which $\Phi_{\max} > 5 \times 10^{-6} Wm^{-2}$ and $\sigma > 50$. The obtained fitted functions, shown by black lines in Figure 10, have the form given by Equation (10), where the corresponding parameters a , b , and c are given in Supplementary Materials (Table S2).
- The changes in N_e within the considered flux domain are greater at the time $t_{TEC_{D\max}}$. This is expected because the perturbation intensity is the most pronounced at that time.

Knowledge of the time evolutions $\beta(t)$ and $H'(t)$ allows us to calculate the D-region electron density time–altitude distribution using Equation (8). In some analyses, the electron density time evolution needs to be fitted. If this fitting is required for many values of h , it is easier to apply Equation (8) to the fitted functions $\beta(t)$ and $H'(t)$ than to perform a fitting of the electron density time evolution for each of the considered heights. Since the agreement of the corresponding time evolutions obtained by these two ways cannot be confirmed a priori, it is necessary to examine whether it is possible to use the first, easier, method with acceptable accuracy. In Figure 10, we show the time evolutions N_e calculated from the fitted values of Wait's parameters by red dashed lines. A comparison of these lines with the black ones representing the results of the second fitting method shows that they practically coincide at the bottom D-region heights. By increasing the height, the values obtained in the first way are less than those obtained by fitting of the originally calculated values N_e . However, these deviations are small. This can be shown by the ratio of the values obtained by the first and second method (r_N) given in Figure 11. Although the form of the dependence $r_N(\log_{10}\Phi_{\max})$ changes with height, it can be seen that the deviations are most significant in the upper D-region part for the largest observed X-ray fluxes. However, these deviations do not exceed 27%, which is not significant considering that the plasma parameters in this atmospheric region are estimated in procedures based on numerous

approximations. For this reason, we can conclude that electron density calculation based on fitted values of Wait's parameters can be used in analyses.

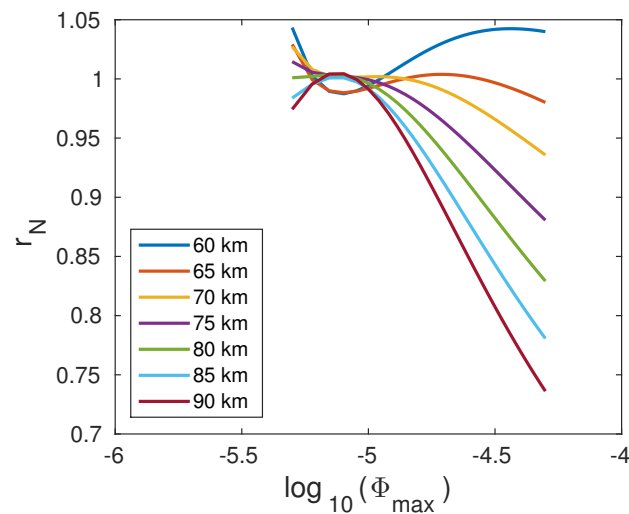


Figure 11. Dependencies of the coefficient r_N on the logarithm of the X-ray flux given in W/m^2 , $\log_{10}(\Phi_{\max})$, at the times of the X-ray flux maxima ($t_{\Phi_{\max}}$).

4.4. Determination of the Total Electron Content in the D-Region

The obtained dependencies $TEC_D(\log_{10}\Phi_{\max})$ at times $t_{\Phi_{\max}}$ and $t_{TEC_{D\max}}$ are shown in Figure 12 (left and right panels, respectively). The obtained graphs show the following:

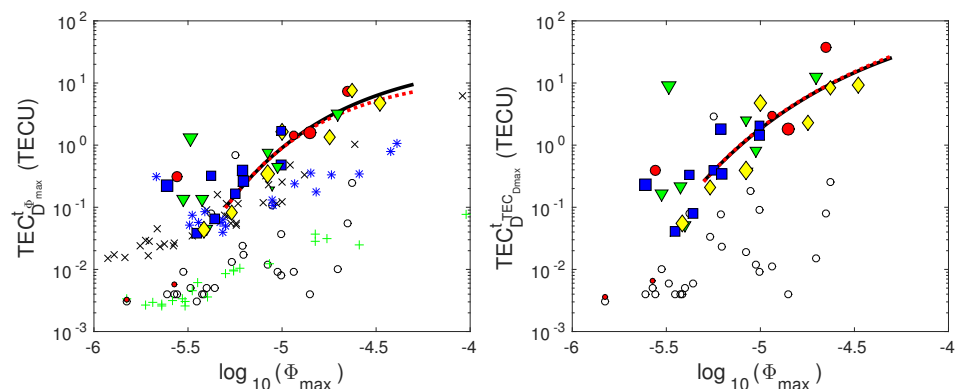


Figure 12. Dependencies of the total electron content in the D-region (TEC_D) on the logarithm of the X-ray flux given in W/m^2 ($\log_{10}(\Phi_{\max})$) at the times of the X-ray flux maxima ($t_{\Phi_{\max}}$) (**left panel**) and at the times of the D-region perturbation maxima ($t_{TEC_{D\max}}$) (**right panel**). The values obtained in this study are presented by blue squares (X-ray flares occurred in winter), green triangles (X-ray flares occurred in spring), red circles (X-ray flares occurred in summer), and yellow diamonds (X-ray flares occurred in autumn). The results obtained from Wait's parameters presented in [18,23,35] are represented by "x", "+", and "*", respectively. The black lines show fitting of the obtained values for the X-ray flares whose flux maxima are greater than $5 \times 10^{-6} Wm^{-2}$ and which occurred on days for which the daily smoothed sunspot number is greater than 50.

- The values of TEC_D are higher at the time $t_{TEC_{D\max}}$. This is consistent with the change in the intensity of the D-region perturbation which is the largest at this time.
- Due to the additional influence of the differences in the X-ray flux time evolutions after the analysed flare intensity maxima, the dispersion of the shown points is more pronounced at the time $t_{TEC_{D\max}}$.
- The influence of seasonal variations is not pronounced.
- The effect of the X-ray flux variation during a solar cycle is visible only for the considered weak flares that occurred in the period around the solar cycle minimum.

- The dispersion of points representing weak flares is expressed at both times due to the significant influence of the initial conditions on the characteristics of the corresponding perturbations.
- The influence of initial conditions on a perturbation decreases with the X-ray flux. This reduces the dispersion of the obtained points and, consequently, allows the fitting of points that represent flares for which $\Phi_{\max} > 5 \times 10^{-6} \text{ Wm}^{-2}$ and $\sigma > 50$ (black lines on the chart). In both cases, the fitted function has the form given by Equation (10), where the corresponding parameters a , b , and c are given in Supplementary Materials (Table S2).
- As in the case of the parameter β , the values of TEC_D obtained by the presented procedure are greater than those obtained for the initial values of Wait's parameters $\beta_0 = 0.3 \text{ km}^{-1}$ and $H'_0 = 74 \text{ km}$ in both observed times (except in one case). The tendency of the dependence $\text{TEC}_D(\log_{10}\Phi_{\max})$ is more pronounced in the first than in the second case.
- Compared to the studies presented in [18,23,35], the values obtained in this paper are in good agreement with:
 - The values obtained from Wait's parameters presented in [23,35] for X-ray flares of mid-intensity class-C;
 - The values obtained from Wait's parameters presented in [18] for two weak X-ray flares that occurred in the period around the solar cycle minimum (2010).

The values obtained in this study are greater in the cases of the other considered weak X-ray flares and in the cases of more intense ones.

- Unlike the shown dependences obtained on the basis of the data presented in [18,23,35], the dependences obtained in this paper are not linear, and the given fittings are not relevant for weak flares due to the significant dispersion of the obtained values.

As in the case of the electron density at higher D-region altitudes, the values obtained by fitting the points determined for the individual considered cases (black lines in Figure 12) are in very good agreement with those calculated on the basis of fitted dependences of Wait's parameters (red lines in Figure 12), except for the most intense flares at time $t_{\Phi_{\max}}$ where a small deviation is visible. The ratio of the obtained values in the second and first case (r_{TEC_D}) at the time $t_{\Phi_{\max}}$ is shown in Figure 13 where one can see that it does not exceed 25%. This deviation is not great considering the necessity of using numerous approximations in ionospheric models. Therefore, we can conclude that the fitted functions of Wait's parameters can be used to determine the dependence $\text{TEC}_D(\log_{10}\Phi_{\max})$.

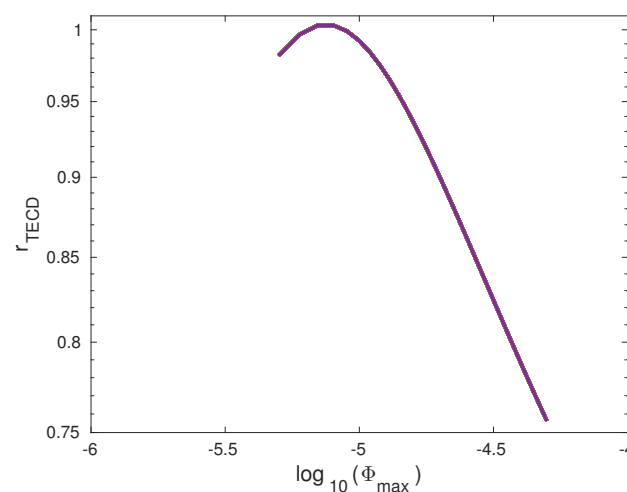


Figure 13. Dependencies of the coefficient r_{TEC_D} on the logarithm of the X-ray flux given in W/m^2 ($\log_{10}(\Phi_{\max})$) at the times of the X-ray flux maxima ($t_{\Phi_{\max}}$)

5. Conclusions

This study presents an upgrade of the quiet ionospheric D-region model. The presented procedure, based on the data obtained by remote sensing of the analysed area during the considered time period, allows for a more precise modelling of the D-region intensively perturbed by a solar X-ray flare. Its most significant contribution refers to a method for the determination of the quiet ionosphere parameters describing the observed area in the period preceding the analysed perturbation. In addition, the developed procedure allows us to reduce the required number of very low/low frequency signals (i.e., transmitters that emit them) to monitor the ionosphere from two (as required in the quiet ionospheric D-region model) to just one. In this way, the observation area is more localised and, consequently, the obtained values of the considered quiet ionosphere parameters are more precise which is, as shown in this study, significant for modelling of the perturbed ionosphere.

In this study, we analyse the “sharpness”, the signal reflection height, the D-region electron density, and the total electron content in the D-region. The obtained results show the following:

- The choice of Wait’s parameters describing the quiet ionosphere affect the time evolutions of the considered parameters during the entire period of a perturbation induced by an X-ray flare.
- The influence of the quiet ionosphere state in the period preceding perturbation on the electron density and total electron content in the perturbed D-region is significant for weak X-ray flares.
- The influence of the initial conditions on the considered ionospheric parameters at the times of the radiation maximum and the most intense D-region perturbation decreases with the X-ray flux.
- Significant differences caused by the variations in the radiation intensity during the 24th solar cycle are obtained for:
 - The “sharpness”—the obtained values are significantly lower for events that occurred in the period around the solar cycle minimum;
 - The electron density in the D-region upper part—the obtained values are significantly lower for weak solar X-ray flares that occurred in the period around the solar cycle minimum;
 - The total electron content in the D-region—the obtained values are significantly lower for weak solar X-ray flares that occurred in the period around the solar cycle minimum.

The stated differences are obtained at the times of the X-ray flux maximum and the most intense D-region disturbance. The variations in the radiation intensity during the 24th solar cycle do not affect the signal reflection height.

- The influence of the seasonal variations on the analysed parameters is not significant at the times of the X-ray flux maximum and the most intense D-region disturbance.
- Due to the pronounced influence of the quiet ionosphere state before perturbation on the analysed parameters in the cases of weak flares, the dispersions of the points describing these events on the corresponding graphs are large. For this reason, we fit only the obtained values describing the X-ray flares of class-C5 or stronger. Due to the differences induced by the variations in the radiation intensity during a solar cycle, the presented fits are relevant for the events which occurred during the days when the smoothed daily sunspot number is greater than 50.
- The obtained results indicate the need to correct the linear dependences of the observed parameters on the logarithm of the X-ray flux maximum obtained in the cases when the initial conditions are considered the same for all analysed cases. The dependences obtained by the method presented in this study indicate a tendency towards saturation of the observed values with the logarithm of the X-ray flux maximum.
- The dispersion of points representing the dependences of the observed parameters on the logarithm of the X-ray flux is higher at the time of maximum D-region perturbation than at the time of maximum X-ray flux. This can be explained by the additional

influence of the difference in the time evolutions of the X-ray flux after its maximum on the ionosphere.

- The fitted functions of Wait's parameters can be used to determine the fitted dependences of the electron density and total electron content in the D-region.

To conclude, the obtained results show that taking into account the specificity of the initial conditions in an individual case gives more intense perturbations of the solar X-ray flare perturbed D-region than in the case when the initial conditions are considered the same in different time periods. Consequently, this result indicates more significant influence of the perturbed D-region on electromagnetic signals. This study confirms the need to include observations of the intensely perturbed D-region in the modelling of satellite signal propagation indicated in recent studies. This is important for the accuracy of satellite data used in many modern technologies and indicates the possibility of practical applications of space weather research.

Supplementary Materials: The following are available at <https://www.mdpi.com/article/10.3390/rs14010054/s1>, Table S1: Wait's parameters obtained by the Quiet ionospheric D-region model (β_0^{QIonDR} and H_0^{QIonDR}) and by the procedure presented in this study (β_0 and H_0') for the considered X-ray flares, Table S2: Parameters a , b and c required for the calculations of the "sharpness" (β), the signal reflection height (H'), the electron density (N_e) at 60 km, 65 km, 70 km, 75 km, 80 km, 85 km, and 90 km, and the total electron content in the D-region (TEC_D) by Equation (10).

Funding: The author acknowledge funding provided by the Institute of Physics Belgrade through the grant by the Ministry of Education, Science, and Technological Development of the Republic of Serbia.

Institutional Review Board Statement: Not applicable.

Informed Consent Statement: Not applicable.

Data Availability Statement: The VLF data used for analysis is available from the corresponding author. Simulation results by IRI-16 model have been provided by the Community Coordinated Modeling Center at Goddard Space Flight Center through their public Runs on Request system (<http://ccmc.gsfc.nasa.gov>, accessed on 11 December 2021). The IRI Model was developed by Dieter Bilitza at the National Aeronautics and Space Administration/Goddard Space Flight Center (NASA/GSFC). Publicly available datasets were analysed in this study. This data can be found here: https://hesperia.gsfc.nasa.gov/goes/goes_event_listings/, accessed on 24 March 2020; <https://satdat.ngdc.noaa.gov/sem/goes/data/full/>, accessed on 7 September 2021; <https://wwwbis.sidc.be/silso/datafiles>, accessed on 3 August 2020; https://ccmc.gsfc.nasa.gov/modelweb/models/iri2016_vitmo.php, accessed on 11 December 2021.

Acknowledgments: The author thank Vladimir Čadež and Tamal Basak for very useful suggestions and comments.

Conflicts of Interest: The author declare no conflict of interest.

References

1. Raulin, J.P.; Trottet, G.; Kretschmar, M.; Macotela, E.L.; Pacini, A.; Bertoni, F.C.P.; Dammasch, I.E. Response of the low ionosphere to X-ray and Lyman- α solar flare emissions. *J. Geophys. Res. Space Phys.* **2013**, *118*, 570–575. [CrossRef]
2. Schmitter, E.D. Modeling solar flare induced lower ionosphere changes using VLF/LF transmitter amplitude and phase observations at a midlatitude site. *Ann. Geophys.* **2013**, *31*, 765–773. [CrossRef]
3. Ammar, A.; Ghalila, H. Ranking of Sudden Ionospheric Disturbances by Means of the Duration of Vlf Perturbed Signal in Agreement with Satellite X-ray Flux Classification. *Acta Geophys.* **2016**, *64*, 2794–2809. [CrossRef]
4. Kumar, S.; Kumar, A.; Menk, F.; Maurya, A.K.; Singh, R.; Veenadhari, B. Response of the low-latitude D region ionosphere to extreme space weather event of 14–16 December 2006. *J. Geophys. Res. Space Phys.* **2015**, *120*, 788–799. [CrossRef]
5. Kumar, S.; NaitAmor, S.; Chanrion, O.; Neubert, T. Perturbations to the lower ionosphere by tropical cyclone Evan in the South Pacific Region. *J. Geophys. Res. Space Phys.* **2017**, *122*, 8720–8732. [CrossRef]
6. Zhao, S.; Shen, X.; Liao, L.; Zhima, Z.; Zhou, C.; Wang, Z.; Cui, J.; Lu, H. Investigation of Precursors in VLF Subionospheric Signals Related to Strong Earthquakes ($M > 7$) in Western China and Possible Explanations. *Remote Sens.* **2020**, *12*, 3563. [CrossRef]

7. Nina, A.; Nico, G.; Odalović, O.; Čadež, V.; Todorović Drakul, M.; Radovanović, M.; Popović, L.Č. GNSS and SAR Signal Delay in Perturbed Ionospheric D-Region During Solar X-ray Flares. *IEEE Geosci. Remote Sens. Lett.* **2020**, *17*, 1198–1202. [[CrossRef](#)]
8. Nina, A.; Radović, J.; Nico, G.; Popović, L.Č.; Radovanović, M.; Biagi, P.F.; Vinković, D. The Influence of Solar X-ray Flares on SAR Meteorology: The Determination of the Wet Component of the Tropospheric Phase Delay and Precipitable Water Vapor. *Remote Sens.* **2021**, *13*, 2609. [[CrossRef](#)]
9. Bilitza, D. IRI the International Standard for the Ionosphere. *Adv. Radio Sci.* **2018**, *16*, 1–11. [[CrossRef](#)]
10. Thomson, N.R.; Rodger, C.J.; Clilverd, M.A. Large solar flares and their ionospheric D region enhancements. *J. Geophys. Res. Space Phys.* **2005**, *110*, A06306. [[CrossRef](#)]
11. Han, F.; Cummer, S.A.; Li, J.; Lu, G. Daytime ionospheric D region sharpness derived from VLF radio atmospheric. *J. Geophys. Res. Space Phys.* **2011**, *116*, 5314. [[CrossRef](#)]
12. McRae, W.M.; Thomson, N.R. VLF phase and amplitude: Daytime ionospheric parameters. *J. Atmos. Sol.-Terr. Phys.* **2000**, *62*, 609–618. [[CrossRef](#)]
13. Nina, A.; Nico, G.; Mitrović, S.T.; Čadež, V.M.; Milošević, I.R.; Radovanović, M.; Popović, L.Č. Quiet Ionospheric D-Region (QIonDR) Model Based on VLF/LF Observations. *Remote Sens.* **2021**, *13*, 483. [[CrossRef](#)]
14. Singh, A.K.; Singh, A.; Singh, R.; Singh, R. Solar flare induced D-region ionospheric perturbations evaluated from VLF measurements. *Astrophys. Space Sci.* **2014**, *350*, 1–9. [[CrossRef](#)]
15. Ferguson, J.A. *Computer Programs for Assessment of Long-Wavelength Radio Communications, Version 2.0*; Space and Naval Warfare Systems Center: San Diego, CA, USA, 1998.
16. Cohen, M.B.; Inan, U.S.; Paschal, E.W. Sensitive Broadband ELF/VLF Radio Reception with the AWESOME Instrument. *IEEE Trans. Geosci. Remote Sens.* **2010**, *48*, 3–17. [[CrossRef](#)]
17. Nina, A.; Čadež, V.M.; Bajčetić, J.; Mitrović, S.T.; Popović, L.Č. Analysis of the Relationship Between the Solar X-ray Radiation Intensity and the D-Region Electron Density Using Satellite and Ground-Based Radio Data. *Sol. Phys.* **2018**, *293*, 64. [[CrossRef](#)]
18. Basak, T.; Chakrabarti, S.K. Effective recombination coefficient and solar zenith angle effects on low-latitude D-region ionosphere evaluated from VLF signal amplitude and its time delay during X-ray solar flares. *Astrophys. Space Sci.* **2013**, *348*, 315–326. [[CrossRef](#)]
19. Grubor, D.P.; Šulić, D.M.; Žigman, V. Classification of X-ray solar flares regarding their effects on the lower ionosphere electron density profile. *Ann. Geophys.* **2008**, *26*, 1731–1740. [[CrossRef](#)]
20. Chakraborty, S.; Basak, T. Numerical analysis of electron density and response time delay during solar flares in mid-latitude lower ionosphere. *Astrophys. Space Sci.* **2020**, *365*, 1–9. [[CrossRef](#)]
21. Thomson, N.R. Experimental daytime VLF ionospheric parameters. *J. Atmos. Terr. Phys.* **1993**, *55*, 173–184. [[CrossRef](#)]
22. Žigman, V.; Grubor, D.; Šulić, D. D-region electron density evaluated from VLF amplitude time delay during X-ray solar flares. *J. Atmos. Sol.-Terr. Phys.* **2007**, *69*, 775–792. [[CrossRef](#)]
23. McRae, W.M.; Thomson, N.R. Solar flare induced ionospheric D-region enhancements from VLF phase and amplitude observations. *J. Atmos. Sol.-Terr. Phys.* **2004**, *66*, 77–87. [[CrossRef](#)]
24. Todorović Drakul, M.; Čadež, V.M.; Bajčetić, J.; Popović, L.Č.; Blagojević, D.; Nina, A. Behaviour of electron content in the ionospheric D-region during solar X-ray flares. *Serb. Astron. J.* **2016**, *193*, 11–18. [[CrossRef](#)]
25. Hayes, L.A.; Gallagher, P.T.; McCauley, J.; Dennis, B.R.; Ireland, J.; Inglis, A. Pulsations in the Earth's Lower Ionosphere Synchronized With Solar Flare Emission. *J. Geophys. Res. Space Phys.* **2017**, *122*, 9841–9847. [[CrossRef](#)]
26. Nina, A.; Čadež, V. Electron production by solar Ly- α line radiation in the ionospheric D-region. *Adv. Space Res.* **2014**, *54*, 1276–1284. [[CrossRef](#)]
27. Kumar, A.; Kumar, S. Solar flare effects on D-region ionosphere using VLF measurements during low- and high-solar activity phases of solar cycle 24. *Earth Planets Space* **2018**, *70*, 29. [[CrossRef](#)]
28. Klobuchar, J.A. Design and characteristics of the GPS ionospheric time delay algorithm for single frequency users. In *PLANS '86—Position Location and Navigation Symposium*; Institute of Electrical and Electronics Engineers: New York, NY, USA, 1986.
29. Zhao, J.; Zhou, C. On the optimal height of ionospheric shell for single-site TEC estimation. *GPS Solut.* **2018**, *22*, 48. [[CrossRef](#)]
30. Daniell, R.J.; Brown, L. *PRISM: A Parameterized Real-Time Ionospheric Specification Model, Version 1.5*; Computational Physics Inc: Newton, MA, USA, 1995.
31. Nava, B.; Coisson, P.; Radicella, S. A new version of the NeQuick ionosphere electron density model. *J. Atmos. Sol.-Terr. Phys.* **2008**, *70*, 1856–1862. [[CrossRef](#)]
32. Scherliess, L.; Schunk, R.W.; Sojka, J.J.; Thompson, D.C.; Zhu, L. Utah State University Global Assimilation of Ionospheric Measurements Gauss-Markov Kalman filter model of the ionosphere: Model description and validation. *J. Geophys. Res. Space Phys.* **2006**, *111*, A11315. [[CrossRef](#)]
33. Mechtly, E.; Bilitza, D. *Models of D-Region Electron Concentration, Report IPW-WB1*; Institut für Physik Weltraumforsch: Freiburg, Germany, 1974.
34. Friedrich, M.; Torkar, K.M. FIRI: A semiempirical model of the lower ionosphere. *J. Geophys. Res.* **2001**, *106*, 21409–21418. [[CrossRef](#)]
35. Pandey, U.; Singh, B.; Singh, O.; Saraswat, V. Solar flare induced ionospheric D-region perturbation as observed at a low latitude station Agra, India. *Astrophys. Space Sci.* **2015**, *357*, 35. [[CrossRef](#)]
36. Nina, A.; Čadež, V.; Bajčetić, J. Contribution of Solar Hydrogen Ly α Line Emission in Total Ionization Rate in Ionospheric D-region During the Maximum of Solar X-flare. *Serb. Astron. J.* **2015**, *191*, 51–57. [[CrossRef](#)]



OPEN ACCESS

EDITED BY

Jing Luo,
Northwest Institute of Eco-
Environment and Resources (CAS),
China

REVIEWED BY

Shufan Zhao,
Ministry of Emergency Management,
China
Sudipta Sasmal,
Indian Centre for Space Physics, India

*CORRESPONDENCE

Aleksandra Nina,
sandrast@ipb.ac.rs

SPECIALTY SECTION

This article was submitted to
Atmosphere and Climate,
a section of the journal
Frontiers in Environmental Science

RECEIVED 28 July 2022

ACCEPTED 06 September 2022

PUBLISHED 29 September 2022

CITATION

Nina A, Biagi PF, Pulinets S, Nico G,
Mitrović ST, Čadež VM, Radovanović M,
Urošev M and Popović LČ (2022),
Variation in the VLF signal noise
amplitude during the period of intense
seismic activity in Central Italy from
25 October to 3 November 2016.
Front. Environ. Sci. 10:1005575.
doi: 10.3389/fenvs.2022.1005575

COPYRIGHT

© 2022 Nina, Biagi, Pulinets, Nico,
Mitrović, Čadež, Radovanović, Urošev
and Popović. This is an open-access
article distributed under the terms of the
[Creative Commons Attribution License
\(CC BY\)](https://creativecommons.org/licenses/by/4.0/). The use, distribution or
reproduction in other forums is
permitted, provided the original
author(s) and the copyright owner(s) are
credited and that the original
publication in this journal is cited, in
accordance with accepted academic
practice. No use, distribution or
reproduction is permitted which does
not comply with these terms.

Variation in the VLF signal noise amplitude during the period of intense seismic activity in Central Italy from 25 October to 3 November 2016

Aleksandra Nina^{1*}, Pier Francesco Biagi², Sergey Pulinets³,
Giovanni Nico⁴, Srđan T. Mitrović⁵, Vladimir M. Čadež⁶,
Milan Radovanović^{7,8}, Marko Urošev⁷ and Luka Č. Popović^{6,9,10}

¹Institute of Physics Belgrade, University of Belgrade, Belgrade, Serbia, ²Physics Department, Università di Bari, Bari, Italy, ³Space Research Institute, Russian Academy of Sciences, Moscow, Russia, ⁴Istituto per le Applicazioni del Calcolo (IAC), Consiglio Nazionale delle Ricerche (CNR), Bari, Italy, ⁵Novelic, Belgrade, Serbia, ⁶Astronomical Observatory, Belgrade, Serbia, ⁷Geographical Institute “Jovan Cvijić” SASA, Belgrade, Serbia, ⁸South Ural State University, Institute of Sports, Tourism and Service, Chelyabinsk, Russia, ⁹Department of Astronomy, Faculty of Mathematics, University of Belgrade, Belgrade, Serbia, ¹⁰Faculty of Science, University of Banja Luka, Banja Luka, Bosnia and Herzegovina

Recent research shows reductions in the VLF signal noise amplitude that begin before particular earthquakes whose epicentres are more than 100 km away from the signal propagation path. In this paper, we extend this research to studying the noise amplitude during periods of intense seismic activity in a localized area. We analyse variations in the VLF signal noise amplitude over a period of 10 days (25 October–3 November 2016) when 981 earthquakes with the minimum magnitude of 2 occurred in Central Italy. Out of these events, 31 had the magnitude equal or greater than 4, while the strongest one had the magnitude of 6.5. We observe the VLF signal emitted by the ICV transmitter located in Sardinia (Italy) and recorded in Belgrade (Serbia). Bearing in mind that the trajectory of this signal crosses the area in which the observed earthquakes occurred, we extend the existing research to study of variations in the noise amplitude of the signal propagating at short distances from the epicentres of the considered earthquakes. In addition, we analyse the impact of a large number earthquakes on characteristics of the noise amplitude and its reductions before particular events. In order to examine the localization of the recorded changes, we additionally analysed the noise amplitude of two reference signals emitted in Germany and Norway. The obtained results show the existence of the noise amplitude reduction preceding individual strong or relatively strong earthquakes, and earthquakes followed by others that occurred in a shorter time interval. However, the additional noise amplitude reductions are either not pronounced or they do not exist before the considered events in periods of the reduced noise amplitude remain from previous earthquakes. Reductions in noise amplitudes for all observed signals indicate a larger perturbed area through which they spread or its closer location to the receiver. The analysis of daily values of parameters describing the noise amplitude reveals their variations start up to 2 weeks before the seismically active period occurs.

KEYWORDS

earthquakes, earthquake precursor, VLF signal, noise amplitude, ionosphere, intense seismic activity

1 Introduction

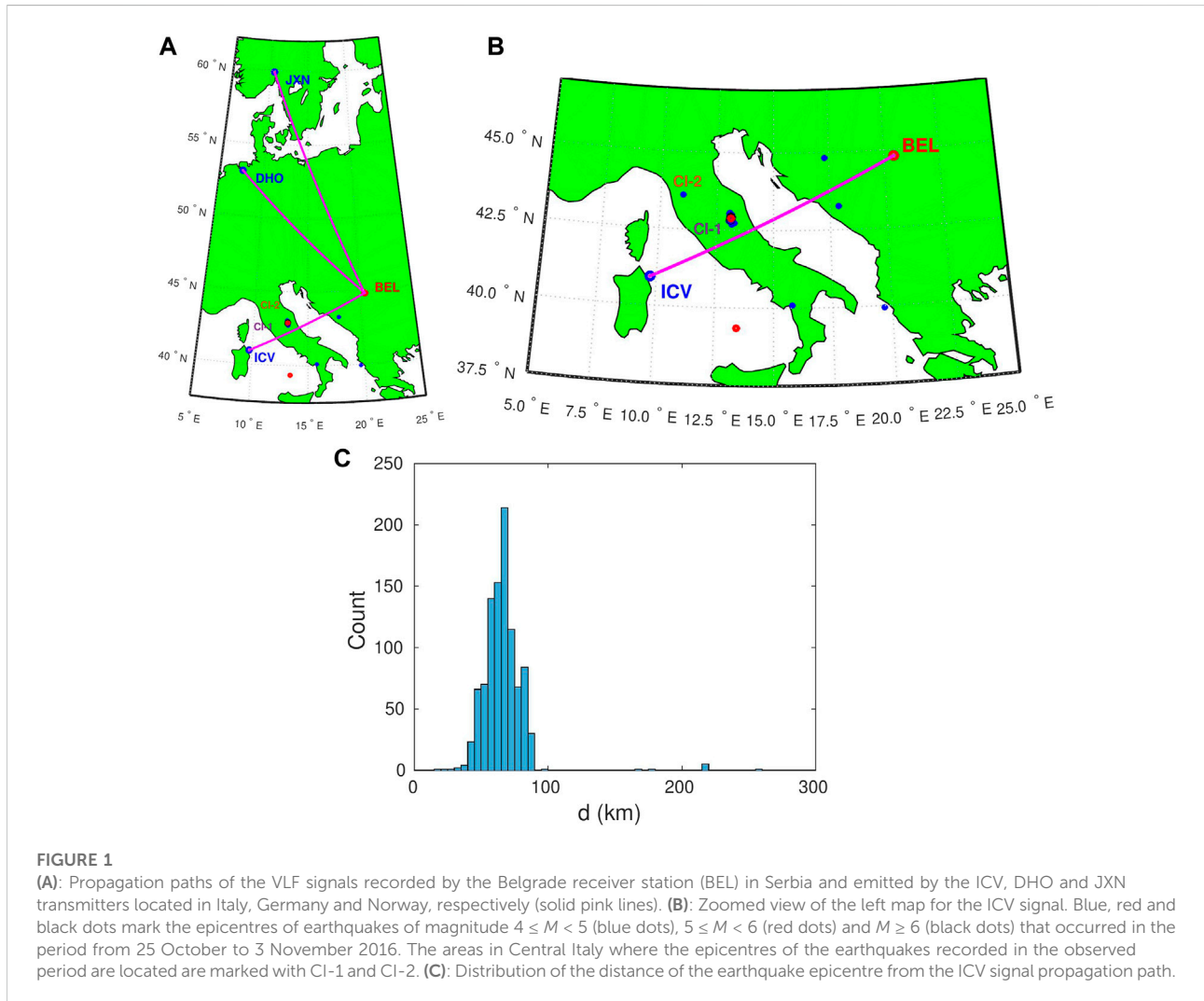
In a large number of scientific studies published in this and the previous century, different types of ionospheric disturbances that precede earthquakes (EQs) are shown (Davies and Baker, 1965; Leonard et al., 1965; Yuen et al., 1969; Calais and Minster, 1998; Maekawa et al., 2006; Sasmal and Chakrabarti, 2009; Chakrabarti et al., 2010; Oyama et al., 2016; Xiong et al., 2021; He et al., 2022; Molina et al., 2022). The repetition of the same or very similar characteristics of these disturbances indicates the possibility that they are precursors of earthquakes, which is why a relevant both theoretical and experimental research is of great importance. In the first case, studies provide several theoretical explanations for the relationship between ionospheric disturbances and lithospheric processes associated with earthquakes, and they are based on thermal and chemical mechanisms as well as on generation of acoustic and electromagnetic waves, and quasi constant local electric field (Sorokin and Yashchenko, 1999; Pulinets and Boyarchuk, 2004; Liperovsky et al., 2008; Korepanov et al., 2009; Pulinets and Ouzounov, 2011; Fu et al., 2015). On the other hand, the observations are based on remote sensing of the high (using ionosonde/digisonde and radar) and lower (using very low/low frequency (VLF/LF) radio signals) ionosphere as well as integral information about the entire ionosphere obtained by the Global Navigation Satellite System (GNSS) signals (Biagi et al., 2001b, 2011; Hegai et al., 2006; Perrone et al., 2018). In addition, measurements by satellites orbiting in the ionosphere (e.g., Detection of Electro-Magnetic Emissions Transmitted from Earthquake Regions (DEMETER) satellite) are used for relevant studies (Němec et al., 2009).

Previous studies indicate that typical perturbations (variations of the electron density (positive and negative) at specific altitudes of the ionosphere registered by ionosondes, the total electron content (TEC) variations registered by GNSS receivers, changes in the VLF/LF signal amplitude (or phase), its periodic fluctuations and the “terminator time” shift) are registered in all ionospheric regions mostly a few days before the occurrence of stronger earthquakes (Hayakawa, 1996; Molchanov et al., 1998; Biagi et al., 2001b, 2006; Miyaki et al., 2001; Molchanov et al., 2001; Pulinets and Boyarchuk, 2004; Rozhnoi et al., 2004; Yamauchi et al., 2007; Hayakawa et al., 2010; Liu et al., 2018; Perrone et al., 2018; Pulinets et al., 2022). However, recent research presented in Nina et al. (2020) and Nina et al. (2021a) points out a possibility for a new type of precursor that occurs up to a few tens of minutes before an EQ (including some cases of weak earthquakes whose magnitude can be less than 3) and manifests itself through a reduction in the VLF

signal amplitude and phase noise, respectively. These studies present analyses of several EQs whose epicentres were relatively close to the considered signal propagation path. In these analysed cases, the detected individual reductions can be clearly associated with individual EQs. In other words, the disturbance in the environment in which the signal propagates either ends quickly enough and do not affect disturbances that could potentially be associated with further EQs or is further amplified before an another event. A possible explanation for this may be the fact that the analysed earthquakes occurred in several remote locations (Serbia, Italy, Tyrrhenian Sea and Western Mediterranean Sea). However, the question arises as to how a large number of EQ events whose epicentres are located in close locations and that occur in a relatively short time period affect the signal noise properties. The importance of this issue can be seen in the fact that in the DHO and GQD signals with a small noise amplitude during the time periods observed in the study Nina et al. (2020) no reduction of the noise amplitude was recorded, which, consequently, requires the examination of the existence of an additional reduction of this parameter if it is already significantly reduced by some previous EQ. The analysis of this issue is the main aim of this paper. In addition, the aims of this research are to explore the VLF signal prior the considered EQs in order to confirm our finding of the noise amplitude reduction in the case of EQs that occurred during the period when the noise amplitude corresponds to that in quiet conditions and, for the first time, to explore the daily characteristics of the VLF signal noise amplitude in time periods before, during and after the considered intensive seismic activity.

In this study, we analyse the time evolution of the noise amplitude of the ICV signal transmitted in Italy and recorded in Serbia in the period from 25 October to 3 November 2016 which was the time period of intense seismic activity (PISA). During this period there were 981 earthquakes in Central Italy of minimum magnitude 2, out of which there were 31 cases with magnitudes equal or greater than 4. In addition, we analyse daily characteristics of the noise amplitude in the time period from 1 October to 22 December in order to examine long-term variations around intense seismic activity located at a small area. To study localization of the perturbed atmospheric part, we analyse two additional VLF signals emitted by the DHO (Germany) and JXN (Norway) transmitters and received in Belgrade, Serbia.

The paper is organised as follows. The descriptions of observations, considered events, and the applied procedures for data processing are presented in Section 2. Section 3 shows the obtained results and their discussion. Finally, the conclusions of this study and the list of the opened questions are given in Section 4.



2 Observations and data processing

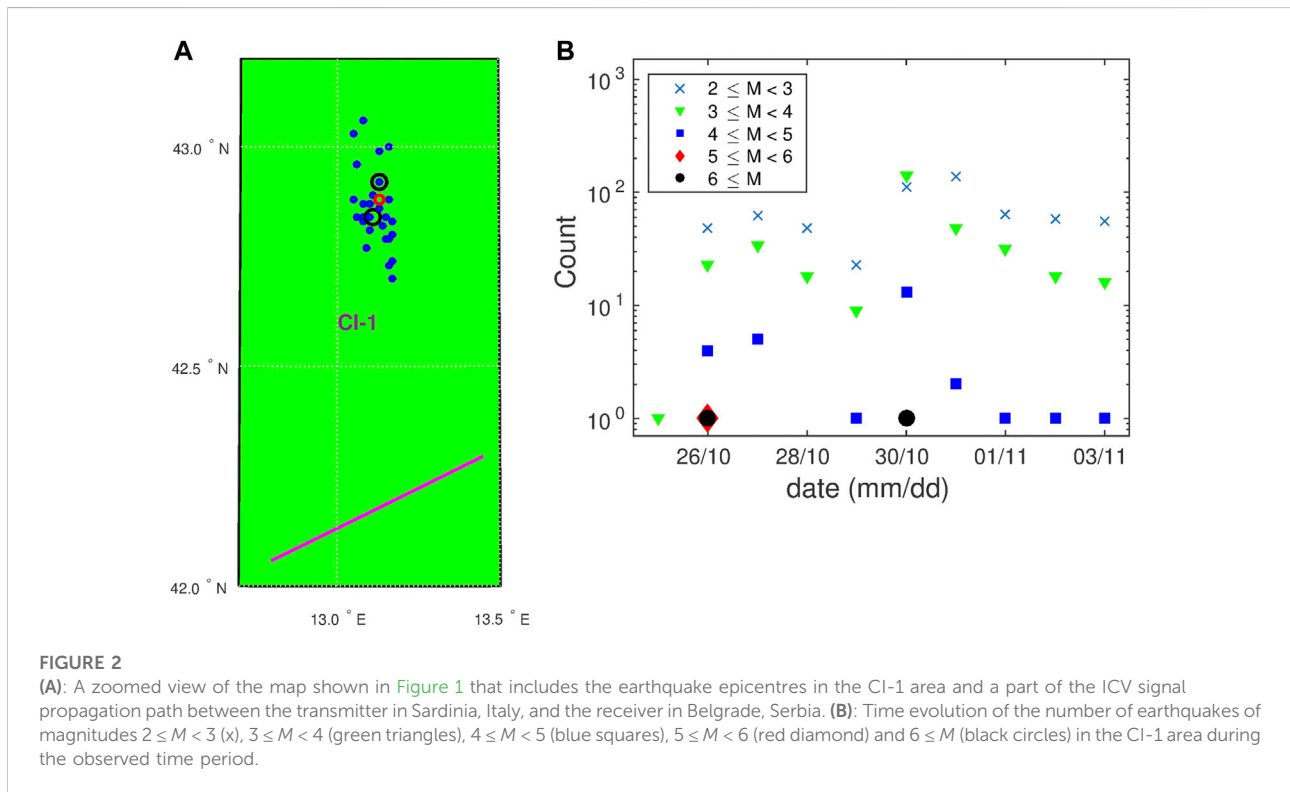
2.1 Observational setup and study area

The study presented in this paper is based on the processing of the VLF signal amplitudes recorded by the Absolute Phase and Amplitude Logger (AbsPAL) receiver in Belgrade, Serbia (44.8 N, 20.4 E). The data recorded by this receiver are used in many analyses (Žigman et al., 2007; Grubor et al., 2008; Kolarski et al., 2011). Here, we analyse three signals emitted by the ICV, DHO and JXN transmitters located in Isola di Tavolara, Sardinia, Italy (40.92 N, 9.73 E), Rhaderfehn, Germany (53.10 N, 7.60 E) and Kolsas, Norway (59.91 N, 10.52 E), respectively. Their propagation paths are shown in Figure 1A.

The focus of this research is on the ICV signal amplitude processing because, as the map shows, its propagation path to Belgrade is closest to the epicentres of the observed set of earthquakes marked as blue, red and black points depending

of their magnitudes (a zoomed map view of the signal propagation area is given in the upper right panel). In addition, a study given in Nina et al. (2020) indicates the appropriate noise amplitude reductions for this signal, and, consequently, shows that it is suitable for relevant analyses. This is important because the influence of the signal characteristics on the possibility of detecting the considered specified form of amplitude change has not been investigated yet, and by choosing this signal we eliminate the possibility of no detection of the observed change due to e.g. insufficient sensitivity of the selected signal to atmospheric noise variations.

We analyse the signals emitted by the DHO and JXN transmitters in order to examine the influence of the receiver, and electronic and electrical devices close to it on the signal noise amplitude, and the localization of the detected changes. Here, we point out that variations in the signal emission relevant for the study are eliminated by analysing its amplitude recorded by the receiver located in Kilpisjärvi, Norway (see Section 2.3).



2.2 Analysed events

In the detailed analysis of the ICV signal amplitude, we observe the time period from 25 October to 3 November 2016 when seismic activity in Central Italy was very intense. In Figure 1, we show a map of the area where the observed signal propagates, and the epicenters of EQs that occurred during the analysed time period, out of which 981 (with the magnitude, M , equal or greater than 2) occurred in Central Italy. For clarity, we show the epicenters of earthquakes of minimum magnitudes 3.9 (blue dots), 5 (red circle) and 6 (black circles) on this map. As can be seen in the map, these epicenters are grouped into two localized areas marked as CI-1 and CI-2 (the maximum earthquake magnitude in this area is 3.9, so we included this value in the epicentre display in the map). The histogram of the distances d between the epicenters of all considered EQs and the signal propagation path is shown in Figure 1C where one can see that d is smaller than 100 km in almost all (more than 99%) cases. The number of the EQ events with $40 \text{ km} < d < 90 \text{ km}$ is 963 which is 98.2% of the total number of observed EQs. The distance d is bigger than 100 km in only 8 cases and corresponds to the events that took place at the CI-2 area.

Considering that the epicenters of EQs that occurred in the CI-2 area are significantly further from the signal propagation path (d is between 168 and 259 km) than those occurred in the CI-1 area (d is below 100 km), and that their magnitudes are below 4, we focus on events in the CI-1 area. A zoomed view of the map for this area

with 31 EQ epicentre locations (for $M \geq 4$) and part of the observed signal path are given in the left panel, while the numbers of EQ events per day with magnitudes between 2 and 3, 3 and 4, 4 and 5, 5 and 6, and greater than 6 are shown in Figure 2B. The list of analysed 31 earthquakes (magnitudes of 4) with their characteristics (times of their events, epicentre locations, depths, magnitude values and types, and epicentre distances from the ICV signal propagation path) is given in Table 1.

As one can see in the map shown in Figure 1, the upper right panel, two additional EQs also occurred relatively close to the considered signal propagation path (in Bosnia and Herzegovina). Their magnitudes are 4.2 (31 October 2016, 09:38:13 UT, (43.26N,17.88E)) and 3.9 (3 November 2016, 15:04:03 UT, (44.82N,17.3E)). In the first case, no reduction of A_{noise} is recorded, while in the period around the second event the ICV signal is not recorded in Belgrade. In the observed period, there were additional two EQs of magnitudes of 2.6 and 2.5 in Bosnia and Herzegovina, and Serbia, respectively. In the first case, the analysed reduction is not recorded, while, in the second case, the time of EQ is in the period of occurrences of two EQs of higher magnitudes (4.6 and 3.9) in the CI-1 area which are much more likely to be associated with the corresponding detected A_{noise} reduction. The strongest EQ outside Central Italy of magnitude 5.8 occurred in the Tyrrhenian Sea (28 October, 20:02:49 UT, (39.35N,13.44E)). As will be seen in Section 3, A_{noise} is low throughout the day and although its slight reduction in the period around this EQ is visible, it is not possible to reliably link these two phenomena.

TABLE 1 List of the main studied earthquakes. Data for EQ date, time t , epicentre locations (latitude (LAT) and longitude (LON)) and magnitudes (M) are given in <http://www.emsc-csem.org/Earthquake/>. Distances between the EQ epicentres and signal propagation path are indicated as d .

No	Date	Time UTC	Latitude	Longitude	Depth	Magnitude Type	Magnitude	Distance
1	2016/11/03	00:35:01	43.03	13.05	8	Mw	4.8	85.0
2	2016/11/02	19:37:52	42.89	13.11	10	ML	4	68.9
3	2016/11/01	07:56:39	43	13.16	10	Mw	4.9	78.0
4	2016/10/31	07:05:45	42.83	13.17	20	Mw	4.2	60.7
5	2016/10/31	03:27:40	42.77	13.09	11	mb	4.3	57.7
6	2016/10/30	18:21:09	42.79	13.15	10	ML	4.2	57.5
7	2016/10/30	13:34:54	42.8	13.17	9	ML	4.6	57.8
8	2016/10/30	12:07:00	42.84	13.08	10	ML	4.6	65.1
9	2016/10/30	11:58:17	42.84	13.06	10	ML	4	65.8
10	2016/10/30	11:21:09	43.06	13.08	2	ML	4.1	86.9
11	2016/10/30	10:19:26	42.82	13.14	11	ML	4.1	60.9
12	2016/10/30	08:35:58	42.83	13.08	10	mb	4.6	64.1
13	2016/10/30	07:34:47	42.92	13.13	10	ML	4	71.1
14	2016/10/30	07:13:06	42.73	13.16	10	mb	4.5	51.2
15	2016/10/30	07:07:54	42.7	13.17	2	ML	4.2	47.9
16	2016/10/30	07:05:56	42.79	13.16	8	ML	4.1	57.1
17	2016/10/30	07:00:40	42.88	13.05	10	ML	4.1	70.1
18	2016/10/30	06:55:40	42.74	13.17	13	ML	4.1	51.8
19	2016/10/30	06:40:18	42.84	13.11	10	Mw	6.5	63.9
20	2016/10/29	16:24:33	42.81	13.1	11	mb	4.4	61.3
21	2016/10/27	17:22:23	42.84	13.1	9	ML	4.2	64.3
22	2016/10/27	08:21:46	42.87	13.1	9	Mw	4.4	67.3
23	2016/10/27	03:50:24	42.99	13.13	9	Mw	4.2	78.1
24	2016/10/27	03:19:27	42.84	13.15	9	mb	4.4	62.5
25	2016/10/27	00:21:32	42.96	13.06	10	mb	4.2	77.7
26	2016/10/26	23:52:32	42.82	13.14	10	mb	4	60.9
27	2016/10/26	21:42:02	42.86	13.13	10	Mw	4.7	65.2
28	2016/10/26	21:24:51	42.87	13.08	9	mb	4.1	68.0
29	2016/10/26	19:18:07	42.92	13.13	8	Mw	6.1	71.1
30	2016/10/26	19:16:57	42.88	13.16	8	ML	4.3	66.1
31	2016/10/26	17:10:36	42.88	13.13	9	Mw	5.5	67.2

Based on the previous analysis, it can be concluded that the noise amplitude reductions can be related to the EQs that occurred in the CI-1 area and that other EQ events do not significantly affect the presented analysis.

In addition to the detailed analysis of the ICV signal amplitude for the indicated 10 days, we analysed the period from 1 October to 22 December to examine long-term variations around the seismological active period.

2.3 Analysis of other potential influences on the signal amplitude

As stated in the literature (Biagi et al., 2011; Nina et al., 2020), there are numerous causes of variations in signal characteristics.

They refer both to natural sources of disturbances and to technical changes in the emission and reception of signals due to, for example, electric or electronic devices operating nearby the receiver, electric cables without good shielding, amateur radios operating in the zone, an improperly grounded receiver, or natural electromagnetic emissions from nearby faults or micro-fractured zones. For this reason, it is necessary to check the presence of influence of these factors on the signal characteristics important for this study.

- Natural conditions. The main potential natural causes of changes in a VLF signal propagation are related to meteorological and geomagnetic conditions, and variations in radiation from the Sun and other sources in the Universe.

- Meteorological conditions can cause disturbances in signal characteristics of different durations. However, typical signal variations caused by lightning (see, for example, Wang et al. (2020) and references therein) do not have the same characteristics as those analysed in Nina et al. (2020) as a potential EQ precursor. In addition, there were no significant meteorological events in the area near the ICV signal route from Sardinia to Belgrade in the observed period according to the European Severe Weather Database (<https://eswd.eu/cgi-bin/eswd.cgi>). The only recorded north wind was on 2 November 2016.
- Geomagnetic conditions. The values of the Kp index were below 5 during this time, except in seven and three three-hour periods when they were ≥ 5 and ≥ 6 , respectively ((Matzka et al., 2021), https://www-app3.gfz-potsdam.de/kp_index/Kp_ap_Ap_SN_F107_since_1932.txt). Although the values of 5 and 6 in the NOAA scale are indicators of minor and moderate geomagnetic storms, respectively (<https://www.swpc.noaa.gov/noaa-scales-explanation>), the comparison of these periods with the time evolution of the noise amplitude show the indicated storms cannot be related to variations in the intensity of this parameter.
- Extraterrestrial electromagnetic radiation. Changes in the D-region electron density (the plasma parameter that is significant for a VLF signal propagation) are dominantly influenced by the solar hydrogen Ly α line in quiet conditions (Mitra, 1974; Nina et al., 2021b) and the soft X-radiation produced during solar X-ray flares (Thomson et al., 2005; Kolarski et al., 2011; Basak and Chakrabarti, 2013; Schmitter, 2013; Ammar and Ghalila, 2016; Chakraborty and Basak, 2020). In both cases, these impacts are significant during the daytime period. Based on the obtained noise amplitude values in Nina et al. (2020), it can be concluded that the noise amplitude of the observed signal is not affected by the daily variations of the mentioned Ly α radiation. In addition, during the observed period, no solar X-ray flares of class C and stronger, which can affect VLF signal characteristics, were recorded (https://hesperia.gsfc.nasa.gov/goes/goes_event_listings/). Based on this, we can conclude that solar radiation cannot be the cause of the significant variations in the noise amplitude analysed in this study.

The changes in the signal that are indicated as the detection of gamma ray burst in Inan et al. (2007) are not recorded, while those shown in Nina et al. (2015) do not correspond to the changes analysed in this study.

- Non-natural conditions. Amplitude variations that result in reductions of its noise amplitude can also be consequences of variations in the signal emission and/or reception. In

order to eliminate the presence of these influences, we analyse the amplitude of the ICV signal recorded by the Kilpisjärvi ULTRA Data receiver (to check variations in the emission of the observed ICV signal) and the DHO and JXN signals emitted in Germany and Norway, respectively, and received by the AbsPAL receiver in Belgrade (to check variations in the reception of the signal by the used receiver). Comparisons with the analysed ICV signal noise amplitude recorded in Belgrade show the following:

- Signal emission. In contrast to the noise amplitude of the ICV signal recorded in Belgrade, which does not have typical daily variations, the noise amplitude of this signal recorded in Kilpisjärva is greater during daytime than during nighttime conditions. Ignoring these periodic changes, the obtained values do not show noise amplitude reductions that match those visible in the data recorded in Belgrade. This suggests that the analysed reduction does not occur in the signal emission.
- Signal reception. In addition to the influence of changes in the signal emission, variations in its reception can occur due to changing characteristics of the environment in which it spreads, and technical problems (including the influence of additional electric and electronic devices near the receiver) during its reception. Bearing in mind that this is one of the pioneer studies and that we cannot *a priori* assume the borders of the area of potential influence of seismic changes on the atmosphere, we compare the noise amplitude of the ICV signal with the corresponding values related to two additional signals recorded by the same receiver in Belgrade. A detailed analysis of this comparison, given in Section 3.1.2, shows that the noise amplitudes reductions recorded for ICV signal also occur for other signals (in all cases for EQs of magnitude over 5, and for the DHO signal for EQs of magnitude below 5 (during October 27)). However, the intensities of these reductions are different, and their relationships cannot be established either with the intensity of the signal amplitudes or with the noise amplitudes corresponding to quiet conditions. For this reason, we can conclude that these reductions are most likely due to changes in the atmosphere, i.e. they do not result from technical problems in reception.

Based on the previously presented checks, we are now able to present the following analysis of the potential relationship of the recorded noise amplitude reductions with the considered EQs.

2.4 Data processing

The procedure for the determination of the noise amplitude, A_{noise} , used in this study is described in Nina et al. (2015) and applied in the studies of the noise reductions in the amplitude

and phase presented in Nina et al. (2020) and Nina et al. (2021a), respectively. It is based on processing of the signal amplitude A recorded by the AbsPAL receiver with time resolution of 0.1 s, and on determining of:

- The basic amplitude $A_{\text{base}}(t)$ at the time t as the mean value of the amplitude values in the time bin $(t - \Delta t, t + \Delta t)$:

$$A_{\text{base}}(t) = \frac{1}{i_{t+\Delta t} - i_{t-\Delta t} + 1} \sum_{i=i_{t-\Delta t}}^{i=i_{t+\Delta t}} A(i) \quad (1)$$

where i_t is the ordinal number of the element in the array of the recorded amplitude values corresponding to the time t .

- The deviation of the signal amplitude $A(t)$ from the basic amplitude A_{base} at the time t using expression:

$$dA(t) = |A(t) - A_{\text{base}}(t)|. \quad (2)$$

- The noise amplitude A_{noise} in the defined time bins as the maximum of the array B obtained by reducing the array $|dA|$ of N values to the array of N^* values by eliminating p percent of the highest values ($B(1 : N^*) = \text{sort}(|dA|)(1 : N^*)$):

$$A_{\text{noise}} = \max(B). \quad (3)$$

As in the study presented in Nina et al. (2020) and Nina et al. (2021a), in this analysis we assumed that $p = 5\%$ (the study given in Nina et al. (2015) indicates that the choice of this value has no essential significance for relevant analyses).

In this study, the examination of variations in daily noise amplitude characteristics is based on the analysis of its minimum, maximum, mean and median values, as well as the standard deviation from 0 to 24 h for the period from 1 October to 22 December.

3 Results and discussions

In this study, we investigate the existence of the VLF signal noise amplitude reductions lasting from several tens of minutes to several hours during the time periods around earthquakes (described in Nina et al. (2020)). Bearing in mind that almost 1000 EQs (31 of them had magnitudes 4 or greater) were registered in Central Italy in just 10 days, we also analyse the presence of long-term variations in the noise amplitude. Therefore, the obtained results and their analysis are presented in two parts related to the noise amplitude time evolution (Section 3.1) and daily characteristics of the noise amplitude (Section 3.2).

3.1 Time evolution of the noise amplitude

During the period from 26 October to 3 November, 31 earthquakes with the minimum magnitude of 4 were registered in the CI-1 area. In this Section we study

characteristics of the ICV signal amplitude (Section 3.1.1) and compare the obtained amplitude noise reduction with those corresponding to two referent signals (Section 3.1.2) in order to examine localization of the considered changes.

3.1.1 Time evolution of the ICV signal noise amplitude

In Figure 3, we show time evolutions of the recorded ICV signal amplitude, A , its deviation from the corresponding basic curve, dA , and the noise amplitude, A_{noise} , for this period and for 1 day that precedes it in order to show the analysed parameters during relatively quiet conditions. The vertical lines in the lower panels indicate the time of the considered EQ occurrences and the horizontal ones (given for a better overview of the A_{noise} reductions and their easier comparison during the observed time interval) represent the noise amplitude values of 1.5 and 1 dB (they are determined as values which are about 0.5 and 1 dB lower than the ICV signals noise amplitude in the “quiet” time period before PISA which is about 2 dB). In these panels one can notice: (1) the absence of mid-term (of several tens of minutes and longer) periodic daily variations of A_{noise} (that is in agreement with the analysis given in Nina et al. (2020)), (2) short-term increases of this parameter during the solar terminator periods (ignored in the further analysis relevant to the potential connection of the considered signal characteristics and earthquakes), and (3) three profiles of the noise amplitude reduction behaviour (seen in Figure 4):

- (1) Type I (left panel)—the amplitude noise reduction is a consequence of both the increasing lower and decreasing higher amplitude values. In this case, the tendency of the A_{base} time evolution does not change. This type is also recorded in the case of Kraljevo EQ (Nina et al., 2020).
- (2) Type II (middle panel)—the amplitude noise reduction is a consequence of increasing lower amplitude values. In this case, the highest amplitude values do not decrease, which affects the increase of the basic amplitude values.
- (3) Type III (right panel)—the amplitude noise reduction is a consequence of decreasing the upper amplitude values to previously minimum values or even lower. In this case, the lower amplitude values do not increase and the basic amplitude decreases.

The analysis of the presented parameters shows the following:

- 25 October. During this day, no strong EQs were recorded in the CI-1 area. A several-hour A_{noise} reduction that is visible in the afternoon corresponds to the time period around EQ of magnitude 3.9 in the CI-2 area. In other periods, the approximate value of A_{noise} is 2 dB, and it can be considered as A_{noise} in quiet conditions.

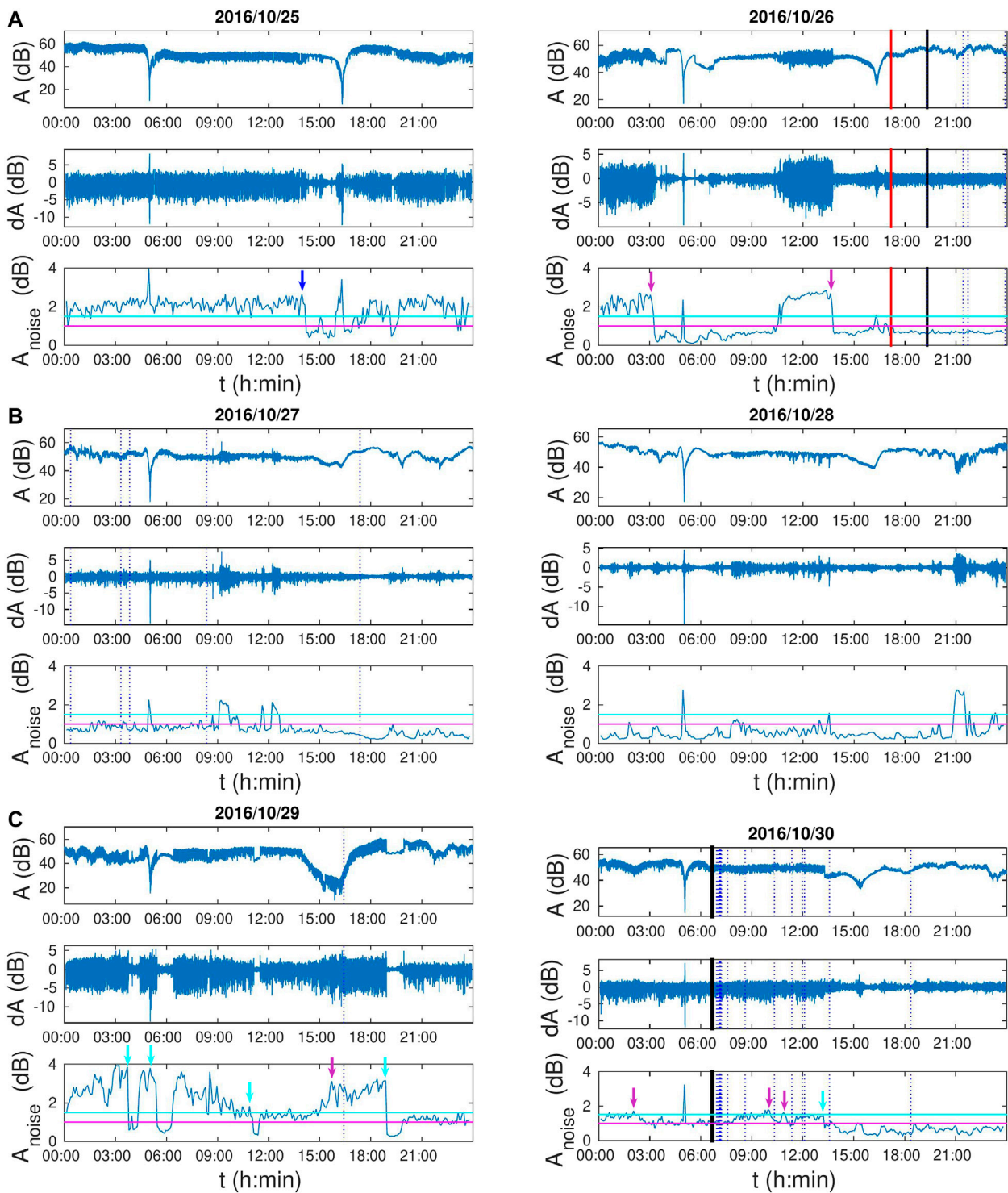
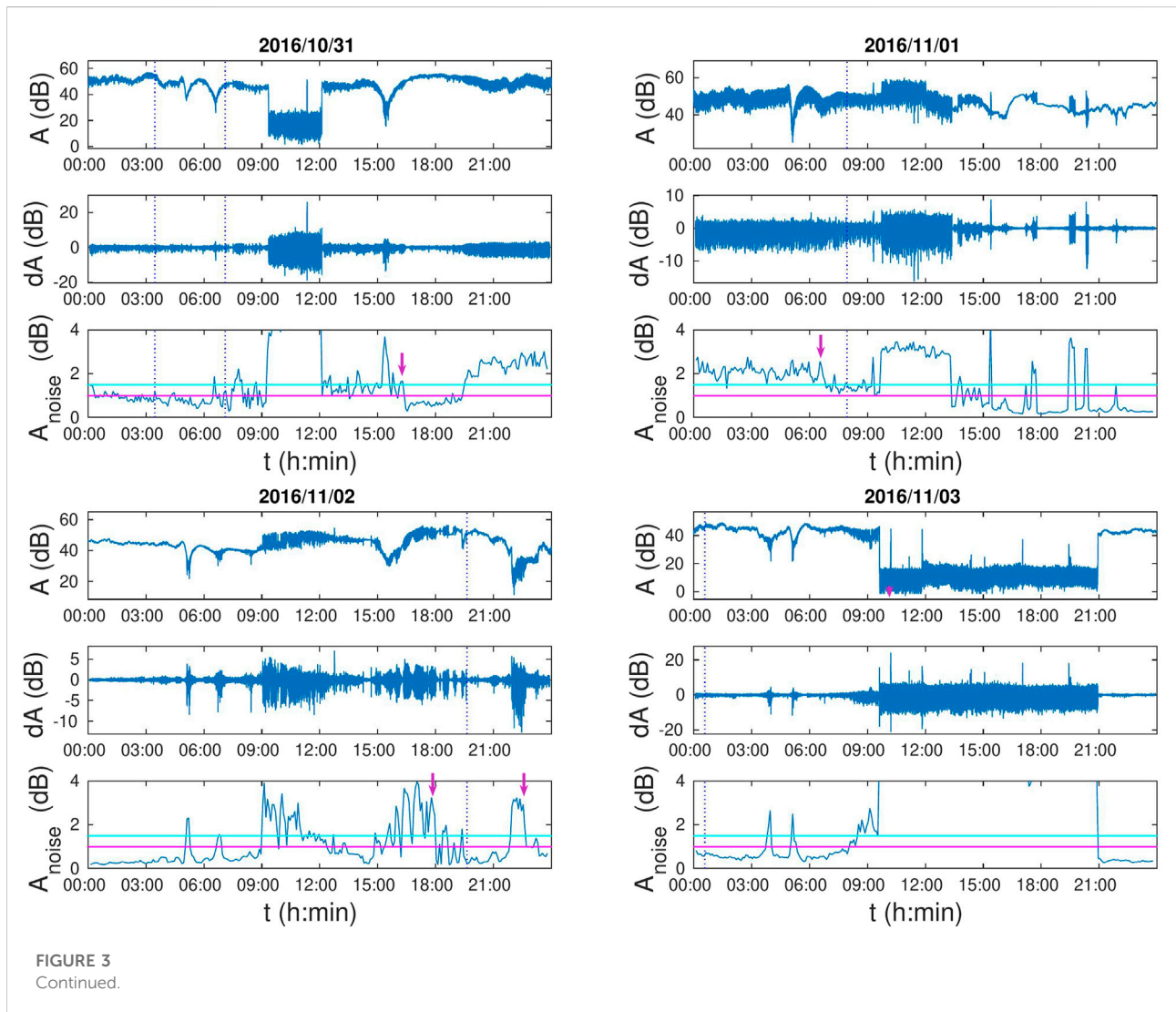


FIGURE 3

The time evolutions of the recorded amplitude A (A), its deviation, dA , from the base curve (B), and the noise amplitude, A_{noise} , (C) for the period of 25 October to 3 November 2016. Vertical lines indicate the times of earthquakes of magnitude $4 \leq M < 5$ (blue dot lines), $5 \leq M < 6$ (red line) and $6 \leq M$ (black lines). Horizontal magenta and cyan lines indicate the amplitude of 1 and 1.5 dB, respectively. The beginnings of the amplitude noise reductions of Type I, II and III are indicated by the magenta, blue and cyan arrows, respectively.



- 26–28 October. The expected values of A_{noise} under quiet conditions are visible at the beginning of 26 October. Its reduction to values below 1 dB begins a little after 3 UT, which is about 14 h before the first considered large EQ of magnitude 5.5. This reduction is followed by an increase of A_{noise} to values between 2 and 3 dB in a period of about 3 h starting at about 10:40 UT. After that, A_{noise} drops again back to values below 1 dB (at approximately 13:40 UT). This second reduction starts about 3.5 h before the mentioned EQ at 17:10 UT. Both of these A_{noise} reductions are of Type I. However, in the case of the first one, no earthquakes were recorded near the considered signal propagation path, which open the question: Can more reduction of A_{noise} occur before a strong earthquake or more (relatively) strong earthquakes (in this case, EQs of magnitudes of 5.5 and 6.1 and 7 EQs of magnitudes of 4–4.7 in a period shorter than 11 h)? The values of A_{noise} continued to be low for the next 2 days. In that

period, 5 EQs (of magnitudes of 4.2 (three events) and of 4.4 (two events)) were recorded on October 27, while there were no earthquakes of magnitude greater than 4 on October 28. It is important to note here that there were no additional significant reductions that could be linked with the mentioned five EQs.

- 29–31 October. A_{noise} exceeds 2 dB at the beginning of 29 October and it is very unstable until about 20 UT. During that period, four reductions of A_{noise} below 1.5 dB (Type 3) that cannot be associated with EQs (not even those of magnitude less than 4) and one of Type 1 preceding EQ of magnitude 4.4 are visible. During the period of this reduction, a large number of less intense EQs were recorded. After 20 UT, A_{noise} is stabilized between 1.5 and 2 dB until around 14 UT on 30 October. During this time period, an EQ of magnitude 6.5 and 12 EQs of magnitude between 4 and 4.6 occurred. Before the

strongest of them, an additional noise amplitude reduction of Type I is recorded. After it, two small additional reductions of Type I which can be connected with EQs are visible. They are followed by one long-lasting additional reduction of Type III, during which four more EQs of magnitudes between 4.2 and 4.9 (two on 30 October and two on 31 October) occurred. The connection of these five EQs with the mentioned reduction is not fully possible to harmonize with the expected possible connections based on the explanation of the previous cases and those given in Nina et al. (2020). Namely, increases in A_{noise} are expected after each of the first three EQs due to their lower intensity and several hours apart from the next one. However, a large number of weaker earthquakes occurred in this period and their impact on the considered signal should not be excluded *a priori* (the potential connection of weaker earthquakes with A_{noise} reductions is reported in Nina et al. (2020)).

- 1–3 November. Before the last three EQs in the observed period, A_{noise} is around 2 dB and higher for a certain period of time and, in all three cases, reductions of this parameter is visible (the first reduction is of Type I, and the second two also correspond mostly to this type).

Based on the above analysis, one can conclude that the reduction of A_{noise} with the characteristics described in Nina et al. (2020) is recorded in the case of all three earthquakes of magnitudes over 5 (5.5, 6.1 and 6.5) (Cheloni et al., 2017; Galli et al., 2017). The earthquakes of magnitudes from 4 to 5 mostly (25 out of 28 cases) occurred after these 3 higher intensity earthquakes when A_{noise} is already reduced. In those cases, the additional observed reduction is either weakened or absent. In three cases when A_{noise} is around 2 dB or higher in the period before the change, visible reductions of A_{noise} are recorded. A corresponding reduction is also recorded before the magnitude 3.9 earthquake with the epicentre in the CI-2 area during the first analysed day (without stronger earthquakes in the CI-1 area). In other words, the obtained results indicate that the detectability of the noise amplitude reduction is reduced if its value is previously reduced due to the influence of other earlier EQ events. This conclusion opens up an additional question: Are signals with low noise amplitude suitable for analyses of its reduction

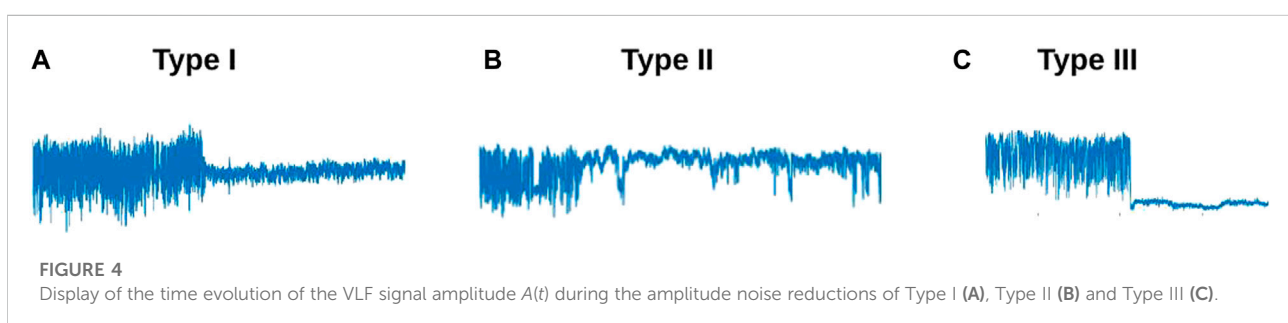
as a potential precursor of earthquakes? In addition, the obtained results indicate the necessity to exclude the temporally close EQs from statistical analyses of effects of various parameters related to the characteristics of the analysed earthquakes, VLF signal and the environment in which it spreads to the noise amplitude reduction properties as such frequent EQs could simultaneously affect the signal.

The analysis of the connection between the A_{noise} reductions of the mentioned types and the occurrence of earthquakes whose magnitude is not less than 4 shows that the majority of Type I reductions (8 out of 10, i.e. 80%) and the only recorded Type II reduction are accompanied by observed phenomenon, which is in agreement with the study given in Nina et al. (2020). Although an earthquake was recorded after the Type III reduction on 30 October 2016, the previous analysis and the absence of that connection in the paper Nina et al. (2020) indicate that these phenomena are most likely not related.

In order to compare the presented analysis for PISA and periods without EQs, we additionally analyse the 6 days before and 6 days after those considered in this study. Based on the corresponding graphs and the detailed analysis given in the Supplementary Material, it can be seen that the reductions of all three types are also visible in these periods. However, out of a total of 18 reductions, 8 (4 of Type I, 3 of Type II and 1 of Type III) are in periods when the intensity of the amplitude is changed (e.g. in ST periods), 3 (all of Type III) are in the period of bad meteorological conditions, 1 (of Type II) in the period when the amplitude is unexpectedly low for the corresponding part of the day, while 4 (1 of Type I and 3 of Type II) have the same value as during most of the day but are preceded by short-term increases in A_{noise} . The only two A_{noise} reductions that have the properties of those described for PISA and in Nina et al. (2020) are reductions of Type III that, based on the previous analysis, cannot be considered as potential earthquake precursors.

3.1.2 The comparison of time evolutions of three VLF signal amplitude characteristics

The analysis presented in the previous section shows that the noise amplitude reductions can be clearly associated with the strongest earthquakes that occurred on 26 and 30 October, as well as the three earthquakes recorded from 1 to 3 November. In



DHO - Germany

JXN - Norway

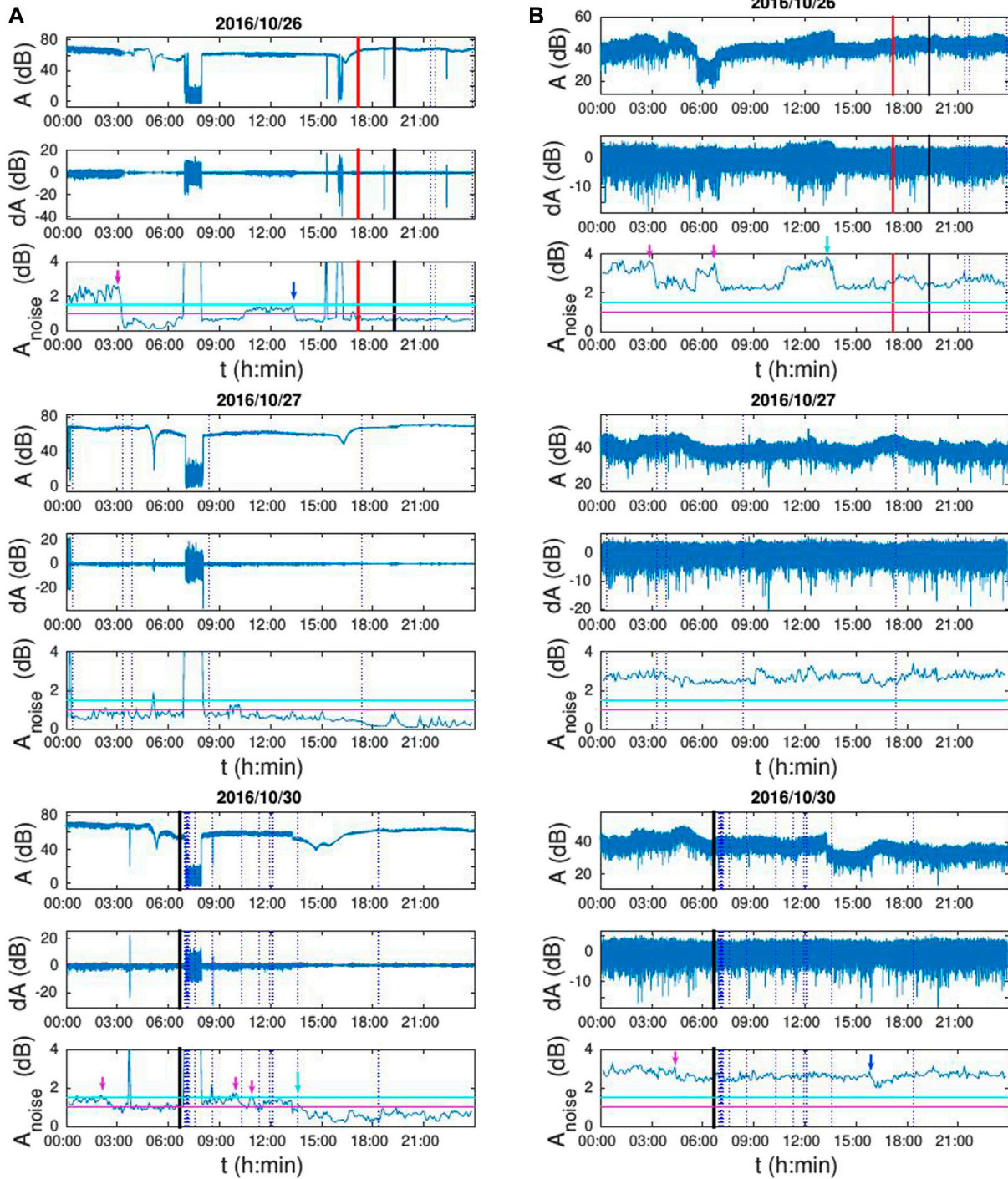
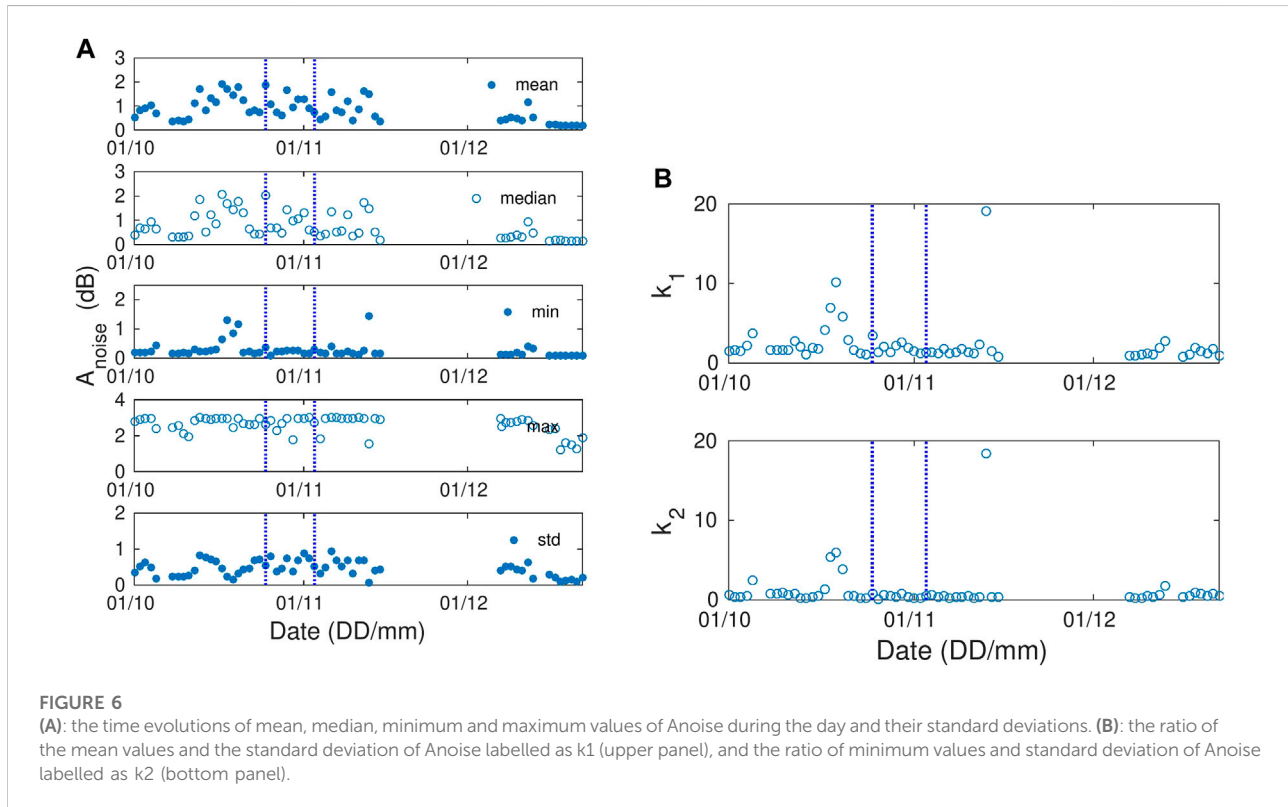


FIGURE 5

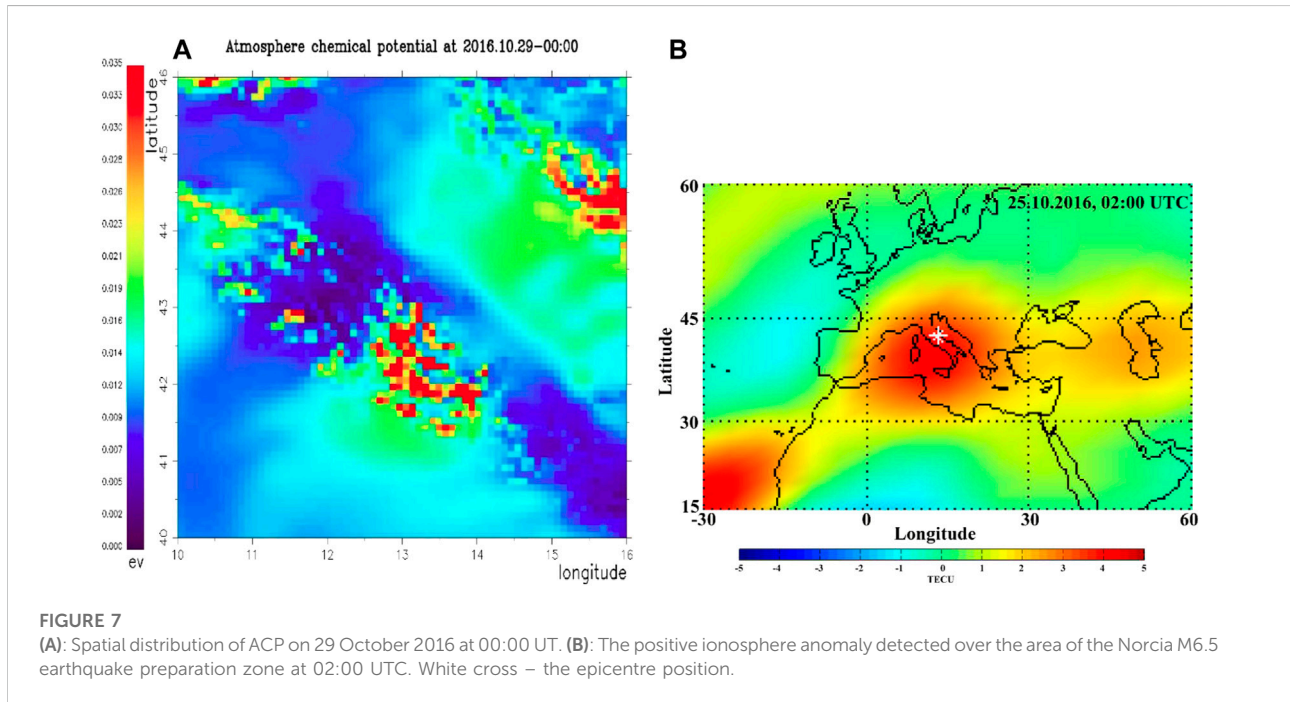
The time evolutions of the recorded amplitude *A* (upper panels), its deviation, *dA*, from the base curve (middle panels), and the sum amplitude, *Anoise*, (lower panels) for the DHO (A) and JXN (B) signal on 26 (upper panels), 27 (middle panels) and 30 (bottom panels) October 2016. Vertical lines indicate the times of earthquakes of magnitude $4 \leq M < 5$ (blue dot lines), $5 \leq M < 6$ (red line) and $6 \leq M$ (black lines). Horizontal magenta and cyan lines indicate the amplitude of 1 and 1.5 dB, respectively. The beginnings of the amplitude noise reductions of Type I, II and III are indicated by the magenta, blue and cyan arrows, respectively.



the following analysis we examine localization of the perturbations by processing two additional signal amplitudes in the case of the three strongest EQs, and during 27 October when no earthquake of magnitude greater than 5 was recorded. We consider the DHO and JYN signals that spread in the areas from their transmitters located in Germany and Norway, respectively, to the receiver in Belgrade. As one can see in Figure 1A the ICV signal propagation path is closest to the CI-1 area and it is located south of the seismic active zone. The paths of the other signals pass through areas north of the epicentres of the observed earthquakes.

The time evolutions of these signals for the mentioned 3 days are shown in Figure 5. In the case of the first day, the two noise amplitude reductions (for the ICV signal) associated in the previous Section with the EQs of magnitudes of 5.5 and 6.1 are visible in both reference signals. The A_{noise} reductions are almost twice smaller for the farthest signal from the CI-1 area (JXN) than for the ICV signal, while in the case of the DHO signal, the increase in A_{noise} between these reductions is significantly smaller than for the ICV signal, which decreases the intensity of the second reduction. In the case of the EQ of the 6.5 magnitude that occurred on 3 November, the A_{noise} reductions are similar for all signals, except that the least pronounced is the JYN signal, which, in addition to being the furthest from the seismically active area, also has the largest A_{noise} during quiet conditions.

Based on this analysis, we can conclude that the A_{noise} reduction is visible in all three signals in the case of the strongest observed earthquakes. This indicates the possibility that the perturbed area has larger dimensions or that it is drifted closer to the receiver (in this way, more observed signals pass through a smaller area). Here it is important to point out that the existence of differences in the changes of A_{noise} , as well as the impossibility of establishing connections between their values, and the values of the signal amplitudes (e.g., the time evolutions of A_{noise} are similar for the ICV and DHO although the amplitude of the DHO signal is significantly higher than the other two) or A_{noise} (e.g., the difference in A_{noise} between the two reductions visible on 26 October between the DHO signal, and the ICV signal although their previous A_{noise} are very similar) are important for this study. Namely, they indicate that, although they are recorded for several signals, these changes are probably not the result of an unstable reception, but rather reflect variations of atmospheric parameters that can be spatially variable. This conclusion is supported by the difference in the time evolutions of the A_{noise} of the JXN signal from those of the other signals (first of all, the absence of the A_{noise} reduction at the end of October 27 in the case of the JXN signal, although they are similar for the remaining two signals), as well as the fact that the observed reductions occurred at different parts of the day when the same influence of man-made factors is not expected.



3.2 Daily characteristics of the noise amplitude

To examine the long-term variations of the signal amplitude, we analyse the time evolutions of noise amplitude characteristics on a daily basis for the time period from 1 October to 22 December (data for some days are missing due to absence of detection of the ICV signal by the AbsPAL receiver in Belgrade). Figure 6A shows the mean, median, minimum, and maximum noise amplitude values during day, as well as the corresponding standard deviation. The displayed values are obtained after eliminating the data during the period when either the signal was not detected by the AbsPAL receiver in Belgrade, or the noise amplitude is unusually high (indicating periods of solar terminators or the presence of some sudden disturbance). For the shown values, the criterion for this elimination is $A_{\text{noise}} = 3$ dB (this value is by 1 dB higher than A_{noise} in quiet conditions, which makes it possible to eliminate the consideration of perturbations that are a consequence of the mentioned causes which are not related to seismic processes). The essential influence of the choice of this value on the obtained conclusions is excluded by an additional check of the limiting values of 2.5 and 3.5 dB.

The obtained time evolutions of the observed parameters show the following:

- The mean and median values of A_{noise} start to increase on October 12 (13 days before PISA). The end point of this

period cannot be exactly determined due to lack of data, but it is evident that from 7 December these values are reduced to those at the beginning of the shown period. In addition to the increases of the considered parameters, the dispersions of the displayed points are also increased in this period. Variations of the standard deviation of the A_{noise} values before PISA are more clearly defined, and its saturation is visible in the last considered week (later than the dependence of daily mean and median values of A_{noise}).

- The minimum values of A_{noise} are very similar during the entire observed time interval with clearly observed peaks at 5–8 days before and 10 days after PISA, respectively.
- The maximum values of A_{noise} are reduced at the beginning and end of the observed time interval as well as during 3 isolated days (1 during PISA and 2 after it).
- The times of the expressed peaks of the mean, median and minima of A_{noise} values before and after PISA correspond to the expressed minima of the standard deviation. This can be clearly seen in the form of pronounced maxima in the right panels in Figure 6 that show the time evolutions of the ratio of the mean values and the standard deviation of A_{noise} , indicated as k_1 (upper panel), and the ratio of minimum values and standard deviation of A_{noise} indicated as k_2 (lower panel).

The above conclusions point to changes in the daily characteristics of A_{noise} that begin about 2 weeks before PISA and end no later than about a month after PISA.

3.3 Comparisons with other studies

The presented analysis of the noise amplitude in a localized area during PISA is a pioneer study and the confirmation of the obtained conclusions requires additional case studies or statistical research which should be carried out in future. However, a comparison of the study of the VLF signal characteristics related to separated relatively strong EQs given in [Nina et al. \(2020\)](#) and [Nina et al. \(2021a\)](#) indicates similarities with conclusions obtained in this study for the corresponding periods. The potential horizontal displacements and enlargements of the area related to the seismic zone indicated in this study are also shown in the studies of the atmospheric chemical potential (ACP) and TEC. Although they refer to atmospheric areas near the surface and, primarily, in the upper ionosphere, respectively, their comparisons with variations in VLF signals propagating between Earth surface and the lower ionosphere are relevant because the seismo-ionospheric anomalies are not limited by some fixed altitude of the ionosphere but are continued to the upper altitudes into the magnetosphere forming the field-aligned irregularities of electron concentration ([Pulinets et al., 2002](#)). The physical nature of ACP, and the physical interfaces of the lithosphere-ionosphere coupling (generation of ACP) and atmosphere-ionosphere coupling (generation of TEC anomalies) are described in, for example, [Pulinets et al. \(2015a\)](#) and [Pulinets et al. \(2018b\)](#). The common agent of the link between the ACP and TEC are the complex ions formed in the process of the Ion Induced Nucleation (INN). The sharp (hyperbolic) growth of large complex ions concentration and their hydration leads to the growth of ACP. Simultaneously the same complex ions sharply decrease the conductivity of the atmospheric column between the ground and ionosphere increasing the ionospheric potential (IP) and forming the positive anomalies of TEC. The physical mechanism of the seismo-ionospheric coupling and statistical proofs of connection of an earthquake with TEC variations is described in [Pulinets and Boyarchuk \(2004\)](#); [Pulinets et al. \(2015b\)](#); [Pulinets et al. \(2018\)](#); [Liu et al. \(2018\)](#). In addition, the observed diurnal changes exhibit some characteristics similar to those identified in many studies describing different types of ionospheric disturbances. In the following text, we point out these similarities and agreements.

3.3.1 The noise amplitude reductions

As stated in [Section 3.1.1](#), the A_{noise} reductions connected with the EQs that occurred during the period when the noise amplitude corresponds to that in quiet conditions have characteristics very similar to those shown in [Nina et al. \(2021b\)](#) for all EQs of magnitudes $M \geq 4$ as well as for 9 EQs of magnitudes $M \leq 4$.

Contrary to the results presented in [Nina et al. \(2021b\)](#) where the noise amplitude reductions are visible only for the ICV signal, the analysis performed in this study shows corresponding changes for several VLF signals. As stated in [Section 3.1.2](#),

this may be due to a larger area influenced by seismic activity or its drifting towards the location of the receiver. Both mentioned phenomena have already been presented in the literature ([Biagi et al., 2012](#)). The study presented in [Sanchez-Dulcet et al. \(2015\)](#) indicates a combination of both possibilities as well as the temporal variability of the spatial distribution of atmospheric disturbances. The larger perturbed area through which the considered VLF signals propagate is also consistent with the spatial distribution of ACP around the time of the Norcia M6.5 earthquake that occurred on 30 October 2016 (see [Figure 7A](#)). This parameter is the so-called integrated parameter actually been the proxy of the radon activity and its measurement at the 100 m altitude can be used for estimation of the disturbed area ([Pulinets et al., 2015](#)). The considered anomaly activity shown in this map covers (and exceeds) the whole region of Italian seismic activity during 2009–2017 presented in [Soldati et al. \(2020\)](#) ([Soldati et al., 2020](#)). Finally, the spatial distribution of TEC, presented in [Figure 7B](#), shows a large disturbed area which includes the region around the receiver location.

3.3.2 Daily characteristics of the noise amplitude

As stated in Introduction, studies in the literature primarily point to ionospheric variations that start a few days or several hours before major earthquakes. These variations apply to both the low and high ionosphere. Variations detected by VLF/LF signals occur in the form of the amplitude minimum time shift during solar terminator periods (the so-called “terminator time”) ([Hayakawa, 1996](#); [Molchanov et al., 1998](#); [Yamauchi et al., 2007](#); [Yoshida et al., 2008](#); [Maurya et al., 2016](#)), signal amplitude variations ([Biagi et al., 2001a,b](#); [Zhao et al., 2020](#)), and periodic fluctuations ([Miyaki et al., 2001](#); [Molchanov et al., 2001](#); [Rozhnoi et al., 2004](#); [Biagi et al., 2006](#); [Hayakawa et al., 2010](#); [Ohya et al., 2018](#)). These variations can be detected using different methods such as analyses of the standard deviation, the Wavelet spectra, the terminator time, deviations from mean values, and the Principal Component Analysis ([Hayakawa, 1996](#); [Biagi et al., 2012](#)). Analyses of the GNSS signals indicate variation in TEC a few days before the considered EQ events. Examples of these changes can be seen in, for example, [Pulinets and Davidenko \(2018a\)](#) and [Abdennasser and Abdelmansour \(2019\)](#). In addition, it is found that the pre-seismic anomalies related to the acoustic-gravity waves, energetic particle burst in radiation belt, magnetic field, electron density, electron temperature and surface latent heat flux are recorded several days before EQs (see, for example, [Sasmal et al. \(2021\)](#); [Chowdhury et al. \(2022\)](#); [Ghosh et al. \(2022\)](#)).

The results obtained in this study are in agreement with those reported in the literature. Namely, as stated in [Section 3.1.2](#), the beginnings of changes in the time evolution of the analysed parameters that describe the noise amplitude are visible about 2 weeks (increases in mean and median values of A_{noise} and dispersion of relevant points in plots of the corresponding time evolutions), a week (peaks of minimum values of A_{noise} and values

of parameters k_1 and k_2), and on the day of the beginning of PISA (increasing the dispersion of the standard deviation A_{noise}).

Based on the comparison mentioned in Sections 3.3.1, 3.3.2, we can conclude that the presented analysis shows a confirmation of the previously presented variations of VLF signals, which are stated as possible precursors of earthquakes.

4 Conclusion

In this paper, we presented an analysis of VLF signal noise amplitude variations during the period of intense seismic activity in Central Italy from 25 October to 3 November 2016. It is a continuation of the study of possible connection between the noise amplitude reduction and earthquakes that can be analysed independently of other relevant connections due to a sufficiently large time interval between earthquake events and, in some cases, large spatial distances between their epicentres. In this study we analysed additional particular earthquake events and extended the global research to examination of a possible influence of the intense seismic activity to the observed signal characteristic changes. That was possible because we observed a time period when almost 1000 earthquakes (31 of them had a magnitude of 4 or greater, and the maximum magnitudes were 5.5, 6.1 and 6.5) were registered in a small area in Central Italy within only 10 days.

In this study we processed the amplitudes of the ICV, DHO and JXN signals emitted in Italy, Germany, the USA and Norway, respectively, and recorded in Belgrade, Serbia. The main analysis is performed for the ICV signal amplitude, while examination of other signal amplitude characteristics was done in order to analyse the localization of changes and possible variations in the noise amplitude due to problems in signal reception.

We presented analyses of: (1) the noise amplitude reduction which were first pointed out as potential precursors of earthquakes in the case of the Kraljevo earthquake that occurred in Serbia on 3 November 2010; (2) the daily characteristics of the VLF signal noise amplitude in the period from 1 October to 22 December, performed for the first time in this study.

Based on the results of the presented research, we can conclude the following facts:

- A significant reduction in the noise amplitude that can be associated with one or more earthquakes affects the possibility of detecting isolated significant reductions that can be associated with a particular earthquake.
- The noise amplitude reduction is recorded for all three earthquakes of magnitudes greater than 5, which is in agreement with the results shown for the earthquakes near Kraljevo, and the Tyrrhenian and Western Mediterranean Sea (presented in the first study that examines the considered correlations). It is important to emphasize that two of these three earthquakes occurred within about 2 h and can be related to the same reduction of the noise amplitude.
- Earthquakes of magnitudes between 4 and 5 that do not follow more intense earthquakes can also be connected with clear specific reductions in the noise amplitude, unlike those after more intense earthquakes for which additional reductions of already low noise amplitudes are small or completely absent.
- There are three types of the noise amplitude reduction depending on whether the noise amplitude reduction is a consequence of the increasing lower and/or decreasing higher amplitude values. Based on the analyses shown in this study and in Nina et al. (2020), correlations between these reductions and earthquakes can be established in cases of the increasing lower and decreasing higher amplitude values (Type I), or when the increase of the lower amplitude values is recorded (Type II). In the cases of decreasing higher amplitude values (Type III), an appropriate correlation with the occurrence of earthquakes was not established.

These conclusions indicate the importance of the noise amplitude value in quiet conditions for the detection of its reduction which can be potentially connected with an earthquake. In other words, the application of low noise amplitude signals for the detection of potential precursors of these natural disasters is questioned. In addition, this study opens more questions that require statistical studies. They relate to the possibility of more the noise amplitude reduction before a strong earthquake or more (relatively) strong earthquakes, increase the unperturbed area through which the VLF signals propagate during the long-term intensification of seismic activity (i.e. a large number of earthquakes in a relatively short period), displacement of the area under influence of the seismic activity relative to the seismically active area, and existence of changes in daily noise amplitude characteristics several days before the intensification of seismic activity (an increase in the noise amplitude mean and median values, clearly defined oscillations of its standard deviation followed by an increase in the dispersion of points in the graph of its time evolution at the beginning of the period of the earthquake series, the short-term (1 day to a few days) peaks of the ratio of the mean/minimum noise amplitude values and its standard deviation before and after the period of intense seismic activity, and the increase of its minimum values). Analyses of these issues should be the focus of future studies. In addition, due to the complexity of the analyzed connection caused by the possibility of the influence of a large number of parameters describing the earthquake, the VLF signal and the environment in which it spreads, it is necessary to carry out a larger number of studies in order to (if possible) define the criteria (in different conditions) for establishing a connection between the noise amplitude reductions and earthquake occurrences.

Here, we point out that analyses of the VLF signal characteristics are not sufficient to obtain the necessary information about localization (vertical and horizontal) of perturbed area. For this reason, it is necessary to do more

studies based on different kinds of observation data so that theoretical analyses and models can be provided. This issue will be subject of future investigation, too.

At the end, we emphasize that the results of this, the second, study of examining the possibility that the noise amplitude reduction of VLF signals is a precursor of earthquakes contribute to the statistic that indicates that such a conclusion is quite realistic. Namely, as in the case of the first relevant study where the observed type of connection was recorded for all recorded earthquakes with magnitude greater than 4 and with epicentres close to the observed signal path (4 events), this analysis also shows that such a connection is detectable in all cases when there is no influence of other events (all 6 events including two events close in time which are connected with the same reduction). This confirmation gives even more importance to the continuation of the relevant research.

Data availability statement

Requests for the VLF data used for analysis can be directed to the corresponding author. The other datasets used for this study can be found in <http://www.emsc-csem.org/Earthquake/>, <https://eswd.eu/cgi-bin/eswd.cgi>, https://www-app3.gfz-potsdam.de/kp_index/Kp_ap_Ap_SN_F107_since_1932.txt, https://hesperia.gsfc.nasa.gov/goes/goes_event_listings/.

Author contributions

Conceptualization, methodology, investigation, resources, formal analysis, writing—original draft, preparation, visualization, AN; Software, data curation, AN, SM, VČ, and MU; Validation, PB, SP, LP, GN, and MR; Writing—review and editing, all authors. All authors have read and agreed to the published version of the manuscript.

Funding

The authors acknowledge funding provided by the Institute of Physics Belgrade, the Astronomical Observatory (the contract

References

- Abdennasser, T., and Abdelmansour, N. (2019). Geodetic contribution to predict the seismological activity of the Italian metropolis by the ionospheric variant of GPS_TEC. *J. Atmos. Solar-Terrestrial Phys.* 183, 1–10. doi:10.1016/j.jastp.2018.12.006
- Ammar, A., and Ghalila, H. (2016). Ranking of sudden ionospheric disturbances by means of the duration of VLF perturbed signal in agreement with satellite X-ray flux classification. *Acta Geophys.* 64, 2794–2809. doi:10.1515/acgeo-2016-0114
- Basak, T., and Chakrabarti, S. K. (2013). Effective recombination coefficient and solar zenith angle effects on low-latitude D-region ionosphere evaluated from vlf

signal amplitude and its time delay during X-ray solar flares. *Astrophys. Space Sci.* 348, 315–326. doi:10.1007/s10509-013-1597-9

Biagi, P., Castellana, L., Maggipinto, T., Piccolo, R., Minafra, A., Ermini, A., et al. (2006). Lf radio anomalies revealed in Italy by the wavelet analysis: Possible preseismic effects during 1997–1998. *Phys. Chem. Earth, Parts A/B/C* 31, 403–408. doi:10.1016/j.pce.2005.10.001

Biagi, P. F., Maggipinto, T., Righetti, F., Loiacono, D., Schiavulli, L., Ligonzo, T., et al. (2011). The European VLF/LF radio network to search for earthquake precursors: Setting up and natural/man-made disturbances. *Nat. Hazards Earth Syst. Sci.* 11, 333–341. doi:10.5194/nhess-11-333-2011

Acknowledgments

The Kilpisjarvi VLF data were supplied by the Sodankyla Geophysical Observatory, University of Oulu, Finland. For checking of the meteorological conditions we used information given on the European Severe Weather Database website. For checking of the geomagnetic conditions we used information provided by the Geomagnetic Observatory Niemegk, GFZ German Research Centre for Geosciences.

Conflict of interest

Author SM was employed by the company Novelic.

The remaining authors declare that the research was conducted in the absence of any commercial or financial relationships that could be construed as a potential conflict of interest.

Publisher's note

All claims expressed in this article are solely those of the authors and do not necessarily represent those of their affiliated organizations, or those of the publisher, the editors and the reviewers. Any product that may be evaluated in this article, or claim that may be made by its manufacturer, is not guaranteed or endorsed by the publisher.

Supplementary material

The Supplementary Material for this article can be found online at: <https://www.frontiersin.org/articles/10.3389/fenvs.2022.1005575/full#supplementary-material>

- Biagi, P. F., Piccolo, R., Ermini, A., Martellucci, S., Bellecci, C., Hayakawa, M., et al. (2001a). Disturbances in LF radio-signals as seismic precursors. *Ann. Geophys.* 44, 4. doi:10.4401/ag-3552
- Biagi, P. F., Piccolo, R., Ermini, A., Martellucci, S., Bellecci, C., Hayakawa, M., et al. (2001b). Possible earthquake precursors revealed by LF radio signals. *Nat. Hazards Earth Syst. Sci.* 1, 99–104. doi:10.5194/nhess-1-99-2001
- Biagi, P., Righetti, F., Maggipinto, T., Schiavulli, L., Ligonzo, T., Ermini, A., et al. (2012). Anomalies observed in VLF and LF radio signals on the occasion of the Western Turkey earthquake (Mw= 5.7). *Int. J. Geosciences* 19, 2011. doi:10.4236/ijg.2012.324086
- Calais, E., and Minster, J. (1998). GPS, earthquakes, the ionosphere, and the space shuttle. *Phys. Earth Planet. Interiors* 105, 167–181. doi:10.1016/S0031-9201(97)00089-7
- Chakrabarti, S. K., Sasmal, S., and Chakrabarti, S. (2010). Ionospheric anomaly due to seismic activities – part 2: Evidence from D-layer preparation and disappearance times. *Nat. Hazards Earth Syst. Sci.* 10, 1751–1757. doi:10.5194/nhess-10-1751-2010
- Chakraborty, S., and Basak, T. (2020). Numerical analysis of electron density and response time delay during solar flares in mid-latitude ionosphere. *Astrophys. Space Sci.* 365, 184–189. doi:10.1007/s10509-020-03903-5
- Cheloni, D., De Novellis, V., Albano, M., Antonioli, A., Anzidei, M., Atzori, S., et al. (2017). Geodetic model of the 2016 central Italy earthquake sequence inferred from InSAR and GPS data. *Geophys. Res. Lett.* 44, 6778–6787. doi:10.1002/2017GL073580
- Chowdhury, S., Kundu, S., Ghosh, S., Hayakawa, M., Schekotov, A., Potirakis, S. M., et al. (2022). Direct and indirect evidence of pre-seismic electromagnetic emissions associated with two large earthquakes in Japan. *Nat. Hazards (Dordr.)* 112, 2403–2432. doi:10.1007/s11069-022-05271-5
- Davies, K., and Baker, D. M. (1965). Ionospheric effects observed around the time of the Alaskan earthquake of March 28, 1964. *J. Geophys. Res.* 70, 2251–2253. doi:10.1029/JZ070i009p02251
- Fu, C.-C., Wang, P.-K., Lee, L.-C., Lin, C.-H., Chang, W.-Y., Giuliani, G., et al. (2015). Temporal variation of gamma rays as a possible precursor of earthquake in the longitudinal valley of eastern Taiwan. *J. Asian Earth Sci.* 114, 362–372. doi:10.1016/j.jseae.2015.04.035
- Galli, P., Castenetto, S., and Peronace, E. (2017). The macroseismic intensity distribution of the 30 October 2016 earthquake in central Italy (M_w 6.6): Seismotectonic implications. *Tectonics* 36, 2179–2191. doi:10.1002/2017TC004583
- Ghosh, S., Chowdhury, S., Kundu, S., Sasmal, S., Politis, D. Z., Potirakis, S. M., et al. (2022). Unusual surface latent heat flux variations and their critical dynamics revealed before strong earthquakes. *Entropy* 24 (1), 23. doi:10.3390/e24010023
- Grubor, D. P., Šulić, D. M., and Žigman, V. (2008). Classification of X-ray solar flares regarding their effects on the lower ionosphere electron density profile. *Ann. Geophys.* 26, 1731–1740. doi:10.5194/angeo-26-1731-2008
- Hayakawa, M., Horie, T., Muto, F., Kasahara, Y., Ohta, K., Liu, J.-Y., et al. (2010). Subionospheric VLF/LF probing of ionospheric perturbations associated with earthquakes: A possibility of earthquake prediction. *SICE J. Control, Meas. Syst. Integration* 3, 10–14. doi:10.9746/jcmsi.3.10
- Hayakawa, M. (1996). The precursory signature effect of the kobe earthquake on VLF subionospheric signals. *J. Comm. Res. Lab.* 43, 169–180. doi:10.1109/ELMAGC.1997.617080
- He, L., Wu, L., Heki, K., and Guo, C. (2022). The conjugated ionospheric anomalies preceding the 2011 Tohoku-Oki earthquake. *Front. Earth Sci. (Lausanne)*. 10, 23. doi:10.3389/feart.2022.850078
- Hegai, V., Kim, V., and Liu, J. (2006). The ionospheric effect of atmospheric gravity waves excited prior to strong earthquake. *Adv. Space Res.* 37, 653–659. doi:10.1016/j.asr.2004.12.049
- Inan, U. S., Lehtinen, N. G., Moore, R. C., Hurley, K., Boggs, S., Smith, D. M., et al. (2007). Massive disturbance of the daytime lower ionosphere by the giant γ -ray flare from magnetar SGR 1806-20. *Geophys. Res. Lett.* 34, L08103. doi:10.1029/2006GL029145
- Kolarski, A., Grubor, D., and Šulić, D. (2011). Diagnostics of the solar X-flare impact on lower ionosphere through seasons based on VLF-NAA signal recordings. *Balt. Astron.* 20, 591–595.
- Korepanov, V., Hayakawa, M., Yampolski, Y., and Lizunov, G. (2009). AGW as a seismo-ionospheric coupling responsible agent. *Phys. Chem. Earth, Parts A/B/C* 34, 485–495. doi:10.1016/j.pce.2008.07.014
- Leonard, R. S., Barnes, J., and Barnes, R. A. (1965). Observation of ionospheric disturbances following the Alaska earthquake. *J. Geophys. Res.* 70, 1250–1253. doi:10.1029/JZ070i005p01250
- Liperovsky, V. A., Pokhotelov, O. A., Meister, C. V., and Liperovskaya, E. V. (2008). Physical models of coupling in the lithosphere-atmosphere-ionosphere system before earthquakes. *Geomagn. Aeron.* 48, 795–806. doi:10.1134/S0016793208060133
- Liu, J.-Y., Hattori, K., and Chen, Y.-I. (2018). Application of total electron content derived from the global navigation satellite system for detecting earthquake precursors. *Am. Geophys. Union (AGU)* 17, 305. doi:10.1002/9781119156949.ch17
- Maekawa, S., Horie, T., Yamauchi, T., Sawaya, T., Ishikawa, M., Hayakawa, M., et al. (2006). A statistical study on the effect of earthquakes on the ionosphere, based on the subionospheric LF propagation data in Japan. *Ann. Geophys.* 24, 2219–2225. doi:10.5194/angeo-24-2219-2006
- Matzka, J., Stolle, C., Yamazaki, Y., Bronkalla, O., and Morschhauser, A. (2021). The geomagnetic kp index and derived indices of geomagnetic activity. *Space weather*. 19, e2020SW002641. doi:10.1029/2020SW002641
- Maurya, A. K., Venkatesham, K., Tiwari, P., Vijaykumar, K., Singh, R., Singh, A. K., et al. (2016). The 25 April 2015 Nepal earthquake: Investigation of precursor in vlf subionospheric signal. *J. Geophys. Res. Space Phys.* 121, 416. doi:10.1002/2016JA022721
- Mitra, A. P. (Editor) (1974). *Ionospheric effects of solar flares* (Dordrecht: Astrophysics and Space Science Library), 46.
- Miyaki, K., Hayakawa, M., and Molchanov, O. (2001). “The role of gravity waves in the lithosphere - ionosphere coupling, as revealed from the subionospheric LF propagation data,” in *Seismo electromagnetics: Lithosphere - atmosphere - ionosphere coupling*” (Tokyo: TERRAPUB), 229–232.
- Molchanov, O., Hayakawa, M., and Miyaki, K. (2001). VLF/LF sounding of the lower ionosphere to study the role of atmospheric oscillations in the lithosphere-ionosphere coupling. *Adv. Polar Up. Atmos. Res.* 15, 146–158.
- Molchanov, O., Hayakawa, M., Oudoh, T., and Kawai, E. (1998). Precursory effects in the subionospheric vlf signals for the kobe earthquake. *Phys. Earth Planet. Interiors* 105, 239–248. doi:10.1016/S0031-9201(97)00095-2
- Molina, C., Boudriki Semlali, B.-E., Park, H., and Camps, A. (2022). A preliminary study on ionospheric scintillation anomalies detected using gnss-r data from NASA CYGNSS mission as possible earthquake precursors. *Remote Sens.* 14, 2555. doi:10.3390/rs14112555
- Némec, F., Santolík, O., and Parrot, M. (2009). Decrease of intensity of ELF/VLF waves observed in the upper ionosphere close to earthquakes: A statistical study. *J. Geophys. Res.* 114, 4. doi:10.1029/2008JA013972
- Nina, A., Biagi, P. F., Mitrović, S. T., Pulinet, S., Nico, G., Radovanović, M., et al. (2021a). Reduction of the VLF signal phase noise before earthquakes. *Atmosphere* 12, 444. doi:10.3390/atmos12040444
- Nina, A., Nico, G., Mitrović, S. T., Čadež, V. M., Milošević, I. R., Radovanović, M., et al. (2021b). Quiet ionospheric D-region (qiondr) model based on VLF/LF observations. *Remote Sens.* 13, 483. doi:10.3390/rs13030483
- Nina, A., Pulinet, S., Biagi, P., Nico, G., Mitrović, S., Radovanović, M., et al. (2020). Variation in natural short-period ionospheric noise, and acoustic and gravity waves revealed by the amplitude analysis of a VLF radio signal on the occasion of the Kraljevo earthquake (mw = 5.4). *Sci. Total Environ.* 710, 136406. doi:10.1016/j.scitotenv.2019.136406
- Nina, A., Simić, S., Srećković, V. A., and Popović, L. Č. (2015). Detection of short-term response of the low ionosphere on gamma ray bursts. *Geophys. Res. Lett.* 42, 8250–8261. doi:10.1002/2015GL065726
- Ohya, H., Tsuchiya, F., Takishita, Y., Shinagawa, H., Nozaki, K., and Shiokawa, K. (2018). Periodic oscillations in the d region ionosphere after the 2011 tohoku earthquake using LF standard radio waves. *J. Geophys. Res. Space Phys.* 123, 5261–5270. doi:10.1029/2018JA025289
- Oyama, K. I., Devi, M., Ryu, K., Chen, C. H., Liu, J. Y., Liu, H., et al. (2016). Modifications of the ionosphere prior to large earthquakes: Report from the ionosphere precursor study group. *Geosci. Lett.* 3, 6. doi:10.1186/s40562-016-0038-3
- Perrone, L., De Santis, A., Abbattista, C., Alfonsi, L., Amoroso, L., Carbone, M., et al. (2018). Ionospheric anomalies detected by ionosonde and possibly related to crustal earthquakes in Greece. *Ann. Geophys.* 36, 361–371. doi:10.5194/angeo-36-361-2018
- Pulinet, S. A., and Davidenko, D. V. (2018a). The nocturnal positive ionospheric anomaly of electron density as a short-term earthquake precursor and the possible physical mechanism of its formation. *Geomagn. Aeron.* 58, 559–570. doi:10.1134/s0016793218040126
- Pulinet, S. A., Ouzounov, D. P., Karelin, A. V., and Davidenko, D. V. (2015a). Physical bases of the generation of short-term earthquake precursors: A complex model of ionization-induced geophysical processes in the lithosphere-atmosphere-ionosphere-magnetosphere system. *Geomagn. Aeron.* 55, 521–538. doi:10.1134/S0016793215040131
- Pulinet, S. A., Ouzounov, D. P., Karelin, A. V., and Davidenko, D. V. (2015b). Physical bases of the generation of short-term earthquake precursors: A complex

model of ionization-induced geophysical processes in the lithosphere-atmosphere-ionosphere-magnetosphere system. *Geomagn. Aeron.* 55, 521–538. doi:10.1134/S0016793215040131

Pulinets, S., Boyarchuk, K., Hegai, V., and Karelin, A. (2002). *Conception and model of seismo-ionosphere-magnetosphere coupling*. Tokyo: TERRAPUB, 353–361.

Pulinets, S., and Boyarchuk, K. (2004). *Ionospheric precursor of earthquakes*. Heidelberg, Germany: Springer.

Pulinets, S., Ouzounov, D., Karelin, A., and Boyarchuk, K. (2022). *Earthquake precursors in the atmosphere and ionosphere: New concepts*. Berlin, Heidelberg, Germany: Springer.

Pulinets, S., Ouzounov, D., Karelin, A., and Davidenko, D. (2018b). *Lithosphere-atmosphere-ionosphere-magnetosphere coupling—a concept for pre-earthquake signals generation*. America: American Geophysical Union AGU. 77–98. doi:10.1002/9781119156949.ch6

Pulinets, S., and Ouzounov, D. (2011). Lithosphere-atmosphere-ionosphere coupling (LAIC) model – An unified concept for earthquake precursors validation. *J. Asian Earth Sci.* 41, 371–382. doi:10.1016/j.jseas.2010.03.005

Rozhnoi, A., Solovieva, M., Molchanov, O., and Hayakawa, M. (2004). Middle latitude lf (40 khz) phase variations associated with earthquakes for quiet and disturbed geomagnetic conditions. *Phys. Chem. Earth, Parts A/B/C* 29, 589–598. doi:10.1016/j.pce.2003.08.061

Sanchez-Dulcet, F., Rodríguez-Bouza, M., Silva, H. G., Herraiz, M., Bezzeghoud, M., and Biagi, P. F. (2015). Analysis of observations backing up the existence of VLF and ionospheric TEC anomalies before the Mw6.1 earthquake in Greece, January 26, 2014. *Phys. Chem. Earth Parts A/B/C* 85, 150–166. doi:10.1016/j.pce.2015.07.002

Sasmal, S., and Chakrabarti, S. K. (2009). Ionospheric anomaly due to seismic activities; part 1: Calibration of the VLF signal of VTX 18.2 kHz station from Kolkata and deviation during seismic events. *Nat. Hazards Earth Syst. Sci.* 9, 1403–1408. doi:10.5194/nhess-9-1403-2009

Sasmal, S., Chowdhury, S., Kundu, S., Politis, D. Z., Potirakis, S. M., Balasis, G., et al. (2021). Pre-seismic irregularities during the 2020 Samos (Greece) earthquake (M = 6.9) as investigated from multi-parameter approach by ground and space-based techniques. *Atmosphere* 12 (8), 1059. doi:10.3390/atmos12081059

Schmitter, E. D. (2013). Modeling solar flare induced lower ionosphere changes using VLF/LF transmitter amplitude and phase observations at a midlatitude site. *Ann. Geophys.* 31, 765–773. doi:10.5194/angeo-31-765-2013

Soldati, G., Cannelli, V., and Piersanti, A. (2020). Monitoring soil radon during the 2016–2017 central Italy sequence in light of seismicity. *Sci. Rep.* 10, 13137. doi:10.1038/s41598-020-69821-2

Sorokin, V., and Yashchenko, A. (1999). Disturbances of conductivity and electric field in the earth-ionosphere layer over an earthquake preparation focus. *Geomagnetism Aeronomy* 39, 228–234. doi:10.1023/A:1021549612290

Thomson, N. R., Rodger, C. J., and Clilverd, M. A. (2005). Large solar flares and their ionospheric D region enhancements. *J. Geophys. Res.* 110, A06306. doi:10.1029/2005JA011008

Wang, J., Huang, Q., Ma, Q., Chang, S., He, J., Wang, H., et al. (2020). Classification of VLF/LF lightning signals using sensors and deep learning methods. *Sensors* 20, 1030. doi:10.3390/s20041030

Xiong, P., Long, C., Zhou, H., Battiston, R., De Santis, A., Ouzounov, D., et al. (2021). Pre-earthquake ionospheric perturbation identification using cses data via transfer learning. *Front. Environ. Sci.* 9, 4. doi:10.3389/fenvs.2021.779255

Yamauchi, T., Maekawa, S., Horie, T., Hayakawa, M., and Soloviev, O. (2007). Subionospheric VLF/LF monitoring of ionospheric perturbations for the 2004 mid-niigata earthquake and their structure and dynamics. *J. Atmos. Solar-Terrestrial Phys.* 69, 793–802. doi:10.1016/j.jastp.2007.02.002

Yoshida, M., Yamauchi, T., Horie, T., and Hayakawa, M. (2008). On the generation mechanism of terminator times in subionospheric VLF/LF propagation and its possible application to seismogenic effects. *Nat. Hazards Earth Syst. Sci.* 8, 129–134. doi:10.5194/nhess-8-129-2008

Yuen, P. C., Weaver, P. F., Suzuki, R. K., and Furumoto, A. S. (1969). Continuous, traveling coupling between seismic waves and the ionosphere evident in May 1968 Japan earthquake data. *J. Geophys. Res.* 74, 2256–2264. doi:10.1029/JA074i009p02256

Zhao, S., Shen, X., Liao, L., Zhima, Z., Zhou, C., Wang, Z., et al. (2020). Investigation of precursors in VLF subionospheric signals related to strong earthquakes (M > 7) in western China and possible explanations 7) in western China and possible explanations. *Remote Sens.* 12, 3563. doi:10.3390/rs12213563

Žigman, V., Grubor, D., and Šulić, D. (2007). D-region electron density evaluated from VLF amplitude time delay during X-ray solar flares. *J. Atmos. Solar-Terrestrial Phys.* 69, 775–792. doi:10.1016/j.jastp.2007.01.012



Article

Quiet Ionospheric D-Region (QIonDR) Model Based on VLF/LF Observations

Aleksandra Nina ^{1,*}, Giovanni Nico ^{2,3}, Srđan T. Mitrović ⁴, Vladimir M. Čadež ⁵, Ivana R. Milošević ¹, Milan Radovanović ^{6,7} and Luka Č. Popović ^{5,8,9}

- ¹ Institute of Physics Belgrade, University of Belgrade, 11080 Belgrade, Serbia; novovic@ipb.ac.rs
 - ² Istituto per le Applicazioni del Calcolo (IAC), Consiglio Nazionale delle Ricerche (CNR), 70126 Bari, Italy; g.nico@ba.iac.cnr.it
 - ³ Department of Cartography and Geoinformatics, Institute of Earth Sciences, Saint Petersburg State University (SPSU), 199034 Saint Petersburg, Russia; g.nico@spbu.ru
 - ⁴ Novelic, 11000 Belgrade, Serbia; mitar027@beotel.net
 - ⁵ Astronomical Observatory, 11060 Belgrade, Serbia; vcadez@aob.rs (V.M.Č.); lpopovic@aob.rs (L.Č.P.)
 - ⁶ Geographical Institute "Jovan Cvijić" SASA, 11000 Belgrade, Serbia; m.radovanovic@gi.sanu.ac.rs
 - ⁷ Institute of Sports, Tourism and Service, South Ural State University, 454080 Chelyabinsk, Russia; milan.georgaf@gmail.com
 - ⁸ Department of Astronomy, Faculty of Mathematics, University of Belgrade, 11000 Belgrade, Serbia; lpopovic@matf.bg.ac.rs
 - ⁹ Faculty of Science, University of Banja Luka, 78000 Banja Luka, Republic of Srpska, Bosnia and Herzegovina; luka.popovic@pmg.unibl.org
- * Correspondence: sandrast@ipb.ac.rs



Citation: Nina, A.; Nico, G.; Mitrović, S.T.; Čadež, V.M.; Milošević, I.R.; Radovanović, M.; Popović, L.Č. Quiet Ionospheric D-Region (QIonDR) Model Based on VLF/LF Observations. *Remote Sens.* **2021**, *13*, 483. <https://doi.org/10.3390/rs13030483>

Academic Editor: Benedikt Soja
Received: 2 December 2020
Accepted: 26 January 2021
Published: 29 January 2021

Publisher's Note: MDPI stays neutral with regard to jurisdictional claims in published maps and institutional affiliations.



Copyright: © 2021 by the authors. Licensee MDPI, Basel, Switzerland. This article is an open access article distributed under the terms and conditions of the Creative Commons Attribution (CC BY) license (<https://creativecommons.org/licenses/by/4.0/>).

Abstract: The ionospheric D-region affects propagation of electromagnetic waves including ground-based signals and satellite signals during its intensive disturbances. Consequently, the modeling of electromagnetic propagation in the D-region is important in many technological domains. One of sources of uncertainty in the modeling of the disturbed D-region is the poor knowledge of its parameters in the quiet state at the considered location and time period. We present the Quiet Ionospheric D-Region (QIonDR) model based on data collected in the ionospheric D-region remote sensing by very low/low frequency (VLF/LF) signals and the Long-Wave Propagation Capability (LWPC) numerical model. The QIonDR model provides both Wait's parameters and the electron density in the D-region area of interest at a given daytime interval. The proposed model consists of two steps. In the first step, Wait's parameters are modeled during the quiet midday periods as a function of the daily sunspot number, related to the long-term variations during solar cycle, and the seasonal parameter, providing the seasonal variations. In the second step, the output of the first step is used to model Wait's parameters during the whole daytime. The proposed model is applied to VLF data acquired in Serbia and related to the DHO and ICV signals emitted in Germany and Italy, respectively. As a result, the proposed methodology provides a numerical tool to model the daytime Wait's parameters over the middle and low latitudes and an analytical expression valid over a part of Europe for midday parameters.

Keywords: ionosphere; D-region; VLF/LF signals; remote sensing; quiet conditions; modeling

1. Introduction

The ionosphere is the upper atmospheric layer that, due to its electrical properties, affects the propagation of electromagnetic waves [1,2]. This property is of high significance in many fields that include application of data obtained by different kinds of microwave signals (like the Global Navigation Satellite System (GNSS) [3–8] and Synthetic aperture radar (SAR) interferometry meteorology [9]), and both signal and ionospheric characteristics have influence on changes in signal propagation within this medium. For example, telecommunication signals emitted from the ground are affected by the ionosphere below

the signal reflection height, while satellite signals are primarily affected by the F-region due to the largest values of electron density in the altitude domain located in this region.

Research of ionospheric properties is a very complex task because of permanent influences coming from outer space and different terrestrial layers. For this reason, it is of crucial importance to include as many observational data as possible in their modeling. For example, although the unperturbed D-region has not visible influences on satellite signal propagation, the recent results presented in Reference [10] show the importance of inclusion of its effects during intensive disturbances that are not considered in existing models (see, for example, References [11–13]).

Application of the specific technique for remote sensing of the ionosphere depends on the altitude domain. In addition, the choice of a particular analysis methodology depends on temporal and spatial characteristics of the collected data. The remote sensing of the lower ionosphere based on the propagation of very low/low frequency (VLF/LF) radio signals is an effective means to collect continuous observations the covering areas. These signals can propagate several thousand kilometres within the Earth-ionosphere waveguide, and the global observational setup is based on numerous worldwide located transmitters, and receivers. The VLF/LF receivers have the possibility of simultaneous monitoring of several signals coming from different directions with time sampling shorter than 1 s. For this reason, the databases collected by a particular receiver contain information that can be used in analyses of local and global, short and long-term variations. Because of these properties, this type of remote sensing is used in studies of how many terrestrial and extraterrestrial phenomena influence the lower ionosphere and, consequently, the propagation of electromagnetic waves which can significantly be affected by the disturbed D-region [14–21].

There are several models for modeling the VLF/LF propagation in the Earth ionosphere waveguide, such as the Long-Wave Propagation Capability (LWPC) program [22], finite-difference time-domain (FDTD) method [23], coupled beams and effective complex impedance model [24], and Modfinder [25]. These models are used in many studies for determination of ionospheric parameters where characteristics of the considered area, the ionospheric state and properties of the analyzed disturbances affect the possibility of applying certain approximations. For example, during quiet conditions or during disturbances that do not affect the horizontal uniformity of the observed D-region it is possible to assume only altitude variations of the ionospheric plasma parameters, while, in the case of local disturbances caused by for example day-night transitions along the propagation path and lightnings, it is necessary to take into account both the vertical and horizontal variations of these parameters. The horizontal uniform ionosphere is analyzed in many papers using the LWPC and Modfinder models [10,26–31]. As an example, some localized perturbations of the ionosphere are considered in Reference [32]. FDTD method was used to model the day-night transitions along the propagation path (see, for example, Reference [23]). Effects of the geomagnetic field and its variations which can induce the need to include gyrotropy and anisotropy into account are most important in analyses of the high-latitude lower ionosphere, while, in the mid-latitude areas, effects of variations in the geomagnetic field should be taken into account during large geophysical disturbances of the Lithosphere-Atmosphere-Ionosphere-Magnetosphere system caused by large magnetic storms, hurricanes, etc. [24]. In this paper, we present a model of the daytime D-region parameters under quiet conditions which is based on data recorded in ionospheric remote sensing by VLF/LF signals and LWPC program that simulates their propagation. The chosen time period, in absence of local intensive geophysical disturbances (induced by, for example, solar terminator, lightnings, and hurricanes) which are followed by significant anisotropy, allows us to assume a horizontally uniform ionosphere. In addition, we consider mid- and low-latitude domains where influence of the magnetic field variations on the considered signals (the presented model is relevant for not too long propagation paths of VLF/LF signals which are reflected at altitudes below 76 km) is not significant under quiet conditions. To calculate the quiet D-region parameters, we also include into

the consideration the analysis of disturbances induced by solar X-ray flares during the mid-day period when the indicated approximations are also justified and already used in many previous studies [10,26–31]. This is possible because solar X-ray flares do not cause local disturbances and induce practically horizontally uniform perturbations, especially within not too large areas, during the mid-day period.

Modeling of the solar X-ray flare perturbed D-region based on data obtained in its remote sensing by the VLF/LF signals assumes two approximations: (1) the lower ionosphere is usually considered as a horizontal uniform medium, and (2) the parameters in quiet conditions are considered as known quantity in which values are determined in previous statistical studies that, generally, do not represent the considered periods and areas. As we already said, the first approximation is good for a not too long propagation path of the considered signal and for daytime periods of a few hours around midday (this period depends on the season) in absence of intensive local disturbances. However, the second approximation can significantly affect the modeling, and this task was a subject of several studies which focused attention on the electron density and Wait's parameters (the "sharpness" and signal reflection height). There are several methodologies used in these studies. They are based on the broad-band detection of radio atmospheric in periods of lightning activities and detection of the narrow-band VLF signals. A technique to measure the local mid-latitude daytime D-region parameters from the Earth-ionosphere waveguide mode interference pattern in spectra of radio atmospheric launched by lightning discharges, presented in Reference [33], is limited to periods of lightning activities. In the cases based on the analysis of narrow-band VLF signals, properties of modeling and necessary approximations which affect certainty of its applications strongly depend on geographical location of the considered transmitters and receivers. Namely, if the propagation path of the considered VLF signal is very long, as, for example, in the case of studies based on data recorded by receiver located in New Zealand from which transmitters are more than 10,000 km away [34–36], it is necessary to include changes in Wait's parameters along the length of the path [34,35]. These changes provide additional possibilities for errors in modeling due to necessary approximations and changes in the ionosphere due to periodical and sudden events. Of course, increasing the propagation path length induces more effects of local disturbances which also affect the model certainty. Analyses of more receivers and transmitters can reduce these problems. A procedure for these ionospheric parameters modeling is given in Reference [37], where data for three signals recorded by six receivers are considered. In the mentioned studies, related to the considered areas, there are presented dependencies of the daytime Wait's parameters on zenith angle during the solar maximum and minimum [34,35], on both zenith angle and local time [33], and dependencies of the signal reflection height on zenith angle for different seasons [35]. Expressions which provide dependencies of Wait's parameters on more variables (zenith angle, season, smoothed sunspot number, latitude, and geomagnetic field) is presented in Reference [38]. However, the equations related to calculation of the signal reflection height cannot be applied to the newer sunspot datasets because one of these equations includes the Zürich sunspot number which refers to production of the sunspot number before 1981.

All these problems and the importance of determination of the quiet D-region parameters for many technologies motivate us to develop a model of the D-region which can be applied to shorter signal paths which significantly reduces disadvantages induced by the long distance signal propagation, and that includes the influences of:

- long-term variations (about 11 years) in solar radiations during solar cycle;
- seasonal variations (due to Earth's revolution);
- daytime periodical changes; and
- sudden mid- and short-term influences

on the D-region properties. In other words, the aim of this study is to develop a procedure that will make it possible to take advantage of densely spaced VLF/LF transmitters and receivers, like those in Europe, to accurately model the D-region parameters in the area of interest and for the considered time period.

In this paper, we present the Quiet Ionospheric D-Region (QIonDR) model which provides a procedure for the determination of the D-region plasma parameters in quiet conditions using the VLF/LF observational data for the considered area in mid- and low-latitude domains, and the considered time period. The QIonDR model provides an analysis of the Wait's parameters "sharpness" and signal reflection height. Determination of these parameters is important because knowing them allows computation of the D-region electron density N and, consequently, many other parameters, using different models [28,31,33,34,39,40]. As a result, in this study we also show the modeled electron density. To visualize the QIonDR model output, we apply it to data for the DHO and ICV signals emitted in Germany and Italy, respectively, and recorded in Serbia.

The article is organized as follows. The proposed methodology is presented in Section 2, while the analyses of observations and events are given in Section 3. Application of the QIonDR model on the DHO and ICV signals recorded in Belgrade is shown in Section 4, and conclusions of this study are given in Section 5.

2. Methodology

In this section, we describe a methodology for modeling Wait's parameters β_0 and H'_0 and the electron density N_{e0} in the quiet ionospheric D-region. This methodology is based on data obtained by the VLF/LF remote sensing of this atmospheric layer, using two VLF/LF signals, and the satellite X-ray flux data needed to determine the periods of ionospheric disturbances induced by solar X-ray flares.

To model propagation of the VLF/LF signal, we use the LWPC program. It models characteristics of the chosen signal considering its propagation in the Earth-ionosphere waveguide. Properties of the bottom boundary are based on the Westinghouse Geophysics Laboratory conductivity map [41], while the upper boundary is characterized by a conductivity that may be specified by the user. In this paper, we used Wait's model of the ionosphere [42] which describes the horizontally homogeneous exponential conductivity profile by conductivity parameter ω_r :

$$\omega_r(h) = \omega_0^2(h)/\nu(h), \quad (1)$$

where $\omega_0(h)$ and $\nu(h)$ are the electron plasma frequency and effective electron-neutral collision frequency, respectively. The first parameter can be obtained from the electron density N_e ($\omega_0^2(h) \approx 3180N_e$), while dependency of the collision frequency ν on the altitude h is given by an approximative equation based on experimental data presented in References [43,44]:

$$\nu(h) = 1.82 \times 10^{11} e^{-0.15h}, \quad (2)$$

Finally, according to the obtained vertical profiles of ω_r shown in Reference [42], an approximative equation for this parameter is given in the following form:

$$\omega_r(h) = 2.5 \times 10^5 e^{\beta(h-H')}, \quad (3)$$

where the parameters β and H' are known as Wait's parameters and called "sharpness" and signal reflection height, respectively. These parameters are input parameters in the LWPC program. ω_r is used for calculation of the reflection coefficient (the phase of the reflection coefficient is referred to the level where $\omega_r = 2.5 \times 10^5 \text{ s}^{-1}$) which is also dependent on the magnetic field. In Reference [42], it is assumed that the geomagnetic field is purely transverse. This approximation is possible because, for arbitrary directions of propagations, it has been indicated that transverse component of the geomagnetic field is most important for reflection of VLF radio waves at highly oblique incidence. Finally, the reflection coefficient is used in a mode theory calculations, which are described in Reference [42]. The output of LWPC program are the modeled amplitude and phase for input parameters and observed signal. Detailed descriptions of the LWPC and Wait's

models are given in References [22,42], while their application in the QIonDR model is described in detail in this Section.

Figure 1 shows the work-logic of the proposed methodology. It is split in the following two procedures related to the time period of the analysis of ionospheric parameters: (1) the Midday procedure (MDP), and (2) the Daytime procedure (DTP), detailed in Sections 2.1 and 2.2, respectively.

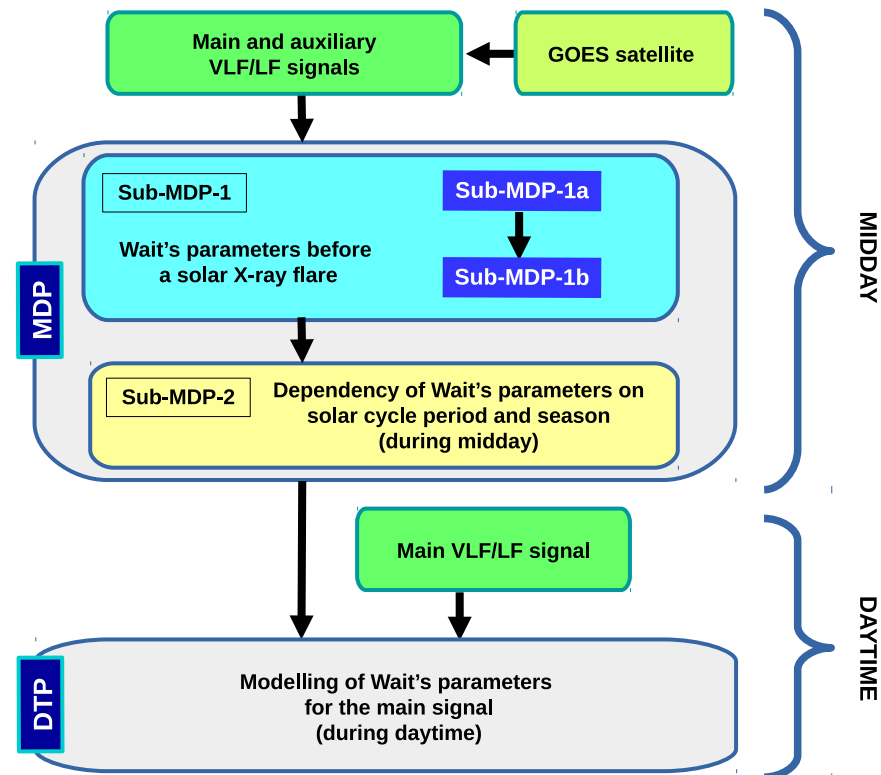


Figure 1. Diagram of the proposed methodology. It consists of two procedures, Midday procedure (MDP) and Daytime procedure (DTP), which are used for the midday and daytime periods. The VLF/LF signals and GOES data are given in input to MDP, which is split in two sub-procedures Sub-MDP-1, to estimate Wait's parameters before a solar X-ray flare, and Sub-MDP-2 to model the dependency of these parameters on the solar cycle period and season at midday. To a finer detail, Sub-MDP-1 is further split in Sub-MDP-1a and Sub-MDP-1b, corresponding to the analyses of a signal s and a disturbed state i of an X-ray flare XF, and determination of Wait's parameters in quiet conditions before a solar X-ray flare XF, respectively. DTP requires as input both the output of MDP and VLF/LF signals to model the daytime evolution of Wait's parameters.

2.1. Midday Periods

First, we analyze the changes in the midday ionospheric parameters induced by solar X-ray flares detected by the GOES satellite which occurred in midday periods. We process the recorded amplitudes and phases of both main and auxiliary VLF/LF signals in order to determine changes of these values at two different times during the solar X-ray flare influence with respect to their values before the disturbance (see Section 2.1.1). These changes are further used as input parameters in MDP (Section 2.1.2) which consists of two sub-procedures, first to determine Wait's parameters before a solar X-ray flare, and second to estimate the dependency of these parameters on the solar cycle period and season at the midday. The first sub-procedure is further split in Sub-MDP-1a and Sub-MDP-1b, corresponding to the analyses of a signal s and a disturbed state i of an X-ray flare XF (XF in general is notation for particular flare; as an example see Table 1), and the determination of Wait's parameters in the quiet conditions before a solar X-ray flare XF, respectively. The output of Sub-MDP-1 consists of Wait's parameters for all considered X-ray flares.

Their values are further fitted in Sub-MDP-2 which provides two functions describing the dependencies of Wait's parameters on the solar sunspot number and season. These two analytical expressions are the output of MDP, and they are used to model the daytime evolution of Wait's parameters in DTP using the amplitude and phase of VLF/LF signals (Section 2.2).

2.1.1. VLF/LF Signal Processing

When an X-ray flare occurs, the main and auxiliary VLF/LF signals are processed, taking both the amplitude and phase, in order to detect changes with respect to their values in quiet conditions before an X-ray flare. Figure 2 shows an example of temporal evolutions of signals' amplitude and phase, where their values in quiet and perturbed conditions are emphasized. These amplitude and phase values are needed in processing steps described in the following:

1. **Determination of the amplitude $A_0^{XF_s}$ of signal s in a quiet state before an X-ray flare XF.** To find this value for both VLF/LF signals, we consider three time bins of length Δt_{bin} (in our processing we use $\Delta t_{bin} = 20$ s) within a time window of a few minutes before the signal perturbation. The amplitude $A_0^{XF_s}$ is defined as the minimum of median values of recorded amplitudes in each bin, while the maximal absolute deviation of the recorded amplitudes in the considered bins from the median value is used as a figure for its absolute error $dA_0^{XF_s}$. In the following, we use "d" for the absolute error and " Δ " to denote the difference between the amplitudes at two different times during the disturbance and quiet state.
2. **Determination of the reference phase $P_{ref}^{XF_s}$ of a signal s during an X-ray flare XF.** The recorded phase of a VLF/LF signal represents the phase deviation of the considered signal with respect to the phase generated at the receiver. For this reason, the recorded phase has a component of constant slope that should be removed. A linear fit is performed through five points, three before the signal perturbation and two at the end of the considered observation interval, is performed. Phase values at these points are determined in the same way as in the procedure for amplitude estimation as described in point 1). For each time bin Δt , we compute the median value of phase samples. Furthermore, the largest deviation of phase values within each bin is used to estimate the absolute error $dP_{ref}^{XF_s}$ of the reference phase.
It is worth noting that disturbances induced by a solar X-ray flare can last from several tenth of minutes to over one hour. For this reason, quiet conditions can be different before and after disturbances. In addition, it is possible that some sudden events or some technical problem affect at least one signal in a time interval starting after the one used in this study. For instance, in Figure 2, we show a visible increase in the "quiet" visible increase in the "quiet" phase of about 15° and 5° for the DHO and ICV signals, respectively.
3. **Determination of differences in the amplitude $\Delta A^{XF_{si}}$ and phase $\Delta P^{XF_{si}}$ of the signal s during a disturbance induced by a solar X-ray flare XF in state i with respect to quiet conditions.** To avoid any dependence of results on the selection of time, we perform twice the analysis of changes in the signal parameters with respect to the initial, unperturbed state, by selecting two different times which are emphasized by vertical dashed and dotted lines in right panels in Figure 2 displaying time evolutions of the amplitude ($\Delta A^{XF_{si}} = A^{XF_s}(t_i) - A_0^{XF_s}$) and phase ($\Delta P^{XF_{si}} = P^{XF_s}(t_i) - P_{ref}^{XF_s}(t)$) changes for both signals during the disturbance induced by the solar X-ray flare occurred on 17 September 2015.
The absolute errors $dA^{XF_{s1}}$ and absolute errors $dA^{XF_{s2}}$ of amplitudes $A^{XF_{s1}}$ and $A^{XF_{s2}}$, and $dP^{XF_{s1}}$ and $dP^{XF_{s2}}$ of phases $P^{XF_{s1}}$ and $P^{XF_{s2}}$, respectively, are determined as for the quiet state, i.e.: (1) we calculate $A^{XF_{s1}}$, $A^{XF_{s2}}$, $P^{XF_{s1}}$ and $P^{XF_{s2}}$ as median values in two bins of width $\Delta t_{bin} = 20$ s around times t_1 and t_2 ; (2) we define absolute errors $dA^{XF_{s1}}$ and $dA^{XF_{s2}}$, and $dP^{XF_{s1}}$ and $dP^{XF_{s2}}$ in terms of maximal absolute deviations

of the corresponding quantities within the bins. The total absolute errors are obtained as follows:

$$d(\Delta A^{XFsi}) = dA_0^{XFsi} + dA^{XFsi}, \quad (4)$$

$$d(\Delta P^{XFsi}) = dP_{ref}^{XFsi} + dP^{XFsi}. \quad (5)$$

where $i = \{1, 2\}$.

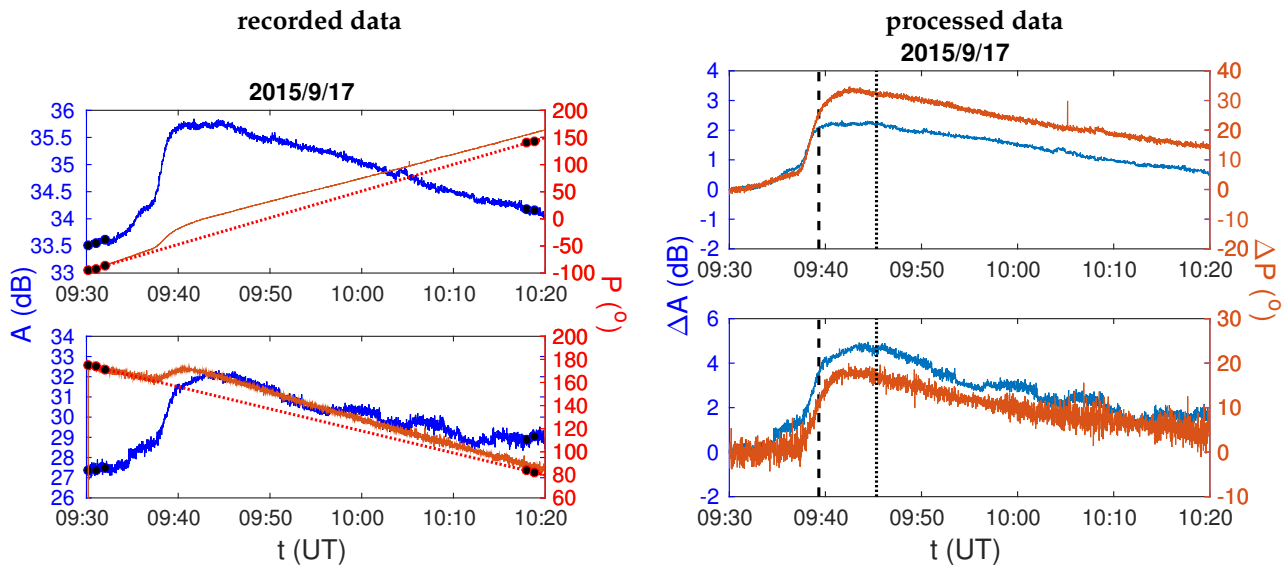


Figure 2. Time evolutions of the recorded amplitude and phase of DHO and ICV signals during the disturbance induced by the solar X-ray flare occurred on 17 September 2015 (**left panels**), and their deviations from the corresponding values in quiet conditions before the disturbance (**right panels**). The upper panels refer to the DHO signal, while the ICV signal data are shown in the bottom panels.

As a result of the above processing, the changes in amplitude and phase at the two times during the disturbance are obtained with respect to their values in quiet conditions.

2.1.2. Modeling

As shown in Figure 1, the procedure for modeling Wait's parameters describing the quiet conditions in midday periods (denoted with MDP in Figure 1) is split into two sub-procedures that provides estimations of: (1) their values for a particular event, and (2) their dependencies on the solar cycle period, described in terms of smoothed daily sunspot number σ , and season parameter $\chi = \text{DOY}/365$, where DOY is the day of year. Here, we approximate the tropical year lasting 365 days (instead 365.24255 days).

Sub-MDP-1: Estimation of Wait's parameters in quiet conditions before a solar X-ray flare.

As can be seen in Figure 1 this procedure consists of two following sub-procedures:

- **Sub-MDP-1a.** This sub-procedure provides values of Wait's parameters in the quiet ionosphere for which the amplitude ΔA_{mod}^{sqd} and phase ΔP_{mod}^{sqd} changes are similar to the corresponding recorded values, ΔA^{XFsi} and ΔP^{XFsi} , respectively. It is based on determination of changes in two sets of the modeled amplitude $\Delta A_{mod}^{sqd} = A_{mod}^{sd} - A_{mod}^{sq}$ and phase $\Delta P_{mod}^{sqd} = P_{mod}^{sd} - P_{mod}^{sq}$ of the signal s , and their deviations from the corresponding recorded values ΔA^{XFsi} and ΔP^{XFsi} for the signal s and disturbed state i . These sets, representing the modeled quiet and disturbed states, q and d , respectively, are performed in simulations of the considered VLF/LF signal propagation using LWPC numerical model developed by the Space and Naval Warfare Systems Center, San Diego, CA,

USA [22]. The input parameters of this numerical model are Wait’s parameters “sharpness” and signal reflection height, while the modeled amplitude and phase are its output (see the diagram in Figure 3).

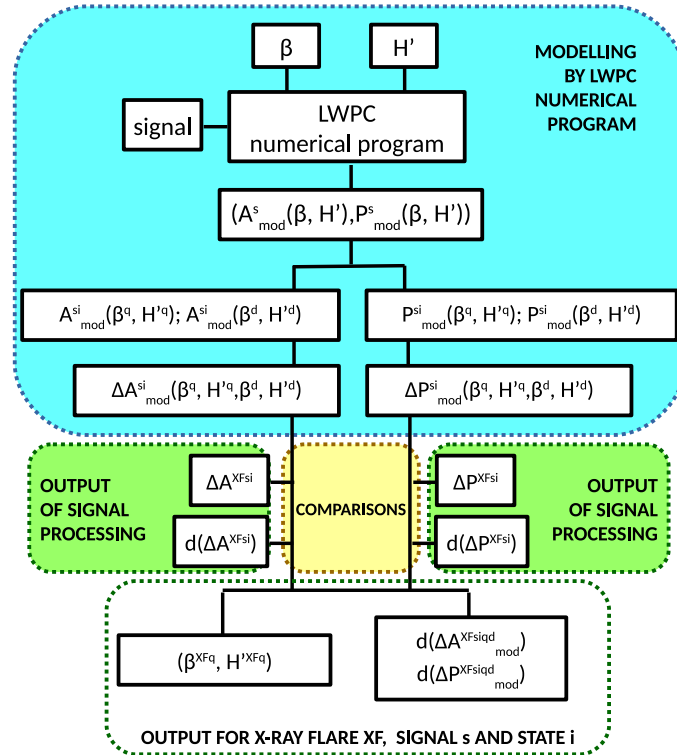


Figure 3. Diagram of sub-procedure MDP-1a.

According to the results presented in literature (see References [26,27,31,33–35]), Wait’s parameters can be considered within intervals 0.2 km^{-1} – 0.6 km^{-1} for β , and 55 km – 76 km for H' , where the quiet conditions can be described within intervals 0.2 km^{-1} – 0.45 km^{-1} for β^q , and 68 km – 76 km for H'^q . To model the parameter values representing a disturbed state d , β^d and H'^d , given those describing a quiet state q , we use conditions $\beta^q < \beta^d$ and $H'^q > H'^d$ which are based on many studies [26,27,31]. In the following, we use these intervals with steps of 0.01 km^{-1} and 0.1 km , respectively, as input in the LWPC numerical program.

The first output of the Sub-MDP-1a are the pairs of Wait’s parameters referring to the quiet state before a solar X-ray flare XF (β^{XFq}, H'^{XFq}) for which the LWPC model can calculate the amplitude and phase differences for both main (m) and auxiliary (a) signals ($s = m, a$) and for both disturbed state ($i = 1, 2$) that satisfy the conditions:

$$d(\Delta A_{\text{mod}}^{\text{XFsiqd}}) = \text{abs}(\Delta A_{\text{mod}}^{\text{sqd}} - \Delta A^{\text{XFsi}}) < d(\Delta A^{\text{XFsi}}), \quad \text{and} \quad (6)$$

$$d(\Delta P_{\text{mod}}^{\text{XFsiqd}}) = \text{abs}(\Delta P_{\text{mod}}^{\text{sqd}} - \Delta P^{\text{XFsi}}) < d(\Delta P^{\text{XFsi}}), \quad (7)$$

where $d(\Delta A^{\text{XFsi}})$ and $d(\Delta P^{\text{XFsi}})$ are the absolute errors in the recorded signal characteristics.

The second output of Sub-MDP-1a are errors in modeling, e.g., the absolute deviations of the modeled changes in the amplitude and phase from their recorded values: $d(\Delta A_{\text{mod}}^{\text{XFsiqd}})$ and $d(\Delta P_{\text{mod}}^{\text{XFsiqd}})$. Both outputs are used in Sub-MDP-1b.

- Sub-MDP-1b.** The goal of this sub-procedure is to find the pair of Wait’s parameters $(\beta_0^{XFmidday}, H_0^{XFmidday})$, from those (β^{XFq}, H^{XFq}) extracted in Sub-MDP-1a, which provides the best agreement between the modeled and measured amplitude and phase changes of the VLF/LF signals. To do that, we analyze both the observation and modeling absolute errors, i.e., $d(\Delta A^{XFsi})$ and $d(\Delta P^{XFsi})$, for observations and $d(\Delta A_{mod}^{XFsiqd})$ and $d(\Delta P_{mod}^{XFsiqd})$ for modeling. These values are used to quantify the observed w_{obs}^{XF} and modeled w_{mod}^{XFq} weights for each extracted pair of Wait’s parameters. Details about the estimations of these weights are provided in Appendix A, while an example of representation of the extracted pairs in the 2D Wait’s parameter space is shown in the left panel of Figure 4. Each pair of Wait’s parameters is represented as a point. The color of points describes their observation and modeling precisions. To find points (i.e., pairs of Wait’s parameters) which best model the amplitude and phase changes, the region around each candidate point is analyzed as follows. The weight of each point, describing the overall observation and modeling precisions, is computed as the product of observed and modeled weights, i.e., $w_{obs}^{XF} w_{mod}^{XFq}$.

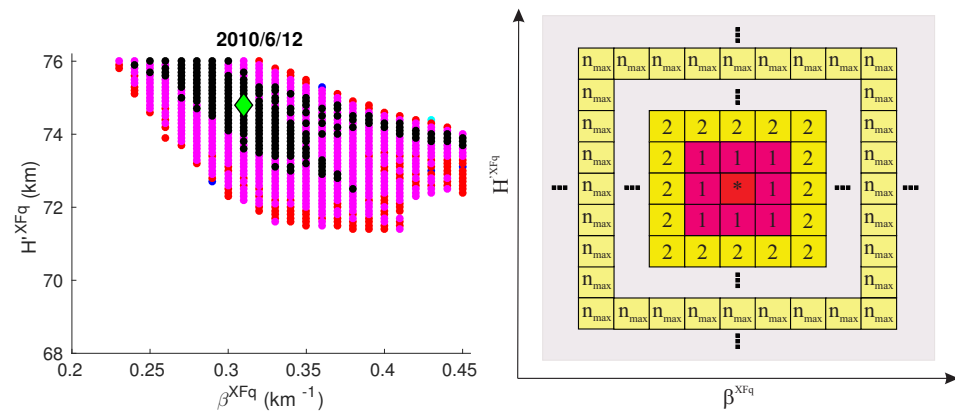


Figure 4. Left panel: Visualization of pairs of Wait’s parameters “sharpness” and signal reflection height (β^{XFq}, H^{XFq}) in quiet state q that satisfy conditions given by Equations (6) and (7) for an X-ray flare XF occurred on 12 June 2010. The color of each point denotes the category of the corresponding pair. Each category includes pairs having all the four relative errors lower than c·10% (see Equation (A1)). Colors black, magenta, red, blue and cyan indicate the c-values increasing from 1 to 5 in steps of 1. The green diamond indicates the pair $(\beta_0^{XFmidday}, H_0^{XFmidday})$ which provides the best agreement of modeled and recorded amplitude and phase changes for the considered X-ray flare. Right panel: Region of Wait’s parameter space around the point “*” with the visualization of the neighbor system. The first neighbors ($n = 1$) are colored pink, the second ones ($n = 2$) orange, and the most distant neighbors considered in the procedure ($n = n_{max}$) are colored yellow.

Furthermore, the weight w_n^{XFq} is introduced to quantify the influence of each point within the region around the candidate point. This weight is defined as

$$w_n^{XFq} = \sum_k \left\{ \frac{1}{n^{qk}} w_{obs}^{XFk} w_{mod}^{XFk} \right\}, \tag{8}$$

where n^{qk} is the distance between the quiet states q and k which refer to pairs (β^{XFq}, H^{XFq}) and (β^{XFk}, H^{XFk}) , respectively.

The total weight w_{tot}^{XFq} for the pair (β^{XFq}, H^{XFq}) is computed as:

$$w_{tot}^{XFq} = w_{obs}^{XFq} w_{mod}^{XFq} + w_n^{XFq}. \tag{9}$$

Finally, the pair of Wait’s parameters $(\beta_0^{XFmidday}, H_0^{XFmidday})$ describing the quiet D-region before a solar X-ray flare XF, which provides the best agree-

ment of the considered modeled and observed amplitude and phase changes, is obtained as the pair with the largest total weight $W_{\text{tot}}^{\text{XF}} = \max_q \{w_{\text{tot}}^{\text{XFq}}\}$. The estimation errors $[e\beta_{0-}^{\text{XF}}, e\beta_{0+}^{\text{XF}}]$ and $[eH'_{0-}^{\text{XF}}, eH'_{0+}^{\text{XF}}]$ of these parameters are obtained from distribution of pairs $(\beta^{\text{XFq}}, H'^{\text{XFq}})$ which satisfy conditions (6) and (7). For instance, the error for $\beta_0^{\text{XFmidday}}$ are computed as follows. For the pair $(\beta_0^{\text{XFmidday}}, H_0'^{\text{XFmidday}})$ represented by green diamonds in Figure 4, the interval $[e\beta_{0-}^{\text{XF}}, e\beta_{0+}^{\text{XF}}]$ is estimated by taking the smaller and larger values of β^{XFq} estimates, for the given $H_0'^{\text{XFmidday}}$. In the same way, we estimate the error for $H_0'^{\text{XFmidday}}$.

Sub-MDP-2: Modeling of Wait's parameters in terms of sunspot number and season.

The aim of this subroutine is to model the behaviour of Wait's parameters by fitting the $(\beta_0^{\text{XFmidday}}, H_0'^{\text{XFmidday}})$ pair. This requires a deeper understanding of the X-ray influences on the D-region. During quiet conditions, the solar hydrogen Ly α radiation has a dominant influence on ionization processes in the ionospheric D-region (see, for example, Reference [45]). The intensity of this radiation varies periodically during the solar cycle and its variation depends on the sunspot number. Because of that, we use the smoothed daily sunspot number σ to represent the intensity of the incoming solar radiation in the Earth's atmosphere. The intensity of this radiation decreases with the solar zenith angle due to larger attenuations in the atmosphere above the considered locations. Generally, the zenith angle changes are due to seasonal and daily variations. However, this study focuses on time intervals around middays which allows us to assume that the seasonal changes represent the zenith angle variations. We introduce the seasonal parameter $\chi = \text{DOY}/365$ where DOY is the day of year. This parameter has values between 0 and 1. Some authors report on possible influences of the geomagnetic field on the Wait's parameter [38,46]. However, this is more pronounced at polar and near polar areas due to shapes of geomagnetic lines that allows charge particle influences on the ionospheric properties. As this study is focused on the low and mid latitude ionosphere, we neglect these effects.

Dependencies of Wait's parameters at midday on solar cycle and seasonal variations can be given as functions:

$$\beta_0^{\text{midday}} = f(\sigma, \chi) \quad (10)$$

and

$$H_0'^{\text{midday}} = g(\sigma, \chi). \quad (11)$$

These relations are not general and have yet to be determined for the location of interest and the time to which the recorded data refer to.

The knowledge of these functions allow us to calculate the vertical distribution of the Wait's horizontally uniform ionosphere, $N_{e0}(h, \sigma, \chi)$, using the equation given in Reference [34] for different values of σ and χ :

$$N_{e0}^{\text{midday}}(\sigma, \chi, h) = 1.43 \cdot 10^{13} e^{-\beta^{\text{midday}}(\sigma, \chi) H'^{\text{midday}}(\sigma, \chi)} e^{[\beta^{\text{midday}}(\sigma, \chi) - 0.15]h}, \quad (12)$$

where N_{e0}^{midday} and β^{midday} are given in m^{-3} and km^{-1} , respectively, and H'^{midday} and altitude h are given in km. This equation was used to determine the temporal $(H_0'(t, h))$ and energy $(H_0'(\epsilon, h))$ distributions of the D-region electron density perturbed by a solar X-ray flare (see, for example, References [31,47,48]).

2.2. Daytime Variations of Ionospheric Parameters

The determination of the daytime variation of Wait's parameters and electron density is based on the comparison of observational and modeling data as for the analysis of midday variations. However, the DTP procedure considers only one VLF/LF signal, e.g.,

the main one. The reason for that is that the approximation of a horizontally uniform ionosphere during the entire daytime period (far from the sunrise and sunset) can be used when the size of the observed area corresponds to a relatively short propagation path of the signal.

2.2.1. VLF/LF Signal Processing

The goal of this procedure is to find the amplitude and phase variations relative to their values in the midday period. We consider data recorded during the daytime period, far from the sunrise and sunset. The midday period is estimated from tendency of the amplitude time evolution $A(t)$. Namely, it rises until the midday and decreases afterwards which allows us to assume the period around the amplitude maximum as the midday period. The duration of this period is a few minutes and it depends on the season and possible existence of unperiodical disturbances which should be excluded from the analysis.

To exclude the short-term amplitude picks that do not represent periodic daily variations, the midday amplitude A^{midday} is estimated as the median amplitude value in the midday period.

Similarly to the analysis in Section 2.1.1, the time evolution of the phase is determined by estimating the linear phase trend obtained by interpolation of phase values estimated within time bins in quiet conditions. The midday phase P^{midday} is estimated from the obtained phase evolution $P(t)$ in the same way like for the midday amplitude.

The final step of this processing is the calculation of amplitude and phase deviations from their reference values, i.e., $\Delta A = A - A^{\text{midday}}$ and $\Delta P = P - P^{\text{midday}}$.

2.2.2. Modeling

The modeling of daytime temporal evolution of Wait's parameters is based on comparison of deviation of observational and modeled changes with respect to their midday values. The modeled midday values $A_{\text{mod}}^{\text{midday}}$ and $P_{\text{mod}}^{\text{midday}}$ are obtained from β_0^{midday} and H_0^{midday} , while the modeled amplitude A_{mod} and phase P_{mod} are outputs of the LWPC program for the given pair of Wait's parameters. Wait's parameters ($\beta(t)$, $H'(t)$) at time t are estimated as those that best satisfy the conditions

$$A - A^{\text{midday}} = A_{\text{mod}} - A_{\text{mod}}^{\text{midday}} \quad (13)$$

and

$$P - P^{\text{midday}} = P_{\text{mod}} - P_{\text{mod}}^{\text{midday}}. \quad (14)$$

Finally, the electron density $N_{e0}(t, \sigma, \chi)$ is obtained from Equation (15):

$$N_{e0}(t, h, \sigma, \chi) = 1.43 \cdot 10^{13} e^{-\beta(t, \sigma, \chi) H'(t, \sigma, \chi)} e^{(\beta(t, \sigma, \chi) - 0.15)h}, \quad (15)$$

where the parameters are given in the same units as in Equation (12).

3. Studied Area and Considered Events

To give an example of this model application, we apply it to data recorded in Belgrade in the lower ionosphere observations by the VLF signals emitted in Germany and Italy, while the information of the X-ray flares occurrences was taken from the website https://hesperia.gsfc.nasa.gov/goes/goes_event_listings/. For a better understanding of the presented procedure, we will first describe observations and then (in Section 4) we present the application of the model to the observed data.

3.1. Remote Sensing of Lower Ionosphere

The lower ionosphere observations are performed by two VLF signals of frequencies 23.4 kHz and 20.27 kHz emitted by the DHO transmitter in Germany (Rhauderfehn, 53.08 N, 7.61 E) and the ICV transmitter in Italy (Isola di Tavolara, 40.92 N, 9.73 E), respectively.

Amplitudes and phases of these signals are recorded by the AWESOME (Atmospheric Weather Electromagnetic System for Observation Modeling and Education) receiver [49] located in Belgrade, Serbia, which was a part of the Stanford/AWESOME Collaboration for Global VLF Research (<http://waldo.world/narrowband-data/>). The locations of the considered transmitters and receiver, as well as the propagation paths, are shown in Figure 5.

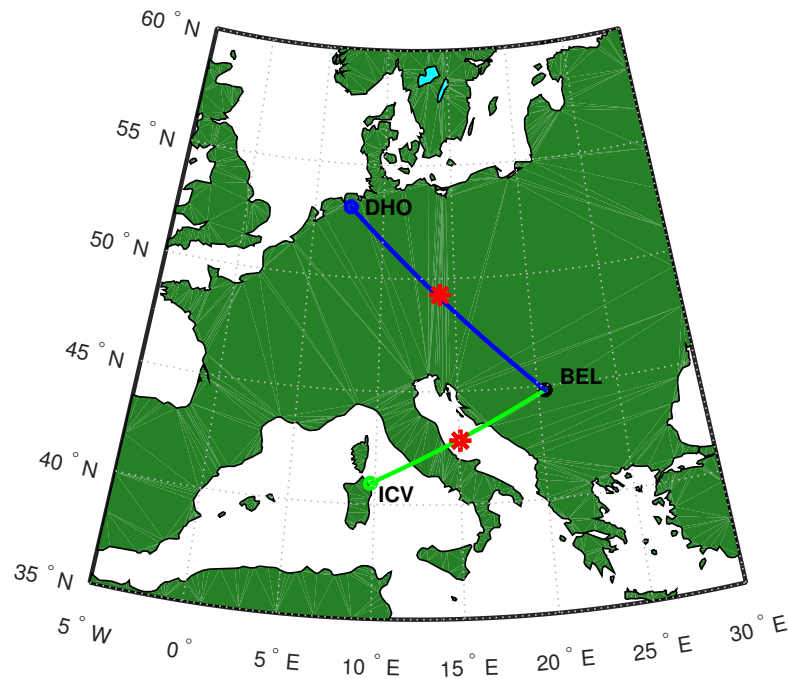


Figure 5. Propagation paths of the main and auxiliary VLF signals emitted by the DHO (Germany) and ICV (Italy) transmitters, respectively, and received in Belgrade (BEL). The stars indicate the locations of the path midpoints.

The best properties of the recorded VLF/LF signals in the Belgrade receiver station are those of the DHO signal. That can be explained by a not too long propagation path and a large emitted power (800 kW). This is why the DHO signal is used in many studies based on data collected by the Belgrade receiver station (see, for example, References [10,50]). Although the distance between the Italian transmitter and Belgrade receiver is shorter than the path in the first case, its emitted power is 40 times lower than that of the signal emitted in Germany. For this reason, we rank the DHO and ICV signals as the main and auxiliary ones, respectively.

3.2. Considered X-ray Flares

As one can see in Section 2, the presented model assumes a horizontally uniform Wait's ionosphere [42] for the area where both signals propagate. That assumption requires analyses of the time period when solar influences is similar above the considered part of Europe, e.g., periods around the midday. In addition, modeling of the electron density by the procedure given in Reference [34] is more appropriate for not too intensive flares. For this reason, we consider flares of up to class M5 (like in Reference [10]). Due to absence or insignificant ionospheric disturbances induced by low intensive flares, we consider events of classes larger than C5.0. In our collected database, we find 9 not too intensive events for which the differences in solar zenith angles, $\Delta\theta = \theta_{\text{DHO}} - \theta_{\text{ICV}}$ (calculated using the website <https://www.esrl.noaa.gov/gmd/grad/solcalc/azel.html> for the latitude/longitude points of the middle propagation paths DHO-BEL (49.28 N, 14.00 E) and ICV-BEL (42.81 N, 15.06 E), obtained in calculations by the program given at the website <https://www.gpsvisualizer.com/calculators>) satisfy the first mentioned

condition. As one can see in Table 1, classes of the considered flares are between C6.1 and M3.2, while differences in the solar zenith angles of the DHO and ICV signal mid-paths, θ_{DHO} and θ_{ICV} , respectively, are lower than 6.4° .

Table 1. Dates, times, and classes of the considered X-ray flares, and zenith angles θ_{DHO} and θ_{ICV} for the latitude/longitude points of the middle propagation paths DHO-BEL and ICV-BEL, respectively. Differences of these angles, $\Delta\theta$, are given in the last column. The positions of the considered VLF signal mid-paths, and corresponding angles θ_{DHO} , θ_{ICV} and $\Delta\theta$ are calculated using tools given at <https://www.gpsvisualizer.com/calculators> and <https://www.esrl.noaa.gov/gmd/grad/solcalc/azel.html>, respectively.

Flare XF	Date	Time (UT)	Flare Class	θ_{DHO} ($^\circ$)	θ_{ICV} ($^\circ$)	$\Delta\theta$ ($^\circ$)
F1	5 May 2010	11:37	C8.8	33.79	27.88	5.91
F2	12 June 2010	09:20	C6.1	35.39	31.25	4.14
F3	3 November 2014	11:23	M2.2	64.84	58.61	6.23
F4	15 November 2014	11:40	M3.2	53.57	51.35	2.22
F5	6 January 2015	11:40	C9.7	72.05	65.76	6.29
F6	21 January 2015	11:32	C9.9	69.25	62.88	6.37
F7	29 January 2015	11:32	M2.1	53.07	50.65	2.42
F8	17 September 2015	09:34	M1.1	50.31	44.28	6.03
F9	14 May 2016	11:28	C7.4	37.50	35.31	2.19

4. Results and Discussion

The proposed methodology is applied to data obtained in observations described in Section 3. Here, we present the results of:

- Modeling the ionospheric parameters in midday periods over the part of Europe included within the location of transmitted signals (Sardinia, Italy, for the ICV signal) and (Lower Saxony, Germany for the DHO signal) and the receiver in Belgrade, Serbia, with respect to the daily smoothed sunspot number and season. This part consists of the following steps:
 - Modeling of pairs of Wait's parameters which satisfy conditions given by Equations (6) and (7) by the LWPC numerical program and determination pair $(\beta_0^{XF}, H_0'^{XF})$ that provides the best fit of observational data for the considered X-ray flares.
 - Determination of dependencies of the midday Wait's parameters, β_0^{midday} and $H_0'^{\text{midday}}$, and the electron density, N^{midday} , from parameters that describe the solar activity and Earth's motion: the smoothed daily sunspot number σ , and parameter χ describing seasonal variations.
- Modeling of daytime variations of ionospheric parameters for a particular day. This procedure consists of:
 - Modeling of time evolutions of Wait's parameters from comparisons of the recorded and modeled amplitude and phase changes with respect to their values in the midday.
 - Modeling of the electron density time evolution for the D-region heights during daytime.

For both analyses, it is necessary to know the modeled amplitude and phase of the considered signals. For this reason, we first present the description of their determination.

4.1. Modeling of the DHO and ICV Signal Amplitudes and Phases by the LWPC Numerical Program

As noticed in Section 2, the LWPC program simulates propagation of the VLF and LF signals from a particular transmitter to a particular receiver of these waves. Wait's parameters, the "sharpness" β and signal reflection height H' are the input values for this program, while the modeled amplitude A_{mod} and phase P_{mod} are its outputs. In this study,

we perform analysis for input values of β and H' in domains 0.2 km^{-1} – 0.6 km^{-1} and 55 km – 76 km , respectively, with corresponding steps of 0.01 km^{-1} and 0.1 km .

Results of modeling by the LWPC program for location of the Belgrade receiver and the DHO and ICV transmitters are shown in Figure 6. Here, it is important to pay attention to the fact that these panels represent the modeled amplitudes and phases (within the domain from -180° to 180°), while the procedure for comparison of recorded and modeled signal characteristics, described in Section 2.1.2, requires changes of these values in the disturbed with respect to quiet conditions. The dependencies of these changes on the input Wait's parameters have the same distributions as the presented corresponding graphs because they have lower than those modeled by the LWPC program for a constant value of modeled amplitude or phase in quiet conditions.

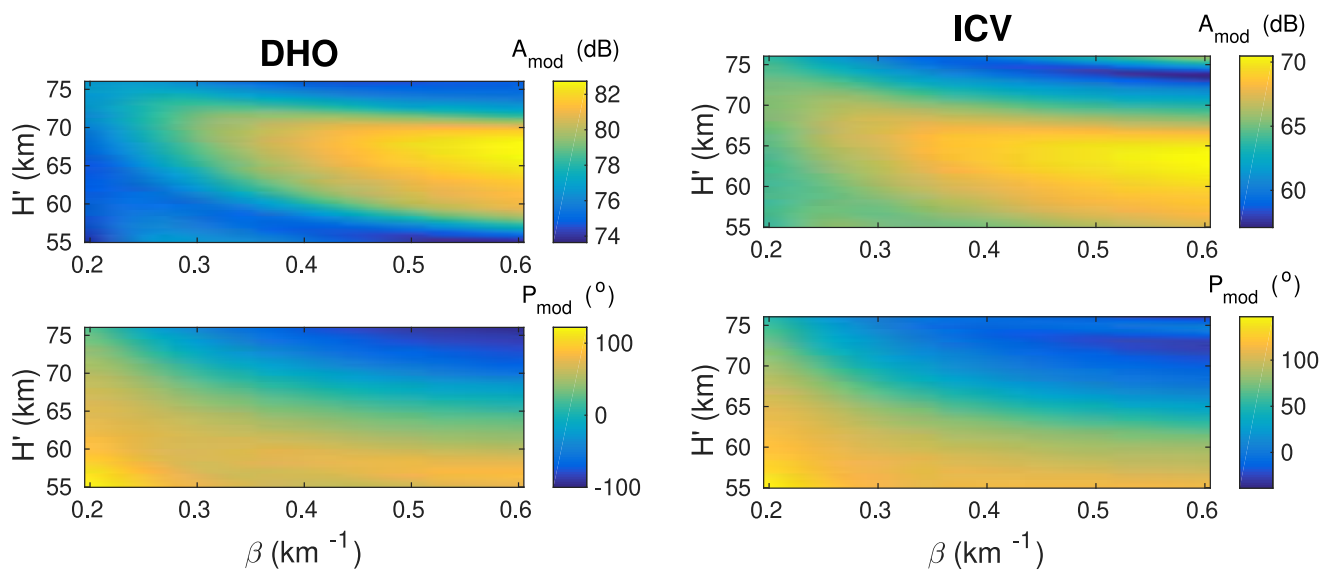


Figure 6. Surface plots of the modeled (by Long-Wave Propagation Capability (LWPC) program) amplitude (**upper panels**) and phase (**lower panels**) of the DHO (**left panels**) and ICV (**right panels**) signal for receiver located in Belgrade, Serbia, as functions of Wait's parameters β and H' .

As one can see in Figure 6, there is no unique pair of Wait's parameters that produce specific LWPC output values. That is why only one presented panel, even though the modeled amplitude/phase in quiet conditions are given, it cannot be used for determination of the input pair that provides the best fit of the observed data. The fact that it is impossible to determine a unique combination of Wait's parameters from a single value of signal characteristic was noticed by other authors (see, e.g., Reference [36]).

4.2. Midday Values—Solar Cycle and Seasonal Variations

The procedure for determination of the considered midday values during the solar cycle and year consists of two parts:

- Determination of pairs (β^{XFq}, H'^{XFq}) which describe quiet states before the considered X-ray flares (Section 4.2.1).
- Determination of dependencies of Wait's parameters and the electron density in midday quiet conditions on σ and χ (Section 4.2.2).

4.2.1. Determination of Pairs (β^{XFq}, H'^{XFq})

Comparison of the recorded and modeled changes in amplitude and phase of the DHO and ICV signals using the procedure described in Section 2.1.2 gives pairs of Wait parameters (β^{XFq}, H'^{XFq}) which satisfy the conditions given by Equations (6) and (7). These values are presented for all considered events in Figure 7. To better visualize the precision in comparisons, we divide the extracted pairs in ten categories depending on relative errors

in modeling of both amplitude and phase of the DHO and ICV signals. The category $c = 1, 2, 3, \dots, 10$ indicates that all relative errors defined by Equation (A1) for pairs (β^{XFq}, H'^{XFq}) have values less than $c \cdot 10\%$. The values of (β^{XFq}, H'^{XFq}) which have the largest total weight calculated by Equation (9), i.e. values $(\beta_0^{XFmidday}, H'_0^{XFmidday})$ for a X-ray flare XF, are indicated by green diamonds.

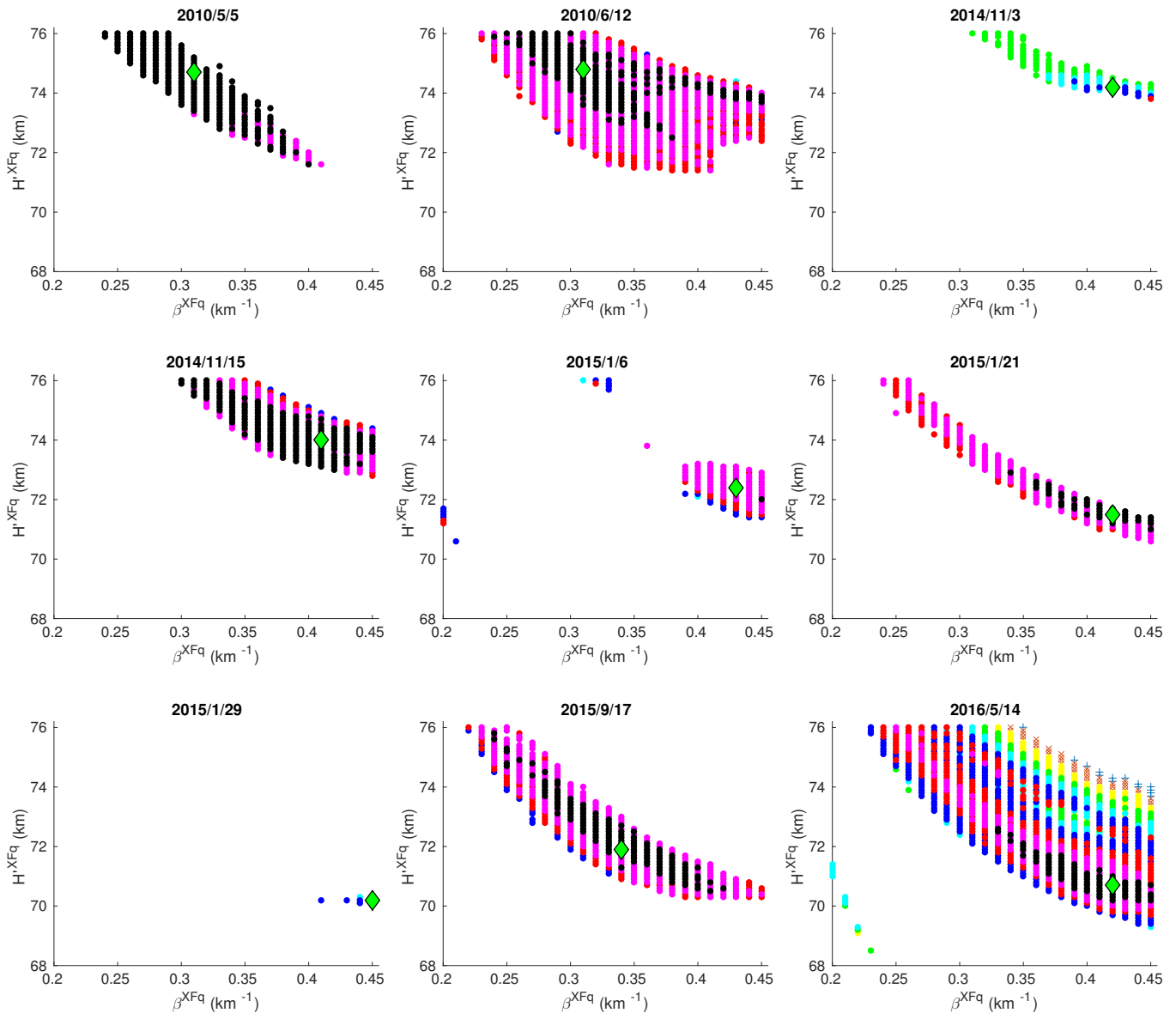


Figure 7. Visualization of pairs of Wait’s parameters “sharpness” and signal reflection height (β^{XFq}, H'^{XFq}) in quiet state q that satisfy conditions given by Equations (6) and (7) for an X-ray flare XF that occurred on the date indicated on the corresponding panel (see Table 1). Categories $c = 1, 2, 3, \dots, 10$, describing relative errors defined by Equation (A1), are shown with different scatters: black, magenta, red, blue, cyan, green and yellow filled circles, x, +, and ·, respectively. The pair (β^{XFq}, H'^{XFq}) which has the largest total weight calculated by Equation (9) for a particular event, i.e., value $(\beta_0^{XFmidday}, H'_0^{XFmidday})$ for a X-ray flare XF, is indicated by green diamonds.

According to the number of neighbors (see Figure 7) that also satisfy the conditions given by Equations (6) and (7), stability of the obtained pairs $(\beta_0^{XFmidday}, H'_0^{XFmidday})$ is good in 8 out of 9 cases. It can be also seen in Table 2 showing the relevant domains with higher $e\beta_{0+}^{XF}$ and eH'_{0+}^{XF} , and lower $e\beta_{0-}^{XF}$ and eH'_{0-}^{XF} values of Wait’s parameters with respect to $\beta_0^{XFmidday}$ and $H'_0^{XFmidday}$ (for fixed other parameter), respectively. Visualization

by different scatters shows that 6 cases have the highest precision of modeling for $c = 1$, while the lowest precision occurs for $c = 3$. The weights $W_{\text{tot}}^{\text{XF}}$, calculated by Equation (9) and given in Table 2, show large differences for the considered events (from 1.4 to 154.5).

Table 2. The obtained Wait’s parameters “sharpness”, β_0^{XFmiddy} , and signal reflection height, H_0^{XFmiddy} , and domains of their possible deviations going to larger ($e\beta_{0+}^{\text{XF}}$ and eH_{0+}^{XF}) and lower values ($e\beta_{0-}^{\text{XF}}$ and eH_{0-}^{XF}) for the considered flares. The last three columns show weights $W_{\text{tot}}^{\text{XF}}$ of the determined pairs of Wait’s parameters (β_0^{XFmiddy} , H_0^{XFmiddy}), smoothed daily sunspot number σ , and seasonal parameter χ .

Flare XF No	β_0^{XFmiddy} (km ⁻¹)	H_0^{XFmiddy} (km)	$e\beta_{0+}^{\text{XF}}$ (km ⁻¹)	$e\beta_{0-}^{\text{XF}}$ (km ⁻¹)	eH_{0+}^{XF} (km)	eH_{0-}^{XF} (km)	W_{tot}	σ	χ
F1	0.31	74.7	0.01	0.04	0.5	1.4	104.0	10.7	0.3452
F2	0.31	74.8	0.08	0.06	1.2	2.6	103.5	23.1	0.4493
F3	0.42	74.2	0.03	0.03	0.3	0.2	5.6	100.5	0.8438
F4	0.41	74.0	0.04	0.05	0.9	0.9	154.5	100.1	0.8767
F5	0.43	72.4	0.02	0.03	0.7	0.9	29.7	112.6	0.0164
F6	0.42	71.5	0.01	0.03	0.2	0.5	56.8	87.6	0.0575
F7	0.45	70.2	0.00	0.02	0.1	0.1	1.4	84.8	0.0795
F8	0.34	71.9	0.04	0.04	1.1	1.0	115.9	54.0	0.7151
F9	0.42	70.7	0.03	0.06	3.6	1.0	111.5	68.6	0.3699

4.2.2. Wait’s Parameters and Electron Density in Quiet Conditions

The final step in determination of midday Wait’s parameters is analysis of their dependencies on daily smoothed solar sunspot number σ and seasonal variations described by parameter χ . To better visualize the difference due to larger solar radiation in the period around the maximum of the solar cycle than in the period around its minimum, we show the relevant points in Figure 8 with a filled and open scatters, respectively. Different seasons are described with blue (winter), green (spring), yellow (summer), and red (autumn) scatters.

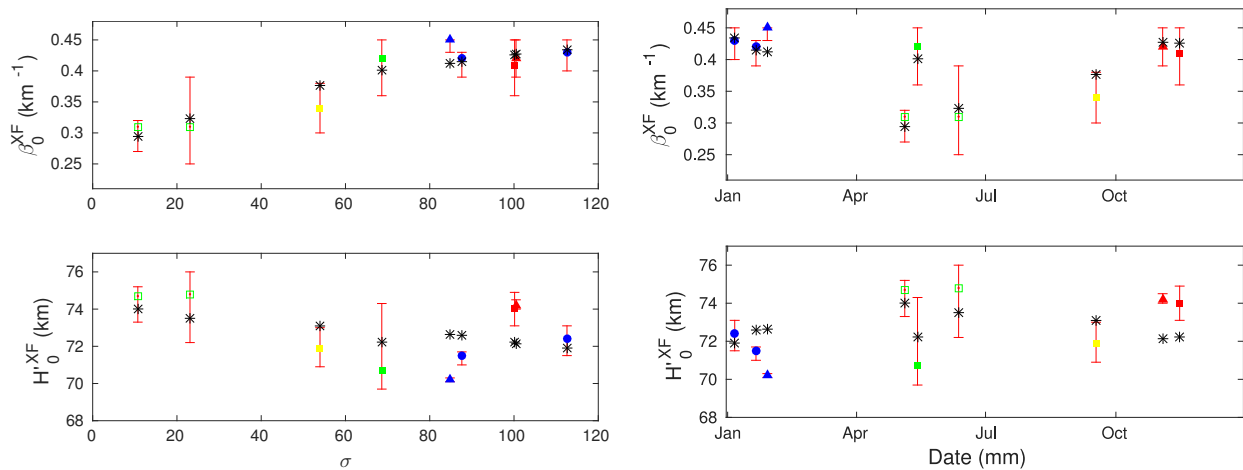


Figure 8. Dependencies of the “sharpness” β (upper panels) and signal reflection height H' on the smoothed daily sunspot number σ (left panels) and season (right panel). The modeled values β_0^{XFmiddy} and H_0^{XFmiddy} are shown as filled (for periods near the solar cycle maximum) and open (for periods near the solar cycle minimum) scatters. Different seasons are described by blue (winter), green (spring), yellow (summer), and red (autumn) scatters. Scatters marked by “*” indicate values obtained from Equations (16) and (17).

Dependencies of the midday Wait’s parameters on the solar sunspot number are shown in the left panels of Figure 8. Here, we consider the smoothed sunspot number (over 21 days) and take the value for the period of 20 days before and the considered day from the database given at <http://sidc.oma.be/silso/datafiles>. The upper panel indicates the increase of the parameter β with σ , while decrease of the signal reflection height with

σ is clearly shown in the bottom panel. These tendencies are in agreement with previous studies of Wait’s parameters during solar X-ray flares where the increase/decrease of the “sharpness”/signal reflection height with the electron density is reported (see, for example, Reference [31]). In this case, the rise of the D-region electron density is a consequence of the $\text{Ly}\alpha$ radiation increase in approaching the solar cycle maximum. In fitting of these dependencies, we assume polynomial functions of the orders 2 and 1, respectively, which is by one order of magnitude larger than in Reference [38] where the dependency of the parameter β is given as a linear function of the sunspot number, while variation of H' with the sunspot number is not suggested. As one can see in the right panels in Figure 8, the seasonal variation is more complex than in the previous case. However, if two scatters related to the solar cycle minimum are excluded we can see approximative sinusoidal shapes in both cases. For this reason, we assume sinusoidal dependencies of Wait’s parameters on parameter χ similarly as in Reference [38] but with daily (instead of monthly) changes and additional phase shifts which provide maximum/minimum values of β/H' for the summer solstice when the expected radiation coming in the considered area reaches its annual maximum.

Tow-dimensional fittings of Wait’s parameters yield the following expressions:

$$\beta_0^{\text{midday}} = 0.2635 + 0.002573 \cdot \sigma - 9.024 \cdot 10^{-6} \sigma^2 + 0.005351 \cdot \cos(2\pi(\varnothing - 0.4712)) \quad (16)$$

and

$$H_0^{\text{midday}} = 74.74 - 0.02984 \cdot \sigma + 0.5705 \cdot \cos(2\pi(\varnothing - 0.4712) + \pi), \quad (17)$$

which provides good agreement of the computed Wait’s parameters with their modeled values given in Table 1. The maximum differences of their values are less than 0.04 km^{-1} , and 2.5 km. These values are in good agreement with those obtained in Reference [51] for the night-time Wait’s parameters and they are similar to the maximum “errors” given in Table 2. Wait’s parameters are visualized in Figure 9 for β_0 (left panel) and H_0' (right panel). The obtained values lie in domains 0.31 km^{-1} – 0.45 km^{-1} and 70.6 km – 74.7 km , respectively. An increase/decrease in dependencies of the “sharpness”/reflection height with σ is visible during the whole year. The minimum/maximum values of β_0/H_0' for the same σ are reached during the summer solstice when the solar radiation has the greatest impact on the ionosphere.

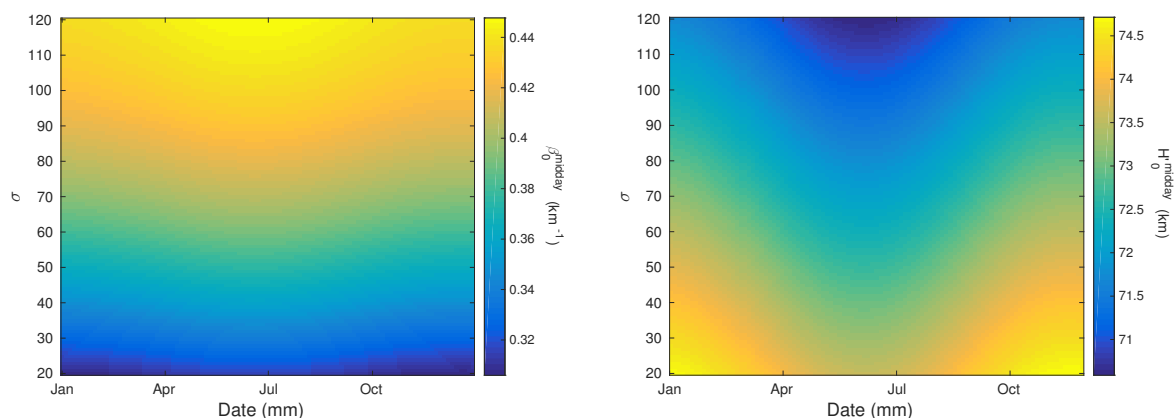


Figure 9. Dependencies of Wait’s parameters in the quiet midday ionosphere, the “sharpness” β_0^{midday} (left panel) and signal reflection height H_0^{midday} (right panel) on season and smoothed daily sunspot number σ .

Introduction of Equations (16) and (17) in Equation (12) gives the midday electron density from σ and χ at altitude h . These dependencies at 70 km, 75 km, and 80 km are shown in Figure 10.

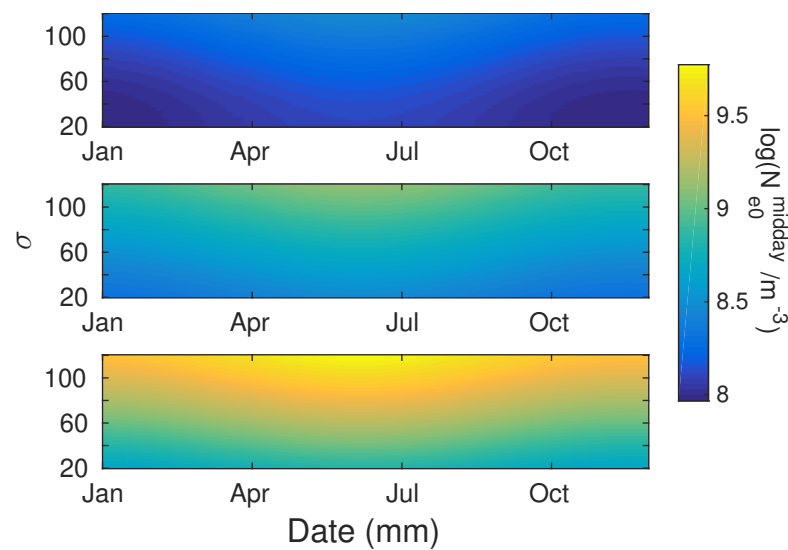


Figure 10. Dependencies of $\log(N_{e0}^{\text{midday}}/1 \text{ m}^{-3})$ at the altitudes of 70 km (upper panel), 75 km (middle panel), and 80 km (bottom panel) on season and smoothed daily sunspot number σ .

As one can see, variations are more visible at larger heights and can reach values near 10^{10} m^{-3} at 80 km for periods with large number of solar sunspot number. Due to the most intensive influences of solar radiation, the electron density has largest values during the summer solstice.

4.3. Daytime Variations

Knowing the midday Wait's parameters allows us to calculate their time evolutions during a quiet day. Here, we present an example using the DHO signal amplitude and phase recorded by the Belgrade VLF receiver on 6 September 2014 (DOY = 250; $\chi = 0.6849$) in which deviations, ΔA and ΔP , from the corresponding midday values are shown in the left panels of Figure 11. We consider a time interval from 9 UT to 15 UT when approximation of a horizontally uniform ionosphere within the medium where the signal propagates. A lack of data between 13 UT and 14 UT is due to a regular pause in the VLF/LF signals monitoring by the AWESOME receiver located in Belgrade.

To obtain the daytime evolution of β and H' , we first calculate their midday values. According to the database given at <http://sidc.oma.be/silso/datafiles>, the mean value of daily sunspot number for 20 days before and for the considered day is $\sigma = 107.1$. Introducing these values in Equations (16) and (17) gives the midday Wait's parameters for the analyzed day: $\beta_0^{\text{midday}} = 0.42 \text{ km}^{-1}$ and $H_0^{\text{midday}} = 72.5 \text{ km}$. The recorded midday amplitude $A_{\text{mod}}^{\text{midday}} = 30.35 \text{ dB}$ and phase $P_{\text{mod}}^{\text{midday}} = 1.11^\circ$ are estimated from time evolutions of the corresponding signal characteristics. Finally, the time evolution of Wait's parameters are calculated by the procedure as described in Section 2.2.2 and shown in the right panels of Figure 11. In the considered time period (excluding a short-term peak), these parameters have values within approximative domains 0.36 km^{-1} – 0.45 km^{-1} and 71.2 km – 74.2 km , respectively. Comparisons of the data obtained by the QIonDR model with those calculated by the LWPC default and IRI (see Reference [52] and references therein; Wait's parameters are calculated from electron density altitude distribution and expression for the electron density given in Reference [34]) models and with data presented in previous studies [27,33,35,53] show the best comparison of the QIonDR modeled amplitude and phase variations with the recorded ones. The QIonDR model fits better than the LWPC default model with data shown in References [27,33,35,53] for both Wait's parameters. The IRI model agrees better with the QIonDR ones for H'_0 , as well as in some periods for β_0 .

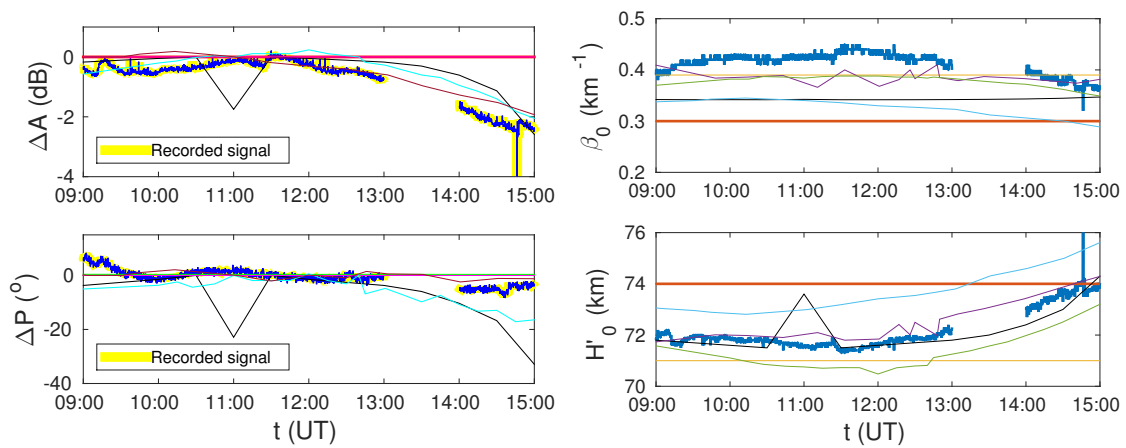


Figure 11. Daytime variations of the amplitude and phase changes (left panels) and Wait’s parameters (right panels) during 6 September 2014 obtained by Quiet Ionospheric D-Region (QIonDR), default Long-Wave Propagation Capability (LWPC), and International Reference Ionosphere (IRI) models and compared with data presented in studies indicated in legend [22,27,33,35,52,53]. The gap between 13 UT and 14 UT is due to the one hour break in data receiving by the Atmospheric Weather Electromagnetic System for Observation Modeling and Education (AWESOME) receiver. — QIonDR; — LWPC default [22]; — IRI [52]; — Thomson et al., 2005 [27]; — Han et al., 2011 [33]; — McRae and Thomson, 2000 [35]; — Thomson et al., 2017 [53].

The daytime variation in the D-region electron density during the considered day, obtained from the calculated Wait’s parameters and Equation (15), is shown in Figure 12. The time variation of electron density is more noticeable at higher altitudes while the vertical changes are most pronounced in the midday period. Similarly to the comparison of Wait’s parameters, the QIonDR model fits better than the LWPC default model with data shown in References [27,33,35,53] for the electron density at 70 km and 80 km. The IRI model agrees better with the QIonDR ones for the electron densities at 70 km.

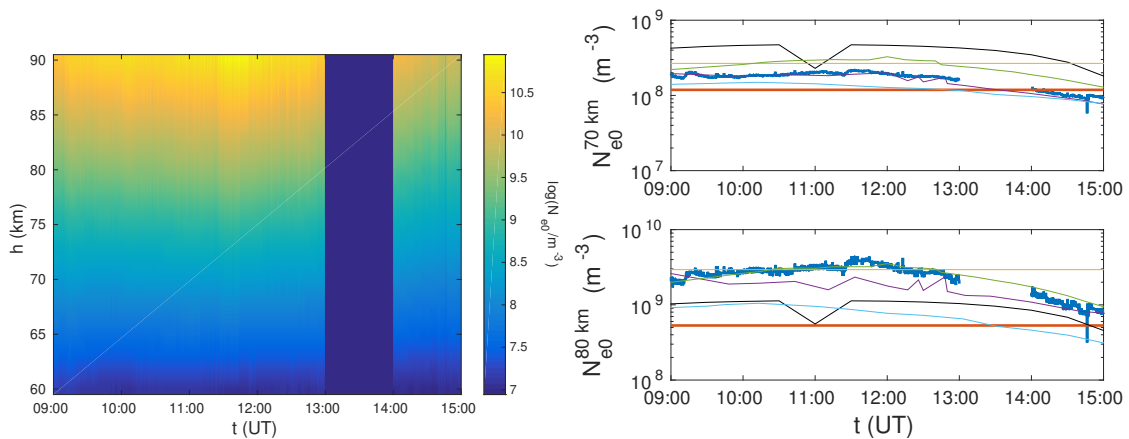


Figure 12. Left panel: Daytime variation of $\log(N_{e0}/1 \text{ m}^{-3})$ during 6 September 2014 obtained by the Quiet Ionospheric D-Region (QIonDR) model. The gap between 13 UT and 14 UT is due to the one hour break in data receiving by the Atmospheric Weather Electromagnetic System for Observation Modeling and Education (AWESOME) receiver. Right panels: Comparisons of the obtained electron density time evolutions at 70 km (upper panel) and 80 km (bottom panel) with those obtained for Wait’s parameters presented in Figure 11. — QIonDR; — LWPC default [22]; — IRI [52]; — Thomson et al., 2005 [27]; — Han et al., 2011 [33]; — McRae and Thomson, 2000 [35]; — Thomson et al., 2017 [53].

A similar analysis is provided also for the D-region disturbed by a solar X-ray flare on 17 September 2015 (signal characteristics for this event are shown in Figure 2). Comparisons of the amplitude and phase changes, as well as time evolutions of Wait’s parameters and the electron density for different values of initial Wait’s parameters, are shown in Figure 13. In these calculations, we applied the LWPC model for the initial Wait’s parameters obtained

by the QIonDR, LWPC default, and IRI models, and based on the studies presented in References [27,35,53]. In all these cases, the modeled amplitude and phase variations are in very good agreement with the recorded ones. For better visibility, we show only the obtained data for the QIonDR and LWPC default models. As one can see in Figure 13a, they are practically completely fitted with the recorded data except for the end of the observed period when minor deviations are noticeable in the case of LWPC default program for the amplitude changes. Agreement of β is better for QIonDR than for the LWPC default model with data obtained by IRI model and data from References [27,35], as well as for data from Reference [53], in some periods. In the cases of H' and electron density time evolutions, the QIonDR better fits with data obtained for initial parameters calculated by the IRI model, used in Reference [27], and, in some periods, for initial parameters given in Reference [35]. In addition, comparison of all parameters is in better agreement for the QIonDR than LWPC default model with data presented in References [26,29] for the maximum X-radiation flux of flares of the same or very similar class as the considered one.

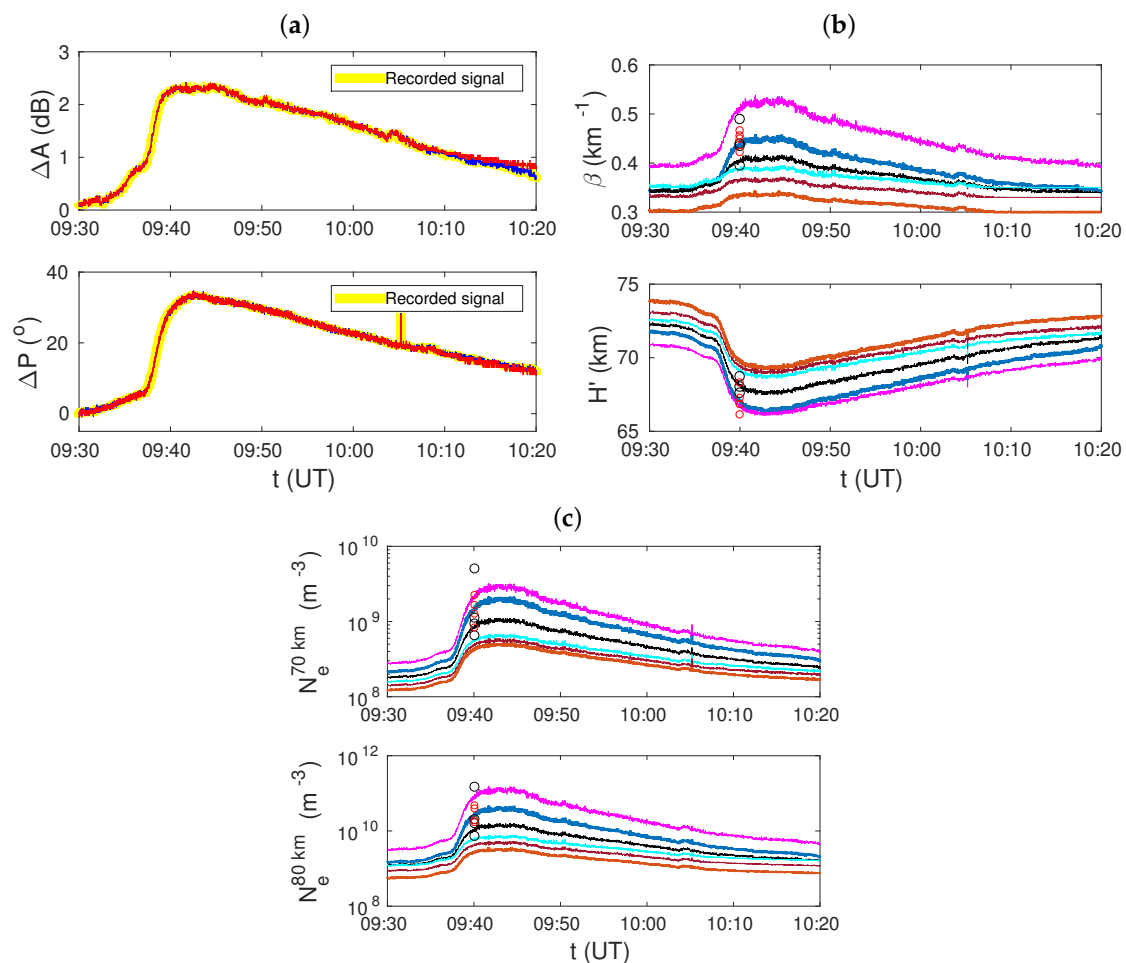


Figure 13. Comparisons for the D-region disturbed by a solar X-ray flare on 17 September 2015. (a) Comparisons of time evolutions of the recorded amplitude (upper panel) and phase (lower panel) changes with their modeled values by the Long-Wave Propagation Capability (LWPC) model for Wait's parameters β_0 and H'_0 determined by the Quiet Ionospheric D-Region (QIonDR) model (blue line) and by default (red line). (b) Comparison of time evolutions of Wait's parameters β and H' obtained by the LWPC program for their initial values modeled by the QIonDR, LWPC default and International Reference Ionosphere (IRI) models, and those presented in literature indicated in the legend [22,27,35,52,53]. The values obtained in References [26,29] at the moment of maximum X-radiation flux for flares of the same or very similar class as the considered one are shown by scatters. (c) Comparison of time evolutions of the electron density at 70 km (upper panel) and 80 km (bottom panel) for Wait's parameters shown in graph (b). — QIonDR; — LWPC default [22]; — IRI [52]; — Thomson et al., 2005 [27]; — McRae and Thomson, 2000 [35]; — Thomson et al., 2017 [53]; o Grubor et al., 2008 [29]; o McRae and Thomson, 2004 [26].

5. Conclusions

In this paper, we present a procedure for calculations of the D-region plasma parameters during quiet conditions. The proposed methodology is applied to areas monitored by the VLF/LF radio signals emitted and recorded by relatively closely located transmitters and receivers like, for example, in Europe. It is based on two different VLF/LF signals acquired by one receiver. We applied the proposed methodology to the DHO and ICV signals emitted in Germany and Italy, respectively, and recorded in Serbia. The obtained results of this study are:

- A new procedure for estimation of Wait's parameters and electron density. It is divided in two parts: (1) determination of dependencies of these parameters on the smoothed daily sunspot number and season at midday, and (2) determination of time evolution of these parameters during daytime;
- Estimation of Wait's parameters and electron density over the part of Europe included within the location of the transmitted signals (Sardinia, Italy, for the ICV signal) and (Lower Saxony, Germany for the DHO signal) and the receiver in Belgrade, Serbia. The obtained results show variations in which inclusion in different analyses of more events or time periods will allow more realistic comparisons and statistic studies;
- Analytical expressions for dependencies of Wait's parameters on the smoothed daily sunspot number and seasonal parameter valid over the studied area.

The determination of the "sharpness" β and signal reflection height H' during quiet conditions are needed for calculations of the electron density and other plasma parameters in the D-region during both the quiet and disturbed conditions. As a consequence, a more realistic modeling of the D-region can be attained based on results obtained by the proposed methodology. This could benefit to statistical analyses of the D-region related to different unperturbed conditions subject to daily and seasonal variations, as well as variations during a solar cycle. Furthermore, the most accurate modeling of the D-region based on the results obtained by the proposed methodology could also improve the mitigation of ionospheric propagation artefacts in telecommunication and microwave Earth Observation applications.

Due to approximation of the horizontally uniform ionosphere and neglect of influence of geomagnetic field variations on the VLF/LF signal propagation, application of the presented model is limited to:

- Time periods during quiet conditions or during disturbances that do not affect the assumed horizontal uniformity of the observed D-region (for example, the midday periods during the influence of solar X-ray flares),
- VLF/LF signals in which propagation paths between transmitters and receivers are relatively short, and
- Mid- and low-latitude areas where the spatial variations of the magnetic field are not significant in the given conditions.

In other words, the presented model cannot be used when losses, gyrotropy and anisotropy in the region of 70–90 km can significantly affect the propagation of VLF/LF signals in the waveguide Earth-Ionosphere, in particular in situations of large geophysical disturbances of the Lithosphere-Atmosphere-Ionosphere-Magnetosphere system caused by large magnetic storms, hurricanes, etc.

The proposed methodology can be applied during the daytime period when the solar influence on the ionosphere is the largest. During this period the electron density can significantly rise due to influence of intensive sudden solar phenomena like a solar X-ray flare, which can further importantly affect propagation of the mentioned electromagnetic waves.

It is worth noting that the proposed methodology can be applied only to relatively small areas like the one studied in this paper. For this reason, it is more relevant for Europe characterized by a high density network of VLF/LF transmitters and receivers. Improvements of the receiver and/or transmitter networks in future will make the application of

the proposed methodology more interesting in providing a real to near-real-time mapping of the D-region electron density above more regions around the world.

Author Contributions: Conceptualization, A.N.; methodology, A.N.; software, A.N. and S.T.M.; validation, G.N., L.Č.P., V.M.Č., S.T.M., I.R.M., and M.R.; formal analysis, A.N., G.N., V.M.Č., and L.Č.P.; investigation, A.N.; resources, A.N.; data curation, A.N. and S.T.M.; writing—original draft preparation, A.N.; writing—review and editing, all authors; visualization, A.N. and I.R.M.; funding acquisition, M.R. and A.N. All authors have read and agree to the published version of the manuscript.

Funding: The authors acknowledge funding provided by the Institute of Physics Belgrade and the Astronomical Observatory (the contract 451-03-68/2020-14/200002) through the grants by the Ministry of Education, Science, and Technological Development of the Republic of Serbia.

Data Availability Statement: Publicly available datasets were analyzed in this study. This data can be found here: https://hesperia.gsfc.nasa.gov/goes/goes_event_listings/; <https://www.gpsvisualizer.com/calculators>; <https://www.esrl.noaa.gov/gmd/grad/solcalc/azel.html>; <http://sidc.oma.be/silso/datafiles>; https://ccmc.gsfc.nasa.gov/modelweb/models/iri2012_vitmo.php.

Acknowledgments: The authors thank Frédéric Clette for help in preparation of our study and anonymous reviewers for very useful suggestions and comments.

Conflicts of Interest: The authors declare no conflict of interest.

Sample Availability: The VLF data used for analysis is available from the corresponding author.

Appendix A

In this appendix, we provide details of determination of the observational, $w_{\text{obs}}^{\text{XF}}$, and modeled, $w_{\text{mod}}^{\text{XFq}}$, weights described in Section 2.1.2. Changes in the signal amplitude and phase can differ by more than one order of magnitude. For this reason, and also due to different unit of amplitude and phase measurements, in the following, we introduce relative errors of these changes. The observation and modeling weights are defined as follows:

- **Weight $w_{\text{obs}}^{\text{XF}}$.** The relative errors of the recorded signal amplitude and phase are obtained as a ratio of their absolute errors and the corresponding observed changes:

$$\delta(\Delta A^{\text{XFsi}}) = \frac{d(\Delta A^{\text{XFsi}})}{\Delta A^{\text{XFsi}}}; \quad \delta(\Delta P^{\text{XFsi}}) = \frac{d(\Delta P^{\text{XFsi}})}{\Delta P^{\text{XFsi}}}. \quad (\text{A1})$$

The total relative error $\delta_{\text{obstot}}^{\text{XF}}$ of the observed changes related to a solar X-ray flare XF is given by:

$$\delta_{\text{obstot}}^{\text{XF}} = \sum_s \sum_i \left[\delta(\Delta A^{\text{XFsi}}) + \delta(\Delta P^{\text{XFsi}}) \right]. \quad (\text{A2})$$

The observational weight for an X-ray flare XF is defined as reciprocal value of the total relative error:

$$w_{\text{obs}}^{\text{XF}} = \frac{1}{\delta_{\text{obstot}}^{\text{XF}}}. \quad (\text{A3})$$

- **Weight $w_{\text{mod}}^{\text{XFq}}$.** This weight is computed for Wait's parameters in a quiet state q for which AT LEAST one corresponding pair $(\beta^{\text{XFd}}, H'^{\text{XFd}})$ is such that Equations (6) and (7) are satisfied for both signals s and both states i. In the case there are more pairs $(\beta^{\text{XFd}}, H'^{\text{XFd}})$ with the quiet state q, the relative error $\delta_{\text{modtot}}^{\text{XFq}}$ is defined as:

$$\delta_{\text{modtot}}^{\text{XFq}} = \min_d \left\{ \sum_s \sum_i \left[\delta(\Delta A_{\text{mod}}^{\text{XFsiqd}}) + \delta(\Delta P_{\text{mod}}^{\text{XFsiqd}}) \right] \right\}. \quad (\text{A4})$$

The modeled weight is calculated as:

$$w_{\text{mod}}^{\text{XFq}} = \frac{1}{\delta_{\text{modtot}}^{\text{XFq}}}. \quad (\text{A5})$$

References

- Kintner, P.M.; Ledvina, B.M. The ionosphere, radio navigation, and global navigation satellite systems. *Adv. Space Res.* **2005**, *35*, 788–811. [\[CrossRef\]](#)
- Meyer, F. Performance requirements for ionospheric correction of low-frequency SAR data. *IEEE Trans. Geosci. Remote Sens.* **2011**, *49*, 3694–3702. [\[CrossRef\]](#)
- Jakowski, N.; Stankov, S.M.; Klaehn, D. Operational space weather service for GNSS precise positioning. *Ann. Geophys.* **2005**, *23*, 3071–3079. [\[CrossRef\]](#)
- Benevides, P.; Nico, G.; Catalão, J.; Miranda, P.M.A. Bridging InSAR and GPS Tomography: A New Differential Geometrical Constraint. *IEEE Trans. Geosci. Remote Sens.* **2016**, *54*, 697–702. [\[CrossRef\]](#)
- Benevides, P.; Nico, G.; Catalão, J.; Miranda, P.M.A. Analysis of Galileo and GPS Integration for GNSS Tomography. *IEEE Trans. Geosci. Remote Sens.* **2017**, *55*, 1936–1943. [\[CrossRef\]](#)
- Su, K.; Jin, S.; Hoque, M.M. Evaluation of Ionospheric Delay Effects on Multi-GNSS Positioning Performance. *Remote Sens.* **2019**, *11*, 171.
- Yang, H.; Yang, X.; Zhang, Z.; Sun, B.; Qin, W. Evaluation of the Effect of Higher-Order Ionospheric Delay on GPS Precise Point Positioning Time Transfer. *Remote Sens.* **2020**, *12*, 2129. [\[CrossRef\]](#)
- Farzaneh, S.; Forootan, E. A Least Squares Solution to Regionalize VTEC Estimates for Positioning Applications. *Remote Sens.* **2020**, *12*, 3545. [\[CrossRef\]](#)
- Miranda, P.M.A.; Mateus, P.; Nico, G.; Catalão, J.; Tomé, R.; Nogueira, M. InSAR Meteorology: High-Resolution Geodetic Data Can Increase Atmospheric Predictability. *Geophys. Res. Lett.* **2019**, *46*, 2949–2955. [\[CrossRef\]](#)
- Nina, A.; Nico, G.; Odalović, O.; Čadež, V.; Drakul, M.T.; Radovanović, M.Č. Popović, L. GNSS and SAR Signal Delay in Perturbed Ionospheric D-Region During Solar X-ray Flares. *IEEE Geosci. Remote Sens. Lett.* **2020**, *17*, 1198–1202. [\[CrossRef\]](#)
- Zhao, J.; Zhou, C. On the optimal height of ionospheric shell for single-site TEC estimation. *GPS Solut.* **2018**, *22*, 48. [\[CrossRef\]](#)
- Nava, B.; Coïsson, P.; Radicella, S. A new version of the NeQuick ionosphere electron density model. *J. Atmos. Solar-Terr. Phys.* **2008**, *70*, 1856–1862. [\[CrossRef\]](#)
- Scherliess, L.; Schunk, R.W.; Sojka, J.J.; Thompson, D.C.; Zhu, L. Utah State University Global Assimilation of Ionospheric Measurements Gauss-Markov Kalman filter model of the ionosphere: Model description and validation. *J. Geophys. Res.-Space* **2006**, *111*, 1–19. [\[CrossRef\]](#)
- Silber, I.; Price, C. On the Use of VLF Narrowband Measurements to Study the Lower Ionosphere and the Mesosphere–Lower Thermosphere. *Surv. Geophys.* **2017**, *38*, 407–441. [\[CrossRef\]](#)
- Nina, A.; Pulnits, S.; Biagi, P.; Nico, G.; Mitrović, S.; Radovanović, M.Č. Popović, L. Variation in natural short-period ionospheric noise, and acoustic and gravity waves revealed by the amplitude analysis of a VLF radio signal on the occasion of the Kraljevo earthquake ($M_w = 5.4$). *Sci. Total Environ.* **2020**, *710*, 136406. [\[CrossRef\]](#) [\[PubMed\]](#)
- Kumar, S.; NaitAmor, S.; Chanrion, O.; Neubert, T. Perturbations to the lower ionosphere by tropical cyclone Evan in the South Pacific Region. *J. Geophys. Res. Space* **2017**, *122*, 8720–8732. [\[CrossRef\]](#)
- Nina, A.; Radovanović, M.; Milovanović, B.; Kovačević, A.; Bajčetić, J.Č. Popović, L. Low ionospheric reactions on tropical depressions prior hurricanes. *Adv. Space Res.* **2017**, *60*, 1866–1877. [\[CrossRef\]](#)
- Biagi, P.F.; Maggipinto, T.; Righetti, F.; Loiacono, D.; Schiavulli, L.; Ligonzo, T.; Ermini, A.; Moldovan, I.A.; Moldovan, A.S.; Buyuksarac, A.; et al. The European VLF/LF radio network to search for earthquake precursors: Setting up and natural/man-made disturbances. *Nat. Hazards Earth Syst. Sci.* **2011**, *11*, 333–341.
- Inan, U.S.; Lehtinen, N.G.; Moore, R.C.; Hurley, K.; Boggs, S.; Smith, D.M.; Fishman, G.J. Massive disturbance of the daytime lower ionosphere by the giant γ -ray flare from magnetar SGR 1806-20. *Geophys. Res. Lett.* **2007**, *34*, 8103. [\[CrossRef\]](#)
- Tanaka, Y.T.; Raulin, J.P.; Bertoni, F.C.P.; Fagundes, P.R.; Chau, J.; Schuch, N.J.; Hayakawa, M.; Hobara, Y.; Terasawa, T.; Takahashi, T. First Very Low Frequency Detection of Short Repeated Bursts from Magnetar SGR J1550-5418. *Astrophys. J. Lett.* **2010**, *721*, L24–L27. [\[CrossRef\]](#)
- Bajčetić, J.; Nina, A.; Čadež, V.M.; Todorović, B.M. Ionospheric D-Region Temperature Relaxation and Its Influences on Radio Signal Propagation After Solar X-Flares Occurrence. *Thermal Sci.* **2015**, *19*, S299–S309. [\[CrossRef\]](#)
- Ferguson, J.A. *Computer Programs for Assessment of Long-Wavelength Radio Communications, Version 2.0*; Space and Naval Warfare Systems Center: San Diego, CA, USA, 1998.
- Marshall, R.A.; Wallace, T.; Turbe, M. Finite-Difference Modeling of Very-Low-Frequency Propagation in the Earth-Ionosphere Waveguide. *IEEE Trans. Antennas Propag.* **2017**, *65*, 7185–7197.
- Rapopot, Y.; Grimalsky, V.; Fedun, V.; Agapitov, O.; Bonnell, J.; Grytsai, A.; Milinevsky, G.; Liashchuk, A.; Rozhnoi, A.; Solovieva, M.; et al. Model of the propagation of very low-frequency beams in the Earth–ionosphere waveguide: Principles of the tensor impedance method in multi-layered gyrotropic waveguides. *Ann. Geophys.* **2020**, *38*, 207–230.

25. Morfitt, D.G.; Shellman, C.H. *MODESRCH, an Improved Computer Program for Obtaining ELF/VLF Mode Constants in an EARTH-Ionosphere Waveguide*; Naval Electronics Laboratory Center: San Diego, CA, USA, 1976.
26. McRae, W.M.; Thomson, N.R. Solar flare induced ionospheric D-region enhancements from VLF phase and amplitude observations. *J. Atmos. Solar Terr. Phys.* **2004**, *66*, 77–87. [[CrossRef](#)]
27. Thomson, N.R.; Rodger, C.J.; Clilverd, M.A. Large solar flares and their ionospheric D region enhancements. *J. Geophys. Res. Space* **2005**, *110*, A06306. [[CrossRef](#)]
28. Žigman, V.; Grubor, D.; Šulić, D. D-region electron density evaluated from VLF amplitude time delay during X-ray solar flares. *J. Atmos. Solar Terr. Phys.* **2007**, *69*, 775–792.
29. Grubor, D.P.; Šulić, D.M.; Žigman, V. Classification of X-ray solar flares regarding their effects on the lower ionosphere electron density profile. *Ann. Geophys.* **2008**, *26*, 1731–1740. [[CrossRef](#)]
30. Basak, T.; Chakrabarti, S.K. Effective recombination coefficient and solar zenith angle effects on low-latitude D-region ionosphere evaluated from VLF signal amplitude and its time delay during X-ray solar flares. *Astrophys. Space Sci.* **2013**, *348*, 315–326. [[CrossRef](#)]
31. Nina, A.; Čadež, V. Electron production by solar Ly- α line radiation in the ionospheric D-region. *Adv. Space Res.* **2014**, *54*, 1276–1284. [[CrossRef](#)]
32. Poulsen, W.L.; Bell, T.F.; Inan, U.S. The scattering of VLF waves by localized ionospheric disturbances produced by lightning-induced electron precipitation. *J. Geophys. Res. Space* **1993**, *98*, 15553–15559. [[CrossRef](#)]
33. Han, F.; Cummer, S.A.; Li, J.; Lu, G. Daytime ionospheric D region sharpness derived from VLF radio atmospheric. *J. Geophys. Res.-Space Phys.* **2011**, *116*, 5314. [[CrossRef](#)]
34. Thomson, N.R. Experimental daytime VLF ionospheric parameters. *J. Atmos. Solar Terr. Phys.* **1993**, *55*, 173–184. [[CrossRef](#)]
35. McRae, W.M.; Thomson, N.R. VLF phase and amplitude: Daytime ionospheric parameters. *J. Atmos. Solar Terr. Phys.* **2000**, *62*, 609–618. [[CrossRef](#)]
36. Thomson, N.R.; Rodger, C.J.; Clilverd, M.A. Daytime D region parameters from long-path VLF phase and amplitude. *J. Geophys. Res.-Space* **2011**, *116*, 11305.
37. Gross, N.C.; Cohen, M.B. VLF Remote Sensing of the D Region Ionosphere Using Neural Networks. *J. Geophys. Res. Space* **2020**, *125*, e2019JA027135.
38. Davis, R.M.; Berry, L.A. *A Revised Model of the Electron Density in the Lower Ionosphere*; Technical Report TR III-77; Defense Communications Agency Command Control Technical Center: Washington, DC, USA, 1977. [[CrossRef](#)]
39. Todorović Drakul, M.; Čadež, V.M.; Bajčetić, J.; L. C. Popović, D.B.; Nina, A. Behaviour of electron content in the ionospheric D-region during solar X-ray flares. *Serb. Astron. J.* **2016**, *193*, 11–18.
40. Srećković, V.; Šulić, D.; Vujičić, V.; Jevremović, D.; Vyklyuk, Y. The effects of solar activity: Electrons in the terrestrial lower ionosphere. *J. Geograph. Inst. Cvijic* **2017**, *67*, 221–233. [[CrossRef](#)]
41. Morgan, R.R. *World-Wide VLF Effective Conductivity Map*; Westinghouse Electric: Cranberry Township, PA, USA, 1968. [[CrossRef](#)]
42. Wait, J.R.; Spies, K.P. *Characteristics of the Earth-Ionosphere Waveguide for VLF Radio Waves*; NBS Technical Note: Boulder, CO, USA, 1964. [[CrossRef](#)]
43. Belrose, J.S.; Burke, M.J. Study of the Lower Ionosphere using Partial Reflection: 1. Experimental Technique and Method of Analysis. *J. Geophys. Res.* **1964**, *69*, 2799–2818. [[CrossRef](#)]
44. Kane, J. Re-evaluation of ionospheric electron densities and collision frequencies derived from rocket measurements of refractive index and attenuation. *J. Atmos. Terr. Phy.* **1961**, *23*, 338–347. [[CrossRef](#)]
45. Mitra, A.P. (Ed.) *Ionospheric Effects of Solar Flares*; Astrophysics and Space Science Library; Springer Nature: Cham, Switzerland, 1974; Volume 46. [[CrossRef](#)]
46. Ferguson, J.A. *Ionospheric Profiles for Predicting Nighttime VLF/LF Propagation*; Technical report; Naval Ocean Systems Center: San Diego, CA, USA, 1980. [[CrossRef](#)]
47. Kumar, A.; Kumar, S. Solar flare effects on D-region ionosphere using VLF measurements during low- and high-solar activity phases of solar cycle 24. *Earth Planets Space* **2018**, *70*, 29. [[CrossRef](#)]
48. Hayes, L.A.; Gallagher, P.T.; McCauley, J.; Dennis, B.R.; Ireland, J.; Inglis, A. Pulsations in the Earth's Lower Ionosphere Synchronized With Solar Flare Emission. *J. Geophys. Res.-Space* **2017**, *122*, 9841–9847.
49. Cohen, M.B.; Inan, U.S.; Paschal, E.W. Sensitive Broadband ELF/VLF Radio Reception With the AWESOME Instrument. *IEEE Trans. Geosci. Remote Sens.* **2010**, *48*, 3–17. [[CrossRef](#)]
50. Nina, A.; Čadež, V.M.; Bajčetić, J.; Mitrović, S.T.; Popović, L.Č. Analysis of the Relationship Between the Solar X-ray Radiation Intensity and the D-Region Electron Density Using Satellite and Ground-Based Radio Data. *Solar Phys.* **2018**, *293*, 64. [[CrossRef](#)]
51. Ammar, A.; Ghalila, H. Estimation of nighttime ionospheric D-region parameters using tweek atmospheric observations for the first time in the North African region. *Adv. Space Res.* **2020**, *66*, 2528–2536.
52. Bilitza, D. IRI the International Standard for the Ionosphere. *Adv. Radio Sci.* **2018**, *16*, 1–11.
53. Thomson, N.R.; Clilverd, M.A.; Rodger, C.J. Midlatitude ionospheric D region: Height, sharpness, and solar zenith angle. *J. Geophys. Res. Space* **2017**, *122*, 8933–8946.



Article

The Influence of Solar X-ray Flares on SAR Meteorology: The Determination of the Wet Component of the Tropospheric Phase Delay and Precipitable Water Vapor

Aleksandra Nina ^{1,*}, Jelena Radović ², Giovanni Nico ^{3,4}, Luka Č. Popović ^{5,6,7}, Milan Radovanović ^{8,9}, Pier Francesco Biagi ¹⁰ and Dejan Vinković ¹¹

¹ Institute of Physics Belgrade, University of Belgrade, 11080 Belgrade, Serbia

² Department of Atmospheric Physics, Faculty of Mathematics and Physics, Charles University, Ke Karlovu 3, 12116 Prague, Czech Republic; 30665473@o365.cuni.cz

³ Istituto per le Applicazioni del Calcolo (IAC), Consiglio Nazionale delle Ricerche (CNR), 70126 Bari, Italy; g.nico@ba.iac.cnr.it

⁴ Department of Cartography and Geoinformatics, Institute of Earth Sciences, Saint Petersburg State University (SPSU), 199034 Saint Petersburg, Russia

⁵ Astronomical Observatory, 11060 Belgrade, Serbia; lpopovic@aob.rs

⁶ Department of Astronomy, Faculty of Mathematics, University of Belgrade, 11000 Belgrade, Serbia

⁷ Faculty of Science, University of Banja Luka, 78000 Banja Luka, Republic of Srpska, Bosnia and Herzegovina

⁸ Geographical Institute "Jovan Cvijić" SASA, 11000 Belgrade, Serbia; m.radovanovic@gi.sanu.ac.rs or milan.georgaf@gmail.com

⁹ Institute of Sports, Tourism and Service, South Ural State University, 454080 Chelyabinsk, Russia

¹⁰ Physics Department, Università di Bari, 70125 Bari, Italy; pf.biagi@gmail.com

¹¹ Science and Society Synergy Institute, B.J. Jelacica 22, 40000 Čakovec, Croatia; dejan@iszd.hr

* Correspondence: sandrast@ipb.ac.rs



Citation: Nina, A.; Radović, J.; Nico, G.; Popović, L.Č.; Radovanović, M.; Biagi, P.F.; Vinković, D. The Influence of Solar X-ray Flares on SAR Meteorology: The Determination of the Wet Component of the Tropospheric Phase Delay and Precipitable Water Vapor. *Remote Sens.* **2021**, *13*, 2609. <https://doi.org/10.3390/rs13132609>

Academic Editor: Piotr Samczynski

Received: 18 May 2021

Accepted: 25 June 2021

Published: 2 July 2021

Publisher's Note: MDPI stays neutral with regard to jurisdictional claims in published maps and institutional affiliations.



Copyright: © 2021 by the authors. Licensee MDPI, Basel, Switzerland. This article is an open access article distributed under the terms and conditions of the Creative Commons Attribution (CC BY) license (<https://creativecommons.org/licenses/by/4.0/>).

Abstract: In this work, we study the impact of high-energy radiation induced by solar X-ray flares on the determination of the temporal change in precipitable water vapor (Δ WPV) as estimated using the synthetic aperture radar (SAR) meteorology technique. As recent research shows, this radiation can significantly affect the ionospheric D-region and induces errors in the estimation of the total electron content (TEC) by the applied models. Consequently, these errors are reflected in the determination of the phase delay and in many different types of measurements and models, including calculations of meteorological parameters based on SAR observations. The goal of this study is to quantify the impact of solar X-ray flares on the estimation of Δ WPV and provide an estimate of errors induced if the vertical total electron content (VTEC) is obtained by single layer models (SLM) or multiple layer models (MLM) (these models do not include ionosphere properties below the altitude of 90 km as input parameters and cannot provide information about local disturbances in the D-region). The performed analysis is based on a known procedure for the determination of the D-region electron density (and, consequently, the vertical total electron content in the D-region (VTEC_D)) using ionospheric observations by very low frequency (VLF) radio waves. The main result indicates that if the D-region, perturbed by medium-sized and intense X-ray flares, is not modeled, errors occur in the determination of Δ WPV. This study emphasizes the need for improved MLMs for the estimation of the TEC, including observational data at D-region altitudes during medium-sized and intense X-ray flare events.

Keywords: ionospheric D-region; VLF/LF signals; remote sensing; SAR meteorology; phase delay; precipitable water vapor; solar X-ray flare; modeling

1. Introduction

Earth observations based on remote sensing by synthetic aperture radar (SAR) signals can be applied to different types of detection and modeling. In particular, SAR interferometry (InSAR) provides useful information in many applications related to the measurement

of displacements and, more recently, in meteorology [1]. SAR meteorology is a recent technique that aims to map precipitable water vapor (PWV) with a high spatial resolution [2–4]. The temporal change of PWV between two SAR observations along the same orbit is related to the propagation delay in the atmosphere through a constant that changes slightly based on the properties of the vertical profiles of the atmospheric temperature [5]. Even if the temporal sampling frequency of SAR PWV maps is lower than that of the global navigation satellite system (GNSS) PWV measurements, their higher spatial resolution has a positive impact when assimilated in numerical weather prediction (NWP) models [6–9]. This can enhance the capability of NWP models to compute the propagation delay in the atmosphere [10] with advantages in other InSAR applications (e.g., the measurement of terrain displacements [11–13] and snow water equivalent (SWE) [14,15]).

The basic assumption of SAR meteorology is that there are no terrain displacements between two passes of a SAR sensor over the area of interest, along the same orbit, and that all other phenomena that can affect the propagation delay are negligible (see [6] for more details). In this case, the temporal change in PWV is related to the temporal change in the wet propagation delay between the two passes. However, as a result of the constant exposure to numerous influences, the properties of a medium, which affect signal propagation, are time dependent, and corrections in the calculations are necessary in some cases. The sources of these variations originate in different terrestrial layers and in outer space. In the second case, the ionosphere has the most significant influence on the variability of SAR signal propagation. For this reason, the determination of the total electron content (TEC), a quantity which describes ionospheric influence on electromagnetic signal delay (P_1), is important. However, insufficient knowledge of perturber characteristics and atmospheric responses make its exact modeling impossible and many approximations must be used because of the various limitations of current remote sensing techniques.

The existing models for the calculation of the vertical total electron content (VTEC) are based on observational data and expressions that give the electron density space dependencies [16–20]. These observational data relate to one (single layer models) or a few (multiple layer models) altitudes which, because of the large electron density, primarily lie in the upper ionosphere. For this reason, these models cannot “see” local ionospheric disturbances at the D-region altitudes (50–90 km) and, consequently, do not provide a good enough approximation of P_1 for satellite signals in periods when intense disturbances dominate the lower ionosphere. This problem is reported for the first time in [21] a study of satellite signal delay in the ionospheric D-region disturbed by a solar X-ray flare.

The increased X-radiation emitted during a solar X-ray flare primarily affects the ionospheric D-region, in which the electron density and corresponding part of the vertical total electron content (VTEC_D) can increase by more than two orders of magnitude with respect to their values under quiet conditions [22–24]. Although the electron density in the D-region is lower than in the F-region, whose contribution is dominant in the TEC, the study presented in [21] indicates that solar X-ray flare-induced disturbances within the D-region can be important in calculating and modeling satellite signal delays. As a consequence, the results obtained in this paper indicate the need for further analyses concerning the influence of solar X-rays on the application of observations by GNSS and SAR signals.

In this paper, we focus on SAR meteorology and the estimations of $\Delta\phi_{\text{wet}}$ and differences in the precipitable water vapor (ΔPWV) during periods in which the master and slave images are recorded by a SAR satellite. We present a procedure for modeling the correction factor that should be included in the determination of $\Delta\phi_{\text{wet}}$ (B_D), and the correction factor that should be included in the determination of ΔPWV (C_D) if the influence of a solar X-ray flare is present in one of the two considered time periods. The study consists of two analyses: first, we consider one particular X-ray flare and calculate B_D and C_D dependencies on the X-ray flux during this event; second, we determine B_D and C_D for maximum X-ray flux for solar X-ray flares using ionospheric parameters derived in [24] and based on the statistical analysis presented in [25]. In both cases, four frequencies are considered: 1.2 GHz

and 5.4 GHz, which are the operating frequencies of radar systems on board the advanced land observing satellite-2 (ALOS-2) and Sentinel-1 satellites, respectively; 0.43 GHz, which is the frequency of the radar system on board the planned BIOMASS mission; and 3.4 GHz, which is one of the two frequencies that will be used by the radar system on board the planned joint mission involving National Aeronautics and Space Administration (NASA) and Indian Space Research Organisation (ISRO), known as the NASA-ISRO Synthetic Aperture Radar (NISAR) (the other frequency is 1.2 GHz, as is the case for ALOS-2).

The paper is organized as follows. After describing the geostationary operational environmental satellite (GOES), very low/low frequency (VLF/LF), and SAR measurements in Section 2, we present our proposed methodology in Section 3. The results of the presented model when apply to the particular event and ionospheric conditions at the X-ray flux maximum, during class-C and -M solar X-ray flares, are shown in Section 4. The conclusions of this study are given in Section 5.

2. Observations

The procedure presented in this study is based on data collected by the GOES satellite measuring the X-ray flux and by VLF/LF receivers using radio waves to sound the lower ionosphere. In addition, the proposed methodology needs the working frequency of SAR systems as an input parameter.

2.1. GOES Satellite Measurements

The measurements of solar X-ray flux provided by the GOES satellite allow for the detection of solar X-ray flares and the analyses of the energy properties of the ionized radiation perturbing the ionospheric D-region. These measurements are captured by two detectors in the energy channels A and B, corresponding to the wavelength domains 0.05 nm–0.4 nm and 0.1 nm–0.8 nm, respectively.

Considering that the temporal evolutions of fluxes recorded by these detectors are different, it is first necessary to pay attention to the determination of the X-ray flux values Φ relevant to this study. The contribution of X-ray photons with wavelength λ in total ionization in the terrestrial ionosphere depends on the altitude (e.g., see [26]). However, the comparison of the temporal evolution of the electron density at a given altitude, and fluxes recorded by the GOES energy channels A and B, presented in [27], shows that the recorded flux in channel A is more relevant for the lower D-region, and that the recorded flux in GOES channel B better describes the influence of an X-ray flare in the upper part of this ionospheric layer. Considering that the electron density increases with altitude, i.e., the upper D-region provides the dominant contribution to the $VTEC_D$, we assume that Φ is the flux recorded by the GOES channel B. The data recorded through this channel are also used in many previous studies of reactions in the low ionosphere [28–30].

Datasets of the X-ray fluxes recorded by the GOES satellites with samples of approximately 2 s are available on the NOAA's National Centers for Environmental Information website (<http://satdat.ngdc.noaa.gov/sem/goes/data>, accessed on 18 May 2021). Values corresponding to the X-ray flare that occurred on 6 January 2015 are shown in the upper left panel of Figure 1.

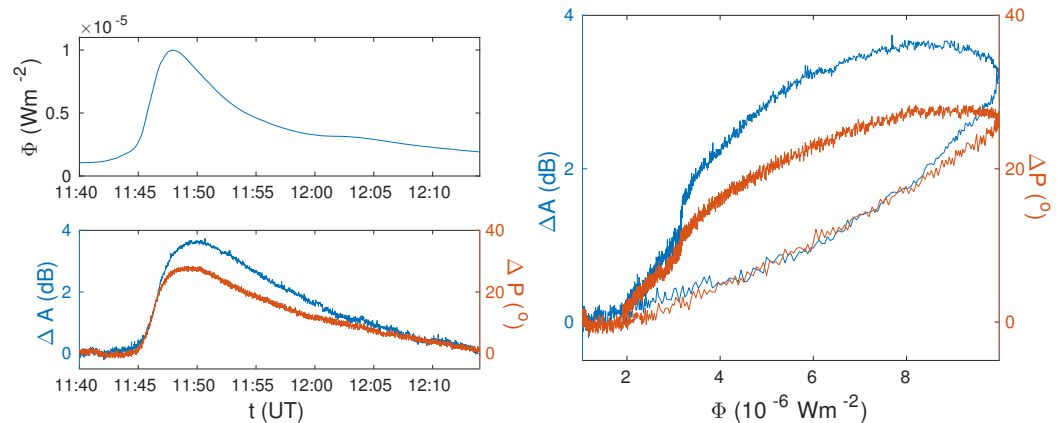


Figure 1. Upper left panel: time dependency of the energy X-ray flux (Φ) during the flare that occurred on 6 January 2015. Bottom left panel: time dependences of the amplitude (ΔA) and phase (ΔP) changes with respect to quiet conditions. Right panel: relationships between ΔA , ΔP , and X-ray flux Φ .

2.2. VLF/LF Measurements

The VLF/LF radio waves propagate in the Earth–ionosphere waveguide, the upper border of which lies in the analyzed atmospheric layer. Applications of this measurement technique in lower ionospheric observations and research are based on the fact that changes in the ionospheric electron density have the most significant influence on variations in the signal amplitude and phase recorded by a VLF/LF receiver. This makes the VLF/LF radio technique a useful tool for remote sensing in the ionosphere D-region. For this reason, we are able to study the influences of many astrophysical and terrestrial phenomena in this layer, such as ionospheric disturbances induced by gamma ray bursts [31,32], solar X-ray flares [33–36], tropical cyclones [37–39], and lightning [40–42]. In addition to independent receivers, there are several networks that are very important for the spatial analyses of local perturbations, such as those induced by earthquakes (the International Network for Frontier Research on Earthquake Precursors (INFREP) [43]) and lightning (the World Wide Lightning Location Network (WWLLN) [44]).

Practical applications of D-region disturbance modeling based on data recorded using this type of observational equipment are very important during solar X-ray flares. In certain cases, intense disturbances can last several hours and the electron density can increase by more than two orders of magnitude [22,23]. For this reason, we chose to analyze periods when this phenomenon affects the Earth’s atmosphere.

Firstly, in relation to the analysis of a particular event, we consider the amplitude (ΔA) and phase (ΔP) changes with respect to quiet conditions for signal emitted by the DHO transmitter in Germany and recorded by the atmospheric weather electromagnetic system for observation modeling and education (AWESOME) receiver [45] located in Belgrade, Serbia. The temporal evolution of the signal characteristics and their dependencies on X-ray flux during the considered flare, which occurred on 6 January 2015, are presented in Figure 1. As one can see, both dependencies on X-ray flux have hysteresis-like shapes; these are the result of the ionospheric plasma properties response to the increase in the photo-ionization rate, which itself depends on electron loss processes.

2.3. SAR Characteristics

Frequency and polarization are the two main characteristics of the SAR signal, useful when modeling their propagation in the ionosphere D-region. Because this paper is focused on the mitigation of ionosphere artifacts in SAR meteorology applications, we only

consider the frequency of the SAR signal. Generally, propagation delay maps are obtained by interferometrically processing two SAR images to derive the interferometric phase [10]:

$$\Delta\varphi_{\text{atm}} = \frac{4\pi}{\lambda} \Delta R_{\text{atm}} = 10^{-6} \frac{4\pi}{\lambda} \int_0^{H_{\text{sat}}} \Delta N dh, \quad (1)$$

where ΔR_{atm} and $\Delta\varphi_{\text{atm}}$ are the temporal changes of the range and interferometric phase delays due to propagation through the whole atmosphere at the acquisition times of the master and slave SAR images, respectively, λ is the radar wavelength, H_{sat} is the altitude of satellite, and ΔN is the temporal change in refractivity along the propagation path of the radar signal. The relationship between the interferometric phase and propagation delay solely depends on the signal frequency. If fully polarized SAR images are used, other effects can be observed and quantified, such as the Faraday rotation effect. However, this effect does not affect the propagation delay and it is not taken into consideration as a possible artifact in SAR meteorology applications. The mapping of temporal change in PWV requires the estimation of the propagation delay caused by the wet component of atmospheric refractivity and the vertical profile of temperature [5]:

$$\Delta\text{PWV} = \Pi ZWD, \quad (2)$$

where Π is a function of the mean temperature along a vertical profile and ZWD is the zenith wet delay obtained by projecting the wet component of the propagation delay in a vertical direction [5]. The estimation of the wet delay is performed by modeling and removing the temporal change of the other components of propagation delay (mainly the hydrostatic components, but also others related to the ionosphere) from the ΔR_{atm} . The impact of uncertainty on the estimation of the propagation delay is studied in [10]. In this paper, we focus on the C-, L-, and P-bands. The C-band is of key importance for SAR meteorology applications as a result the free access to Sentinel-1 SAR data. The L-band is more applicable in atmospheric studies, because it is directly comparable to GNSS measurements, which work in the L-band. However, thus far, the L-band ALOS-2 mission does not provide data with the same temporal revisiting time as Sentinel-1. The new satellites for observation and communications (SAOCOM) mission of Argentina's space agency [46] and NISAR, the joint mission between NASA and ISRO, [47], will increase the availability of L-band SAR data. ALOS-2 and SAOCOM work in the following frequencies: $f = 1.200$ GHz and $f = 1.275$ GHz, respectively. NISAR will carry both an L-band ($\lambda = 24$ cm) and S-band: ($\lambda = 9$ cm) radar. In this work, we also consider the P-frequency band that will be used by the BIOMASS mission planned to be launched by the European Space Agency in 2022 [48]. The frequencies and wavelengths of these satellites are summarized in Table 1.

Table 1. The ranges, operating frequencies (f), wavelengths (λ), and angles (θ) of the considered satellites.

Satellite	Range	f (GHz)	λ (cm)	θ [°]
Sentinel-1A/B	C	5.4	5.5	29.1–46
NISAR	S	3.2	9.3	33–47
ALOS-2	L	1.2	24	8–70
SAOCOM	L	1.275	24	8–70
NISAR	L	1.2	24	33–47
BIOMASS	P	0.43	70	23–60

3. Modeling ΔPWV Corrections Resulting from the Influence of a Solar X-ray Flare

In this section, we describe a methodology for modeling the influence of the X-ray flare-perturbed D-region on the measurements of ΔPWV currently obtained by InSAR

meteorology and provide a means to estimate the necessary correction resulting from X-ray flare effects. Modeling of the solar X-ray-perturbed D-region influence on ΔPWV can be divided into two steps: 1. calculations of the electron density (N_e) and, consequently, $VTEC_D$; 2. the determination of the corresponding correction factors B_D and C_D , in calculations of $\Delta\phi_{wet}$ and ΔPWV , respectively. A description of these steps is given in the following, and a schematic view of this methodology is presented in Figure 2.

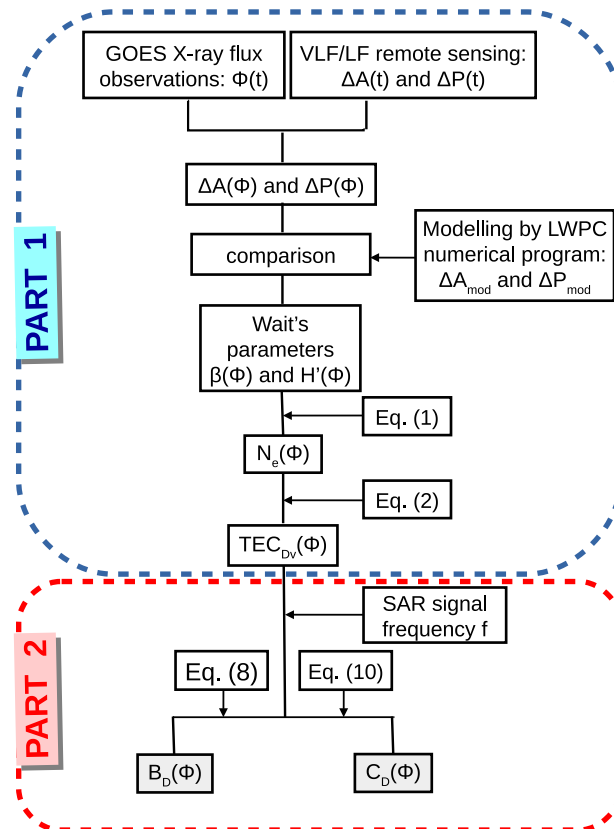


Figure 2. Flow-chart of the proposed methodology.

3.1. Determination of $VTEC_D$

The determination of $VTEC_D$ during a solar X-ray flare is explained in [21] in detail. In this study, we apply very similar procedures, which substitutes dependencies on the time evolution to dependencies on the X-ray flux. It consists of the observation and modeling, and its main steps are as follows:

- The determination of the period when the considered X-ray flare affected the terrestrial atmosphere from data collected by a GOES satellite;
- The determination of the considered time period from the temporal evolution of the DHO signal amplitude and phase recorded by the AWESOME VLF receiver in Belgrade. These variations are used because the ionosphere perturbations last longer than the increase in the X-radiation;
- The extraction of time series data recorded by the GOES energy channel B ($\Phi(t)$), and the VLF receiver ($\Delta A(t)$, and $\Delta P(t)$) in the considered time interval;
- The determination of $\Delta A(\Phi)$ and $\Delta P(\Phi)$. As presented in Figure 2, these relationships are obtained in comparison with the recorded datasets (given in time);
- The determination of $N_e(\Phi, h)$ in the D-region altitude domain. We use the Wait model of the ionosphere [49], which is based on two ionospheric parameters: the “sharpness” (β) which describes the electron density vertical gradient, and signal reflection height (H') which shows at what altitude the VLF or LF signal is reflected from the ionosphere. These parameters are determined by comparing the recorded values ΔA and ΔP

with corresponding values modeled using the long-wave propagation capability (LWPC) numerical program for the simulation of the signal propagation in the Earth–ionosphere waveguide developed by the Space and Naval Warfare Systems Center, San Diego, USA [50]. This procedure is explained in [51] and is applied in several previous studies [22,52,53]. The initial values of Wait’s parameters β and H' in quiet conditions before the influence of the considered flare are determined using the Quiet Ionospheric D-Region (QIonDR) model [54]. Knowledge of the time evolution of Wait’s parameters allows the electron density time-altitude distribution to be calculated using equation [55]:

$$N_e(t, h) = 1.43 \times 10^{13} e^{-\beta(t)H'(t)} e^{(\beta(t)-0.15)h}, \quad (3)$$

which is used in numerous previous papers [56–59]. Here, N_e , β , and H' and the considered D-region altitude h are given in m^{-3} , km^{-1} and km , respectively;

- The determination of the vertical total electron content time evolution $VTEC_D(t)$ within the D-region altitude domain h_D (60–90 km) using Equation [24]:

$$VTEC_D(\Phi) = \int_{h_D} N_e(\Phi, h) dh. \quad (4)$$

The obtained values of $VTEC_D$ are input values in the second part of the presented procedure.

3.2. Determination of B_D and C_D

The determination of B_D and C_D depends on both the D-region and SAR signal properties. In this study, we present a procedure for its estimation. Before describing this method, it is important to note that a solar X-ray flare significantly influences the determination of $\Delta\phi_{wet}$ and ΔPWV during one or both periods relevant for master and slave SAR images. However, the second case is very rare and, for this reason, we focus our attention on the first.

Considering that $\Delta\phi_{wet}$ is one of the components of the phase delay $\Delta\phi$, it can be calculated from Equation [9]:

$$\Delta\phi = \Delta\phi_{top} + \Delta\phi_{wet} + \Delta\phi_{hyd} + \Delta\phi_{ion}, \quad (5)$$

where $\Delta\phi_{top}$, $\Delta\phi_{hyd}$, and $\Delta\phi_{ion}$ relate to changes in the terrain morphology, the hydrostatic component of tropospheric delay, and ionospheric delay during the two considered periods, respectively. Because a solar X-ray flare has no influence on terrain morphology or tropospheric parameters, Equation (5) demonstrates that parameter B_D represents the difference in $\Delta\phi_{wet}$, in cases in which the influence of X radiation is and is not considered (relevant values in the following are indicated by “*” and “o” in the superscript, respectively) [16]:

$$B_D = \Delta\phi_{ion}^o - \Delta\phi_{ion}^*. \quad (6)$$

The phase delay in the ionosphere due VTEC is given by the following [16]:

$$\phi_{ion} = \frac{4\pi}{\lambda} \frac{K}{f^2 \cos(\theta_{look})} VTEC, \quad (7)$$

which gives their differences: $\Delta\phi_{ion}^o = \frac{4\pi}{\lambda} \frac{K}{f^2 \cos(\theta_{look})} \Delta VTEC$ and $\Delta\phi_{ion}^{m/s} = \frac{4\pi}{\lambda} \frac{K}{f^2 \cos(\theta_{look})} (\Delta VTEC \mp VTEC_D)$. Here, $K = 40.28 \text{ m}^3/\text{s}^2$, $\Delta VTEC$ is the difference in the VTEC between the slave and master acquisition times, where $t_{slave} > t_{master}$, and $VTEC_D$ is the additional VTEC variation due to an anomaly in the D-region. This quantity is added to or subtracted from $\Delta VTEC$ if this X-ray flare occurs at the slave or master acquisition time, respectively. Cases in which a flare affects the atmosphere at the master and slave acquisition times are

indicated by subscripts “m” and “s”, respectively. The combination of these relationships with Equations (6) and (7) gives the equation for $B_{D_{m/s}}$ in the following form:

$$B_{D_{m/s}} = \pm \frac{4\pi}{\lambda} \frac{K}{f^2 \cos(\vartheta_{\text{look}})} \text{VTEC}_D, \quad (8)$$

where one can see that B_D is proportional to VTEC_D and $\cos^{-1}(\vartheta_{\text{look}})$. ΔPWV can be determined from the unwrapped phase $\Delta\phi$, which is obtained by filtering and unwrapping the wet component of the tropospheric delay $\delta\phi$ [5]:

$$\Delta\text{PWV} = \frac{\lambda}{4\pi} \frac{\cos(\vartheta_{\text{look}})}{\rho\xi} \delta\phi, \quad (9)$$

where λ is the radar wavelength, ϑ_{look} is the look angles along the swath, and ρ and ξ are constants, whose values are $1000 \text{ kg}\cdot\text{m}^{-3}$ (the density of water) and 6.4, respectively.

Assuming $\delta\phi^o - \delta\phi^* \approx B_{D_{m/s}}$, Equations (8) and (9) give

$$C_{D_{m/s}} = \Delta\text{PWV}^o - \Delta\text{PWV}^* = \pm \frac{K}{f^2 \rho \xi} \text{VTEC}_D. \quad (10)$$

This equation shows that correction factor C_D is proportional to VTEC_D and to f^{-2} . In other words, the influence of an X-ray flare on ΔPWV increases with its intensity, and has a larger effect on SAR signals with a lower frequency. In addition, it is important to note that the presented procedure demonstrates that the look angles along the swath ϑ_{look} do not affect C_D . This fact is a consequence of the linear dependence of $\Delta\phi_{\text{wet}}$ on $\cos(\vartheta_{\text{look}})$, and the reverse relationship between VTEC_D and $\cos(\vartheta_{\text{look}})$.

As one can see from Equations (8) and (10), absolute values of both correction factors are the same in cases when a solar X-ray flare occurs at the master and slave acquisition time. For this reason, we further analyze B_D and C_D , e.g., the absolute values of quantities $B_{D_{m/s}}$ and $C_{D_{m/s}}$, respectively.

4. Results and Discussion

The presented methodology for the estimation of the correction factors B_D and C_D is applied to two analyses relating to: 1. the dependencies of B_D and C_D on the X-ray flux (Φ) during one solar X-ray flare, and 2. the dependencies of B_D and C_D on the maximum X-ray flux (Φ_{max}) for flares of classes C and M.

4.1. Particular X-ray Flare Event

As it can be seen in previous studies (see, for example, [58]), variations in the D-region electron density during solar X-ray flares have very similar characteristics, which allows us to study the properties of the dependences $B_D(\Phi)$ and $C_D(\Phi)$ in analysis of one event. Here, we present a detailed analysis for period during the class-C9.9 X-ray flare, which occurred on 6 January 2015. In addition, we show the results obtained for two more flares of classes C8.8 and C6.1, which occurred on 5 May 2010 and 8 January 2014, respectively (see Supplementary Material).

According the methodology shown in Figure 2, the comparison of the observed amplitude ΔA and phase ΔP changes (see Figure 1), and the corresponding values obtained by modeling the considered VLF signal propagation using the LWPC numerical model gives us Wait's parameters β and H' for each value of the X-ray flux Φ (upper panel of Figure 3). As one can see, β first increases with Φ . Although Φ decreases after Φ_{max} , β continues to increase for some time and reaches a maximum value for $\Phi \approx 8.7 \times 10^{-6} \text{ Wm}^{-2}$, after which it begins to decrease. The changes in H' run counter to those of the first parameter. In both cases, the values are not equal for the same Φ before and after the X-ray flux maximum and these dependencies have hysteresis-like shapes. During the period in which Φ increases, the changes in Wait's parameters are slower for the smallest values of Φ . The properties are better visible in the dependencies of the electron density N_e on Φ and

altitude h before (the second panel) and after (the third panel) the X-ray flux maximum, as calculated by Equation (3). These properties are in agreement with the analysis given in [27], which describes them in detail. Here, we indicate that they can be explained according to complex processes in the ionospheric plasma, i.e., electron density changes depend on both ionization and electron loss processes, which induce an increase and decrease in N_e . The rate of the first type of processes (G) is larger than the second (L) during the increase in Φ and some time after its maximum value. In this period, N_e increases. After that, $G < L$ and N_e have the tendency to reach their initial values. Considering that L depends on the ionospheric state, its values are not the same for the same Φ before and after Φ_{\max} , which, together with the changes in the spectrum of the incoming X radiation in the considered area, explains the corresponding differences in N_e 's (and Wait's parameters') dependencies on Φ .

Finally, $VTEC_D$'s dependence on Φ is shown in the bottom panel of Figure 2. Its shape is the same as β , while the maximum difference for the same Φ is about one order of magnitude.

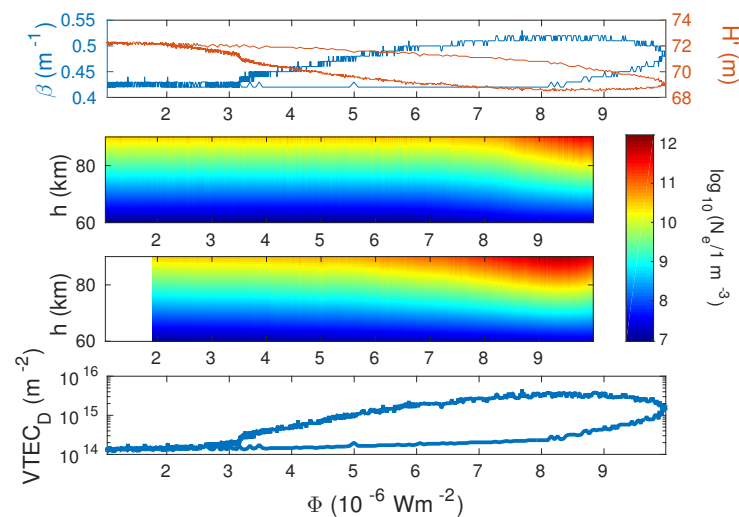


Figure 3. Dependencies of the modeled parameters on the X-ray flux (Φ) during the considered flare, which occurred on 6 January 2015. Upper panel: dependencies of Wait's parameters "sharpness" (β) and signal reflection height (H') on Φ . Middle panels: dependencies of $\log_{10}(N_e/1\text{ m}^{-3})$, where N_e is the electron density given in 1 m^{-3} , before (upper middle panel) and after (bottom middle panel) the X-ray flux maximum on Φ and altitude h . Bottom panel: dependencies of the vertical total electron content in the D-region ($VTEC_D$) on Φ .

The application of Equations (8) and (10) to the obtained values of $VTEC_D$, and signal frequencies $f_1 = 0.43\text{ GHz}$, $f_2 = 1.2\text{ GHz}$, $f_3 = 3.2\text{ GHz}$, and $f_4 = 5.4\text{ GHz}$, gives dependencies $B_D(\Theta, \Phi)$ and $C_D(\Phi)$, respectively.

To better visualize the signal frequency influence on $B_D(\Theta, \Phi)$, we use the same color map scale for all four graphs in Figure 4, which present the results for the BIOMASS (upper left graph), ALOS-2 (upper right graph), NISAR (bottom left graph), and Sentinel-1 (bottom right graph) satellites. The upper panels for each satellite correspond to the period before Φ_{\max} , while values obtained for the period after Φ_{\max} are presented in the bottom panels. As one can see, B_D varies more than one order of magnitude for all satellites and all angles during the considered flare. Its values strongly depend on the signal frequency ($\sim f^{-2}$) and differ more than one order of magnitude for the satellites with the lowest (BIOMASS) and the largest (Sentinel-1) frequency when the other parameters are the same. The maximal values of B_D are 25.36° , 18.86° , 3.55° , and 2.06° for the BIOMASS, ALOS-2, NISAR, and Sentinel-1 satellites, respectively. According to Equation (8), the maximal values of B_D correspond to Φ measured at the peak of $VTEC_D$. Variations with Θ are weak and they are more pronounced for the ALOS-2 satellite, in which the operating angle domain is the

widest and reaches the lowest values (as $B_D \sim \cos^{-1}(\Theta)$, these variations increase with Θ , which is clearly visible in the relevant graph). The maxima of B_D are for the largest Θ , which can be seen from Equation (8) and from the fact that Θ has values lower than 90° .

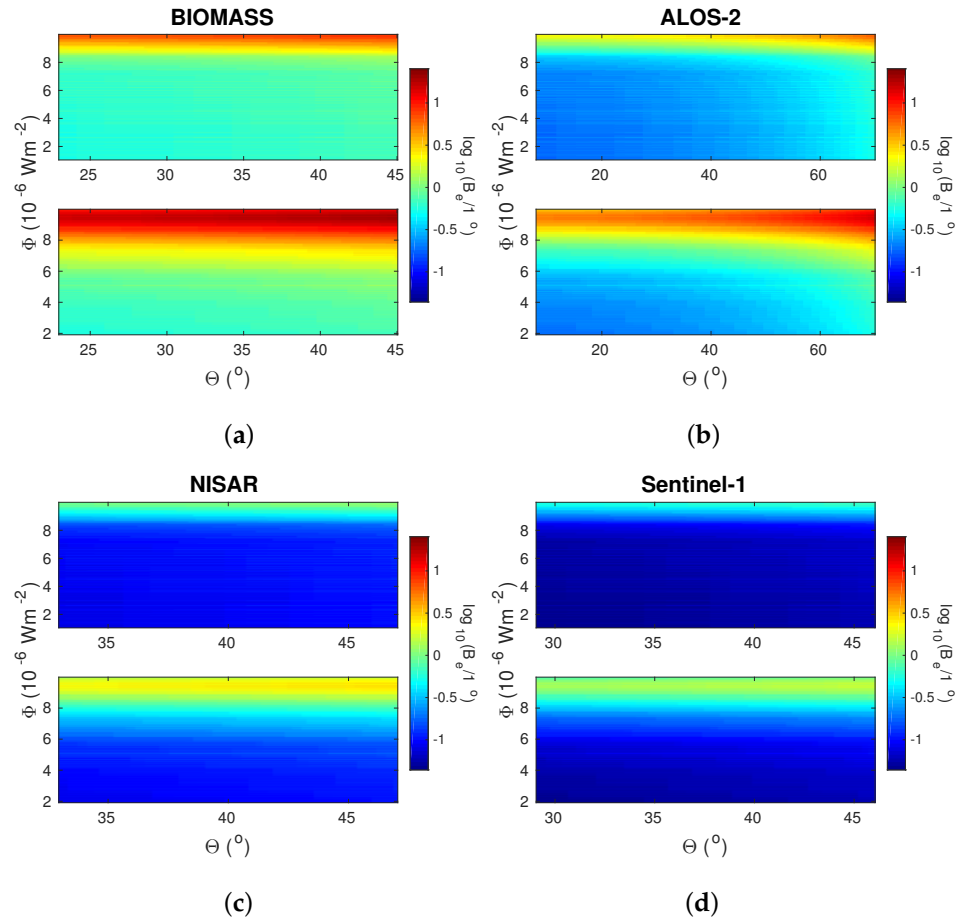


Figure 4. Dependencies of the correction factor in the determination of changes in the wet component of tropospheric phase delay (B_D) on the angle (Θ) and the X-ray flux (Φ) during the considered event for the four considered spaceborne synthetic aperture radar (SAR) systems: (a) BIOMASS (L-band); (b) advanced land observing satellite-2 (ALOS-2) (L-band); (c) National Aeronautics and Space Administration (NASA), Indian Space Research Organisation (ISRO), and synthetic aperture radar (NISAR) (S-band); and (d) Sentinel-1 (C-band).

Dependencies of C_D on Φ are shown in Figure 5. Their quantitative description (for one frequency) is the same as that for β and $VTEC_D$. As in the case of B_D , this correction factor is proportional to $VTEC_D$ and f^{-2} (see Equation (10)). For all frequencies, C_D reaches values that are more than one order of magnitude larger in the moment of the most intense D-region disturbance. Its maxima are 0.16 mm, 0.02 mm, 0.003 mm, and 0.001 mm for the BIOMASS, ALOS-2, NISAR, and Sentinel-1 satellites, respectively. To estimate the importance of these values, which represent errors in the modeling of ΔPWV due to the influence of the increased X-radiation during a solar X-ray flare, we calculated their ratio with absolute values of ΔPWV obtained in [60]. The domain of ΔPWV is from about -22 mm to 8 mm. Although they include the results of calculations with absolute values lower than 1 mm, we do not present them in Figure 6. This is because despite providing a large considered ratio $\delta C_D = \frac{C_D}{|\Delta PWV|} \times 100\%$, they are not as important for practical applications. As it can be seen in Figure 6, the obtained δC_D increases with $VTEC_D$ and reaches 15.6%, 2.0%, 0.3%, and 0.1% for the BIOMASS, ALOS-2, NISAR, and Sentinel-1 satellites, respectively. Here, we can see that the signal frequency is important in the

determination of the considered error, which, in the case of this flare of class C, is only larger than 10% for the BIOMASS satellite.

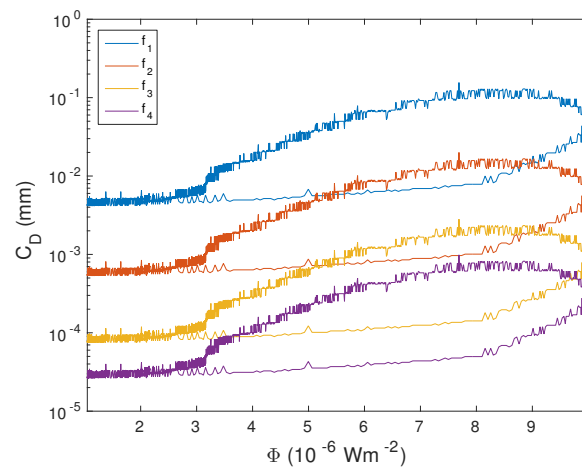


Figure 5. Dependence of the correction factor in the determination of changes in the precipitable water vapor (C_D) on the X-ray flux (Φ) during the considered event.

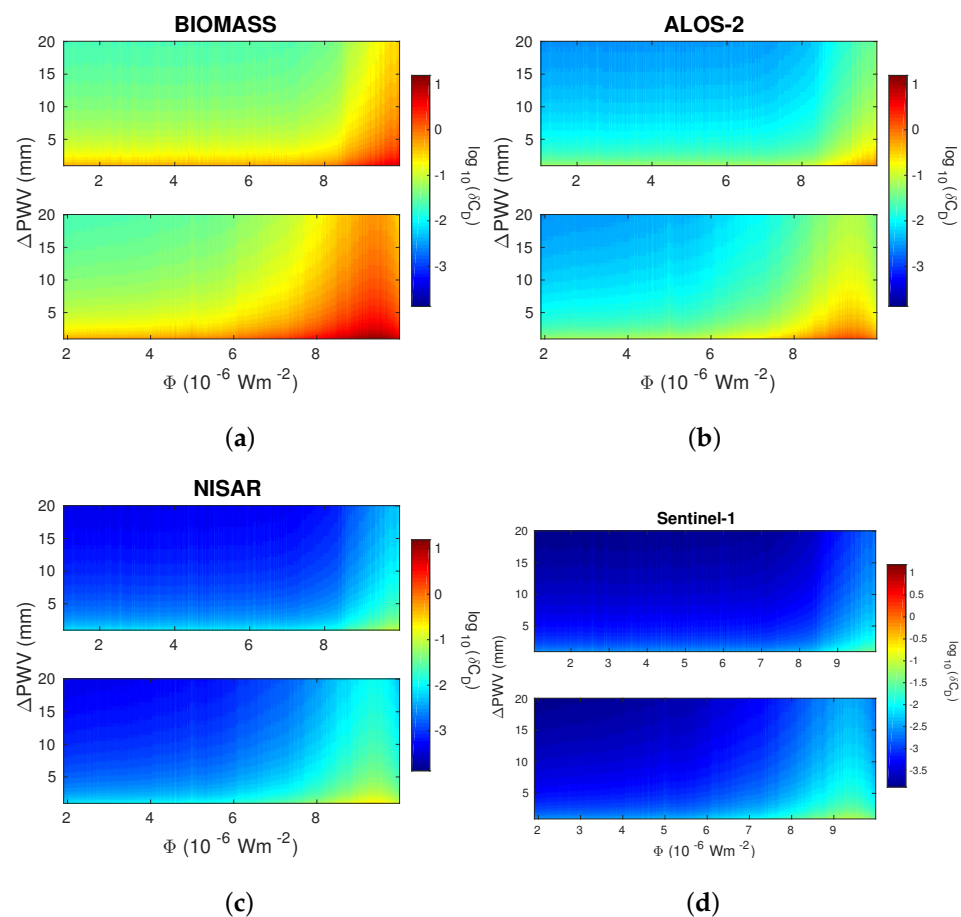


Figure 6. Dependencies of the ratio (in percent) of the correction factor in the determination of changes in the precipitable water vapor and absolute values of changes in the precipitable water vapor presented in [60] (δC_D) on the X-ray flux (Φ) and changes in the precipitable water vapor (ΔPWV) during the considered event for the four considered spaceborne synthetic aperture radar (SAR) systems: (a) BIOMASS (L-band); (b) advanced land observing satellite-2 (ALOS-2) (L-band); (c) National Aeronautics and Space Administration (NASA), Indian Space Research Organisation (ISRO), and synthetic aperture radar (NISAR) (S-band); and (d) Sentinel-1 (C-band).

As one can see in Supplementary Materials, very similar graphs are obtained for the other two analyzed X-ray flares. The plots are quite similar like those described in the previous text, and B_D , C_D , and δC_D reaches similar values like in the case of the first analyzed flare.

4.2. Maximum X Radiation Flux

To analyze the influence of the X-ray flare class on the determination of $\Delta\phi_{\text{wet}}$ and ΔPWV in SAR meteorology, we study the dependence of B_D and C_D on the radiation flux maximum Φ_{max} . In this case, we calculate the VTEC_D using expressions for Wait's parameters derived in [24] by processing data based on the observation and statistical study in [21,25]. Considering that the application of Equation (3) better fits with the values obtained by other models for flares of classes C and M than for flares of class X, we consider the dependency for $\Phi_{\text{max}} \leq 5 \times 10^{-5} \text{ Wm}^{-2}$. All calculations are performed using the same equations as in the previous corresponding analyses.

The dependences of Wait's parameters, the electron density at D-region heights, and the total electron content on Φ_{max} are shown in Figure 7. As one can see, all quantities increase with Φ_{max} except H' which has the opposite tendency. The maximum calculated VTEC_D ($2.4 \times 10^{16} \text{ m}^{-3}$) is more than five times that of the flare analyzed in the first part of this study ($4.6 \times 10^{15} \text{ m}^{-3}$), which again provides larger errors in the estimation of $\Delta\phi_{\text{wet}}$ and ΔPWV .

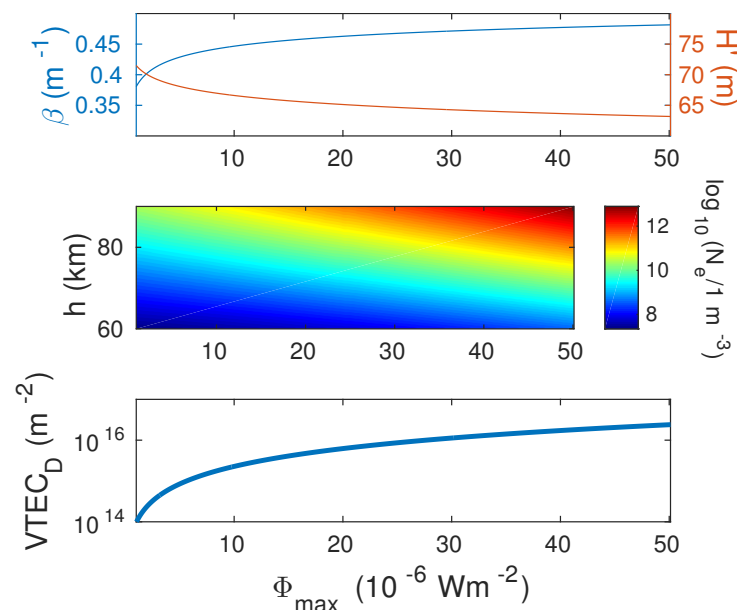


Figure 7. Dependences of the Wait's parameters “sharpness” (β) and signal reflection height (H') (upper panel) obtained in [24] based on data presented in [25], $\log_{10}(N_e/1 \text{ m}^{-3})$, where N_e is the electron density given in m^{-3} , at the D-region altitudes (h) (middle panel) and the vertical total electron content in the D-region (VTEC_D) (bottom panel) on the maximum X-ray flux (Φ_{max}).

The influences of f , Θ , and Φ_{max} on B_D are illustrated in Figure 8. According to Equation (8), B_D is proportional to f^{-2} and $\cos^{-1}(\Theta)$, as in the case of one event. However, in this analysis, B_D monotonically increases with Φ_{max} because of the increase in VTEC_D with this radiation flux. For the considered domains, the most important variations are recorded for different Φ_{max} (of more than two orders of magnitude). The influence of the chosen frequency is also important (they can provide variations in B_D for more than one order of magnitude), while the lowest significance has Θ , which, as in the first case, is the most pronounced for the ALOS-2 satellite. The maximum obtained values are 132.8° , 98.8° , 18.6° , and 10.8° for the BIOMASS, ALOS-2, NISAR, and Sentinel-1 satellites, respectively. This is more than five times larger than in the case of the flare considered in the first

part of this study, which indicates that the intensity of the considered X-ray flare has a significant influence.

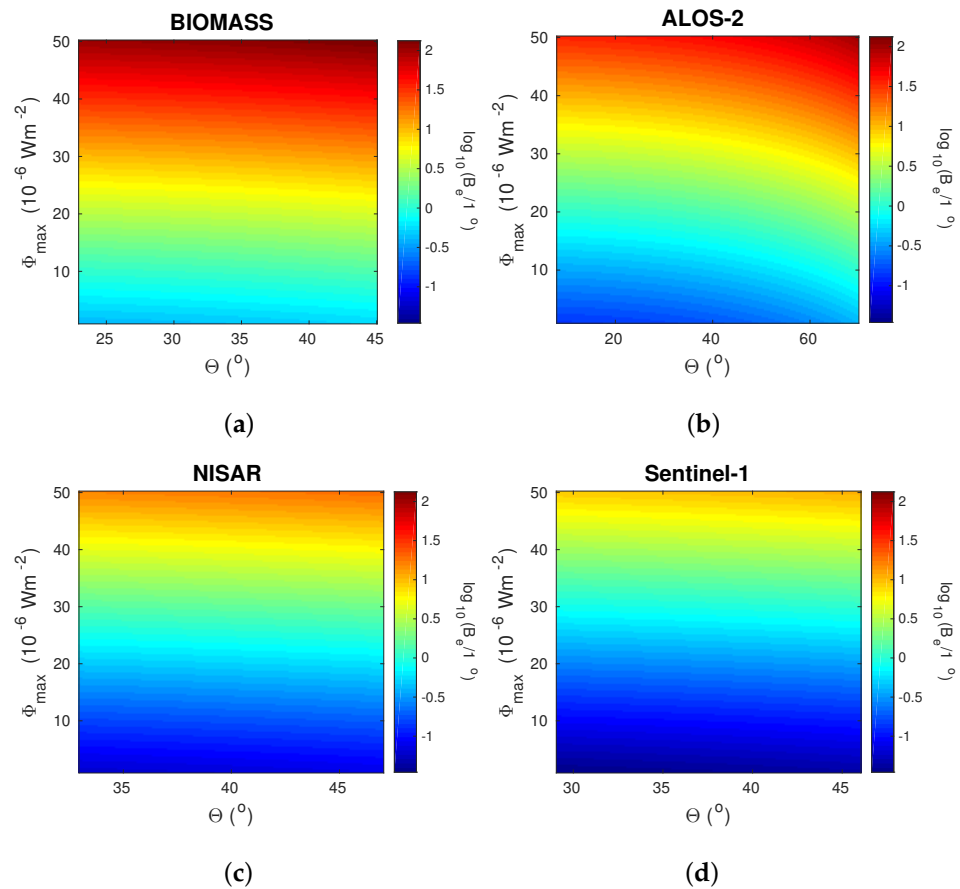


Figure 8. Dependencies of the correction factor in the determination of changes in the wet component of tropospheric phase delay (B_D) on the angle (Θ) and the X-ray flux maximum (Φ_{max}) for the four considered spaceborne synthetic aperture radar (SAR) systems: (a) BIOMASS (L-band); (b) advanced land observing satellite-2 (ALOS-2) (L-band); (c) National Aeronautics and Space Administration (NASA), Indian Space Research Organisation (ISRO), and synthetic aperture radar (NISAR) (S-band); and (d) Sentinel-1 (C-band).

Increases in C_D with Φ_{max} are shown in Figure 9. As is the case for the analysis of one flare, the considered correction factor decreases with signal frequency and, for M5 X-ray flares, reaches values of 0.81 mm, 0.10 mm, 0.015 mm, and 0.0052 mm for the BIOMASS, ALOS-2, NISAR, and Sentinel-1 satellites, respectively. The maximum obtained values reach 81.7%, 10.5%, 1.5%, and 0.5% of those for ΔPWV presented in [60] for the considered satellites, respectively.

The tendencies of the obtained dependencies $B_D(\Phi_{max})$ and $C_D(\Phi_{max})$ indicate that more intense flares (firstly, class X flares) can induce non-negligible errors in the determination of ϕ_{wet} and ΔPWV for the BIOMASS and ALOS-2 satellites (Figure 10).

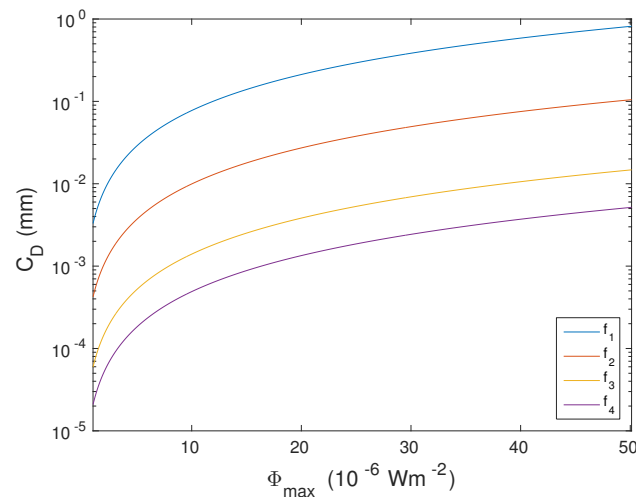


Figure 9. Dependence of the correction factor C_D on the X-ray flux maximum Φ_{max} .

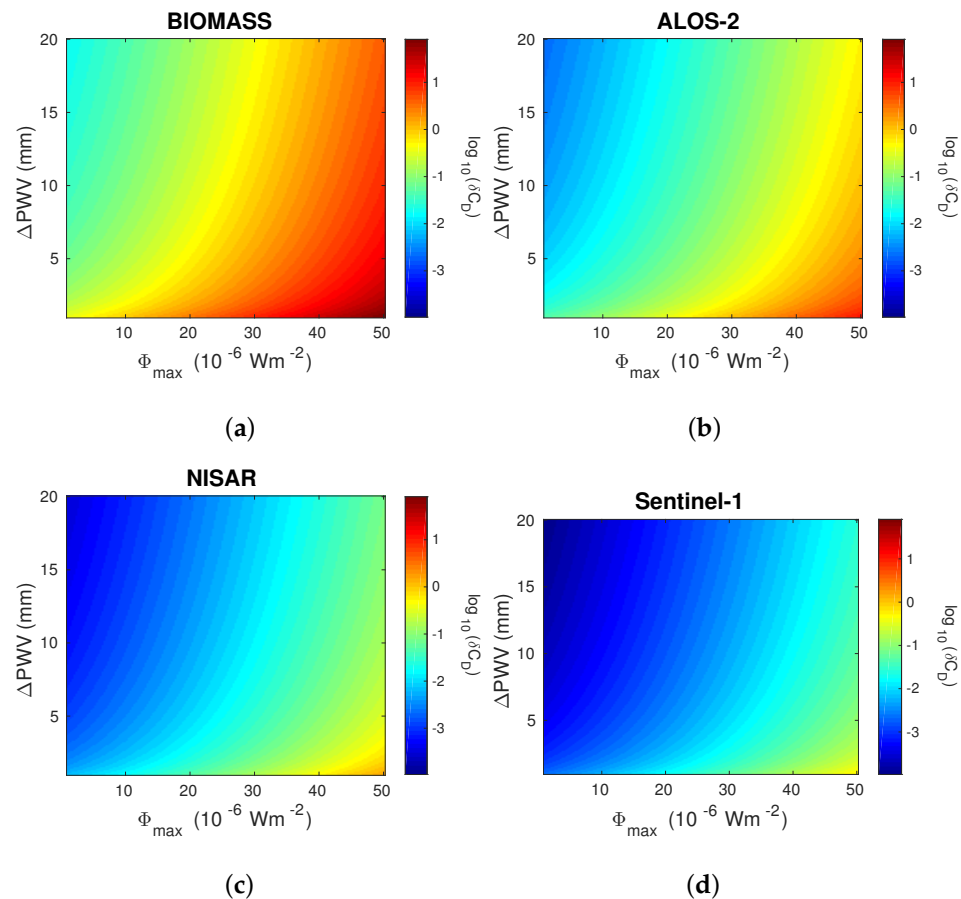


Figure 10. Dependencies of the ratio (in percent) of the correction factor in the determination of changes in the precipitable water vapor and absolute values of changes in the precipitable water vapor presented in [60] (δC_D) on the X-ray flux maximum (Φ_{max}) and changes in the precipitable water vapor (ΔPWV) for the four considered spaceborne synthetic aperture radar (SAR) systems: (a) BIOMASS (L-band); (b) advanced land observing satellite-2 (ALOS-2) (L-band); (c) National Aeronautics and Space Administration (NASA), Indian Space Research Organisation (ISRO), and synthetic aperture radar (NISAR) (S-band); and (d) Sentinel-1 (C-band).

5. Conclusions

In this paper, we study how neglecting the D-region electron density temporal variations in the determination of the total electron content by single and multiple layer models affects results in synthetic aperture radar meteorology when this ionospheric region is significantly disturbed. We present an analysis of the correction factors that should be included in the determination of differences in the wet component of tropospheric phase delay and precipitable water vapor obtained by synthetic aperture radar meteorology during a solar X-ray flare event. We study the dependence of these correction factors on X-ray flux during an X-ray flare event, and C- and M-class flares at the time of their maximum radiation intensity. The obtained results show the following:

- The correction factors for the same radiation flux are larger in the period after than in the period before the radiation maximum;
- During a solar X-ray flare event, the maxima of the considered correction factors pertain to the radiation flux that is lower than its maximum value and that occurred after the radiation maximum. For the X-ray flare that occurred on 6 January 2015, the correction factor that should be included in the determination of differences in the wet component of tropospheric phase delay reaches 25.36° , while the correction factor that should be included in the determination of temporal changes in the precipitable water vapor can reach 0.16 mm (this value can be more than 15% of the values for precipitable water vapor changes given in [60]);
- The correction factors increase with the maximum X-ray flux. For the considered fluxes, the correction factor that should be included in the determination of differences in the wet component of tropospheric phase delay can reach more than 130° while the correction factor that should be included in the determination of changes in the precipitable water vapor can reach 0.8 mm, which can be more than 80% of the values for precipitable water vapor changes given in [60];
- The correction factors are inversely proportional to the square of the frequency. The differences for the considered maximal and minimal frequencies are more than two orders of magnitude for the correction factor in the determination of changes in the wet component of tropospheric phase delay, and more than one order of magnitude for the correction factor in the determination of changes in the precipitable water vapor, in the case of the same X-ray intensity. The changes are also pronounced as regards the variation in the X-ray flux, while changes in B_D with the signal angle are the weakest (they are the largest in the case of the advanced land observing satellite-2 due to the wider operating angle range and the largest angles).

To conclude, this is the first study to analyze the errors induced by intense ionospheric D-region disturbances (in this study, induced by a solar X-ray flare) in the practical application of synthetic aperture radar signals. We found that the inclusion of the D-region altitude in the calculation of the total electron content, which is used to determine changes in the wet component of tropospheric phase delay and precipitable water vapor using synthetic aperture radar meteorology, is necessary during larger solar X-ray flare events. It has a larger influence on lower frequency signals and is most important for the BIOMASS satellite.

Supplementary Materials: The following are available online at <https://www.mdpi.com/article/10.3390/rs13132609/s1>, Table S1: The maximal values of the correction factor in the determination of changes in the wet component of tropospheric phase delay (BDmax), correction factor in the determination of changes in the precipitable water vapor (CDmax), and ratio (in percent) of the correction factor in the determination of changes in the precipitable water vapor and absolute values of changes in the precipitable water vapor presented in [1] (dCDmax) during a solar X-ray flare, which occurred on 5 May 2010 for the BIOMASS, ALOS-2, NISAR, and Sentinel-1 satellites, Table S2: The maximal values of the correction factor in the determination of changes in the wet component of tropospheric phase delay (BDmax), correction factor in the determination of changes in the precipitable water vapor (CDmax), and ratio (in percent) of the correction factor in the determination

of changes in the precipitable water vapor and absolute values of changes in the precipitable water vapor presented in [1] (dCDmax) during a solar X-ray flare, which occurred on 8 January 2014 for the BIOMASS, ALOS-2, NISAR, and Sentinel-1 satellites.

Author Contributions: Conceptualization, A.N.; methodology, A.N.; software, A.N.; validation, G.N., L.Č.P., P.F.B. and D.V.; formal analysis, A.N., J.R., G.N. and L.Č.P.; investigation, A.N.; resources, A.N.; data curation, A.N.; writing—original draft preparation, A.N. and G.N.; writing—review and editing, all authors; visualization, A.N.; funding acquisition, A.N., G.N. and M.R. All authors have read and agreed to the published version of the manuscript.

Funding: This research was funded by OT-4CLIMA Project, which was funded by the Italian Ministry of Education, University, and Research (D.D. 2261 del 6.9.2018, PON R&I 2014–2020). This research was also funded by the Institute of Physics Belgrade, Geographical Institute “Jovan Cvijić” SASA and Astronomical Observatory (the contract 451-03-68/2020-14/200002) through the grants by the Ministry of Education, Science, and Technological Development of the Republic of Serbia.

Institutional Review Board Statement: Not applicable.

Informed Consent Statement: Not applicable.

Data Availability Statement: Publicly available datasets were analyzed in this study. These data can be found here: <https://satdat.ngdc.noaa.gov/sem/goes/data/full/>, accessed on 18 May 2021.

Acknowledgments: This research is also provided within the COST Action CA15211.

Conflicts of Interest: The authors declare no conflict of interest.

References

- Miranda, P.M.A.; Mateus, P.; Nico, G.; Catalão, J.; Tomé, R.; Nogueira, M. InSAR Meteorology: High-Resolution Geodetic Data Can Increase Atmospheric Predictability. *Geophys. Res. Lett.* **2019**, *46*, 2949–2955. [\[CrossRef\]](#)
- Mateus, P.; Catalão, J.; Nico, G.; Benevides, P. Mapping Precipitable Water Vapor Time Series From Sentinel-1 Interferometric SAR. *IEEE Trans. Geosci. Remote Sens.* **2020**, *58*, 1373–1379. [\[CrossRef\]](#)
- Kinoshita, Y.; Shimada, M.; Furuya, M. InSAR observation and numerical modeling of the water vapor signal during a heavy rain: A case study of the 2008 Seino event, central Japan. *Geophys. Res. Lett.* **2013**, *40*, 4740–4744. [\[CrossRef\]](#)
- Hanssen, R.F.; Weckwerth, T.M.; Zebker, H.A.; Klees, R. High-Resolution Water Vapor Mapping from Interferometric Radar Measurements. *Science* **1999**, *283*, 1297–1299. [\[CrossRef\]](#) [\[PubMed\]](#)
- Mateus, P.; Nico, G.; Catalão, J. Maps of PWV Temporal Changes by SAR Interferometry: A Study on the Properties of Atmosphere’s Temperature Profiles. *IEEE Geosci. Remote Sens. Lett.* **2014**, *11*, 2065–2069. [\[CrossRef\]](#)
- Mateus, P.; Tomé, R.; Nico, G.; Catalão, J. Three-Dimensional Variational Assimilation of InSAR PWV Using the WRFDA Model. *IEEE Trans. Geosci. Remote Sens.* **2016**, *54*, 7323–7330. [\[CrossRef\]](#)
- Mateus, P.; Miranda, P.M.A.; Nico, G.; Catalão, J.; Pinto, P.; Tomé, R. Assimilating InSAR Maps of Water Vapor to Improve Heavy Rainfall Forecasts: A Case Study With Two Successive Storms. *J. Geophys. Res. Atmos.* **2018**, *123*, 3341–3355. [\[CrossRef\]](#)
- Kinoshita, Y.; Furuya, M. Localized Delay Signals Detected by Synthetic Aperture Radar Interferometry and Their Simulation by WRF 4DVAR. *SOLA* **2017**, *13*, 79–84. [\[CrossRef\]](#)
- Pierdicca, N.; Maiello, I.; Sansosti, E.; Venuti, G.; Barindelli, S.; Ferretti, R.; Gatti, A.; Manzo, M.; Monti-Guarnieri, A.V.; Murgia, F.; et al. Excess Path Delays From Sentinel Interferometry to Improve Weather Forecasts. *IEEE J. Sel. Top. Appl. Earth Obs. Remote Sens.* **2020**, *13*, 3213–3228. [\[CrossRef\]](#)
- Mateus, P.; Nico, G.; Catalão, J. Uncertainty Assessment of the Estimated Atmospheric Delay Obtained by a Numerical Weather Model (NMW). *IEEE Trans. Geosci. Remote Sens.* **2015**, *53*, 6710–6717. [\[CrossRef\]](#)
- Catalão, J.; Raju, D.; Nico, G. InSAR Maps of Land Subsidence and Sea Level Scenarios to Quantify the Flood Inundation Risk in Coastal Cities: The Case of Singapore. *Remote Sens.* **2020**, *12*, 296. [\[CrossRef\]](#)
- Aobpaet, A.; Cuenca, M.C.; Hooper, A.; Trisirisatayawong, I. InSAR time-series analysis of land subsidence in Bangkok, Thailand. *Int. J. Remote Sens.* **2013**, *34*, 2969–2982. [\[CrossRef\]](#)
- Chaussard, E.; Amelung, F.; Abidin, H.; Hong, S.H. Sinking cities in Indonesia: ALOS PALSAR detects rapid subsidence due to groundwater and gas extraction. *Remote Sens. Environ.* **2013**, *128*, 150–161. [\[CrossRef\]](#)
- Conde, V.; Nico, G.; Mateus, P.; Catalão, J.; Kontu, A.; Gritsevich, M. On The Estimation of Temporal Changes of Snow Water Equivalent by Spaceborne Sar Interferometry: A New Application for the Sentinel-1 Mission. *J. Hydrol. Hydromech.* **2019**, *67*, 93–100. [\[CrossRef\]](#)
- Gneriussen, T.; Hogda, K.A.; Johnsen, H.; Lauknes, I. InSAR for estimation of changes in snow water equivalent of dry snow. *IEEE Trans. Geosci. Remote Sens.* **2001**, *39*, 2101–2108. [\[CrossRef\]](#)
- Klobuchar, J.A. Design and characteristics of the GPS ionospheric time delay algorithm for single frequency users. In *PLANS '86-Position Location and Navigation Symposium*; Institute of Electrical and Electronics Engineers: New York, NY, USA, 1986.

17. Zhao, J.; Zhou, C. On the optimal height of ionospheric shell for single-site TEC estimation. *GPS Solut.* **2018**, *22*, 48. [[CrossRef](#)]
18. Daniell, R.J.; Brown, L. *PRISM: A Parameterized Real-Time Ionospheric Specification Model, Version 1.5*; Defense Technical Information Center: Fort Belvoir, VA, USA, 1995.
19. Nava, B.; Coisson, P.; Radicella, S. A new version of the NeQuick ionosphere electron density model. *J. Atmos. Sol. Terr. Phys.* **2008**, *70*, 1856–1862. [[CrossRef](#)]
20. Scherliess, L.; Schunk, R.W.; Sojka, J.J.; Thompson, D.C.; Zhu, L. Utah State University Global Assimilation of Ionospheric Measurements Gauss-Markov Kalman filter model of the ionosphere: Model description and validation. *J. Geophys. Res. Space Phys.* **2006**, *111*, A11315. [[CrossRef](#)]
21. Nina, A.; Nico, G.; Odalović, O.; Čadež, V.; Drakul, M.T.; Radovanović, M.; Popović, L.Č. GNSS and SAR Signal Delay in Perturbed Ionospheric D-Region During Solar X-ray Flares. *IEEE Geosci. Remote Sens. Lett.* **2020**, *17*, 1198–1202. [[CrossRef](#)]
22. Nina, A.; Čadež, V.; Srečković, V.; Šulić, D. Altitude distribution of electron concentration in ionospheric D-region in presence of time-varying solar radiation flux. *Nucl. Instrum. Methods B* **2012**, *279*, 110–113. [[CrossRef](#)]
23. Singh, A.K.; Singh, A.; Singh, R.; Singh, R. Solar flare induced D-region ionospheric perturbations evaluated from VLF measurements. *Astrophys. Space Sci.* **2014**, *350*. [[CrossRef](#)]
24. Drakul, M.; Čadež, V.M.; Bajčetić, J.; Popović, L.Č.; Blagojević, D.; Nina, A. Behaviour of electron content in the ionospheric D-region during solar X-ray flares. *Serb. Astron. J.* **2016**, *193*, 11–18. [[CrossRef](#)]
25. McRae, W.M.; Thomson, N.R. Solar flare induced ionospheric D-region enhancements from VLF phase and amplitude observations. *J. Atmos. Sol. Terr. Phys.* **2004**, *66*, 77–87. [[CrossRef](#)]
26. Pacini, A.A.; Raulin, J.P. Solar X-ray flares and ionospheric sudden phase anomalies relationship: A solar cycle phase dependence. *J. Geophys. Res. Space Phys.* **2006**, *111*. [[CrossRef](#)]
27. Nina, A.; Čadež, V.M.; Bajčetić, J.; Mitrović, S.T.; Popović, L.Č. Analysis of the Relationship Between the Solar X-ray Radiation Intensity and the D-Region Electron Density Using Satellite and Ground-Based Radio Data. *Sol. Phys.* **2018**, *293*, 64. [[CrossRef](#)]
28. Basak, T.; Chakrabarti, S.K. Effective recombination coefficient and solar zenith angle effects on low-latitude D-region ionosphere evaluated from VLF signal amplitude and its time delay during X-ray solar flares. *Astrophys. Space Sci.* **2013**, *348*, 315–326. [[CrossRef](#)]
29. Grubor, D.P.; Šulić, D.M.; Žigman, V. Influence of solar X-ray flares on the earth-ionosphere waveguide. *Serb. Astron. J.* **2005**, *171*, 29–35. [[CrossRef](#)]
30. Chakraborty, S.; Basak, T. Numerical analysis of electron density and response time delay during solar flares in mid-latitude lower ionosphere. *Astrophys. Space Sci.* **2020**, *365*, 184. [[CrossRef](#)]
31. Inan, U.S.; Lehtinen, N.G.; Moore, R.C.; Hurlley, K.; Boggs, S.; Smith, D.M.; Fishman, G.J. Massive disturbance of the daytime lower ionosphere by the giant γ -ray flare from magnetar SGR 1806-20. *Geophys. Res. Lett.* **2007**, *34*, 8103. [[CrossRef](#)]
32. Nina, A.; Simić, S.; Srečković, V.A.; Popović, L.Č. Detection of short-term response of the low ionosphere on gamma ray bursts. *Geophys. Res. Lett.* **2015**, *42*, 8250–8261. [[CrossRef](#)]
33. Thomson, N.R.; Clilverd, M.A. Solar flare induced ionospheric D-region enhancements from VLF amplitude observations. *J. Atmos. Sol. Terr. Phys.* **2001**, *63*, 1729–1737. [[CrossRef](#)]
34. Kolarski, A.; Grubor, D.; Šulić, D. Diagnostics of the Solar X-Flare Impact on Lower Ionosphere through Seasons Based on VLF-NAA Signal Recordings. *Balt. Astron.* **2011**, *20*, 591–595. [[CrossRef](#)]
35. Srečković, V.; Šulić, D.; Vujičić, V.; Jevremović, D.; Vykylyuk, Y. The effects of solar activity: Electrons in the terrestrial lower ionosphere. *J. Geogr. Inst. Cvijic* **2017**, *67*, 221–233. [[CrossRef](#)]
36. Thomson, N.R.; Rodger, C.J.; Clilverd, M.A. Large solar flares and their ionospheric D region enhancements. *J. Geophys. Res. Space Phys.* **2005**, *110*, A06306. [[CrossRef](#)]
37. Kumar, S.; NaitAmor, S.; Chanrion, O.; Neubert, T. Perturbations to the lower ionosphere by tropical cyclone Evan in the South Pacific Region. *J. Geophys. Res. Space Phys.* **2017**, *122*, 8720–8732. [[CrossRef](#)]
38. Nina, A.; Radovanović, M.; Milovanović, B.; Kovačević, A.; Bajčetić, J.; Popović, L.Č. Low ionospheric reactions on tropical depressions prior hurricanes. *Adv. Space Res.* **2017**, *60*, 1866–1877. [[CrossRef](#)]
39. NaitAmor, S.; Cohen, M.B.; Kumar, S.; Chanrion, O.; Neubert, T. VLF Signal Anomalies During Cyclone Activity in the Atlantic Ocean. *Geophys. Res. Lett.* **2018**, *45*, 10185–10192. [[CrossRef](#)]
40. Inan, U.S.; Cummer, S.A.; Marshall, R.A. A survey of ELF and VLF research on lightning-ionosphere interactions and causative discharges. *J. Geophys. Res. Space Phys.* **2010**, *115*. [[CrossRef](#)]
41. Peter, W.B.; Inan, U.S. Electron precipitation events driven by lightning in hurricanes. *J. Geophys. Res. Space Phys.* **2005**, *110*, 5305. [[CrossRef](#)]
42. Li, D.; Luque, A.; Rachidi, F.; Rubinstein, M.; Azadifar, M.; Diendorfer, G.; Pichler, H. The Propagation Effects of Lightning Electromagnetic Fields Over Mountainous Terrain in the Earth-Ionosphere Waveguide. *J. Geophys. Res. Atmos.* **2019**, *124*, 14198–14219. [[CrossRef](#)]
43. Biagi, P.F.; Maggipinto, T.; Righetti, F.; Loiacono, D.; Schiavulli, L.; Ligonzo, T.; Ermini, A.; Moldovan, I.A.; Moldovan, A.S.; Buyuksarac, A.; et al. The European VLF/LF radio network to search for earthquake precursors: Setting up and natural/man-made disturbances. *Nat. Hazards Earth Syst. Sci.* **2011**, *11*, 333–341. [[CrossRef](#)]
44. Lay, E.H.; Holzworth, R.H.; Rodger, C.J.; Thomas, J.N.; Pinto, O., Jr.; Dowden, R.L. WWLL global lightning detection system: Regional validation study in Brazil. *Geophys. Res. Lett.* **2004**, *31*. [[CrossRef](#)]

45. Cohen, M.B.; Inan, U.S.; Paschal, E.W. Sensitive Broadband ELF/VLF Radio Reception With the AWESOME Instrument. *IEEE Trans. Geosci. Remote Sens.* **2010**, *48*, 3–17. [[CrossRef](#)]
46. Official Website for the Marketing of SAOCOM[®] Products. Available online: <https://saocom.veng.com.ar/en/> (accessed on 18 May 2021).
47. NISAR-ISRO SAR Mission (NISAR). Available online: <https://nisar.jpl.nasa.gov/> (accessed on 18 May 2021).
48. Biomass. Available online: <https://earth.esa.int/web/guest/missions/esa-future-missions/biomass> (accessed on 18 May 2021).
49. Wait, J.R.; Spies, K.P. *Characteristics of the Earth-Ionosphere Waveguide for VLF Radio Waves*; NBS Technical Note: Boulder, CO, USA, 1964.
50. Ferguson, J.A. *Computer Programs for Assessment of Long-Wavelength Radio Communications, Version 2.0*; Space and Naval Warfare Systems Center: San Diego, CA, USA, 1998.
51. Grubor, D.P.; Šulić, D.M.; Žigman, V. Classification of X-ray solar flares regarding their effects on the lower ionosphere electron density profile. *Ann. Geophys.* **2008**, *26*, 1731–1740. [[CrossRef](#)]
52. Šulić, D.; Srećković, V.A. A comparative study of measured amplitude and phase perturbations of VLF and LF radio signals induced by solar flares. *Serb. Astron. J.* **2014**. [[CrossRef](#)]
53. Žigman, V.; Grubor, D.; Šulić, D. D-region electron density evaluated from VLF amplitude time delay during X-ray solar flares. *J. Atmos. Sol. Terr. Phys.* **2007**, *69*, 775–792. [[CrossRef](#)]
54. Nina, A.; Nico, G.; Mitrović, S.T.; Čadež, V.M.; Milošević, I.R.; Radovanović, M.; Popović, L.Č. Quiet Ionospheric D-Region (QIonDR) Model Based on VLF/LF Observations. *Remote Sens.* **2021**, *13*, 483. [[CrossRef](#)]
55. Thomson, N.R. Experimental daytime VLF ionospheric parameters. *J. Atmos. Terr. Phys.* **1993**, *55*, 173–184. [[CrossRef](#)]
56. Hayes, L.A.; Gallagher, P.T.; McCauley, J.; Dennis, B.R.; Ireland, J.; Inglis, A. Pulsations in the Earth's Lower Ionosphere Synchronized With Solar Flare Emission. *J. Geophys. Res. Space Phys.* **2017**, *122*, 9841–9847. [[CrossRef](#)]
57. Ammar, A.; Ghalila, H. Estimation of nighttime ionospheric D-region parameters using tweek atmospheric observations for the first time in the North African region. *Adv. Space Res.* **2020**, *66*, 2528–2536. [[CrossRef](#)]
58. Nina, A.; Čadež, V. Electron production by solar Ly- α line radiation in the ionospheric D-region. *Adv. Space Res.* **2014**, *54*, 1276–1284. [[CrossRef](#)]
59. Kumar, A.; Kumar, S. Solar flare effects on D-region ionosphere using VLF measurements during low- and high-solar activity phases of solar cycle 24. *Earth Planets Space* **2018**, *70*, 29. [[CrossRef](#)]
60. Mateus, P.; Catalão, J.; Nico, G. Sentinel-1 Interferometric SAR Mapping of Precipitable Water Vapor Over a Country-Spanning Area. *IEEE Trans. Geosci. Remote Sens.* **2017**, *55*, 2993–2999. [[CrossRef](#)]

M22

Article

Reduction of the VLF Signal Phase Noise Before Earthquakes

Aleksandra Nina ^{1,*}, Pier Francesco Biagi ², Srđan T. Mitrović ³, Sergey Pulinetz ⁴, Giovanni Nico ^{5,6}, Milan Radovanović ^{7,8} and Luka Č. Popović ^{9,10,11}

¹ Institute of Physics Belgrade, University of Belgrade, 11080 Belgrade, Serbia

² Physics Department, Università di Bari, 70125 Bari, Italy; pf.biagi@gmail.com

³ Novelic, 11000 Belgrade, Serbia; mitar027@beotel.net

⁴ Space Research Institute, Russian Academy of Sciences, 117997 Moscow, Russia; pulse1549@gmail.com

⁵ Istituto per le Applicazioni del Calcolo (IAC), Consiglio Nazionale delle Ricerche (CNR), 70126 Bari, Italy; g.nico@ba.iac.cnr.it

⁶ Department of Cartography and Geoinformatics, Institute of Earth Sciences, Saint Petersburg State University (SPSU), 199034 Saint Petersburg, Russia

⁷ Geographical Institute "Jovan Cvijić" SASA, 11000 Belgrade, Serbia; m.radovanovic@gi.sanu.ac.rs

⁸ Institute of Sports, Tourism and Service, South Ural State University, 454080 Chelyabinsk, Russia

⁹ Astronomical Observatory, 11060 Belgrade, Serbia; lpopovic@aob.rs

¹⁰ Department of Astronomy, Faculty of mathematics, University of Belgrade, 11000 Belgrade, Serbia

¹¹ Faculty of Science, University of Banja Luka, 78000 Banja Luka, R. Srpska, Bosnia and Herzegovina

* Correspondence: sandrast@ipb.ac.rs

Abstract: In this paper we analyse temporal variations of the phase of a very low frequency (VLF) signal, used for the lower ionosphere monitoring, in periods around four earthquakes (EQs) with magnitude greater than 4. We provide two analyses in time and frequency domains. First, we analyse time evolution of the phase noise. And second, we examine variations of the frequency spectrum using Fast Fourier Transform (FFT) in order to detect hydrodynamic wave excitations and attenuations. This study follows a previous investigation which indicated the noise amplitude reduction, and excitations and attenuations of the hydrodynamic waves less than one hour before the considered EQ events as a new potential ionospheric precursors of earthquakes. We analyse the phase of the ICV VLF transmitter signal emitted in Italy recorded in Serbia in time periods around four earthquakes occurred on 3, 4 and 9 November 2010 which are the most intensive earthquakes analysed in the previous study. The obtained results indicate very similar changes in the noise of phase and amplitude, and show an agreement in recorded acoustic wave excitations. However, properties in the obtained wave attenuation characteristics are different for these two signal parameters.

Keywords: ionosphere; earthquakes; observations; VLF signal; signal processing; acoustic and gravity waves



Citation: Nina, A.; Biagi, F.P.; Mitrović, S.T.; Pulinetz, S.; Nico, G.; Radovanović, M.; Popović, L.Č. Reduction of the VLF Signal Phase Noise Before Earthquakes. *Atmosphere* **2021**, *12*, 444. <https://doi.org/10.3390/atmos12040444>

Academic Editor: Victor Ivanovich Zakharov

Received: 5 March 2021

Accepted: 30 March 2021

Published: 31 March 2021

Publisher's Note: MDPI stays neutral with regard to jurisdictional claims in published maps and institutional affiliations.



Copyright: © 2021 by the authors. Licensee MDPI, Basel, Switzerland. This article is an open access article distributed under the terms and conditions of the Creative Commons Attribution (CC BY) license (<https://creativecommons.org/licenses/by/4.0/>).

1. Introduction

In addition to periodical ionospheric changes, which can be predicted and estimated by different models (see, for example, [1,2] and references therein), sudden events can induce significant ionospheric disturbances and affect many contemporary technologies based on satellite and ground-based electromagnetic (EM) signal propagation [3]. Consequently, variations of the recorded EM signal properties can be used for detections and analyses of influences of many phenomena on this atmospheric layer including processes which induce different kinds of natural disasters [4–8].

In the last several decades, studies of the lower ionosphere disturbances are mostly based on observations by very low/low frequency (VLF/LF) radio signals [9–13] and processing of the corresponding recorded data in both the time and frequency domains. Increases or decreases of the signal amplitude and/or phase are recorded in many studies focused on research of ionospheric disturbances induced by earthquakes [9], solar activity [14–18], tropical cyclones [19,20], solar eclipse [21,22] etc.

The acoustic gravity waves (AGW) are recently mentioned in association with earthquakes mainly as a result of the strong oscillations caused by the seismic shock (Jin et al., 2015 [23]) or tsunami (Manta et al., 2020 [24]). But for a long period of time they were considered as a main agent of the seismo-ionospheric coupling as the earthquake precursor (Korepanov et al., 2009 [25]). But the main problem was the lack of convincing experimental evidences of the AGW generation before earthquakes and corresponding physical mechanism of their generation. As the possible sources the mosaic distribution of gas emission before earthquakes was proposed (Mareev et al., 2002 [26]), or the surface thermal anomalies (Molchanov et al., 2004 [27]). Research of AGW in the lower ionosphere is also presented in several studies. They relate to disturbances induced by the solar terminator [28], geomagnetic storms [29,30], tropical cyclones [19,31,32] earthquakes [33], solar eclipse [34], and they are based on analyses of the VLF/LF signals.

Studies of the ionospheric changes as precursors of earthquakes report changes usually a few days before events [9,13,35]. These lower ionosphere disturbances are detected as the solar terminator shift [13,36,37] and deviations of the time evolutions of signal characteristics from values recorded during days with unperturbed conditions [5,38] (in time domain), and as variations in the wavelet power spectrum [5,39] (in frequency domain), and all of these changes are shown for both signal amplitude and phase. The recent analysis presented in [33] shows reduction of the amplitude noise of the VLF signal less than one hour before the earthquake occurred near Kraljevo, Serbia, on 3 November 2010 (the seismotectonic model of this event is presented in [40]), as well as excitation and attenuation of the acoustic waves. In addition, the similar changes in the amplitude noise are also recorded for 12 other earthquakes with different magnitudes during three whole days. It was concluded that all considered EQs with the magnitude larger than 4 were connected with the recorded noise amplitude reduction. However, contrary to the previous cases this pioneer study which indicates a possible new ionospheric precursor of earthquake is provided only for the amplitude i.e., variations of the phase, is not considered. For this reason, in this study we extend the research presented in [33] and investigate if the recorded changes in amplitude noise are also visible in analysis of the VLF signal phase, and if excitations and attenuations of the acoustic and gravity waves can be visualized from the recorded phase. We show analysis of the phase of the ICV signal emitted in Italy and recorded in Serbia in periods around four EQs with magnitude greater than 4 which are connected with the noise amplitude reductions in study shown in [33].

The paper is organized as follows. Descriptions of observations and data processing are given in Section 2. Results of this study are divided in two parts: those related to reduction of the phase noise is shown in Section 3.1 and those related to analysis of the acoustic and gravity waves are presented in Section 3.2. Finally, conclusions of this study are summarized in Section 4.

2. Observations and Data Processing

In this study we analyse phase of the ICV signal emitted by a transmitter located in Isola di Tavolara, Italy (40.92 N, 9.73 E) and received in Belgrade, Serbia (44.8 N, 20.4 E) in time periods around four EQs, considered in [33] and connected to the short-term noise amplitude reduction. Two of these events occurred near Kraljevo, Serbia, one in the Tyrrhenian Sea (TS) and one in the Western Mediterranean Sea (WMS) (their epicentres are shown in map given in Figure 1). As it can be seen in Table 1, their magnitudes were greater than 5 for two events (the first one near Kraljevo, and in the Tyrrhenian Sea) while other two had magnitude larger than 4. These magnitudes are larger than those related to other EQs considered in [33].

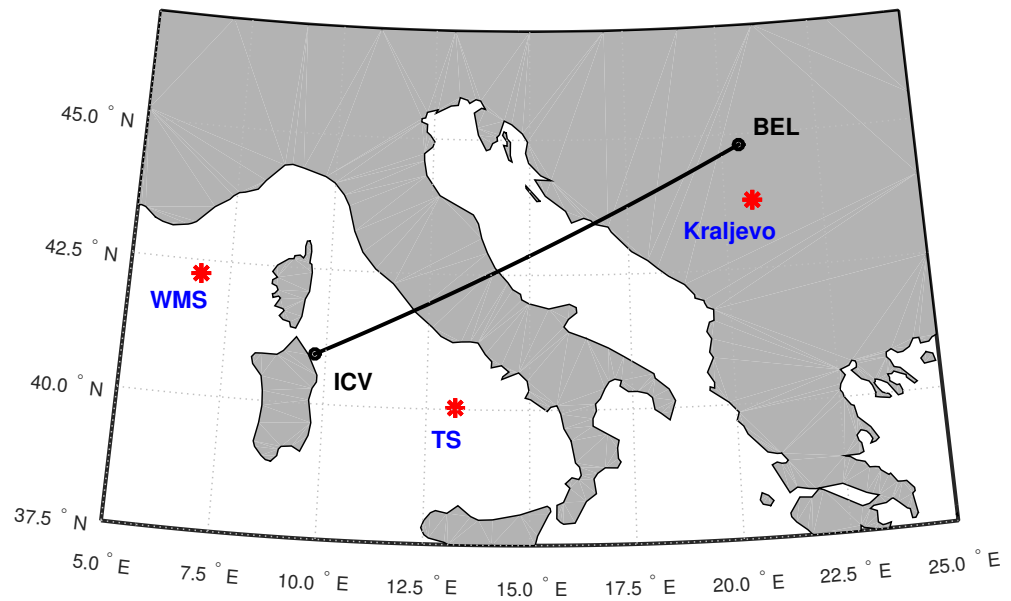


Figure 1. Propagation paths of the VLF signals recorded by the Belgrade receiver station (BEL) in Serbia and emitted by the transmitters ICV in Italy. Locations of the main considered EQs are shown as stars. One EQ occurred in the Tyrrhenian Sea (TS) and Western Mediterranean Sea (WMS), while two EQs were near Kraljevo (their epicentres are shown by the same star).

Table 1. List of the main earthquakes considered in this study. EQ date, time *t*, epicentre locations (latitude (LAT) and longitude (LON)) and magnitudes (M) are given in <http://www.emsc-csem.org/Earthquake/> (accessed on 25 February 2021). The variable *d* denotes the distance between the EQ epicentres and signal propagation path.

No.	Date	<i>t</i> (UTC)	LAT (°)	LON (°)	<i>d</i> (km)	M	Location
Kraljevo—03/11/2010							
1	2010/11/03	00:56:54	43.74	20.69	126.0	5.4	Serbia (near Kraljevo)
31 EQs until 8 UT—31 in Serbia, 3 in Italy and 1 in Bosnia and Herzegovina							
Tyrrhenian Sea (TS)—03/11/2010							
2	2010-11-03	17:12:30	42.4	13.35	11.4	2	Central Italy
	2010-11-03	17:48:04	43.75	20.7	120.7	2.5	Serbia (near Kraljevo)
	2010/11/03	18:13:10	40.03	13.2	219.1	5.1	TS
	2010-11-03	18:47:23	43.73	20.67	121.7	2.1	Serbia (near Kraljevo)
Kraljevo—04/11/2010							
1	2010-11-04	20:33:01	43.75	20.7	120.7	1.9	Serbia (near Kraljevo)
	2010/11/04	21:09:05	43.78	20.62	114.9	4.4	Serbia (near Kraljevo)
	2010-11-04	21:55:40	45.81	7.55	562.9	1.2	Northern Italy
	2010-11-04	23:43:05	43.78	20.62	114.9	3.3	Serbia (near Kraljevo)
	2010-11-05	00:16:14	43.74	20.64	119.6	2.8	Serbia (near Kraljevo)
	2010-11-05	01:38:48	43.76	20.69	119.4	2.5	Serbia (near Kraljevo)
Western Mediterranean Sea (WMS)—03/11/2010							
4	2010-11-09	16:45:13	43.59	12.36	165.9	2.3	Central Italy
	2010-11-09	18:23:36	42.25	6.77	287.7	4.3	WMS

During the considered four time intervals, additional weaker EQs also occurred near the considered signal propagation path. After the most intensive EQ (Kraljevo, 3/11/2010) 31 additional EQs occurred before 8 UT. 27 of these events were in Serbia, 3 in Italy and 1 in Bosnia and Herzegovina. Their magnitudes were lower than 3 except in one case when it was 3.3. Because of this large number we only give common information of their occurrences in Table 1. Processes in the lithosphere below the monitored ionospheric area were not so intensive during the other three time intervals. For this reason all additional EQ events are indicated in Table 1.

In this analysis, we process the 0.1-s resolution datasets. This procedure consists of three parts: (1) phase unwrapping, (2) determination of the unwrapped phase noise, and

(3) application of Fast Fourier Transform (FFT) to the unwrapped phase in order to examine excitations and attenuations of the acoustic and gravity waves.

- **Phase unwrapping.** The recorded signal phase P_{data} represents the deviation of the signal phase with respect to the phase generated at the receiver. Because of that it has a component of constant slope. However, this component does not affect the presented analysis, and for this reason we did not remove it. On the other side, all recorded values are given within a principal phase interval and for further analysis it is necessary to unwrap it. The obtained time evolutions of the unwrapped phase P are shown in Figure 2 where the vertical lines indicate times of EQ occurrences. Red lines represent the main EQ considered in corresponding time periods while the additional events listed in Table 1 are coloured in black. To visualize the magnitudes of these additional events, we divided them in three categories: 1. magnitude below 2.5, 2. magnitudes from 2.5 to 3, and 3. magnitudes from 3 to 4. These categories are represented by thin dotted, thin dashed and tick dotted black lines, respectively.
- **Determination of the phase noise.** To obtain the noise P_{noise} of the unwrapped phase P we calculate its deviation $dP(t) = P(t) - P_{\text{base}}(t)$ from the basic phase P_{base} at time t . Here, P_{base} is obtained in a procedure described in [33] as the mean value of unwrapped phase in the defined time bins around time t . Finally, noise of P is determined as the maximum of $|dP|$ after elimination of the largest p percent of its values. To find this value, we first sorted the values of $|dP|$ into an ascending array $dP_{\text{as}} = \text{sort}(|dP|)$ of N members, and determined the value of the phase noise as the value of the term that is $i_{\text{noise}} = N \cdot (100 - p)/100$ in this array:

$$P_{\text{noise}} = dP_{\text{as}}(i_{\text{noise}}). \tag{1}$$

In this study we use $p = 5\%$ like in [33].

- **Acoustic and gravity waves—excitations and attenuations.** Research of the acoustic and gravity waves in this paper is based on processing of the VLF signal phase. We analyse their excitations and attenuations in periods around the considered EQs using the procedure given in [33]. It is based on the application of the Fast Fourier Transform (FFT) on fixed window time intervals (WTI) within the considered time periods. Keeping in mind that WTI affects the maximum of observable wave period and precision in the analysis of the observed variations we choose three WTIs of 20 min, 1 h and 3 h.

The goal of this procedure is to analyse the recorded phase in frequency domain and connect the wave-periods for which important changes are recorded to the acoustic and gravity waves. The acoustic cut-off τ_0 and the Brunt-Väisälä τ_{BV} wave-periods representing minimal and maximal periods for the acoustic and gravity waves, respectively, are determined from the expressions:

$$\tau_0 = \frac{4\pi v_s}{\gamma g}, \quad \tau_{\text{BV}} = \frac{2\pi}{N_{\text{BV}}}, \tag{2}$$

where $\gamma = 5/3$ is the standard ratio of specific heats and $g = 9.6 \text{ m/s}^2$ is gravitational acceleration. The adiabatic sound speed squared $v_s^2 = \gamma k_B T_0 / m_a$ is obtained for the gass temperature $T_0 = 220 \text{ K}$ (estimated from the International Reference Ionosphere (IRI) model [41] and assumed average mass of atoms $m_a \approx 10^{-25} \text{ kg}$. The Boltzmann constant k_B is $1.3807 \cdot 10^{-23} \text{ J/K}$. Details of this procedure can be found in, for example, [42,43].

As it is obtained in [33] waves with periods $T < \tau_0 = 176.7, \text{ s}$ and $T > \tau_{\text{BV}} = 180.4 \text{ s}$, represents acoustic and gravity modes, respectively.

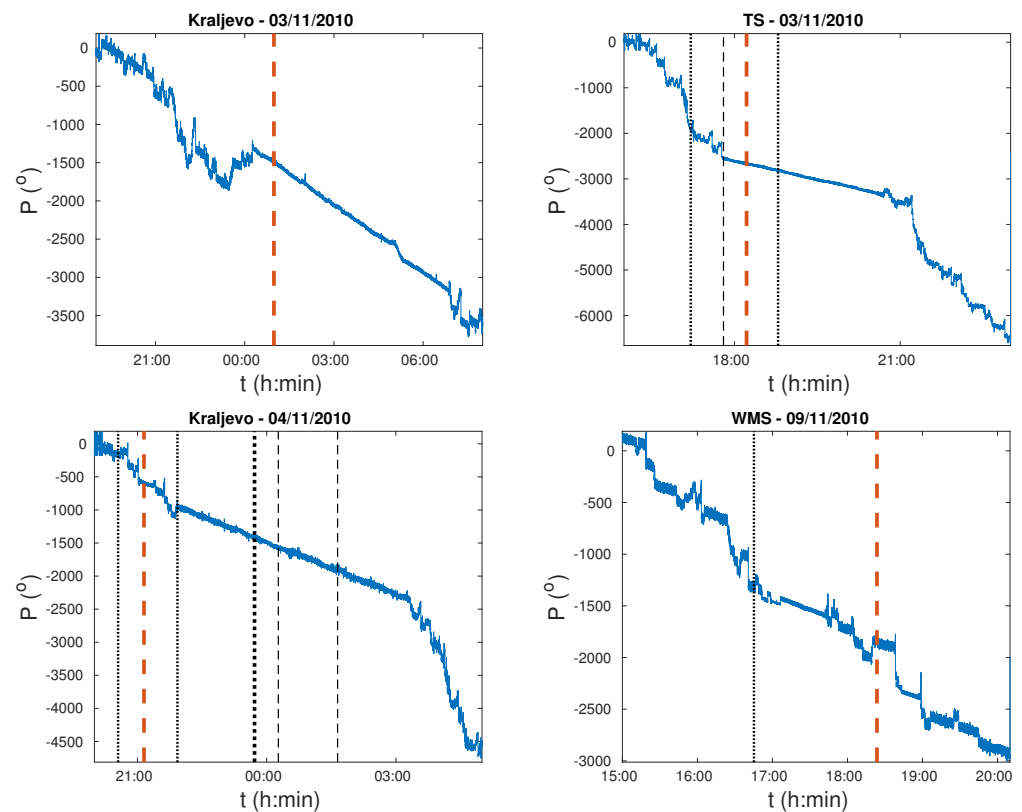


Figure 2. Time evolutions of the unwrapped phase P for the considered periods. Red lines represent the main EQ considered in corresponding time periods. The additional events listed in Table 1 are coloured in black. Times of the additional considered EQ events with magnitude below 2.5, from 2.5 to 3, and from 3 to 4 are represented by thin dotted, thin dashed and tick dotted black lines, respectively.

Here we point out that during the considered time periods there are not recorded other events which can influence the signal phase. Detailed analysis, described in [33], indicated that influences of receiver, transmitter, meteorological and geomagnetic conditions, which are suggested as the most important non-ionospheric sources of the VLF signal variations [44], can be ignored.

3. Results and Discussions

Results of determination of the phase noise and periods of the excited and attenuated acoustic and gravity waves are presented in Sections 3.1 and 3.2, respectively.

3.1. Signal Phase Noise

Time evolutions of deviation of the wrapped phase from its basic values dP and the phase noise P_{noise} obtained by the proposed methodology are shown in Figures 3 and 4, respectively. As one can see, reduction of the phase noise is recorded for all four main EQ events and it is clearly visible in the first two cases whose magnitudes are greater than 5.

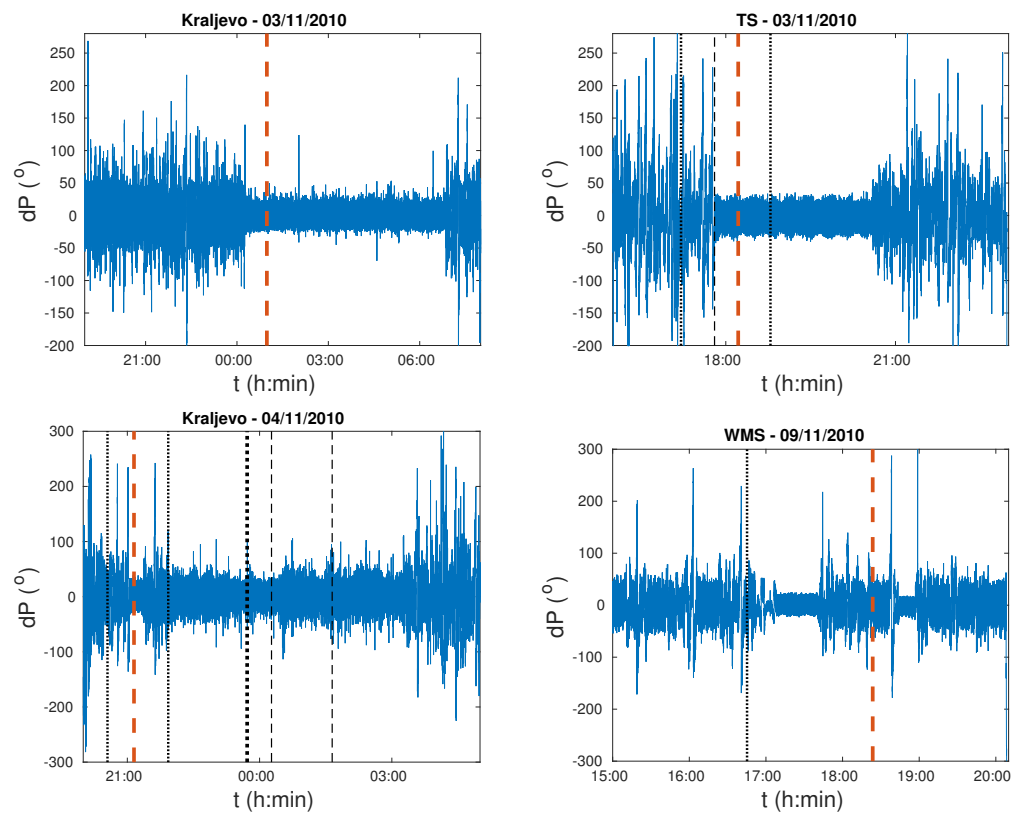


Figure 3. The same as in Figure 2 but for phase deviation $dP = P_{data} - P_{base}$.

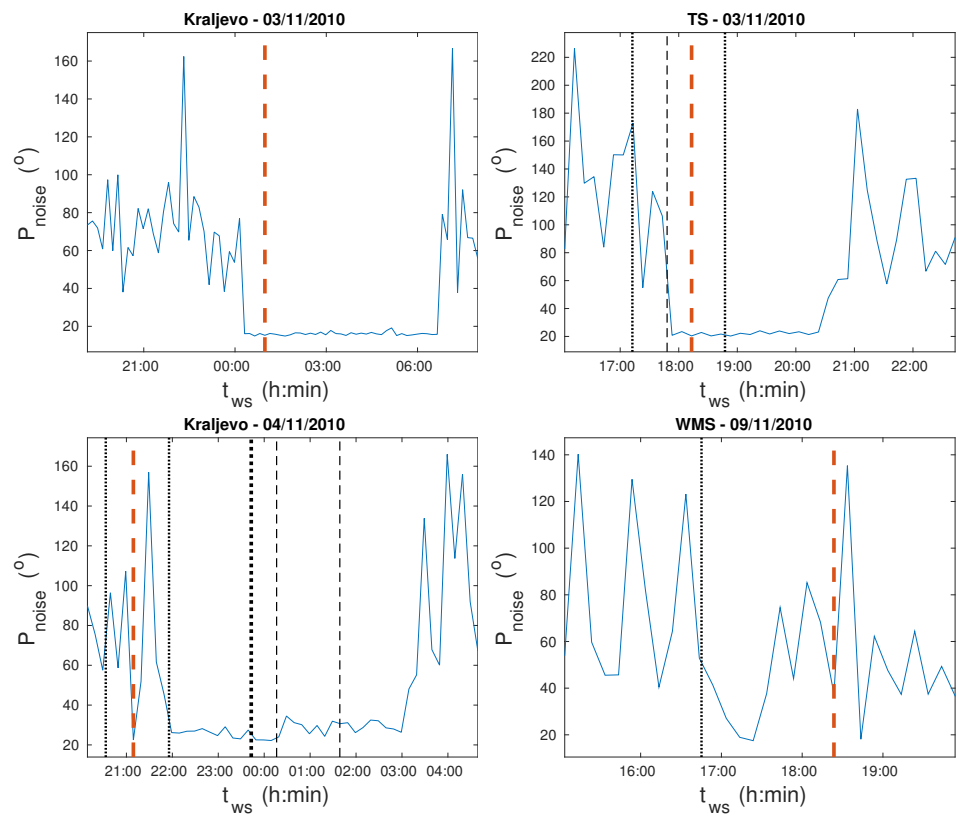


Figure 4. The same as in Figure 2 but for the phase noise P_{noise} .

It is worth noting that after the first EQ event near Kraljevo which occurred on 3 November 2010, additional 31 EQs occurred in areas near the considered signal propagation path. Twenty nine of them occurred when the phase noise reduction is clearly visible, while two events of weak intensities (magnitudes of 2.1 and 2.2) occurred after increasing of the phase noise. The most intensive additional EQ had magnitude of 3.3. However, despite the large number of accompanying earthquakes, no significant variations were observed either in dP or in P_{noise} . The absence of these variations is also noticeable in the second case (EQ in Tyrrhenian Sea of magnitude 5.1) when three more earthquakes (magnitudes of 2, 2.1 and 2.5) were recorded within about 1.5 h.

In the cases of the other two EQs which magnitudes were between 4 and 5, analysis of dP and P_{noise} time evolutions is not so simple like in the first two considered time intervals. Namely, although the reductions in phase noise are recorded before and after these events, they are not related each other. In the case of the EQ which occurred near Kraljevo on 4 November 2010 significant reduction in P_{noise} is recorded several minutes before the EQ and lasts about 20 min. This phase reduction is followed by the short-term increase in P_{noise} and additional significant decrease which yield to the second reduction lasting about 5 h. During the second reduction four additional EQs are recorded. The first one occurred in North Italy while the other three near Kraljevo (like the main one) with magnitudes of 3.3, 2.8 and 2.5. As one can see in the bottom left panels of Figures 3 and 4, although the small increase in noise is recorded after the second additional EQ near Kraljevo, significant reduction which can be related with EQ events observed within a time window of about 3 h and includes the time of the last EQ.

Reduction of the phase noise begins about 1 h before the EQ in the Western Mediterranean Sea but it is also possible relate it with the EQ occurred in Central Italy just before the decrease in dP . This reduction is followed by noise increase which begins more than a half of hour before the EQ and lasts about 1 h before the reduction is recorded again. This event is interesting because position of the EQ epicentre is, contrary to the other events, northern than the signal propagation path. The possible recorded time shift of the reduction time opens a question of influence of position of the EQ epicentre with respect to the signal propagation path. This task requires a specific statistical analysis and it will be in focus of our forthcoming research.

By comparison with noise amplitude reduction analysed in [33] we can conclude that the characteristics of phase reduction are the same for the first two cases: they last for several hours, begin before and end after an EQ event, and there are not observed changes that could be related to other earthquakes of lower intensity. In the third and fourth cases phase noise reductions are also recorded, but they are shortly interrupted by the noise amplifications. Also, it cannot be claimed that the strongest earthquake in the observed period masks the potential relationship between phase noise reduction and weaker EQs.

3.2. Acoustic and Gravity Waves

In the second part of this study we analyse signal phase in frequency domain. We apply FFT to the recorded data to research possible excitations and attenuations of the acoustic and gravity waves that can be considered as ionospheric disturbances connected to earthquakes.

To better visualize periods of the excited/attenuated waves we apply the same procedures like in [33]: (1) we consider three WTI of 20 min, 1 h and 3 h and, (2) in order to better present changes for smaller and greater wave periods T , the obtained values for all WTIs are considered for smaller and greater wave period domains separately. In this study we showed lower periods T for the first WTI, and greater periods for all the three WTIs. The results of the analyses for the considered four time periods are shown in Figures 5–8.

Kraljevo—03/11/2010

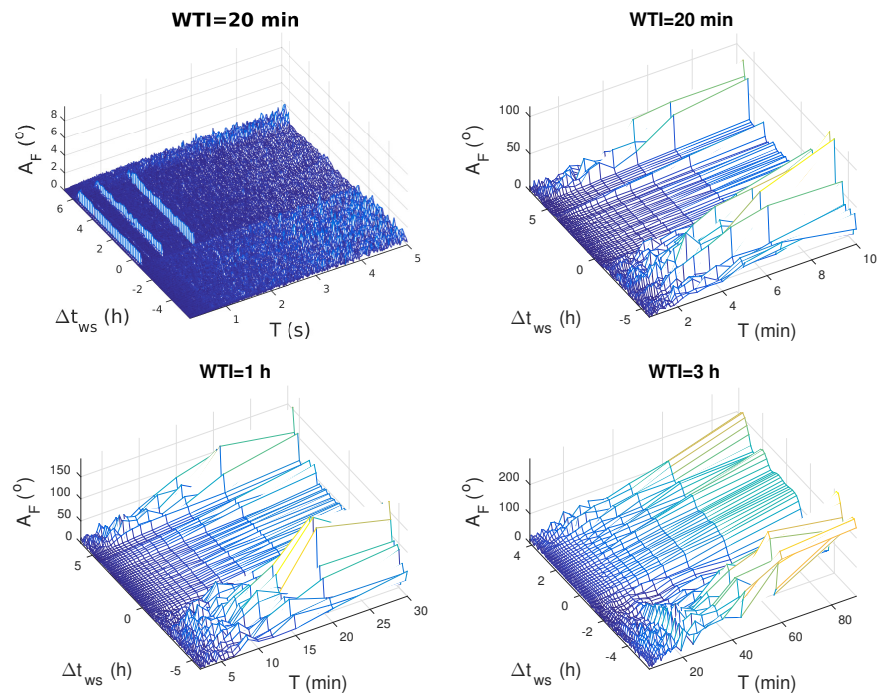


Figure 5. Fourier amplitude of waves with period T obtained by applying FFT to the ICV signal phase recorded in time around EQ occurred near Kraljevo on 3 November 2010 with window time intervals (WTI) of 20 min (upper panels), 1 h (bottom left panel), and 3 h (bottom right panel) which begin with a Δt_{WS} shift with respect to the EQ time.

Tyrrhenian Sea—03/11/2010

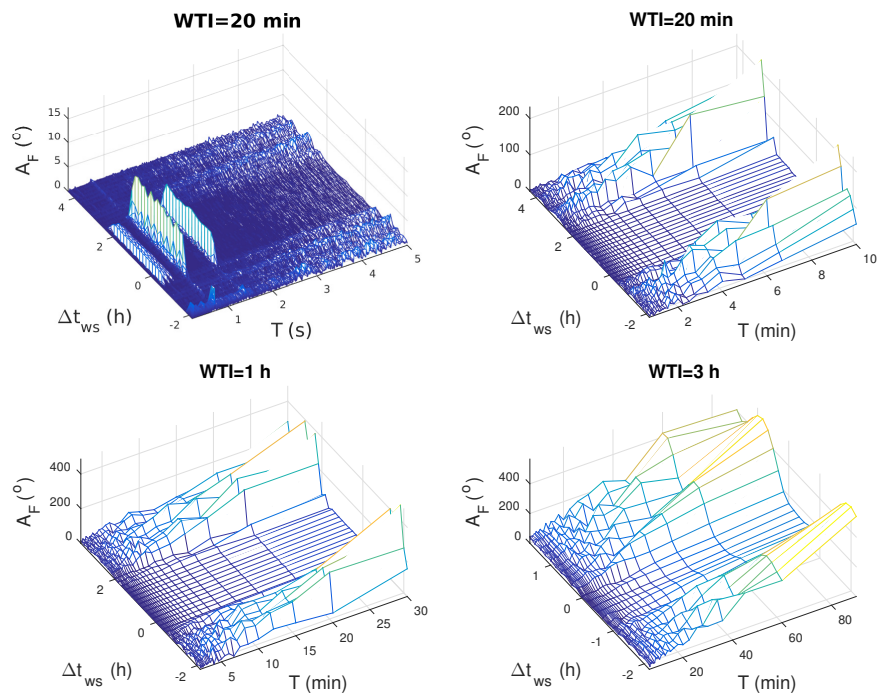


Figure 6. Fourier amplitude of waves with period T obtained by applying FFT to the ICV signal phase recorded in time around EQ occurred in the Tyrrhenian Sea on 3 November 2010 with window time intervals (WTI) of 20 min (upper panels), 1 h (bottom left panel), and 3 h (bottom right panel) which begin with a Δt_{WS} shift with respect to the EQ time.

Kraljevo—04/11/2010

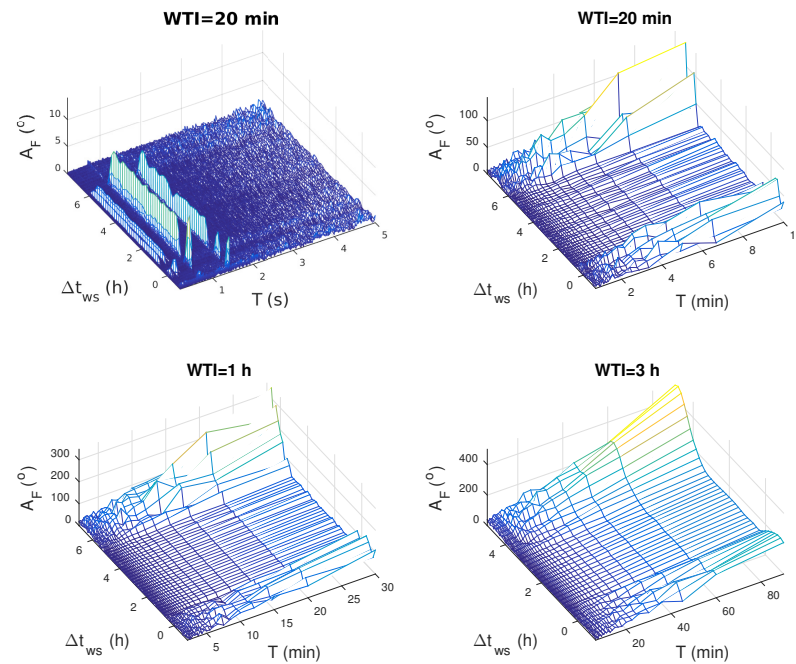


Figure 7. Fourier amplitude of waves with period T obtained by applying FFT to the ICV signal phase recorded in time around EQ occurred near Kraljevo on 4 November 2010 with window time intervals (WTI) of 20 min (upper panels), 1 h (bottom left panel), and 3 h (bottom right panel) which begin with a Δt_{WS} shift with respect to the EQ time.

Western Mediterranean Sea—09/11/2010

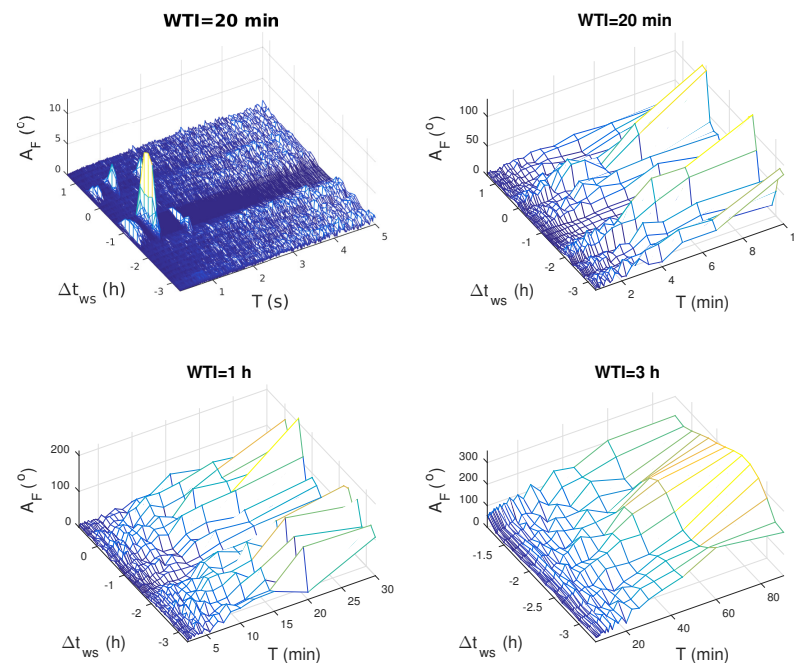


Figure 8. Fourier amplitude of waves with period T obtained by applying FFT to the ICV signal phase recorded in time around EQ occurred in the Western Mediterranean Sea on 9 November 2010 with window time intervals (WTI) of 20 min (upper panels), 1 h (bottom left panel), and 3 h (bottom right panel) which begin with a Δt_{WS} shift with respect to the EQ time.

Similarly to the analysis of the noise amplitude shown in [33], excitations are recorded in periods when phase noise is reduced at several values of T which are smaller than 1.5 s:

- Kraljevo—03/11/2010: 0.2 s, 0.23 s, 0.47 s (weak increase of the Fourier amplitude), 0.7 s and 1.4 s.
- Tyrrhenian Sea—03/11/2010: 0.23 s, 0.35 s, 0.47 s, 0.7 s and 1.4 s.
- Kraljevo—04/11/2010: 0.23 s, 0.35 s, 0.7 s and 1.4 s;
- Western Mediterranean Sea—09/11/2010: 0.23 s, 0.35 s, 0.47 s (during the first time period when noise reduction is recorded), 0.7 s and 1.4 s.

As one can see, the common periods are 0.23 s, 0.35 s, and 1.4 s while waves at period of 0.47 s are excited in three cases whereby these excitations are weak in the first case, while in the fourth case they are recorded only for one of two periods of phase noise reduction. Excited waves at 0.2 s are recorded only for the first considered EQ event. Because the obtained values are lower than calculated maximum period of the acoustic waves ($\tau_0 = 176.7$) we can conclude that acoustic waves are excited in periods when noise reduction occurs.

Although the previous results related to the noise reductions and excitations of the acoustic waves are very similar as those shown in analysis of the amplitude, there is a difference in wave attenuation. Namely, the Fourier amplitude for several discrete values before the reduction time are reported in [33]. In this study, these peaks are not recorded. In addition, in all four considered periods attenuations are clearly visible at all periods T (except those values for which excitation is recorded) for phase while these attenuations are much less pronounced in the case of the amplitude for time period around Kraljevo EQ on 3 November 2010. Recent results obtained for the Kumamoto M7.2 earthquake on 15 April 2016 in Japan [45] are in close correlation with our results, so we can suppose that registered oscillations are the acoustic gravity waves of the same origin as is described in this paper. A similar correlation of our results can be also found in their comparison with data presented in analysis of the M7.8 earthquake with the epicenter in Nepal on 25 April 2015 [46].

4. Conclusions

In this paper we analysed the VLF signal phase in time periods around four earthquakes which magnitude were greater than 4. The goal of this study was to extend analyses of reductions of the noise amplitude of VLF signals, excitations and attenuations of the acoustic and gravity waves presented in [33] to the corresponding analyses of the phase of the VLF signal. We analysed data recorded by the receiver located in Belgrade, Serbia for VLF signal emitted by the ICV transmitter in Italy.

The obtained results of this study can be summarised as follows:

- In the cases of EQs with magnitudes greater than 5, a multi-hour noise reductions was observed. As in the case of the amplitude, they begin before the earthquake. In these cases, no changes that could be related to other earthquakes of lower intensity were observed.
- In the cases of EQs with magnitudes between 4 and 5, phase noise reductions are also recorded, but they are shortly interrupted by the noise amplifications. Specific reductions are potentially related to different EQs, i.e., it cannot be claimed that the strongest earthquake in the observed period masks the potential relationship between phase noise reduction and weaker EQs.
- Because the recorded phase reductions are very similar like those in the case of the amplitude the choice of the signal characteristic which can be used in the corresponding studies depends only on the quality of the recorded data and do not affect the results of study.
- Excitations of the acoustic waves are recorded for all four periods. The obtained wave-periods are below 1.5 s which is in agreement with results obtained in analysis of the amplitude.

- Attenuations of the acoustic and gravity waves are recorded continuously with wave-period except for those T corresponding to wave excitations. This result does not agree with those obtained when analysing amplitude variations where attenuations are primarily recorded for discrete values of wave periods, while similar continuous attenuations are much less pronounced.

Author Contributions: Conceptualization, methodology, investigation, resources, formal analysis, writing—original draft, preparation, visualization, A.N.; software, data curation, A.N. and S.T.M.; validation, P.F.B., S.P., L.Č.P. and M.R.; writing—review and editing, all authors. All authors have read and agreed to the published version of the manuscript.

Funding: The authors acknowledge funding provided by the Institute of Physics Belgrade, the Astronomical Observatory (the contract 451-03-68/2020-14/200002) through the grants by the Ministry of Education, Science, and Technological Development of the Republic of Serbia.

Institutional Review Board Statement: Not applicable.

Informed Consent Statement: Not applicable.

Data Availability Statement: Publicly available datasets were analysed in this study. This data can be found here: <http://www.emsc-csem.org/Earthquake/> (accessed on 28 February 2021); https://ccmc.gsfc.nasa.gov/modelweb/models/iri2012_vitmo.php (accessed on 29 February 2021). The VLF data used for analysis is available from the corresponding author.

Acknowledgments: This research was supported by COST Actions CA18109 and CA15211.

Conflicts of Interest: The authors declare no conflict of interest.

References

1. Bilitza, D. IRI the International Standard for the Ionosphere. *Adv. Radio Sci.* **2018**, *16*, 1–11. [[CrossRef](#)]
2. Nina, A.; Nico, G.; Mitrović, S.T.; Čadež, V.M.; Milošević, I.R.; Radovanović, M.; Popović, L.Č. Quiet Ionospheric D-Region (QIonDR) Model Based on VLF/LF Observations. *Remote Sens.* **2021**, *13*, 483. [[CrossRef](#)]
3. Nina, A.; Nico, G.; Odalović, O.; Čadež, V.M.; Drakul, M.T.; Radovanović, M.; Popović, L.Č. GNSS and SAR Signal Delay in Perturbed Ionospheric D-Region During Solar X-Ray Flares. *IEEE Geosci. Remote Sens. Lett.* **2020**, *17*, 1198–1202. [[CrossRef](#)]
4. Pulintets, S.; Boyarchuk, K. *Ionospheric Precursor of Earthquakes*; Springer: Berlin/Heidelberg, Germany, 2004. [[CrossRef](#)]
5. Rozhnoi, A.; Solovieva, M.; Molchanov, O.; Hayakawa, M. Middle latitude LF (40 kHz) phase variations associated with earthquakes for quiet and disturbed geomagnetic conditions. *Phys. Chem. Earth* **2004**, *29*, 589–598. [[CrossRef](#)]
6. Hayakawa, M. VLF/LF Radio Sounding of Ionospheric Perturbations Associated with Earthquakes. *Sensors* **2007**, *7*, 1141–1158. [[CrossRef](#)]
7. Liu, Y.; Jin, S. Ionospheric Rayleigh Wave Disturbances Following the 2018 Alaska Earthquake from GPS Observations. *Remote Sens.* **2019**, *11*, 901. [[CrossRef](#)]
8. Zhong, M.; Shan, X.; Zhang, X.; Qu, C.; Guo, X.; Jiao, Z. Thermal Infrared and Ionospheric Anomalies of the 2017 Mw6.5 Jiuzhaigou Earthquake. *Remote Sens.* **2020**, *12*, 2843. [[CrossRef](#)]
9. Biagi, P.F.; Piccolo, R.; Ermini, A.; Martellucci, S.; Bellecci, C.; Hayakawa, M.; Kingsley, S.P. Disturbances in LF radio-signals as seismic precursors. *Ann. Geophys.* **2001**, *44*, 5–6. [[CrossRef](#)]
10. Hayakawa, M. Probing the lower ionospheric perturbations associated with earthquakes by means of subionospheric VLF/LF propagation. *Earthq. Sci.* **2011**, *24*, 609–637. [[CrossRef](#)]
11. Nina, A.; Radovanović, M.; Milovanović, B.; Kovačević, A.; Bajčetić, J.; Popović, L.Č. Low ionospheric reactions on tropical depressions prior hurricanes. *Adv. Space Res.* **2017**, *60*, 1866–1877. [[CrossRef](#)]
12. Rozhnoi, A.; Shalimov, S.; Solovieva, M.; Levin, B.; Hayakawa, M.; Walker, S. Tsunami-induced phase and amplitude perturbations of subionospheric VLF signals. *J. Geophys. Res. Space* **2012**, *117*, 9313. [[CrossRef](#)]
13. Molchanov, O.; Hayakawa, M.; Oudoh, T.; Kawai, E. Precursory effects in the subionospheric VLF signals for the Kobe earthquake. *Phys. Earth Planet. Inter.* **1998**, *105*, 239–248. [[CrossRef](#)]
14. Žigman, V.; Grubor, D.; Šulić, D. D-region electron density evaluated from VLF amplitude time delay during X-ray solar flares. *J. Atmos. Sol. Terr. Phys.* **2007**, *69*, 775–792. [[CrossRef](#)]
15. Srećković, V.; Šulić, D.; Vujičić, V.; Jevremović, D.; Vyklyuk, Y. The effects of solar activity: Electrons in the terrestrial lower ionosphere. *J. Geogr. Inst. Cvijic* **2017**, *67*, 221–233. [[CrossRef](#)]
16. Raulin, J.P.; Trotter, G.; Kretzschmar, M.; Macotela, E.L.; Pacini, A.; Bertoni, F.C.P.; Dammasch, I.E. Response of the low ionosphere to X-ray and Lyman- α solar flare emissions. *J. Geophys. Res. Space* **2013**, *118*, 570–575. [[CrossRef](#)]

17. Basak, T.; Chakrabarti, S.K. Effective recombination coefficient and solar zenith angle effects on low-latitude D-region ionosphere evaluated from VLF signal amplitude and its time delay during X-ray solar flares. *Astrophys. Space Sci.* **2013**, *348*, 315–326. [[CrossRef](#)]
18. Chakraborty, S.; Basak, T. Numerical analysis of electron density and response time delay during solar flares in mid-latitude lower ionosphere. *Astrophys. Space Sci.* **2020**, *365*, 1–9. [[CrossRef](#)]
19. Kumar, S.; NaitAmor, S.; Chanrion, O.; Neubert, T. Perturbations to the lower ionosphere by tropical cyclone Evan in the South Pacific Region. *J. Geophys. Res. Space* **2017**, *122*, 8720–8732. [[CrossRef](#)]
20. Rozhnoi, A.; Solovieva, M.; Levin, B.; Hayakawa, M.; Fedun, V. Meteorological effects in the lower ionosphere as based on VLF/LF signal observations. *Nat. Hazards Earth Syst. Sci.* **2014**, *14*, 2671–2679. [[CrossRef](#)]
21. Singh, R.; Veenadhari, B.; Maurya, A.K.; Cohen, M.B.; Kumar, S.; Selvakumaran, R.; Pant, P.; Singh, A.K.; Inan, U.S. D-region ionosphere response to the total solar eclipse of 22 July 2009 deduced from ELF-VLF tweek observations in the Indian sector. *J. Geophys. Res. Space* **2011**, *116*, 10301. [[CrossRef](#)]
22. Ilić, L.; Kuzmanoski, M.; Kolarž, P.; Nina, A.; Srećković, V.; Mijić, Z.; Bajčetić, J.; Andrić, M. Changes of atmospheric properties over Belgrade, observed using remote sensing and in situ methods during the partial solar eclipse of 20 March 2015. *J. Atmos. Sol. Terr. Phys.* **2018**, *171*, 250–259. [[CrossRef](#)]
23. Jin, S.; Occhipinti, G.; Jin, R. GNSS ionospheric seismology: Recent observation evidences and characteristics. *Earth Sci. Rev.* **2015**, *147*, 54–64. [[CrossRef](#)]
24. Manta, F.; Occhipinti, G.; Feng, L.; Hill, E.M. Rapid identification of tsunamigenic earthquakes using GNSS ionospheric sounding. *Sci. Rep.* **2020**, *10*, 1–10. [[CrossRef](#)]
25. Korepanov, V.; Hayakawa, M.; Yampolski, Y.; Lizunov, G. AGW as a seismo-ionospheric coupling responsible agent. *Phys. Chem. Earth* **2009**, *34*, 485–495. [[CrossRef](#)]
26. Mareev, E.A. Mosaic source of internal gravity waves associated with seismic activity. *Seism. Electromagn. Lithosphere Atmos. Ionos.* **2002**, 335–343. [[CrossRef](#)]
27. Molchanov, O.; Fedorov, E.; Schekotov, A.; Gordeev, E.; Chebrov, V.; Surkov, V.; Rozhnoi, A.; Andreevsky, S.; Iudin, D.; Yunga, S.; et al. Lithosphere-atmosphere-ionosphere coupling as governing mechanism for preseismic short-term events in atmosphere and ionosphere. *Nat. Haz. Earth Syst. Sci.* **2004**, *4*, 757–767. [[CrossRef](#)]
28. Nina, A.; Čadež, V.M. Detection of acoustic-gravity waves in lower ionosphere by VLF radio waves. *Geophys. Res. Lett.* **2013**, *40*, 4803–4807. [[CrossRef](#)]
29. Kumar, S.; Kumar, A.; Menk, F.; Maurya, A.K.; Singh, R.; Veenadhari, B. Response of the low-latitude D region ionosphere to extreme space weather event of 14–16 December 2006. *J. Geophys. Res. Space* **2015**, *120*, 788–799. [[CrossRef](#)]
30. Maurya, A.K.; Venkatesham, K.; Kumar, S.; Singh, R.; Tiwari, P.; Singh, A.K. Effects of St. Patrick’s Day Geomagnetic Storm of March 2015 and of June 2015 on Low-Equatorial D Region Ionosphere. *J. Geophys. Res. Space* **2018**, *123*, 6836–6850. [[CrossRef](#)]
31. NaitAmor, S.; Cohen, M.B.; Kumar, S.; Chanrion, O.; Neubert, T. VLF Signal Anomalies During Cyclone Activity in the Atlantic Ocean. *Geophys. Res. Lett.* **2018**, *45*, 10,185–10,192. [[CrossRef](#)]
32. Kumar, S.; Kumar, A.; Maurya, A.K.; Singh, R. Changes in the D region associated with three recent solar eclipses in the South Pacific region. *J. Geophys. Res. Space* **2016**, *121*, 5930–5943. [[CrossRef](#)]
33. Nina, A.; Pulnits, S.; Biagi, P.; Nico, G.; Mitrović, S.; Radovanović, M.; Popović, Č.L. Variation in natural short-period ionospheric noise, and acoustic and gravity waves revealed by the amplitude analysis of a VLF radio signal on the occasion of the Kraljevo earthquake (Mw = 5.4). *Sci. Total Environ.* **2020**, *710*, 136406. [[CrossRef](#)]
34. Maurya, A.K.; Phanikumar, D.V.; Singh, R.; Kumar, S.; Veenadhari, B.; Kwak, Y.S.; Kumar, A.; Singh, A.K.; Niranjana Kumar, K. Low-mid latitude D region ionospheric perturbations associated with 22 July 2009 total solar eclipse: Wave-like signatures inferred from VLF observations. *J. Geophys. Res.* **2014**, *119*, 8512–8523. [[CrossRef](#)]
35. Yamauchi, T.; Maekawa, S.; Horie, T.; Hayakawa, M.; Soloviev, O. Subionospheric VLF/LF monitoring of ionospheric perturbations for the 2004 Mid-Niigata earthquake and their structure and dynamics. *J. Atmos. Sol. Terr. Phys.* **2007**, *69*, 793–802. [[CrossRef](#)]
36. Maekawa, S.; Horie, T.; Yamauchi, T.; Sawaya, T.; Ishikawa, M.; Hayakawa, M.; Sasaki, H. A statistical study on the effect of earthquakes on the ionosphere, based on the subionospheric LF propagation data in Japan. *Ann. Geophys.* **2006**, *24*, 2219–2225. [[CrossRef](#)]
37. Maurya, A.K.; Venkatesham, K.; Tiwari, P.; Vijaykumar, K.; Singh, R.; Singh, A.K.; Ramesh, D.S. The 25 April 2015 Nepal Earthquake: Investigation of precursor in VLF subionospheric signal. *J. Geophys. Res. Space* **2016**, *121*, 10,403–10,416. [[CrossRef](#)]
38. Zhao, S.; Shen, X.; Liao, L.; Zhima, Z.; Zhou, C.; Wang, Z.; Cui, J.; Lu, H. Investigation of Precursors in VLF Subionospheric Signals Related to Strong Earthquakes (M > 7) in Western China and Possible Explanations. *Remote Sens.* **2020**, *12*, 3563. [[CrossRef](#)]
39. Biagi, P.; Castellana, L.; Maggipinto, T.; Maggipinto, G.; Minafra, A.; Ermini, A.; Molchanov, O.; Rozhnoi, A.; Solovieva, M.; Hayakawa, M. Anomalies in VLF radio signals related to the seismicity during November–December 2004: A comparison of ground and satellite results. *Phys. Chem. Earth Parts A/B/C* **2009**, *34*, 456–463. [[CrossRef](#)]
40. Knezevic Antonijevic, S.; Arroucau, P.; Vlahovic, G. Seismotectonic Model of the Kraljevo 3 November 2010 Mw 5.4 Earthquake Sequence. *Seismol. Res. Lett.* **2013**, *84*, 600–610. [[CrossRef](#)]
41. International Reference Ionosphere—IRI-2012. Available online: https://ccmc.gsfc.nasa.gov/modelweb/models/iri2012_vitmo.php (accessed on 28 February 2021).

42. Yeh, K.C.; Liu, C.H. *Theory of Ionospheric Waves*; Academic Press: New York, NY, USA, 1972.
43. Goedbloed, H.; Poedts, S. *Principles of Magnetohydrodynamics: With Applications to Laboratory and Astrophysical Plasmas*; Cambridge University Press: Cambridge, UK, 2004.
44. Biagi, P.F.; Maggipinto, T.; Righetti, F.; Loiacono, D.; Schiavulli, L.; Ligonzo, T.; Ermini, A.; Moldovan, I.A.; Moldovan, A.S.; Buyuksarac, A.; et al. The European VLF/LF radio network to search for earthquake precursors: Setting up and natural/man-made disturbances. *Nat. Hazards Earth Syst. Sci.* **2011**, *11*, 333–341. [[CrossRef](#)]
45. Yang, S.S.; Asano, T.; Hayakawa, M. Abnormal Gravity Wave Activity in the Stratosphere Prior to the 2016 Kumamoto Earthquakes. *J. Geophys. Res. Space* **2019**, *124*, 1410–1425. [[CrossRef](#)]
46. Chum, J.; Liu, J.-Y.; Laštovička, J.; Fišer, J.; Mošna, Z.; Sun, Y.-Y. Ionospheric signatures of the 25 April 2015 Nepal earthquake and the relative role of compression and advection for Doppler sounding of infrasound in the ionosphere. *Earth Planets Space* **2019**, *68*, 24. [[CrossRef](#)]

VARIATIONS IN IONOSPHERIC D-REGION RECOMBINATION PROPERTIES DURING INCREASE OF ITS X-RAY HEATING INDUCED BY SOLAR X-RAY FLARE

by

**Aleksandra M. NINA^{a*}, Vladimir M. ČADEŽ^b, Maša D. LAKIĆEVIĆ^b,
Milan M. RADOVANOVIĆ^{c,d}, Aleksandra B. KOLARSKI^e,
and Luka Č. POPOVIĆ^{b,f}**

^a Institute of Physics Belgrade, University of Belgrade, Belgrade, Serbia

^b Astronomical Observatory of Belgrade, Belgrade, Serbia

^c Geographical Institute Jovan Cvijić SASA, Belgrade, Serbia

^d South Ural State University, Institute of Sports, Tourism and Service, Chelyabinsk, Russia

^e STC NIS-Naftagas LLC, Novi Sad, Serbia

^f Faculty of Science, University of Banja Luka, Banja Luka,
Republic of Srpska, Bosnia and Herzegovina

Original scientific paper

<https://doi.org/10.2298/TSCI190501313N>

In this paper we present an analysis of parameters describing the effective recombination processes in the upper ionospheric D-region in the period of its additional heating by the X-radiation emitted during a solar X-ray flare. We present a procedure for calculation of the effective recombination coefficient and electron loss rate in the period when the X-radiation flux detected by the GOES satellite in the wavelength domain between 0.1 and 0.8 nm increases. The developed procedure is based on observational data obtained in the low ionospheric monitoring by the very low/low frequency radio waves and it is related to the considered area and time period. The obtained expressions are applied to data for the very low frequency signal emitted in Germany and recorded in Serbia during the solar X-ray flare detected by the GOES-14 satellite on May 5, 2010.

Key words: *effective recombination coefficient, electron loss rate, ionospheric D-region, solar X-ray flares*

Introduction

Due to influences of numerous geo and astrophysical phenomena, the thermal properties of the ionosphere can significantly vary in time. One of the most important phenomena which induce intensive low ionospheric disturbances is emission of high-energy electromagnetic radiation from the Sun in the X-spectral domain called a solar X-ray flare. This radiation primarily disturbs the ionospheric plasma in the D-region (60-90 km) and research of these effects is a subject of many studies [1-4]. Earlier investigations show that changes in plasma parameters induced by these astrophysical phenomena depend on the radiation intensity as well as on the atmospheric properties (see for example [5]) and that relative changes of plasma parameters due to heating by high-energy photons can reach a few orders of magnitude.

* Corresponding author, e-mail: sandrast@ipb.ac.rs

Because of complexity of radiation characteristics and processes in Earth's atmosphere, analysis of space and time distributions of a particular parameter require different approximations. Consequently, divisions in both space and time domains are necessary for many studies. In the case of the ionospheric D-region, which is in the focus of this research, the differences in modeling depending on the altitude are mainly consequences of variation of dominant electron loss processes. Namely, in the upper part, the recombination processes can be considered as the most important in reduction of the electron density while electron attachment processes have dominant role in the lowest D-region altitudes [6]. On the other side, approximations which can be applied to different parameters depend on the flare phase. For this reason, many studies are related to quiet conditions or the relaxation period [7, 8], time of radiation flux maximum [6, 9], *etc.*

Although solar X-ray flares can provide significant variations in the D-region properties which are connected with thermal processes, research of temperature dependent parameters during disturbed conditions are not enough analyzed. In this paper we investigate the influence of the X-radiation increase on parameters describing recombination processes in the D-region part between 75 km and 80 km. First, we give a new procedure for calculation of time evolution of the effective recombination coefficient which describes the dominant processes in the electron density reduction within the considered altitude domain. This procedure is based on experimental very low frequency/low frequency (VLF/LF) data and long-wave propagation capability (LWPC) numerical model for simulation of the VLF/LF signal propagation [10] and it follows the research presented in [5] and [7] and references therein. In the second part we analyze properties of the electron loss rate in the considered altitude domain. We consider the time period when the X-radiation intensity increases to its maximum value. The obtained theoretical equations are applied to a particular case of the D-region perturbation induced by the solar X-ray flare of class C8.8 occurred on May 5, 2010. It is interesting that this flare was in the beginning of NASA Solar Dynamics Observatory (SDO) observations and that its characteristics are very well analyzed [11].

Experimental set-up, observations and data processing

The presented study requires data obtained in observations of the solar X-ray radiation and in the D-region monitoring which can be obtained by a GOES satellite and ionospheric sounding by the VLF/LF radio signals, respectively.

For general descriptions of the space-time dependencies of plasma parameters located in the considered area, it is practically sufficient to consider one particular flare event. Namely, the major characteristics of the D-region response to the solar X-ray flares are very similar (see for example comparison given in [7]) and statistical analyses give additional information related only to dependencies of the considered values on the ionospheric state and radiation properties. In this study the major goal is determination of expressions for time evolution of plasma parameters (the effective recombination coefficient α_{eff} and electron loss rate L) which allow us to use one particular flare event as an example. Here we chose to study the perturbation induced by the solar X-flare occurred on May 5, 2010 with photon flux I registered by the GOES-14 satellite of National Oceanic and Atmospheric Administration (NOAA), USA (fig. 1, upper panel) at the wavelengths range 0.1-0.8 nm for two reasons: this is the best example of the dominant influence of a solar X-ray on the D-region (seen in fig. 1 as very flat amplitude and phase time evolutions, as recorded by the AWESOME VLF receiver [12], which correspond to time evolution of the X-radiation time evolution and this study is an extension of complementary research given in [7, 8] related to the unperturbed conditions and relaxation period, respectively. Due

to the first reason this flare has also been considered in several previous investigations (see [13] and references therein). One of the open questions of this study is related to research of the radiation and atmospheric properties on the electron reduction in the considered flare phase. This task exceeds the topic of this paper and should be a subject of the incoming research.

The time evolution of the solar X-ray radiation is important for determination of the time period within the ionospheric parameters that should be analyzed. In fig. 1 it is seen that the flux increase is recorded from about 10:48 UT to near 11:53 UT. However, the beginning of the considered period is chosen to be about 11:49 UT because of the time delay of the ionospheric response (seen as the beginning of variations in signal amplitude A_{rec} and phase P_{rec}) with respect to the start of the flare occurrence.

Processing of the recorded amplitude and phase (using the LWPC numerical model for simulation of the VLF signal propagation [10]) is directed to determination of Wait's parameters *sharpness* β [km^{-1}] and signal reflection height H' [km] which are required for calculation of the electron density $N_e(h,t)$ [m^{-3}] at fixed altitude h [km] using Wait's model [14] and expression given in [15]:

$$N_e(h,t) = 1.43 \cdot 10^{13} e^{-\beta(t)H'(t)} e^{[\beta(t)-0.15]h} \quad (1)$$

which is the standard procedure applied in numerous studies of the low ionospheric disturbances induced by different events [6, 16, 17].

The Wait's parameters are modeled using criteria given in [16] and applied in many papers [6, 18, 19]. The obtained values and the relevant fitted curves (polynomial functions of the order 4) are shown in fig. 2 (upper panel). The surface plot of the electron density time and altitude dependences, shown in the bottom panel of this figure, are in agreement with relevant data presented in [6, 9, 16].

D-region modelling

In the upper horizontal uniform D-region, where the recombination processes dominate in the free electron number reduction, the electron density dynamics can be described by expression [20]:

$$\frac{dN_e(h,t)}{dt} = G_0(h) + K(h,t)I(t) - \alpha_{\text{eff}}(h,t)N_e^2(h,t) \quad (2)$$

where $G_0(h)$ is the electron gain rate in the unperturbed D-region at altitude, h , whose determination is explained in details in [7], $I(t)$ – the X-radiation flux detected by the GOES satellite in energy channel for wavelengths between 0.1 nm and 0.8 nm at time, t . The coefficient $K(h,t)$ is a space and time dependent scaling coefficient described in [5] while α_{eff} is the effective re-

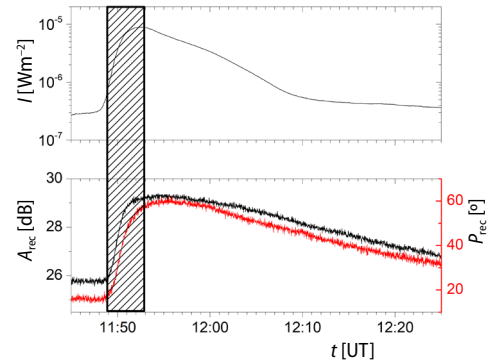


Figure 1. Increase of the X-radiation flux recorded by the GOES-14 satellite at wavelengths domain 0.1-0.8 nm (upper panel) and reaction of the phase and amplitude (bottom panel) of the VLF signal emitted by the DHO transmitter located in Germany and received by the AWESOME receiver in Serbia. The shaded domain represents the considered period analyzed when the recorded X-radiation flux increases in time after beginning of the ionospheric response

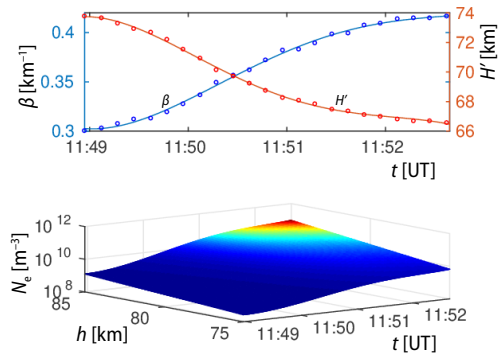


Figure 2. Time evolutions of Wait's parameters (upper panel) and the electron density in the altitude domain between 75 km and 85 km (bottom panel) for the considered X-ray flare event

upper D-region heights. The developed procedure and the obtained results open possibility for further modeling other plasma parameters in the upper part of the D-region disturbed by the solar X-ray flare and they enable study of the flare phase between its maximum flux and recombination regime which will be in focus of our upcoming research.

Modelling the time evolution of the effective recombination coefficient

As we already said, determination of the time evolution of the effective recombination coefficient is a very complex task and, due to lack of real observations which are necessary for calculation of plasma parameters at the considered location and time period, it is necessary to use some approximations. In this study we present a model for calculation of the effective recombination coefficient at altitude domain between 75 km and 85 km during increase of the X-ray flux. Our procedure is divided in three steps:

- Determination of an analytical expression for dependency of the effective recombination coefficient on the X-ray flux at a fixed altitude using data given in literature,
- Correction of the obtained dependence on calculated effective recombination coefficient in quiet conditions obtained from a real low ionospheric observation relevant to the considered case and transformation of the flux dependency in time evolution of the effective recombination coefficient corrected to the initial condition for the considered case.
- Correction of the obtained dependency on the calculated effective recombination coefficient in the maximum X-radiation flux obtained from a real low ionospheric observation relevant to the considered case.

In this way, we provide a model for calculation of the effective recombination coefficient based on real observations which means that the obtained values are related to the considered event and the observed area.

Dependence of effective recombination coefficient on X-ray flux

Research presented in [5] shows that dependence of the electron density and its time derivative on the X-ray flux detected by the GOES satellite has complex shapes. However, in the period between times of relatively small increase of the electron density and maximum of the considered X-radiation flux these dependences are very close to linear dependences in the exp-exp scale. Furthermore, the time evolution of radiation at wavelengths which dominate

combination coefficient that also vary in space and time.

Although we can neglect transport processes (they become important at altitudes above 120-150 km [21]) and although the time and altitude dependencies of $N_e(h,t)$ and $G_0(h)$ in the horizontal uniform ionosphere can be determined, eq. (2) is very complex because of lack of observational data needed for calculation of the coefficients K and α_{eff} during the disturbance. For this reason, it is necessary to use some approximations for one of these parameters.

In this study we use the previous research presented in [7] and [22] to model the effective recombination coefficient time evolutions at the

in ionization in the upper ionosphere indicates that the expected variations in the parameter K near the radiation maximum (primarily induced by variation in the X-radiation spectrum) is not significant. Because of these properties and assuming that ionization without the X-radiation, $G_0(h)$, is stationary (*e. g.* that X-radiation is the dominant source of the ionization rate increase) we assumed that the fitted dependence of the effective recombination coefficient in maxima of the X-radiation fluxes detected by the GOES satellite at the wavelength domain 0.1-0.8 nm for different flare events can be used as the dependence of this plasma parameter on the X-radiation flux during its increase in one particular X-ray flare event. Here we consider the X-ray flux detected by the GOES energy channel for the wavelength domain 0.1-0.8 nm because it better describes the X-ray photoionization in the upper D-region than the other energy channel (0.05-0.4 nm) [5].

Dependencies of the effective recombination coefficient in the X-radiation flux maxima is given in several studies [6, 22, 23]. In our investigation we use the results presented in [22] which are related to the altitude of 80 km. As seen in fig. 3, the influence of the radiation characteristics and atmospheric conditions relevant for different flare events is important. For this reason, we fit these values to estimate the analytical expression for the $\psi_{\text{eff}}(\Phi)$ dependence at this altitude. Here we notice that the letters ψ and Φ are used for the effective recombination coefficient and X-radiation flux in the maximum X-radiation of events analyzed in [22] to indicate the difference of these parameters from those calculated by data obtained in real observations of the particular studied events which are designated as α and I , respectively. To choose the fitting function for fit data given in [22] we use the criterion that $\psi_{\text{eff}}(\Phi)$ should saturate going to lower fluxes *e. g.* going to quiet conditions. In fig. 3 we show the obtained fitted curves for $\log(\psi^*)(\log(\Phi^*))$ by formula:

$$\log(\psi_{\text{eff}}^*) = -14.13109 + \frac{-11.2868 + 14.13109}{1 + 10^{\log(\Phi^*) - \log(-11.32906)}} \quad (3)$$

Here we fitted the logarithmic values of the considered physical parameters divided by relevant unique values, $\log(\psi_{\text{eff}}^*) = \log(\psi_{\text{eff}}/1 \text{ m}^3\text{s}^{-1})$ and $\log(\Phi^*) = \log(\Phi/1 \text{ Wm}^{-2})$, to obtain better determination of representative fits related to values which lies within more than one order of magnitude.

The fact that the considered altitude domain is characterized by very similar processes allows us to use eq. (3) as approximation in the entire considered altitude domain. This assumption is in agreement with results obtained in [23].

The obtained values are relevant for the set of data given in [22] that describes specific conditions in the ionosphere relevant for the events analyzed in that study. To obtain the procedure for determination the dependence of the effective recombination coefficient on the radiation flux (or in other words, to reduce the influence of the considered geographical locations and

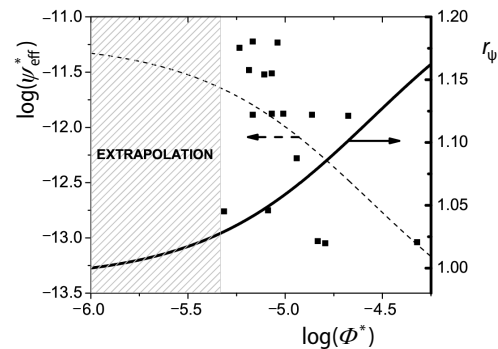


Figure 3. Left axis: Dependences of ψ_{eff} normalized to its unit values $1 \text{ m}^3\text{s}^{-1}$ on the X-radiation flux normalized to its unit values 1 Wm^{-2} . Scatters represent values obtained in [22] while dashed line is obtained by fitting these values with eq. (3). Right axis: tick solid line represents normalized values of fitted curve on value of $\log(\psi_{\text{eff}}^*)$ related to quiet state. These calculations are made using eq. (4)

other parameters), in our model we modified the fitted curve using observational data relevant to quiet conditions and values at the moment of the radiation flux maximum for the considered X-ray flare and observed D-region area.

Correction on the quiet condition

To fit the obtained curve to the values obtained by real observations we first normalize the dependence $\log(\psi_{\text{eff}}^o)$ given by eq. (3) on its value relevant for the unperturbed conditions $\log(\psi_{\text{eff}}^{o*})$:

$$r_{\psi^*} = \frac{\log[\psi_{\text{eff}}^{o*}(\Phi)]}{\log(\psi_{\text{eff}}^{o*})} \quad (4)$$

This expression gives us the final information from the data given in [22] and it is further used as an input set of data for calculation the time evolution of this plasma parameter for the considered flare event.

The next step in our procedure is applying eq. (4) (dependent on flux) in calculation of the first correction coefficient, r^o , (describing the correction on the initial unperturbed conditions) which is time dependent. To do that, we use the GOES satellite data set for the X-ray flux time evolution and find pairs of parameters t and Φ specific for the considered flare event. These parameters allow us to transform the energy dependence that is given in eq. (4) and shown in fig. 3 to r^o : $r_{\psi^*}(\Phi) \rightarrow r^o(t)$. Here we notice that transformation should first be made for the relevant form with logarithm expressions and after that, using the exponential function, the required corrected parameter should be calculated.

The product of coefficient, r^o , and the initial effective recombination coefficient α_{eff}^o gives the effective recombination coefficient corrected only to the unperturbed conditions. Here, α_{eff}^o can be determined from eq. (2) assuming $dN_e/dt \approx 0$ and $G_0(h) \gg K(h, t)I(t)$.

$$\alpha_{\text{eff}}^o(h) = \frac{G_0(h)}{N_e^{o2}(h)} \quad (5)$$

where N_e^o represents the electron density in the quiet ionospheric D-region. As we already said, N_e^o and $G_0(h)$ can be obtained by procedures explained in [7] and [15], respectively.

Correction on properties at time of the X-radiation flux maximum

In the second correction we normalize the obtained dependence by function r :

$$r = \frac{\Phi - \Phi^o}{\Phi^{(\text{Imax})} - \Phi^o} r^{(\text{Imax})} \quad (6)$$

which fits the modeled effective recombination coefficient corrected on quiet conditions in procedure explained in section *Correction on the quiet condition* to its value α_{eff} obtained in the modeling based on real observation of the analyzed event at the time of the X-radiation intensity maximum. Here, $\Phi^{(\text{Imax})}$ and $r^{(\text{Imax})}$ are Φ and r at the time of the X-radiation intensity maximum, respectively.

Similarly like in the procedure given for the first correction, $\alpha_{\text{eff}}^{\text{Imax}}$ can be obtained from eq. (2). As we here consider the maximum of the X-radiation, we can assume that the time derivative of KI is equal to 0. In addition, from the fact that the electron reduction rate still increases in this period [24] we can conclude that N_e^2 (it increases in time) dominates α_{eff} in time

variation of this term *e. g.* that $d\alpha_{\text{eff}}/dt < dN_e^2/dt$. For this reason, we use $d(\alpha_{\text{eff}}N_e^2)/dt \approx \alpha_{\text{eff}}dN_e^2/dt$. By these assumptions, the time derivative of eq. (2) gives:

$$\alpha_{\text{eff}}^{\text{Imax}}(h) = -\frac{d^2 N_e(h,t)}{dt^2} \left[\frac{dN_e^2(h,t)}{dt} \right]^{-1} \Bigg|_{t=t_{\text{Imax}}} \quad (7)$$

Finally, the obtained expression for the effective recombination coefficient is:

$$\alpha_{\text{eff}}^{\text{Imax}}(h) = C(h)\alpha_{\text{eff}}^o(h) \quad (8)$$

where normalized coefficient C is given by:

$$C = \frac{\Phi - \Phi^o}{\Phi^{(\text{Imax})} - \Phi^o} r^o r^{(\text{Imax})} \quad (9)$$

Modeling of the electron loss rate

As one can see in eq. (2), knowledge of the electron density and effective recombination coefficient allows us to calculate the electron loss rate $L(h, t)$ using the expression:

$$L(h,t) = \alpha_{\text{eff}}(h,t)N_e^2(h,t) \quad (10)$$

where the electron recombination coefficient α_{eff} and the electron density N_e are given by eqs. (8) and (1), respectively.

Results and discussions

In this paper we apply the model presented in section *D-region modelling* to the X-ray flux data detected by the GOES-14 satellite and to data on the amplitude and phase of the 23.4 kHz signal emitted by the VLF transmitter in Germany and received by the Belgrade receiver station in Serbia. These values, recorded during the period of influence of the solar X-ray flare of class C8.8 occurred on May 5, 2010, are given in section *Experimental set-up, observations and data processing*, fig. 1.

As we can see in section *D-region modelling*, to determine the time evolution of the effective recombination coefficient it is necessary to know its values in quiet conditions and at the moment of the solar X-radiation maximum. Calculations based on eqs. (5) and (7) give the lower values of α_{eff} during a maximum of the radiation intensity than when the state is quasi stationary, and its variation within one order of magnitude at fixed altitude during the considered flare influence. In both cases α_{eff} decreases with altitude.

Although research of the altitude dependence of the coefficient α_{eff} is presented in several studies the comparison of obtained results is not simple due to variations with geographical position and periodical changes in quiet Sun radiation and unperturbed atmospheric properties. During perturbed periods, additional differences in atmospheric dynamic can be consequences of various X-radiation spectral characteristics. These deviations are visualized in [24, 25] where one can see that the presented values at fixed altitude can lie within about three orders of magnitude. However, it is important to point out that α_{eff} decreases with altitude, as visible in fig. 4, is also obtained in 8 of 10 and in 9 of 10 analyses shown in [24, 25], respectively.

The obtained values in the case of quiet conditions are in a good agreement with those presented in earlier investigations. In fig. 4 we can see that our model, applied to the considered conditions, gives a very similar shape in comparison with those shown in [26]

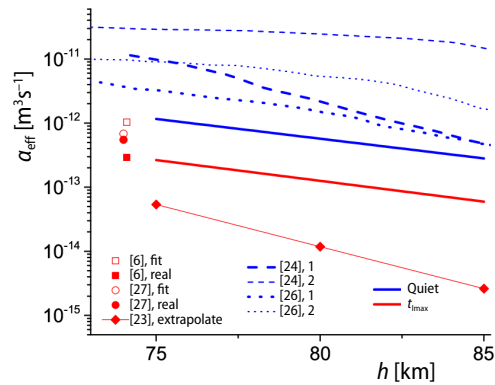


Figure 4. Altitude distribution of α_{eff} in a quiet state and at time of the X-ray flux maximum obtained in our model and their comparison with curves presented in [24, 25] for quiet conditions (blue lines) and presented or derived from data given in [6, 23, 26] for the maximum radiation (red line or scatters). Detailed description is given in text (for color image see journal web site)

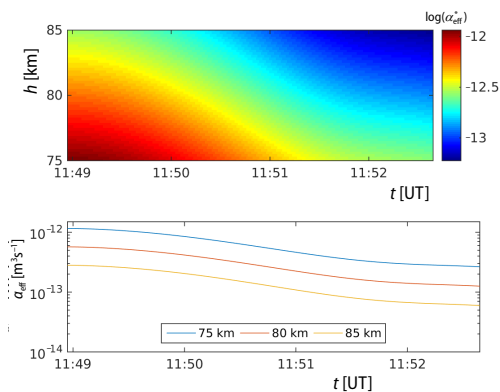


Figure 5. Upper panel: Surface plot α_{eff} normalized to its unit values $1 \text{ m}^3 \text{ s}^{-1}$ as a function of time, t , and altitude, h , during increase of the X-ray flux of the considered solar X-ray flare. Bottom panel: Time evolution of α_{eff} at altitudes of 75 km, 80 km and 85 km during increase of the X-ray flux of the considered solar X-ray flare (for color image see journal web site)

of fig. 5. As one can see, the shapes of these dependences are the same for the logarithmic y scale and, for the considered X-ray flare event, their values differ within an order of magnitude at a fixed altitude.

Properties of the monotonous time and altitude dependences of the electron loss rate, calculated using eq. (10) for the known α_{eff} and N_e are opposite of what was obtained in the previous analysis. Namely, it can be seen in the upper panel of fig. 6 that this parameter reaches a

(blue dotted lines). Comparison with one curve given in [24] (tick dashed blue line) is better for higher altitudes while the second curve given in [24] (thin dashed blue line) has larger values of α_{eff} than in the cases of all presented dependencies (this deviation is more pronounced at higher altitudes).

Comparison of the obtained dependence $\alpha_{\text{eff}}(h)$ at the moment of the X-radiation maximum is harder than for quiet condition because of the lack of relevant data for the X-ray flares of the considered class. In fig. 4 we show the relevant data for 74.1 km and 74 km obtained by fitting of dependencies α_{eff} in the maximum X-radiation flux presented in [6, 27] (fill and open scatters, respectively). In addition, in these studies we give calculated values for events of class very similar to the X-ray flare which we analyze. Here, one can see that all these values and the expected value in our calculation which can be seen as extrapolation of the red line to 74 km, differ within one order of magnitude. The lower values of $\alpha_{\text{eff}}(h)$ are obtained by extrapolation of data presented in [23] (red line with scatters). In this case better comparison is obtained for lower altitude (within one order of magnitude below about 80 km). At 85 km, these values are within two orders of magnitude.

Time evolutions of the effective recombination coefficient, α_{eff} , in altitude domain between 75 km and 85 km during the period of the X-ray flux increase are presented in fig. 5 for the considered flare. The upper panel shows that both time and altitude dependences are monotonous functions. Namely, the values of α_{eff} at fixed altitude decrease during the entire considered period and, on the other side, they increase going to the Earth surface at a fixed time, t .

Time evolutions of α_{eff} at altitudes 75 km, 80 km and 85 km are shown in the bottom panel

maximum at the end of the considered time interval and that its value increases with altitude during the entire time period.

Contrary to the same shapes of the time evolution of the parameter α_{eff} at different heights, the comparison of the electron loss rate during the considered time period at 75 km, 80 km, and 85 km shows a larger increase of its values going to the upper D-region boundary. According eq. (10), this difference can be explained by a more pronounced increase of the electron density ($L \sim N_e^2$) relative to the decrease of the effective recombination coefficient ($L \sim \alpha_{\text{eff}}$) occurring with altitude.

Keeping in mind that the electron loss rate is approximatively equal to the electron gain rate induced by the Ly α radiation in the quiet period, we can say that the obtained values before the X-ray flare perturbation in this case are in agreement with values presented for the other two flares in [7] and those given in [24, 28, 29, 30]. Comparison of the noticed dependences are shown in [7]. In addition, as we already said, the electron density at the maximum of the X-radiation is in the domain of values reported in other papers (see for example [6, 9, 16]). For this reason and owing to the indicated agreement of the effective recombination coefficient, we can conclude that eq. (10) for the electron loss rate at the maximum of the X-radiation flux yields acceptable values.

Conclusions

In this study we presented a procedure for determination of changes of plasma parameters in the upper D-region during the increase of ionospheric heating by solar radiation during an X-ray flare. We considered the effective recombination coefficient and electron loss rate and apply the developed procedure to determine their time evolutions at the altitude domain between 75 km and 85 km from data obtained from the low ionospheric monitoring by the VLF signal emitted in Germany and received in Serbia during the influence of the solar X-ray flare which occurred on May 5, 2010.

The obtained results show a decrease of the effective recombination coefficient with strengthening of the X-radiation at altitudes between 75 and 85 km with the same profiles in the lin-exp scale. Nevertheless, the electron loss rate increases in time and with altitude. Also, the variations of this rate in the considered height domain increase in time, e.g. with the radiation flux.

This procedure includes data obtained in real observations which indicates the relevance of obtained results for research of the considered part of the D-region and the considered event that cause perturbations. It is an extension of research of plasma parameters to D-region during influence of a solar X-ray flare. Namely, the existing studies are primarily directed to the quiet conditions before the flare occurrence, at radiation flux maximum, or in the relaxation period after termination of the flare influence on the atmosphere. Our results, however, introduce the effects of temporal transition between the first two quasi stationary states and can also be used for modeling the temporal transition to the third domain (between the radiation flux maximum and beginning of the relaxation period) which, to our knowledge, has not yet been done from real observation data.

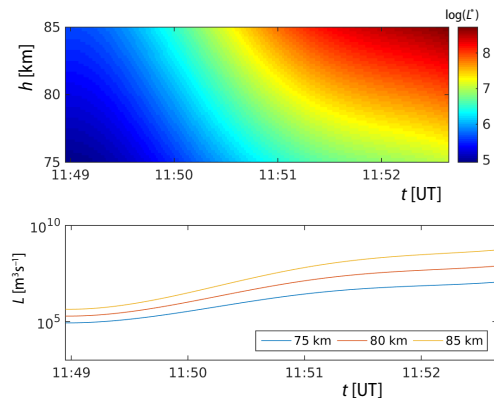


Figure 6. The same as in fig. 5 but for the electron loss rate L (for color image see journal web site)

Because this method is applicable to numerous data sets obtained by the VLF/LF receiver network (it observes a large part of the terrestrial low ionosphere), the presented procedure allows further studies of spatial variation of the considered ionospheric parameters and enables research of influence of different spectral properties of solar X-ray flare events. The obtained results also open a possibility for modeling parameters relevant to electron gain processes using the equation for electron density dynamics. Here, we point out that this research requires a detailed analysis of the influence of the X-ray photon energies on the upper D-region altitude domain and that inclusion of time evolution of the X-radiation should be analyzed in more details for a better determination of these parameters.

Acknowledgment

The authors thank the Ministry of Education, Science and Technological Development of the Republic of Serbia through the projects III 44002 176001, 176002, 176004 and III47007. The data for this paper collected by the GOES-14 satellite is available at NOAA's National Centers for Environmental information (http://satdat.ngdc.noaa.gov/sem/goes/data/new_full/2010/05/goes14/csv). Requests for the VLF data used for analysis can be directed to the corresponding author.

Nomenclature

A_{rec}	– recorded signal amplitude	β	– sharpness, [km^{-1}]
C	– normalized coefficient	ψ_{eff}	– fitted effective recombination coefficient, [m^3s^{-1}]
G_0	– electron gain rate under unperturbed conditions, [m^3s^{-1}]	<i>Superscripts</i>	
H^p	– signal reflection height, [km]	*	– normalized on unique values
h	– altitude [km]	o	– unperturbed conditions
I	– X-radiation flux, [Wm^{-2}]	<i>Acronyms</i>	
K	– scaling coefficient, [$\text{W}^{-1}\text{m}^{-1}\text{s}^{-1}$]	AWESOME – atmospheric weather electromagnetic system for observation modelling and education	
L	– electron loss rate, [m^3s^{-1}]	LWPC – long-wave propagation capability	
N_e	– electron density, [Wm^{-2}]	VLF – very low frequency	
P_{rec}	– recorded signal phase		
r	– correction coefficient, [–]		
t	– time, [s]		
<i>Greek letters</i>			
α_{eff}	– effective recombination coefficient, [m^3s^{-1}]		

References

- [1] Singh, A. K., *et al.*, Solar Flare Induced D-region Ionospheric Perturbations Evaluated from VLF Measurements, *Astrophysics and Space Science*, 350 (2014), 1, pp. 1-9
- [2] Srećković, V. A., *et al.*, The Effects of Solar Activity: Electrons in the Terrestrial Lower Ionosphere, *Journal of the Geographical Institute "Jovan Cvijic" SASA*, 67 (2017), 3, pp. 221-233
- [3] Todorović Drakul, M., *et al.*, Behaviour of Electron Content in the Ionospheric D-region During Solar X-ray Flares, *Serbian Astronomical Journal*, 2016 (2016), 193, pp. 11-18
- [4] Nina, A., *et al.*, Diagnostics of Plasma in the Ionospheric D-region: Detection and Study of Different Ionospheric Disturbance Types, *European Physical Journal D*, 71 (2017), 7, 189
- [5] Nina, A., *et al.*, Analysis of the Relationship Between the Solar X-ray Radiation Intensity and the D-region Electron Density Using Satellite and Ground-based Radio Data, *Solar Physics*, 293 (2018), Apr., 64
- [6] Žigman, V., *et al.*, D-region Electron Density Evaluated from VLF Amplitude Time Delay During X-ray Solar Flares, *Journal of Atmospheric and Solar-Terrestrial Physics*, 69 (2007), 7, pp. 775-792
- [7] Nina, A., Čadež, V. M., Electron Production by Solar Ly- α Line Radiation in the Ionospheric D-region, *Advances in Space Research*, 54 (2014), 7, pp. 1276-1284

- [8] Bajčetić, J., et al., Ionospheric D-region Temperature Relaxation and its Influences on Radio Signal Propagation after Solar X-flares Occurrence, *Thermal Science*, 19 (2015), Suppl. 2, pp. S299-S309
- [9] Thomson, N. R. et al., Large Solar Flares and their Ionospheric D Region Enhancements, *Journal of Geophysical Research (Space Physics)*, 110 (2015), A6, pp. A06306: 1-10
- [10] Ferguson, J. A., *Computer Programs for Assessment of Long-Wavelength Radio Communications*, Version 2.0, Space and Naval Warfare Systems Center, San Diego, Cal., USA, 1998
- [11] Woods, T. N., et al., New Solar Extreme-ultraviolet Irradiance Observations, *The Astrophysical Journal*, 739 (2011), 2, pp. 59-71
- [12] Cohen, M. B., et al., Sensitive Broadband ELF/VLF Radio Reception with the AWESOME Instrument, *IEEE Transactions on Geoscience and Remote Sensing*, 48 (2010), 1, pp. 3-17
- [13] Radovanović, M, Investigation of Solar Influence on the Terrestrial Processes: Activities in Serbia, *Journal of the Geographical Institute "Jovan Cvijic" SASA*, 68 (2018), 1, pp. 149-155
- [14] Wait, J. R., Spies, K. P., Characteristics of the Earth-Ionosphere Waveguide for VLF Radio Waves, NBS Technical Note, Col., USA, 1964
- [15] Thomson, N. R, Experimental Daytime VLF Ionospheric Parameters, *Journal of Atmospheric and Terrestrial Physics*, 55 (1993), 2, pp. 173-184
- [16] Grubor, D. P., et al., Classification of X-ray Solar Flares Regarding their Effects on the Lower Ionosphere Electron Density Profile, *Annales Geophysicae*, 26 (2008), 7, pp. 1731-1740
- [17] Kumar, S., et al., Perturbations to the Lower Ionosphere by Tropical Cyclone Evan in the South Pacific Region, *Journal of Geophysical Research: Space Physics*, 122 (2017), 8, pp. 8720-8732
- [18] Nina, A., et al., Altitude Distribution of Electron Concentration in Ionospheric D-region in Presence of Time-varying Solar Radiation Flux, *Nuclear Instruments and Methods in Physics Research B*, 279 (2012), May, pp. 110-113
- [19] Kolarski, A., Davorka Grubor, D., Sensing the Earth's Low Ionosphere During Solar Flares Using VLF Signals and GOES Solar X-ray Data, *Advances in Space Research*, 53 (2014), 11, pp. 1595-1602
- [20] McEwan, M., Phillips, F., *Chemistry of the Atmosphere*, Mir, Moscow, Russia, 1978
- [21] Blaunstein, N., Christodoulou, C., *Radio Propagation and Adaptive Antennas for Wireless Communication Links: Terrestrial, Atmospheric and Ionospheric*, John Wiley and Sons, Inc., Hoboken, New Jersey, 2006
- [22] Deshpande, S. D., Mitra, A. P., Ionospheric Effects of Solar Flares – III. the Quantitative Relationship of Flare X-rays to SID's, *Journal of Atmospheric and Terrestrial Physics*, 34 (1972), 2, pp. 243-253
- [23] Hayes, L. A., et al., Pulsations in the Earth's Lower Ionosphere Synchronized with Solar Flare Emission, *Journal of Geophysical Research: Space Physics*, 122 (2017), 10, pp. 9841-9847
- [24] Mitra, A. P., *Ionospheric Effects of Solar Flares*, Mir, Moscow, Russia, 1974
- [25] Sato, T., The Response of the Lower Ionosphere to the Great Solar Flare of August 7, 1972, *Journal of Geomagnetism and Geoelectricity*, 27 (1975), 5, pp. 383-407
- [26] Osepian, A., et al., D-region Electron Density and Effective Recombination Coefficients During Twilight – Experimental Data and Modelling During Solar Proton Events, *Annales Geophysicae*, 27 (2009), 10, pp. 3713-3724
- [27] Basak, T., Chakrabarti, S. K., Effective Recombination Coefficient and Solar Zenith Angle Effects on Low-latitude D-Region Ionosphere Evaluated from VLF Signal Amplitude and its Time Delay During X-ray Solar Flares, *Astrophysics and Space Science*, 348 (2013), 2, pp. 315-326
- [28] Rowe, J. N., Model Studies of the Lower Ionosphere, Sci. Rep.No. 406, Pennsylvania State Univ., Univ. Park, Penn., USA, 1972
- [29] Aikin, A. C., et al., Some Results of Rocket Experiments in the Quiet D Region, *Journal of Geophysical Research*, 69 (1964), 21, pp. 4621-4628
- [30] Bourdeau, R. E., et al., The Lower Ionosphere at Solar Minimum, Greenbelt, Md.: NASA, Goddard Space Flight Center. 1965

M23

Influence of variations in the solar hydrogen Ly α radiation on the ionospheric D-region electron density during a year and solar cycle

A. Nina¹ , V.M. Čadež², L.Č. Popović^{2,3,4} and M. Radovanović^{5,6}

¹ *Institute of Physics Belgrade, University of Belgrade, 11080 Belgrade, Serbia (E-mail: sandrast@ipb.ac.rs)*

² *Astronomical Observatory, 11060 Belgrade, Serbia*

³ *Department of Astronomy, Faculty of mathematics, University of Belgrade, 11000 Belgrade, Serbia*

⁴ *Faculty of Science, University of Banja Luka, 78000 Banja Luka, R. Srpska, Bosnia and Herzegovina*

⁵ *Geographical Institute Jovan Cvijić SASA, 11000 Belgrade, Serbia*

⁶ *South Ural State University, Institute of Sports, Tourism and Service, 454080 Chelyabinsk, Russia*

Received: July 15, 2022; Accepted: October 10, 2022

Abstract. The hydrogen Ly α radiation emitted from the Sun is the main source of photo-ionization processes and, consequently, of the free electron production in the ionospheric D-region. Variations in the intensity of the incoming Ly α radiation affect changes in the electron density and they show up as periodic daily and seasonal changes, and changes during a solar cycle. The Quiet Ionospheric D-Region (QIonDR) model describes these periodic changes. In this study, we analyse how changes during a year and changes in the smoothed daily sunspot number (both processes affect the intensity of incoming radiation in the D-region) affect the electron density changes related to quiet conditions. The presented modelling is based on the results of the QIonDR model obtained for the part of Europe defined by the positions of the very low frequency (VLF) signal transmitters ICV (Sardinia, Italy) and DHO (Lower Saxony, Germany), and the AWESOME (Atmospheric Weather Electromagnetic System for Observation Modeling and Education) receiver position (Belgrade, Serbia) in application of the QIonDR model on real signals.

Key words: solar hydrogen Ly α line – ionospheric D-region – QIonDR model – VLF signals

1. Introduction

Study of the electron density dynamics in the ionosphere is of crucial importance for scientific research of many plasma parameters, and physical and chemical

processes in this atmospheric layer, as well as for modelling of the ionospheric influence on different kinds of electromagnetic waves. Variations in the ionospheric electron density occur as a result of numerous permanent influences coming from the outer space (Basak & Chakrabarti, 2013; Chakraborty & Basak, 2020; Nina, 2022) and terrestrial layers (Kumar et al., 2017; Nina et al., 2020), and their influence can be both periodical and aperiodical.

The most important source of the free electron production in the ionosphere is the solar radiation. Depending on the wavelength of the photons of this radiation, the efficiency in the considered photo-ionization processes depends on the altitude. Thus, the most significant parts of the spectrum that ionize the ionospheric D-region are the Ly α (121.6 nm) during quiet conditions and X-radiation generated by solar X-ray flares.

In this paper we analyse periodical variations of the ionospheric D-region electron density induced by local variations in the intensity of the solar hydrogen Ly α radiation at the considered area. We perform calculations based on Wait's model (Wait & Spies, 1964) by considering the ionosphere as a horizontally uniform medium with the electron density increasing exponentially with height according to an expression described by two independent, the so-called Wait's, parameters: the "sharpness", and the signal reflection height.

There are several procedures for the quiet ionosphere parameters determination. Generally, they are based on the broad-band detection of radio atmospherics in periods of lightning activities (Han et al., 2011; Ammar & Ghalila, 2020) and detection of the narrow-band very low frequency (VLF) signals (Thomson, 1993; McRae & Thomson, 2000; Thomson et al., 2011; Nina et al., 2021). In this paper, we analyse variations of the D-region electron density N depending on the smoothed daily sunspot number, σ , and on its variations in time (t) and on the day of year (DOY). We apply the Quiet ionospheric D-region (QIonDR) model (Nina et al., 2021) that provides dependencies of Wait's parameters on σ and DOY for the part of Europe defined by the positions of the VLF signal transmitters ICV (Sardinia, Italy) and DHO (Lower Saxony, Germany), and the AWESOME (Atmospheric Weather Electromagnetic System for Observation Modeling and Education) receiver (Belgrade, Serbia) which are used to develop this model. The mentioned dependences of these parameters in the QIonDR model were obtained by fitting relevant values calculated in processing of observational data during perturbations caused by 9 solar X-ray flares that occurred during all four seasons in the midday periods from 2009 to 2016. The application of the obtained functions enables the modelling of White's parameters and, consequently, the electron density in the D-region during quiet midday conditions without observational data only by DOY and σ (it can be obtained based on the appropriate data available on the Internet) entering into the calculations for the considered day.

2. Modelling

The electron density modelling is based on Wait's model of the ionosphere, which involves a horizontally uniform ionosphere described by two independent Wait's parameters, the "sharpness" (β) and the signal reflection height (H') and the expression from Thomson (1993):

$$N(\sigma, \chi, h) = 1.43 \cdot 10^{13} e^{-\beta(\sigma, \chi) H'(\sigma, \chi)} e^{[\beta(\sigma, \chi) - 0.15]h}, \quad (1)$$

where N , β and H' are given in m^{-3} , km^{-1} and km , respectively.

The dependencies of Wait's parameters on σ and the seasonal parameter χ are calculated using the QIonDR model (Nina et al., 2021):

$$\beta_0 = 0.2635 + 0.002573 \cdot \sigma - 9.024 \cdot 10^{-6} \sigma^2 + 0.005351 \cdot \cos(2\pi(\chi - 0.4712)), \quad (2)$$

and

$$H'_0 = 74.74 - 0.02984 \cdot \sigma + 0.5705 \cdot \cos(2\pi(\chi - 0.4712) + \pi). \quad (3)$$

These equations were obtained in the aforementioned study based on observational data of the DHO and ICV signals emitted in Germany (53.08 N, 7.61E) and Italy (40.92 N, 9.73 E), respectively, and recorded in Serbia (44.8 N, 20.4 E). For this reason, they are relevant for the area between these transmitters and receivers, i.e. approximately for the D-region above Central Europe.

Here, we point out that the uncertainties of the mentioned procedure are caused both by the approximations related to the White model of the ionosphere and by the approximations applied in the QIonDR model. These approximations primarily refer to considering the D-region as a horizontally uniform medium and the electron density distribution as an exponential function of height. In addition, the functional dependences of Wait's parameters on DOY and σ in the QIonDR model were obtained by fitting the relevant values of observational data for 9 analysed cases that met the analysis criteria. In specific cases, deviations of the relevant values from those given by these fitted functions are expected due to the constant influence of a large number of events and processes on the ionosphere.

The absolute variations of electron density due to changes in the observed σ and DOY are calculated based on the expressions:

$$\frac{\Delta N(\sigma(i), \chi(j), h)}{\Delta \sigma} = \frac{1}{2} (N(\sigma(i+1), \chi, h) - N(\sigma(i-1), \chi, h)), \quad (4)$$

and

$$\frac{\Delta N(\sigma(i), \chi(j), h)}{\Delta d} = \frac{1}{2} (N(\sigma(i), \chi(j+1), h) - N(\sigma(i), \chi(j-1), h)) \quad (5)$$

where the i -th value of $\sigma(i)$ is calculated using the expression $\sigma(i) = 19 + i$ ($i = 1, 2, 3, \dots, 101$), and the value of $\chi(j) = j/\text{NDY}$ ($j=1, 2, 3, \dots, \text{NDY}$, where NDY is the number of days in a year).

In this paper, the relative changes of the electron density with σ and DOY are analysed. They are calculated by dividing Eqs. (4) and (5) with the corresponding value of the electron density, respectively.

3. Results and discussion

In this Section, we present the results of modelling the electron density changes with σ (Section 3.1) and with DOY (Section 3.2). In both cases, we observe absolute and relative changes in the electron density at heights $H= 60$ km, 70 km, 80 km and 90 km for all combinations of DOY and σ ranging between 20 to 120.

3.1. Solar cycle variations

The electron density changes during a year and solar cycle. Consequently, variations in the solar hydrogen Ly α radiation do not have the same effect on the D-region characteristics at different periods. To examine how changes in σ affect changes in electron density under different conditions, we study the dependencies of the derivatives $\frac{\Delta N}{\Delta \sigma}$ versus DOY and σ . The results of this modelling, based on the expressions given in Section 2, are shown in Fig. 1. Based on the obtained panels we can conclude the following:

- The tendencies of the absolute changes of N are the same for all D-region heights.
- The intensity of these changes increases with altitude. For observed heights that differ by 10 km, the values on the scales differ by more than one order of magnitude.

For small values of σ at 70 km, the obtained values of $\frac{\Delta N}{\Delta \sigma}$ are below 10^{-6} m $^{-3}$. Because of approximations taken in the QIonDR model, these values can be considered approximately equal to 0. By decreasing the height, the maximum values of σ to which this approximation is applied increase (the exact value depends on DOY).

- Changes in the electron density for the same DOY increase with σ .
- The most pronounced changes in $\frac{\Delta N}{\Delta \sigma}$ for all values of σ occur in the period around the summer solstice.

Bearing in mind that the electron density changes with height, we analyse its relative changes with sigma to determine the local significance of changes in emitted solar hydrogen Ly α radiation. For this reason, we apply the procedure

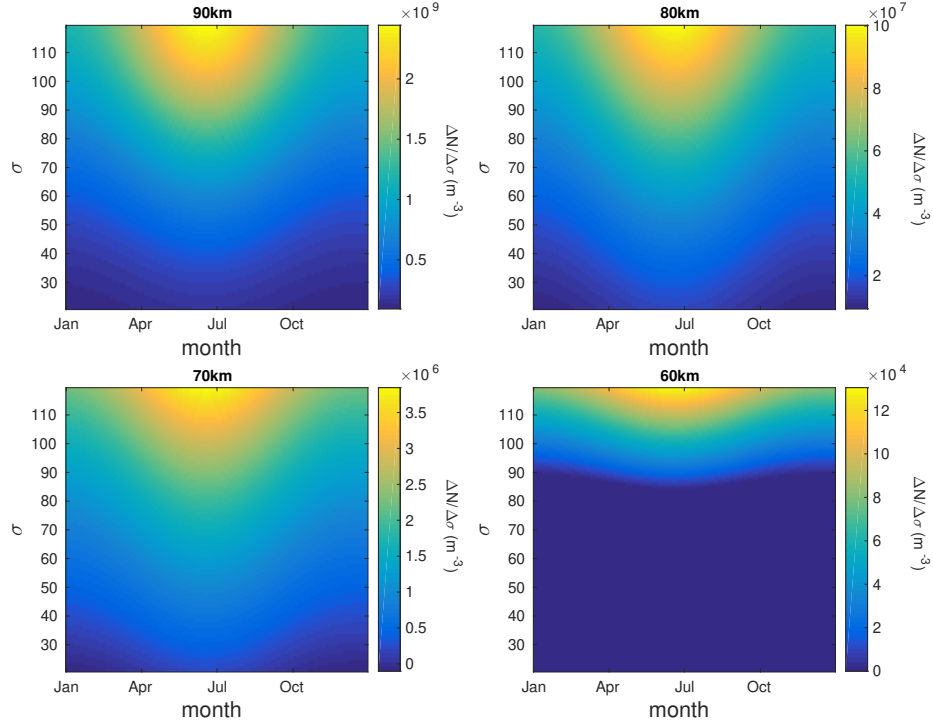


Figure 1. Ratio of variations ΔN and $\Delta\sigma \frac{\Delta N}{\Delta\sigma}$, versus DOY and σ at heights $h=60, 70, 80$ and 90 km.

shown in the previous case to determine the dependencies $\frac{1}{\Delta\sigma} \frac{\Delta N}{N}$. Based on the obtained results visualized in Fig. 2, the following characteristics of $\frac{1}{\Delta\sigma} \frac{\Delta N}{N}$ changes can be observed:

- The maximum values of $\frac{1}{\Delta\sigma} \frac{\Delta N}{N}$ at all D-region heights are within one order of magnitude for the observed values of σ , and they increase with height;
- The maximum considered relative changes occur in the summer solstice period.
- The maximum relative changes of N with the smoothed daily sunspot number occur at smaller values of σ with increasing height.
- As a consequence of the small values of $\frac{\Delta N}{\Delta\sigma}$ in the lower part of the D-region for lower values of σ , it can be concluded that the relative changes in these parameters are negligible.

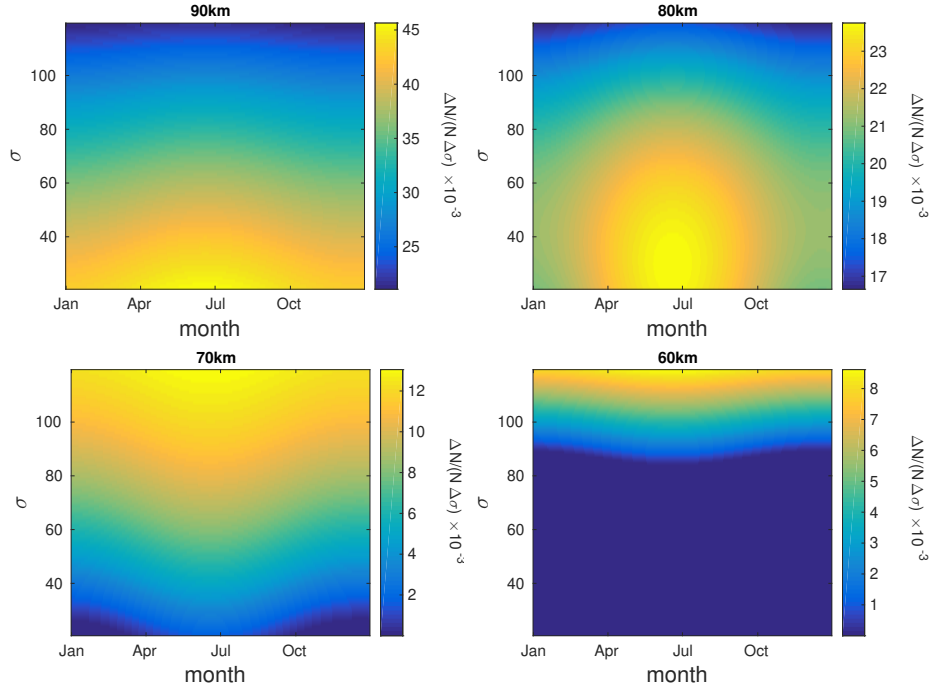


Figure 2. Dependencies of the relative changes in the electron density with the changes of the smoothed daily sunspot number, $\frac{\Delta N}{N \Delta \sigma}$, on DOY and σ at $h = 60, 70, 80$ and 90 km.

3.2. Seasonal variations

The analysis of the electron density absolute and relative changes with DOY is shown in a similar way as in the previous case.

Based on the obtained 3D dependencies of the electron density absolute changes shown in Fig. 3, the following conclusions can be drawn:

- The intensity of these changes increases with the height, and their maxima at the lower and upper boundaries of the D-region differ by about 4 orders of magnitude.
- From the winter to summer solstice $\frac{\Delta N}{\Delta d}$ is positive, while going from a summer to a winter solstice, this parameter is negative. Changes in the electron density with DOY are most pronounced during equinoxes.
- The influence of σ on $\frac{\Delta N(\sigma(i), X(j), h)}{\Delta d}$ increases with height.

The relative changes of the electron density (presented in Fig. 4) show the following characteristics:

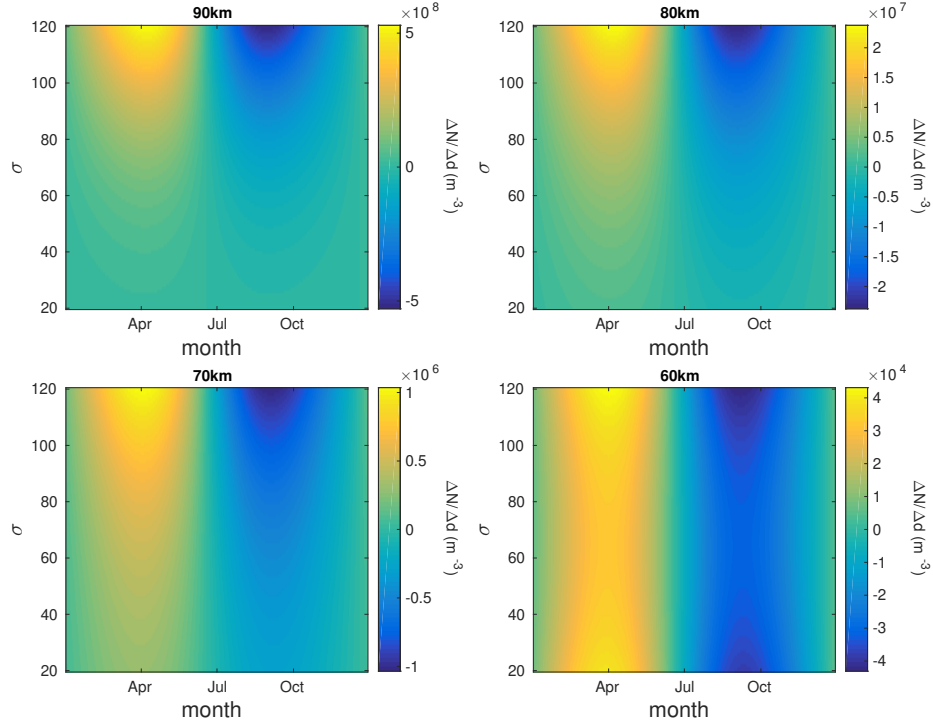


Figure 3. Dependencies of the absolute changes in the electron density with the day $\frac{\Delta N}{\Delta d}$, versus DOY and σ .

- The values of $\frac{1}{\Delta d} \frac{\Delta N}{N}$ for the same σ and for the same day are within one order of magnitude in the entire D-region.
- The influence of σ on the observed changes is not expressed. It is most pronounced during the summer and winter solstices.
- As in the case of absolute changes, $\frac{1}{\Delta d} \frac{\Delta N}{N}$ is positive in the period between the winter solstice and summer solstice, while going from the summer to winter solstice it is negative.

4. Conclusions

In this paper, the absolute and relative changes of the mid-day D-region electron density during a year and a solar cycle were analysed. The analyses are based on modelling the undisturbed ionospheric D-region by the QIonDR model. The obtained results show the following:

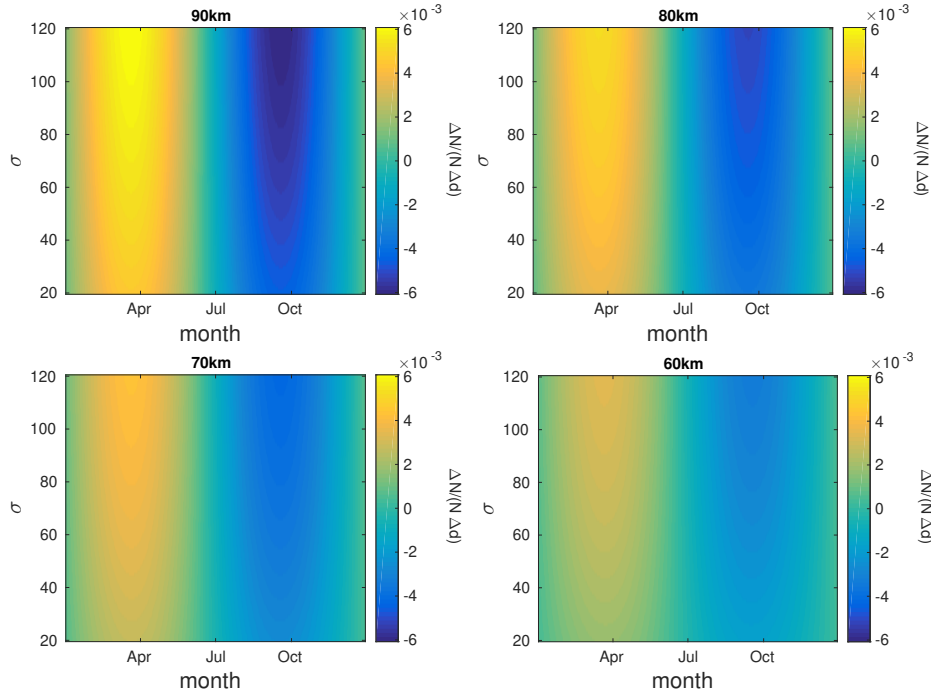


Figure 4. Dependencies of the relative changes in the electron density with the day $\frac{\Delta N}{N \Delta d}$, versus DOY and σ .

- Both, the absolute and relative changes in the electron density with the smoothed daily sunspot number and with the day of year increase with altitude.
- The maximum absolute changes at the upper and lower limits differ by about four orders of magnitude, while the corresponding maximum relative changes differ by about 2 times.
- Due to the small values of changes in the electron density with the smoothed daily sunspot number at the lower altitudes of the D-region, it can be considered that they are negligible for smaller values of the smoothed daily sunspot number.
- The maximum values of the observed changes in the electron density with the smoothed daily sunspot number are in the period of the solstices, while those changes with the day of year are most intense in the periods of equinoxes.

- The resulting assessment of the influence of the smoothed daily sunspot number on the observed changes in the electron density based on the QIonDR model has more complex characteristics than in the case of seasonal changes:
 - The absolute changes in the electron density with the smoothed daily sunspot number increase with this number at all altitudes throughout a year.
 - The maximum relative changes of the electron density with the smoothed daily sunspot number occur during the period of the summer solstice. The smoothed daily sunspot number corresponding to these maximum changes decrease with the D-region heights.
 - At higher altitudes, the absolute changes in the electron density with days at higher altitudes increase with the smoothed daily sunspot number.
 - The relative changes in the electron density with days increase with the smoothed daily sunspot number at all altitudes.

Finally, it should be emphasized that it is not possible to check the obtained dependencies on the basis of other models. Namely, some of the other existing models do not give dependences on both observed parameters, while some expressions use dependences on the Zürich sunspot number, which has been replaced by the international sunspot numbers since 1980. Therefore, it is necessary to verify the obtained conclusions in the future.

Acknowledgements. The authors acknowledge funding provided by the Institute of Physics Belgrade, the Astronomical Observatory (the contract 451-03-68/2020-14/200002) and the Geographical Institute "Jovan Cvijić" SASA through the grants by the Ministry of Education, Science, and Technological Development of the Republic of Serbia.

References

- Ammar, A. & Ghalila, H., Estimation of nighttime ionospheric D-region parameters using tweek atmospherics observed for the first time in the North African region. 2020, *Advances in Space Research*, **66**, 2528, DOI: 10.1016/j.asr.2020.08.025
- Basak, T. & Chakrabarti, S. K., Effective recombination coefficient and solar zenith angle effects on low-latitude D-region ionosphere evaluated from VLF signal amplitude and its time delay during X-ray solar flares. 2013, *Astrophysics and Space Science*, **348**, 315, DOI: 10.1007/s10509-013-1597-9
- Chakraborty, S. & Basak, T., Numerical analysis of electron density and response time delay during solar flares in mid-latitudinal lower ionosphere. 2020, *Astrophysics and Space Science*, **365**, 184, DOI: 10.1007/s10509-020-03903-5
- Han, F., Cummer, S. A., Li, J., & Lu, G., Daytime ionospheric D region sharpness derived from VLF radio atmospherics. 2011, *Journal of Geophysical Research (Space Physics)*, **116**, 5314, DOI: 10.1029/2010JA016299

- Kumar, S., NaitAmor, S., Chanrion, O., & Neubert, T., Perturbations to the lower ionosphere by tropical cyclone Evan in the South Pacific Region. 2017, *Journal of Geophysical Research: Space Physics*, **122**, 8720, DOI: 10.1002/2017JA024023
- McRae, W. M. & Thomson, N. R., VLF phase and amplitude: daytime ionospheric parameters. 2000, *Journal of Atmospheric and Solar-Terrestrial Physics*, **62**, 609, DOI: 10.1016/S1364-6826(00)00027-4
- Nina, A., Modelling of the Electron Density and Total Electron Content in the Quiet and Solar X-ray Flare Perturbed Ionospheric D-Region Based on Remote Sensing by VLF/LF Signals. 2022, *Remote Sensing*, **14**, DOI: 10.3390/rs14010054
- Nina, A., Nico, G., Mitrović, S. T., et al., Quiet Ionospheric D-Region (QIonDR) Model Based on VLF/LF Observations. 2021, *Remote Sensing*, **13**, DOI: 10.3390/rs13030483
- Nina, A., Pulnests, S., Biagi, P., et al., Variation in natural short-period ionospheric noise, and acoustic and gravity waves revealed by the amplitude analysis of a VLF radio signal on the occasion of the Kraljevo earthquake (Mw = 5.4). 2020, *Science of the Total Environment*, **710**, 136406, DOI: 10.1016/j.scitotenv.2019.136406
- Thomson, N. R., Experimental daytime VLF ionospheric parameters. 1993, *Journal of Atmospheric and Terrestrial Physics*, **55**, 173, DOI: 10.1016/0021-9169(93)90122-F
- Thomson, N. R., Rodger, C. J., & Clilverd, M. A., Daytime D region parameters from long-path VLF phase and amplitude. 2011, *Journal of Geophysical Research (Space Physics)*, **116**, 11305, DOI: 10.1029/2011JA016910
- Wait, J. R. & Spies, K. P. 1964, *Characteristics of the Earth-ionosphere waveguide for VLF radio waves*, , NBS Technical Note, CO

Influence of the solar hydrogen Ly α line on the GNSS signal delay in the ionospheric D-region

D. Petković¹, O. Odalović¹ and A. Nina²

¹ Faculty of Civil Engineering, University of Belgrade, Bulevar kralja Aleksandra 73, 11000 Belgrade, Serbia

² Institute of Physics Belgrade, University of Belgrade, Pregrevica 118, 11080 Belgrade, Serbia (E-mail: sandrast@ipb.ac.rs)

Received: July 20, 2022; Accepted: October 2, 2022

Abstract. Recent research indicates that the influence of the ionospheric D-region on the propagation of satellite signals cannot be ignored during the intense X-radiation emitted during solar X-ray flares. In this paper, we investigate the influence of changes in the solar hydrogen Ly α radiation, which is manifested in variations of the D-region electron density and, consequently, the total electron content in this region, on the propagation of the Global Navigation Satellite System (GNSS) signals. We consider changes during a solar cycle and year, represented by the smoothed daily sunspot number and the day of year. The obtained results indicate that the influence of the D-region on these signals is not negligible for positioning with a single signal recorded by a single receiver during the period around the maximum of a solar cycle.

Key words: solar hydrogen Ly α radiation – total electron content – ionosphere – GNSS signal delay

1. Introduction

The terrestrial atmosphere is constantly exposed to the influence of solar radiation, which significantly affects the characteristics of its upper part. The consequence of that influence is the formation of the ionized layer called the ionosphere (50 km - 1000 km) in which ionization processes occur in collisions of atmospheric particles with different kinds of particles and photons. Photo-ionization processes depend on the incident photons wavelengths and the considered location. Namely, solar photons in the upper ionosphere, which play a dominant role in photo-ionization processes in these altitude domain, have wavelengths in the soft X-domain of the electromagnetic spectrum, while, during quiet solar conditions, the solar hydrogen Ly α photons are the most significant source of these processes in the lowest ionospheric layer called the D-region.

Free electrons produced in the photo-ionization processes play a significant role in the propagation of electromagnetic waves, including the satellite signals emitted by the Global Navigation Satellite System (GNSS). This system refers

to any constellation of satellites used to provide accurate and three-dimensional positioning and navigation on a global or regional scale. The United States Department of Defense has been established NAVSTAR GPS (Global Positioning System) as the very first system of its kind. Following that lead, five other positioning systems were built during the last two decades, including Russia's Global Navigation Satellite System (GLONASS), China's BeiDou (or COMPASS), the Navigation with Indian Constellation (NavIC) (or the Indian Regional Navigation Satellite System (IRNSS)), Japanese Quasi-Zenith Satellite System (QZSS), and the European Union's GALILEO (Hofmann-Wellenhof et al., 2008).

GNSS signals play a very important role in modern life, which is why the study of the ionospheric electron density changes also has practical applications. The influence of the atmosphere on their propagation is significant in the ionosphere and troposphere. At the same time, the ionospheric effect on signal propagation is more important in the upper ionosphere due to a significantly higher electron density than at its lower altitudes. However, recent research indicates that the influence of the perturbed D-region cannot be ignored (Nina et al., 2020). Bearing in mind that even in the absence of sudden disturbances, the characteristics of this ionospheric layer change significantly due to changes in the intensity of incoming Ly α radiation during a solar cycle, year and time of day, the question arises as to how these changes affect the propagation of a GNSS signal. The aim of this paper is to investigate the influence of changes in Ly α radiation during a solar cycle on the delay of the GNSS signal during a year. In this study, we analyse the maximum daily influence of the D-region on the signals, which occurs at noon. This analysis is based on Wait's model of the ionosphere (Wait & Spies, 1964), which describes the ionosphere with two parameters: the "sharpness", β and the signal reflection height, H' , and on the Quiet Ionospheric D-Region (QIonDR) model (Nina et al., 2021), which provides these parameters at noon of the selected day. According to the QIonDR model, White's parameters are counted as functions of the ordinal number of this day in year (Day of Year, DOY) and the smoothed daily sunspot number, σ , relevant for the considered day.

2. Modelling

The solar ionizing radiation (particles and photons in the soft X and UV domains) produces the free electrons in the ionosphere in sufficient quantities to directly affect the radio waves propagation (from 3 kHz up to 300 GHz). The ionospheric parameter which has a significant role in quantification of the ionosphere's state impact on the electromagnetic wave propagation is the Total Electron Content (TEC). It represents the total number of electrons in a column with a 1 m² cross-section area along the signal path from a transmitter

(satellite) to the receiver. Thus, it can be expressed by the simple line integral (Seeber, 2003; Hofmann-Wellenhof et al., 2008):

$$TEC(t) = \int_S^R N_e dh, \quad (1)$$

in which N_e stands for the electron density, R and S are the upper and lower ionosphere boundary, and h is the altitude. TEC is expressed in the Total Electron Content Units (TECU), which amounts to 10^{16} free electrons per m^2 .

TEC delays signal propagation from satellite to receiver. Relationship between TEC and signal delay (P_{ION}) is defined by following equation (Hofmann-Wellenhof et al., 2008):

$$P_{ION} = \pm \frac{40.3}{f^2} \cdot \int_S^R N_e dh = \pm \frac{40.3}{f^2} \cdot TEC, \quad (2)$$

where f denotes frequency of the considered electromagnetic wave, i.e. the used satellite signal.

In this paper, we focus attention on the D-region influence on the signal propagation. For this reason, we modify Equations (1) and (2) such that they only apply to this ionospheric region. If we slightly modify integration boundaries, by setting the upper and lower bounds of the D region instead, i.e. $S = h_{low} = 60$ km and $R = h_{upp} = 90$ km, Equation (1) can be rewritten as follows:

$$TEC_D(t) = \int_{h_{low}}^{h_{upp}} N_e dh, \quad (3)$$

where index D in TEC_D indicates that the TEC value is for ionospheric D-region. In a manner that is analogous to the example given earlier, we are going to refer to the signal delay in the D-region as P_D :

$$P_D = 40.3 \frac{TEC_D}{f^2}. \quad (4)$$

It is necessary to point out that Equations (1) and (3) represents the TEC calculation for the electromagnetic wave that is coming in from the zenith direction (signal path goes perpendicular to the D-region boundary). In the case that the satellite signal does not arrive from the zenith direction, slant TEC ($STEC$ or $STEC_D$ for D-region only) is introduced. $STEC$ can be calculated using the vertical TEC value and the mapping function $S(\theta)$ corresponding to the actual zenith angle θ :

$$STEC_D(t) = S(\theta) \cdot TEC_D(t) = \frac{TEC_D(t)}{\cos(\theta)}. \quad (5)$$

As can be seen Equation (3), the TEC in both the vertical and slant directions is a function of the electron density N_e . Equation that can be used to calculate the electron density is as follows (Thomson, 1993):

$$N_e(\beta, H', h) = 1.43 \cdot 10^{13} \cdot e^{-\beta \cdot H'} \cdot e^{[\beta - 0.15]h}, \quad (6)$$

where the "sharpness", β , and the signal reflection height, H' , are given in km^{-1} and km , respectively. For quiet solar conditions, these parameters can be determined using the expressions developed in (Nina et al., 2021) for the Central Europe using the Quiet Ionosphere D-region (QIonDR) Model. β can be obtained from:

$$\beta(\sigma, \chi) = 0.2635 + 0.002573 \cdot \sigma - 9.024 \cdot 10^{-6} \cdot \sigma^2 + 0.005351 \cdot \cos(2\pi(\chi - 0.4712)). \quad (7)$$

while H' can be calculated as:

$$H'(\sigma, \chi) = 74.74 - 0.02984 \cdot \sigma + 0.5705 \cdot \cos(2\pi(\chi - 0.4712) + \pi). \quad (8)$$

As one can see in previous expressions, both, β and H' , depend on the two parameters which represent dependency on a solar cycle period, described in terms of the smoothed daily sunspot number, σ , and dependency on the season parameter $\chi = \text{DOY}/365$, where DOY is the day of year (Nina et al., 2021).

The following expression, derived from Equations (3) and (6), can be used to calculate the TEC value in the D-region (Todorović Drakul et al., 2016):

$$TEC_D(t) = 1000 \frac{N_e(\beta, H', h_t) - N_e(\beta, H', h_t)}{\beta(\sigma, \chi) - 0.15}. \quad (9)$$

As one can see, the signal delay, P_D , is a function of the seasonal parameter, χ , smoothed daily sunspot number, σ , zenith angle from which electromagnetic wave reached ionospheric layer, θ , and frequency of the considered signal f . In this study, we analyse the dependencies on χ and σ for the three fixed values of θ , and the two f which are used for satellite signals important for the GNSS positioning.

In addition to analysis of P_D dependencies of the indicated parameters, we also provide analysis of its changes with σ (i.e. changes of derivative $\frac{\Delta P_D}{\Delta \sigma}$) depending on the same parameters.

3. Results and discussion

In this contribution, we calculated signal delay P_D for TEC values as function of DOY and the smoothed daily sunspot number. The values of the zenith angles are chosen to cover the best and worst case scenarios regarding the application of GNSS technology - zenith angle values of $\theta = 0^\circ$ and $\theta = 70^\circ$, as well as

their mean value $\theta = 35^\circ$. Calculations of TEC values are performed to cover all seasons and values of smoothed daily sunspot number σ in the range of 20 to 120. Fig. 1 illustrates vertical TEC values. It shows that TEC reaches its peak during the summer months (summer solstice), and increases with σ .

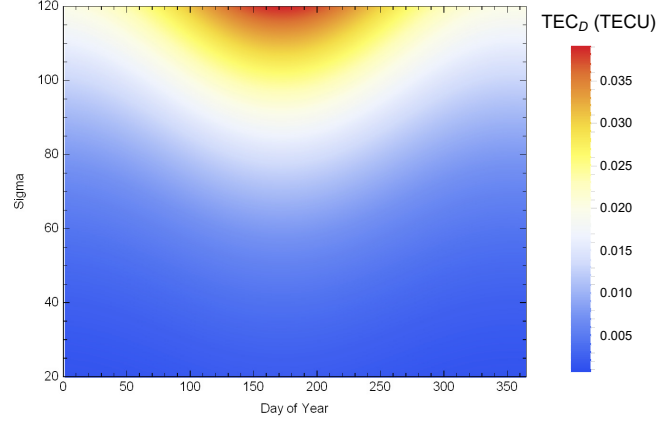


Figure 1. Dependency of vertical TEC_D on the day of year and σ values.

Calculations of the slant TEC are performed based on vertical TEC values and Equation (5). Fig. 2 illustrates those values for zenith angle of $\theta = 35^\circ$ and $\theta = 70^\circ$, respectively. The maximum TEC values for θ values of 0° , 35° , and 70° are respectively 0.04, 0.05, and 0.11 TECU. According to those, we shown that values grow as the zenith angle increases (e.g. as satellite reaches horizon).

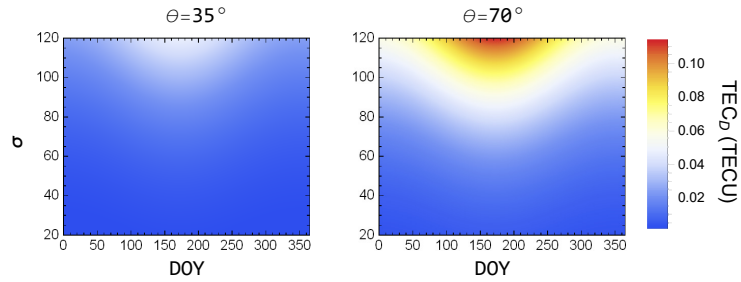


Figure 2. Dependency of the slant TEC_D on the day of year, DOY, and the smoothed daily sunspot number, σ , for the zenith angles $\theta = 35^\circ$ (left) and $\theta = 70^\circ$ (right).

In addition to the TEC values, we analyse the signal delay due to influence of the ionospheric D-region. We consider the frequencies used to broadcast satellite

signals of the satellite systems mentioned in Introduction which are in the range of approximately 1.2 GHz to 1.6 GHz (Hofmann-Wellenhof et al., 2008). In this study we provide calculations for $f_1 = 1.2$ GHz and $f_2 = 1.6$ GHz.

The calculated delays are presented in Fig. 3. In the case of the frequency f_2 , signal delay reached values of 6 mm, 8 mm, and 18 mm for $\theta = 0^\circ$, 35° , and 70° . Within the same spirit, for the frequency f_1 , correspondent delay values are 11mm, 13 mm, and 32 mm. The comparison of the signal delays for the used frequencies are given in the third row of Fig. 3. Analysing this comparison, we can conclude that, even in a relatively small considered frequency range of 0.4 GHz, differences reaches 5 mm, 6 mm, and 14 mm for 0° , 35° , and 70° .

The obtained results indicate that even with the most intense impacts of solar hydrogen Ly α photons on the ionospheric D-region, changes in the propagation of the GNSS signal are significantly smaller than in periods of intense perturbations of this ionospheric layer caused by e.g. solar X-ray flares when P_D can exceed 1 m (Nina et al., 2020). However, for large values of θ parameter, the obtained P_D exceed 1 cm, which represents the minimum value that is included in the total signal delay in Wautelet (2013). For this reason, as well as the fact that the sunspot number can be higher than 120 (the maximum value of σ considered in this analysis), one can conclude that the positioning error that a quiet D-region at solar cycle maxima can cause is not negligible. In other words, variations in the hydrogen Ly α photons that arrive in this layer can provide enough large changes in propagation of a single GNSS signal that using of one GNSS signal and one receiver is not relevant for precise positioning, among others, due to the influence of the quiet D-region during intense radiation from the Sun.

Table 1. The signal delay P_D modelled for Waits parameters presented in Ferguson (1998) (Long Wavelength Propagation Capability (LWPC) numerical model), Bilitza (2018) (International Reference Ionosphere (IRI) model), Thomson et al. (2005), Han et al. (2011), McRae & Thomson (2000) and Thomson et al. (2017) for the signal zenith angle, θ , of 0° , 35° , and 70° , and GNSS signal frequencies, f , of 1.2 GHz and 1.6 GHz.

source of Wait's parameters	P_D ($\theta = 0^\circ$)	P_D ($\theta = 35^\circ$)	P_D ($\theta = 70^\circ$)
		(mm)	
		$f = 1.2/1.6$ GHz	
Ferguson (1998)	0.44/0.25	0.54/0.30	1.29/0.72
Bilitza (2018)	1.59/0.89	1.94/1.09	4.65/2.61
Thomson et al. (2005)	3.77/2.12	4.61/2.59	11.04/6.21
Han et al. (2011)	8.98/5.05	10.97/6.17	26.27/14.78
McRae & Thomson (2000)	4.48/2.52	5.47/3.08	13.11/7.37
Thomson et al. (2017)	1.06/0.59	1.29/0.73	3.09/1.74

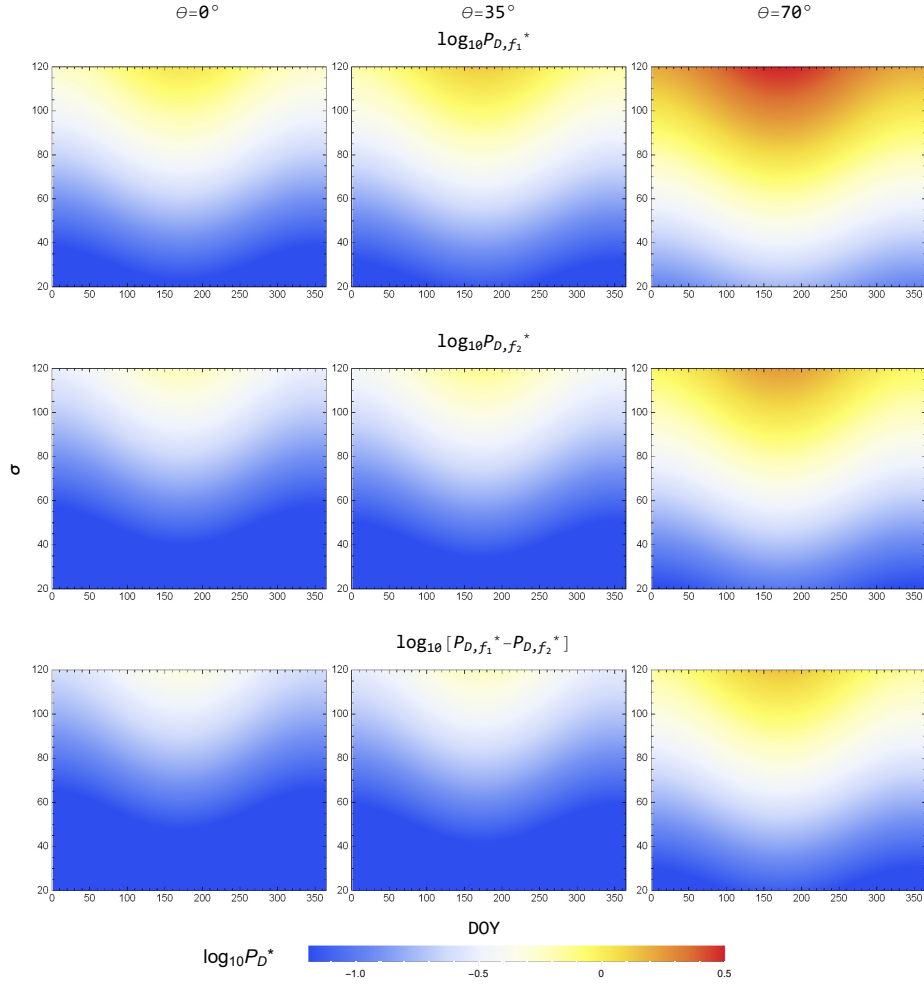


Figure 3. Dependencies of the GNSS signal delay logarithm ($\log_{10}(P_D^*)$) in the ionospheric D-region on the day of year, DOY, and the smoothed daily sunspot number σ . Here, $P_D^* = P_D/1\text{cm}$. The considered zenith angle of the signal are $\theta = 0^\circ$ (first column), $\theta = 35^\circ$ (second column), and $\theta = 70^\circ$ (third column). First two rows represent the signal delay for the specific frequencies $f_1 = 1.2\text{ GHz}$ and $f_2 = 1.6\text{ GHz}$, and the third one represents the difference between those delays.

The obtained values of P_D are in good agreement with those modelled by the presented procedure for the values of Wait's parameters given in [Ferguson \(1998\)](#) (Long Wavelength Propagation Capability (LWPC) numerical model), [Bilitza \(2018\)](#) (International Reference Ionosphere (IRI) model), [Thomson et al.](#)

(2005), Han et al. (2011), McRae & Thomson (2000) and Thomson et al. (2017). Namely, based on the data given in the Tab. 1, it can be seen that all the stated values are within the corresponding ranges obtained in this study.

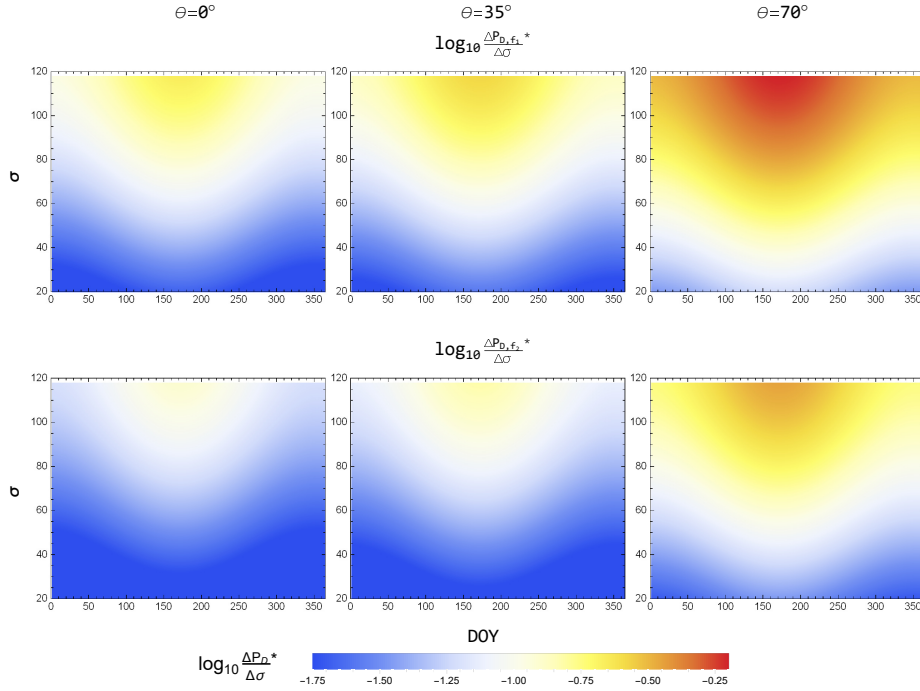


Figure 4. Dependencies of logarithm of the derivative of the GNSS signal delay in the ionospheric D-region with the smoothed daily sunspot number σ ($\log \frac{\Delta P_D^*}{\Delta \sigma}$) on the day of year, DOY, and σ . The considered zenith angle of the signal θ are $\theta = 0^\circ$ (first column), $\theta = 35^\circ$ (second column), and $\theta = 70^\circ$ (third column). The rows represent the considered quantities for the specific frequencies $f_1 = 1.2$ GHz and $f_2 = 1.6$ GHz.

In order to examine the influence of the changes in the solar hydrogen Ly α radiation intensity on changes in P_D , we present an analysis of the dependencies of $\frac{\Delta P_D}{\Delta \sigma}$ on DOY and σ . In Fig. 4, where this dependence is presented for the previously observed values of θ and f , it can be seen that the influence of changes in the sunspot number, i.e. the observed Ly α radiation, on the propagation of the GNSS signal is the greatest during the summer solstice and that it increases with θ . Also, it is important to emphasize that this influence is much more pronounced in the maximum than in the minimum of a solar cycle.

4. Conclusions

In this study, we present a study of the influence of a solar cycle (represented as the smoothed daily sunspot number) and season (represented as the day of year) period, on propagation of the GNSS signals, with the fixed frequency and incident zenith angle, in the ionospheric D-region. We perform the total electron content and signal delay in this ionospheric layer in order to investigate if influence of the quiet D-region can be ignored under all conditions.

The most important conclusion of this study is that variations in the hydrogen Ly α photons arriving in this layer can provide enough large changes in propagation of a single GNSS signal that using of one GNSS signal and one receiver is not relevant for precise positioning.

In addition, the obtained results show the following:

- The total electron content and signal delay increase with the zenith angle and the daily smoothed sunspot number. They are larger in the summer than in the winter months, and reached their maximum values during the summer solstice.
- The obtained signal delays are smaller than in periods of intense perturbations of this ionospheric layer caused by e.g. solar X-ray flares.

Furthermore, various initial conditions affect the ionospheric D-region differently, which consequently affects the propagation of the satellite signals. These influences will be the subject of future research.

Acknowledgements. The authors acknowledge funding provided by the Institute of Physics Belgrade and the Faculty of Civil Engineering, University of Belgrade, through the Ministry of Education, Science, and Technological Development of the Republic of Serbia grants.

References

- Bilitza, D., IRI the International Standard for the Ionosphere. 2018, *Advances in Radio Science*, **16**, 1, DOI: 10.5194/ars-16-1-2018
- Ferguson, J. A. 1998, *Computer Programs for Assessment of Long-Wavelength Radio Communications, Version 2.0*, ed. Space and Naval Warfare Systems Center, San Diego, CA
- Han, F., Cummer, S. A., Li, J., & Lu, G., Daytime ionospheric D region sharpness derived from VLF radio atmospherics. 2011, *Journal of Geophysical Research (Space Physics)*, **116**, 5314, DOI: 10.1029/2010JA016299
- Hofmann-Wellenhof, B., Lichtenegger, H., & Wasle, E. 2008, *GNSS Global Navigation Satellite Systems: GPS, GLONASS, Galileo, and more*, ed. Springer, Vienna, Austria

- McRae, W. M. & Thomson, N. R., VLF phase and amplitude: daytime ionospheric parameters. 2000, *Journal of Atmospheric and Solar-Terrestrial Physics*, **62**, 609, DOI: 10.1016/S1364-6826(00)00027-4
- Nina, A., Nico, G., Mitrović, S., et al., Quiet Ionospheric D-Region (QIonDR) Model Based on VLF/LF Observations. 2021, *Remote Sensing*, **13**, 483, DOI: 10.3390/rs13030483
- Nina, A., Nico, G., Odalović, O., et al., GNSS and SAR Signal Delay in Perturbed Ionospheric D-Region During Solar X-Ray Flares. 2020, *IEEE Geoscience and Remote Sensing Letters*, **17**, 1198, DOI: 10.1109/LGRS.2019.2941643
- Seeber, G. 2003, *Satellite Geodesy*, Walter de Gruyter, Berlin, Germany
- Thomson, N. R., Experimental daytime VLF ionospheric parameters. 1993, *Journal of Atmospheric and Terrestrial Physics*, **55**, 173, DOI: 10.1016/0021-9169(93)90122-F
- Thomson, N. R., Clilverd, M. A., & Rodger, C. J., Midlatitude ionospheric D region: Height, sharpness, and solar zenith angle. 2017, *Journal of Geophysical Research: Space Physics*, **122**, 8933, DOI: 10.1002/2017JA024455
- Thomson, N. R., Rodger, C. J., & Clilverd, M. A., Large solar flares and their ionospheric D region enhancements. 2005, *Journal of Geophysical Research (Space Physics)*, **110**, A06306, DOI: 10.1029/2005JA011008
- Todorović-Drakul, M., Čadež, V., Bajčetić, J., et al., Behaviour of electron content in the ionospheric D-region during solar X-ray flares. 2016, *Serbian Astronomical Journal*, **2016**, 11, DOI: 10.2298/SAJ160404006T
- Wait, J. R. & Spies, K. P. 1964, *Characteristics of the Earth-ionosphere waveguide for VLF radio waves*, NBS Technical Note, CO
- Wautelet, G. 2013, Characterization of Ionospheric Irregularities and Their Influence on High-Accuracy Positioning with GPS over Mid-Latitudes, Doctoral dissertation, University of Liège, Belgium



Variation of electron loss rate due to recombination processes in the upper ionospheric D-region plasma after a solar X-ray flare: a study case

A. Nina^{1,a}  and V. M. Čadež²

¹ Institute of Physics Belgrade, University of Belgrade, Pregrevica 118, Belgrade 11080, Serbia

² Astronomical Observatory, Volgina 7, Belgrade 11060, Serbia

Received 30 January 2021 / Accepted 25 February 2021 / Published online 12 March 2021

© The Author(s), under exclusive licence to EDP Sciences, SIF and Springer-Verlag GmbH Germany, part of Springer Nature 2021

Abstract. In this paper, we study electron loss rate resulting from recombination processes in the upper part of the ionospheric D-region after being influenced by a solar X-ray flare activity. We analyse the altitude and time dependences of the governing plasma electron loss rate and its spatial and temporal derivatives. The presented numerical modelling is based on data recorded through remote sensing of the lower ionosphere utilizing the reflected very low-frequency radio signal emitted by the DHO transmitter in Germany and received in Belgrade, Serbia. Ionospheric parameters were calculated by a procedure based on a comparison of the observed changes in the signal amplitude and phase with their values modelled by the Long-Wave Propagation Capability numerical model. We consider the time period after influence of the solar X-ray flare of the class C8.8 occurred on 5 May, 2010 between 11:37 UT and 11:58 UT with the maximum at 11:52 UT. Due to the same tendencies of the D-region plasma parameters variation, the obtained conclusions can be extended and generalized to any solar X-ray flare.

1 Introduction

The terrestrial ionosphere is under permanent influence of different natural events located in various parts of the outer space and Earth's layers. The astrophysical phenomena which induce sudden ionospheric disturbances (SIDs) are, for example, solar radiations [1] and gamma ray bursts [2,3]. In addition, events occurring in the terrestrial atmosphere (lightning [4], atmospheric convective motions [5], tropical cyclones and depressions [6–8]), earthquakes [9–11] and ocean motions including tsunamis [12] can also be related to SIDs.

Properties of relaxation processes depend on characteristics of the perturber, their impact on the considered area, properties of local medium and possible presence of other influences. Even in the absence of sudden events, ionospheric properties in quiet conditions depend on periodical changes during day, year and solar cycle [13]. However, in many cases, these differences in relaxation properties are only quantitative, while qualitative descriptions remain the same. One of the phenomena producing the same tendencies of temporal and

space variations of plasma parameters is a solar X-ray flare which induces disturbances whose relaxation is analysed in this study. For this reason and clearer presentation of the considered changes, we present an example case study showing the analysis for the time period after influence of the solar X-ray flare of the class C8.8 occurred on 5 May 2010. Because of a very clear D-region response and absence of other significant influences during the entire disturbed period, several studies focused on variations induced by this event were already performed (see, for example, [14–16]).

In this paper, we consider the D-region altitude domain above 70 km where recombination dominates in the electron loss processes. In previous studies, the relaxation period is considered in the analysis of both the rate of electron gain due to photoionization induced by the Ly α photons (this process dominates in electron production within the D-region) [17] and the effective recombination coefficient [18]. Here, we extend this research to the electron loss rate by analysing its variations with altitude and time. In addition, we also study properties of both its vertical gradient and time derivative.

The observations of the D-region are done by the 23.4 kHz very low-frequency (VLF) signal emitted from the DHO transmitter in Germany and recorded in Serbia by the AWESOME (Atmospheric Weather Electromagnetic System for Observation Modeling and Education) receiver [19].

Advances in Physics of Ionized Gases and Spectroscopy of Isolated Complex Systems: from Biomolecules to Space Particles - SPIG 2020. Guest editors: Duško Borka, Dragana Ili, Aleksandar Milosavljevic, Christophe Nicolas, Vladimir Srećković, Luka Č. Popović, Sylwia Ptasinska.

^a e-mail: sandrast@ipb.ac.rs (corresponding author)

2 Observations and modelling

Diagnostics of the ionospheric D-region is performed by the method based on analysis of recorded VLF radio signals constantly emitted by a worldwide network of transmitters, which further enables registrations of both the global and local disturbances in the D-region as well as perturbations caused by both the predictable periodic and unpredictable phenomena. This is why such a telecommunication method is being applied in numerous studies of the low ionosphere (see, for example, [20–23]).

Modelling of the electron plasma density $N(h, t)$ (in m^{-3}) at fixed altitude h (in km) can be done by applying Wait's model of a horizontally uniform ionosphere [24] to measured changes ΔA_{rec} and phase ΔP_{rec} . This model assumes that the D-region electron density $N_e(h, t)$ is a given function of two independent parameters: the signal reflection height H' (in km) and sharpness β (in km^{-1}) [25]:

$$N_e(h, t) = 1.43 \cdot 10^{13} e^{-\beta(t)H'(t)} e^{(\beta(t)-0.15)h}. \quad (1)$$

The numerical procedure for their computation is based on matching the recorded changes of amplitude $\Delta A_{\text{rec}}(\beta, H') = A_{\text{rec}}(\beta, H') - A_{\text{rec}}(\beta_0, H'_0)$ and phase $\Delta P_{\text{rec}}(\beta, H') = P_{\text{rec}}(\beta, H') - P_{\text{rec}}(\beta_0, H'_0)$ with the corresponding values $\Delta A_{\text{sim}}(\beta, H') = A_{\text{sim}}(\beta, H') - A_{\text{sim}}(\beta_0, H'_0)$ and $\Delta P_{\text{sim}}(\beta, H') = P_{\text{sim}}(\beta, H') - P_{\text{sim}}(\beta_0, H'_0)$ obtained in simulations by the Long-Wave Propagation Capability (LWPC) numerical model for simulation of the VLF signal propagations [26] as explained in [27]:

$$\Delta A_{\text{sim}}(\beta, H') \approx \Delta A_{\text{rec}}(\beta, H') \quad (2)$$

and

$$\Delta P_{\text{sim}}(\beta, H') \approx \Delta P_{\text{rec}}(\beta, H'). \quad (3)$$

Here, index 0 indicates the unperturbed values. This method is applied in numerous papers ([17, 18] showing a good agreement with other methods (see, for example, comparisons in [17] for different flare stages).

Knowledge of the electron density temporal and spatial distributions allows us to model some other plasma parameters that are important in the electron density dynamics described by the expression [28, 29]:

$$\frac{dN(h, t)}{dt} = G(h, t) - L(h, t), \quad (4)$$

where $G(h, t)$ and $L(h, t)$ are the electron gain and electron loss rate, respectively, at altitude h and at time t . Here, the influence of transport processes is neglected as they become important at altitudes above 120–150 km [30] and they are generally not included in models of the D-region plasma [31, 32].

In the absence of sudden radiation impacts in the upper part of the D-region and for approximately stationary intensity of the Ly α line, we can assume:

$$G(h, t) = G_0(h), \quad (5)$$

where $G_0(h)$ is the electron gain rate induced by this spectral line. A detailed explanation of the applied procedure for this calculation, which is based on analysis of the VLF/LF signal data for the period of the D-region relaxation after a solar X-ray flare or some other source of intensive ionospheric disturbance, is given in [17].

According to Eqs. (4) and (5), the electron loss rate L can be express as:

$$L(h, t) = G_0(h) - \frac{dN(h, t)}{dt}. \quad (6)$$

3 Results and discussions

In this study, we consider the time period of the ionospheric parameter relaxation after influence of the solar X-ray flare occurred on 5 May, 2010. Figure 1 shows the time evolutions of the X-radiation flux I between 0.1 nm and 0.1 nm recorded by the GOES-14 satellite, and the amplitude A_{rec} and phase P_{rec} of the DHO signal recorded by the AWESOME receiver in Belgrade. The considered time interval (the shaded domain in Fig. 1) is estimated in [14]: its beginning is determined by the moment when the X-radiation flux, after passing through its maximum, drops to the value it had at the time when the signal characteristics started to response to the considered event. Here, we assume that the intensity of X-radiation below this value does not play a significant role in the D-region ionization process, which is of importance in drawing conclusions and for the discussion concerning the electron density dynamics (see Eq. (4) and its explanation).

As it is explained in Sect. 2, calculation of the electron loss rate L requires knowledge of the electron density time derivative dN/dt and the electron gain rate G . In this paper, we used their values from the analysis presented in [17].

The electron density is calculated by Eq. (1). Figure 2 shows the time evolutions of the fitted values of Wait's parameters β and H' which are obtained by using the criteria given by Eqs. (2) and (3). These evolutions are already used in [17] for calculation of the electron gain rate due to ionization by the Ly α photons. We can see that, in the considered time period, the variation of β is very small (about 0.001 km^{-1}), while a shift of the reflection height H' of more than half a kilometre is not negligible in comparison with about 8 km of the maximum lowering of the upper Earth-ionosphere boundary of the waveguide where the considered VLF signal propagates [14, 15, 17].

Time and altitude distributions of the electron density N calculated by Eq. (1) and its time derivative

dN/dt are shown in Fig. 2, middle and bottom panels, respectively.

As one can see in the middle panel, the time variation of the electron density is slow within the entire considered altitude domain. This property is also visible from the comparison of the scales in middle and bottom panels. Relative decrease in the electron density within the considered altitude domain is from 0.05% to 0.005% per second.

Analysis of the electron gain rate is done in [17]. As said in Sect. 2, this physical quantity can be considered stationary within the observed time period. Its vertical profile can be approximately calculated from the expression [17]:

$$G_0(h) \approx G_0(75)e^{(\beta^*-0.15)(h-75)}. \tag{7}$$

where $G(75) = 95000 \text{ m}^{-3} \text{ s}^{-1}$ and $\beta^* = 0.304 \text{ km}^{-1}$ for the considered X-ray flare. (These values are obtained from the analysis given in [17].)

The resulting time and altitude dependence $L(t, h)$ given by Eq. (6) are shown in Fig. 3. The left panel shows a 2D graph while the right panel clearly visualizes time evolutions at fixed altitudes as indicated in the legend. The same presentation is given for all values in the following analysis. As one can see, L decreases with t and increases with h and lie within range $43775 \text{ m}^{-3} \text{ s}^{-1}$ – $2573500 \text{ m}^{-3} \text{ s}^{-1}$, i.e. within near two orders of magnitude.

Variations of the vertical gradient dL/dh (Fig. 4) have the same tendencies like L and also lie within two orders of magnitude ($6838 \text{ m}^{-3} \text{ s}^{-1}/\text{km}$ – $403720 \text{ m}^{-3}\text{s}^{-1}/\text{km}$).

Finally, Fig. 5 shows a negative time derivative dL/dt which indicates decreasing of L in time. Description of its absolute values corresponds to those for L and dL/dh . dL/dt takes values from $-4006 \text{ m}^{-3}\text{s}^{-1}/\text{km}$ to $-12 \text{ m}^{-3}\text{s}^{-1}/\text{km}$.

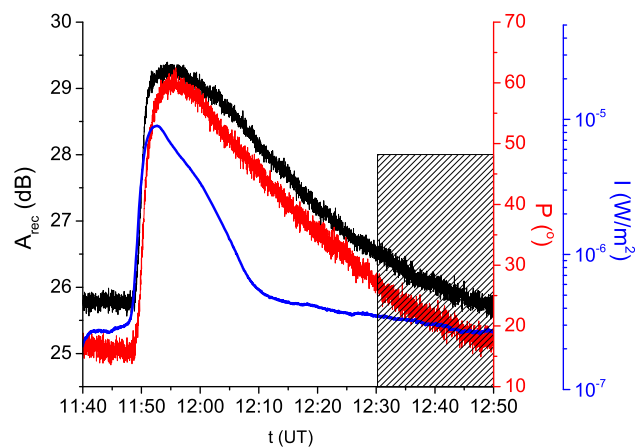


Fig. 1 Time evolutions of the X-radiation flux I between 0.1 nm and 0.1 nm recorded by the GOES-14 satellite, and the recorded amplitude A_{rec} and phase P_{rec} of the DHO signal by the AWESOME receiver. Shaded domain indicates the time period considered in this study

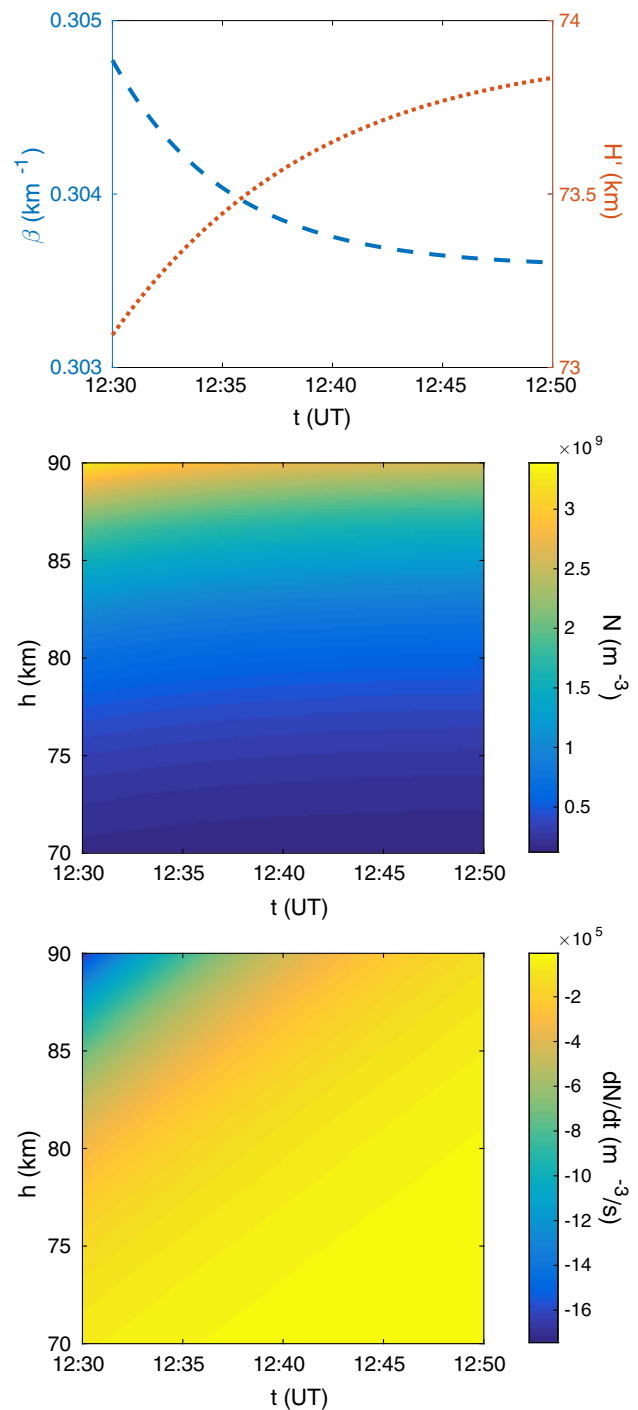


Fig. 2 Upper panel: Time evolutions of the Wait’s parameters β and H' after influence of the considered X-ray flare. Middle panel: surface plot of the electron density $N(h, t)$ within altitude domain between 70 km and 90 km in the considered time period. Bottom panel: the same as in the middle panel but for the electron density time derivative dN/dt

The spatial and time dependence of L can also be visualized by introducing two standard e-folding scaling quantities: the vertical scale length, S_h , and scale time S_t representing a typical length in vertical direction and typical time, respectively, for change of L :

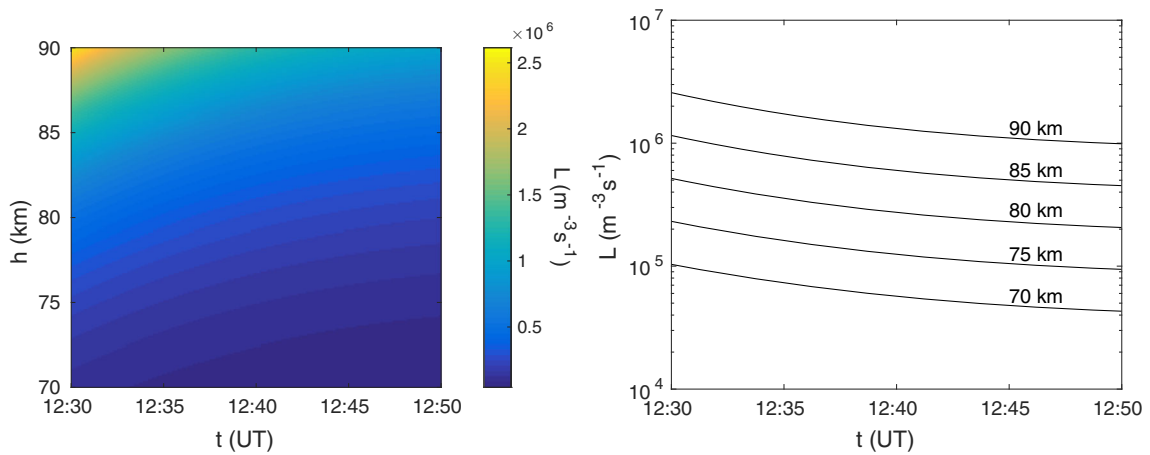


Fig. 3 Left panel: Surface plot of the electron loss rate $L(h, t)$ within the altitude domain between 70 km and 90 km after the influence of the considered X-ray flare. Right panel: Time evolutions of the electron loss rate $L(h, t)$ at 70 km, 75 km, 80 km, 85 km and 90 km during considered time period

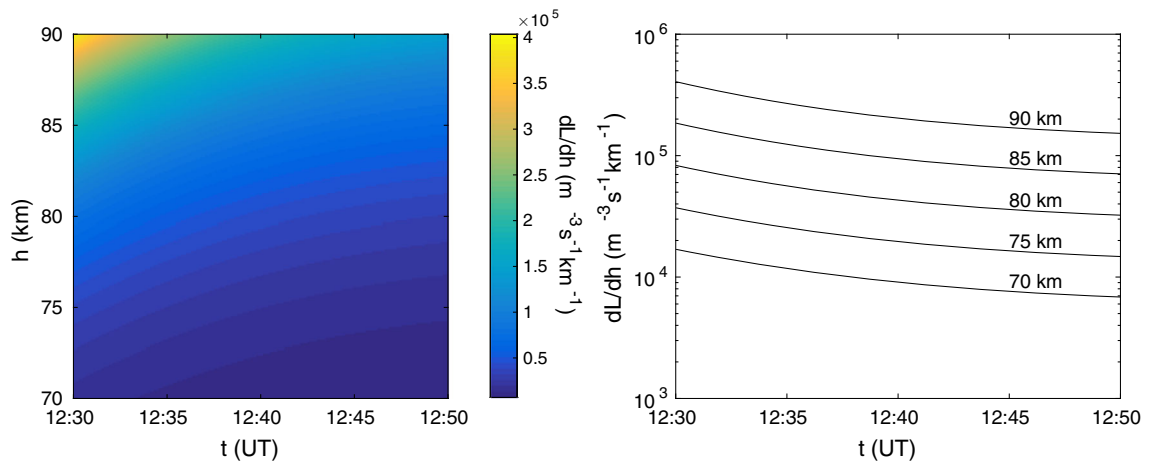


Fig. 4 Same as in Fig. 3 but for vertical gradient dL/dh of the electron loss rate

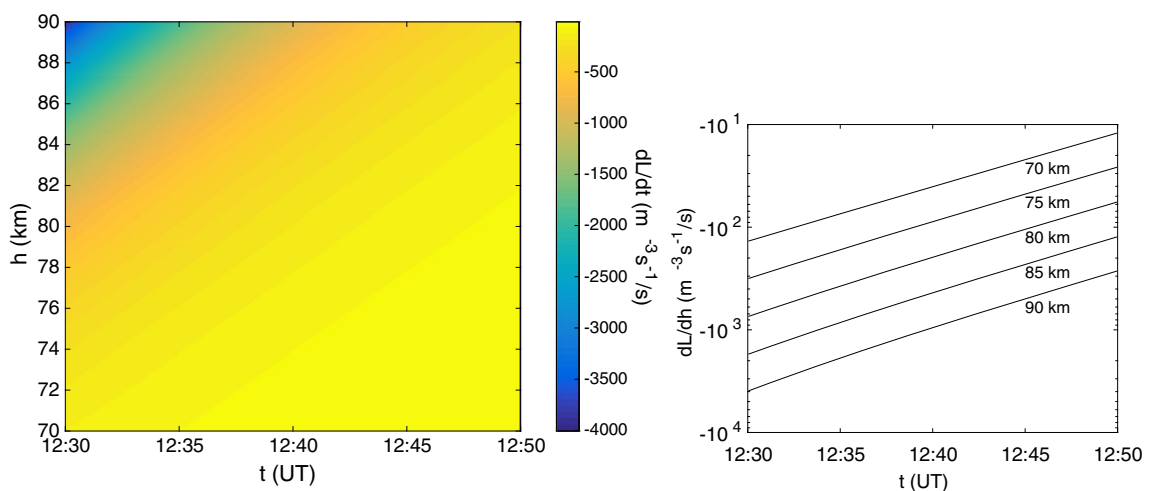


Fig. 5 Same as in Fig. 3 but for time derivative dL/dh of the electron loss rate

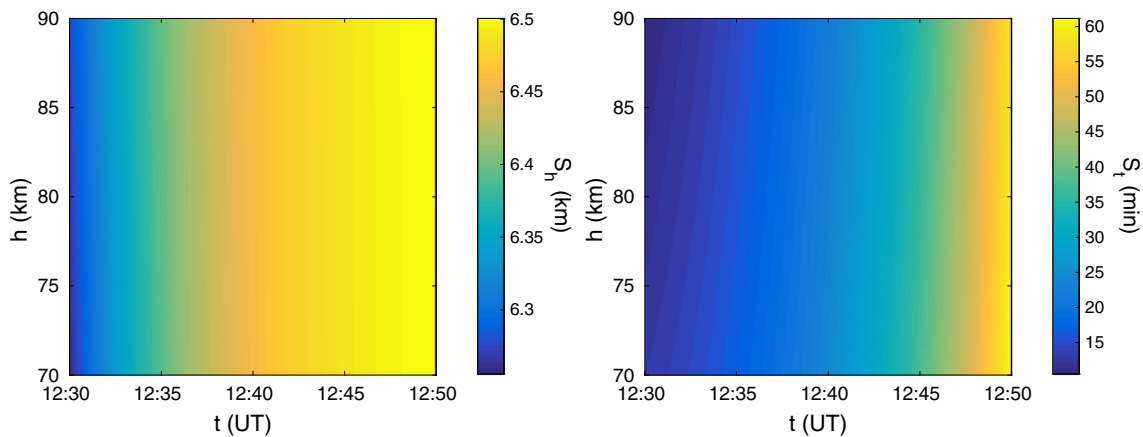


Fig. 6 Vertical scale length S_h (left panel) and scale time S_t (right panel) variations between 70 km and 90 km after influence the considered X-ray flare

$$S_h \equiv L \left| \frac{dL}{dh} \right|^{-1} \quad \text{and} \quad S_t \equiv L \left| \frac{dL}{dt} \right|^{-1} \quad (8)$$

As shown in Fig. 6, both scaling parameters S_h and S_t are practically only time dependent at altitudes between $h = 70$ km and $h = 90$ km meaning that here changes of $L(h, t)$ with altitude h and time t are everywhere with the same rates at the given time instant. These rates, i.e. the scaling coefficients S_h and S_t , are time dependent in sense that they grow with time approaching their values typical of the vertically nonuniform stationary state of the D-region existing before the perturbation caused by the considered flare event. Thus, Fig. 6 shows that the typical scale length S_h tends to a finite value of ~ 6.5 km representing the vertical distance with natural e-fold growth of L under unperturbed conditions, while, at the same time, the typical scale time S_t for temporal changes grows from the initial ~ 8 min to $\sim > 60$ min typical of practically stationary pre-flare conditions if compared with the considered 20 min time period of t (UT) in Fig. 6.

Figure 7 contains a comparison of the obtained electron loss rate at the end of the relaxation period (when it can be considered approximately equal to the electron loss rate L_q in quiet conditions) with the electron gain rate G_q in quiet conditions (when $L_q \approx G_q$) showing a good agreement with vertical distributions of the electron gain rate in [16] based on data from [17, 33–36]. In addition, it can be seen that the obtained altitude distribution of L is in good agreement with those obtained from the expression $L = \alpha_{\text{eff}} N^2$, where vertical distribution of the effective recombination coefficient α_{eff} is taken from [28, 37, 38].

4 Summary

In this work, we analyse the altitude and time variations of the electron loss rate $L(h, t)$ and its vertical gradient and time derivative, (dL/dh) and (dL/dt) , respectively,

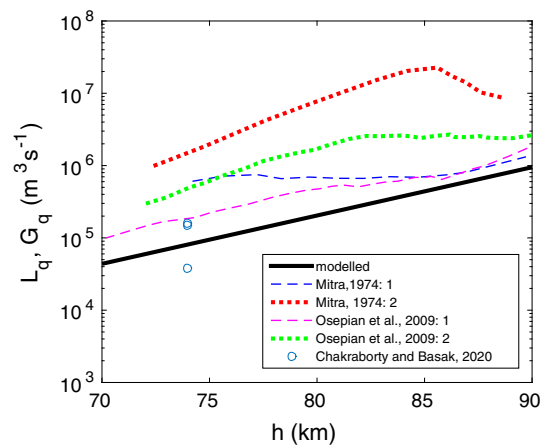


Fig. 7 Comparison of the obtained electron loss L_q and gain G_q rates in quiet conditions

within the upper part of the ionospheric D-region in the period after a solar X-ray flare influence on Earth’s atmosphere. Calculations are based on applications of the LWPC numerical model and existing analytical procedures on a data set related to the 23.4 kHz VLF signal emitted by the DHO transmitter in Germany and collected by the AWESOME radio receiver located in Serbia.

The main conclusions related to tendencies of the considered parameters during relaxations after a solar X-ray flare are:

- The electron loss rate L and its vertical gradient dL/dh decrease with time and increase with altitude.
- Time derivative of the electron loss rate dL/dt has negative values. Its absolute values increase with altitude and decrease with time.

The presented study relates to the relaxation period after the solar X-ray flare occurred on 5 May 2010. However, the same general properties of the D-region

relaxation after other solar X-ray flares in the absence of additional influences allows us to generalize the obtained conclusions to all X-ray flare events.

Acknowledgements The authors acknowledge funding provided by the Institute of Physics Belgrade and the Astronomical Observatory (the contract 451-03-68/2020-14/200002) through the grants by the Ministry of Education, Science, and Technological Development of the Republic of Serbia. The authors are grateful to the anonymous reviewers and editor for comments and suggestions that improved this paper.

Data Availability Statement This manuscript has no associated data or the data will not be deposited. [Authors' comment: The data for this paper collected by the GOES-14 satellite are available at NOAA's National Centers for Environmental information (<http://satdat.ngdc.noaa.gov/sem/goes/data/new/hbox/tim/char95full/2010/05/goes14/csv>). Requests for the VLF data used for analysis can be directed to the corresponding author.]

References

- V. Srećković, D. Šulić, V. Vujičić, D. Jevremović, Y. Vykylyuk, J. Geograph. Inst. Cvijic **67**, 221 (2017)
- U.S. Inan, N.G. Lehtinen, R.C. Moore, K. Hurley, S. Boggs, D.M. Smith, G.J. Fishman, Geophys. Res. Lett. **34**, L08103 (2007)
- A. Nina, S. Simić, V.A. Srećković, L.Č. Popović, Geophys. Res. Lett. **42**, 8250 (2015)
- U.S. Inan, S.A. Cummer, R.A. Marshall, J. Geophys. Res.-Space **115**, A00E36 (2010)
- T. Šindelářová, D. Burešová, J. Chum, Studia Geophys. Geod. **53**, 403 (2009)
- W.B. Peter, U.S. Inan, J. Geophys. Res.-Space **110**, A05305 (2005)
- S. Kumar, S. NaitAmor, O. Chanrion, T. Neubert, J. Geophys. Res.-Space **122**, 8720 (2017)
- A. Nina, M. Radovanović, B. Milovanović, A. Kovačević, J. Bajčetić, L.Č. Popović, Adv. Space Res. **60**, 1866 (2017)
- P.F. Biagi, R. Piccolo, A. Ermini, S. Martellucci, C. Bellecci, M. Hayakawa, V. Capozzi, S.P. Kingsley, Nat. Hazard Earth Sys. **1**, 99 (2001)
- S. Pulinets, K. Boyarchuk, *Ionospheric precursor of earthquakes* (Springer, Heidelberg, Germany, 2004)
- A. Nina, S. Pulinets, P. Biagi, G. Nico, S. Mitrović, M. Radovanović, L.Č. Popović, Sci. Total Environ. **710**, 136406 (2020)
- A. Rozhnoi, S. Shalimov, M. Solovieva, B. Levin, M. Hayakawa, S. Walker, J. Geophys. Res.-Space **117**, A09313 (2012)
- A. Nina, G. Nico, S.T. Mitrović, V.M. Čadež, I.R. Milošević, M. Radovanović, L.Č. Popović, Remote Sens. **13**, 3 (2021)
- J. Bajčetić, A. Nina, V.M. Čadež, B.M. Todorović, Therm. Sci. **19**, S299 (2015)
- M. Todorović Drakul, V.M. Čadež, J. Bajčetić, D.B.L.C. Popović, A. Nina, Serb. Astron. J. **193**, 11 (2016)
- A. Nina, V.M. Čadež, J. Bajčetić, S.T. Mitrović, L.Č. Popović, Solar Phys. **293**, 64 (2018)
- A. Nina, V. Čadež, Adv. Space Res. **54**, 1276 (2014)
- A. Nina, V. Čadež, D. Šulić, V. Srećković, V. Žigman, Nucl. Instrum. Meth. B **279**, 106 (2012)
- M.B. Cohen, U.S. Inan, E.W. Paschal, I.E.E.E.T. Geosci, Remote **48**, 3 (2010)
- M.A. Clilverd, C.J. Rodger, R.M. Millan, J.G. Sample, M. Kokorowski, M.P. McCarthy, T. Ulich, T. Raita, A.J. Kavanagh, E. Spanswick, J. Geophys. Res.-Space **112**, A12 (2007)
- A. Kolarski, D. Grubor, Adv. Space Res. **53**, 1595 (2014)
- A.K. Singh, A. Singh, R. Singh, R. Singh, Astrophys. Space Sci. **350**, 1 (2014)
- A. Nina, G. Nico, O. Odalović, V. Čadež, M.T. Drakul, M. Radovanović, L.Č. Popović, I.E.E.E. Geosci, Remote S. **17**, 1198 (2020)
- J.R. Wait, K.P. Spies, *Characteristics of the Earth-Ionosphere Waveguide for VLF Radio Waves* (NBS Technical Note, CO, 1964)
- N.R. Thomson, J. Atmos. Terr. Phys. **55**, 173 (1993)
- J.A. Ferguson, Computer Programs for Assessment of Long-Wavelength Radio Communications, Version 2.0 (1998)
- D.P. Grubor, D.M. Šulić, V. Žigman, Ann. Geophys. **26**, 1731 (2008)
- A.P. Mitra, ed., *Ionospheric effects of solar flares*, Vol. 46 of Astrophys. Space Sc. L., (Springer, Dordrecht, Holland, 1974)
- M. McEwan, F. Phillips, *Chemistry of the Atmosphere*, Mir Publishers (Moscow, Russia, 1978)
- N. Blaunstein, C. Christodoulou, *Radio Propagation and Adaptive Antennas for Wireless Communication Links: Terrestrial, Atmospheric and Ionospheric* (Wiley, Hoboken, New Jersey, 2006)
- E. Turunen, J. Tolvanen, H. Matveinen, H. Ranta, *D Region Ion Chemistry Model* (SCOSTEP Secretariat, Boulder, Colorado 1992)
- S. William, C.I. Foley, *Steady-state Multi-ion Disturbed D-region Model* (Environmental Research Papers Air Force Geophysics Lab., Hanscom AFB, Massachusetts, 1978)
- A.P. Mitra, *Ionospheric Effects of Solar Flares* (Mir, Moscow, Russia 1977)
- J.N. Rowe, *Model studies of the lower ionosphere*, Sci. Rep. No. 406 (Pennsylvania State University, University Park, 1972)
- A.C. Aikin, J.A. Kane, J. Troim, J. Geophys. Res. **69**, 4621 (1964)
- R.E. Bourdeau, A.C. Aiken, D.J. L., *The Lower Ionosphere at Solar Minimum*, Greenbelt, Md.: NASA, Goddard Space Flight Center (1965)
- A. Osepian, S. Kirkwood, P. Dalin, V. Tereschenko, Ann. Geophys. **27**, 3713 (2009)
- S. Chakraborty, T. Basak, Astrophys. Space Sci. **365**, 184 (2020)

M28b



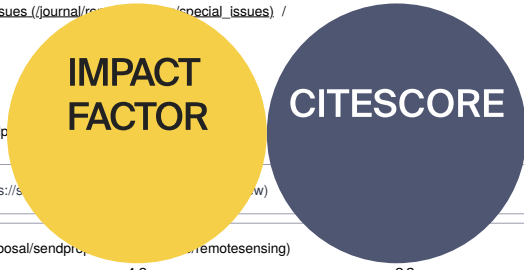
[Sign In / Sign Up \(/user/login\)](#)

[Submit \(https://susy.mdpi.com/user/manuscripts/upload?journal=remotesensing \)](https://susy.mdpi.com/user/manuscripts/upload?journal=remotesensing)

Search for Articles:

Advanced Search

[Journals \(/about/journals\)](#) / [Remote Sensing \(/journal/remotesensing\)](#) / [Special Issues \(/journal/remotesensing/special_issues\)](#) / [Advances in Remote Sensing Applications in Natural Hazards Research](#) /



[Submit to Remote Sensing \(https://susy.mdpi.com/user/manuscripts/upload?journal=remotesensing\)](https://susy.mdpi.com/user/manuscripts/upload?journal=remotesensing)

[Review for Remote Sensing \(https://susy.mdpi.com/user/manuscripts/upload?journal=remotesensing\)](https://susy.mdpi.com/user/manuscripts/upload?journal=remotesensing)

[Propose a Special Issue \(/journalproposalsendproposal?journal=remotesensing\)](#)

[\(/journal/remotesensing/stats\)](#)

<https://www.scopus.com/sourceid/86430>

Journal Menu

► **Journal Menu**

- [Remote Sensing Home \(/journal/remotesensing\)](#)
- [Aims & Scope \(/journal/remotesensing/about\)](#)
- [Editorial Board \(/journal/remotesensing/editors\)](#)
- [Reviewer Board \(/journal/remotesensing/submission_reviewers\)](#)
- [Topical Advisory Panel \(/journal/remotesensing/topical_advisory_panel\)](#)
- [Photography Exhibition \(/journal/remotesensing/exhibition\)](#)
- [Instructions for Authors \(/journal/remotesensing/instructions\)](#)
- [Special Issues \(/journal/remotesensing/special_issues\)](#)
- [Topics \(/topics?journal=remotesensing\)](#)
- [Sections & Collections \(/journal/remotesensing/sections\)](#)
- [Article Processing Charge \(/journal/remotesensing/apc\)](#)
- [Indexing & Archiving \(/journal/remotesensing/indexing\)](#)
- [Editor's Choice Articles \(/journal/remotesensing/editors_choice\)](#)
- [Most Cited & Viewed \(/journal/remotesensing/most_cited\)](#)
- [Journal Statistics \(/journal/remotesensing/stats\)](#)
- [Journal History \(/journal/remotesensing/history\)](#)
- [Journal Awards \(/journal/remotesensing/awards\)](#)
- [Society Collaborations \(/journal/remotesensing/societies\)](#)
- [Conferences \(/journal/remotesensing/events\)](#)
- [Editorial Office \(/journal/remotesensing/editorial_office\)](#)

Journal Browser

► **Journal Browser**

- > [Forthcoming issue \(/2072-4292/16/23\)](#)
- > [Current issue \(/2072-4292/16/22\)](#)

- [Vol. 16 \(2024\) \(/2072-4292/16\)](#)
- [Vol. 15 \(2023\) \(/2072-4292/15\)](#)
- [Vol. 14 \(2022\) \(/2072-4292/14\)](#)
- [Vol. 13 \(2021\) \(/2072-4292/13\)](#)
- [Vol. 12 \(2020\) \(/2072-4292/12\)](#)
- [Vol. 11 \(2019\) \(/2072-4292/11\)](#)
- [Vol. 10 \(2018\) \(/2072-4292/10\)](#)
- [Vol. 9 \(2017\) \(/2072-4292/9\)](#)
- [Vol. 8 \(2016\) \(/2072-4292/8\)](#)
- [Vol. 7 \(2015\) \(/2072-4292/7\)](#)
- [Vol. 6 \(2014\) \(/2072-4292/6\)](#)
- [Vol. 5 \(2013\) \(/2072-4292/5\)](#)
- [Vol. 4 \(2012\) \(/2072-4292/4\)](#)
- [Vol. 3 \(2011\) \(/2072-4292/3\)](#)
- [Vol. 2 \(2010\) \(/2072-4292/2\)](#)
- [Vol. 1 \(2009\) \(/2072-4292/1\)](#)

Advances in Remote Sensing Applications in Natural Hazards Research

- [Special Issue Editors](#)



Special Issue Information

Keywords

Benefits of Publishing in a Special Issue

Published Papers

A special issue of *Remote Sensing* (journal/remotesensing) (ISSN 2072-4292). This special issue belongs to the section "[Earth Observation for Emergency Management](http://journal/remotesensing/sections/earth_observation_emergency_management) (journal/remotesensing/sections/earth_observation_emergency_management)".

Deadline for manuscript submissions: **closed (15 June 2024)** | Viewed by 6987

Share This Special Issue

 (mailto:??&subject=From%20MDPI%3A%20%22Advances%20in%20Remote%20Sensing%20Applications%20in%20Natural%20Hazards%20Research"&body=Special%20Issue%20Title%3A%20Advances%20in%20Remote%20Sensing%20Applications%20in%20Natural%20Hazards%20Research%0A%0AWebsite%3A%20https%3A%2F%2Fwww.mdpi.com%2F%2F166566%0A%0AGuest%20Editors%3A%0A%0AName%3A%20Dr.%20Aleksandra%20Nina%0AAffiliation%3A%20Institute%20of%20Physics%20Belgrade%2C%20University%20of%20Belgrade%2C%20Pregrevice%20118%2C%2011080%20Belgrade%2C%20Serbia%0A%0AName%3A%20Prof.%20Dr.%20Milan%20Radovanovi%C4%87%0AAffiliation%3A%20Geographical%20Institute%20of%20Jovan%20Cvijic%2E%80%9D%20Serbian%20Academy%20of%20Sciences%20and%20Arts%2C%20Djure%20Jak%C5%A1i%C4%87a%209%2C%2011000%20Belgrade%2C%20Serbia%0A%0AName%3A%20Prof.%20Dr.%20Luka%20%C4%8C.%20Popovi%C4%87%0AAffiliation%3A%201.%20Astronomical%20Observatory%2C%20in%20Belgrade%2C%20Boljina%207%2C%2011160%20Belgrade%2C%20Serbia%0D%0A2.%20Faculty%20of%20Mathematics%20University%20of%20Belgrade%2C%20Studentski%20Trg%2016%2C%20Belgrade%2C%20Serbia%0A%0A) (https://twitter.com/intent/tweet?text=Advances+in+Remote+Sensing+Applications+in+Natural+Hazards+Research&hashtags=mdpiremotesensing&url=https%3A%2F%2Fwww.mdpi.com%2F%2F166566&via=RemoteSens_MDPI) (<http://www.linkedin.com/shareArticle?mini=true&url=https%3A%2F%2Fwww.mdpi.com%2F%2F166566&title=Advances%20in%20Remote%20Sensing%20Applications%20in%20Natural%20Hazards%20Research%26source%3Dhttps%3A%2F%2Fwww.mdpi.com%26summary%3DDear%20Colleagues%2C%0D%0ANatural%20disasters%20are%20phenomena%20whose%20impact%20on%20the%20lives%20and%20health%20of%20people%20and%20other%20living%20beings%20is%20very%20often%2C%20many%20of%20these%20phenomena%20are%20very%20difficult%20or%20still%20impossible%20to%20predict%20with%20sufficient%20%5B...%5D>)  (<https://www.facebook.com/sharer.php?u=https://www.mdpi.com/si/166566>)

Special Issue Editors



Dr. Aleksandra Nina

E-Mail ([\)](mailto:) **Website** (<https://loop.frontiersin.org/people/831163/bio>)

Guest Editor

Institute of Physics Belgrade, University of Belgrade, Pregrevice 118, 11080 Belgrade, Serbia

Interests: ionosphere; VLF/LF signals; remote sensing; natural hazards

Special Issues, Collections and Topics in MDPI journals



Prof. Dr. Milan Radovanović

E-Mail ([\)](mailto:) **Website** (https://www.researchgate.net/profile/Milan_Radovanovic4)

Guest Editor

Geographical Institute "Jovan Cvijic" Serbian Academy of Sciences and Arts, Djure Jakićeva 9, 11000 Belgrade, Serbia

Interests: My field of interest is influences of the sun on the atmospheric processes and environment on earth. In last few years my team and I have tried to develop models by which the relationship can be explained between the influx of charged particles from the sun and forest fires. Additionally, I am involved in the research of physical geography, natural hazards and tourism.

Special Issues, Collections and Topics in MDPI journals



Prof. Dr. Luka Č. Popović

E-Mail ([\)](mailto:) **Website** (<http://popovic.aob.rs/>)

Guest Editor

1. Astronomical Observatory, in Belgrade, Boljina 7, 11160 Belgrade, Serbia

2. Faculty of Mathematics University of Belgrade, Studentski Trg 16, Belgrade, Serbia

Interests: active galactic nuclei; gravitational lensing; plasma physics; ionosphere

Special Issues, Collections and Topics in MDPI journals

Special Issue Information

Dear Colleagues,

Natural disasters are phenomena whose impact on the lives and health of people and other living beings is very often tragic. Unfortunately, many of these phenomena are very difficult or still impossible to predict with sufficient temporal and spatial precision. Therefore, all research in this area is very important.

Different techniques based on remote sensing are constantly being developed, which, among others, affects the research of natural hazards, as well as the possibilities for predicting natural disasters and developing procedures for gathering information necessary for emergency management. In this Special Issue, we emphasize multidisciplinary in relevant research and point out the importance of integrating science, technology, engineering, programming, and other activities in order to make faster and more efficient progress in reducing the risk of natural disasters such as earthquakes, volcanic eruptions, tropical cyclones, and other meteorological phenomena, as well as in order to develop emergency management.

This Special Issue aims to present new research in this area and its practical applications. This Special Issue welcomes papers related to natural hazards and disasters, including the following:

- Remote sensing of different Earth systems;
- Modeling of different terrestrial areas using data obtained through various types of remote sensing;
- Possible applications of conclusions derived from the processing and modeling of relevant data.

Additionally, other papers that deal with the applications of remote sensing related to natural hazards and disasters are welcome.

Dr. Aleksandra Nina

Prof. Dr. Milan Radovanović

Prof. Dr. Luka Č. Popović

Guest Editors

Manuscript Submission Information

Manuscripts should be submitted online at www.mdpi.com (<https://www.mdpi.com>) by **registering** (<https://www.mdpi.com/user/register/>) and **logging in to this website** (<https://www.mdpi.com/user/login/>). Once you are registered, **click here to go to the submission form** (<https://susy.mdpi.com/user/manuscripts/upload/?journal=remotesensing>). Manuscripts can be submitted until the deadline. All submissions that pass pre-check are peer-reviewed. Accepted papers will be published

continuously in the journal (as soon as accepted) and will be listed together on the special issue website. Research articles, review articles as well as short communications are invited. For planned papers, a title and short abstract (about 100 words) can be sent to the Editorial Office for announcement on this website.

Submitted manuscripts should not have been published previously, nor be under consideration for publication elsewhere (except conference proceedings papers). All manuscripts are thoroughly refereed through a single-blind peer-review process. A guide for authors and other relevant information for submission of manuscripts is available on the [Instructions for Authors](https://www.mdpi.com/journal/remotesensing/instructions) (<https://www.mdpi.com/journal/remotesensing/instructions>) page. *Remote Sensing* (<https://www.mdpi.com/journal/remotesensing/>) is an international peer-reviewed open access semimonthly journal published by MDPI.

Please visit the [Instructions for Authors](https://www.mdpi.com/journal/remotesensing/instructions) (<https://www.mdpi.com/journal/remotesensing/instructions>) page before submitting a manuscript. The **Article Processing Charge (APC)** (<https://www.mdpi.com/about/apc/>) for publication in this **open access** (<https://www.mdpi.com/about/openaccess/>) journal is 2700 CHF (Swiss Francs). Submitted papers should be well formatted and use good English. Authors may use MDPI's [English editing service](https://www.mdpi.com/authors/english) (<https://www.mdpi.com/authors/english>) prior to publication or during author revisions.

Keywords

- natural hazards
- natural disasters
- remote sensing
- modelling
- emergency management

Benefits of Publishing in a Special Issue

- Ease of navigation: Grouping papers by topic helps scholars navigate broad scope journals more efficiently.
- Greater discoverability: Special Issues support the reach and impact of scientific research. Articles in Special Issues are more discoverable and cited more frequently.
- Expansion of research network: Special Issues facilitate connections among authors, fostering scientific collaborations.
- External promotion: Articles in Special Issues are often promoted through the journal's social media, increasing their visibility.
- e-Book format: Special Issues with more than 10 articles can be published as dedicated e-books, ensuring wide and rapid dissemination.

Further information on MDPI's Special Issue policies can be found [here](https://www.mdpi.com/special_issues_guidelines) (https://www.mdpi.com/special_issues_guidelines).

Published Papers (4 papers)

[Download All Papers](#)

Order results

Content type

Result details

Normal

[Show export options](#) ▾

Research

Open Access Article 24 pages, 7317 KIB ([/2072-4292/16/6/1029/pdf?version=1710407473](https://doi.org/10.3390/rs16061029/pdf?version=1710407473))

Natural Gas Induced Vegetation Stress Identification and Discrimination from Hyperspectral Imaging for Pipeline Leakage Detection ([2072-4292/16/6/1029](https://doi.org/10.3390/rs16061029))

by Pengfei Ma, Ying Zhuo, Genda Chen and Joel G. Burken

Remote Sens. **2024**, *16*(6), 1029; <https://doi.org/10.3390/rs16061029> (<https://doi.org/10.3390/rs16061029>) - 14 Mar 2024

Cited by 2 ([2072-4292/16/6/1029#metrics](https://doi.org/10.3390/rs16061029#metrics)) | Viewed by 1386

Abstract Remote sensing detection of natural gas leaks remains challenging when using ground vegetation stress to detect underground pipeline leaks. Other natural stressors may co-present and complicate gas leak detection. This study explores the feasibility of identifying and distinguishing gas-induced stress from other natural [...][Read more](#). (This article belongs to the Special Issue **Advances in Remote Sensing Applications in Natural Hazards Research** ([/journal/remotesensing/special_issues/614751CUMG](https://www.mdpi.com/journal/remotesensing/special_issues/614751CUMG)))

[► Show Figures](#)

https://pub.mdpi-res.com/remotesensing/remotesensing-16-01029/article_deploy/html/images/remotesensing-16-01029-g001-550.jpg?1710407594 (https://pub.mdpi-res.com/remotesensing/remotesensing-16-01029/article_deploy/html/images/remotesensing-16-01029-g002-550.jpg?1710407596) (https://pub.mdpi-res.com/remotesensing/remotesensing-16-01029/article_deploy/html/images/remotesensing-16-01029-g003-550.jpg?1710407597) ([https://pub.mdpi-res.com/remotesensing/remotesensing-16-01029-g004-550.jpg?1710407598](https://pub.mdpi-res.com/remotesensing/remotesensing-16-01029/article_deploy/html/images/remotesensing-16-01029-g004-550.jpg?1710407598)) ([https://pub.mdpi-res.com/remotesensing/remotesensing-16-01029-g005-550.jpg?1710407599](https://pub.mdpi-res.com/remotesensing/remotesensing-16-01029/article_deploy/html/images/remotesensing-16-01029-g005-550.jpg?1710407599)) ([https://pub.mdpi-res.com/remotesensing/remotesensing-16-01029-g006-550.jpg?1710407601](https://pub.mdpi-res.com/remotesensing/remotesensing-16-01029/article_deploy/html/images/remotesensing-16-01029-g006-550.jpg?1710407601)) ([https://pub.mdpi-res.com/remotesensing/remotesensing-16-01029-g007-550.jpg?1710407602](https://pub.mdpi-res.com/remotesensing/remotesensing-16-01029/article_deploy/html/images/remotesensing-16-01029-g007-550.jpg?1710407602)) (<https://pub.mdpi-res.com/remotesensing/remotesensing-16-01029-g008-550.jpg?1710407603>) (<https://pub.mdpi-res.com/remotesensing/remotesensing-16-01029-g009-550.jpg?1710407605>) (<https://pub.mdpi-res.com/remotesensing/remotesensing-16-01029-g010-550.jpg?1710407606>) (<https://pub.mdpi-res.com/remotesensing/remotesensing-16-01029-g011-550.jpg?1710407609>) (<https://pub.mdpi-res.com/remotesensing/remotesensing-16-01029-g012-550.jpg?1710407610>)

Open Access Article 19 pages, 2113 KIB ([/2072-4292/16/2/397/pdf?version=170567634](https://doi.org/10.3390/rs16020397/pdf?version=170567634))

Analysis of VLF Signal Noise Changes in the Time Domain and Excitations/Attenuations of Short-Period Waves in the Frequency Domain as Potential Earthquake Precursors ([2072-4292/16/2/397](https://doi.org/10.3390/rs16020397))

by Aleksandra Nina

Remote Sens. **2024**, *16*(2), 397; <https://doi.org/10.3390/rs16020397> (<https://doi.org/10.3390/rs16020397>) - 19 Jan 2024

Cited by 1 ([2072-4292/16/2/397#metrics](https://doi.org/10.3390/rs16020397#metrics)) | Viewed by 1127

Abstract In this paper, we complete pioneering research that indicates the very low frequency (VLF) signal amplitude and phase noise reductions, and short-period wave excitations and attenuations as new potential earthquake precursors. We consider changes in the VLF signal broadcast in Italy by the [...][Read more](#). (This article belongs to the Special Issue **Advances in Remote Sensing Applications in Natural Hazards Research** ([/journal/remotesensing/special_issues/614751CUMG](https://www.mdpi.com/journal/remotesensing/special_issues/614751CUMG)))

[► Show Figures](#)

https://pub.mdpi-res.com/remotesensing/remotesensing-16-00397/article_deploy/html/images/remotesensing-16-00397-ag-550.jpg?1705678569 ([https://pub.mdpi-res.com/remotesensing/remotesensing-16-00397-g001-550.jpg?170567708](https://pub.mdpi-res.com/remotesensing/remotesensing-16-00397/article_deploy/html/images/remotesensing-16-00397-g001-550.jpg?170567708)) ([https://pub.mdpi-res.com/remotesensing/remotesensing-16-00397-g002-550.jpg?170567709](https://pub.mdpi-res.com/remotesensing/remotesensing-16-00397/article_deploy/html/images/remotesensing-16-00397-g002-550.jpg?170567709))

https://pub.mdpi-res.com/remotesensing/remotesensing-16-00397/article_deploy/html/images/remotesensing-16-00397-g002-550.jpg?1705657710 (https://pub.mdpi-res.com/remotesensing/remotesensing-16-00397/article_deploy/html/images/remotesensing-16-00397-g003-550.jpg?1705657712) (https://pub.mdpi-res.com/remotesensing/remotesensing-16-00397/article_deploy/html/images/remotesensing-16-00397-g004-550.jpg?1705657713) (https://pub.mdpi-res.com/remotesensing/remotesensing-16-00397/article_deploy/html/images/remotesensing-16-00397-g005-550.jpg?1705657714) (https://pub.mdpi-res.com/remotesensing/remotesensing-16-00397/article_deploy/html/images/remotesensing-16-00397-g006-550.jpg?1705657716) (https://pub.mdpi-res.com/remotesensing/remotesensing-16-00397/article_deploy/html/images/remotesensing-16-00397-g007-550.jpg?1705657718) (https://pub.mdpi-res.com/remotesensing/remotesensing-16-00397/article_deploy/html/images/remotesensing-16-00397-g008-550.jpg?1705657719)

Open Access Article

18 pages, 20974 KiB [\(2072-4292/16/1/41/pdf?version=1703155478\)](#)**Water Quality and Flooding Impact of the Record-Breaking Storm Gloria in the Ebro Delta (Western Mediterranean) (2072-4292/16/1/41)**

by Isabel Caballero, Mar Roca, Martha B. Dunbar and Gabriel Navarro

Remote Sens. **2024**, *16*(1), 41; <https://doi.org/10.3390/rs16010041> (<https://doi.org/10.3390/rs16010041>) - 21 Dec 2023Cited by 1 ([2072-4292/16/1/41#metrics](#)) | Viewed by 1943**Abstract** Extreme events are increasing in frequency and severity due to climate change, making the littoral zone even more vulnerable and requiring continuous monitoring for its optimized management. The low-lying Ebro Delta ecosystem, located in the NW Mediterranean, was subject to Storm Gloria in [...]. [Read more](#).(This article belongs to the Special Issue **Advances in Remote Sensing Applications in Natural Hazards Research** ([/journal/remotesensing/special_issues/614751CUMG](#)))**Show Figures**

https://pub.mdpi-res.com/remotesensing/remotesensing-16-00041/article_deploy/html/images/remotesensing-16-00041-ag-550.jpg?1703487662 (https://pub.mdpi-res.com/remotesensing/remotesensing-16-00041/article_deploy/html/images/remotesensing-16-00041-g001-550.jpg?1703155555) (https://pub.mdpi-res.com/remotesensing/remotesensing-16-00041/article_deploy/html/images/remotesensing-16-00041-g002-550.jpg?1703155558) ([https://pub.mdpi-res.com/remotesensing/remotesensing-16-00041-g003-550.jpg?1703155559](https://pub.mdpi-res.com/remotesensing/remotesensing-16-00041/article_deploy/html/images/remotesensing-16-00041-g003-550.jpg?1703155559)) ([https://pub.mdpi-res.com/remotesensing/remotesensing-16-00041-g004-550.jpg?1703155562](https://pub.mdpi-res.com/remotesensing/remotesensing-16-00041/article_deploy/html/images/remotesensing-16-00041-g004-550.jpg?1703155562)) (https://pub.mdpi-res.com/remotesensing/remotesensing-16-00041/article_deploy/html/images/remotesensing-16-00041-g005-550.jpg?1703155564) (https://pub.mdpi-res.com/remotesensing/remotesensing-16-00041/article_deploy/html/images/remotesensing-16-00041-g006-550.jpg?1703155568) (https://pub.mdpi-res.com/remotesensing/remotesensing-16-00041/article_deploy/html/images/remotesensing-16-00041-g007-550.jpg?1703155571) (https://pub.mdpi-res.com/remotesensing/remotesensing-16-00041/article_deploy/html/images/remotesensing-16-00041-g008-550.jpg?1703155573) (https://pub.mdpi-res.com/remotesensing/remotesensing-16-00041/article_deploy/html/images/remotesensing-16-00041-g009-550.jpg?1703155577) (https://pub.mdpi-res.com/remotesensing/remotesensing-16-00041/article_deploy/html/images/remotesensing-16-00041-g010-550.jpg?1703155581)

Open Access Article

24 pages, 9896 KiB [\(2072-4292/15/21/5262/pdf?version=1699285458\)](#)**Automatic Identification for the Boundaries of InSAR Anomalous Deformation Areas Based on Semantic Segmentation Model (2072-4292/15/21/5262)**

by Yiwen Liang, Yi Zhang, Yuanxi Li and Jiaqi Xiong

Remote Sens. **2023**, *15*(21), 5262; <https://doi.org/10.3390/rs15215262> (<https://doi.org/10.3390/rs15215262>) - 6 Nov 2023Cited by 1 ([2072-4292/15/21/5262#metrics](#)) | Viewed by 1675**Abstract** Interferometric synthetic aperture radar (InSAR) technology has become one of the mainstream techniques for active landslide identification over a large area. However, the method for interpreting anomalous deformation areas derived from InSAR data is still mainly manual delineation through human-computer interaction. This study [...]. [Read more](#).(This article belongs to the Special Issue **Advances in Remote Sensing Applications in Natural Hazards Research** ([/journal/remotesensing/special_issues/614751CUMG](#)))**Show Figures**

https://pub.mdpi-res.com/remotesensing/remotesensing-15-05262/article_deploy/html/images/remotesensing-15-05262-g001a-550.jpg?1699285528 (https://pub.mdpi-res.com/remotesensing/remotesensing-15-05262/article_deploy/html/images/remotesensing-15-05262-g001b-550.jpg?1699285530) (https://pub.mdpi-res.com/remotesensing/remotesensing-15-05262/article_deploy/html/images/remotesensing-15-05262-g002-550.jpg?1699285533) (https://pub.mdpi-res.com/remotesensing/remotesensing-15-05262/article_deploy/html/images/remotesensing-15-05262-g003-550.jpg?1699285534) (https://pub.mdpi-res.com/remotesensing/remotesensing-15-05262/article_deploy/html/images/remotesensing-15-05262-g004-550.jpg?1699285538) ([https://pub.mdpi-res.com/remotesensing/remotesensing-15-05262-g005-550.jpg?1699285540](https://pub.mdpi-res.com/remotesensing/remotesensing-15-05262/article_deploy/html/images/remotesensing-15-05262-g005-550.jpg?1699285540)) ([https://pub.mdpi-res.com/remotesensing/remotesensing-15-05262-g006-550.jpg?1699285542](https://pub.mdpi-res.com/remotesensing/remotesensing-15-05262/article_deploy/html/images/remotesensing-15-05262-g006-550.jpg?1699285542)) (https://pub.mdpi-res.com/remotesensing/remotesensing-15-05262/article_deploy/html/images/remotesensing-15-05262-g007-550.jpg?1699285545) (https://pub.mdpi-res.com/remotesensing/remotesensing-15-05262/article_deploy/html/images/remotesensing-15-05262-g008-550.jpg?1699285547) (https://pub.mdpi-res.com/remotesensing/remotesensing-15-05262/article_deploy/html/images/remotesensing-15-05262-g009-550.jpg?1699285549) (https://pub.mdpi-res.com/remotesensing/remotesensing-15-05262/article_deploy/html/images/remotesensing-15-05262-g010-550.jpg?1699285554) (https://pub.mdpi-res.com/remotesensing/remotesensing-15-05262/article_deploy/html/images/remotesensing-15-05262-g011-550.jpg?1699285555) (https://pub.mdpi-res.com/remotesensing/remotesensing-15-05262/article_deploy/html/images/remotesensing-15-05262-g012-550.jpg?1699285559) (https://pub.mdpi-res.com/remotesensing/remotesensing-15-05262/article_deploy/html/images/remotesensing-15-05262-g013-550.jpg?1699285563) (https://pub.mdpi-res.com/remotesensing/remotesensing-15-05262/article_deploy/html/images/remotesensing-15-05262-g014-550.jpg?1699285567)

Show export options 

Displaying articles 1-4

Remote Sens. ([/journal/remotesensing](#)). EISSN 2072-4292, Published by MDPI[RSS \(/rss/journal/remotesensing\)](#) [Content Alert \(/journal/remotesensing/toc-alert\)](#)

Further Information

[Article Processing Charges \(/apc\)](#)[Pay an Invoice \(/about/payment\)](#)[Open Access Policy \(/openaccess\)](#)[Contact MDPI \(/about/contact\)](#)[Jobs at MDPI \(https://careers.mdpi.com\)](#)

Guidelines

[For Authors \(/authors\)](#)[For Reviewers \(/reviewers\)](#)[For Editors \(/editors\)](#)

- [For Librarians \(/librarians\)](#)
- [MDPI](#)
- [For Publishers \(/publishing_services\)](#)
- [For Societies \(/societies\)](#)
- [MDPI Initiatives](#)
- [For Conference Organizers \(/conference_organizers\)](#)
- [SciForum \(https://sciforum.net\)](#)
- [MDPI Books \(https://www.mdpi.com/books\)](#)
- [Preprints.org \(https://www.preprints.org\)](#)
- [Scilit \(https://www.scilit.net\)](#)
- [SciProfiles \(https://sciprofiles.com?utm_source=mpdi.com&utm_medium=bottom_menu&utm_campaign=initiative\)](#)
- [Encyclopedia \(https://encyclopedia.pub\)](#)
- [JAMS \(https://jams.pub\)](#)
- [Proceedings Series \(/about/proceedings\)](#)



Follow MDPI

- [LinkedIn \(https://www.linkedin.com/company/mdpi\)](https://www.linkedin.com/company/mdpi)
- [Facebook \(https://www.facebook.com/MDPIOpenAccessPublishing\)](https://www.facebook.com/MDPIOpenAccessPublishing)
- [Twitter \(https://twitter.com/MDPIOpenAccess\)](https://twitter.com/MDPIOpenAccess)



Subscribe to receive issue release notifications and newsletters from MDPI journals

Select options

Enter your email address...

© 1996-2024 MDPI (Basel, Switzerland) unless otherwise stated

[Disclaimer](#) [Terms and Conditions \(/about/terms-and-conditions\)](#) [Privacy Policy \(/about/privacy\)](#)

< Frontiers in Environmental Science

Atmospheric Disturbances: Responses to Phenomena from Lithosphere to Outer Space

8.4K views

24 authors

5 articles



EDITORIAL

09 May 2023

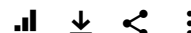
Editorial: Atmospheric disturbances: responses to phenomena from lithosphere to outer space

Aleksandra Nina, Boško Milovanović, Slavica Malinović-Milićević and Sergey Pulinets

A large number of processes and phenomena that occur both in the Earth's layers (Veronis et al., 1999; Beletsky et al., 2003; Bochev and Dimitrova, 2003; Balan et al., 2008; Utada et al., 2011; Simões et al., 2012; Nina et al., 2020h) and in outer space

al., 2017; Nina et al., 2018; Nina et al., 2021; Kolarski et al., 2022) constantly affect the terrestrial atmosphere. Although the effects that phenomena created in different areas produce in atmospheric layers depend on their characteristics and the

710 views 0 citations



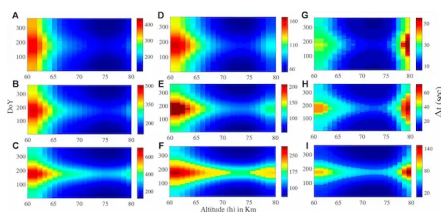
areas that include several atmospheric layers. Also, there are numerous influences on one atmospheric area (Nina et al., 2017; Silber and Price, 2017). In addition, changes in the atmosphere as a medium, in which other processes take place, have an impact on various processes and technologies in modern life (Jakowski et al., 2005; Stankov

et al., 2021). Therefore, the monitoring and understanding of spatio-temporal atmospheric changes are important for research in a number of scientific disciplines as well as for geoinformation technologies. Here, first of all, the importance of research into atmospheric changes related to natural disasters should be

Editors 4



Impact



ORIGINAL RESEARCH
28 November 2022

On the altitude profile of lower ionospheric D-region response time

1,172 views 2 citations



ORIGINAL RESEARCH
29 September 2022

Variation in the VLF signal noise amplitude during the period of intense seismic activity in Central Italy from 25 October to 3 November 2016

Aleksandra Nina, 7 more and
1,473 views 5 citations



The D-region ionosphere is sluggish in nature while responding to the incoming solar radiation. We study the altitude (h) profile of mid-latitude D-region response time delay (Δt) during three chosen solar flares, namely,

ORIGINAL RESEARCH

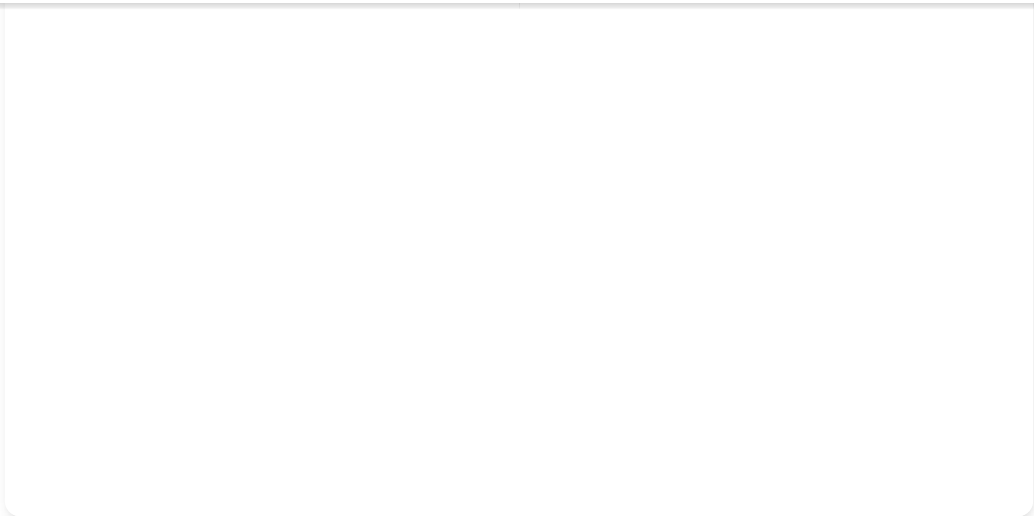
26 August 2022

Multi-instrumental investigation of the solar flares impact on the ionosphere on 05–06 December 2006

Veronika Barta, 4 more and Desanka Šulic

2,462 views 10 citations





ORIGINAL RESEARCH

24 June 2022

Very-Short-Term Variations of Sea Surface and Atmospheric Parameters Before the Ms 6.2 Zhangbei (China) Earthquake in 1998

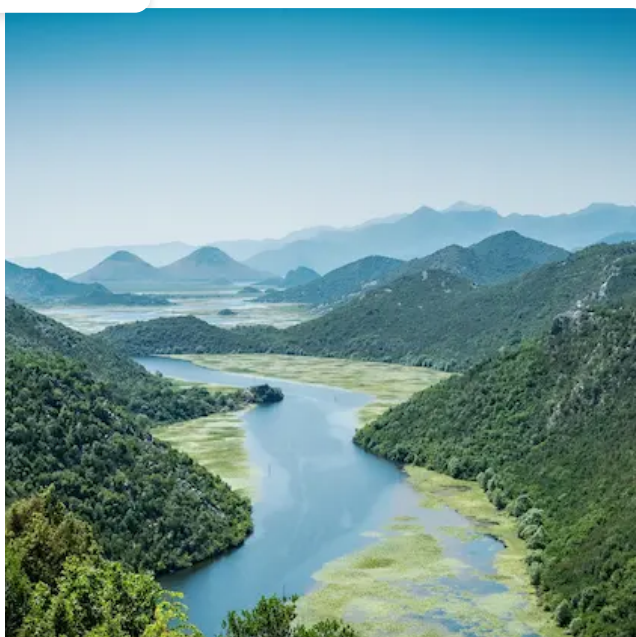
Yingjia Liu, 2 more and Yifan Ding

1,404 views 3 citations



Frontiers in Environmental Science

The Atmospheric and Environmental Impact of Anthropogenic



Cryosphere: A Multidisciplinary

 Recommended Research Topics  



Frontiers in Environmental
Science

Observations and Modelling of Recent Extreme Wild Fire Events and their Impact on the Environment and Climate

Edited by Corinna Kloss,
Pasquale Sellitto,
Christoph Rüdiger,
Solene Turquet

Frontiers in Environmental
Science

Atmospheric Dust: How it affects climate, environment and life on Earth?

Edited by Qinjian Jin, Dr.
Diana FRANCIS, Sagar
Parajuli, Chen Siyu, Charu
Singh

Frc
Sci
In
Cl
Li
Ed
Ya
Zh

Home / ... / ... / Research Topics

Enjoyed this Research Topic? Share it using



Atmospheric Disturbances:





Sections ▾

Articles

Research Topics

Editorial board

At

Atmosphere to Outer Space

8.4K views

| 24 authors





OPEN ACCESS

EDITED AND REVIEWED BY
Yongliang Zhang,
Johns Hopkins University, United States

*CORRESPONDENCE
Aleksandra Nina,
✉ sandrast@ipb.ac.rs

RECEIVED 03 April 2023
ACCEPTED 02 May 2023
PUBLISHED 09 May 2023

CITATION
Nina A, Milovanović B,
Malinović-Milićević S and Pulinets S
(2023), Editorial: Atmospheric
disturbances: responses to phenomena
from lithosphere to outer space.
Front. Environ. Sci. 11:1199573.
doi: 10.3389/fenvs.2023.1199573

COPYRIGHT
© 2023 Nina, Milovanović, Malinović-
Milićević and Pulinets. This is an open-
access article distributed under the terms
of the [Creative Commons Attribution
License \(CC BY\)](#). The use, distribution or
reproduction in other forums is
permitted, provided the original author(s)
and the copyright owner(s) are credited
and that the original publication in this
journal is cited, in accordance with
accepted academic practice. No use,
distribution or reproduction is permitted
which does not comply with these terms.

Editorial: Atmospheric disturbances: responses to phenomena from lithosphere to outer space

Aleksandra Nina^{1*}, Boško Milovanović²,
Slavica Malinović-Milićević² and Sergey Pulinets³

¹Institute of Physics Belgrade, University of Belgrade, Belgrade, Serbia, ²Geographical Institute "Jovan Cvijić" SASA, Belgrade, Serbia, ³Space Research Institute, Russian Academy of Sciences, Moscow, Russia

KEYWORDS

atmospheric disturbances, modelling, *in situ* measurements, remote sensing, natural disasters, environmental impact assessment, community responses

Editorial on the Research Topic

Atmospheric disturbances: responses to phenomena from lithosphere to outer space

A large number of processes and phenomena that occur both in the Earth's layers (Veronis et al., 1999; Beletsky et al., 2003; Bochev and Dimitrova, 2003; Balan et al., 2008; Utada et al., 2011; Simões et al., 2012; Nina et al., 2020b) and in outer space (Inan et al., 2007; Srećković et al., 2017; Nina et al., 2018; Nina et al., 2021; Kolarski et al., 2022) constantly affect the terrestrial atmosphere. Although the effects that phenomena created in different areas produce in atmospheric layers depend on their characteristics and the observed geographical location, changes can very often be detected in large areas that include several atmospheric layers. Also, there are numerous influences on one atmospheric area (Nina et al., 2017; Silber and Price, 2017). In addition, changes in the atmosphere as a medium, in which other processes take place, have an impact on various processes and technologies in modern life (Jakowski et al., 2005; Stankov et al., 2009; Su et al., 2019; Nina et al., 2020a; Hunting et al., 2021). Therefore, the monitoring and understanding of spatio-temporal atmospheric changes are important for research in a number of scientific disciplines as well as for geoinformation technologies. Here, first of all, the importance of research into atmospheric changes related to natural disasters should be emphasized (Molchanov et al., 2004; Price et al., 2007; Maurya et al., 2016; Kumar et al., 2017; Vyklyuk et al., 2017, 2019; Manta et al., 2020; Malinović-Milićević et al., 2023). For example, the Lithosphere-Atmosphere-Ionosphere Coupling (LAIC) model based on the effects of ionisation provided by radon released from active tectonic faults before earthquakes is created in Pulinets et al. (2022).

In this Research Topic, studies of solar flare and seismic processes (possible) influences on the atmosphere are presented. Here, we briefly review and summarize these articles.

Barta et al. analysed the ionosphere during influences of solar flares that occurred on 5 and 6 December 2006. This study is based on data obtained in ground-based (by ionosonde and very low frequency (VLF) radio signals) and satellite (by GNSS and DEMETER satellites) observations. The obtained results show 1) an increase in VTEC (2%–5%)

during a stronger flare and the absence of its change in the case of a weaker flare, 2) a latitude dependent enhancement of f_{min} (first echo trace observed on ionograms) during both observed events in relation for quiet periods. In addition, a change in absorption of VLF signal from ground transmitters detected in low Earth orbit, and electron density profile versus ionospheric D-region altitude are presented.

Liu et al. proposed a way to explore the seismic activity of submarine faults. The study analyses disturbances in the atmosphere in the days leading up to, during, and after the Ms 6.2 Zhangbei earthquake that occurred on 10 January 1998, 150 km northwest of Beijing, using observations from satellites, reanalysis data, and satellite infrared cloud images. A positive thermal infrared (TIR) anomaly was detected in the area between the sea surface and the atmosphere above the Bohai Sea 2–3 days prior to the earthquake. The TIR strip was caused by clouds of low level arising from the release of gas from the Tancheng-Lujiang fault, which has a higher temperature than land surface gas, but not from the Zhangbei-Bohai fault that was previously considered. It was concluded that strip-shaped clouds that are the consequence of seismic activity and underwater release of gas were forced by a certain wind field and lowering boundary layer of the atmosphere.

Nina et al. extend research of VLF signal noise amplitude reductions before an earthquake to their studying during intense seismic activity. They analysed a time period from 25 October to 3 November 2016 when 981 earthquakes with magnitudes between 2 and 6.5 occurred in Central Italy. VLF observations confirm the noise amplitude reduction before individual not weak earthquakes that do not follow earthquakes after which the analyzed change is already present. In addition, this study point out the beginning of noise amplitude changes 2 weeks before the considered seismically active period.

Chakraborty et al. studied the altitude (h) profile of mid-latitude D-region response time delay (Δt) during solar flares of different classes. By solving “electron continuity equation” they estimated the variation of solar irradiation onto the ionosphere and investigated latitudinal variation (over both Northern and Southern hemispheres within the latitude range from 30° to 60°) and seasonal variation (throughout the year) of $\Delta t - h$ profiles of each of these solar flares separately. They found h dependency of Δt for all of the flares and

their significant latitudinal variation. The methodology shown in the paper is not limited to the $\Delta t - h$ profiles just for the classes of solar flares in case, but is applicable to the entire range of available solar flares.

Author contributions

AN, BM, SM-M, and SP all made substantial contributions to the conception and design of the work and to drafting and revising it for important intellectual content. All authors listed have made a substantial, direct, and intellectual contribution to the work and approved it for publication. All authors contributed to the article and approved the submitted version.

Funding

The authors acknowledge funding provided by the Institute of Physics Belgrade and the Geographical Institute “Jovan Cvijić” SASA through the grants by the Ministry of Science, Technological Development and Innovation of the Republic of Serbia.

Conflict of interest

The authors declare that the research was conducted in the absence of any commercial or financial relationships that could be construed as a potential conflict of interest.

Publisher’s note

All claims expressed in this article are solely those of the authors and do not necessarily represent those of their affiliated organizations, or those of the publisher, the editors and the reviewers. Any product that may be evaluated in this article, or claim that may be made by its manufacturer, is not guaranteed or endorsed by the publisher.

References

- Balan, N., Alleyne, H., Walker, S., Reme, H., McCrea, I., and Aylward, A. (2008). Magnetosphere-ionosphere coupling during the CME events of 07–12 November 2004. *Jo. Atmos. Solar-Terr. Phys.* 70, 2101–2111. doi:10.1016/j.jastp.2008.03.015
- Beletsky, A. B., Afraimovich, E. L., Gress, O. G., Lesyuta, O. S., Mikhalev, A. V., and Shalin, A. Y. (2003). “Wave disturbances in the Earth’s atmosphere during the passage of Leonid’s meteor stream on November 16–18, 2001,” in *Society of photo-optical instrumentation engineers (SPIE) conference series*. Editors G. G. Matvienko and V. P. Lukin, 5027, 216–223. doi:10.1117/12.497322
- Bochev, A. Z., and Dimitrova, I. I. A. (2003). Magnetic cloud and magnetosphere - ionosphere response to the 6 November 1997 CME. *Adv. Space Res.* 32, 1981–1987. doi:10.1016/S0273-1177(03)90636-3
- Hunting, E. R., Matthews, J., Fernández de Arróyabe Hernández, P., England, S. J., Kourtidis, K., Koh, K., et al. (2021). Challenges in coupling atmospheric electricity with biological systems. *Int. J. Biometeorol.* 65, 45–58. doi:10.1007/s00484-020-01960-7
- Inan, U. S., Lehtinen, N. G., Moore, R. C., Hurley, K., Boggs, S., Smith, D. M., et al. (2007). Massive disturbance of the daytime lower ionosphere by the giant γ -ray flare from magnetar SGR 1806-20. *Geophys. Res. Lett.* 34, L08103. doi:10.1029/2006GL029145
- Jakowski, N., Stankov, S. M., and Klaehn, D. (2005). Operational space weather service for GNSS precise positioning. *Ann. Geophys.* 23, 3071–3079. doi:10.5194/angeo-23-3071-2005
- Kolarski, A., Sreckovic, V., and Mijic, Z. (2022). Monitoring solar activity during 23/24 solar cycle minimum through VLF radio signals. *Contrib. Astron. Obs. Skaln. Pleso* 52, 105–115. doi:10.31577/caosp.2022.52.3.105
- Kumar, S., NaitAmor, S., Chanrion, O., and Neubert, T. (2017). Perturbations to the lower ionosphere by tropical cyclone Evan in the south Pacific region. *J. Geophys. Res. Space* 122, 8720–8732. doi:10.1002/2017JA024023
- Malinović-Miličević, S., Radovanović, M. M., Radenković, S. D., Vyklyuk, Y., Milovanović, B., Milanović Pešić, A., et al. (2023). Application of solar activity time series in machine learning predictive modeling of precipitation-induced floods. *Mathematics* 11, 795. doi:10.3390/math11040795
- Manta, F., Occhipinti, G., Feng, L., and Hill, E. M. (2020). Rapid identification of tsunamigenic earthquakes using GNSS ionospheric sounding. *Sci. Rep.* 10, 11110. doi:10.1038/s41598-020-68097-w

- Maurya, A. K., Venkatesham, K., Tiwari, P., Vijaykumar, K., Singh, R., Singh, A. K., et al. (2016). The 25 april 2015 Nepal earthquake: Investigation of precursor in VLF subionospheric signal. *J. Geophys. Res. Space*. 121(10), 416. doi:10.1002/2016JA022721
- Molchanov, O., Fedorov, E., Schekotov, A., Gordeev, E., Chebrov, V., Surkov, V., et al. (2004). Lithosphere-atmosphere-ionosphere coupling as governing mechanism for preseismic short-term events in atmosphere and ionosphere. *Nat. Haz. Earth Sys. Sci.* 4, 757–767. doi:10.5194/nhess-4-757-2004
- Nina, A., Čadež, V. M., Bajčetić, J., Mitrović, S. T., and Popović, L. Č. (2018). Analysis of the relationship between the solar X-ray radiation intensity and the D-region electron density using satellite and ground-based radio data. *Sol. Phys.* 293, 64. doi:10.1007/s11207-018-1279-4
- Nina, A., Čadež, V. M., Popović, L. Č., and Srećković, V. A. (2017). Diagnostics of plasma in the ionospheric D-region: Detection and study of different ionospheric disturbance types. *Eur. Phys. J. D.* 71, 189. doi:10.1140/epjd/e2017-70747-0
- Nina, A., Nico, G., Mitrović, S. T., Čadež, V. M., Milošević, I. R., Radovanović, M., et al. (2021). Quiet ionospheric D-region (QIonDR) model based on VLF/LF observations. *Remote Sens.* 13, 483. doi:10.3390/rs13030483
- Nina, A., Nico, G., Odalović, O., Čadež, V., Todorović Drakul, M., Radovanović, M., et al. (2020a). GNSS and SAR signal delay in perturbed ionospheric D-region during solar X-ray flares. *IEEE Geosci. Remote Sens. Lett.* 17, 1198–1202. doi:10.1109/LGRS.2019.2941643
- Nina, A., Pulinets, S., Biagi, P., Nico, G., Mitrović, S., Radovanović, M., et al. (2020b). Variation in natural short-period ionospheric noise, and acoustic and gravity waves revealed by the amplitude analysis of a VLF radio signal on the occasion of the Kraljevo earthquake (Mw = 5.4). *Sci. Total Environ.* 710, 136406. doi:10.1016/j.scitotenv.2019.136406
- Price, C., Yair, Y., and Asfur, M. (2007). East African lightning as a precursor of Atlantic hurricane activity. *Geophys. Res. Lett.* 34, L09805. doi:10.1029/2006GL028884
- Pulinets, S., Ouzounov, D., Karelin, A., and Boyarchuk, K. (2022). *Earthquake precursors in the atmosphere and ionosphere: New concepts*. Berlin, Heidelberg, Germany: Springer.
- Silber, I., and Price, C. (2017). On the use of VLF narrowband measurements to study the lower ionosphere and the mesosphere–lower thermosphere. *Surv. Geophys.* 38, 407–441. doi:10.1007/s10712-016-9396-9
- Simões, F., Pfaff, R., Berthelier, J.-J., and Klenzing, J. (2012). A review of low frequency electromagnetic wave phenomena related to tropospheric-ionospheric coupling mechanisms. *Space Sci. Rev.* 168, 551–593. doi:10.1007/s11214-011-9854-0
- Srećković, V., Šulić, D., Vujičić, V., Jevremović, D., and Vyklyuk, Y. (2017). The effects of solar activity: Electrons in the terrestrial lower ionosphere. *J. Geogr. Inst. Cvijic* 67, 221–233. doi:10.2298/IJGI1703221S
- Stankov, S., Warnant, R., and Stegen, K. (2009). Trans-ionospheric GPS signal delay gradients observed over mid-latitude Europe during the geomagnetic storms of October–November 2003. *Advan. Space Res.* 43, 1314–1324. doi:10.1016/j.asr.2008.12.012
- Su, K., Jin, S., and Hoque, M. M. (2019). Evaluation of ionospheric delay effects on multi-GNSS positioning performance. *Remote Sens.* 11, 171. doi:10.3390/rs11020171
- Utada, H., Shimizu, H., Ogawa, T., Maeda, T., Furumura, T., Yamamoto, T., et al. (2011). Geomagnetic field changes in response to the 2011 off the pacific coast of tohoku earthquake and tsunami. *Earth Planet. Sc. Lett.* 311, 11–27. doi:10.1016/j.epsl.2011.09.036
- Veronis, G., Pasko, V. P., and Inan, U. S. (1999). Characteristics of mesospheric optical emissions produced by lightning discharges. *J. Geophys. Res.* 104, 12645–12656. doi:10.1029/1999JA900129
- Vyklyuk, Y., Radovanović, M., Milovanović, B., Leko, T., Milenković, M., Milošević, Z., et al. (2017). Hurricane Genesis modelling based on the relationship between solar activity and hurricanes. *Nat. Hazards* 85, 1043–1062. doi:10.1007/s11069-016-2620-6
- Vyklyuk, Y., Radovanović, M. M., Milovanović, B., Milenković, M., Petrović, M., Doljak, D., et al. (2019). Space weather and hurricanes irma, jose and katia. *Astrophys. Space Sci.* 364, 154. doi:10.1007/s10509-019-3646-5



[Sign In / Sign Up \(/user/login\)](#)

[Submit \(https://susy.mdpi.com/user/manuscripts/upload?journal=atmosphere \)](https://susy.mdpi.com/user/manuscripts/upload?journal=atmosphere)

Search for Articles:

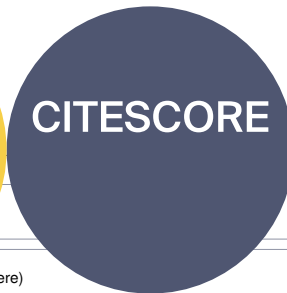
Advanced Search

[Journals \(/about/journals\)](#) / [Atmosphere \(/journal/atmosphere\)](#) / [Special Issues \(/journal/atmosphere/special_issues\)](#) / [Atmospheric Disturbances: Detecting, Modelling and Influences on Natural Phenomena and...](#)



atmosphere

[\(/journal/atmosphere\)](#)



[Submit to Atmosphere \(https://susy.mdpi.com/user/manuscripts/upload?form\[journal_id\]=35\)](https://susy.mdpi.com/user/manuscripts/upload?form[journal_id]=35)

[Submit to Atmosphere \(https://susy.mdpi.com/user/manuscripts/upload?form\[journal_id\]=35\)](https://susy.mdpi.com/user/manuscripts/upload?form[journal_id]=35)

[https://susy.mdpi.com/user/manuscripts/upload?form\[journal_id\]=35](https://susy.mdpi.com/user/manuscripts/upload?form[journal_id]=35)

[Review for Atmosphere \(https://susy.mdpi.com/user/manuscripts/upload?form\[journal_id\]=35\)](https://susy.mdpi.com/user/manuscripts/upload?form[journal_id]=35)

[Propose a Special Issue \(/journalproposals/sendproposal?journal=atmosphere\)](#)

[Review for Atmosphere \(/volunteer/journals\)](#)

Journal Menu

[/volunteer/journals](#)

[Journal Menu](#)

[Journal Menu](#)

[Journal Menu](#)

[Journal Menu](#)

[Journal Menu](#)

[Journal Menu](#)

[Journal Menu](#)

[Journal Menu](#)

[Journal Menu](#)

[Journal Menu](#)

[Journal Menu](#)

[Journal Menu](#)

[Journal Menu](#)

[Journal Menu](#)

[Journal Menu](#)

[Journal Menu](#)

[Journal Menu](#)

[Journal Menu](#)

[Journal Menu](#)

[Journal Menu](#)

[Journal Menu](#)

[Journal Menu](#)

[Journal Menu](#)

[Journal Menu](#)

[Journal Menu](#)

[Journal Menu](#)

[Journal Menu](#)

[Journal Menu](#)

[Journal Menu](#)

[Journal Menu](#)

[Journal Menu](#)

[Journal Menu](#)

[Journal Menu](#)

[Journal Menu](#)

[Journal Menu](#)

[Journal Menu](#)

[Journal Menu](#)

[Journal Menu](#)

[Journal Menu](#)

[Journal Menu](#)

[Journal Menu](#)

[Journal Menu](#)

[Journal Menu](#)

[Journal Menu](#)

[Journal Menu](#)

[Journal Menu](#)

[Journal Menu](#)

[Journal Menu](#)

[Journal Menu](#)

[Journal Menu](#)

[Journal Menu](#)

[Journal Menu](#)

[Journal Menu](#)

[Journal Menu](#)

[Journal Menu](#)

[Journal Menu](#)

[Journal Menu](#)

[Journal Menu](#)

[Journal Menu](#)

[Journal Menu](#)

[Journal Menu](#)

[Journal Menu](#)

[Journal Menu](#)

Journal Browser

[Journal Browser](#)

[> Forthcoming issue \(/2073-4433/15/12\)](#)

[> Current issue \(/2073-4433/15/11\)](#)

[Vol. 15 \(2024\) \(/2073-4433/15\)](#)

[Vol. 14 \(2023\) \(/2073-4433/14\)](#)

[Vol. 13 \(2022\) \(/2073-4433/13\)](#)

[Vol. 12 \(2021\) \(/2073-4433/12\)](#)

[Vol. 11 \(2020\) \(/2073-4433/11\)](#)

[Vol. 10 \(2019\) \(/2073-4433/10\)](#)

[Vol. 9 \(2018\) \(/2073-4433/9\)](#)

[Vol. 8 \(2017\) \(/2073-4433/8\)](#)

[Vol. 7 \(2016\) \(/2073-4433/7\)](#)

[Vol. 6 \(2015\) \(/2073-4433/6\)](#)

[Vol. 5 \(2014\) \(/2073-4433/5\)](#)

[Vol. 4 \(2013\) \(/2073-4433/4\)](#)

[Vol. 3 \(2012\) \(/2073-4433/3\)](#)



Changes in atmospheric parameters due to extra-terrestrial and terrestrial phenomena affect the propagation of electromagnetic signals in the atmosphere. The analysis of these changes and the study of their relationships with the aforementioned phenomena is becoming increasingly interesting for Earth scientists. The multidisciplinary character of these studies and the need for different kinds of data, both in situ measurements and Earth observation datasets acquired by satellite and ground-based infrastructures, require the collaboration of researchers working in different scientific fields and the collection and processing heterogeneous datasets.

This Special Issue will present new advances in techniques to detect atmospheric disturbances, models, investigations of their relationship with natural phenomena (e.g., earthquakes, hurricanes, etc.) and mitigation of their impact on the propagation of telecommunication, GNSS and EO signals.

We encourage submissions of new researches related, but not limited, to the following topics:

- Techniques for detection of atmospheric disturbance;
- Modelling of atmospheric disturbances;
- Relationship between natural phenomena (e.g., earthquakes, hurricanes, etc.) and atmospheric disturbances;
- Databases and Earth observation datasets useful for studies on atmospheric disturbances;
- Impacts of atmospheric disturbances on telecommunication, GNSS and Earth observation signal propagation.

Dr. Aleksandra Nina

Dr. Vladimir Srećković
Guest Editors

Manuscript Submission Information

Manuscripts should be submitted online at www.mdpi.com (<https://www.mdpi.com/>) by [registering](https://www.mdpi.com/user/register/) (<https://www.mdpi.com/user/register/>) and [logging in to this website](https://www.mdpi.com/user/login/) (<https://www.mdpi.com/user/login/>). Once you are registered, [click here to go to the submission form](https://susy.mdpi.com/user/manuscripts/upload/?journal=atmosphere) (<https://susy.mdpi.com/user/manuscripts/upload/?journal=atmosphere>). Manuscripts can be submitted until the deadline. All submissions that pass pre-check are peer-reviewed. Accepted papers will be published continuously in the journal (as soon as accepted) and will be listed together on the special issue website. Research articles, review articles as well as short communications are invited. For planned papers, a title and short abstract (about 100 words) can be sent to the Editorial Office for announcement on this website.

Submitted manuscripts should not have been published previously, nor be under consideration for publication elsewhere (except conference proceedings papers). All manuscripts are thoroughly refereed through a single-blind peer-review process. A guide for authors and other relevant information for submission of manuscripts is available on the [Instructions for Authors](https://www.mdpi.com/journal/atmosphere/instructions) (<https://www.mdpi.com/journal/atmosphere/instructions>) page. *Atmosphere* (<https://www.mdpi.com/journal/atmosphere/>) is an international peer-reviewed open access monthly journal published by MDPI.

Please visit the [Instructions for Authors](https://www.mdpi.com/journal/atmosphere/instructions) (<https://www.mdpi.com/journal/atmosphere/instructions>) page before submitting a manuscript. The **Article Processing Charge (APC)** (<https://www.mdpi.com/about/apc/>) for publication in this [open access](https://www.mdpi.com/about/openaccess/) (<https://www.mdpi.com/about/openaccess/>) journal is 2400 CHF (Swiss Francs). Submitted papers should be well formatted and use good English. Authors may use MDPI's [English editing service](https://www.mdpi.com/authors/english) (<https://www.mdpi.com/authors/english>) prior to publication or during author revisions.

Keywords

- atmospheric disturbances
- earth observations
- modelling
- data processing
- SAR
- GNSS
- space weather
- natural hazards

Benefits of Publishing in a Special Issue

- Ease of navigation: Grouping papers by topic helps scholars navigate broad scope journals more efficiently.
- Greater discoverability: Special Issues support the reach and impact of scientific research. Articles in Special Issues are more discoverable and cited more frequently.
- Expansion of research network: Special Issues facilitate connections among authors, fostering scientific collaborations.
- External promotion: Articles in Special Issues are often promoted through the journal's social media, increasing their visibility.
- e-Book format: Special Issues with more than 10 articles can be published as dedicated e-books, ensuring wide and rapid dissemination.

Further information on MDPI's Special Issue policies can be found [here](https://www.mdpi.com/special_issues_guidelines) (https://www.mdpi.com/special_issues_guidelines).

Published Papers (7 papers)

[Download All Papers](#)

Order results

Result details

[Show export options](#) ▾

Research

Jump to: [Review](#)

Open Access Article

34 pages, 10822 KiB [\(2073-4433/12/10/1276/pdf?version=1634174229\)](#)

[Back to TopTop](#)



MDPI (0)

Different Methods to Determine Starting Altitudes for Dry Air Atmosphere by GNSS-RO Data (*I2073-4433/12/10/1276*)
 by **Andrea Andrisani** and **Francesco Vespe**
Atmosphere **2021**, *12*(10), 1276; <https://doi.org/10.3390/atmos12101276> (<https://doi.org/10.3390/atmos12101276>) - 30 Sep 2021
 Submitted to *Atmosphere* on 12 October 2020
 (https://susy.mdpi.com/user/manuscripts/upload?formid=35) Q ☰

Abstract Boundary profile evaluation (BPV) is an approach proposed in order to estimate water vapor content in the atmosphere. It exploits radio occultation (RO) observations of the signals emitted by the satellites of global navigation systems (GNSS) which are eclipsing (rising) as viewed by [...] [Read more](#).
 (This article belongs to the Special Issue **Atmospheric Disturbances: Detecting, Modelling and Influences on Natural Phenomena and Propagation of Telecommunication, GNSS and EO Signal Propagation** (*/journal/atmosphere/special_issues/Atmospheric_Disturbances*))

[Review for Atmosphere](#)
 (https://susy.mdpi.com/volunteer/journals/review)

[Propose a Special Issue](#)
 (/journalproposals/sendproposals/atmosphere)

[Show Figures](#)
 (https://pub.mdpi-res.com/atmosphere/atmosphere-12-01276/article_deploy/html/images/atmosphere-12-01276-g001-550.jpg?1634174346) (https://pub.mdpi-res.com/atmosphere/atmosphere-12-01276/article_deploy/html/images/atmosphere-12-01276-g002-550.jpg?1634174346) (https://pub.mdpi-res.com/atmosphere/atmosphere-12-01276/article_deploy/html/images/atmosphere-12-01276-g003-550.jpg?1634174346) (https://pub.mdpi-res.com/atmosphere/atmosphere-12-01276/article_deploy/html/images/atmosphere-12-01276-g004-550.jpg?1634174346) (https://pub.mdpi-res.com/atmosphere/atmosphere-12-01276/article_deploy/html/images/atmosphere-12-01276-g005-550.jpg?1634174346) (https://pub.mdpi-res.com/atmosphere/atmosphere-12-01276/article_deploy/html/images/atmosphere-12-01276-g006-550.jpg?1634174346) (https://pub.mdpi-res.com/atmosphere/atmosphere-12-01276/article_deploy/html/images/atmosphere-12-01276-g007-550.jpg?1634174346) (https://pub.mdpi-res.com/atmosphere/atmosphere-12-01276/article_deploy/html/images/atmosphere-12-01276-g008-550.jpg?1634174346) (https://pub.mdpi-res.com/atmosphere/atmosphere-12-01276/article_deploy/html/images/atmosphere-12-01276-g009-550.jpg?1634174346) (https://pub.mdpi-res.com/atmosphere/atmosphere-12-01276/article_deploy/html/images/atmosphere-12-01276-g010-550.jpg?1634174346) (https://pub.mdpi-res.com/atmosphere/atmosphere-12-01276/article_deploy/html/images/atmosphere-12-01276-g011-550.jpg?1634174346) (https://pub.mdpi-res.com/atmosphere/atmosphere-12-01276/article_deploy/html/images/atmosphere-12-01276-g012-550.jpg?1634174346) (https://pub.mdpi-res.com/atmosphere/atmosphere-12-01276/article_deploy/html/images/atmosphere-12-01276-g013-550.jpg?1634174346) (https://pub.mdpi-res.com/atmosphere/atmosphere-12-01276/article_deploy/html/images/atmosphere-12-01276-g014-550.jpg?1634174346) (https://pub.mdpi-res.com/atmosphere/atmosphere-12-01276/article_deploy/html/images/atmosphere-12-01276-g015a-550.jpg?1634174346) (https://pub.mdpi-res.com/atmosphere/atmosphere-12-01276/article_deploy/html/images/atmosphere-12-01276-g015b-550.jpg?1634174346) (https://pub.mdpi-res.com/atmosphere/atmosphere-12-01276/article_deploy/html/images/atmosphere-12-01276-g016-550.jpg?1634174346) (https://pub.mdpi-res.com/atmosphere/atmosphere-12-01276/article_deploy/html/images/atmosphere-12-01276-g017-550.jpg?1634174346) (https://pub.mdpi-res.com/atmosphere/atmosphere-12-01276/article_deploy/html/images/atmosphere-12-01276-g018-550.jpg?1634174346)

Open Access Article 15 pages, 1032 KiB [\(I2073-4433/12/6/765/pdf?version=1623579934\)](#)

Numerical Modeling of Coseismic Tropospheric Disturbances Arising from the Unstable Acoustic Gravity Wave Energetics (*I2073-4433/12/6/765*)
 by **Esfhan A. Kherani**, **Saul A. Sanchez** and **Eurico R. de Paula**
Atmosphere **2021**, *12*(6), 765; <https://doi.org/10.3390/atmos12060765> (<https://doi.org/10.3390/atmos12060765>) - 13 Jun 2021
 Cited by **3** (*I2073-4433/12/6/765#metrics*) | Viewed by 2420

Abstract Numerous recent studies report the Coseismic Tropospheric Disturbances (CTDs) during large earthquakes. Their presence suggests the importance of atmospheric seismology in a possible earthquake forecasting scenario. The origin mechanism and associated energetics of CTDs are not well understood though the observations associate them [...] [Read more](#).
 (This article belongs to the Special Issue **Atmospheric Disturbances: Detecting, Modelling and Influences on Natural Phenomena and Propagation of Telecommunication, GNSS and EO Signal Propagation** (*/journal/atmosphere/special_issues/Atmospheric_Disturbances*))

[Show Figures](#)
 (https://pub.mdpi-res.com/atmosphere/atmosphere-12-00765/article_deploy/html/images/atmosphere-12-00765-g001-550.jpg?1623580034) (https://pub.mdpi-res.com/atmosphere/atmosphere-12-00765/article_deploy/html/images/atmosphere-12-00765-g002-550.jpg?1623580034) (https://pub.mdpi-res.com/atmosphere/atmosphere-12-00765/article_deploy/html/images/atmosphere-12-00765-g003-550.jpg?1623580034) (https://pub.mdpi-res.com/atmosphere/atmosphere-12-00765/article_deploy/html/images/atmosphere-12-00765-g004-550.jpg?1623580034) (https://pub.mdpi-res.com/atmosphere/atmosphere-12-00765/article_deploy/html/images/atmosphere-12-00765-g005-550.jpg?1623580034) (https://pub.mdpi-res.com/atmosphere/atmosphere-12-00765/article_deploy/html/images/atmosphere-12-00765-g006-550.jpg?1623580034) (https://pub.mdpi-res.com/atmosphere/atmosphere-12-00765/article_deploy/html/images/atmosphere-12-00765-g007-550.jpg?1623580034) (https://pub.mdpi-res.com/atmosphere/atmosphere-12-00765/article_deploy/html/images/atmosphere-12-00765-g008-550.jpg?1623580034) (https://pub.mdpi-res.com/atmosphere/atmosphere-12-00765/article_deploy/html/images/atmosphere-12-00765-g009-550.jpg?1623580034)

Open Access Article 13 pages, 1973 KiB [\(I2073-4433/12/4/444/pdf?version=1618189990\)](#)

Reduction of the VLF Signal Phase Noise Before Earthquakes (*I2073-4433/12/4/444*)
 by **Aleksandra Nina**, **Pier Francesco Biagi**, **Srdan T. Mitrović**, **Sergey Pulinet**, **Giovanni Nico**, **Milan Radovanović** and **Luka Č. Popović**
Atmosphere **2021**, *12*(4), 444; <https://doi.org/10.3390/atmos12040444> (<https://doi.org/10.3390/atmos12040444>) - 31 Mar 2021
 Cited by **8** (*I2073-4433/12/4/444#metrics*) | Viewed by 2270

Abstract In this paper we analyse temporal variations of the phase of a very low frequency (VLF) signal, used for the lower ionosphere monitoring, in periods around four earthquakes (EQs) with magnitude greater than 4. We provide two analyses in time and frequency domains. [...] [Read more](#).
 (This article belongs to the Special Issue **Atmospheric Disturbances: Detecting, Modelling and Influences on Natural Phenomena and Propagation of Telecommunication, GNSS and EO Signal Propagation** (*/journal/atmosphere/special_issues/Atmospheric_Disturbances*))

[Show Figures](#)
 (https://pub.mdpi-res.com/atmosphere/atmosphere-12-00444/article_deploy/html/images/atmosphere-12-00444-g001-550.jpg?1628011469) (https://pub.mdpi-res.com/atmosphere/atmosphere-12-00444/article_deploy/html/images/atmosphere-12-00444-g002-550.jpg?1628011469) (https://pub.mdpi-res.com/atmosphere/atmosphere-12-00444/article_deploy/html/images/atmosphere-12-00444-g003-550.jpg?1628011469) (https://pub.mdpi-res.com/atmosphere/atmosphere-12-00444/article_deploy/html/images/atmosphere-12-00444-g004-550.jpg?1628011469) (https://pub.mdpi-res.com/atmosphere/atmosphere-12-00444/article_deploy/html/images/atmosphere-12-00444-g005-550.jpg?1628011469) (https://pub.mdpi-res.com/atmosphere/atmosphere-12-00444/article_deploy/html/images/atmosphere-12-00444-g006-550.jpg?1628011469) (https://pub.mdpi-res.com/atmosphere/atmosphere-12-00444/article_deploy/html/images/atmosphere-12-00444-g007-550.jpg?1628011469) (https://pub.mdpi-res.com/atmosphere/atmosphere-12-00444-g008-550.jpg?1628011469)

Open Access Article 17 pages, 5658 KiB [\(I2073-4433/11/12/1298/pdf?version=1606918668\)](#)

The Effect of Boreal Summer Intraseasonal Oscillation on Evaporation Duct and Electromagnetic Propagation over the South China Sea (*I2073-4433/11/12/1298*)
 by **Wentao Jia**, **Weimin Zhang**, **Jiahua Zhu** and **Jilin Sun**
Atmosphere **2020**, *11*(12), 1298; <https://doi.org/10.3390/atmos11121298> (<https://doi.org/10.3390/atmos11121298>) - 30 Nov 2020

MDPI (0) [4433/11/12/1298#metrics](#) | Viewed by 2550
Abstract Intraseasonal oscillation of the evaporation duct, lasting 30–60 days, has been identified over the South China Sea (SCS) summer monsoon region based on multiple reanalyses and observational data. The boreal summer intraseasonal oscillation (BSISO) causes anomalies at the air–sea boundary and thus plays [...] [Read more.](#)
(This article belongs to the Special Issue **Atmospheric Disturbances: Detecting, Modelling and Influences on Natural Phenomena and Propagation of Telecommunication, GNSS and EO Signal Propagation.** (/journal/atmosphere/special_issues/Atmospheric_Disturbances))

[Show Figures](#)
(https://pub.mdpi-res.com/atmosphere/atmosphere-11-01298/article_deploy/html/images/atmosphere-11-01298-g001-550.jpg?1607102768) (https://pub.mdpi-res.com/atmosphere/atmosphere-11-01298/article_deploy/html/images/atmosphere-11-01298-g002a-550.jpg?1607102768) (https://pub.mdpi-res.com/atmosphere/atmosphere-11-01298/article_deploy/html/images/atmosphere-11-01298-g002b-550.jpg?1607102768) (https://pub.mdpi-res.com/atmosphere/atmosphere-11-01298/article_deploy/html/images/atmosphere-11-01298-g003-550.jpg?1607102768) (https://pub.mdpi-res.com/atmosphere/atmosphere-11-01298/article_deploy/html/images/atmosphere-11-01298-g004-550.jpg?1607102768) (https://pub.mdpi-res.com/atmosphere/atmosphere-11-01298/article_deploy/html/images/atmosphere-11-01298-g005-550.jpg?1607102768)

Propose a Special Issue
(https://pub.mdpi-res.com/atmosphere/atmosphere-11-01298/article_deploy/html/images/atmosphere-11-01298-g006-550.jpg?1607102768) (https://pub.mdpi-res.com/atmosphere/atmosphere-11-01298/article_deploy/html/images/atmosphere-11-01298-g007-550.jpg?1607102768) (https://pub.mdpi-res.com/atmosphere/atmosphere-11-01298/article_deploy/html/images/atmosphere-11-01298-g008-550.jpg?1607102768) (https://pub.mdpi-res.com/atmosphere/atmosphere-11-01298/article_deploy/html/images/atmosphere-11-01298-g009-550.jpg?1607102768) (https://pub.mdpi-res.com/atmosphere/atmosphere-11-01298/article_deploy/html/images/atmosphere-11-01298-g010-550.jpg?1607102768) (https://pub.mdpi-res.com/atmosphere/atmosphere-11-01298/article_deploy/html/images/atmosphere-11-01298-g011-550.jpg?1607102768) (https://pub.mdpi-res.com/atmosphere/atmosphere-11-01298/article_deploy/html/images/atmosphere-11-01298-g012-550.jpg?1607102768)

Open Access Article 12 pages, 4468 KIB (</2073-4433/11/9/897/pdf?version=1598347833>)

Statistical Approach to Observe the Atmospheric Density Variations Using Swarm Satellite Data (</2073-4433/11/9/897>)

by Md Wahiduzzaman, Alea Yeasmin, Jing-Jia Luo, Md. Arfan Ali, Muhammad Bilal and Zhongfeng Qiu
Atmosphere 2020, 11(9), 897; <https://doi.org/10.3390/atmos11090897> (<https://doi.org/10.3390/atmos11090897>) - 24 Aug 2020
Cited by 5 (</2073-4433/11/9/897#metrics>) | Viewed by 4894

Abstract Over time, the initial algorithms to derive atmospheric density from accelerometers have been significantly enhanced. In this study, we discussed one of the accurate accelerometers—the Earth’s Magnetic Field and Environment Explorers, more commonly known as the Swarm satellites. Swarm satellite–C level 2 (measurements [...] [Read more.](#)

(This article belongs to the Special Issue **Atmospheric Disturbances: Detecting, Modelling and Influences on Natural Phenomena and Propagation of Telecommunication, GNSS and EO Signal Propagation.** (/journal/atmosphere/special_issues/Atmospheric_Disturbances))

[Show Figures](#)
(https://pub.mdpi-res.com/atmosphere/atmosphere-11-00897/article_deploy/html/images/atmosphere-11-00897-g001-550.jpg?1598347906) (https://pub.mdpi-res.com/atmosphere/atmosphere-11-00897/article_deploy/html/images/atmosphere-11-00897-g002-550.jpg?1598347906) (https://pub.mdpi-res.com/atmosphere/atmosphere-11-00897/article_deploy/html/images/atmosphere-11-00897-g003-550.jpg?1598347906) (https://pub.mdpi-res.com/atmosphere/atmosphere-11-00897/article_deploy/html/images/atmosphere-11-00897-g004-550.jpg?1598347906) (https://pub.mdpi-res.com/atmosphere/atmosphere-11-00897/article_deploy/html/images/atmosphere-11-00897-g005-550.jpg?1598347906) (https://pub.mdpi-res.com/atmosphere/atmosphere-11-00897/article_deploy/html/images/atmosphere-11-00897-g006-550.jpg?1598347906) (https://pub.mdpi-res.com/atmosphere/atmosphere-11-00897/article_deploy/html/images/atmosphere-11-00897-g007-550.jpg?1598347906) (https://pub.mdpi-res.com/atmosphere/atmosphere-11-00897/article_deploy/html/images/atmosphere-11-00897-g008-550.jpg?1598347907) (https://pub.mdpi-res.com/atmosphere/atmosphere-11-00897/article_deploy/html/images/atmosphere-11-00897-g009-550.jpg?1598347907)

Review

Jump to: [Research](#)

Open Access Review 21 pages, 3790 KIB (</2073-4433/12/11/1424/pdf?version=1637229437>)

Sound Propagation Modelling for Manned and Unmanned Aircraft Noise Assessment and Mitigation: A Review (</2073-4433/12/11/1424>)

by Rohan Kapoor, Nicola Kloet, Alessandro Gardi, Abdulghani Mohamed and Roberto Sabatini
Atmosphere 2021, 12(11), 1424; <https://doi.org/10.3390/atmos12111424> (<https://doi.org/10.3390/atmos12111424>) - 28 Oct 2021
Cited by 12 (</2073-4433/12/11/1424#metrics>) | Viewed by 5091

Abstract This paper addresses one of the recognized barriers to the unrestricted adoption of Unmanned Aircraft (UA) in mainstream urban use—noise—and reviews existing approaches for estimating and mitigating this problem. The aircraft noise problem is discussed upfront in general terms by introducing the sound [...] [Read more.](#)

(This article belongs to the Special Issue **Atmospheric Disturbances: Detecting, Modelling and Influences on Natural Phenomena and Propagation of Telecommunication, GNSS and EO Signal Propagation.** (/journal/atmosphere/special_issues/Atmospheric_Disturbances))

[Show Figures](#)
(https://pub.mdpi-res.com/atmosphere/atmosphere-12-01424/article_deploy/html/images/atmosphere-12-01424-g001-550.jpg?1637229608) (https://pub.mdpi-res.com/atmosphere/atmosphere-12-01424/article_deploy/html/images/atmosphere-12-01424-g002-550.jpg?1637229608) (https://pub.mdpi-res.com/atmosphere/atmosphere-12-01424/article_deploy/html/images/atmosphere-12-01424-g003-550.jpg?1637229608) (https://pub.mdpi-res.com/atmosphere/atmosphere-12-01424/article_deploy/html/images/atmosphere-12-01424-g004-550.jpg?1637229608) (<https://pub.mdpi-res.com/atmosphere/atmosphere-12-01424-g005-550.jpg?1637229608>) (<https://pub.mdpi-res.com/atmosphere/atmosphere-12-01424-g006-550.jpg?1637229608>) (<https://pub.mdpi-res.com/atmosphere/atmosphere-12-01424-g007-550.jpg?1637229608>) (<https://pub.mdpi-res.com/atmosphere/atmosphere-12-01424-g008-550.jpg?1637229608>) (<https://pub.mdpi-res.com/atmosphere/atmosphere-12-01424-g009-550.jpg?1637229608>) (<https://pub.mdpi-res.com/atmosphere/atmosphere-12-01424-g010-550.jpg?1637229608>) (<https://pub.mdpi-res.com/atmosphere/atmosphere-12-01424-g011-550.jpg?1637229608>)

Open Access Review 47 pages, 7666 KIB (</2073-4433/12/7/918/pdf?version=1627040907>)

Laser Beam Atmospheric Propagation Modelling for Aerospace LIDAR Applications (</2073-4433/12/7/918>)

by Thomas Fahey, Maidul Islam, Alessandro Gardi and Roberto Sabatini
Atmosphere 2021, 12(7), 918; <https://doi.org/10.3390/atmos12070918> (<https://doi.org/10.3390/atmos12070918>) - 17 Jul 2021
Cited by 41 (</2073-4433/12/7/918#metrics>) | Viewed by 19060

...eric effects have a significant impact on the performance of airborne and space laser systems. Traditional models used to predict propagation effects rely heavily on simplified assumptions of the atmospheric properties and their interactions with laser systems. In the engineering domain, these models [...] [Read more.](#)

Submit to [Atmosphere](#) (journal) | This article belongs to the Special Issue [Atmospheric Disturbances: Detecting, Modelling and Influences on Natural Phenomena and Propagation of Telecommunication, GNSS and EO Signal Propagation](#) ([/journal/atmosphere/special_issues/Atmospheric_Disturbances](#))

- [Show Figures](#) ([journal_id=55](#)) (https://pub.mdpi-res.com/atmosphere/atmosphere-12-00918/article_deploy/html/images/atmosphere-12-00918-g001-550.jpg?1627041025) (https://pub.mdpi-res.com/atmosphere/atmosphere-12-00918/article_deploy/html/images/atmosphere-12-00918-g002-550.jpg?1627041025) (https://pub.mdpi-res.com/atmosphere/atmosphere-12-00918/article_deploy/html/images/atmosphere-12-00918-g003-550.jpg?1627041025) (https://pub.mdpi-res.com/atmosphere/atmosphere-12-00918/article_deploy/html/images/atmosphere-12-00918-g004-550.jpg?1627041025) (https://pub.mdpi-res.com/atmosphere/atmosphere-12-00918/article_deploy/html/images/atmosphere-12-00918-g005-550.jpg?1627041025) (https://pub.mdpi-res.com/atmosphere/atmosphere-12-00918/article_deploy/html/images/atmosphere-12-00918-g006-550.jpg?1627041025) (https://pub.mdpi-res.com/atmosphere/atmosphere-12-00918/article_deploy/html/images/atmosphere-12-00918-g007-550.jpg?1627041025) (https://pub.mdpi-res.com/atmosphere/atmosphere-12-00918/article_deploy/html/images/atmosphere-12-00918-g008-550.jpg?1627041025) (https://pub.mdpi-res.com/atmosphere/atmosphere-12-00918/article_deploy/html/images/atmosphere-12-00918-g009-550.jpg?1627041025) (https://pub.mdpi-res.com/atmosphere/atmosphere-12-00918/article_deploy/html/images/atmosphere-12-00918-g010-550.jpg?1627041025) (https://pub.mdpi-res.com/atmosphere/atmosphere-12-00918/article_deploy/html/images/atmosphere-12-00918-g011-550.jpg?1627041025) (https://pub.mdpi-res.com/atmosphere/atmosphere-12-00918/article_deploy/html/images/atmosphere-12-00918-g012-550.jpg?1627041025) (https://pub.mdpi-res.com/atmosphere/atmosphere-12-00918/article_deploy/html/images/atmosphere-12-00918-g013-550.jpg?1627041025) ([https://pub.mdpi-res.com/atmosphere/atmosphere-12-00918-g014-550.jpg?1627041025](https://pub.mdpi-res.com/atmosphere/atmosphere-12-00918/article_deploy/html/images/atmosphere-12-00918-g014-550.jpg?1627041025)) ([https://pub.mdpi-res.com/atmosphere/atmosphere-12-00918-g015-550.jpg?1627041025](https://pub.mdpi-res.com/atmosphere/atmosphere-12-00918/article_deploy/html/images/atmosphere-12-00918-g015-550.jpg?1627041025)) ([https://pub.mdpi-res.com/atmosphere/atmosphere-12-00918-g016-550.jpg?1627041025](https://pub.mdpi-res.com/atmosphere/atmosphere-12-00918/article_deploy/html/images/atmosphere-12-00918-g016-550.jpg?1627041025)) ([https://pub.mdpi-res.com/atmosphere/atmosphere-12-00918-g017-550.jpg?1627041025](https://pub.mdpi-res.com/atmosphere/atmosphere-12-00918/article_deploy/html/images/atmosphere-12-00918-g017-550.jpg?1627041025)) ([https://pub.mdpi-res.com/atmosphere/atmosphere-12-00918-g018-550.jpg?1627041025](https://pub.mdpi-res.com/atmosphere/atmosphere-12-00918/article_deploy/html/images/atmosphere-12-00918-g018-550.jpg?1627041025)) ([https://pub.mdpi-res.com/atmosphere/atmosphere-12-00918-g019-550.jpg?1627041025](https://pub.mdpi-res.com/atmosphere/atmosphere-12-00918/article_deploy/html/images/atmosphere-12-00918-g019-550.jpg?1627041025)) (https://pub.mdpi-res.com/atmosphere/atmosphere-12-00918/article_deploy/html/images/atmosphere-12-00918-g020-550.jpg?1627041025) ([https://pub.mdpi-res.com/atmosphere/atmosphere-12-00918-g021-550.jpg?1627041025](https://pub.mdpi-res.com/atmosphere/atmosphere-12-00918/article_deploy/html/images/atmosphere-12-00918-g021-550.jpg?1627041025)) ([https://pub.mdpi-res.com/atmosphere/atmosphere-12-00918-g022-550.jpg?1627041025](https://pub.mdpi-res.com/atmosphere/atmosphere-12-00918/article_deploy/html/images/atmosphere-12-00918-g022-550.jpg?1627041025)) ([https://pub.mdpi-res.com/atmosphere/atmosphere-12-00918-g023-550.jpg?1627041025](https://pub.mdpi-res.com/atmosphere/atmosphere-12-00918/article_deploy/html/images/atmosphere-12-00918-g023-550.jpg?1627041025)) ([https://pub.mdpi-res.com/atmosphere/atmosphere-12-00918-g024-550.jpg?1627041025](https://pub.mdpi-res.com/atmosphere/atmosphere-12-00918/article_deploy/html/images/atmosphere-12-00918-g024-550.jpg?1627041025)) ([https://pub.mdpi-res.com/atmosphere/atmosphere-12-00918-g025-550.jpg?1627041025](https://pub.mdpi-res.com/atmosphere/atmosphere-12-00918/article_deploy/html/images/atmosphere-12-00918-g025-550.jpg?1627041025)) ([https://pub.mdpi-res.com/atmosphere/atmosphere-12-00918-g026-550.jpg?1627041025](https://pub.mdpi-res.com/atmosphere/atmosphere-12-00918/article_deploy/html/images/atmosphere-12-00918-g026-550.jpg?1627041025)) ([https://pub.mdpi-res.com/atmosphere/atmosphere-12-00918-g027-550.jpg?1627041025](https://pub.mdpi-res.com/atmosphere/atmosphere-12-00918/article_deploy/html/images/atmosphere-12-00918-g027-550.jpg?1627041025)) ([https://pub.mdpi-res.com/atmosphere/atmosphere-12-00918-g028-550.jpg?1627041025](https://pub.mdpi-res.com/atmosphere/atmosphere-12-00918/article_deploy/html/images/atmosphere-12-00918-g028-550.jpg?1627041025))

[Show export options](#) ▾

Displaying articles 1-7

Atmosphere ([/journal/atmosphere](#)), EISSN 2073-4433, Published by MDPI

[RSS \(/rss/journal/atmosphere\)](#) [Content Alert \(/journal/atmosphere/toc-alert\)](#)

Further Information

- [Article Processing Charges \(/apc\)](#)
- [Pay an Invoice \(/about/payment\)](#)
- [Open Access Policy \(/openaccess\)](#)
- [Contact MDPI \(/about/contact\)](#)
- [Jobs at MDPI \(https://careers.mdpi.com\)](#)

Guidelines

- [For Authors \(/authors\)](#)
- [For Reviewers \(/reviewers\)](#)
- [For Editors \(/editors\)](#)
- [For Librarians \(/librarians\)](#)
- [For Publishers \(/publishing_services\)](#)
- [For Societies \(/societies\)](#)
- [For Conference Organizers \(/conference_organizers\)](#)
- MDPI Initiatives
- [Sciforum \(https://sciforum.net\)](#)
- [MDPI Books \(https://www.mdpi.com/books\)](#)
- [Preprints.org \(https://www.preprints.org\)](#)
- [Scilit \(https://www.scilit.net\)](#)
- [SciProfiles \(https://sciprofiles.com?utm_source=mdpi.com&utm_medium=bottom_menu&utm_campaign=initiative\)](#)
- [Encyclopedia \(https://encyclopedia.pub\)](#)
- [JAMS \(https://jams.pub\)](#)
- [Proceedings Series \(/about/proceedings\)](#)

Follow MDPI

- [LinkedIn \(https://www.linkedin.com/company/mdpi\)](#)
- [Facebook \(https://www.facebook.com/MDPIOpenAccessPublishing\)](#)
- [Twitter \(https://twitter.com/MDPIOpenAccess\)](#)





Submit to Atmosphere
([https://susy.mdpi.com/user/manuscripts/upload?form\[journal_id\]=25](https://susy.mdpi.com/user/manuscripts/upload?form[journal_id]=25))



Select options

Review for Atmosphere
(<https://susy.mdpi.com/volunteer/journals/review>)

Subscribe

Propose a Special Issue 2024 MDPI (Basel, Switzerland) unless otherwise stated

([journalproposal/sendproposalspecialissue/atmosphere](https://susy.mdpi.com/journalproposal/sendproposalspecialissue/atmosphere))

[Disclaimer](#) [Terms and Conditions \(/about/terms-and-conditions\)](#) [Privacy Policy \(/about/privacy\)](#)





[Journals \(/about/journals\)](#) [Topics \(/topics\)](#) [Information \(/authors\)](#) [Editing Services \(/authors/english\)](#) [Initiatives \(/about/initiatives\)](#) [About \(/about\)](#)

[Sign In / Sign Up \(/user/login\)](#)

[Submit \(https://susy.mdpi.com/user/manuscripts/upload?journal=remotesensing\)](https://susy.mdpi.com/user/manuscripts/upload?journal=remotesensing)

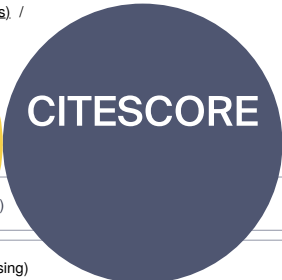
Search for Articles:

Advanced Search

[Journals \(/about/journals\)](#) / [Remote Sensing \(/journal/remotesensing\)](#) / [Special Issues \(/journal/remotesensing/special_issues\)](#) / [Extraterrestrial Influences on Remote Sensing in the Earth's Atmosphere /](#)



[remote sensing \(/journal/remotesensing\)](#)



[Submit to Remote Sensing \(https://susy.mdpi.com/user/manuscripts/upload?journal=remotesensing\)](https://susy.mdpi.com/user/manuscripts/upload?journal=remotesensing)

[Review for Remote Sensing \(https://susy.mdpi.com/user/manuscripts/upload?journal=remotesensing\)](#)

[Propose a Special Issue \(/journalproposals/sendproposal?journal=remotesensing\)](#)

4.2
[\(/journal/remotesensing/stats\)](#)

8.3
<https://www.scopus.com/sourceid/86430>

Journal Menu

Journal Menu

- [Remote Sensing Home \(/journal/remotesensing\)](#)
- [Aims & Scope \(/journal/remotesensing/about\)](#)
- [Editorial Board \(/journal/remotesensing/editors\)](#)
- [Reviewer Board \(/journal/remotesensing/submission_reviewers\)](#)
- [Topical Advisory Panel \(/journal/remotesensing/topical_advisory_panel\)](#)
- [Photography Exhibition \(/journal/remotesensing/exhibition\)](#)
- [Instructions for Authors \(/journal/remotesensing/instructions\)](#)
- [Special Issues \(/journal/remotesensing/special_issues\)](#)
- [Topics \(/topics?journal=remotesensing\)](#)
- [Sections & Collections \(/journal/remotesensing/sections\)](#)
- [Article Processing Charge \(/journal/remotesensing/apc\)](#)
- [Indexing & Archiving \(/journal/remotesensing/indexing\)](#)
- [Editor's Choice Articles \(/journal/remotesensing/editors_choice\)](#)
- [Most Cited & Viewed \(/journal/remotesensing/most_cited\)](#)
- [Journal Statistics \(/journal/remotesensing/stats\)](#)
- [Journal History \(/journal/remotesensing/history\)](#)
- [Journal Awards \(/journal/remotesensing/awards\)](#)
- [Society Collaborations \(/journal/remotesensing/societies\)](#)
- [Conferences \(/journal/remotesensing/events\)](#)
- [Editorial Office \(/journal/remotesensing/editorial_office\)](#)

Journal Browser

Journal Browser

- > [Forthcoming issue \(/2072-4292/16/23\)](#)
- > [Current issue \(/2072-4292/16/22\)](#)

- [Vol. 16 \(2024\) \(/2072-4292/16\)](#)
- [Vol. 15 \(2023\) \(/2072-4292/15\)](#)
- [Vol. 14 \(2022\) \(/2072-4292/14\)](#)
- [Vol. 13 \(2021\) \(/2072-4292/13\)](#)
- [Vol. 12 \(2020\) \(/2072-4292/12\)](#)
- [Vol. 11 \(2019\) \(/2072-4292/11\)](#)
- [Vol. 10 \(2018\) \(/2072-4292/10\)](#)
- [Vol. 9 \(2017\) \(/2072-4292/9\)](#)
- [Vol. 8 \(2016\) \(/2072-4292/8\)](#)
- [Vol. 7 \(2015\) \(/2072-4292/7\)](#)
- [Vol. 6 \(2014\) \(/2072-4292/6\)](#)
- [Vol. 5 \(2013\) \(/2072-4292/5\)](#)
- [Vol. 4 \(2012\) \(/2072-4292/4\)](#)
- [Vol. 3 \(2011\) \(/2072-4292/3\)](#)

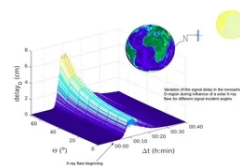


Extraterrestrial Influences on Remote Sensing in the Earth's Atmosphere

- [Print Special Issue Flyer \(/journal/remotesensing/special_issue_flyer_pdf_v2/Extraterrestrial_Atmo\)](#)
- [Special Issue Editors](#)
- [Special Issue Information](#)
- [Keywords](#)
- [Benefits of Publishing in a Special Issue](#)
- [Published Papers](#)

A special issue of [Remote Sensing \(/journal/remotesensing\)](#) (ISSN 2072-4292). This special issue belongs to the section "[Atmospheric Remote Sensing \(/journal/remotesensing/sections/Atmosphere_Remote_Sensing\)](#)".


Deadline for manuscript submissions: **closed (31 March 2022)** | Viewed by 12418




Share This Special Issue

[\(mailto:?&subject=From%20MDPI%3A%20%22Extraterrestrial%20Influences%20on%20Remote%20Sensing%20in%20the%20Earth%E2%80%99s%20Atmosphere%22&body=Special%20Issue%20Title%3A%20Extraterrestrial%20Influences%20on%20Remote%20Sensing%20in%20the%20Earth%E2%80%99s%20Atmosphere%0A%0AWebsite%3A%20https%3A%2F%2Fwww.mdpi.com%2Fsi%2F67190%0A%0AGuest%20Editors%3A%0A%0AName%3A%20Dr.%20Aleksandra%20Nina%0AAffiliation%3A%20Institute%20of%20Physics%20Belgrade%2C%20University%20of%20Belgrade%2C%20Pregrevice%20118%2C%2011080%20Belgrade%2C%20Serbia%0A%0AName%3A%20Prof.%20Dr.%20Milan%20Radovanovi%C4%87%0AAffiliation%3A%20Geographical%20Institute%20E2%80%9CJovan%20Cvijic%E2%80%9D%20Serbian%20Academy%20of%20Sciences%20and%20Arts%2C%20Djure%20Jak%C5%A1i%C4%87a%209%2C%2011000%20Belgrade%2C%20Serbia%0A%0AName%3A%20Prof.%20Dr.%20Luka%20%C4%8C.%20Popovi%C4%87%0AAffiliation%3A%201.%20Astronomical%20Observatory%2C%20in%20Belgrade%2C%20Bolgina%207%2C%202011160%20Belgrade%2C%20Serbia%0D%0A2.%20Faculty%20of%20Mathematics%20University%20of%20Belgrade%2C%20Studentski%20Trg%202016%2C%20Belgrade%2C%20Serbia%0A%0A\) \(<https://twitter.com/intent/tweet?text=Extraterrestrial+Influences+on+Remote+Sensing+in+the+Earth%E2%80%99s+Atmosphere&hashtags=mdpiremotesensing&url=https%3A%2F%2Fwww.mdpi.com%2Fsi%2F67190&via=RemoteSens+MDPI>\) \(<http://www.linkedin.com/shareArticle?mini=true&url=https%3A%2F%2Fwww.mdpi.com%2Fsi%2F67190&title=Extraterrestrial%20Influences%20on%20Remote%20Sensing%20in%20the%20Earth%E2%80%99s%20Atmosphere%26source%3Dhttps%3A%2F%2Fwww.mdpi.com%26summary%3DDear%20Colleagues%2C%0D%0APropagation%20of%20the%20electromagnetic%20signals%20used%20for%20different%20kinds%20of%20remote%20sensing%20depends%20on%20the%20atmosphere%2C%20such%20as%20the%20electron%20density%20and%20temperature.%20Spatial%20and%20temporal%20variations%20of%20these%20%5B...%5D>\) \(<https://www.facebook.com/sharer.php?u=https://www.mdpi.com/si/67190>\)](mailto:?&subject=From%20MDPI%3A%20%22Extraterrestrial%20Influences%20on%20Remote%20Sensing%20in%20the%20Earth%E2%80%99s%20Atmosphere%22&body=Special%20Issue%20Title%3A%20Extraterrestrial%20Influences%20on%20Remote%20Sensing%20in%20the%20Earth%E2%80%99s%20Atmosphere%0A%0AWebsite%3A%20https%3A%2F%2Fwww.mdpi.com%2Fsi%2F67190%0A%0AGuest%20Editors%3A%0A%0AName%3A%20Dr.%20Aleksandra%20Nina%0AAffiliation%3A%20Institute%20of%20Physics%20Belgrade%2C%20University%20of%20Belgrade%2C%20Pregrevice%20118%2C%2011080%20Belgrade%2C%20Serbia%0A%0AName%3A%20Prof.%20Dr.%20Milan%20Radovanovi%C4%87%0AAffiliation%3A%20Geographical%20Institute%20E2%80%9CJovan%20Cvijic%E2%80%9D%20Serbian%20Academy%20of%20Sciences%20and%20Arts%2C%20Djure%20Jak%C5%A1i%C4%87a%209%2C%2011000%20Belgrade%2C%20Serbia%0A%0AName%3A%20Prof.%20Dr.%20Luka%20%C4%8C.%20Popovi%C4%87%0AAffiliation%3A%201.%20Astronomical%20Observatory%2C%20in%20Belgrade%2C%20Bolgina%207%2C%202011160%20Belgrade%2C%20Serbia%0D%0A2.%20Faculty%20of%20Mathematics%20University%20of%20Belgrade%2C%20Studentski%20Trg%202016%2C%20Belgrade%2C%20Serbia%0A%0A)

Special Issue Editors

 **Dr. Aleksandra Nina**
 E-Mail ([\)](mailto:) Website (<https://loop.frontiersin.org/people/831163/bio>)
Guest Editor
 Institute of Physics Belgrade, University of Belgrade, Pregrevice 118, 11080 Belgrade, Serbia
Interests: ionosphere; VLF/LF signals; remote sensing; natural hazards
Special Issues, Collections and Topics in MDPI journals

 **Prof. Dr. Milan Radovanović**
 E-Mail ([\)](mailto:) Website (https://www.researchgate.net/profile/Milan_Radovanovic4)
Guest Editor
 Geographical Institute "Jovan Cvijic" Serbian Academy of Sciences and Arts, Djure Jakšića 9, 11000 Belgrade, Serbia
Interests: My field of interest is influences of the sun on the atmospheric processes and environment on earth. In last few years my team and I have tried to develop models by which the relationship can be explained between the influx of charged particles from the sun and forest fires. Additionally, I am involved in the research of physical geography, natural hazards and tourism.
Special Issues, Collections and Topics in MDPI journals

 **Prof. Dr. Luka Č. Popović**
 E-Mail ([\)](mailto:) Website (<http://ipopovic.aob.rs/>)
Guest Editor
 1. Astronomical Observatory, in Belgrade, Bolgina 7, 11160 Belgrade, Serbia
 2. Faculty of Mathematics University of Belgrade, Studentski Trg 16, Belgrade, Serbia
Interests: active galactic nuclei; gravitational lensing; plasma physics; ionosphere
Special Issues, Collections and Topics in MDPI journals

Special Issue Information

Dear Colleagues,



Propagation properties of the electromagnetic signals used for different kinds of remote sensing depends on the atmospheric parameters, such as the electron density and temperature. Spatial and temporal variations of these parameters affect signal propagations and, consequently, corresponding applications of the used technique such as observations and positioning. One of the most important sources of the atmospheric disturbances is solar electromagnetic and charged particles radiation. In addition, cosmic rays, including both electromagnetic and particle radiation, can provide enough intensive perturbations of the outer Earth's layer that can affect the signal propagation path. The sources of these perturbations can be relatively close to our planet, but also can be located in the deep Universe. Perturber intensities, lengths and locations in the Earth's atmosphere can be quite different, which can induce various signal deviations.

The aim of this Issue is to present the latest research linking events and processes in the outer space with changes in the propagation of the satellite and ground-based signals used in remote sensing. This Special issue welcomes papers that explore the following:

- Detection of the extra-terrestrial radiation and modelling of the induced atmospheric disturbances using different kinds of remote sensing techniques;
- Changes in signals used for remote sensing and the quality of their applications during influences of extra-terrestrial events;
- Influences of events from outer space on the detection of terrestrial or extra-terrestrial events and corresponding modelling, such as masking less intense perturbations with solar influences, etc.

Additionally, other papers that deal with the Earth's atmosphere's perturbations due to extra-terrestrial events (e.g., meteor perturbations) that may affect signal propagation are welcome.

Dr. Aleksandra Nina
Prof. Dr. Milan Radovanović
Prof. Dr. Luka Č. Popović
Guest Editors

Manuscript Submission Information

Manuscripts should be submitted online at www.mdpi.com (<https://www.mdpi.com>) by [registering](https://www.mdpi.com/user/register/) (<https://www.mdpi.com/user/register/>) and [logging in to this website](https://www.mdpi.com/user/login/) (<https://www.mdpi.com/user/login/>). Once you are registered, [click here to go to the submission form](https://susy.mdpi.com/user/manuscripts/upload/?journal=remotesensing) (<https://susy.mdpi.com/user/manuscripts/upload/?journal=remotesensing>). Manuscripts can be submitted until the deadline. All submissions that pass pre-check are peer-reviewed. Accepted papers will be published continuously in the journal (as soon as accepted) and will be listed together on the special issue website. Research articles, review articles as well as short communications are invited. For planned papers, a title and short abstract (about 100 words) can be sent to the Editorial Office for announcement on this website.

Submitted manuscripts should not have been published previously, nor be under consideration for publication elsewhere (except conference proceedings papers). All manuscripts are thoroughly refereed through a single-blind peer-review process. A guide for authors and other relevant information for submission of manuscripts is available on the [Instructions for Authors](https://www.mdpi.com/journal/remotesensing/instructions) (<https://www.mdpi.com/journal/remotesensing/instructions>) page. *Remote Sensing* (<https://www.mdpi.com/journal/remotesensing/>) is an international peer-reviewed open access semimonthly journal published by MDPI.

Please visit the [Instructions for Authors](https://www.mdpi.com/journal/remotesensing/instructions) (<https://www.mdpi.com/journal/remotesensing/instructions>) page before submitting a manuscript. The **Article Processing Charge (APC)** (<https://www.mdpi.com/about/apc/>) for publication in this **open access** (<https://www.mdpi.com/about/openaccess/>) journal is 2700 CHF (Swiss Francs). Submitted papers should be well formatted and use good English. Authors may use MDPI's [English editing service](https://www.mdpi.com/authors/english) (<https://www.mdpi.com/authors/english>) prior to publication or during author revisions.

Keywords

- Atmosphere
- Observations
- Signal processing
- Modelling
- Extraterrestrial radiation
- Solar radiation
- Disturbances
- Remote sensing

Benefits of Publishing in a Special Issue

- Ease of navigation: Grouping papers by topic helps scholars navigate broad scope journals more efficiently.
- Greater discoverability: Special Issues support the reach and impact of scientific research. Articles in Special Issues are more discoverable and cited more frequently.
- Expansion of research network: Special Issues facilitate connections among authors, fostering scientific collaborations.
- External promotion: Articles in Special Issues are often promoted through the journal's social media, increasing their visibility.
- e-Book format: Special Issues with more than 10 articles can be published as dedicated e-books, ensuring wide and rapid dissemination.

Further information on MDPI's Special Issue policies can be found [here](https://www.mdpi.com/special_issues_guidelines) (https://www.mdpi.com/special_issues_guidelines).

Published Papers (4 papers)

[Download All Papers](#)

Order results

Content type

Result details

Normal

[Show export options](#) ▾

Editorial

Jump to: [Research](#)



Open Access Editorial

4 pages, 242 KIB

[\(/2072-4292/13/5/890/pdf?version=1614846116\)](#)**Extraterrestrial Influences on Remote Sensing in the Earth's Atmosphere (2072-4292/13/5/890)**

by Aleksandra Nina, Milan Radovanović and Luka Popović

Remote Sens. **2021**, *13*(5), 890; <https://doi.org/10.3390/rs13050890> (<https://doi.org/10.3390/rs13050890>) - 26 Feb 2021**Cited by 2** ([/2072-4292/13/5/890#metrics](#)) | Viewed by 2815**Abstract** Atmospheric properties have a significant influence on electromagnetic (EM) waves, including the propagation of EM signals used for remote sensing. For this reason, changes in the received amplitudes and phases of these signals can be used for the detection of the atmospheric disturbances [...] [Read more](#).(This article belongs to the Special Issue [Extraterrestrial Influences on Remote Sensing in the Earth's Atmosphere](#) ([/journal/remotesensing/special_issues/Extraterr_Atmo](#)))**Show Figures**https://pub.mdpi-res.com/remotesensing/remotesensing-13-00890/article_deploy/html/images/remotesensing-13-00890-g001-550.jpg?1614846202

Research

Jump to: [Editorial](#)

Open Access Communication

9 pages, 506 KIB

[\(/2072-4292/14/11/2560/pdf?version=1653628850\)](#)**September 2017 Solar Flares Effect on the Middle Atmosphere (2072-4292/14/11/2560)**

by Polina Pikulina, Irina Mironova, Eugene Rozanov and Arseniy Karagodin

Remote Sens. **2022**, *14*(11), 2560; <https://doi.org/10.3390/rs14112560> (<https://doi.org/10.3390/rs14112560>) - 27 May 2022**Cited by 10** ([/2072-4292/14/11/2560#metrics](#)) | Viewed by 1900**Abstract** This paper examines the response of the upper atmosphere to increased radiation following exceptional solar activity in September 2017. The active region of the Sun AR2673 has caused intense solar-terrestrial disturbance. This active region has generated several powerful X-class solar flares. The strongest [...] [Read more](#).(This article belongs to the Special Issue [Extraterrestrial Influences on Remote Sensing in the Earth's Atmosphere](#) ([/journal/remotesensing/special_issues/Extraterr_Atmo](#)))**Show Figures**https://pub.mdpi-res.com/remotesensing/remotesensing-14-02560/article_deploy/html/images/remotesensing-14-02560-g001-550.jpg?1653628937 (https://pub.mdpi-res.com/remotesensing/remotesensing-14-02560/article_deploy/html/images/remotesensing-14-02560-g002-550.jpg?1653628934) (https://pub.mdpi-res.com/remotesensing/remotesensing-14-02560/article_deploy/html/images/remotesensing-14-02560-g003-550.jpg?1653628937) ([https://pub.mdpi-res.com/remotesensing/remotesensing-14-02560-g004-550.jpg?1653628939](https://pub.mdpi-res.com/remotesensing/remotesensing-14-02560/article_deploy/html/images/remotesensing-14-02560-g004-550.jpg?1653628939)) ([https://pub.mdpi-res.com/remotesensing/remotesensing-14-02560-g005-550.jpg?1653628936](https://pub.mdpi-res.com/remotesensing/remotesensing-14-02560/article_deploy/html/images/remotesensing-14-02560-g005-550.jpg?1653628936))

Open Access Article

22 pages, 2988 KIB

[\(/2072-4292/14/1/54/pdf?version=1640335151\)](#)**Modelling of the Electron Density and Total Electron Content in the Quiet and Solar X-ray Flare Perturbed Ionospheric D-Region Based on Remote Sensing by VLF/LF Signals (2072-4292/14/1/54)**

by Aleksandra Nina

Remote Sens. **2022**, *14*(1), 54; <https://doi.org/10.3390/rs14010054> (<https://doi.org/10.3390/rs14010054>) - 23 Dec 2021**Cited by 9** ([/2072-4292/14/1/54#metrics](#)) | Viewed by 2911**Abstract** Many analyses of the perturbed ionospheric D-region and its influence on the propagation of ground-based and satellite signals are based on data obtained in ionospheric remote sensing by very low/low frequency (VLF/LF) signals. One of the most significant causes of errors in these [...] [Read more](#).(This article belongs to the Special Issue [Extraterrestrial Influences on Remote Sensing in the Earth's Atmosphere](#) ([/journal/remotesensing/special_issues/Extraterr_Atmo](#)))**Show Figures**https://pub.mdpi-res.com/remotesensing/remotesensing-14-00054/article_deploy/html/images/remotesensing-14-00054-ag-550.jpg?1640335255) (https://pub.mdpi-res.com/remotesensing/remotesensing-14-00054/article_deploy/html/images/remotesensing-14-00054-g001-550.jpg?1640335255) (https://pub.mdpi-res.com/remotesensing/remotesensing-14-00054/article_deploy/html/images/remotesensing-14-00054-g002-550.jpg?1640335255) ([https://pub.mdpi-res.com/remotesensing/remotesensing-14-00054-g003-550.jpg?1640335255](https://pub.mdpi-res.com/remotesensing/remotesensing-14-00054/article_deploy/html/images/remotesensing-14-00054-g003-550.jpg?1640335255)) ([https://pub.mdpi-res.com/remotesensing/remotesensing-14-00054-g004-550.jpg?1640335255](https://pub.mdpi-res.com/remotesensing/remotesensing-14-00054/article_deploy/html/images/remotesensing-14-00054-g004-550.jpg?1640335255)) ([https://pub.mdpi-res.com/remotesensing/remotesensing-14-00054-g005-550.jpg?1640335255](https://pub.mdpi-res.com/remotesensing/remotesensing-14-00054/article_deploy/html/images/remotesensing-14-00054-g005-550.jpg?1640335255)) ([https://pub.mdpi-res.com/remotesensing/remotesensing-14-00054-g006-550.jpg?1640335255](https://pub.mdpi-res.com/remotesensing/remotesensing-14-00054/article_deploy/html/images/remotesensing-14-00054-g006-550.jpg?1640335255)) ([https://pub.mdpi-res.com/remotesensing/remotesensing-14-00054-g007-550.jpg?1640335255](https://pub.mdpi-res.com/remotesensing/remotesensing-14-00054/article_deploy/html/images/remotesensing-14-00054-g007-550.jpg?1640335255)) ([https://pub.mdpi-res.com/remotesensing/remotesensing-14-00054-g008-550.jpg?1640335255](https://pub.mdpi-res.com/remotesensing/remotesensing-14-00054/article_deploy/html/images/remotesensing-14-00054-g008-550.jpg?1640335255)) (https://pub.mdpi-res.com/remotesensing/remotesensing-14-00054/article_deploy/html/images/remotesensing-14-00054-g009a-550.jpg?1640335255) (https://pub.mdpi-res.com/remotesensing/remotesensing-14-00054/article_deploy/html/images/remotesensing-14-00054-g009b-550.jpg?1640335255) (https://pub.mdpi-res.com/remotesensing/remotesensing-14-00054/article_deploy/html/images/remotesensing-14-00054-g010a-550.jpg?1640335255) (https://pub.mdpi-res.com/remotesensing/remotesensing-14-00054/article_deploy/html/images/remotesensing-14-00054-g010b-550.jpg?1640335255) (https://pub.mdpi-res.com/remotesensing/remotesensing-14-00054/article_deploy/html/images/remotesensing-14-00054-g011-550.jpg?1640335255) (https://pub.mdpi-res.com/remotesensing/remotesensing-14-00054/article_deploy/html/images/remotesensing-14-00054-g012-550.jpg?1640335255) (https://pub.mdpi-res.com/remotesensing/remotesensing-14-00054/article_deploy/html/images/remotesensing-14-00054-g013-550.jpg?1640335255)


Open Access Article

10 pages, 1985 KIB

[\(/2072-4292/13/20/4161/pdf?version=1634538810\)](#)**Ionization in the Earth's Atmosphere Due to Isotropic Energetic Electron Precipitation: Ion Production and Primary Electron Spectra (2072-4292/13/20/4161)**

by Irina Mironova, Gennadiy Kovaltsov, Alexander Mishev and Anton Artamonov

Remote Sens. **2021**, *13*(20), 4161; <https://doi.org/10.3390/rs13204161> (<https://doi.org/10.3390/rs13204161>) - 18 Oct 2021**Cited by 10** ([/2072-4292/13/20/4161#metrics](#)) | Viewed by 2614**Abstract** Energetic electron precipitation (EEP) via atmospheric ion production rates is a natural force acting on the atmosphere and climate systems. The correct estimation of EEP ion production and spectra for the computation of ionization rates is an important issue for estimating climate forces. [...] [Read more](#).(This article belongs to the Special Issue [Extraterrestrial Influences on Remote Sensing in the Earth's Atmosphere](#) ([/journal/remotesensing/special_issues/Extraterr_Atmo](#)))**Show Figures**https://pub.mdpi-res.com/remotesensing/remotesensing-13-04161/article_deploy/html/images/remotesensing-13-04161-g001-550.jpg?1634538888) (https://pub.mdpi-res.com/remotesensing/remotesensing-13-04161/article_deploy/html/images/remotesensing-13-04161-g002-550.jpg?1634538888) (https://pub.mdpi-res.com/remotesensing/remotesensing-13-04161/article_deploy/html/images/remotesensing-13-04161-g003-550.jpg?1634538888)

 [remotesensing-13-04161/article_deploy/html/images/remotesensing-13-04161-g003a-550.jpg?1634538888](https://pub.mdpi-res.com/remotesensing/remotesensing-13-04161/article_deploy/html/images/remotesensing-13-04161-g003a-550.jpg?1634538888) (https://pub.mdpi-res.com/remotesensing/remotesensing-13-04161/article_deploy/html/images/remotesensing-13-04161-g003b-550.jpg?1634538888)

Show export options ▾



Displaying articles 1-4

Remote Sens. ([journal/remotesensing](https://www.mdpi.com/journal/remotesensing)), EISSN 2072-4292, Published by MDPI

[RSS \(/rss/journal/remotesensing\)](https://www.mdpi.com/rss/journal/remotesensing) [Content Alert \(/journal/remotesensing/toc-alert\)](https://www.mdpi.com/content/alert/journal/remotesensing/toc-alert)

Further Information

[Article Processing Charges \(/apc\)](#)

[Pay an Invoice \(/about/payment\)](#)

[Open Access Policy \(/openaccess\)](#)

[Contact MDPI \(/about/contact\)](#)

[Jobs at MDPI \(https://careers.mdpi.com\)](https://careers.mdpi.com)

Guidelines

[For Authors \(/authors\)](#)

[For Reviewers \(/reviewers\)](#)

[For Editors \(/editors\)](#)

[For Librarians \(/librarians\)](#)

[For Publishers \(/publishing_services\)](#)

[For Societies \(/societies\)](#)

[For Conference Organizers \(/conference_organizers\)](#)

MDPI Initiatives

[Sciforum \(https://sciforum.net\)](https://sciforum.net)

[MDPI Books \(https://www.mdpi.com/books\)](https://www.mdpi.com/books)

[Preprints.org \(https://www.preprints.org\)](https://www.preprints.org)

[Scilit \(https://www.scilit.net\)](https://www.scilit.net)

[SciProfiles \(https://sciprofiles.com?utm_source=mdpi.com&utm_medium=bottom_menu&utm_campaign=initiative\)](https://sciprofiles.com?utm_source=mdpi.com&utm_medium=bottom_menu&utm_campaign=initiative)

[Encyclopedia \(https://encyclopedia.pub\)](https://encyclopedia.pub)

[JAMS \(https://jams.pub\)](https://jams.pub)

[Proceedings Series \(/about/proceedings\)](#)

Follow MDPI

[LinkedIn \(https://www.linkedin.com/company/mdpi\)](https://www.linkedin.com/company/mdpi)

[Facebook \(https://www.facebook.com/MDPIOpenAccessPublishing\)](https://www.facebook.com/MDPIOpenAccessPublishing)

[Twitter \(https://twitter.com/MDPIOpenAccess\)](https://twitter.com/MDPIOpenAccess)



Subscribe to receive issue release notifications and newsletters from MDPI journals

Select options ▾

Enter your email address...

Subscribe

© 1996-2024 MDPI (Basel, Switzerland) unless otherwise stated

[Disclaimer](#) [Terms and Conditions \(/about/terms-and-conditions\)](#) [Privacy Policy \(/about/privacy\)](#)



Extraterrestrial Influences on Remote Sensing in the Earth's Atmosphere

Aleksandra Nina ^{1,*}, Milan Radovanović ^{2,3} and Luka Popović ^{4,5,6}

¹ Institute of Physics Belgrade, University of Belgrade, 11080 Belgrade, Serbia

² Geographical Institute "Jovan Cvijić" SASA, 11000 Belgrade, Serbia; m.radovanovic@gi.sanu.ac.rs

³ Institute of Sports, Tourism and Service, South Ural State University, 454080 Chelyabinsk, Russia

⁴ Astronomical Observatory, 11060 Belgrade, Serbia; lpopovic@aob.rs

⁵ Department of Astronomy, Faculty of mathematics, University of Belgrade, 11000 Belgrade, Serbia

⁶ Faculty of Science, University of Banja Luka, 78000 Banja Luka, Republic of Srpska, Bosnia and Herzegovina

* Correspondence: sandrast@ipb.ac.rs

Abstract: Atmospheric properties have a significant influence on electromagnetic (EM) waves, including the propagation of EM signals used for remote sensing. For this reason, changes in the received amplitudes and phases of these signals can be used for the detection of the atmospheric disturbances and, consequently, for their investigation. Some of the most important sources of the temporal and space variations in the atmospheric parameters come from the outer space. Although the solar radiation dominates in these processes, radiation coming out of the solar system also can induce enough intensive disturbance in the atmosphere to provide deflections in the EM signal propagation paths. The aim of this issue is to present the latest research linking events and processes in outer space with changes in the propagation of the satellite and ground-based signals used in remote sensing.

Keywords: atmosphere; observations; signal processing; modelling; extraterrestrial radiation; solar radiation; disturbances; remote sensing



Citation: Nina, A.; Radovanović, M.; Popović, L. Extraterrestrial Influences on Remote Sensing in the Earth's Atmosphere. *Remote Sens.* **2021**, *13*, 890. <https://doi.org/10.3390/rs13050890>

Received: 17 February 2021

Accepted: 22 February 2021

Published: 26 February 2021

Publisher's Note: MDPI stays neutral with regard to jurisdictional claims in published maps and institutional affiliations.



Copyright: © 2021 by the authors. Licensee MDPI, Basel, Switzerland. This article is an open access article distributed under the terms and conditions of the Creative Commons Attribution (CC BY) license (<https://creativecommons.org/licenses/by/4.0/>).

1. Introduction

As the highest terrestrial layer, the atmosphere is under permanent influences from outer space. For this reason and due to link with many processes in different areas of Earth, the temporal and space distributions of atmospheric parameters are very complex and have been the focus of a number of studies in different research fields. The application of these studies is important for pure sciences but also for applied sciences and technology.

Since the measurement of atmospheric parameters using on-site methods is very complex, remote sensing has very important role in observations of different-altitude domains. The propagation properties of a signal which have been used for different kinds of remote sensing depend on the different atmospheric parameters, such as the electron density and temperature. The spatial and temporal variations in these parameters affect signal propagations and, consequently, the corresponding applications of the used technique, such as observations and positioning. Some of the most important sources of atmospheric disturbances are solar wind and radiation. In addition, cosmic rays can provide intensive perturbations of the outer Earth's layer [1–3]. The perturbation intensity, duration, and location in the Earth's atmosphere can be quite different, which can induce various signal deviations.

The focus of this Special Issue is: (1) the detection of extraterrestrial events and induced atmospheric disturbance modelling, and (2) the influences of atmospheric parameter variations on EM signal propagation.

2. Extraterrestrial Influences on the Earth Atmosphere—Remote Sensing of Disturbances

The properties of the atmospheric disturbances induced by extraterrestrial events and processes depend on the characteristics of the disturbance sources (intensities, source type etc.), the considered atmospheric area (due to interaction of incoming radiation or bodies with particles within them), and the space between them (due to the interaction of incoming radiation or bodies with the atmosphere part before its arrival at the considered location). Charged particles primarily disturb the upper ionosphere as well as the polar and near-polar latitudes (due to the geomagnetic field), while the influence of the EM radiation depends on the radiation intensity, wavelength, impact angle in the atmosphere, and the area within its propagation.

These variations can be periodical because of, for example, variations during a solar cycle, year (due to Earth's revolution), and day (due to Earth's rotation), and sudden due to expected or unexpected outer space phenomena (see Figure 1). The periodical changes in the atmospheric parameters and the precision of their determination are primarily connected with the solar radiation. They are recorded within all atmospheric layers, from the ionosphere and magnetosphere in the upper atmosphere [4–6] to the troposphere and stratosphere in the lower atmosphere [7]. The sources of these sudden perturbations can be the Sun, solar system, galaxy, or the wider Universe [3,8]. The intensity and duration of their influences on the atmosphere are different: from very weak and very hard to detect to extremely intensive when the atmospheric parameters are changed by several orders of magnitude [9,10], and from short-lasting (several milliseconds) [2] to perturbations of several days or more [11].

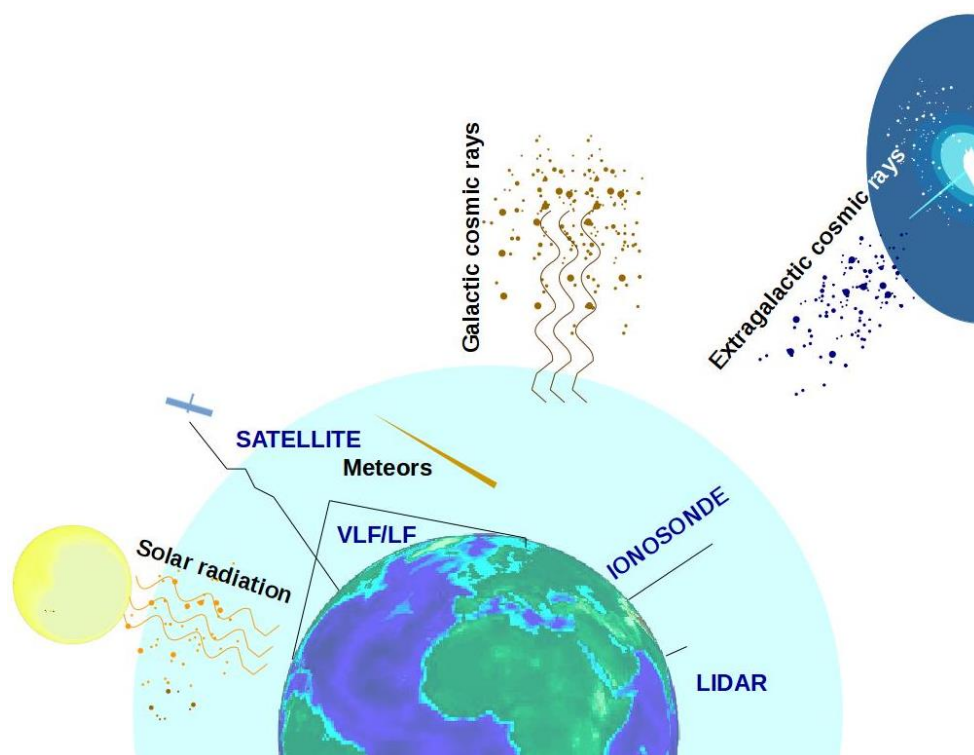


Figure 1. Scheme of outer space's influence on the Earth's atmosphere. Extraterrestrial electromagnetic and particle radiation coming from the Sun, our galaxy, and the wider universe, and impact of meteors in the Earth's atmosphere. Several examples of the remote sensing of the atmosphere: troposphere observations by LIDAR, VLF/LF signal monitoring of the lower ionosphere, ionospheric monitoring using signals emitted by ionosondes, satellite observations.

The application of an observation technique depends on the considered altitude domain. In addition, the detection of the short-term variations requires the good temporal

resolution of the observed data, while the monitoring of the unpredictable phenomena is possible with continuous measurements provided by, for example, the Global Navigation Satellite System (GNSS) [12] or lower ionosphere monitoring by very low/low frequency radio waves [2,3,13,14].

The recorded data are included in many methodologies for the modelling of the spatial and temporal distributions of atmospheric parameters. In some cases, their estimation within a local area require a more than one data set and more than one monitoring techniques [15–17] which provides more precious estimates of atmospheric properties.

3. Extraterrestrial Influences on Electromagnetic Signal Propagation

The investigation of the signal propagation changes induced by extraterrestrial events and processes, primarily with origins in the solar system, is very important due to possible errors in their use in observations and modelling. This task can be crucial for precision in technologies based on, for example, satellite signal propagation, which is reason why the corresponding research took place many decades ago and why it is still of high importance.

In this field, solar radiation is the subject of most relevant studies. Its influence on satellite signals dominates in the upper ionosphere due to the largest electron density in this atmospheric layer, which is often used as an approximation in the estimation of the total electron content (TEC), the ionospheric parameter required in the modelling of signal propagation [18–20]. However, the recent study presented in [21] shows that errors due to the neglect of the D-region electron density increase induced by a solar X-ray flare can be important for the precision of satellite signal propagation modelling. Lower ionosphere disturbances as well as F-region disturbances below the altitude of the electron density maximum are important for the propagation of ground-based signals emitted at the surface and reflected from the ionosphere. A well-known example of extreme solar radiation influence on radio signal propagation is black out [22].

The influence of the Solar radiation on the quality of signals is also reported in lower atmospheric observations. As an example, in [23] the authors analysed solar radiation's influence on error in temperature measurements.

4. Summary

The main goal of this Special Issue is to collect studies about extraterrestrial influences on remote sensing in the Earth's atmosphere. Attention is focused on research on the following topics:

- The detection of extra-terrestrial radiation and the modelling of the induced atmospheric disturbances using different kinds of remote sensing techniques;
- Changes in signals used for remote sensing and the quality of their applications during influences of extra-terrestrial events;
- Influence of events from outer space on the detection of terrestrial or extra-terrestrial events and corresponding modelling, such as masking less intense perturbations with solar influences;
- The Earth's atmosphere's perturbations due to extra-terrestrial events (e.g., meteor perturbations) that may affect signal propagation, etc.

Studies in different research fields should emphasise the multidisciplinary character of both observations and modelling corresponding to extraterrestrial influences on remote sensing in the Earth's atmosphere

Author Contributions: Conceptualization, original draft preparation, and visualization, A.N.; review and editing, all authors. All authors have read and agreed to the published version of the manuscript.

Funding: The authors acknowledge funding provided by the Institute of Physics Belgrade and the Astronomical Observatory (the contract 451-03-68/2020-14/200002) through the grants by the Ministry of Education, Science, and Technological Development of the Republic of Serbia.

Acknowledgments: The authors thank to Zoran Mijić and Nikola Veselinović for help in preparation of this paper, and Srđan Mitrović for help in promotion of this Special Issue. We also would like to thank the Remote Sensing editorial team for its support in preparation of this SI.

Conflicts of Interest: The authors declare no conflict of interest.

References

1. Siingh, D.; Singh, R. The role of cosmic rays in the Earth's atmospheric processes. *Pramana J. Phys.* **2010**, *74*, 153–168. [[CrossRef](#)]
2. Nina, A.; Simić, S.; Srećković, V.A.; Popović, L.Č. Detection of short-term response of the low ionosphere on gamma ray bursts. *Geophys. Res. Lett.* **2015**, *42*, 8250–8261. [[CrossRef](#)]
3. Inan, U.S.; Lehtinen, N.G.; Moore, R.C.; Hurley, K.; Boggs, S.; Smith, D.M.; Fishman, G.J. Massive disturbance of the daytime lower ionosphere by the giant γ -ray flare from magnetar SGR 1806-20. *Geophys. Res. Lett.* **2007**, *34*, 8103. [[CrossRef](#)]
4. Jerez, G.O.; Hernández-Pajares, M.; Prol, F.S.; Alves, D.B.M.; Monico, J.F.G. Assessment of Global Ionospheric Maps Performance by Means of Ionosonde Data. *Remote Sens.* **2020**, *12*, 3452. [[CrossRef](#)]
5. Lühr, H.; Maus, S. Solar cycle dependence of quiet-time magnetospheric currents and a model of their near-Earth magnetic fields. *Earth Planets Space* **2010**, *62*, 14. [[CrossRef](#)]
6. Nina, A.; Nico, G.; Mitrović, S.T.; Čadež, V.M.; Milošević, I.R.; Radovanović, M.; Popović, L.Č. Quiet Ionospheric D-Region (QIonDR) Model Based on VLF/LF Observations. *Remote Sens.* **2021**, *13*, 483. [[CrossRef](#)]
7. Wiencke, L.; Rizi, V.; Will, M.; Allen, C.; Botts, A.; Calhoun, M.; Carande, B.; Claus, J.; Coco, M.; Emmert, L.; et al. Joint elastic side-scattering LIDAR and Raman LIDAR measurements of aerosol optical properties in south east Colorado. *J. Instrum.* **2017**, *12*, P03008. [[CrossRef](#)]
8. Tsurutani, B.T.; Verkhoglyadova, O.P.; Mannucci, A.J.; Lakhina, G.S.; Li, G.; Zank, G.P. A brief review of “solar flare effects” on the ionosphere. *Radio Sci.* **2009**, *44*, 1. [[CrossRef](#)]
9. Singh, A.K.; Singh, A.; Singh, R.; Singh, R. Solar flare induced D-region ionospheric perturbations evaluated from VLF measurements. *Astrophys. Space Sci.* **2014**, *350*, 1–9. [[CrossRef](#)]
10. Chakraborty, S.; Basak, T. Numerical analysis of electron density and response time delay during solar flares in mid-latitude lower ionosphere. *Astrophys. Space Sci.* **2020**, *365*, 184. [[CrossRef](#)]
11. Gil, A.; Modzelewska, R.; Moskwa, S.; Siluszyk, A.; Siluszyk, M.; Wawrzynczak, A.; Pozoga, M.; Tomasik, L. The Solar Event of 14–15 July 2012 and Its Geoeffectiveness. *Sol. Phys.* **2020**, *295*, 135. [[CrossRef](#)]
12. Curto, J.J.; Juan, J.M.; Timoté, C.C. Confirming geomagnetic Sfe by means of a solar flare detector based on GNSS. *J. Space Weather Space Clim.* **2019**, *9*, A42. [[CrossRef](#)]
13. Srećković, V.; Šulić, D.; Vujičić, V.; Jevremović, D.; Vyklyuk, Y. The effects of solar activity: Electrons in the terrestrial lower ionosphere. *J. Geograph. Inst. Cvijic* **2017**, *67*, 221–233. [[CrossRef](#)]
14. Nina, A.; Čadež, V.M.; Popović, L.Č.; Srećković, V.A. Diagnostics of plasma in the ionospheric D-region: Detection and study of different ionospheric disturbance types. *Eur. Phys. J. D* **2017**, *71*, 189. [[CrossRef](#)]
15. An, X.; Meng, X.; Chen, H.; Jiang, W.; Xi, R.; Chen, Q. Modelling Global Ionosphere Based on Multi-Frequency, Multi-Constellation GNSS Observations and IRI Model. *Remote Sens.* **2020**, *12*, 439. [[CrossRef](#)]
16. Benevides, P.; Nico, G.; Catalão, J.; Miranda, P.M.A. Analysis of Galileo and GPS Integration for GNSS Tomography. *IEEE Trans. Geosci. Remote Sens.* **2017**, *55*, 1936–1943. [[CrossRef](#)]
17. Mateus, P.; Tomé, R.; Nico, G.; Catalão, J. Three-Dimensional Variational Assimilation of InSAR PWV Using the WRFDA Model. *IEEE Trans. Geosci. Remote Sens.* **2016**, *54*, 7323–7330. [[CrossRef](#)]
18. Zhao, J.; Zhou, C. On the optimal height of ionospheric shell for single-site TEC estimation. *GPS Solut.* **2018**, *22*, 48. [[CrossRef](#)]
19. Scherliess, L.; Schunk, R.W.; Sojka, J.J.; Thompson, D.C.; Zhu, L. Utah State University Global Assimilation of Ionospheric Measurements Gauss-Markov Kalman filter model of the ionosphere: Model description and validation. *J. Geophys. Res. Space* **2006**, *111*, A11315. [[CrossRef](#)]
20. Nava, B.; Coïsson, P.; Radicella, S. A new version of the NeQuick ionosphere electron density model. *J. Atmos. Sol.-Terr. Phys.* **2008**, *70*, 1856–1862. [[CrossRef](#)]
21. Nina, A.; Nico, G.; Odalović, O.; Čadež, V.; Drakul, M.T.; Radovanović, M.; Popović, L.Č. GNSS and SAR Signal Delay in Perturbed Ionospheric D-Region During Solar X-Ray Flares. *IEEE Geosci. Remote Sens. Lett.* **2020**, *17*, 1198–1202. [[CrossRef](#)]
22. Frissell, N.A.; Vega, J.S.; Markowitz, E.; Gerrard, A.J.; Engelke, W.D.; Erickson, P.J.; Miller, E.S.; Luetzelschwab, R.C.; Bortnik, J. High-Frequency Communications Response to Solar Activity in September 2017 as Observed by Amateur Radio Networks. *Space Weather* **2019**, *17*, 118–132. [[CrossRef](#)]
23. Martucci, G.; Navas-Guzman, F.; Renaud, L.; Romanens, G.; Gamage, S.M.; Hervo, M.; Jeannet, P.; Haefele, A. Validation of temperature data from the Raman Lidar for Meteorological Observations (RALMO) at Payerne. An application to liquid cloud supersaturation. *Atmos. Meas. Tech. Discuss.* **2020**, *2020*, 1–32. [[CrossRef](#)]

M29B

(018)533-015, 226-310 | pmfinfo@pmf.ni.ac.rs (mailto:pmfinfo@pmf.ni.ac.rs)

[🏠](#) [Nastavnički portal](#) [Studentski portal](#) [E-servisi](#) ▾ [Linkovi](#) [Kontakt](#) ▾ [🔍](#) [🇷🇸](#) [Lat](#) ▾



UNIVERZITET U NIŠU
PRIRODNO-MATEMATIČKI
FAKULTET U NIŠU

(<https://www.pmf.ni.ac.rs/>)

[STUDIJE](#) ▾ [ZA BUDUĆE STUDENTE](#) ▾ [NAUKA](#) ▾
[VESTI](#) ▾

Aims and scope

Volumes

Guide for authors

Guide for Reviewers

Editorial Board

Editorial Board

Editor-in-Chief

Ranko Dragović (/sj_geosciences/ranko-dragovic/)

Department of Geography, Faculty of Sciences and Mathematics,
University of Niš, Serbia

Associate Editors

Branislav Bajat (/sj_geosciences/branislav-bajat/)

Department of Geodesy and Geoinformatics, Faculty of Civil
Engineering, University of Belgrade, Serbia

Vladica Cvetković (/sj_geosciences/vladica-cvetkovic/)

University of Belgrade – Faculty of Mining and Geology

Milan Đorđević (/sj_geosciences/milan-djordjevic/)

Department of Geography, Faculty of Sciences and Mathematics,
University of Niš, Serbia

Pablo Fernández de Arróyabe Hernáez (/sj_geosciences/pablo-fernandez-de-arroyabe-hernaez/)

Dept. of Urban Geography, Urban and Regional Planning, Univ. de
Cantabria, Spain

Ivan Filipović (/sj_geosciences/ivan-filipovic/)

Department of Geography, Faculty of Sciences and Mathematics,
University of Niš, Serbia

Bosko Gajić (/sj_geosciences/bosko-gajic/)

Soil Management department, Faculty of Agriculture, University of
Belgrade, Serbia

Andjelija Ivkov-Džigurski (/sj_geosciences/andjelija-ivkov-dzigurski/)

Department of Geography, Tourism and Hotel Management, Faculty
of Sciences, University of Novi Sad, Serbia

Pavlos Kassomenos (/pavlos-kassomenos-serbian-journal-of-geosciences/)

Department of Physics, University of Ioannina, Greece

Jovan Kovačević (/sj_geosciences/jovan-kovacevic/)

Geological Survey of Serbia, University of Belgrade, Serbia

Slobodan B. Marković (/sj_geosciences/slobodan-b-markovic/)

Department of Geography, Tourism and Hotel Management, Faculty of Sciences, University of Novi Sad, Serbia

Aleksandra Nina (/aleksandra-nina-serbian-journal-geo/)

Institute of Physics Belgrade – National Institute of the Republic of Serbia, University of Belgrade, Serbia

Antonije Onija (/si_geosciences/antonije-onija/)

Faculty of Technology and Metallurgy of University of Belgrade, Serbia

Mila A. Pavlović (/sj_geosciences/mila-a-pavlovic/)

Faculty of Geography, University of Belgrade, Serbia

Irma Potočnik Slavič (/sj_geosciences/irma-potocnik-slavic/)

Department of Geography, Faculty of Arts, University of Ljubljana, Slovenia

Aleksandar Radivojević (/sj_geosciences/aleksandar-radivojevic/)

Department of Geography, Faculty of Sciences and Mathematics, University of Niš, Serbia

Milan M. Radovanovic (/sj_geosciences/milan-m-radovanovic/)

Geographical Institute "Jovan Cvijic", University of Belgrade, Serbia

Reviewers

UNIVERZITET U NIŠU, PRIRODNO-MATEMATIČKI FAKULTET U NIŠU

Adresa:

18106 Niš • Višegradska 33 • Poš. fah : 224 (<https://goo.gl/maps/nVE2KmV5Eeu>)

Telefoni:

Centrala (018) 533-015, 226-310

M31

PROCEEDINGS
of the XX Serbian Astronomical Conference
Belgrade, October 16 – 20, 2023

ЗБОРНИК РАДОВА
XX Српске астрономске конференције
Београд, 16 – 20. октобар 2023.

Edited by Jelena Petrović, Dušan Marčeta and Ana Lalović



Б Е О Г Р А Д
2024

REDUCTION OF THE VLF SIGNAL NOISE AS POTENTIAL EARTHQUAKE PRECURSOR: PILOT STUDIES

ALEKSANDRA NINA 

*Institute of Physics Belgrade, University of Belgrade,
Pregrevica 118, 11080 Belgrade, Serbia
E-mail: sandrast@ipb.ac.rs*

Abstract. Studies of pre-earthquake disturbances in the ionosphere since the middle of the last century point to several types of potential precursors to these natural events. A large number of them are detected as disturbances in the Global navigation satellite system (GNSS) and very low / low frequency (VLF/LF) signals a few days before the earthquake. However, the analysis of the VLF signal emitted in Italy and received in Belgrade in the period around the earthquake in Kraljevo that occurred on 3 November, 2010 indicates a potentially new type of these precursors. It is visible as a reduction of the VLF signal noise which starts several minutes or several tens of minutes before earthquake. In addition, Fourier transform of the recorded data indicates wave excitations at discrete waveperiods under 1.5 s, and wave attenuations at other waveperiods. In this paper, pilot studies of the noise reduction of the amplitude and phase of the mentioned VLF signal in both time and frequency domains are presented. The data recorded by the Absolute Phase and Amplitude Logger (AbsPAL) receiver located at the Institute of Physics Belgrade on November 3, 4 and 9, 2010, and during the period of intense seismic activity when almost 1000 earthquakes occurred in Central Italy from October 25 to November 3, 2016, are analyzed. The obtained results indicate possible differences in the signal noise reduction in cases when the observed earthquake follow and not follow previous earthquakes in approximately the same area. Namely, in the first case, the signal noise reduction may already be present so that no new reductions occur before subsequent earthquakes. On the analyzed sample of 35 earthquakes of minimum magnitude 4, the signal noise is reduced in over 90% of cases. In the remaining three cases, it cannot be clearly concluded whether this reduction exists due to its reduced value over a longer time period, which can be explained by the intense seismic activity in that period.

1. INTRODUCTION

Investigations of natural disasters are one of the most striking examples of the importance of scientific studies. This primarily refers to efforts to find changes that can be considered as their precursors.

One of the natural phenomena that causes the greatest consequences for human lives and the environment in which they occur are earthquakes. There are various methods used to study the earthquakes, and attempts to establish their precursors. One of these methods is based on the analysis of very low/low frequency (VLF/LF) radio signals used to monitor the low ionosphere (Biagi et al. 2006, 2011, Hayakawa et al. 2010, Maurya et al. 2016, Molchanov et al. 1998, 2001, Nina et al. 2020, Ohya et al. 2018, Yamauchi, 2004, Yamauchi et al. 2004). The analyses of these signals are based on the processing of their amplitudes and phases in the time and frequency

domains. Changes that are considered in the time domain as potential precursors of earthquakes are manifested in variations of signal parameter values and their noise before the earthquake, as well as, the changes in solar terminator times a few days earlier. In the frequency domain, wave excitations and attenuations are observed, which are obtained by applying a wavelet transform or the Fast Fourier Transform to the sets of recorded data relevant to both signal parameters.

This paper presents pioneering studies of new potential earthquake precursors that were first observed in the analysis of data recorded by the Absolute Phase and Amplitude Logger (AbsPAL) receiver located at the Institute of Physics Belgrade in Serbia about the period around the earthquake near Kraljevo, Serbia, which occurred on November 3, 2010. This investigation is present in Nina et al. 2020, Nina et al. 2021, and Nina et al. 2022. Although the earthquake was not very strong, it was the strongest earthquake that occurred in Serbia during the period of operation of the Belgrade VLF/LF receiving station. It was the motivation for the beginning of the aforementioned research. Unlike previous studies which were mostly done with data recorded with a minute resolution, the data sets used in the three studies mentioned above have a time resolution of 0.1 s. This improvement in time resolution enabled a more detailed analysis that resulted in the changes in signal parameters starting a few minutes or a few tens of minutes before an earthquake.

2. OBSERVATIONS

2. 1. OBSERVATIONAL SETUP

The studies of the indicated new possible earthquake precursors are based on data obtained in the monitoring of the lower ionosphere with VLF signals, and recorded by the AbsPAL receiver located at the Institute of Physics Belgrade in Serbia. In the performed analyses we considered four VLF signals emitted by the VLF transmitters located in Italy (ICV transmitter), Germany (DHO transmitter), the UK (GQD transmitter), and Norway (JXN transmitter). The locations of these transmitters and receiver as well as the corresponding signal propagation paths are shown in Figure 1.

2. 2. ANALYZED EVENTS

As stated in Introduction, in the studies of the aforementioned new potential earthquake precursors that have been published so far, analysis is made for two groups of earthquakes:

- Earthquakes that occurred in periods when seismic activity was not intense (in an area where there was no long-term seismic activity manifested by numerous earthquakes over a period of several days). In this case, the analysis is focused on four earthquakes whose magnitudes are above 4 and that occurred near Kraljevo in Serbia on November 3 (K1 earthquake) and 4 (K2 earthquake), 2010, in the Tyrrhenian Sea (TS earthquake) on November 3, 2010, and in the Western Mediterranean Sea on November 9, 2010. During these three days, more earthquakes of smaller magnitudes were recorded, which is why analysis is made for these as well.

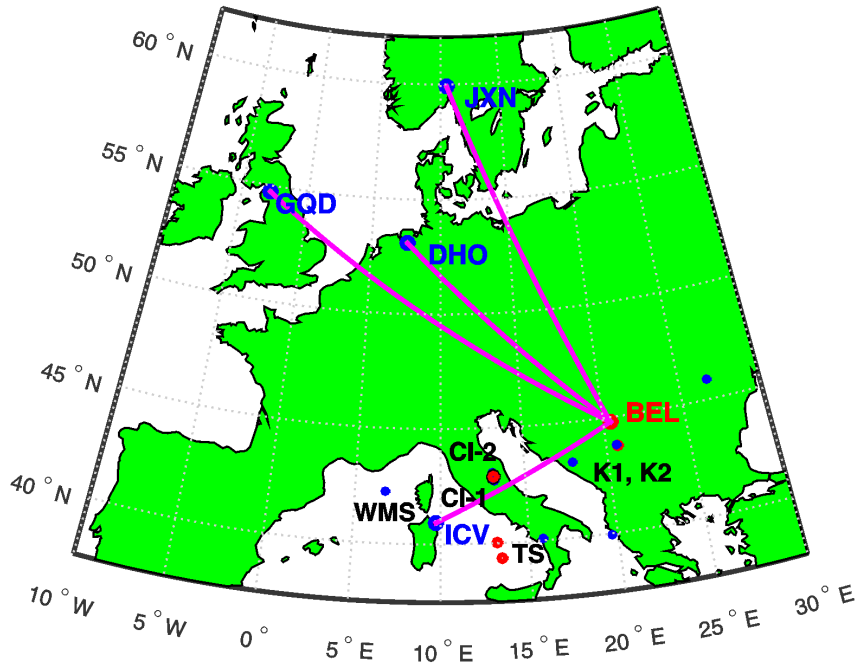


Figure 1: Propagation paths of the VLF signals recorded by the Belgrade receiver station (BEL) in Serbia and emitted by the ICV, DHO and JXN transmitters located in Italy, Germany and Norway. Blue, red and black dots mark the epicenters of considered earthquakes of magnitude $4 \leq M < 5$ (blue dots), $5 \leq M < 6$ (red dots) and $M \geq 6$ (black dots).

- Earthquakes that occurred during periods of intense seismic activity. In this case, the period from October 25 to November 3, 2016 when almost 1000 earthquakes occurred in Central Italy (dominantly grouped in the locations marked as CI-1 and CI-2 on the map) is considered.

2. 3. SIGNAL PROCESSING

In these studies of the new potential earthquake precursors, data sets related to the amplitude and phase of VLF signals recorded with the sampling period of 0.1 s were analyzed. This analysis was performed in the time and frequency domains.

In the time domain we analyze the amplitude and phase noise. These parameters are defined in the analysis of short-term disturbances of the VLF signal amplitude which follow the detection of gamma ray bursts by the Swift satellite. The used parameters are defined as the maximum absolute values of the deviations of the recorded amplitude and phase values from their smoothed curves. In order to avoid consideration of short-term effects of other phenomena (e.g. those caused by lightning), this maximum absolute value is determined after sorting the relevant deviations in the observed time interval and removing p -percent of their highest values. Specifically, we assumed that $p = 5\%$, so that, in the observed interval of e.g. 20 minutes in which 6000 values are recorded for one of these two signal parameters, the 300 highest absolute values are discarded and the highest absolute value is taken from the remaining part of the considered sample.

In the frequency domain we analyze the Fourier amplitude obtained after application of the Fast Fourier Transform to the recorded amplitude and phase.

3. RESULTS AND DISCUSSION

The research on the amplitude and phase changes of VLF signals that are considered as new potential earthquake precursors, started in 2018 at the Institute of Physics Belgrade, Serbia, and several studies on this topic have been published so far. These studies present the results published in Nina et al. 2020, Nina et al. 2021, and Nina et al. 2022, in which the amplitudes and phases of the considered VLF signals are processed in the time and frequency domains. The studies considered earthquakes that occurred in the periods when intense seismic activity in the observed area did not occur for several days as well as, in the periods when it was recorded. All the combinations of different types of analyses used on the mentioned parameters and conditions which are relevant for this research are given in the scheme in Figure 2. The specific analyses given in the mentioned studies are listed in Table 1 where ”-” mark indicates that the relevant research has not yet been published.

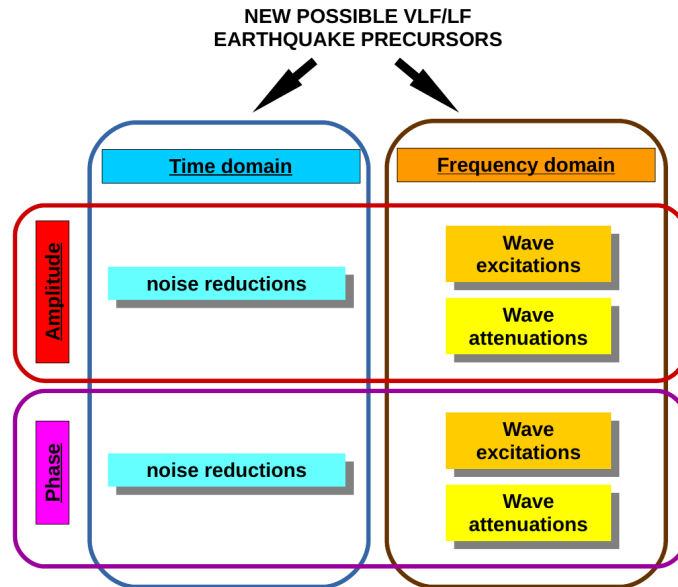


Figure 2: Scheme of the relevant analyses of the signal parameters (amplitude and phase) in the time and frequency domains.

3. 1. ANALYSES IN THE TIME DOMAIN

The first relevant analysis (Nina et al. 2020) is provided for the ICV, DHO, and GQD amplitudes on November 3, 4, and 9, 2010 with focus on the period around Kraljevo earthquake that occurred on November 3, 2010. It shows that the ICV amplitude noise reductions occur a few minutes or tens of minutes before many earthquakes that occurred in those days. The mentioned reduction is recorded at 8 out of 10 earthquakes with a minimum magnitude of 2.5 that occurred near Kraljevo (on 3, 4, and November 9, 2010). Also, 13 of the recorded 15 amplitude noise reductions during those three days can be accompanied by earthquakes with epicentres close to the propagation path of the observed VLF signal.

The amplitude noise reduction is recorded before all four earthquakes with the magnitude larger than 4 which occurred during the observed three days. In this case,

Table 1: References to the studies of ICV signal amplitude and phase in the case of non-intensive seismic activity occurrences (upper half) which are conducted in time and frequency domains in the periods around K1, TS, K2, and WMS earthquakes, respectively; and in the case of earthquakes in Central Italy, during the intensive seismic activity (bottom half). Terms [1], [2], and [3] refer to the studies reported in Nina et al. 2020, Nina et al. 2021, and Nina et al. 2022, respectively.

Domain	Amplitude	Phase
No intensive seismic activity		
Time	[1],[1],[1],[1]	[2],[2],[2],[2]
Frequency	[1],-,,-	[2],[2],[2],[2]
Intensive seismic activity		
Time	[3]	-
Frequency	-	-

the similar reduction of the phase noise is also recorded (Nina et al. 2021). The amplitude noise reduction is also observed before the earthquakes with magnitude greater than 4 which are not preceded by strong earthquakes during the period of intense seismic activity in central Italy from October 25 to November 3, 2016 (Nina et al. 2022).

The results given in Nina et al. 2020 show that in the case when multiple earthquakes occur in a short time interval in an area, only one long-term amplitude noise reduction can be associated with all of them. This is important for the detection of relevant precursors before a particular earthquake during intense seismic activities. As study of the ICV signal amplitude noise reduction during the period of intense seismic activity when almost 1000 earthquakes occurred in Central Italy shows, many earthquakes occurred during a period of one amplitude noise reduction. At the same time, no significant variations are detected in those reductions, which makes it impossible to detect the precursors of individual earthquakes.

The integration of the studies given in Nina et al. 2020 and shows that over 90% of 35 analyzed cases occurred during periods when the amplitude noise is reduced. In the remaining three cases, it cannot be clearly concluded whether this reduction exists due to its reduced value over a longer time period, which can be explained by the intense seismic activity in that period.

An example of precursors which preceded the two earthquakes that occurred on November 9, 2010 (their characteristics are given in <http://www.emsc-csem.org/Earthquake/>) is given in Figure 3. As can be seen, there are two successive amplitude noise reductions and each of them is followed by earthquakes after several tents of minutes. This example is interesting for two reasons. First, both of these earthquakes have a small magnitude (2.5 and 3.2, respectively), which indicates a potentially very high sensitivity of the presented method. And secondly, the earthquakes occurred in a short time interval (at 01:32:14 UT, and 02:24:24 UT, respectively) but in different locations (in Central Italy and in Serbia). Based on the time evolution of the amplitude noise, it can be seen that the second noise reduction builds on the first one before its end, which indicates the temporal closeness (but spatial distance) of the observed earthquakes.

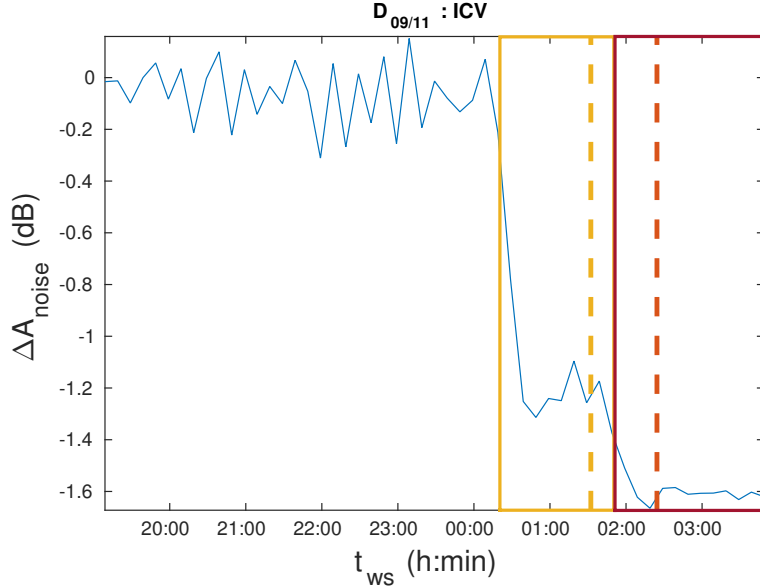


Figure 3: The time evolution of the amplitude noise with respect to its value in a quiet condition ΔA_{noise} in the period around the two earthquakes which times are indicated by vertical dashed lines. The yellow box indicates the period in which the decrease in amplitude noise can be associated with the first earthquake, while the additional decrease in the period indicated by the red box can be associated with the second earthquake.

3. 2. ANALYSES IN THE FREQUENCY DOMAIN

The detection of wave excitations with periods T below 1.5 s and their attenuations for also small values of T is firstly presented on the example of the Mw 5.4 earthquake that occurred near Kraljevo on November 3, 2010 in Nina et al. 2020.

Examples of the increase and decrease of the Fourier amplitude for the two values of T showing the relevant excitation and attenuation, respectively, are given in Figure 4.

Very similar characteristics are obtained in the analyses of the wave excitations and attenuations in the ICV signal phase in the periods around four earthquakes (Nina et al. 2022). The only difference that can be observed in these cases is the attenuation of the waves at all periods relevant to the analysis (up to half the duration of the phase noise reduction in the analyzed cases).

4. SUMMARY

In this study, we present the pioneer research of the new types of potential earthquake precursors manifested as 1) the reduction of the noise of the VLF signal amplitude and phase starting several minutes or several tens of minutes before an earthquake, and 2) wave excitations and attenuations at short wave periods.

The main obtained results indicate the following:

- 90% of the analyzed earthquakes with the magnitude larger than 4 occurred in the periods when the amplitude noise reduction is recorded.

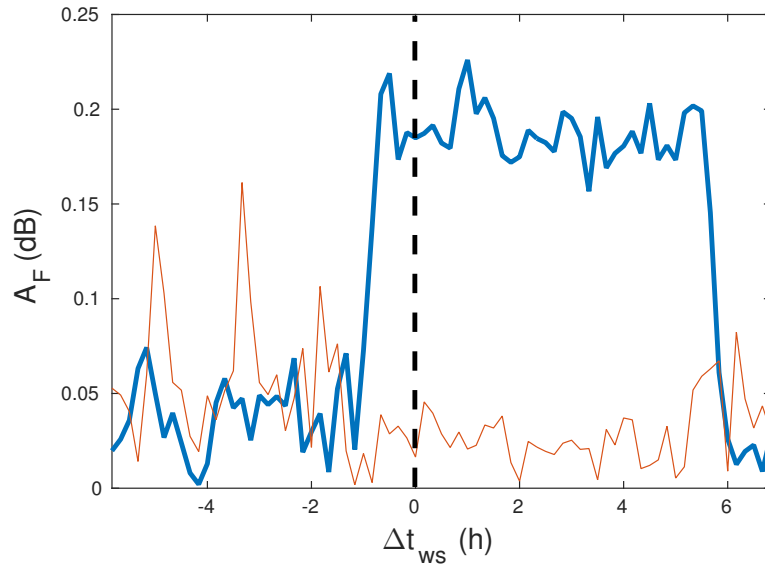


Figure 4: Examples of the Fourier amplitude time evolution A_F given for two wave periods for which excitations (blue line) and attenuations (red line) of waves with beginnings before the earthquake are detected. The vertical dashed line indicates the time of the earthquake, and the time difference from that time Δt_{ws} is given on the x-axis.

- Studies of phase characteristics in all four analyzed cases show that the reductions in its noise, as well as, wave excitation at periods below 1.5 s and attenuation of waves with other periods below several minutes, are also registered for this signal parameter. As in the case of the amplitude, all these changes last several tens of minutes and begin before the occurrence of the analyzed earthquakes.
- A reduction in the amplitude noise can be associated with more earthquakes. This can affect the possibility of detecting isolated significant reductions that can be associated with a particular earthquake. In other words, if several earthquakes are registered in a certain area in a short time interval, reductions in the amplitude noise do not have to occur individually for each earthquake, but one can last during the occurrence of several earthquakes. This means that during the seismically active period or in the case of several earthquakes in a small area that occur within a few hours, amplitude noise reductions are not precursors to individual earthquakes, but only to the first in a series, and that during the entire period of amplitude noise reduction, other earthquakes can be expected.

Finally, we would like to emphasize that, although the presented analyses refer to an insufficient number of earthquakes to be able to claim with certainty that the mentioned changes are precursors of earthquakes, the obtained results indicate a significant possibility that they are. For this reason, it is necessary to continue with this research. Also, it is important to emphasize that in addition to relevant studies, the development of new networks of VLF receivers as well as new software for automatic data analysis and alerting is necessary.

Acknowledgements

The author acknowledges funding provided by the Institute of Physics Belgrade through the support by the Ministry of Science, Technological Development and Innovation of the Republic of Serbia (contract no. 451-03-66/2024-03/1).

References

- Biagi, P.F., Castellana, L., Maggipinto, T., Piccolo, R., Minafra, A., Ermini, A., Martellucci, S., Bellecci, C., Perna, G., Capozzi, V., et al.: 2006, *Physics and Chemistry of the Earth, Parts A/B/C*, **31**, 403.
- Biagi, P.F., Maggipinto, T., Righetti, F., Loiacono, D., Schiavulli, L., Ligonzo, T., Ermini, A., Moldovan, I.A., Moldovan, A.S., Buyuksarac, A., et al.: 2011, *Natural Hazards and Earth System Sciences*, **11**, 333.
- Hayakawa, M., Horie, T., Muto, F., Kasahara, Y., Ohta, K., Liu, J.Y., Hobara, Y.: 2010, *SICE Journal of Control, Measurement, and System Integration*, **3**, 10.
- Maurya, A.K., Venkatesham, K., Tiwari, P., Vijaykumar, K., Singh, R. Singh, A.K., Ramesh, D.S.: 2016, *Journal of Geophysical Research: Space Physics*, **121**, 10403.
- Molchanov, O., Hayakawa, M., Oudoh, T., Kawai, E.: 1998, *Physics of the Earth and Planetary Interiors*, **105**, 239.
- Molchanov, O., Hayakawa, M., Miyaki, K.: 2001, *Adv. Polar Upper Atmos. Res.*, **15**, 146.
- Nina, A., Simić, S., Srećković, V., Popović, L.Č.: 2015, *Geophysical Research Letters*, **42**, 8250.
- Nina, A., Pulinets, S., Biagi, P., Nico, G., Mitrović, S., Radovanović, M., Popović, L.Č.: 2020, *Science of the Total Environment*, **710**, 136406.
- Nina, A., Biagi, P.F., Mitrović, S.T., Pulinets, S., Nico, G., Radovanović, M., Popović, L.Č.: 2021, *Atmosphere*, **12**, 444.
- Nina, A., Biagi, P.F., Pulinets, S., Nico, G., Mitrović, S.T., Čadež, V.M., Radovanović, M., Urošev, M., Popović, L.Č.: 2022, *Frontiers in Environmental Science*, 10.
- Ohya, H., Tsuchiya, F., Takishita, Y., Shinagawa, H., Nozaki, K., Shiokawa, K.: 2018, *Journal of Geophysical Research: Space Physics*, **123**, 5261.
- Rozhnoi, A., Solovieva, M., Molchanov, O., Hayakawa, M.: 2004, *Physics and Chemistry of the Earth, Parts A/B/C*, **29**, 589.
- Yamauchi, T., Maekawa, S., Horie, T., Hayakawa, M., Soloviev, O.: 2004, *Journal of Atmospheric and Solar-Terrestrial Physics*, **69**, 793.

**PROCEEDINGS OF THE XII SERBIAN-BULGARIAN
ASTRONOMICAL CONFERENCE**

Sokobanja, Serbia, September 25-29, 2020

**Eds. Luka Č. Popović, Vladimir A. Srećković,
Milan S. Dimitrijević and Anđelka Kovačević**



**БЕОГРАД
2020**

ACTIVITIES OF SERBIAN SCIENTISTS IN EUROPLANET

ALEKSANDRA NINA¹, MILAN RADOVANOVIĆ²,
LUKA Č. POPOVIĆ³, ANA ČERNOK⁴, BRATISLAV P. MARINKOVIĆ¹,
VLADIMIR A. SREĆKOVIĆ¹, ANĐELKA KOVAČEVIĆ⁵,
JELENA RADOVIĆ⁶, VLADAN ČELEBONOVIĆ¹,
IVANA MILIĆ ŽITNIK³, ZORAN MIJIĆ¹, NIKOLA VESELINOVIĆ¹,
ALEKSANDRA KOLARSKI⁷ and ALENA ZDRAVKOVIĆ⁸

¹*Institute of Physics Belgrade, University of Belgrade, Pregrevica 118, 11080 Belgrade, Serbia*

²*Geographical Institute Jovan Cvijić SASA, 11000 Belgrade, Serbia*

³*Astronomical Observatory, Volgina 7, 11060 Belgrade, Serbia*

⁴*Royal Ontario Museum, Center for the applied planetary mineralogy, Toronto, ON, Canada*

⁵*Department of astronomy, Faculty of Mathematics, University of Belgrade Studentski trg 16, 11000 Belgrade, Serbia*

⁶*Charles University, Faculty of Mathematics and Physics, Ke Karlovu 3, 12116, Prague 2*

⁷*Technical Faculty "Mihajlo Pupin", University of Novi Sad, 23000 Zrenjanin, Serbia*

⁸*Faculty of Mining and Geology, University of Belgrade, Belgrade*

E-mail: sandrast@ipb.ac.rs, bratislav.marinkovic@ipb.ac.rs, vlada@ipb.ac.rs, vladan@ipb.ac.rs, zoran.mijic@ipb.ac.rs, veselinovic@ipb.ac.rs

E-mail: m.radovanovic@gi.sanu.rs, lpopovic@aob.rs, ivana@aob.rs, acernok@rom.on.ca, andjelka@matf.bg.ac.rs, radovicj95@gmail.com, aleksandrakolarski@gmail.com, alena.zdravkovic@rgf.bg.ac.rs

Abstract. The Europlanet Society, an organization which promotes the advancement of European planetary science and related fields, has 10 hubs. The Serbian Europlanet Group (SEG) is included in the Europlanet South Eastern European Hub (ESEEH) and, currently, has 20 active scientists.

In this work, we present activities of SEG. Primarily, we describe two Europlanet workshops organized in the Petnica Science Center: "Geology and geophysics of the solar system bodies" and "Integrations of satellite and ground-based observations and multi-disciplinarity in research and prediction of different types of hazards in Solar system" that occurred in 2018 and 2019, respectively, and the Europlanet session during XII Serbian-

Bulgarian Astronomical Conference that occurred in Sokobanja 2020. In addition, we present other activities that were primarily aimed at connecting SEG members coming from six institutions as well as the promotion of the Europlanet and ESEEH organizations.

1. INTRODUCTION

The Europlanet society is an organization which promotes the European planetary science and related fields. Its aims are to support the development of planetary science at a national and regional level, particularly in countries and areas that are currently under-represented within the community, and early career researchers who establish their network within the Europlanet: the Europlanet Early Career (EPEC) network (<https://www.europlanet-society.org/early-careers-network/>).

Two Europlanet projects (the Europlanet 2020 Research Infrastructure and the Europlanet 2024 Research Infrastructure (RI)) are funded through the European Commission's Horizon 2020 programme. The first one, lasting 4 years, ended 2020, while the second one runs for four years from February 2020 until January 2024. The latest is led by the University of Kent, UK, and has 53 beneficiary institutions from 21 countries in Europe and around the world, with a further 44 affiliated partners. It provides free access to the world's largest collection of planetary simulation and analysis facilities, data services and tools, a ground-based observational network and programme of community support activities.

The Europlanet consists of 10 Regional Hubs:

- Benelux
- Central Europe: Austria, Czech Republic, Hungary, Poland, Slovenia and Slovakia
- France
- Germany
- Ireland and UK
- Italy
- Northern Europe: Denmark, Estonia, Finland, Iceland, Latvia, Lithuania, Norway and Sweden
- Southeast Europe: Bulgaria, Croatia, Cyprus, Greece, Romania, and Serbia
- Spain and Portugal
- Switzerland

As one can see, Serbia is one of, current six countries included in the South-east European Hub that is established in 2019.

More information about organization and activities of this society can be found at the website <https://www.europlanet-society.org/>.

2. SERBIAN EUROPLANET GROUP

The Serbian Europlanet Group (SEG) currently consists of 20 members from 6 institutions. Details of members and activities of SEG can be found at

<https://www.europlanet-society.org/europlanet-society/regional-hubs/southeast-europe/>.

The main activities of Serbian scientists in the Europlanet were:

- Organization of two Europlanet meetings and one session,
- Establishing of SEG webpage,
- Participations in the Europlanet science congresses and meetings,
- Participations in the Europlanet NA1 Expert Exchange Program, and
- Participations in the Europlanet committees.

In this paper we describe these activities and present scientific research of SEG members related to the Europlanet fields.

3. EUROPLANET MEETING ORGANIZATIONS

Serbian scientist organized two Europlanet workshops in Petica Science Center near Valjevo in Serbia:

- "Geology and geophysics of the solar system bodies" (24 June– 1 July, 2018), and
- "Integrations of satellite and ground-based observations and multidisciplinary in research and prediction of different types of hazards in the Solar system" (10-13 May, 2019),

and Europlanet session during the XII Serbian-Bulgarian Astronomical Conference (XII SBAC) in Sokobanja, Serbia 25-29 September, 2020.

3.1. Europlanet workshops

3.1.1. Workshop in Geology and Geophysics of the Solar System

The workshop took place in Petnica Science Center, Petnica, Serbia (23 June – 1 July 2018) and further details can be found at <http://petnica.rs/planetary2017>. It was designed to cover a wide range of topics related to the formation, structure and dynamics of the Solar System and aimed to attract students and young researchers of various backgrounds and of different levels of experience in the fields of planetary sciences and space exploration. The workshop attended 43 participants, of which 24 PhD, 13 master and 6 undergraduate students. They were from 19 different home countries, including 15 from Eastern Europe, 3 from Russia and 4 from Northern Afrika. Other participants came from as far as India, Australia, and USA. The scientific organizers of the workshop were Dr. Katarina Miljkovic (Curtin University, Australia), Dr. Ana Cernok (The Open University, UK) and Dr. Matija Cuk (SETI Institute, USA), supported by the local organizers Dusan Pavlovic (Petnica Science Centre, Serbia) and Andrea Rajsic, deputy (University of Belgrade, Serbia). In total, there were 14 lecturers (7 female and 7 male). Although there was only one lecturer from a Serbian institution (University of Bel-

grade), there were 5 other lecturers (including the organizers) who were originally from Serbia. This planetary sciences workshop was supported by the Europlanet 2020 RI NA1 (Innovation through Science Networking) Task 5 (Coordination of ground-based observations) and Europlanet 2020 RI NA2 (Impact through outreach and engagement).

3.1.2. Workshop in Hazards in the Solar system

This workshop was focused on integrations of satellite and ground-based observations and multidisciplinary in research and prediction of different types of hazards in the Solar system. The main of this meeting was connection of young researchers and scientists from under-represented countries, and experts in corresponding scientific fields. The organizer was the Geographical Institute "Jovan Cvijic" of Serbian Academy of Sciences and Arts. The chairs of the Scientific committee were Aleksandra Nina, Milan Radovanović from Serbia and Giovanni Nico from Italy. In this committee participated 11 scientists from 9 countries. Aleksandra Nina and Milan Radovanović were co-chairs, and Gorica Stanojević, Vladimir Čadež, Dejan Doljak, Vladimir Srećković and Dragoljub Štrbac were members of the Local Organizing Committee. The meeting attended 33 participants (of which 11 early career scientists) from 8 European countries: Bulgaria, Croatia, Greece, Hungary, Italy, Russia, Ukraine and Serbia. Their research fields relate to different theoretical and observation areas as well as to data sciences. In addition, two participants were from industry. This event was supported by the Europlanet 2020 RI NA1 - Innovation through Science Networking, Task 2: Scientific working groups (Europlanet 2020 RI has received funding from the European Union's Horizon 2020 research and innovation programme under grant No. 654208) and the Ministry for Education, Science and Technological Development of Republic of Serbia. More information about this event can be found at <http://www.gi.sanu.ac.rs/site/index.php/en/activities/conferences-organisation/998-hazards-sos>.

3.3. Europlanet session organised by SEG

Serbian scientists organized a Europlanet session during XII Serbian-Bulgarian Astronomical Conference (SBAS 12) that was held in Sokobanja from 25-29 of September 2020 (see Popović *et al.* 2020). Several lectures were held, a discussion, as well as the report of work of our group in the previous period was presented. At this Europlanet special session and during SBAC 12, possible directions for expanding cooperation were discussed with Bulgarian colleagues and also with colleagues from Europlanet Southeast HUB countries.

3.4. Participations in the Europlanet Science Congresses

Serbian scientists participated at the Europlanet Science Congresses (EPSC). The number of participants from Serbia is increasing. 7 scientists from Serbia participated in the EPSC-2020 and presented 3 lectures.



Figure 1: Participants of the workshop “Integrations of satellite and ground-based observations and multidisciplinary in research and prediction of different types of hazards in the Solar system” held in Petnica Science Center on 10-13 May, 2019 (photo: Veljko Vujičić). From left to right:

Upper row: Konstantinos Kourtidis (Greece) , Pál Gábor Vizi (Hungary), Jelena Petrović (Serbia), Anđelka Kovačević (Serbia), Duško Borka (Serbia), Gorica Stanojević (Serbia), Zorica Marinković (Serbia), Bratislav Marinković (Serbia) and Dejan Doljak (Serbia);

Middle row: Georgi Simeonov (Bulgaria), Inna Pulinets (Russia), Bozhidar Srebrov (Bulgaria), Dejan Vinković (Croatia), Yaroslav Vykyuk (Ukraine), Pier Francesco Biagi (Italy), Aleksandra Kolarski (Serbia), Lelica Popović (Serbia), Nikola Veselinović (Serbia) and Zoran Mijić (Serbia);

Bottom row: Predrag Jovanović (Serbia), Vesna Borka Jovanović (Serbia), Sergey Pulinets (Russia), Milan Radovanović (Serbia), Aleksandra Nina (Serbia), Vladimir Srećković (Serbia), Giovanni Nico (Italy), Milan S. Dimitrijević (Serbia), Luka Č. Popović (Serbia), Nataša Todorović (Serbia), Slavica Malinović-Milićević (Serbia) and Dragoljub Štrbac (Serbia).

3.5. Participations in the Regional Hubs Meetings

On the 4th and 5th June 2019, in Hotel Gellért, Budapest the Regional Hubs Meeting was organized by Melinda Dósa from Wigner RCP with the presence of the representatives from the Europlanet Society, Benelux Hub (represented by Ann Carine Vandaele, vice-president of Europlanet Society), Central European Hub, France, Italy, Northern European Hub, Spain & Portugal and Southeast European Hub, in total there were 23 researchers present. After the participants introduced themselves, the talk by Anita Heward, communication officer, was given on the Role of the hubs in the Europlanet Society and building a sustainable future from Europlanet 2020 RI. Following discussion was about the importance of widening in Europlanet. The focus of the meeting was on Planetary science – technology – industry synergy: aims and possibilities & Towards a strategy definition. As a result of this meeting the participation and formal enrollment in Europlanet Society by Serbian researchers has been substantially increased.

3.6. Participation in the Europlanet NA1 Expert Exchange Program

Supported through the Europlanet NA1 Expert Exchange Program, Dr. Alena Zdravković, curator of the Mineral and Rock Collection of the Faculty of Mining and Geology in Belgrade, Serbia, visited The Open University in October 2017 to work with Dr. Ana Cernok and other experts in meteorite science. During this visit, six meteorite samples from the Marquis de Mauroy collection of the Mineral and Rock Collection (01. Lancon, 02. Bath, 03. Powder Mill Creek, 04. Morrisyown Hamblen, 05. Merceditas and 06. Hex River, with numbers representing a handing number at the Open University) were used for polished thin- and thick-section preparation at the Open University, Milton Keynes, UK. Lancon and Bath are fragmented chondrite meteorites, Powder Mill Creek and Morrisyown Hamblen are mesosiderites, and Merceditas and Hex River are iron meteorites. Since the meteorite samples belong to a very old collection, dating from 1899, due to inadequate equipment and unprecise preparation facilities in the laboratory of Faculty of Mining and Geology in Belgrade, those kind of samples were never used for utilizing cut and polishing preparations. This visit aimed at meteorite thin-section preparation was an important milestone for this Serbian collection. It was the first such opportunity to open and present the collection to an international scientific community. More importantly, those are the only thin sections of meteorite samples available at Belgrade University, and will therefore serve as precious teaching material for students educating, as well as for initiating meteorite research.

3.7. Participations in the Europlanet committees

As a member of the Southeastern European Hub Committee, Aleksandra Nina participated in two teleconferences and one meeting of the Selection committee for Europlanet funding.

3.8. Other activities

Lecture during XIX Serbian astronomical conference (19 SAC) held at the Serbian Academy of Sciences and Arts in Belgrade, from October 13 – 17, 2020 (see Kovačević et al. 2020).

4. SOME STUDIES OF SEG MEMBERS

SEG members are scientists in four research fields: astronomy, geophysics, physics and geography. Here we present a few research that are in Europlanet areas.

4.1. Astronomy

4.1.1. The functional relation between mean motion resonances and Yarkovsky force on small eccentricities

We examined asteroid's motion with orbital eccentricity in the range (0.1, 0.2) across the 2-body mean motion resonance (MMRs) with Jupiter due to the Yarkovsky effect. We calculated time delays dtr caused by the resonance on the mobility of an asteroid with the Yarkovsky drift speed. We derived a functional relation that accurately describes dependence between the average time lead/lag dtr , the strength of the resonance SR , and the semimajor axis drift speed da/dt with asteroids' orbital eccentricities in the range (0.1, 0.2). We analysed average values of dtr using this functional relation comparing with obtained values of dtr from the numerical integrations. On the basis of the obtained results and analyses, we conclude that our equation can be used for the 2-body MMRs with strengths in the range $[1.3 \times 10^{-8}, 2.2 \times 10^{-4}]$, for Yarkovsky drift speeds in the range $[2.6 \times 10^{-4}, 2 \times 10^{-3}]$ au/Myr and for asteroids' orbital eccentricities in the range (0.1, 0.2) (Milić Žitnik 2020a).

4.1.2. The specific property of motion of resonant asteroids with very slow Yarkovsky drift speeds

We examined the specific characteristics of the motion of asteroids with very slow Yarkovsky drift speeds across the 2-body MMRs with Jupiter, whose strengths cover a wide range. It was found that the test asteroids with very small Yarkovsky drift speeds moved extremely rapidly across MMRs (order of magni-

tude 10^{-5} au/Myr or less). This result may indicate that, below a certain boundary value of da/dt asteroids typically move quickly across MMRs. From the obtained results, it is concluded that the boundary value of the Yarkovsky drift speed is 7×10^{-5} au/Myr (Milić Žitnik 2019).

4.1.3. The relationship between the 'limiting' Yarkovsky drift speed and asteroid families' Yarkovsky V -shape

We examined the relationship between asteroid families' V -shapes and the 'limiting' diameters in the $(a, 1/D)$ plane. Following the recently defined 'limiting' value of the Yarkovsky drift speed at 7×10^{-5} au/Myr, we decided to investigate the relation between the asteroid family Yarkovsky V -shape and the 'limiting' Yarkovsky drift speed of asteroid's semi-major axes. We have used the known scaling formula to calculate the Yarkovsky drift speed in order to determine the inner and outer 'limiting' diameters (for the inner and outer V -shape borders) from the 'limiting' Yarkovsky drift speed. The method was applied to 11 asteroid families of different taxonomic classes, origin type and age, located throughout the Main Belt. Our main conclusion is that the 'breakpoints' in changing V -shape of the very old asteroid families, crossed by relatively strong MMRs on both sides very close to the parent body, are exactly the inverse of 'limiting' diameters in the a versus $1/D$ plane. This result uncovers a novel interesting property of asteroid families' Yarkovsky V -shapes (Milić Žitnik 2020b).

4.1.4. Improvement of modelling of atmospheres using A&M data

We continued to work on topics of modelling various atmospheres (using new software packages and supercomputers) and diagnostic of the astrophysical (terrestrial and space) and laboratory plasma using A&M datasets e.g. rate coefficients, Stark broadening parameters, line profiles (the shape of atomic spectral lines in plasmas contains information on the plasma parameters, and can be used as a diagnostic tool), etc. Results which are of interest for Europlanet community are presented in our recently published papers (see e.g. Ignjatović *et al.* 2019, Srećković *et al.* 2020, Majlinger *et al.* 2020, Dimitrijević *et al.* 2020) as well as in database MolD <http://servo.aob.rs/mold> (Marinković *et al.* 2019) hosted on SerVO at AOB.

4.1.5. Correlation of solar wind parameters with cosmic rays observed with ground station

It has been well known for more than half a century that solar activity has a strong influence on galactic cosmic ray (GCR) flux reaching Earth (anti-correlation). Coronal mass ejections (CMEs) structure and shockwave can additionally modulate GCRs, which could result in a transient decrease in observed GCR intensity, known as Forbush decrease (FD). These FDs can be detected even

with ground muon detector (Savić et al. 2019). Variation of GCR can be analyzed correlating in situ measurement of the particles species present in solar wind with ground observations. Correlation between the 1-hour variations of GCR and several different one-hour averaged particle fluxes was found during FDs and it depends on energy of the particles of the solar wind as well as cut-off rigidities of secondary cosmic rays detectors on ground.

4.1.6. Habitability of exoplanets

Balbi, Hami and Kovačević (2020) present a new investigation of the habitability of the Milky Way bulge, that expands previous studies on the Galactic Habitable Zone. This work discusses existing knowledge on the abundance of planets in the bulge, metallicity and the possible frequency of rocky planets, orbital stability and encounters, and the possibility of planets around the central supermassive black hole. The paper focuses the two aspects that can present substantial differences with respect to the environment in the disk: (i) the ionizing radiation environment, due to the presence of the central black hole and to the highest rate of supernovae explosions and (ii) the efficiency of putative lithopanspermia mechanism for the diffusion of life between stellar systems. Authors devised analytical models of the star density in the bulge to provide estimates of the rate of catastrophic events and of the diffusion timescales for life over interstellar distances.

This article has been published as an invited contribution in the Special Issue "Frontiers of Astrobiology" edited by Manasvi Lingam.

Another concern for habitability is the presence of the supermassive black hole in the Galactic center, but also in nearby Active galactic nuclei, that could have resulted in a substantial flux of ionizing radiation during its past active phase, causing increased planetary atmospheric erosion and potentially harmful effects to surface life as shown by Wisłocka, Kovačević, Balbi (2019).

The goal of this paper is to improve our knowledge of the erosion of exoplanetary atmospheres through radiation from supermassive black holes (SMBHs) undergoing an active galactic nucleus (AGN) phase.

Authors extended the well-known energy-limited mass-loss model to include the case of radiation from AGNs. In the paper was calculated the possible atmospheric mass loss for 54 known exoplanets (of which 16 are hot Jupiters residing in the Galactic bulge and 38 are Earth-like planets, EPs) due to radiation from the Milky Way's (MW) central SMBH, Sagittarius A* (Sgr A*), and from a set of 107 220 AGNs generated using the 33 350 AGNs at $z < 0.5$ of the Sloan Digital Sky Survey database.

It was found that planets in the Galactic bulge might have lost up to several Earth atmospheres in mass during the AGN phase of Sgr A*, while the EPs are at a safe distance from Sgr A* (>7 kpc) and have not undergone any atmospheric erosion in their lifetimes. It was also found that the MW EPs might experience a mass loss up to 15 times the Mars atmosphere over a period of 50 Myr as the result of exposure to the cumulative extreme-UV flux FXUV from the AGNs up to z

= 0.5. This work was featured in famous *Forbes Magazine* in their section Innovation.

4.2. Geophysics

4.2.1. Investigation of a possible new type of lower ionosphere precursor of earthquakes

Analysis of the signal transmitted in Italy and received by the AbsPAL receiver in Belgrade in the period around the earthquake that occurred in the vicinity of Kraljevo on November 3, 2010 indicated a change in the amplitude of the signal less than an hour before this event. Although this change has not been reported in the literature, an additional study of several earthquakes indicates the existence of this change in other cases as well. The first study of this phenomenon is presented in Nina et al. (2020), and a broader statistical analysis is underway.

4.2.2. Modelling of solar X-ray flare influence on propagation of satellite signals

Due to the low electron density, the unperturbed D-region has practically no effect on the propagation of satellite signals. Therefore, it is generally not involved in modeling of signal propagation path or, if it is, its influence is given by analytical expressions based on observational data from higher altitudes. In Nina et al. (2020b), it is shown that during intense perturbations of this ionospheric layer due to the influence of solar X-ray flares (they do not perturb significantly higher ionospheric layers except when their intensity is very strong) it is necessary to include observational data for the D-region in modeling the propagation of satellite signals.

4.2.3. Satellite radar technique for atmospheric water vapor measurement and modelling effects of the ionospheric disturbances

Atmospheric water vapor measurement can be carried out in many different ways. One of the techniques for observing and measuring atmospheric water vapor is through satellite radars, precisely the Synthetic Aperture Radar (SAR) used and carried on the platform of many active satellites. In Radović (2020) are introduced four of such satellites and the water vapor modelling technique called SAR Interferometry is described as well. Along with the above mentioned in Radović (2020) it is demonstrated how neglecting the ionospheric disturbances that can occur during the satellite radar measurement of the water vapor can influence the modelling of certain parameters which are connected to the measured atmospheric water vapor.

4.2.4. Remote sensing of the atmospheric aerosol

Atmospheric aerosol plays one of the most important roles in climate changes and environmental issues through direct (scattering and absorption of solar and terrestrial radiation) and indirect (modification of cloud condensation nuclei through aerosol-cloud interaction) effects. In Mijić and Perišić (2019), study the relationship between satellite aerosol optical depth (AOD) measurements by Moderate Resolution Imaging Spectroradiometer (MODIS) and PM (Particulate Matter) concentrations data set from the Belgrade region was investigated. The preliminary results showed that AOD retrieved from a satellite sensor can be considered as a good proxy for ground observed PM mass concentrations. Within the EARLINET (European Aerosol Research Lidar Network) network a stand-alone lidar-based method (Papagiannopoulos et al. 2020) for detecting airborne hazards for aviation in near real time (NRT) is developed. In addition, Belgrade lidar station has been involved in ESA ADM-Aeolus mission (the first high-spectral resolution lidar in space) Cal/Val activity through validation of L2A products of aerosol and cloud profiles of backscatter, extinction and lidar-ratio.

4.2.5. Atmospheric disturbances due to severe stormy weather over Balkan region

Strong release of energy by atmospheric lightning discharges induced ionization changes along the propagation path of several Very Low Frequency (VLF) radio signals that had been received and recorded by Absolute Phase and Amplitude Logger (AbsPAL) system located in Belgrade (44.85° N, 20.38° E), at the Institute of Physics Belgrade, University of Belgrade, Serbia. Increased ionization is apparent in the perturbation of the signal amplitude and phase delay with respect to regular undisturbed ionospheric conditions. Integrated ground-based observations were performed with the aim to find coincidence and possible relationship between phenomena of VLF signal perturbations, optically documented Transient Luminous Events (TLEs) and documented lightning stroke events, during the stormy night of 27th-28th of May, 2009. The survey enclosed data from three independent sources: 1) VLF signal records from Belgrade Institute for Physics database, 2) video records of sprite events from ITALIAN METEOR and TLE NETWORK (I.M.T.N.) database and 3) detected lightning strokes from European Cooperation for Lightning Detection (EUCLID) network database. In most cases, the correspondence between VLF perturbations and CG strokes and on the other hand, VLF perturbations and TLE events, was found. In some cases the correspondence between all three phenomena was found (Kolarski 2019, 2020).

4.3. Physics

4.3.1. V. Čelebonović has been working on the problem of impact craters on the surfaces of solid planetary and satellite bodies. He showed that using standard solid state physics and measured properties of the craters, one can derive various parameters of the impactors. The calculations were checked on several known examples, and the agreement is reasonable.

4.3.2. The role of electron induced dissociation in the comet's coma and the findings during Rosetta spacecraft mission have been the subject of investigation published in Marinković *et al.* (2017). Data needs for modelling electron processes in cometary coma and their influence on the interpretation of the observed data by Rosetta instruments, have been discussed together with the currently available data and databases, where BEAMDB (Belgrade Electron/Atom(Molecule) DataBase - <http://servo.aob.rs/emol>) is given as an example (Marinković *et al.* 2019).

4.4. Geography

4.4.1. Our research was devoted to the determination of the causal relationship between the flow of particles that are coming from the Sun and the hurricanes Irma, Jose, and Katia. As a result of the preliminary analysis, using 12,274,264 linear models by parallel calculations, six of them were chosen as best. The identified lags were the basis for refinement of models with the artificial neural networks. Multilayer perceptrons with back propagation and recurrent LSTM have been chosen as commonly used artificial neural networks. Comparison of the accuracy of both linear and artificial neural networks results confirmed the adequacy of these models and made it possible to take into account the dynamics of the solar wind. Sensitivity analysis has shown that F10.7 has the greatest impact on the wind speed of the hurricanes. Despite low sensitivity of pressure to change the parameters of the solar wind, their strong fluctuations can cause a sharp decrease in pressure, and therefore the appearance of hurricanes (Vykyuk, *et al.* 2019).

4.4.2. Forest fires that occurred in Portugal on 18 June 2017 caused several tens of human casualties. The cause of their emergence, as well as many others that occurred in Western Europe at the same time remained unknown. Taking into account consequences, including loss of human lives and endangerment of ecosystem sustainability, discovering of the forest fires causes is the very significant question. The heliocentric hypothesis has indirectly been tested, according to which charged particles are a possible cause of forest fires. We must point out that it was not possible to verify whether in this specific case the particles by reaching the ground and burning the plant mass create the initial phase of the formation of the flame. Therefore, we have tried to determine whether during the critical period, *i.e.* from 15–19 June there is a certain statistical connection between certain parameters of the solar wind and meteorological elements. Based on the 2 hourly values of the charged particles flow, a correlation analysis was performed with

hourly values of individual meteorological elements including time lag at Monte Real station. The application of the Adaptive Neuro Fuzzy Inference System models has shown that there is a high degree of connection between the flow of protons and the analysed meteorological elements in Portugal. However, further verification of this hypothesis requires further laboratory testing (Radovanović et al. 2019).

5. CONCLUSION

In this paper we present activities of Serbian scientists in the Europlanet. We describe two Europlanet workshops organized in the Petnica Science Center: "Geology and geophysics of the solar system bodies" and "Integrations of satellite and ground-based observations and multi-disciplinarity in research and prediction of different types of hazards in Solar system" that occurred in 2018 and 2019, respectively, and the Europlanet session during XII Serbian-Bulgarian Astronomical Conference that occurred in Sokobanja 2020. In addition, we present other activities that were primarily aimed at connecting SEG members coming from six institutions as well as the promotion of the Europlanet and ESEEH organizations. Several studies relevant for the Europlanet research fields are presented in the second part of this paper.

Acknowledgments

This research is supported by the Europlanet. The authors acknowledge funding provided by the Institute of Physics Belgrade, Astronomical Observatory (the contract 451-03-68/2020-14/200002), Faculty of Mathematics University of Belgrade (the contract 451-03-68/2020-14/200104) through the grants by the Ministry of Education, Science, and Technological Development of the Republic of Serbia.

References

- Balbi A., Hami M., Kovačević A.: 2020, The Habitability of the Galactic Bulge, *Life*, 10, 132-145.
- Čelebonović V.: 2020, The origin of impact craters, some ideas. *Bulg. Astron. J*, 33, 21.
- Dimitrijević M. S., Srećković V. A., Ignjatović Lj. M., Marinković B. P.: 2021, The role of some collisional processes in AGNs: rate coefficients needed for modeling, *New Astronomy*, 84, 101529.
- Ignjatović Lj. M., Srećković V. A., Dimitrijević M. S.: 2019. The collisional atomic processes of Rydberg alkali atoms in geo-cosmical plasmas. *Monthly Notices of the Royal Astronomical Society*, 483(3), 4202-4209.
- Kolarski A.: 2019, *Atmospheric disturbances due to severe stormy weather*, Book of Abstracts, "Integrations of satellite and ground-based observations and multi-disciplinarity in research and prediction of different types of hazards in Solar system", Petnica, Science Center, May 10-13, 2019, Valjevo, Serbia, Geographical Institute "Jovan Cvijić" SASA, Belgrade, Serbia, p. 42.

- Kolarski A.: 2020, *Storm activity over Balkan region during May 2009*, Book of Abstracts, "XII Serbian-Bulgarian Astronomical Conference (XII SBAC)" September 25-29, 2020, Sokobanja, Serbia, Astronomical Observatory, Belgrade, Serbia, p. 75.
- Kovačević A., Kovačević Dojčinović A., Marčeta D., Onić D.: 2020, Book of abstracts XIX Serbian Astronomical Conference October 13 - 17, 2020, Belgrade, Serbia.
- Majlinger Z., Dimitrijević M. S., Srećković V. A.: 2020, Stark broadening of Co II spectral lines in hot stars and white dwarf spectra, *Monthly Notices of the Royal Astronomical Society*, 496(4), 5584-5590.
- Marinković B. P., Bredehöft J. H., Vujčić V., Jevremović D., Mason N. J.: 2017, Rosetta Mission: Electron Scattering Cross Sections - Data Needs and Coverage in BEAMDB Database, *Atoms*, 5(4), 46 [18pp].
- Marinković B. P., Srećković V. A., Vujčić V., Ivanović S., Uskoković N., Nešić M., Ignjatović Lj. M., Jevremović D., Dimitrijević M. S., Mason N. J.: 2019, BEAMDB and MOLD – Databases at the Serbian Virtual Observatory for collisional and radiative processes, *Atoms*, 7(1), 11 [14pp].
- Mijić Z., Perišić M.: 2019, *Comparison of Modis aerosol observations and ground-based PM measurement for the Belgrade region*, Book of abstracts, "Integrations of satellite and ground-based observations and multi-disciplinarity in research and prediction of different types of hazards in Solar system", pp.51-52, Petnica Science Center, 10-13 May, 2019, Geographical Institute "Jovan Cvijić" SASA, Belgrade.
- Milić Žitnik I.: 2019, The specific property of motion of resonant asteroids with very slow Yarkovsky drift speeds, *MNRAS*, 486, 2435-2439.
- Milić Žitnik I.: 2020a, The functional relation between mean motion resonances and the Yarkovsky force for small eccentricities, *MNRAS*, 498(3), 4465-4471.
- Milić Žitnik I.: 2020b, The relationship between the 'limiting' Yarkovsky drift speed and asteroid families' Yarkovsky V-shapes, *SAJ*, 200, 25-41.
- Nina A., Radovanović M., Srećković V. A.: 2019, Book of abstracts, "Integrations of satellite and ground-based observations and multi-disciplinarity in research and prediction of different types of hazards in Solar system", Petnica Science Center, 10-13 May, 2019, Geographical Institute "Jovan Cvijić" SASA, Belgrade.
- Nina A., Pulinets S., Biagi P. F., Nico G., Mitrović S. T., Radovanović M., Popović L. Č.: 2020a, *Sci. Total Environ.*, 710, 136406.
- Nina A., Nico G., Odalović O., Čadež M., V., Todorović Drakul M., Radovanović M., Popović L. Č.: 2020b, *IEEE Geosci. Remote Sens. Lett.*, 17(7), 1198 – 1202.
- Papagiannopoulos N., D'Amico G., Gialitaki A., Ajtai N., Alados-Arboledas L., Amodeo A., Amiridis V., Baars H., Balis D., Binietoglou I., Comerón A., Dionisi D., Falconieri A., Fréville P., Kampouri A., Mattis I., Mijić Z., Molero F., Papayannis A., Pappalardo G., Rodríguez-Gómez A., Solomos S., Mona L.: 2020, An EARLINET early warning system for atmospheric aerosol aviation hazards, *Atmos. Chem. Phys.*, 20, 10775–10789.
- Popović L. Č., Srećković V. A., Dimitrijević M. S., Kovačević A.: 2020, *Book of Abstracts*, "XII Serbian-Bulgarian Astronomical Conference (XII SBAC)" September 25 - 29, 2020, Sokobanja, Serbia, Astronomical Observatory, Belgrade, Serbia
- Radovanović M. M., Vyklyuk Y., Stevančević T. M., Milenković Đ. M., Jakovljević D., Petrović M., Malinović Miličević S., Vuković N., Vujko A., Yamashkin A., Sydor P., Vuković D., Škoda M.: 2019, Forest fires in Portugal — case study, 18 June 2017, *Thermal Science*, 23(1), 73-86.

- Radović J.: 2020, *Satellite radar technique for atmospheric water vapor measurement and modelling effects of the ionospheric disturbances*, Master thesis, Faculty of Physics, University of Belgrade, Serbia.
- Savić M., Veselinović N., Dragić A., Maletić D., Joković D., Banjanac R., Udovičić V.: 2019, Rigidity dependence of Forbush decreases in the energy region exceeding the sensitivity of neutron monitors, *Advances in Space Research*, 63(4), 1483-1489.
- Srećković V. A., Dimitrijević M. S., Ignjatović Lj. M.: 2020, The influence of collisional-ionization and recombination processes on spectral line shapes in stellar atmospheres and in the hydrogen clouds in broad-line region of AGNs, *Contrib. Astron. Obs. Skalnaté Pleso*, 50, 171-178.
- Vyklyuk Y, Radovanović M. M, Milovanović B, Milenković M, Petrović M, Doljak D, Malinovic Miličević S, Vuković N, Vujko A, Matsiuk N, Mukherjee S.: 2019, Space weather and hurricanes Irma, Jose and Katia, *Astrophys Space Sci*, 364, 154.
- Wisłocka A. M., Kovačević A. B., Balbi A.: 2019, Comparative analysis of the influence of Sgr A* and nearby active galactic nuclei on the mass loss of known exoplanets, *Astron. Astrophys.*, 624, A71 [17 pp].

M32



**30th Summer School and
International Symposium on
the Physics of Ionized Gases**

Šabac, Serbia,
August 24 -28, 2020

CONTRIBUTED PAPERS
&
**ABSTRACTS of INVITED LECTURES,
TOPICAL INVITED LECTURES and PROGRESS REPORTS**

Editors:
Luka Č. Popović, Duško Borka,
Dragana Ilić and Vladimir Srećković



**БЕОГРАД
2020**

PROPAGATION OF ELECTROMAGNETIC WAVES IN PERTURBED LOWER IONOSPHERIC PLASMA

A. NINA

*Institute of Physics Belgrade, University of Belgrade, Pregrevica 118,
11080 Belgrade, Serbia
E-mail sandrast@ipb.ac.rs*

Abstract. Remote sensing of the lower ionospheric plasma has scientific and practical applications. Namely, this atmospheric layer is continuously exposed to numerous astronomical and terrestrial events, and analyses of variations in its plasma parameters are important for detection of these events as well as modeling of influences of perturbed ionospheric plasma on the propagation of electromagnetic waves within it. Here, we present the recent research related to the lower ionospheric disturbances around the periods of natural disasters, and changes in propagation of satellite signals during D-region perturbations induced by solar X-ray flares. In the first part, attention is focused on research of possible ionospheric earthquake precursor visualized as reduction of the noise of the amplitude of a very low frequency radio signal used for monitoring the lower ionosphere (Nina et al. 2020). Analysis of importance of the perturbed D-region for satellite signal delay is subject of the second part of this study (Nina et al. 2019).

Acknowledgments. The author acknowledges funding provided by the Institute of Physics Belgrade, through the grant by the Ministry of Education, Science, and Technological Development of the Republic of Serbia.

References

- Nina, A., Nico, G., Odalović, O., Čadež, V. M., Todorović Drakul, N., Radovanović, M., Popović, L. Č.: 2019, *IEEE Geosci. Remote Sens. Lett.*, **1-5**, DOI: 10.1109/LGRS.2019.2941643
- Nina, A., Pulnits, S., Biagi, P. F., Nico, G., Mitrović, S. T., Radovanović, M., Popović, L. Č.: 2020, *Sci. Total Environ.*, **710**, 136406.

M33



All



ADVANCED SEARCH

Conferences > 2021 IEEE International Geosc...

Using VLF Time Series from the INFREP Network for the Study of Pre-Seismic Radio Anomalies

Publisher: IEEE

Cite This



Manilo Monaco ; Giovanni Nico ; Pier Francesco Biagi ; Anita Ermini ; Aleksandra Nina ; Mario G.C.A. Cimino All Authors

67 Full Text Views

Abstract

Document Sections

- 1. Introduction
- 2. INFREP Network
- 3. Methodology
- 4. Results

Authors

Figures

References

Keywords

Metrics

More Like This

Abstract:

This work presents an application of the Perceptually Important Points (PIP) technique for the analysis of VLF time series. The aim of the analysis is to detect anomalies... **View more**

Metadata

Abstract:

This work presents an application of the Perceptually Important Points (PIP) technique for the analysis of VLF time series. The aim of the analysis is to detect anomalies with respect to the normal variations of the data trends. Such anomalies could reveal possible radio precursors of the earthquake. Since 2009, several radio receivers have been installed throughout Europe in order to realize the INFREP European radio network for studying the VLF (10-50 kHz) and LF (150-300 kHz) radio precursors of earthquakes. The time series used for experiments was collected during the Dodecanese islands earthquakes ($MW = 5.6$ and $MW = 5.7$) occurred on January 30, 2020.

Published in: 2021 IEEE International Geoscience and Remote Sensing Symposium IGARSS

Date of Conference: 11-16 July 2021

DOI: 10.1109/IGARSS47720.2021.9553599

Date Added to IEEE Xplore: 12 October 2021

Publisher: IEEE

ISBN Information:

Electronic ISBN:978-1-6654-0369-6

USB ISBN:978-1-6654-0368-9

Print on Demand(PoD)

ISBN:978-1-6654-4762-1

Conference Location: Brussels, Belgium

ISSN Information:

Electronic ISSN: 2153-7003

Print on Demand(PoD) ISSN: 2153-6996

Manilo Monaco



Department of Information Engineering, University of Florence, Florence, Italy

Giovanni Nico

Institute of Applied Mathematics, National Research Council, Bari, Italy

Pier Francesco Biagi

Department of Physics, University of Bari, Bari, Italy

Anita Ermini

Department of Industrial Engineering, University of Tor Vergata, Rome, Italy

Aleksandra Nina

Institute of Physics Belgrade, University of Belgrade, Belgrade, Serbia

Mario G.C.A. Cimino

Department of Information Engineering, University of Pisa, Pisa, Italy

Gigliola Vaglini

Department of Information Engineering, University of Pisa, Pisa, Italy

Contents

1. Introduction

Different factors, such as meteorological conditions, solar bursts and geomagnetic activity, affect VLF/LF radio waves propagation. At the same time, variations of some parameters in the ground, in the atmosphere and in the ionosphere, occur during the preparatory phase of earthquakes. Such variations can produce disturbances in the propagation of previous signals along their radio paths, which are the radio precursors. Since 2009, several VLF/LF radio receivers have been installed throughout Europe in order to realize a European radio network for studying the VLF/LF radio precursors of earthquakes, called the INFREP network [1]-[4].

Authors

Manilo Monaco

Department of Information Engineering, University of Florence, Florence, Italy

Giovanni Nico

Institute of Applied Mathematics, National Research Council, Bari, Italy

Pier Francesco Biagi

Department of Physics, University of Bari, Bari, Italy

Anita Ermini

Department of Industrial Engineering, University of Tor Vergata, Rome, Italy

Aleksandra Nina

Institute of Physics Belgrade, University of Belgrade, Belgrade, Serbia

Mario G.C.A. Cimino

Department of Information Engineering, University of Pisa, Pisa, Italy

Gigliola Vaglini

Department of Information Engineering, University of Pisa, Pisa, Italy



USING VLF TIME SERIES FROM THE INFREP NETWORK FOR THE STUDY OF PRE-SEISMIC RADIO ANOMALIES

¹Manilo Monaco, ²Giovanni Nico, ³Pier Francesco Biagi, ⁴Anita Ermini, ⁵Aleksandra Nina, ⁶Mario G.C.A. Cimino, ⁶Gigliola Vaglini

¹Department of Information Engineering, University of Florence, Florence, Italy

²Institute of Applied Mathematics, National Research Council, Bari, Italy

³Department of Physics, University of Bari, Bari, Italy

⁴Department of Industrial Engineering, University of Tor Vergata, Rome, Italy

⁵Institute of Physics Belgrade, University of Belgrade, Belgrade, Serbia

⁶Department of Information Engineering, University of Pisa, Pisa, Italy

ABSTRACT

This work presents an application of the Perceptually Important Points (PIP) technique for the analysis of VLF time series. The aim of the analysis is to detect anomalies with respect to the normal variations of the data trends. Such anomalies could reveal possible radio precursors of the earthquake. Since 2009, several radio receivers have been installed throughout Europe in order to realize the INFREP European radio network for studying the VLF (10-50 kHz) and LF (150-300 kHz) radio precursors of earthquakes. The time series used for experiments was collected during the Dodecanese islands earthquakes (MW=5.6 and MW=5.7) occurred on January 30, 2020.

Index Terms— Ionosphere, VLF signal, Earthquake, Time series, Perceptually important points

1. INTRODUCTION

Different factors, such as meteorological conditions, solar bursts and geomagnetic activity, affect VLF/LF radio waves propagation. At the same time, variations of some parameters in the ground, in the atmosphere and in the ionosphere, occur during the preparatory phase of earthquakes. Such variations can produce disturbances in the propagation of the previous signals along their radio paths, which are the radio precursors. Since 2009, several VLF/LF radio receivers have been installed throughout Europe in order to realize a European radio network for studying the VLF/LF radio precursors of earthquakes, called the INFREP network [1-4].

At the end of January 2020 an intense seismic crisis occurred on Dodecanese islands; the main earthquakes (Mw = 5.6 and Mw = 5.7) happened on January 30. This seismic activity occurred in the "sensitive" zone of the INFREP receiver located in Cyprus.

The visual analysis of the raw radio data revealed clear pre-seismic anomalies on the three VLF radio signals (19.58, 20.27, 23.40 kHz) collected by the Cyprus receiver and crossing the zone of the previous seismic activity. The temporal trend of these VLF signals, from the beginning of January 24 till the end of January 31, 2020 is shown in Fig. 1. The analysis of daily day/night trend of these signals points out a clear anomaly during the night of January 29, 2020, one day before the occurrence of the main shocks of the seismic crisis.

In this work an approach based on computational intelligence is experimented for anomaly detection. In the first phase of the approach, a time series segmentation is carried out, to remove the noise and divide the series into discrete segments revealing the major dynamics. As a segmentation method, the Perceptually Important Points (PIP) technique is applied. The PIP is able to preserve the shape of the data [5][6]. In the second phase, the time series of PIPs is statistically compressed using the median for each time window. Finally, the set of median points is separated into low and high dynamics using the K-means clustering algorithm. As a consequence, anomalies are automatically located outside the generated clusters. The effectiveness of the approach has been experimented.

2. INFREP NETWORK

The International Network for Frontier Research on Earthquake Precursors (INFREP) network currently consists of nine receivers located as follows: one in Austria, Cyprus, Italy, Portugal and Serbia, two in Romania and Greece.

The radio receivers measure the intensity (electric field strength) of radio signals radiated by existing VLF-LF broadcasting stations in the bands VLF (20 - 80 kHz) and LF (150 - 300 kHz), with one-minute sampling rate. The location of the transmitters and receivers are available on the INFREP web site (www.infrep-network.eu).

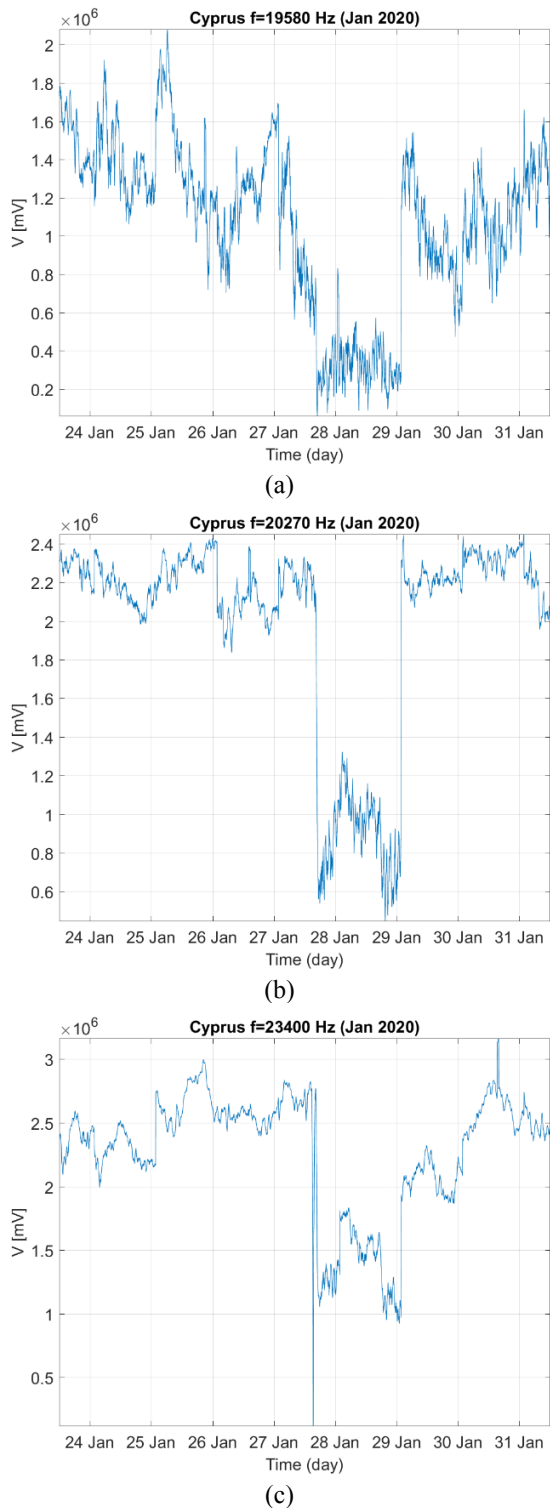


Fig. 1 - VLF signals collected by the Cyprus receiver from 24 to 30 January 2020: (a) 19.58 kHz, (b) 20.27 kHz and (c) 23.40 kHz. An anomalous decrease appears on 29 January.

The data collected are transmitted every day to the server. The different temporal trends of signals collected at the receivers are also available on the INFREP web site.

3. METHODOLOGY

The problem on how to represent a time series in multi-resolution is fundamental, because time series data is hard to manage in its original structure. Moreover, before processing and analyzing time series, computational intelligence applications is needed to reduce the high dimensionality of the data while retaining the information associated with important points. For example, financial analysis often depends on the shape of data and the significance of points to identify technical patterns. Most time series dimensionality reduction approaches, such as principal component analysis (PCA), discrete Fourier transform (DFT), discrete wavelet transform (DWT), piecewise aggregate approximation (PAA), often lose important data points and fail to retain the general shape of the time series after compression [7]. A method to dynamically segment time series into subsequences of unequal length, preserving the shape of the data, is based on choosing points that are important in the human vision identification process. These data points are known as Perceptually Important Points (PIPs). PIPs were initially introduced to exploit salient points from a price series and then have also been used to identify specific technical patterns [5]. In the context of data mining, PIPs have been used mainly for purposes of dimension reduction (time series representation) and for clustering reasons (see [8] and references therein).

Fig. 2 shows the workflow for detecting anomalies in VLF time series. Specifically, the input is made by the VLF time series $v_i(t)$, $i=1,2,3$, collected at three different frequencies. A windowing is then carried out, selecting the values that are enclosed in the current sliding interval, characterized by size τ and shift $\delta\tau$. Let $\bar{v}_{i,n}(t)$ be the resulting windowed signal extracted with the n -th window. A segmentation is applied, in which the input time-series is divided into a sequence of $\sigma-1$ linear segments, generating the time series $\tilde{v}_{i,n}(t)$. As an example, Fig. 3 shows 10 points located with a PIPs identification algorithm on a time series initially made up of 241 samples. Starting with the time series $\bar{v}_{i,n}(t)$, the algorithm allows to identify σ data points: $\tilde{v}_{i,n,1}, \dots, \tilde{v}_{i,n,\sigma}$ via a reordering process of points in the input data series by their importance. The first two PIPs found are the first and last points of $\bar{v}_{i,n}(t)$. In order to identify the next PIPs, the most classical algorithms calculate the distance between all remaining points and two adjacent PIPs, and label as the next PIP the one with the maximum distance. Three metrics are generally used as a distance, namely Euclidean distance (ED), perpendicular distance (PD) and vertical distance (VD) [8].

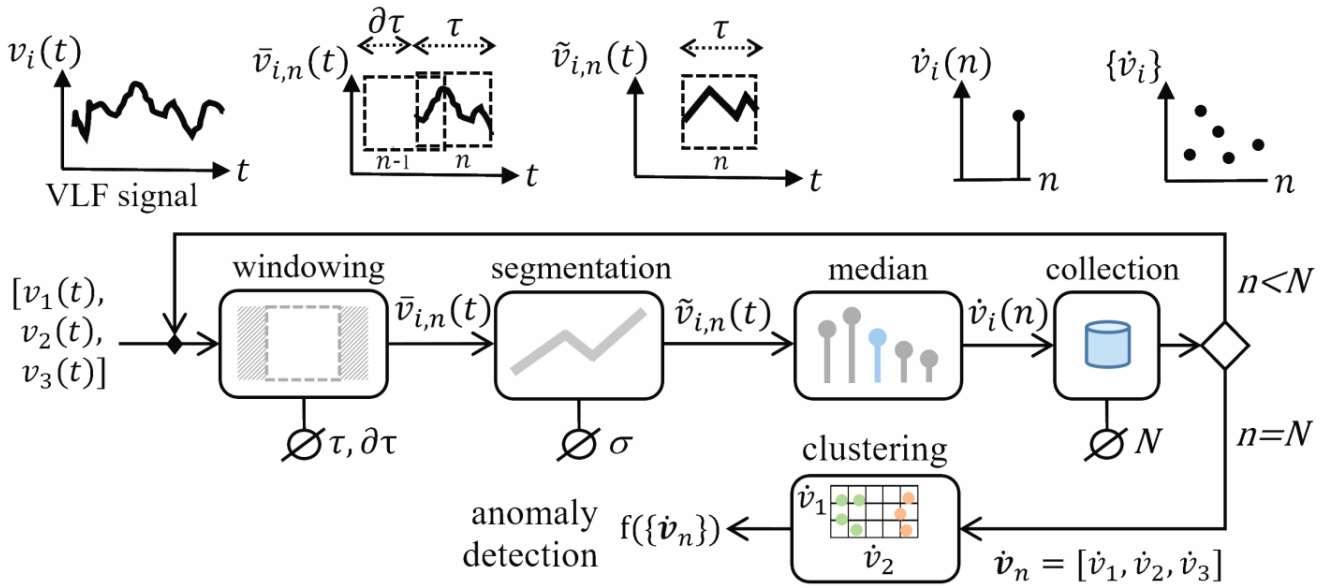


Fig. 2 –Workflow for detecting anomalies in VLF time series

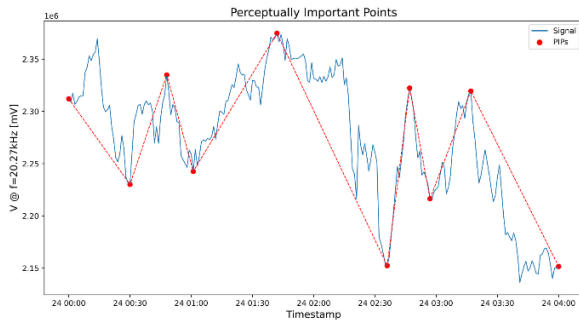


Fig. 3 - PIPs identified on a time series of 241 samples

In this paper, a particular approach has been used to locate the next PIPs. First, the slope of the line joining two PIPs is considered, to identify the main trend of the subsequence. Then, the next one or two (possibly) PIPs are determined, considering the maximum percentage retracement of the main trend. A retracement is defined as a temporary reversal of the trend of a time series. The PIPs identification process continues until σ points in $\bar{v}_{i,n}(t)$ are attached to a list. If $\sigma+1$ points are identified, then the first PIP is discarded as the least significant, since it is the oldest. Subsequently, the median of the σ PIPs $\tilde{v}_{i,n,1}, \dots, \tilde{v}_{i,n,\sigma}$ is computed. In the case in point, a vector of three medians is delivered for each n -th window, i.e., $\hat{v}_n = [\hat{v}_1(n), \hat{v}_2(n), \hat{v}_3(n)]$. Median vectors are continuously collected and stored. When N vectors are available, the anomaly detection process can start. In general, an anomaly detection approach is comprehensive if it is able to both detect and identify the emerging anomalies and characterize the essence of these

anomalies by visualizing the structures discovered within data in a way that is understandable to the end-user [9]. In this paper, the k -means clustering algorithm is used as a basis for anomaly detection and characterization. Indeed, clustering is an effective way to visualize and understand the variation of dynamics within data. Specifically, K -means is a fast, iterative algorithm that has been used in many clustering applications. Formally, it is a point-based clustering method that starts with the cluster centers (centroids) arranged at arbitrary positions and proceeds by moving at each step the centroids in order to minimize the clustering error. The method has the disadvantage of being sensitive to the initial positions of the centroids. Therefore, in order to obtain near optimal solutions using the k -means algorithm, several runs must be scheduled changing the initial positions of the cluster centers [10]. Actually, in our approach the clustering is iteratively applied on overlapping sliding windows of N points. As a consequence, after the first clustering, the subsequent ones can be initialized with the previous centroids.

In particular, the clustering is configured to detect 2 cluster: normal and anomalous vector. As a result, two types of analyses can be carried out. In the *offline analysis*, the colored clusters are represented in 3D space as animated frames (one frame per clustering). With this kind of analysis, the labeling generated by clusters exhibit the differences over time between normal and anomalous behaviors [11]. In the *online analysis*, an anomaly score is calculated, in order to detect anomalous events, i.e, a drift in the cluster composition. In our approach, the silhouette index [12] has been used as an aggregated value of anomaly. It measures how similar an object is to its own cluster (cohesion) compared to other clusters (separation). The silhouette index ranges from -1 to

+1: high values indicate that the point matches to its own cluster and not to the others. If most points have a high value, the clustering configuration is well defined. In contrast, overlapped clusters exhibit low or negative values. In our approach, as anomaly index the average silhouette index of all points is used to assess an unfolding anomaly.

An important aspect related to the horizontal scalability of this approach, is that different sources of information can be derived from VLF signals, originating a multimodal decision-making process. In order to keep the 3D visualization effective, the context-based clustering can be considered. The context is a sub-aspect of the domain, related to different factors or sub-regions of the monitored sources. A suitable architecture for this purpose is based on receptive fields [13].

4. RESULTS

In order to show the potential of the approach of Fig.2, in this section a pilot case is discussed. Specifically, the window size τ is set to 90 samples, the shift $\partial\tau$ is set to 1, and the segmentation σ is set to 30 PIPs. Fig. 4 shows the result of the cluster analysis. Here, the coordinates of each point are given by the signal amplitude at the three frequencies 19.58 kHz, 20.27 kHz and 23.40 kHz (see Fig. 1). In figure different colors are used to denote points referring to the eight days from January 24 to January 31. Two well separated clusters are clearly visible. The anomalous cluster is the group of points at bottom right, characterized by the green and red points grouped in the days 28 and 29 January.

The purpose of this paper is to introduce a novel analysis perspective of pre-seismic radio anomalies based on VLF time series. A small case study has been briefly discussed to show the potential of the approach. Further research is necessary to achieve significant results. To this aim, future work will focus on further experimentation and investigation, as well as on further integration with other methods.

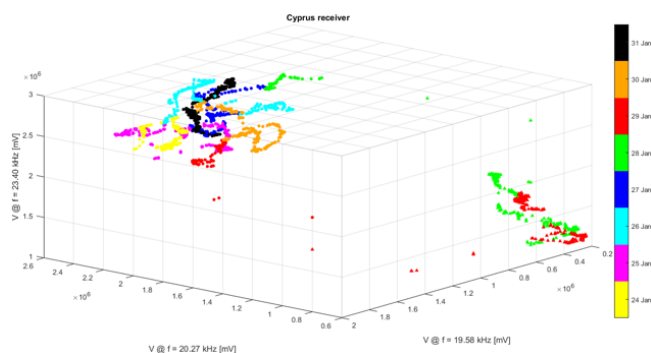


Fig. 4 - Cluster analysis applied to the VLF time series using k -means algorithm and two clusters

REFERENCES

[1] P.F. Biagi, T. Maggipinto, F. Righetti, D. Loiacono, L. Schiavulli, T. Ligonzo, A. Ermini, I.A. Moldovan, A.S.

Moldovan, A. Buyuksarac, M. Buyuksarac, H.G. Silva, M. Bezzeghoud and M.E. Contadakis, "The European VLF/LF radio network to search for earthquake precursors: setting up and natural/man-made disturbances," *Natural Hazards and Earth System Sciences*, Vol. 11(2), pp. 333-341, February 2011.

[2] P. Dolea, O. Cristea, P. V. Dascal, I. A. Moldovan and P.F. Biagi, "Aspects regarding the use of the INFREP network for identifying possible seismic precursors," *Physics and Chemistry of the Earth*, Vol. 85-86(1), pp. 34-43, 2015.

[3] A. Nina, S. Pulinets, P.F. Biagi, G. Nico, S.T. Mitrović, M. Radovanović, L.Č. Popović, "Variation in natural short-period ionospheric noise, and acoustic and gravity waves revealed by the amplitude analysis of a VLF radio signal on the occasion of the Kraljevo earthquake (Mw = 5.4)," *Science of The Total Environment*, Vol. 710, Paper N. 136406, March 2020.

[4] M.E. Contadakis, D.N. Arabelos, G.N. Vergos, C. Skeberis, T.D. Xenos, P.F. Biagi, E.M. Scordilis, "Ionospheric turbulence from TEC variations and VLF/LF transmitter signal observations before and during the destructive seismic activity of August and October 2016 in Central Italy," *Annals of Geophysics*, Vol. 63(5), PA546, 2020.

[5] T. Fu, F. Chung, R. Luk, C. Ng, "Stock Time Series Pattern Matching: Template-based vs. Rule-based Approaches," *Engineering Applications of Artificial Intelligence*, Elsevier, Vol. 20(3), pp. 347-364, April 2007.

[6] M.G.C.A. Cimino, F. Dalla Bona, P. Foglia, M. Monaco, C.A. Prete, G. Vaglini, "Stock price forecasting over adaptive timescale using supervised learning and receptive fields." International Conference on Mining Intelligence and Knowledge Exploration. Springer, Cham, 2018.

[7] T. Fu, F. Chung, R. Luk, C. Ng, "Representing Financial Time Series Based on Data Point Importance," *Engineering Applications of Artificial Intelligence*, Elsevier, Vol. 21(2), pp. 277-300, March 2008.

[8] P. E. Tsinaslanidis, D. Kugiumtzis, "A Prediction Scheme Using Perceptually Important Points and Dynamic Time Warping," *Expert Systems with Applications*, Elsevier, Vol. 41(15), pp. 6848-6860, 1 November 2014.

[9] H. Izakian, W. Pedrycz, "Anomaly Detection and Characterization in Spatial Time Series Data: a Cluster-Centric Approach," *IEEE Transactions in Fuzzy Systems*, IEEE, Vol. 22(6), pp. 1612-1624, 24 January 2014.

[10] A. Likas, N. Vlassis, J. J. Verbeek, "The Global K-Means Clustering Algorithm," *Pattern Recognition*, Elsevier, Vol. 36(2), pp. 451-461, February 2003.

[11] E. Keogh, J. Lin, A. Fu, "HOT SAX: Efficiently Finding the Most Unusual Time Series Subsequence," *In Proceedings of the Fifth IEEE International Conference on Data Mining*, IEEE, Houston, TX, USA, pp. 226-233, 27-30 November 2005.

[12] A. Dudek, "Silhouette Index as Clustering Evaluation Tool". In *Conference of the Section on Classification and Data Analysis of the Polish Statistical Association* pp. 19-33. 2019, Springer, Cham.

[13] M.G. Cimino, W. Pedrycz, B. Lazzerini, and F. Marcelloni, "Using multilayer perceptrons as receptive fields in the design of neural networks". *Neurocomputing*, 72(10-12), pp.2536-2548, 2009.



**30th Summer School and
International Symposium on
the Physics of Ionized Gases**

Šabac, Serbia,
August 24 -28, 2020

CONTRIBUTED PAPERS
&
**ABSTRACTS of INVITED LECTURES,
TOPICAL INVITED LECTURES and PROGRESS REPORTS**

Editors:
Luka Č. Popović, Duško Borka,
Dragana Ilić and Vladimir Srećković



**БЕОГРАД
2020**

**REDUCTION OF LOWER IONOSPHERE PLASMA FLUCTUATION –
NEW EARTHQUAKE PRECURSOR?**

A. NINA¹, S. PULINETS², P. F. BIAGI³, G. NICO⁴, S. T. MITROVIĆ⁵,
M. RADOVANOVIĆ⁶ and L. Č. POPOVIĆ⁷

¹*Institute of Physics Belgrade, University of Belgrade, Pregrevica 118,
11080 Belgrade, Serbia
E-mail sandrast@ipb.ac.rs*

²*Space Research Institute, Russian Academy of Sciences, Moscow, Russia
E-mail pulse1549@gmail.com*

³*Università di Bari, Physics Department, Bari, Italy
E-mail pf.biagi@gmail.com*

⁴*Istituto per le Applicazioni del Calcolo (IAC), Consiglio Nazionale delle Ricerche
(CNR), Bari, Italy
E-mail g.nico@ba.iac.cnr.it*

⁵*Novelic, Belgrade, Serbia
E-mail mitar027@beotel.net*

⁶*Geographical Institute Jovan Cvijić SASA, Belgrade 11000, Serbia
E-mail m.radovanovic@gi.sanu.ac.rs*

⁷*Astronomical Observatory, Volgina 7, 11060 Belgrade, Serbia
E-mail lpopovic@aob.rs*

Abstract. We present analysis of the lower ionosphere plasma short-term disturbances during period around the Kraljevo earthquake that occurred in Serbia on 3 November, 2010. Study is based on analysis of the short-term phase noise of the very low frequency (VLF) radio signal emitted by ICV transmitter located in Italy and received in Serbia. In this study we applied the procedure already described in recent research related to the signal amplitude in period around the considered event which point out the amplitude noise reduction as potential new ionospheric precursor of earthquakes. In this work, we process phase of ICV signal and results indicating phase noise reduction similar like those in the case of the amplitude shows that both signal characteristics, the amplitude and phase, can be used in future research of ionospheric plasma variations as possible precursors of earthquakes.

1. INTRODUCTION

As numerous studies performed during this and previous centuries show, variations in the ionospheric plasma can be considered as earthquake (EQ) precursors (Pulinets and Boyarchuk 2004). Observations of these variations are based on different satellite and ground-based techniques and their applications primarily depend on the considered altitude domain.

In this study we focused on the lower ionosphere and its remote sensing by the very low frequency (VLF) radio waves. This technique provides continuous information related to the waveguide within signal propagate and can be used for the lower ionosphere changes in different time scales. In addition, there are several networks of the VLF receivers which, in combination with numerous VLF transmitters located worldwide, allows monitoring large part of the lower ionosphere and detections of local disturbances like those possible connected with processes relevant for earthquakes. One of these networks, the International Network for Frontier Research on Earthquake Precursors (INFREP, Biagi et al. 2011), is located in the Europe. The data collected with its receivers located in seven European countries showed a typical variation in signal amplitudes several days before earthquake events (see for example Biagi et al. 2011). In addition, the recent research of the short-term amplitude noise shows that its reduction is recorded less than one hour before the Kraljevo EQ occurred in Serbia on 3 November, 2010.

In order to examine if these short-term ionospheric variations can be described also as changes in time evolution of another signal parameter, phase, in this work we analyze the phase noise of the VLF signal emitted by ICV transmitter located in Italy and received in Serbia (Grubor et al. 2005).

2. OBSERVATIONS AND SIGNAL PROCESSING

We analyze data obtained by remote sensing of the lower ionosphere during night-time when Kraljevo EQ occurred with 20.27 kHz signal emitted by ICV transmitter from Isola di Tavolara, Italy (40.92 N, 9.73 E) and received by the Absolute Phase and Amplitude Logger (AbsPAL) receiver located at the Institute of Physics Belgrade in Belgrade, Serbia (44.8 N, 20.4 E). The distance between the propagation path of this signal and the EQ epicentre is 126 km that is usually large for detection of long-term ionosphere variations before not so strong EQs like the considered one. However, better data sampling of 0.1 s provided in our observations allows us to analyze short-term signal changes which, as it is show in Nina et al. (2020), are recorded (in analysis of the signal amplitude) for several EQ events occurred more than 100 km from signal propagation path. Here we analyze the signal phase on the same way like in the previous research of the amplitude.

Changes of the phase noise is visualized in this analysis as variations in time evolution of phase deviation dP defined as difference between recorded, P , and

basic phase P_{base} (mean value of P within defined time bean around time t): $dP(t) = P(t) - P_{\text{base}}(t)$.

3. RESULTS AND DISCUSSIONS

Time evolution of phase deviation dP is shown in Fig. 1 where, in order to remove non-natural changes, we exclude values larger and smaller than 60° and -60° , respectively. As one can see, significant noise reduction is recorded less than one hour before the EQ event whose time occurrence is indicated with vertical dashed line.

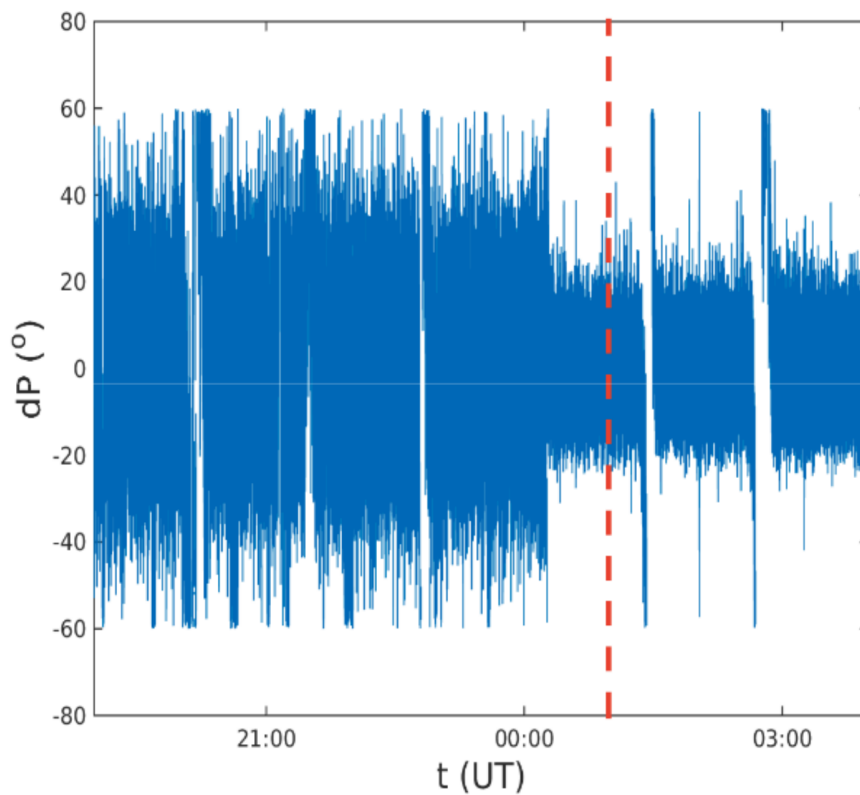


Figure 1: Time evolutions of phase deviation dP of the ICV signal in night-time of the Kraljevo earthquake. Vertical dashed line indicates the time of occurrence of the considered EQ.

In comparison with the amplitude noise, which has been analyzed in Nina et al. 2020, we can conclude that the noticed changes are very similar and that both analyses point out that reduction in lower ionosphere short-term fluctuations can be considered as new possible EQ precursor.

4. SUMMARY

In this paper, we analyzed time evolution of short-term fluctuations of the lower ionosphere plasma processing of data for the phase of the ICV signal recorded in Belgrade around time of Kraljevo EQ occurrence. As in the case of amplitude analysis, the obtained results show that significant reduction of phase noise started less than one hour before the EQ event.

Keeping in mind that this analysis presents a case study, confirmation that the recorded ionospheric changes can be a new type of ionosphere precursors of earthquakes requires statistical analyses. Here, we should point out that recent study shows reductions of amplitude noise are recorded before several other EQ events occurred during 3, 4 and 9 November, 2010 near the propagation path of the considered signal even in some cases of very weak EQ events. Although variations are visible for all of 4 EQs of magnitude greater than 4, studies with larger sample should be made before we can confirm the analyzed relationship and find its possible characteristics.

Acknowledgments

The authors acknowledge funding provided by the Institute of Physics Belgrade, the Astronomical Observatory (the contract 451-03-68/2020-14/200002), and project No 176001 through the grants by the Ministry of Education, Science, and Technological Development of the Republic of Serbia.

References

- Biagi, P. F., Maggipinto, T., Righetti, F., Loiacono, D., Schiavulli, L., Ligonzo, T., Ermini, A., Moldovan, I. A., Moldovan, A. S., Buyuksarac, A., Silva, H. G., Bezzeghoud, M., Contadakis, M. E.: 2011, *Nat. Hazards Earth Syst. Sci.*, **11**, 333.
- Nina, A., Pulinets, S., Biagi, P. F., Nico, G., Mitrović, S. T., Radovanović, M., Popović, L. Č.: 2020, *Sci. Total Environ.*, **710**, 136406.
- Pulinets, S., Boyarchuk, K.: 2004, *Ionospheric precursor of earthquakes*. Heidelberg: Springer.

IONOSPHERIC D-REGION INFLUENCE ON SAR SIGNAL PROPAGATION

J. RADOVIĆ¹, A. NINA² and G. NICO^{3,4}

¹*Faculty of Physics, University of Belgrade, 11000 Belgrade, Serbia
E-mail radovicj95@gmail.com*

²*Institute of Physics Belgrade, University of Belgrade, 11080 Belgrade, Serbia
E-mail sandrast@ipb.ac.rs*

³*Instituto per le Applicazioni del Calcolo (IAC), Consiglio Nazionale delle Ricerche (CNR), 70126 Bari, Italy
E-mail g.nico@ba.iac.cnr.it*

⁴*Department of Cartography and Geoinformatics, Institute of Earth Sciences, Saint Petersburg State University (SPSU), 199034 Saint Petersburg, Russia*

Abstract. Many studies have suggested that the signals used for satellite observations can be interrupted by the influence of a certain part of the ionosphere. In the course of our research we observed the perturbed D-region and its influence on the Synthetic Aperture Radar (SAR) signal delay that occurred as a consequence of the perturbation induced by a solar X-ray flare. To model the D-region plasma disturbance we analyse a very low frequency signal emitted by the DHO transmitter located in Germany and recorded in Serbia using Wait's model of the ionosphere. The results of the conducted research can help in further improvement and precision in modeling and measuring regarding SAR instruments.

1. INTRODUCTION

Satellite measurements and their contribution in observing and monitoring the planet Earth has become significant in many scientific fields. Some types of satellites only detect the radiation that comes from the Earth or outer space, whereas others are emitting their own signals which propagate towards the Earth's layers and reflect from some area.

In this paper we only consider the latter type of satellites. Satellites such as Sentinel-1, NASA-ISRO Synthetic Aperture Radar (NISAR) and Constellation of Small Satellites for Mediterranean basin Observations or (SkyMed) hold a

Synthetic Aperture Radar (SAR) which transmits microwave signals towards the Earth. SAR has the ability to operate at wavelengths not hindered by a cloud cover and acquires data over a specific place during day time or night time regardless the weather conditions. Synthetic aperture radar interferometry (InSAR) is a specific method of making observations which has many applications such as providing data for meteorological purposes. In order to acquire information about the target, the satellite emits the signal such as electromagnetic radiation of a certain frequency. During its path through the atmosphere the signal becomes prone to its current state. Moreover, one of the atmospheric layers which can significantly influence the signal and the layer which we contemplated is the ionosphere. Specifically, the D-region which when perturbed can cause a delay which cannot be neglected. The main reason for the signal deviation is the increased electron density which affects signal propagation path. The electron density has larger values in the upper part of the ionosphere, and its and the influences of the lower ionosphere above 100 km are taken into account in various models. However, during perturbations caused by solar X-ray flares the total electron content (TEC) present in the ionospheric D-region (60 km – 90 km) can affect the SAR signal propagation (see Nina et al. 2020). The main goal of this study is to show the example of how the perturbed D-region can affect the propagation of a SAR signal and calculate the D-region phase delay (P_D) for different frequencies and incident angles. To calculate the D-region electron density and TEC in the D-region (TEC_D), we process DHO VLF signal used for the lower ionosphere observations and Wait's model of the ionosphere (Wait and Spies 1946).

2. OBSERVATIONS AND MODELLING

The event which caused perturbations in the ionosphere considered in this paper is the X-ray solar flare which happened on 1 May, 2013. Data used for modeling are derived by the $23.4kHz$ VLF signal emitted by the DHO transmitter located in Rhauderfehn, Germany, and received at the Institute of Physics in Belgrade, Serbia, (Nina et al. 2020). Furthermore, the contemplated SAR frequencies are $f_1 = 1.257GHz$, $f_2 = 5.405GHz$ and $f_3 = 9.6 GHz$ used in NISAR mission, Sentinel-1 and COSMO-SkyMed, respectively. In order to calculate the influence that the D-region has on the signal propagation it is necessary to determine the total electron content present in the mentioned region (TEC_D) represented by

$$TEC_D = \int_{l_D} N_e dl_D, \quad (1)$$

where l_D represents the signal propagation path in the D-region and N_e represents the electron density. The vertical and temporal electron density distribution is calculated by equation (Tomson 1993):

$$N_e(h, t) = 1.43 \times 10^{13} e^{-\beta(t)H'(t)} e^{(\beta(t)-0.15)h}, \quad (2)$$

where temporal evolution of the “sharpness” β and signal reflection height H' are obtained as the best fit of the recorded and modeled amplitude and phase of the analyzed VLF signal using procedure based on Wait’s model of the ionosphere (Wait and Spies, 1964) explained in Grubor et al. 2008 and references therein. In order to calculate TEC, the D-region is divided into N_D horizontally uniform layers of thickness δH_D , each with its own electron density N_{ei} . Ultimately, equation used for calculating the phase delay P_D produced by the D-region can be expressed as (Nina et al. 2019):

$$P_D = \frac{C\delta H_D}{f^2} \sum_{i=1}^{N_D} \frac{N_{ei}n_i}{\sqrt{n_i^2 - (n_0 \sin(\theta_0))^2}} \quad (3)$$

where $C = 40.3$ and n_i is the refractive index in the layer i . θ_0 is the incident angle of the SAR signal in the D-region and f stands for the signal frequency.

3. RESULTS AND DISCUSSION

As mentioned above there are three different SAR frequencies from three different satellites. The first frequency is $f_1 = 1.257$ GHz (NISAR Earth-observing mission) and it belongs to L-band satellite frequency range (1-2 GHz). Furthermore, the second frequency is $f_2 = 5.405$ GHz, and it is taken from Sentinel-1 SAR instrument. This frequency is the part of the C-band range (4-8 GHz). Finally, the third frequency is from the X-band range (8-12 GHz). Its value is $f_3 = 9.6$ GHz, and it is taken from COSMO-SkyMed satellites.

We observed dependency of signal delay in the D-region at the moment when the D-region electron density maximum is attained which happened during disturbance induced by the analyzed solar X-ray flare. It is visible from Fig. 1 that the signal delay increases with incident angle for each of the three frequencies. Apparently the signal delay is the smallest for the highest frequency which is in our case f_3 and the highest for the lowest frequency which is f_1 frequency. It is worth noting that the value of P_D decreases as the value frequency is doubled, (see Eq. (3)) which implies that with increasing the frequency value one can get smaller ionospheric D-region influence on the signal.

The highest signal delay is obtained for the lowest, f_1 , frequency and it reaches $30mm$ which is not negligible for modeling and applications of SAR signals. Bearing in mind the above-mentioned one can conclude that the signal delay induced by the X-ray solar flare needs to be taken into account.

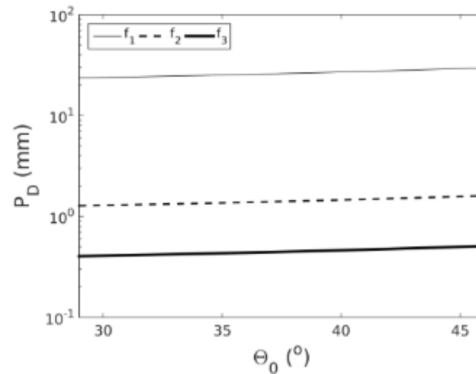


Figure 1: P_D dependence on the signal incident angle θ_0 in the range from 29° to 46° and SAR frequencies $f_1=1.257$ GHz, $f_2=5.405$ GHz and $f_3=9.6$ GHz.

3. SUMMARY

The final outcome of this work was to present the signal delay that occurs during the ionospheric D-region disturbance. This was achievable by using the proposed modeling methods and the collected data. The signal delay dependence on the signal incident angle was calculated for three different SAR signal frequencies. For each one of the frequencies the signal delay was observed, which indicates the influence that the perturbed D-region has. One prominent thing which needs to be pointed out is that the signal delay decreases with the SAR signal frequency. Furthermore, the increase of the signal incident angle results in higher signal delay. Acquired values of the signal delay, obtained during a not so strong solar flare, indicate that the D-region influence on the SAR signal propagation cannot be neglected.

Acknowledgments

The authors acknowledge funding provided by the Institute of Physics Belgrade, through the grant by the Ministry of Education, Science, and Technological Development of the Republic of Serbia.

References

- Grubor, P. D., Šulić, D. M., Žigman, V.: 2008, *Ann. Geophys.*, **26**, 1731–1740.
- Nina, A., Nico, G., Odalović, O., Čadež, V. M., Todorović Drakul, N., Radovanović, M., Popović, L. Č.: 2019, *IEEE Geosci. Remote Sens. Lett.*, **1-5**, DOI: 10.1109/LGRS.2019.2941643
- Tomson, N. R.: 1993, *J. Atmos. Terr. Phys.*, **55**, pp. 173–184
- Wait, J., R., Spies, K. P.: 1967, *Characteristics Earth-ionosphere waveguide for VLF radio waves*, Tech. Note 300, Nat. Bureau Standards, Boulder, CO, USA.



All



ADVANCED SEARCH

Conferences > 2020 XXXIIIrd General Assembl...

Studying the temporal variations of atmosphere physical properties at different spatial and temporal scales by VLF radio signals and space geodesy techniques

Publisher: IEEE

[Cite This](#)



PDF

G. Nico ; A. Nina ; P. Biagi ; R. Colella ; A. Ermini **All Authors** ...

51

Full
Text Views



Abstract

Document Sections

- 1 Introduction
- 2 Study of VLF Propagation In Atmosphere
- 3 INFREP Network
- 4 Effects of D-Region Disturbances On Space Geodesy Techniques
- 4 Conclusions

Authors

Figures

References

Keywords

Metrics

More Like This

Abstract:

In this work we study the physical variations of atmosphere at different spatial and temporal scales. The temporal evolution of the amplitude of Very Low Frequency (VLF) ... **View more**

▼ **Metadata**

Abstract:

In this work we study the physical variations of atmosphere at different spatial and temporal scales. The temporal evolution of the amplitude of Very Low Frequency (VLF) radio signals is used as a means to characterize the seasonal variations of atmosphere. The microwave-based GNSS and Synthetic Aperture radar (SAR) interferometry techniques are used as a means to characterize anomalies in the physical properties of atmosphere due to solar X-ray flares.

Published in: 2020 XXXIIIrd General Assembly and Scientific Symposium of the International Union of Radio Science

Date of Conference: 29 August 2020 - 05 September 2020

DOI: 10.23919/URSIGASS49373.2020.9232381

Publisher: IEEE

Date Added to IEEE Xplore: 20 October 2020

Conference Location: Rome, Italy

▼ **ISBN Information:**

Electronic ISBN:978-9-4639-6800-3

Print on Demand(PoD)

ISBN:978-1-7281-5690-3

^ **ISSN Information:**

Electronic ISSN: 2642-4339

Print on Demand(PoD) ISSN: 2640-7027

G. Nico
IAC-CNR, Bari, Italy

A. Nina
Institute of Physics Belgrade, University of Belgrade, Belgrade, Serbia

P. Biagi
Department of Physics, University of Bari, Bari, Italy

R. Colella
STIIMA-CNR, Bari, Italy

A. Ermini
Department of Industrial Engineering, University of Rome Tor Vergata, Rome, Italy

☰ **Contents**

1 Introduction

The propagation of radio and microwaves in the atmosphere can help to study the properties of atmosphere at different spatial scales. In this work we focus on two specific frequency ranges: 1) Very Low Frequency (VLF) radio waves and 2) microwaves used by GNSS and spaceborne SAR systems. The first frequency range has an important application in the study of many phenomena including earthquake precursors [1- 4], tropical cyclones [5], influence of solar X-ray flares [6], gamma ray bursts [7]. The second frequency range is of interest in space geodesy with applications spanning a large set of examples from geology to GNSS and SAR interferometry (InSAR) meteorology [8- 11]. In both cases, meteorological conditions, solar bursts and geomagnetic activity affect propagation of signals. The intensity of solar radiation is main driving factor shaping the spatial and temporal distribution of electron density and daytime/nighttime variations of ionosphere properties. During daytime, the ionosphere is divided in three layers: F, E





Studying the temporal variations of atmosphere physical properties at different spatial and temporal scales by VLF radio signals and space geodesy techniques

G. Nico ⁽¹⁾, A. Nina ⁽²⁾, P. Biagi ⁽³⁾, R. Colella⁽⁴⁾ and A. Ermini⁽⁵⁾

(1) IAC-CNR, Bari, Italy

(2) Institute of Physics Belgrade, University of Belgrade, Belgrade, Serbia

(3) Department of Physics, University of Bari, Bari, Italy

(4) STIIMA-CNR, Bari, Italy

(5) Department of Industrial Engineering, University of Rome Tor Vergata, Rome, Italy

Abstract

In this work we study the physical variations of atmosphere at different spatial and temporal scales. The temporal evolution of the amplitude of Very Low Frequency (VLF) radio signals is used as a means to characterize the seasonal variations of atmosphere. The microwave-based GNSS and Synthetic Aperture radar (SAR) interferometry techniques are used as a means to characterize anomalies in the physical properties of atmosphere due to solar X-ray flares.

1 Introduction

The propagation of radio and microwaves in the atmosphere can help to study the properties of atmosphere at different spatial scales. In this work we focus on two specific frequency ranges: 1) Very Low Frequency (VLF) radio waves and 2) microwaves used by GNSS and spaceborne SAR systems. The first frequency range has an important application in the study of many phenomena including earthquake precursors [1-4], tropical cyclones [5], influence of solar X-ray flares [6], gamma ray bursts [7]. The second frequency range is of interest in space geodesy with applications spanning a large set of examples from geology to GNSS and SAR interferometry (InSAR) meteorology [8-11]. In both cases, meteorological conditions, solar bursts and geomagnetic activity affect propagation of signals. The intensity of solar radiation is main driving factor shaping the spatial and temporal distribution of electron density and daytime/nighttime variations of ionosphere properties. During daytime, the ionosphere is divided in three layers: F, E and D. The electron density is the largest in F-region while it attains a minimal value in the D-region. In the nighttime the lowest layers of ionosphere dissipate their electron density due to decrease of incoming solar radiation and, consequently, have a lower ionization. Significant differences in ionosphere are also observed moving from the equator towards the polar region. These changes are a due to the morphology of the geomagnetic field. As a consequence, the ionosphere can be divided in equatorial, middle-latitude

and polar ionosphere. The knowledge of all these variations is important not only to describe the quiet ionosphere but also to study the influences of different geophysical and astrophysical events and processes on local plasma characteristics which can be quasi-permanent, periodical and sudden in time. For example, the influence of X-radiation on D-region perturbation is more important than on the upper ionosphere [12], while entering and penetration of charged particles depend on the geomagnetic field and their influence is the most important at polar region. In this study we describe a methodology to study the lower ionosphere based on the use of VLF waves. The dominant sources of ionization in the D regions are Lyman alpha radiation during quiet conditions. We will study this phenomenon using the VLF receivers of the INFREP, a European radio network of several VLF/LF radio receivers which have been installed throughout Europe since 2009 [1-3].

2 Study of VLF propagation in atmosphere

VLF radio signals have a frequency in the bands 20-80 kHz. As a good approximation, we can model the propagation of VLF radio signals as characterized by a ground-wave and a sky-wave propagation mode. The first one generates a radio signal that propagates in the channel ground-troposphere, while the second one generates a signal which propagates using the lower ionosphere as a reflector. Generally, due to the different conditions of the ionosphere, the VLF radio signals are less disturbed during the night than during the day. Figure 1 shows examples of intensities of VLF signals measured at the INFREP receivers. VLF signals recorded during night can be used to study propagation in the atmosphere quite undisturbed conditions. We use long time-series of VLF signals propagating during night to study possible seasonal effects due to temporal variations in the physical properties of troposphere. A graph theory approach is used to investigate the spatial correlation of the aforementioned effects at different receivers. A multivariate analysis is also applied

to identify common temporal changes observed at VLF receivers.

However, also during daytime disturbed VLF signals can provide useful information. During daytime the GOES satellite can be used to measure the temporal evolution of X-ray radiation from sun and so study the corresponding variation of physical properties in the D-region of ionosphere by means of VLF signals.

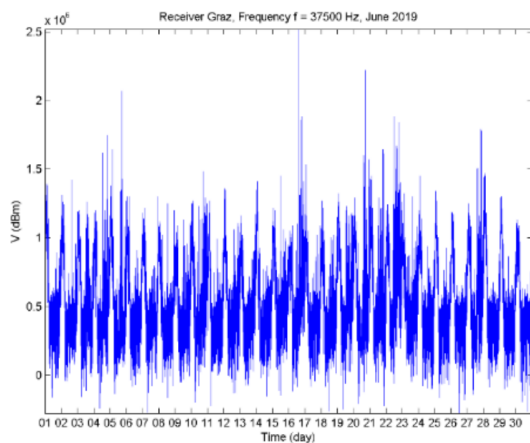


Figure 1. Amplitude of VLF signal vs time. The different behavior during day (lower amplitude) and night (higher amplitude) times can be observed.

3 INFREP network

The INFREP network currently consists of nine receivers located in different countries in southern Europe: two in Romania and Greece, one in Italy, Austria, Portugal, Cyprus and Serbia. The receivers measure the intensity of 10 radio signals in the band VLF (10-50 kHz) and LF (150-300 kHz), using a 1-min sampling rate. The transmitters are standard radio broadcasting (LF) or systems used for radio-navigation, time signal and mainly for military purpose (VLF). Figure 2 display the location of receivers and VLF/LF transmitters. More information about the activity of the INFREP network is available at the URL www.infrep-network.eu where interested users can register, download data and visualize results.

4 Effects of D-region disturbances on space geodesy techniques

The influences of upper ionospheric disturbances on space geodesy technique have been already studied. Here we focus on the influence of D-region disturbances on GNSS and SAR interferometry (InSAR) space geodesy techniques. We focus on this lower part of ionosphere as it can be studied by VLF signals and so it is a good case study for the aim of this paper. The most important influence on the mid latitude D-region coming from the Sun.



Figure 2. INFREP network: current set of the receivers and VLF/LF transmitters overlaid to a Google[®] map. More information is available at the URL www.infrep-network.eu.

However, effects of photons and charged particles are different. Namely, in addition to Ly- α radiation, increased X radiation during solar X-ray flares significantly disturb this atmospheric part, while ionization of the mid latitude D-region by charged particles is not so important.

Disturbances on GNSS and InSAR signals in the D-region perturbed by solar X-ray flares has been studied, recently [13]. Besides being a problem for these space geodesy techniques as it causes artifacts to be mitigated, it has been proposed to use InSAR images to study this phenomenon at a higher spatial resolution [14].

On the other side, variations in the D-region properties are primary studied at high latitude. In Figure 3 we present time evolutions of NRK and NAA VLF signals emitted in Iceland and the USA and received in Belgrade by the AWESOME (Atmospheric Weather Electromagnetic System for Observation Modeling and Education) receiver on 24 January, 2012 when charged particles rates increase due to a coronal mass ejection. In the three upper panels time evolution of electrons with energies larger than 0.8, 2 and 4 MeV are presented. As one can see, there is not clear similarity in these evolutions. Further work is needed to detect the effects of D-region perturbations in VLF radio signals and image them by means of SAR interferometry.

4 Conclusions

In this work we discussed the use of VLF radio signals, GNSS data and InSAR images as a means to study the temporal evolution of physical properties of atmosphere at different temporal and spatial scales. We focused on the D-region of ionosphere as it is the most affected during X-ray flares, the less modeled in GNSS and InSAR applications and the region where the synergy between VLF, GNSS and InSAR data is the most fruitful.

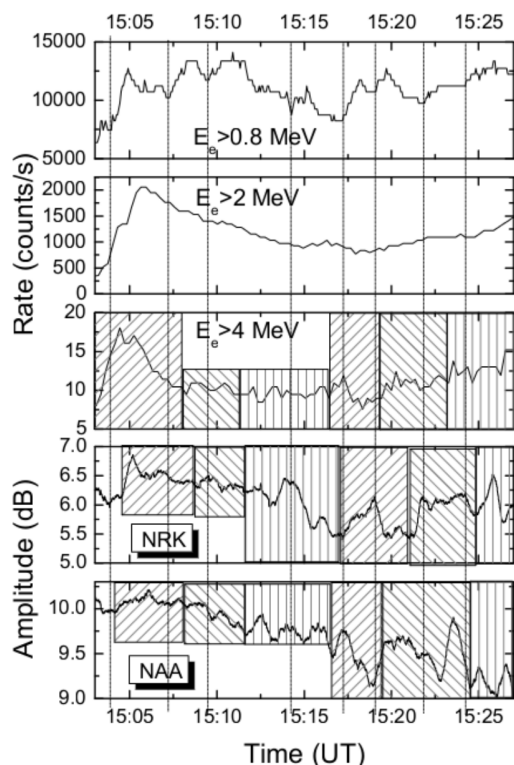


Figure 3. Time evolutions of detection rates of electrons with energies of 0.8, 2 and 4 MeV by the GOES satellite (upper three panels), and amplitudes of NRK and NAA VLF signals emitted in Iceland and the USA and received in Belgrade by the AWESOME receiver (bottom two panels) on 24 January, 2012.

6 Acknowledgements

This work was supported by the Ministero dell'Istruzione, dell'Università e della Ricerca (MIUR), Italy, under the project OT4CLIMA. This research is supported by the Ministry of Education, Science and Technological Development of the Republic of Serbia, under the projects 176002 and III44002.

7 References

1. P. F. Biagi, T. Maggipinto, F. Righetti, D. Loiacono, L. Schiavulli, T. Ligonzo, A. Ermini, I.A. Moldovan, A.S. Moldovan, A. Buyuksarac, M. Buyuksarac, H.G. Silva, M. Bezzeghoud and M.E. Contadakis, "The European VLF/LF radio network to search for earthquake precursors: setting up and natural/man-made disturbances," *Natural Hazards and Earth System Sciences*, **11**, 2, February 2011, pp. 333-341, doi: 10.5194/nhess-11-333-2011.
2. P. Dolea, O. Cristea, P. V. Dascal, I. A. Moldovan and P. F. Biagi, "Aspects regarding the use of the INFREP network for identifying possible seismic precursors," *Physics and Chemistry of the Earth*, 85-86, 1, June 2015, pp. 34-43, doi: 10.1016/j.pce.2015.05.010.

3. P. F. Biagi, R. Colella, L. Schiavulli, A. Ermini, M. Boudjada, H. Eichelberger, K. Schwingenschuh, K. Katzzis, M. E. Contadakis, C. Skeberis, I. A. Moldovan and M. Bezzeghoud, "The INFREP Network: Present Situation and Recent Results," *Open Journal of Earthquake Research*, **8**, 2, May 2019, Article ID: 92641, 15 pages, doi: 10.4236/ojer.2019.82007.
4. A. Nina, S. Pulinet, P. F. Biagi, G. Nico, S. T. Mitrović, M. Radovanović and L. Č. Popović, "Variation in natural short-period ionospheric noise, and acoustic and gravity waves revealed by the amplitude analysis of a VLF radio signal on the occasion of the Kraljevo earthquake (Mw = 5.4)," *Science of the Total Environment*, **710**, November 2020, pp. 136406, doi:10.1016/j.scitotenv.2019.136406.
5. A. Nina, M. M. Radovanović, B. M. Milovanović, A. B. Kovačević, J. B. Bajčetić and L. Č. Popović, "Low ionospheric reactions on tropical depressions prior hurricanes," *Advances in Space Research*, **60**(8), October 2017, pp. 1866-1877, doi:10.1016/j.asr.2017.05.024.
6. A. Nina, V. M. Čadež, J. Bajčetić, S.T. Mitrović and L. Č. Popović, "Analysis of the Relationship Between the Solar X-Ray Radiation Intensity and the D-Region Electron Density Using Satellite and Ground-Based Radio Data," *Solar Physics*, **293**(4), April 2018, Article 64, pp. 1-19, doi:10.1007/s11207-018-1279-4.
7. A. Nina, S. Simić, V. A. Srećković, and L. Č. Popović, "Detection of short-term response of the low ionosphere on gamma ray bursts," *Geophysical Research Letters*, **42**(19), September 2015, pp. 8250-8261, doi:10.1002/2015GL065726.
8. D. Massonnet, K. L. Feigl, "Radar interferometry and its application to changes in the Earth's surface", *Review of Geophysics*, **36**(4), November 1998, pp. 441-500, doi: 10.1029/97RG03139.
9. P. Mateus, J. Catalão, G. Nico, "Sentinel-1 interferometric SAR mapping of precipitable water vapor over a country-spanning area," *IEEE Transactions on Geoscience and Remote Sensing*, **55**(5), May 2017, pp. 2993-2999, doi: 10.1109/TGRS.2017.2658342.
10. P. Mateus, P. M. A. Miranda, G. Nico, J. Catalão, J. Pinto, R. Tomé, "Assimilating InSAR maps of water vapor to improve heavy rainfall forecasts: a case study with successive storms", *Journal of Geophysical Research: Atmospheres*, **123**(7), February 2018, pp. 3341-3355, doi: 10.1002/2017JD027472.
11. P. M. A. Miranda, P. Mateus, G. Nico, J. Catalão, R. Tomé, M. Nogueira, "InSAR meteorology: high resolution geodetic data can increase atmospheric predictability," *Geophysical Research Letters*, **46**(5), February 2019, pp. 2949-2955, doi:10.1029/2018GL081336.
12. D. M. Todorović, V. M. Čadež, J. Bajčetić, D. Blagojević, A. Nina, "Behaviour of electron content in the ionospheric D-region during solar X-ray flares", *Serbian Astronomical Journal*, **193**, 2016, pp. 11-18, doi:10.2298/SAJ160404006T.
13. A. Nina, G. Nico, O. Odalović, V. M. Čadež, Miljana T. Drakul, M. Radovanović, L. Č. Popović, "GNSS and SAR Signal Delay in Perturbed Ionospheric D-Region During Solar X-Ray Flares", *IEEE Geoscience and Remote*

Sensing Letters, (in press), October 2019, pp. 1-5,
doi:10.1109/LGRS.2019.2941643.

14. G. Nico, A. Nina, M. Radovanović, “Can spaceborne Synthetic Aperture Radar be useful for the mapping of ionospheric disturbances in the Arctic region?”, Proceedings of the International Conference “InterCarto InterGIS”, 2019, pp. 290-297, doi:10.35595/2414-9179-2019-1-25-290-297.

M34

MONITORING SOLAR FLARES AND GAMMA RAY BURSTS: MULTI-INSTRUMENTAL APPROACH INVESTIGATION

Aleksandra Kolarski[✉], Aleksandra Nina[✉], Vladimir A.
Srećković[✉], Filip Arnaut[✉]

*Institute of Physics Belgrade, University of Belgrade, Pregrevica 118,
11080 Belgrade, Serbia*

*E-mail: aleksandra.kolarski@ipb.ac.rs, vlada@ipb.ac.rs,
arnaut@ipb.ac.rs*

In this paper ionospheric phenomena were studied by utilization of VLF (Very Low Frequency radio signals, 3-30 kHz) technology for monitoring of lower ionospheric plasma response to driving agents originating both within our solar system, e.g. on Sun like solar flare (SF) events, and beyond our solar system, e.g. like gamma ray bursts (GRBs), with time span that encompasses period of several years. The data on X-ray fluxes measured by Geostationary Operational Environmental Satellites (GOES) were taken from NOAA National Centers for Environmental Information database, while data on GRBs were taken from Swift satellite database. VLF signal amplitude and phase data were monitored along multiple radio signal paths using network of VLF transmitters globally positioned worldwide and received in Belgrade, Serbia by BEL receiving system, covering mainly European subcontinent. Short-termed ionospheric perturbation associated with GRBs and relatively longer-lasting ionospheric perturbations associated with

SFs were compared in order to study similarities and differences in ionospheric plasma responses to these fundamentally different driving mechanisms.

Acknowledgments

The authors acknowledge the support from the Institute of Physics Belgrade which was made possible by grants from the Ministry of Science, Technological Development and Innovation of the Republic of Serbia.

EGU24-6001, updated on 17 Nov 2024

<https://doi.org/10.5194/egusphere-egu24-6001>

EGU General Assembly 2024

© Author(s) 2024. This work is distributed under the Creative Commons Attribution 4.0 License.



Investigation of VLF/LF electric field variations related to magnitude $M_w \geq 5.5$ earthquakes in the Mediterranean region for the year 2023

Hans Eichelberger¹, Mohammed Y. Boudjada¹, Konrad Schwingenschuh¹, Bruno P. Besser¹, Daniel Wolbang¹, Maria Solovieva², Pier F. Biagi³, Patrick H. M. Galopeau⁴, Ghulam Jaffer⁵, Christoph Schirninger⁶, Aleksandra Nina⁷, Gordana Jovanovic⁸, Giovanni Nico⁹, Manfred Stachel¹, Özer Aydogar¹, Cosima Muck¹, Josef Wilfinger¹, Irmgard Jernej¹, and Werner Magnes¹

¹Space Research Institute, Austrian Academy of Sciences, Graz, Austria (hue@oeaw.ac.at)

²Schmidt Institute of Physics of the Earth, RAS, Moscow, Russia

³Department of Physics, University of Bari, Bari, Italy

⁴LATMOS-CNRS, UVSQ Université Paris-Saclay, Guyancourt, France

⁵SpaSys, SnT – Interdisciplinary Centre for Security, Reliability and Trust, University of Luxembourg, Luxembourg

⁶Institute for Physics, University of Graz, Graz, Austria

⁷Institute of Physics Belgrade, Belgrade, Serbia

⁸Faculty of Science and Mathematics, University of Montenegro, Podgorica, Montenegro

⁹Institute of Applied Mathematics, Italian National Research Council, Bari, Italy

Strong natural hazards together with their societal impact are usually accompanied by multiple physical phenomena which can be an important information source about the underlying processes.

In this study we statistically analyze the lithosphere–atmosphere–ionosphere couplings of magnitude $M_w 5.5+$ earthquakes (EQs) in the year 2023 with the aid of sub-ionospheric VLF/LF radio links. The electric field amplitude and phase measurements with a temporal resolution of one second are from the seismo-electromagnetic receiver facility in Graz (GRZ), Austria (Galopeau et al., 2023), which is part of the INFREP network. The spatial extend of the study area has the range $[-10^\circ\text{E} \leq \text{longitude} \leq 40^\circ\text{E}]$ and $[20^\circ\text{N} \leq \text{latitude} \leq 50^\circ\text{N}]$, in total are 17 EQs according to the United States Geological Survey (USGS) data base, among them the Turkey–Syria EQs (main shocks $M_w 7.8$ and $M_w 7.5$) and the Morocco $M_w 6.8$ EQ. We apply the night-time amplitude method (Hayakawa et al., 2010) for all available paths, of particular importance are the transmitter links TBB (26.70 kHz, Bafa, Turkey), ITS (45.90 kHz, Niscemi, Sicily, Italy), and ICV (20.27 kHz, Tavolara, Italy). Relevant crossings are determined by the size of the Dobrovolsky–Bowman relationship (Dobrovolsky et al., 1979; Bowman et al., 1998).

A major finding is the statistically significant electric field variation of the TBB–GRZ link related to the Turkey–Syria EQ sequence. A physical interpretation is based on atmospheric gravity waves (AGWs) which could alter the E-layer in the lower ionosphere during nighttime and modulate the height of the waveguide cavity.

References:

Galopeau et al., A VLF/LF facility network for preseismic electromagnetic investigations, *Geosci. Instrum. Method. Data Syst.*, 12, 231–237, 2023, <https://doi.org/10.5194/gi-12-231-2023>

Dobrovolsky et al., Estimation of the size of earthquake preparation zones, *PAGEOPH* 117, 1025–1044, 1979, <https://doi.org/10.1007/BF00876083>

Bowman et al., An observational test of the critical earthquake concept, *JGR Solid Earth*, 103, B10, 24359–24372, 1998, <https://doi.org/10.1029/98JB00792>

Hayakawa et al., A statistical study on the correlation between lower ionospheric perturbations as seen by subionospheric VLF/LF propagation and earthquakes, *JGR Space Physics*, 115(A9), 09305, 2010, <https://doi.org/10.1029/2009JA015143>

International Conference on Recent Trends in Geoscience Research and Applications 2023

October 23–27, 2023, Belgrade, Serbia & virtual

BOOK OF ABSTRACTS AND CONTRIBUTED PAPERS

eosciRA23

Edited by Aleksandra Nina, Snežana Dragović, and Dejan Doljak



Belgrade
2023

NEW POTENTIAL EARTHQUAKE PRECURSOR: REDUCTION OF THE VLF SIGNAL NOISE

Aleksandra Nina^{1*}, Pier Francesco Biagi², Sergey Pulinetz³, Srđan Mitrović⁴, Giovanni Nico⁵, Luka Č. Popović^{6,7}

¹Institute of Physics Belgrade, University of Belgrade, Belgrade, Serbia; e-mail: sandrast@ipb.ac.rs

²University of Bari, Department of Physics, Bari, Italy; e-mail: pf.biagi@gmail.com

³Russian Academy of Sciences, Space Research Institute, Moscow, Russia; e-mail: pulse1549@gmail.com

⁴Novelic, Belgrade, Serbia; e-mail: mitar027@beotel.net

⁵Institute of Applied Mathematics (IAC), National Research Council of Italy (CNR), Bari, Italy; e-mail: giovanni.nico@gmail.com

⁶Astronomical Observatory, Belgrade, Serbia; e-mail: lpopovic@aob.ac.rs

⁷University of Belgrade, Faculty of Mathematics, Department of Astronomy, Belgrade, Serbia; e-mail: lpopovic@matf.bg.ac.rs.

In this study we present a possible new earthquake precursor which is manifested as the reduction of very low frequency (VLF) signal noise several minutes or tents of minutes before an event. We analyse changes in the signal amplitude and phase in both the time and frequency domains. The observed events are divided in the two groups related to the seismic activity in a localised area during a short time period. Namely, the results show that the intensive seismic activity can induce long-term reduction of the signal noise which includes more earthquakes with magnitude larger than four. We analyse the VLF signal emitted in Italy and received in Belgrade by the Absolute Phase and Amplitude Logger (AbsPAL) receiver located at the Institute of Physics Belgrade. In the first group of the earthquakes occurred when intensive seismic activity were not recorded, we analyse periods around the four events with magnitudes larger than four which occurred near Kraljevo (November 3 and 4, 2010), in the Tyrrhenian Sea (November 3, 2010), and in the Western Mediterranean Sea (November 9, 2010). In the second group, we present a study of the signal noise reduction during the period of intense seismic activity when almost 1,000 earthquakes occurred in Central Italy from October 25 to November 3, 2016.

Acknowledgements

The authors acknowledge funding provided by the Institute of Physics Belgrade and the Astronomical Observatory (the contract 451-03-47/2023-01/200002) through the grants by the Ministry of Science, Technological Development and Innovation of the Republic of Serbia.

*Corresponding author, e-mail: sandrast@ipb.ac.rs

ON THE DETECTION OF ANOMALIES IN TIME SERIES OF VLF SIGNALS RELATED TO SEISMIC ACTIVITY

Giovanni Nico^{1*}, Manilo Monaco², Pier Francesco Biagi³, Anita Ermini⁴, Aleksandra Nina⁵

¹Institute of Applied Mathematics, Italy's National Research Council, Bari, Italy; e-mail: giovanni.nico@cnr.it

²Italian Space Agency, Matera, Italy; e-mail: manilo.monaco@asi.it

³University of Bari, Department of Physics, Bari, Italy; e-mail: pf.biagi@gmail.com

⁴University of Tor Vergata, Department of Industrial Engineering, Rome, Italy; e-mail: ermini@uniroma2.it

⁵University of Belgrade, Institute of Physics Belgrade, Belgrade, Serbia; e-mail: sandrast@ipb.ac.rs

In this work we present an application of the Perceptually Important Points (PIP) technique for the analysis of time series of VLF signals collected during some earthquakes ($M_w = 5.0$ – 6.0) occurred in the European area. The aim of the analysis is to detect “anomalies” of VLF signals with respect to the normal variations of the data trends; these anomalies could reveal possible radio precursors of the earthquakes. Since 2009, several radio receivers have been installed throughout Europe in order to realize the INFREP European radio network for studying the VLF (10–60 kHz) and LF (150–300 kHz) radio precursors of earthquakes (Biagi et al., 2011), (Righetti et al., 2012). The analysis has been applied to earthquakes with $M_w \geq 5.0$ located inside the 5th Fresnel zone defined by each receiver and transmitter or inside a circle with a 300km radius around each receiver or transmitter. The time series which have been analyzed are referring to earthquakes that occurred on 2009-09-06 ($M_w = 5.6$), 2010-02-06 ($M_w = 5.0$), 2010-03-08 ($M_w = 6.0$), and 2020-01-30 ($M_w = 5.6$).

References

- Biagi, P. F., Maggipinto, T., Righetti, F., Loiacono, D., Schiavulli, L., Ligonzo, T., Ermini, A., Moldovan, I. A., Moldovan, A. S., Buyuksarac, A., Silva, H. G., Bezzeghoud, M., and Contadakis, M. E. (2011). The European VLF/LF radio network to search for earthquake precursors: setting up and natural/man-made disturbances. *Natural Hazards and Earth System Sciences*, 11(2), 333–341. <https://doi.org/10.5194/nhess-11-333-2011>
- Righetti, F., Biagi, P. F., Maggipinto, T., Schiavulli, L., Ligonzo, T., Ermini, A., Moldovan, I. A., Moldovan, A. S., Buyuksarac, A., Silva, H. G., Bezzeghoud, M., Contadakis, M. E., Arabelos, D. N., & Xenos, T. D. (2012). Wavelet analysis of the LF radio signals collected by the European VLF/LF network from July 2009 to April 2011. *Annals of Geophysics*, 55, 171–180. <https://ui.adsabs.harvard.edu/abs/2012AnGp...55..171R/abstract>

*Corresponding author, e-mail: giovanni.nico@cnr.it

IONOSPHERIC D-REGION DISTURBANCES INDUCED BY OUTER SPACE EVENTS

Aleksandra Nina^{1}, Vladimir Čadež², Luka Č. Popović^{2,3}*

¹Institute of Physics Belgrade, University of Belgrade, Belgrade, Serbia; e-mail: sandrast@ipb.ac.rs

²Astronomical Observatory, Belgrade, Serbia; e-mails: vcazez@aob.ac.rs, lpopovic@aob.rs

³University of Belgrade, Faculty of Mathematics, Department of Astronomy, Belgrade, Serbia; e-mail: lpopovic@matf.bg.ac.rs

In the ionospheric D-region, which extends within the altitude domain of about 50–90 km above the Earth's surface, there is a weakly ionized plasma whose characteristics are spatially and temporally variable. The main source of these variations is solar radiation, which causes both periodic variations due to changes in incoming solar hydrogen Ly α radiation (daily, seasonal, and variations during a solar cycle) as well as non-periodic changes due to sudden processes on the Sun (from these processes, solar X-ray flares have the most significant influence on the D-region). In addition to solar radiation, this ionospheric layer is influenced by galactic and extragalactic radiation from space as well as processes in the different terrestrial layers. Monitoring of the D-region is carried out using very low/low frequency (VLF/LF) radio signals. In this paper, we present the changes in the characteristics of VLF/LF signals that are detected by the receiver in Belgrade, Serbia, and induced by solar radiation and gamma ray bursts. In addition, we present the modeling of the periodic changes in the D-region electron density, as well as changes in this parameter during the influence of the solar X-ray flare.

Acknowledgements

The authors acknowledge funding provided by the Institute of Physics Belgrade, and the Astronomical Observatory (the contract 451-03-47/2023-01/200002) through the grants by the Ministry of Science, Technological Development and Innovation of the Republic of Serbia.

*Corresponding author, e-mail: sandrast@ipb.ac.rs

**XIII SERBIAN CONFERENCE
ON SPECTRAL LINE SHAPES IN
ASTROPHYSICS**

BOOK OF ABSTRACTS

**Eds. Anđelka Kovačević, Luka Č. Popović
and Saša Simić**



Astronomical Observatory, 2021

**Ly α RADIATION INFLUENCE TO IONOSPHERIC D-REGION:
QUIET IONOSPHERIC D-REGION (QIONDR) MODEL**

**A. Nina¹, G. Nico², S. T. Mitrović³, V. M. Čadež⁴, I. R. Milošević¹,
M. Radovanović^{5,6} and L. Č. Popović⁴**

¹*Institute of Physics Belgrade, University of Belgrade, 11080 Belgrade, Serbia*

²*Istituto per le Applicazioni del Calcolo (IAC), Consiglio Nazionale
delle Ricerche (CNR), 70126 Bari, Italy*

³*Novelic, 11000 Belgrade, Serbia*

⁴*Astronomical Observatory, Volgina 7, 11060 Belgrade, Serbia*

⁵*Geographical Institute "Jovan Cvijić" SASA, 11000 Belgrade, Serbia*

⁶*Institute of Sports, Tourism and Service, South Ural State University,
454080 Chelyabinsk, Russia*

E-mail: sandrast@ipb.ac.rs

We present the Quiet Ionospheric D-Region (QIonDR) model to analyze periodical variations of ionospheric parameters induced by changes in the incoming solar hydrogen Ly α line intensity. The model is based on data collected in the ionospheric D-region observations utilizing very low/low frequency (VLF/LF) signals. It provides: (1) a procedure for estimation of ionospheric parameters during quiet midday periods as a function of the daily sunspot number, related to the long-term variations during solar cycle, and the seasonal parameter, providing the seasonal variations, and (2) a procedure for determination of ionospheric parameters during the entire daytime using their midday values. QIonDR model is applied to VLF data acquired in Serbia that are related to the DHO and ICV signals emitted in Germany and Italy, respectively. We show time evolutions of the daytime Wait's parameters over the middle and low latitudes, and analytical expressions for midday parameters valid over a part of Europe.

Acknowledgment. The authors acknowledge funding provided by the Institute of Physics Belgrade, Geographical Institute "Jovan Cvijić" SASA and Astronomical Observatory (the contract 451-03-68/2020-14/200002) through the grants by the Ministry of Education, Science, and Technological Development of the Republic of Serbia.

**XII SERBIAN - BULGARIAN
ASTRONOMICAL
CONFERENCE 2020**

25 - 29. September 2020, Sokobanja, Serbia



BOOK OF ABSTRACTS

**Eds. Luka Č. Popović, Vladimir A. Srećković,
Milan S. Dimitrijević and Anđelka Kovačević**



BELGRADE, 2020

Poster paper

LOWER IONOSPHERE DISTURBANCES: THEIR POSSIBLE RELATIONSHIP WITH EARTHQUAKES, AND INFLUENCE ON SATELLITE SIGNALS

A. Nina¹, S. Pulinets², P. F. Biagi³, G. Nico⁴, V. M. Čadež⁵,
S. T. Mitrović⁶, M. Radovanović⁷ and L. Č. Popović⁵

¹*Institute of Physics Belgrade, University of Belgrade, Belgrade, Serbia*
²*Space Research Institute, Russian Academy of Sciences, Moscow, Russia*
³*Università di Bari, Physics Department, Bari, Italy*
⁴*Istituto per le Applicazioni del Calcolo (IAC), Consiglio Nazionale delle
Ricerche (CNR), Bari, Italy*
⁵*Astronomical Observatory, Belgrade, Serbia*
⁶*Novelic, Belgrade, Serbia*
⁷*Geographical Institute Jovan Cvijić SASA, Belgrade, Serbia*
E-mail: sandrast@ipb.ac.rs

We present two directions in recent studies of the lower ionosphere related to natural hazards and to the satellite signal propagation. In the first part, we focus attention on variations in the short-period noise amplitude within the time period around an earthquake onset which can be considered as a possible earthquake precursor (Nina, Pulinets et al. 2020). The second part contains detailed explanations about effects of the perturbed D-region on propagation of satellite signals utilized for positioning and Earth observation purposes (Nina, Nico et al. 2019).

Acknowledgments. The authors acknowledge funding provided by the Institute of Physics Belgrade, the Astronomical Observatory (the contract 451-03-68/2020-14/200002), and project No 176001 through the grants by the Ministry of Education, Science, and Technological Development of the Republic of Serbia.

References

- Nina, A., Nico, G., Odalović, O., Čadež, V. M., Todorović Drakul, N., Radovanović, M., Popović, L. Č.: 2019, *IEEE Geosci. Remote Sens. Lett.*, 1-5, DOI: 10.1109/LGRS.2019.2941643.
- Nina, A., Pulinets, S., Biagi, P. F., Nico, G., Mitrović, S. T., Radovanović, M., Popović, L. Č.: 2020, *Sci. Total Environ.*, **710**, 136406.



EGU21-7659, updated on 04 Mar 2021
<https://doi.org/10.5194/egusphere-egu21-7659>
EGU General Assembly 2021
© Author(s) 2021. This work is distributed under
the Creative Commons Attribution 4.0 License.



Ray paths of VLF/LF transmitter radio signals in the seismic Adriatic regions

Mohammed Y. Boudjada et al. ▶

We analyze the radio wave propagations of VLF/LF transmitter signals along subionospheric paths using two different reception systems localized in the Graz seismo-electromagnetic facility (15.43E,47.06N). Those systems allow the simultaneous detection of more than fifteen transmitter signals emitting in the northern (i.e. France, Germany and United Kingdom) and southern (i.e. Italy and Turkey) parts of Europe. In this work, we investigate the transmitter radio wave propagations associated with two earthquakes (EQs) which occurred, at two occasions, in nearly the same Croatian regions (Geo. Long.=16°E; Geo. Lat.=45°N). The first and second EQs happened, respectively, on March 22 and December 29, 2020, with magnitudes M_w equal to 5.4 and 6.4. The use of two complementary reception systems, i.e. INFREP (Biagi et al., Open Journal of Earthquake Research, 8, 2019) and UltraMSK (Schwingenschuh et al., Nat. Hazards Earth Syst. Sci., 11, 2011), and the proximity to the epicenters lead us to characterize the behavior of the transmitter signal amplitudes particularly above the Croatian seismic regions. We analyze the amplitude variation for a given transmitter frequency starting few weeks before the earthquakes occurrences. We discuss the observed anomalies in the transmitter signals which may be considered as precursors due to the ionospheric disturbances of the transmitter ray paths above the earthquakes preparation zones.

How to cite: Boudjada, M. Y., Eichelberger, H. U., Biagi, P. F., Schwingenschuh, K., Nico, G., Solovieva, M., Ermini, A., Moldovan, I. A., Contadakis, M. E., Nina, A., Katzis, K., Bezzeghoud, M., Lammer, H., Galopecau, P. H. M., Besser, B., and Aydogar, Ö.: Ray paths of VLF/LF transmitter radio signals in the seismic Adriatic regions, EGU General Assembly 2021, online, 19–30 Apr 2021, EGU21-7659, <https://doi.org/10.5194/egusphere-egu21-7659>, 2021.



Displays

Display file



EGU21-5154, updated on 04 Mar 2021
<https://doi.org/10.5194/egusphere-egu21-5154>
EGU General Assembly 2021
© Author(s) 2021. This work is distributed under
the Creative Commons Attribution 4.0 License.



Wavelet analysis applied on temporal data sets in order to reveal possible pre-seismic radio anomalies and comparison with the trend of the raw data

Giovanni Nico et al. ▶

Since 2009, several radio receivers have been installed throughout Europe in order to realize the INFREP European radio network for studying the VLF (10-50 kHz) and LF (150-300 kHz) radio precursors of earthquakes. Precursors can be related to “anomalies” in the night-time behavior of VLF signals. A suitable method of analysis is the use of the Wavelet spectra. Using the “Morlet function”, the Wavelet transform of a time signal is a complex series that can be usefully represented by its square amplitude, i.e. considering the so-called Wavelet power spectrum.

The power spectrum is a 2D diagram that, once properly normalized with respect to the power of the white noise, gives information on the strength and precise time of occurrence of the various Fourier components, which are present in the original time series. The main difference between the Wavelet power spectra and the Fourier power spectra for the time series is that the former identifies the frequency content along the operational time, which cannot be done with the latter. Anomalies are identified as regions of the Wavelet spectrogram characterized by a sudden increase in the power strength.

On January 30, 2020 an earthquake with $M_w = 6.0$ occurred in Dodecanese Islands. The results of the Wavelet analysis carried out on data collected some INFREP receivers is compared with the trends of the raw data. The time series from January 24, 2020 till January 31, 2020 was analyzed. The Wavelet spectrogram shows a peak corresponding to a period of 1 day on the days before January 30. This anomaly was found for signals transmitted at the frequencies 19,58 kHz, 20, 27 kHz, 23,40 kHz with an energy in the peak increasing from 19,58 kHz to 23,40 kHz. In particular, the signal at the frequency 19,58 kHz, shows a peak on January 29, while the frequencies 20,27 kHz and 23,40 kHz are characterized by a peak starting on January 28 and continuing to January 29. The results presented in this work shows the perspective use of the Wavelet spectrum analysis as an operational tool for the detection of anomalies in VLF and LF signal potentially related to EQ precursors.

How to cite: Nico, G., Biagi, P. F., Ermini, A., Boudjada, M. Y., Eichelberger, H. U., Katzis, K., Contadakis, M., Skeberis, C., Moldovan, I. A., Bezzeghoud, M., and Nina, A.: Wavelet analysis applied on temporal data sets in order to reveal possible pre-seismic radio anomalies and comparison with the trend of the raw data, EGU General Assembly 2021, online, 19–30 Apr 2021, EGU21-5154, <https://doi.org/10.5194/egusphere-egu21-5154>, 2021.



Displays

Display file



EGU21-1047
<https://doi.org/10.5194/egusphere-egu21-1047>
EGU General Assembly 2021
© Author(s) 2021. This work is distributed under
the Creative Commons Attribution 4.0 License.



A possible radio anomaly observed on the occasion of the $M_W=6.0$ earthquake occurred in Dodecanese islands at the end of January 2020

Pier Francesco Biagi et al. ▶

Since 2009, several VLF/LF radio receivers have been installed throughout Europe in order to realize a European radio network for studying the radio precursors of earthquakes, called the INFREP network. The current network has nine VLF/LF receiving stations, two in Romania and Greece, one in Italy, Austria, Portugal, Cyprus, and Serbia. The receivers can measure with 1 min sampling rate the intensity of 10 radio signals in the band VLF (10-50 kHz) and LF (150-300 kHz). The scope of existing transmitters is manifold, e.g. they are used for radio broadcast (LF), for radio-navigation or time signals and mainly for military purposes in the VLF range. At the end of January 2020 an intense seismic crisis occurred in Dodecanese Islands; the main event ($M_w=6.0$) occurred on January 30. This seismic activity occurred in the "sensitive" area of the INFREP network. The analysis of the data collected by INFREP receivers has revealed clear anomalies in three VLF signals appearing some days before the main earthquake. The anomalies appear in the trends collected by the Cyprus receiver and the epicenter is inside the 5th Fresnel ellipses defined by transmitters-receiver. Here we report the data analysis and we present in detail the anomalies. The possibility that they are precursors of the quoted earthquake seems significant.

Biagi, P.F., Colella, R., Schiavulli, L., Ermini, A., Boudjada, M., Eichelberger, H., Schwingenschuh, K., Katzis, K., Contadakis, M.E., Skeberis, C., Moldovan, I.A. and Bezzeghoud, M. (2019) The INFREP Network: Present Situation and Recent Results. *Open Journal of Earthquake Research*, 8, 101-115. <https://doi.org/10.4236/ojer.2019.82007>

How to cite: Biagi, P. F., Ermini, A., Boudjada, M., Eichelberger, H., Katzis, K., Contadakis, M., Skeberis, C., Moldovan, I., Bezzeghoud, M., Nina, A., and Nico, G.: A possible radio anomaly observed on the occasion of the $M_W=6.0$ earthquake occurred in Dodecanese islands at the end of January 2020, EGU General Assembly 2021, online, 19–30 Apr 2021, EGU21-1047, <https://doi.org/10.5194/egusphere-egu21-1047>, 2021.



Displays

Display file



EGU2020-9197
<https://doi.org/10.5194/egusphere-egu2020-9197>
EGU General Assembly 2020
© Author(s) 2021. This work is distributed under
the Creative Commons Attribution 4.0 License.



On the characterization of VLF radio signal propagation in atmosphere in quite solar conditions

Giovanni Nico et al. ▶

In this work we use Very Low Frequency (VLF) radio signals, having a frequency in the bands 20-80 kHz, to study the VLF signal propagation in the atmosphere quite undisturbed conditions by selecting the signals recorded during night. As a good approximation, we can model the propagation of VLF radio signals as characterized by a ground-wave and a sky-wave propagation mode. The first one generates a radio signal that propagates in the channel ground-troposphere, while the second one generates a signal which propagates using the lower ionosphere as a reflector. The VLF receivers of the INFREP (European Network of Electromagnetic Radiation) network are used. These receivers have been installed since 2009 mainly in southern and central Europe and currently the INFREP network consists of 9 receivers. A 1-minute sampling interval is used to record the amplitude of VLF signals. Long time-series of VLF signals propagating during night are extracted from recorded signals to study possible seasonal effects due to temporal variations in the physical properties of troposphere. A graph theory approach is used to investigate the spatial correlation of the aforementioned effects at different receivers. A multivariate analysis is also applied to identify common temporal changes observed at VLF receivers.

This work was supported by the Ministero dell'Istruzione, dell'Università e della Ricerca (MIUR), Italy, under the project OT4CLIMA. This research is supported by the Ministry of Education, Science and Technological Development of the Republic of Serbia, under the projects 176002 and III44002.

How to cite: Nico, G., Nina, A., Ermini, A., and Biagi, P.: On the characterization of VLF radio signal propagation in atmosphere in quite solar conditions, EGU General Assembly 2020, Online, 4–8 May 2020, EGU2020-9197, <https://doi.org/10.5194/egusphere-egu2020-9197>, 2020





EGU2020-9200
<https://doi.org/10.5194/egusphere-egu2020-9200>
EGU General Assembly 2020
© Author(s) 2021. This work is distributed under
the Creative Commons Attribution 4.0 License.



Variations revealed by INFREP Radio Network in correspondence of six earthquakes with M_w greater than 5.0 occurred in the Balkan Peninsula and Adriatic Sea on 26 and 27 November, 2019

Pier Francesco Biagi et al. ▶

In this work we analyse variations in VLF/LF radio signal amplitudes recorded by the INFREP network in the period 16 November – 6 December, 2019 characterized by very intensive seismic activities in the Balkan peninsula, Crete, and Adriatic, Aegean and Black seas. Namely, 38 earthquakes with magnitude greater than 4.0 occurred in this area during the noticed period; the most intensive of them occurred on 26 and 27 November: three events in Albania ($M_w= 6.4, 5.3, 5.1$), one in Crete ($M_w= 6$), one in Bosnia and Herzegovina ($M_w= 5.4$) and two in Adriatic sea ($M_w= 5.4, 5.3$). We study both long- and short- term variations that are already recorded in earlier studies. The long-term variations relate to changes in the amplitude intensities in periods of several days and their existence is shown in many previous studies. The recent analyses also indicate short-term variations in signal amplitude noises started about several tents of minutes before the earthquake (Nina et al. 2020). In this work, we analyse different areas using INFREP network, which allow us to study local changes in the atmosphere. In order to examine possible precursors we considered longer time started and ended 10 days before and after the most intensive of the considered earthquakes, respectively.

This research is supported by the Ministry of Education, Science and Technological Development of the Republic of Serbia, under the projects 176002 and III44002.

References

Nina, A., S. Pulinet, P. F. Biagi, G. Nico, S. T. Mitrović, M. Radovanović and L. Č. Popović. Science of the Total Environment 710 (2020) 136406

How to cite: Biagi, P. F., Nina, A., Ermini, A., and Nico, G.: Variations revealed by INFREP Radio Network in correspondence of six earthquakes with M_w greater than 5.0 occurred in the Balkan Peninsula and Adriatic Sea on 26 and 27 November, 2019, EGU General Assembly 2020, Online, 4–8 May 2020, EGU2020-9200, <https://doi.org/10.5194/egusphere-egu2020-9200>, 2020



M36

International Conference on Recent Trends in Geoscience Research and Applications 2023

October 23–27, 2023, Belgrade, Serbia & virtual

BOOK OF ABSTRACTS AND CONTRIBUTED PAPERS



Edited by Aleksandra Nina, Snežana Dragović, and Dejan Doljak



Belgrade
2023

Scientific Committee

Aleksandra Nina, Serbia, chair
Snežana Dragović, Serbia, co-chair
Ivan Lizaga, Belgium, co-chair
Oleg Odalović, Serbia, co-chair

Pier Francesco Biagi, Italy
Jozsef Bor, Hungary
Ranko Dragović, Serbia
Slobodan Đorđević, UK
Hans Eichelberger, Austria
Emil Fulajtar, Austria
Boško Gajić, Serbia
Maria Gritsevich, Finland
Pavlos Kassomenos, Greece
Konstantinos Kourtidis, Greece

Slavica Malinović-Milićević, Serbia
Ana Milanović Pešić, Serbia
Boško Milovanović, Serbia
Irina Mironova, Russia
Giovanni Nico, Italy
Antonije Onjia, Serbia
Marko D. Petrović, Serbia
Luka Č. Popović, Serbia
Sergey Pulinets, Russia
Milan Radovanović, Serbia
Ivana Smičklas, Serbia
Vladimir Srećković, Serbia
Mirela Voiculescu, Romania
Desmond Walling, UK

Local Organizing Committee

Aleksandra Nina, Serbia, chair
Ana Milanović Pešić, Serbia, co-chair

Filip Arnaut, Serbia
Jovana Brankov, Serbia
Stefan Denda, Serbia
Dejan Doljak, Serbia
Milan Đorđević, Serbia

Sanja Grekulović, Serbia
Dejana Jakovljević, Serbia
Aleksandra Kolarski, Serbia
Maja Kuzmanoski, Serbia
Suzana Lović Obradović, Serbia
Dušan Petković, Serbia
Miljana Todorović Drakul, Serbia
Đorđe Trajković, Serbia

Scientific Rationale

Geoscience research and applications are of crucial interest in science and many areas of modern life. For this reason, exchanging knowledge in various relevant areas is essential for development in scientific, engineering and programming activities. The conference aims to highlight the importance of joint research of experts in these fields and provide a platform for knowledge exchange.

Venue: Institute of Physics Belgrade, Belgrade, Serbia & virtual

Organizers: Faculty of Civil Engineering, University of Belgrade and Institute of Physics Belgrade, University of Belgrade

Published by: Faculty of Civil Engineering, University of Belgrade; Institute of Physics Belgrade, University of Belgrade; and Geographical Institute "Jovan Cvijić" SASA

The publication of this issue is financially supported by the Ministry for Education, Science and Technological Development of Serbia

Picture on the first cover: Dejan Doljak

ISBN 978-86-7518-239-9

eISBN 978-86-7518-240-5

Printed by: Curent Print, Tvrtka Velikog 14, Beograd

Number of copies: 50

M53

Analysis of the solar terminator shift determined from the VLF signal amplitude in the period around the intense seismic activity in Central Italy from 25 October to 3 November 2016

Aleksandra Nina¹ , Pier Francesco Biagi² , Sergey Pulinetz³ , Giovanni Nico⁴ ,
Srđan T. Mitrović⁵ , Vladimir M. Čadež⁶ , Milan Radovanović^{7,8} , Luka Č. Popović^{6,9,10} 

¹Institute of Physics Belgrade, University of Belgrade, Pregrevica 118, 11080 Belgrade, Serbia,

²Physics Department, Università di Bari, 70125 Bari, Italy,

³Space Research Institute, Russian Academy of Sciences, 117997 Moscow, Russia,

⁴Istituto per le Applicazioni del Calcolo (IAC), Consiglio Nazionale delle Ricerche (CNR), 70126 Bari, Italy,

⁵Novelic, 11000 Belgrade, Serbia,

⁶Astronomical Observatory, Volgina 7, 11060 Belgrade, Serbia,

⁷Geographical Institute "Jovan Cvijić" SASA, Đure Jakšića 9, 11000 Belgrade, Serbia,

⁸South Ural State University, Institute of Sports, Tourism and Service, 454080 Chelyabinsk, Russia,

⁹Department of Astronomy, Faculty of Mathematics, University of Belgrade, 11000 Belgrade, Serbia,

¹⁰Faculty of Science, University of Banja Luka, 78000 Banja Luka, R. Srpska, Bosnia and Herzegovina

Received 22.11.2022 · Accepted for publication 26.01.2023 · Published 15.02.2023

Keywords:

Lower ionosphere,
Earthquakes,
VLF signal.

Abstract

Since the middle of the last century, numerous studies indicate the possibility that ionospheric perturbations can be precursors of earthquakes (EQs). At the same time, different types of perturbations related to various ionospheric areas were observed. Among them, shifts in the times of occurrence of minimum amplitudes of very low/low frequency (VLF/LF) signals used for monitoring the lower ionosphere in the sunrise and sunset periods (the so-called Solar terminator time - STT) are shown in several studies. In this paper, we analyse STT of the 20.27 kHz ICV signal emitted in Italy and recorded in Serbia in the period from October 15 to November 13, 2016. This period includes 10 days (October 25 - November 3, 2016) when 981 EQs with the minimum magnitude of 2 out of which 31 had the minimum amplitude of 4 were registered in Central Italy. The obtained results show that the STT shifts during sunrise are predominantly due to seasonal changes, while the additional sudden shifts (most pronounced before and at the beginning of intense seismic activity (PISA) in Central Italy) are observed during sunset.

1. Introduction

Although studies connecting ionospheric perturbations with seismic activity began to be published in the mid-sixties of the last century (Davies and Baker, 1965; Leonard et al., 1965), this topic is still relevant and is the subject of numerous researches in recent years (He et al., 2022; Molina et al., 2022). In addition to theoretical studies and models that indicate the influence of lithospheric processes on the upper

atmosphere through waves and the influence of the electric field (see, for example, Pulinetz and Ouzounov, 2011), the analyses are based on data recorded by various forms of monitoring. First of all, these techniques are based on propagation of the Global Navigation Satellite System (GNSS) signals (their characteristic variations can predominantly be associated with the upper ionosphere perturbations due to

the significantly higher electron density that affects the signal propagation more than in the lower ionosphere (Molina et al., 2022)), and very low/low frequency (VLF/LF) signals (they are used for the lower ionosphere observations (Hayakawa, 2007)), as well as on monitoring by satellites orbiting in the ionosphere (Němec et al., 2009)).

Processing of recorded amplitudes and phases of VLF signals shows several types of changes that can be considered as possible earthquake (EQ) precursors. They refer to changes in the values of these parameters and the solar terminator time (STT) shift, usually visible a few days before the individual EQs, and the reduction of the signal amplitude/phase noise a few tens of minutes before EQ (Hayakawa, 1996; Molchanov et al., 1998; Yamauchi et al., 2007; Biagi et al., 2001a; Rozhnoi et al., 2010; Biagi et al., 2006; Hayakawa et al., 2010; Miyaki et al., 2001; Molchanov et al., 2001; Rozhnoi et al., 2004; Nina et al., 2020, 2021, 2022).

The subject of this research is the examination of STT shifts during a one-month time interval that includes a ten-day period of intense seismic activity (PISA) occurred in Central Italy in 2016. We analyse the ICV signal whose path from the transmitter in Sardinia (Italy) to the receiver in Belgrade (Serbia) passes close to the area where almost a thousand EQs of minimum magnitude 2 were recorded during the considered PISA.

2. Observations and study area

The research presented in this paper is based on the analysis of STTs determined from the ICV signal amplitude time evolution. This signal is used to monitor the lower ionosphere between the transmitter and receiver locations in Isola di Tavolara (Sardinia, Italy) and Belgrade (Serbia), respectively. In this study, we consider the time period from October 15 to November 13, 2016. It begins 10 days before and ends 10 days after PISA (October 25 - November 3, 2016), which enables us to analyse possible connection between the STT shifts in both sunrise and sunset periods and seismic activities during PISA when 981 EQs of minimum magnitude 2 were recorded (<http://www.emsc-csem.org/Earthquake/>).

The propagation path of the observed 20.27 kHz VLF signal is given on the map shown in Nina et al., 2022 (Figure 1). The EQ epicentres are marked with white and magenta crosses, and blue, red and black circles for the EQ magnitudes (M) between 2 and 3, 3 and 4, 4 and 5, and 5 and 6, and for magnitudes greater than 6, respectively (the magnitude types are given in <http://www.emsc-csem.org/Earthquake/> and, for the considered EQs with $M \geq 4$, in Nina et al., 2022 (Table 1)). As can be seen from this map, the locations of the epicentres are primarily grouped in the area where their distances from the ICV signal path (D) are less than 100 km

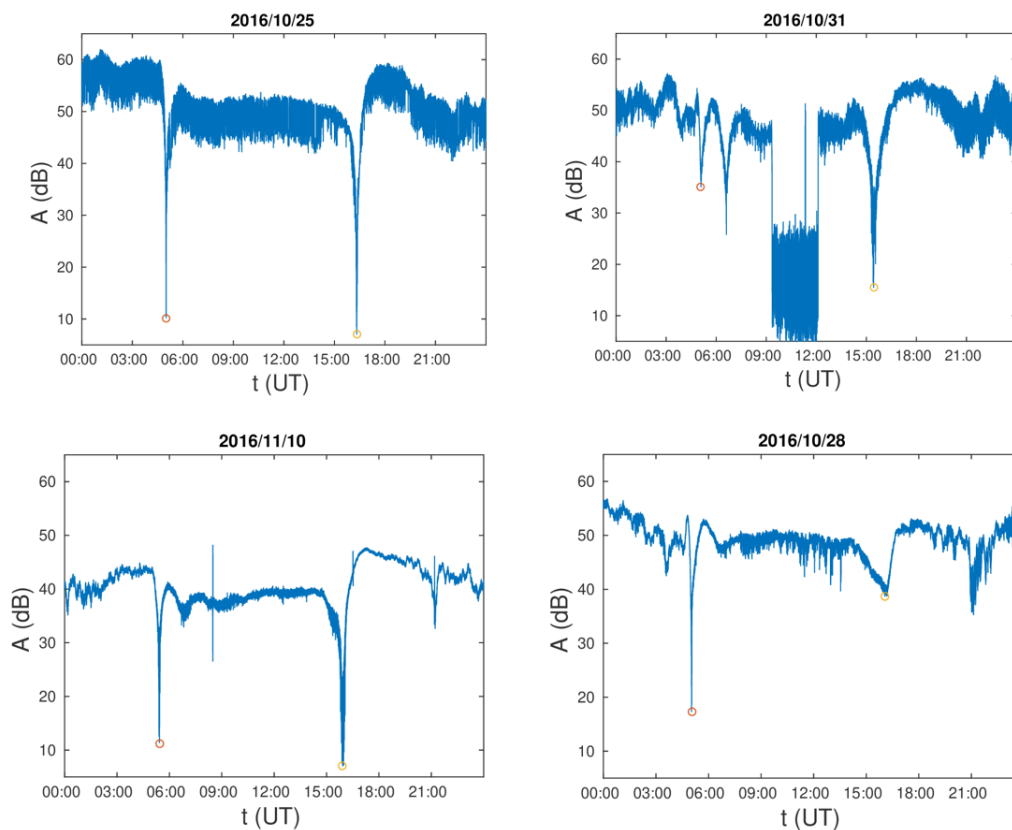


Figure 1. Examples of the ICV signal amplitude time evolutions during selected four days.

(since the greatest distance from the signal path of this group of epicenters is 99.86 km, in the analysis we chose that the border distance of the considered area is 100 km). Table 1 shows that there were 973 (99.2%) of these EQs, while there were 8 (0.8%) EQs whose epicenters were further away ($D > 100$ km from the ICV signal path). Given that all 8 more distant EQs had a magnitude of less than 4, it is realistic to assume that the potential impact of seismic activity on the ICV signal can primarily be related to events closer to its path.

Bearing in mind that a large number of factors affect the propagation of a VLF signal, the analysis of the possible impact of seismic activities on its characteristics, including the non-periodic changes in STT, requires the exclusion of other factors that may have an impact on the obtained results. As stated in Biagi et al., 2011 and Nina et al., 2020, these factors are primarily related to meteorological and geomagnetic conditions, extraterrestrial radiation, and non-natural conditions that are based on changes in emission and reception (caused, for example, by the influence of additional electric and electronic devices near the receiver). In the analysis of possible influences of the mentioned factors given in Nina et al. 2022, it is shown that they did not have a significant contribution to the signal characteristics in the observed time period. In addition, it should be noted that several individual EQs were recorded close to the observed ICV signal propagation path in other areas, but the maximum magnitude of these EQs was only 4.2 (the corresponding event occurred in Bosnia and Herzegovina on 31 October, 2016), which is why their significant impact on the STT shift is not expected. This conclusion is based on previous studies where corresponding changes are recorded for only much stronger earthquakes (see, for example, Hayakawa et al., 1996 and Biswas et al., 2022).

3. Signal processing

VLF signal receivers record two signal characteristics: amplitude and phase. The first of these parameters is significantly more stable and more suitable for multi-day analyses, which is the reason why its temporal evolution is the subject of this study. The used data are recorded by the Absolute Phase and Amplitude Logger (AbsPAL) receiver in Belgrade, Serbia. This receiver records two sets of data with time samplings of 0.1 s and 1 min. Unlike the analysis of the signal characteristics (the amplitude and phase) of noise reductions which requires data with a better time resolution (Nina et al., 2020, 2021, 2022), the second data set is more suitable for the STT analysis due to the elimination of short-lasting peaks caused

Table 1. Number of the considered EQs of the magnitudes (M) between 2 and 3, 3 and 4, 4 and 5, and 5 and 6, and for M greater than 6, and the domains of the distances between the considered epicenters and ICV signal propagation path (D).

Magnitude	D<100 km		D>100 km	
	N _o	Range of D (km)	N _o	Range of D (km)
2≤M<3	604	18.91 - 99.86	5	168.12 - 258.83
3≤M<4	338	31.01 - 88.21	3	216.38 - 217.98
4≤M<5	28	47.85 - 86.85	0	-
5≤M<6	1	67.17	0	-
M≥6	2	63.95 and 71.14	0	-

by various influences whose effects on a VLF signal we cannot precisely determine.

As stated in Introduction, the non-periodic STT shifts before and after the occurrence of individual EQs are presented in several studies. In this paper, we analyse STT before, during and after the observed PISA.

Generally speaking, signal amplitudes at the sunrise and sunset periods have characteristic forms of temporal evolution that are manifested in pronounced minima. As can be seen in Figure 1, the number of these amplitude minima is not unambiguous. In addition, their determination in some cases is not simple. This can be seen in the case of the amplitude minimum (about 7 UT) from which the signal starts to rise to its maximum daytime value. These minima are in some cases pronounced (e.g. October 31, 2016), in others they are weaker (e.g. October 28 and November 10, 2016), while in some days they are not visible at all (e.g. October 25, 2016). For this reason, in this study we observe the times of the minimum amplitude during the sunrise period (from 4:30 UT to 6:00 UT), and the sunset period (from 15:00 UT to 17:00 UT) in which the analysed minima are clearly defined and present every day.

4. Results and discussion

In order to examine the STT shifts during the periods of sunrise (sunrise time (SRT) shift) and sunset (sunset time (SST) shift), it is necessary to observe a longer time period, which in its middle part includes the considered EQ day or PISA. In this study, we observe the time period from 15 October to 14 November, 2016 which includes PISA starting on 25 October and ending on 3 November, 2016. Here it should be indicated that the AbsPAL receiver did not record a quality signal during 4 sunrise and 5 sunset periods, which is why the corresponding data of SRT and SST for the corresponding days are missing.

In the upper panel of Figure 2 where the time evolution of SRT is shown, the seasonal changes manifested in the SRT shift towards daytime (DT) from day to day can be clearly

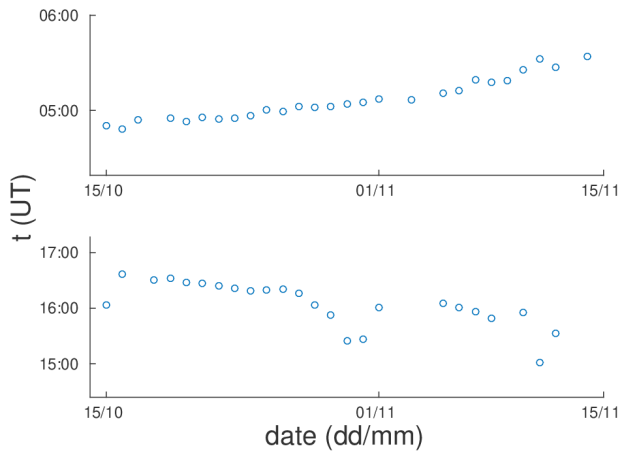


Figure 2. Time evolutions of the sunrise (upper panel) and sunset (bottom panel) time shifts in the considered time period.

visible. Additional changes that can potentially be related to intense seismic activity in Central Italy are not observed. In contrast to SRT, the time evolution of SST (lower panel of Figure 2) indicates a combination of the influence of several phenomena. In addition to the tendency of the SST shift towards DT with days, additional changes are also visible in three time intervals. The first of them is visible as a SST shift towards DT as compared to the expected time in quiet conditions and it relates only on the first observed day. Much more interesting are the changes in the middle of the observed time interval. The beginning of the deviation from the expected SRT evolution shape is manifested in a slight SRT shift towards nighttime (NT) on 22 and 23 October 22, i.e. three and two days before PISA. After that, a sharp shift of SST towards DT is noticeable. It reaches more than half an hour from the expected value during quiet conditions on 28 October. From 29 October, SST shifts towards NT and returns

to the expected values that reach around 6 October, with a previous larger shift towards NT. These non-periodic changes have a quasi-symmetrical shape in relation to the day of minimum SST. On the third and second day from the end of the observed time interval, the SST shifts towards NT and DT, respectively, are seen, but on the next day the SST is already similar to its expected value in the case without the influence of sudden events.

As mentioned in the Introduction, several studies have analyzed SRT in time periods around several EQs. A comparison of the data obtained in this research with the results of two other studies related to EQs that occurred in Kobe, Japan (Hayakawa et al., 1996), and near the Samos island in Greece (Biswas et al., 2022) are given in Table 2. The basic characteristics given in them are the existence of the SRT and SST shift in both days before and after the EQ. As can be seen from Table 2, these parameters do not have the same characteristics for all the mentioned cases.

Sudden changes in SRT (defined as the time of the minimum phase of the Omega signal recorded near Tokyo, Japan, in Hayakawa et al., 1996) are observed before Kobe EQ (M=7.2) that occurred on 17 January, 1995. In contrast to the results obtained in our study, the SRT shift is only towards NT and is visible both at sunrise and at sunset, but it is not significantly expressed in the days after the EQ day.

The analysis of the SRT shifts in the period around the time of Niigata EQ that occurred in Japan (23 October, 2004) with magnitude of 6.8 indicates the importance of signal selection in determining the characteristics of possible EQ precursors (Yamauchi et al., 2006). As can be seen from Table 2,

Table 2. Sunrise (SRT) and sunset (SST) time shifts toward daytime (DT) and night time (NT) before, during and after the considered EQs in this study, and Kobe EQ and EQ near the Samos island, Greece.

No	EQ epicentre	Reference	VLF transmitter / receiver location	SRT shift toward			SST shift toward		
				before EQ	During PISA or EQ day	After EQ	before EQ	During PISA or EQ day	After EQ
1	Central Italy	This study	ICV (Italy) / Belgrade (Serbia)	-	-	-	NT – DT (DT is dominated)	DT – NT (DT is dominated)	NT
2	Kobe, Japan	Hayakawa et al., 1996	Omega (Japan) / Inubo (Japan)	NT	-	-	NT	NT	-
			JJY (Japan) / MCR (Japan)	DT	-	NT	No data	No data	
			JJY (Japan) / KOC (Japan)	DT	-	-	No data	No data	
3	Niigata	Yamauchi et al., 2006	JJI (Japan) / CHO (Japan)		No data		DT	-	NT
			JJI (Japan) / CBA (Japan)		No data		NT	-	-
			JJI (Japan) / MCR (Japan)		No data		-	-	-
			JJI (Japan) / KOC (Japan)		No data		-	-	-
3	Near Samos island, Greece	Biswas et al., 2022	ISR (Israel) / Athens (Greece)	NT	NT	DT	DT	-	-
			TBB (Turkey) / Athens (Greece)	DT-NT	No data	NT	NT-DT	-	-

two VLF signals emitted by JJY and JJI transmitters and recorded at four receivers (MCR, KOC, CHO and CBA) are considered in this study. Two (JJY-MCR and JJY-KOC) and four (JJI-CHO, JJI-CBA, JJI-MCR and JJI-KOC) signal paths are considered in analysis of the SRT and SST shifts, respectively. The significant SRT shifts before EQ toward DT are recorded for two signal paths, while the SST shift toward NT is visible for one path after EQ. The significant SST shifts are recorded before (toward DT and NT) and after (toward NT) EQ for two and one paths, respectively, and they are not recorded for two paths. The importance of signal selection in corresponding research is also indicated in analysis of the period around the time of EQ that occurred near the Samos island, Greece (30 October, 2020) with magnitude of 6.9 (Biswas et al., 2022). In this study, the ISR and TBB signals emitted in Israel and Turkey, respectively, and recorded in Athens, Greece, are analyzed. The SRT shifts are visible both before and after the EQ day in both signals, as well as on that day (towards NT) for the ISR signals (the TBB signal was not recorded in that period, so the corresponding information is not available). However, the shifts are not directed towards the same time of the day (SRT is shifted towards NT and in both directions before EQ, and towards DT and NT after EQ day for the ISR and TBB signal, respectively; SST is shifted towards DT and towards both times of the day for ISR and TBB signal, respectively, before EQ). Based on the presented data, it can be seen that the SST shifts are detected before EQs in all cases, as well as that they can be registered on the day of EQ or PISA and endure during the following days. In all cases, they can be directed both to DT and to NT.

The explanation of the SRT shifts is very complicated due to the large number of simultaneous influences on a VLF signal and data that only provide information on integral changes in the amplitude and phase of the considered signal throughout the Earth-ionosphere waveguide through which it extends and its boundaries. A possible explanation for these changes lies in the change in the height of the reflection of a VLF signal from the ionosphere. The study presented in Yoshida et al., 2008 shows a SST modeling for different signal reflection heights (h) for a relatively small distance between the transmitter and receiver (less than 2000 km). This study shows that for the JJY signal registered in Kochi (786 km away from the JJY transmitter) a decrease in h of 2 km causes SRT and SST shifts to later and to earlier hours, respectively, which is usually observed in the experiments in periods around the Kobe EQ.

5. Conclusions

In this paper, we analysed the shifts in solar terminator times detected by the ICV signal emitted in Italy and recorded in Serbia during a period of one month which includes the period of intense seismic activity recorded in Central Italy. We analysed both the sunrise and sunset periods.

The obtained results related to the observed time period indicate:

- Absence of the sudden shifts in the solar terminator time during the sunrise period. In this time intervals, only changes in the solar terminator time which are a clear consequence of seasonal changes are recorded.

- Existence of non-periodic variations of solar terminator times during sunset. These changes occur in combination with the expected periodic seasonal changes in which the solar terminator time continuously decreases due to earlier sunset.

Comparison with other analyses indicates that the sunset time shifts were detected before an earthquake in all considered cases, and that they can be registered on the day when an earthquake occurred or during a period of intense seismic activity, and persist during the following days. In all cases, they can be directed to both the daytime and nighttime.


This research represents an extension of the previous studies which primarily refer to strong individual earthquakes to the examination of potential precursors of intense seismic activity manifested in a large number of earthquakes during a time period of several days. In addition, due to the complexity of analyses of characteristics of radio signals used to monitor the ionosphere, a statistical analysis that includes a large number of earthquakes and periods of intense seismic activity is necessary for drawing reliable conclusions. For this reason, the presented study can be included in the corresponding wider research and its results can be used in different statistical analyses.


Acknowledgements

The authors acknowledge funding provided by the Institute of Physics Belgrade, the Astronomical Observatory (the contract 451-03-68/2020-14/200002) and the Geographical Institute "Jovan Cvijić" SASA through the grants by the Ministry of Education, Science, and Technological Development of the Republic of Serbia.

ORCID iDs

Aleksandra Nina  <https://orcid.org/0000-0003-0462-8383>

Pier Francesco Biagi  <https://orcid.org/0000-0003-2584-8481>

Sergey Pulinets  <https://orcid.org/0000-0003-3944-6686>

Giovanni Nico  <https://orcid.org/0000-0001-7621-5014>
 Srđan T. Mitrović  <https://orcid.org/0000-0002-1287-2792>
 Vladimir M. Čadež  <https://orcid.org/0000-0001-9154-8298>
 Milan Radovanović  <https://orcid.org/0000-0002-9702-3879>
 Luka Č. Popović  <https://orcid.org/0000-0003-2398-7664>

References

- Biagi, P.F., Piccolo, R., Ermini, A., Martellucci, S., Bellecci, C., Hayakawa, M., Capozzi, V., Kingsley, S.P., 2001a. Possible earthquake precursors revealed by LF radio signals. *Nat. Hazards Earth Syst. Sci.* 1, 99–104.
- Biagi, P., Castellana, L., Maggipinto, T., Piccolo, R., Minafra, A., Ermini, A., Martellucci, S., Bellecci, C., Perna, G., Capozzi, V., Molchanov, O., Hayakawa, M., 2006. LF radio anomalies revealed in Italy by the wavelet analysis: possible preseismic effects during 1997–1998. *Phys. Chem. Earth* 31, 403–408.
- Biswas, S., Chowdhury, S., Sasmal, S., Politis D.Z., Potirakis S.M. Hayakawa, M., 2022. Numerical modelling of sub-ionospheric Very Low Frequency radio signal anomalies during the Samos (Greece) earthquake (M = 6.9) on October 30, 2020, *Adv. Space Res.*, 70(5), 1453–1471.
- Davies, K., and Baker, D. M., 1965. Ionospheric effects observed around the time of the Alaskan earthquake of March 28, 1964. *J. Geophys. Res.* 70, 2251–2253.
- Hayakawa, M. 2007. VLF/LF Radio Sounding of Ionospheric Perturbations Associated with Earthquakes, *Sensors* 7(7), 1141–1158.
- Hayakawa, M., Molchanov, O.A., Ondoh, T., Kawai, E., 1996. Precursory signature effect of the Kobe earthquake on VLF subionospheric signals. *J. Atmos. Electr.*, 16(3), 247–257.
- Hayakawa, M., Horie, T., Muto, F., Kasahara, Y., Ohta, K., Liu, J.Y., Hobara, Y., 2010. Subionospheric VLF/LF probing of ionospheric perturbations associated with earthquakes: a possibility of earthquake prediction. *SICE J. Control Meas. Syst. Integr.* 3, 10–14.
- He, L., Wu, L., Heki, K., and Guo, C., 2022. The conjugated ionospheric anomalies preceding the 2011 Tohoku-Oki earthquake. *Front. Earth Sci.* 10, 23.
- Leonard, R. S., Barnes, J., and Barnes, R. A., 1965. Observation of ionospheric disturbances following the Alaska earthquake. *J. Geophys. Res.* 70, 1250–1253.
- Miyaki, K., Hayakawa, M., Molchanov, O., 2001. The role of gravity waves in the lithosphere - ionosphere coupling, as revealed from the subionospheric LF propagation data. *Seismo Electromagnetics: Lithosphere - Atmosphere-Ionosphere Coupling*; TERRAPUB: Tokyo. pp. 229–232.
- Molchanov, O., Hayakawa, M., Oudoh, T., Kawai, E., 1998. Precursory effects in the subionospheric VLF signals for the Kobe earthquake. *Phys. Earth Planet. Inter.* 105, 239–248.
- Molchanov, O., Hayakawa, M., Miyaki, K., 2001. VLF/LF sounding of the lower ionosphere to study the role of atmospheric oscillations in the lithosphere-ionosphere coupling. *Adv. Polar Upper Atmos. Res.* 15, 146–158.
- Molina, C., Boudriki Semaili, B.-E., Park, H., and Camps, A., 2022. A preliminary study on ionospheric scintillation anomalies detected using GNSS-r data from NASA CYGNSS mission as possible earthquake precursors, 2022, *Remote Sens.* 14(11), 2555.
- Němec, F., Santolík, O., and Parrot, M. (2009). Decrease of intensity of ELF/VLF waves observed in the upper ionosphere close to earthquakes: A statistical study. *J. Geophys. Res.*, 114(A4), A04303.
- Nina, A., Pulinets S., Biagi P.F, Nico G., Mitrović S.T., Radovanović M, Popović, Č., 2020. Variation in natural short-period ionospheric noise, and acoustic and gravity waves revealed by the amplitude analysis of a VLF radio signal on the occasion of the Kraljevo earthquake (Mw = 5.4). *Sci. Total Environ.* 710, 136406.
- Nina, A., Biagi, P. F., Mitrović, S. T., Pulinets, S., Nico, G., Radovanović, M., Popović, L.Č., 2021. Reduction of the VLF signal phase noise before earthquakes. *Atmosphere* 12, 444.
- Nina A, Biagi PF, Pulinets S, Nico G, Mitrović ST, Čadež VM, Radovanović M, Urošev M and Popović L.Č. (2022). Variation in the VLF signal noise amplitude during the period of intense seismic activity in Central Italy from 25 October to 3 November 2016. *Front. Environ. Sci.*, 10:1005575.
- Pulinets, S., and Ouzounov, D., 2011. Lithosphere-atmosphere-ionosphere coupling (LAIC) model – An unified concept for earthquake precursors validation. *J. Asian Earth Sci.* 41, 371–382.
- Rozhnoi, A., Solovieva, M., Molchanov, O., Hayakawa, M., 2004. Middle latitude LF (40 kHz) phase variations associated with earthquakes for quiet and disturbed geomagnetic conditions. *Phys. Chem. Earth* 29, 589–598.
- Yamauchi, T., Maekawaa, S., Horie, T., Hayakawaa, M., Soloviev, O., 2007. Subionospheric VLF/LF monitoring of ionospheric perturbations for the 2004 Mid-Niigata earthquake and their structure and dynamics. *J. Atmos. Solar—Terr. Phys.* 69, 793–802.
- Yoshida, M., Yamauchi, T., Horie, T., Hayakawa, M., 2008. On the generation mechanism of terminator times in subionospheric VLF/LF propagation and its possible application to seismogenic effects. *Nat. Hazards Earth Syst. Sci.*, 8 (1), 129–134.

M61



VIII International Congress

**BIOMEDICINE AND GEOSCIENCES -
INFLUENCE OF ENVIRONMENT ON
HUMAN HEALTH**

Hotel *Kraljevi čardaci*, Kopaonik Mt., December 7-9, 2020

**Under the auspices of Ministry of Education, Science and
Technological Development of the Republic of Serbia**



PROCEEDINGS

The 8th International Congress **BIOMEDICINE AND GEOSCIENCES - INFLUENCE OF ENVIRONMENT ON HUMAN HEALTH**

Editor

Prof.Dr Snežana Komatina, AGES, Belgrade, Serbia

Editorial Board

Prof.Dr Miomir Komatina, AGES, Belgrade, Serbia

Prof.Dr Milovan Urošević, Dept. of Exploration Geophysics, Curtin University of Technology, Perth, Australia

Prof.Dr Bayraktutan Memet Salih, Igdir University, Faculty of Engineering, Igdir, Turkey

Prof.Dr Vladislav Brkić, University of Zagreb, Zagreb, Croatia

Assist.Prof.dr Toni Nikolić, University "Džemal Bijedić", Faculty of Civil Engineering, Mostar, Bosnia and Herzegovina

Publisher

Association of Geophysicists and Environmentalists of Serbia (AGES)

For Publisher

Snežana Komatina, AGES, Belgrade, Serbia

Cover design

Durica Surla, Technical Faculty "Mihajlo Pupin", University of Novi Sad, Zrenjanin, Serbia

Technical preparation

Durica Surla, Technical Faculty "Mihajlo Pupin", University of Novi Sad, Zrenjanin, Serbia

Printed by

Copy Link Studio d.o.o., Belgrade, Serbia

Published: 2021, Belgrade, Serbia

Copies: 200

All papers in Proceedings are reviewed.

The Book of Papers has been published by the financial support of the Ministry of Education, Science and Technological Development of Serbia.



ORGANIZERS

Association of Geophysicists and Environmentalists of Serbia (AGES), Belgrade, Serbia

ORGANIZING COMMITTEE

Prof.Dr. Snežana Komatina, AGES, Belgrade, Serbia - President

Assist.Prof.Dr. Snežana Filip, Technical Faculty "Mihajlo Pupin", University of Novi Sad, Zrenjanin, Serbia - Vice-President

Prof.Dr Vladislav Brkić, University of Zagreb, Zagreb, Croatia

Prof.dr Bayraktutan Memet Salih, Igdır University, Faculty of Engineering, Igdır, Turkey

Assist.Prof.Dr. Aleksandra Kolarski, Technical Faculty "Mihajlo Pupin", University of Novi Sad, Zrenjanin, Serbia

Magdalena Marković Juhlin, Uppsala University, Sweden

M.Sc. Mila Đuričić, Technical Faculty "M. Pupin", University of Novi Sad, Zrenjanin, Serbia

M.Sc. Una Petrović, AGES, Belgrade, Serbia

M.Sc. Marko Vanić, NTC NIS-GazpromNeft, Novi Sad, Serbia

Gordana Leković, Ministry of Education, Science and Technological Development of the Republic of Serbia, Belgrade, Serbia

Đurica Surla, Technical Faculty "Mihajlo Pupin", University of Novi Sad, Zrenjanin, Serbia

Dejan Bajić, Technical Faculty "Mihajlo Pupin", University of Novi Sad, Zrenjanin, Serbia

Isidora Popov, Technical Faculty "M. Pupin", University of Novi Sad, Zrenjanin, Serbia

Milica Vukić, AGES, Novi Sad, Serbia

M.Sc. Tomo Obrenović, AGES, Brčko, Brčko district, BiH

SCIENTIFIC COMMITTEE

Prof.Dr. Snežana Komatina, AGES, Belgrade, Serbia - President

Assist.Prof.Dr. Aleksandra Kolarski, Technical Faculty "Mihajlo Pupin", University of Novi Sad, Zrenjanin, Serbia - Vice-President

Prof.Dr Vladislav Brkić, University of Zagreb, Zagreb, Croatia

Dr. Dan Herold, Executive Vice President, Parallel Geoscience Corp., USA

Prof.dr Bayraktutan Memet Salih, Igdır University, Faculty of Engineering, Igdır, Turkey

Dr. Sergey Buryak, DECO Geophysical SC, Moscow, Russia

Prof.Dr. Miomir Komatina, AGES, Belgrade, Serbia

Assist.Prof.Dr. Snežana Filip, Technical Faculty "Mihajlo Pupin", University of Novi Sad, Zrenjanin, Serbia

M.Sc. Magdalena Marković Juhlin, Uppsala University, Sweden

M.Sc. Mila Đuričić, Technical Faculty "Mihajlo Pupin", University of Novi Sad, Zrenjanin, Serbia

Assist.Prof.dr Toni Nikolić, University "Džemal Bijedić", Faculty of Civil Engineering, Mostar, Bosnia and Herzegovina



CIP - Каталогизација у публикацији - Народна библиотека Србије, Београд

614.2(082)
502/504(082)

МЕЂУНАРОДНИ Конгрес Биомедицина и геонауке - утицај животне средине на људско здравље (8 ; 2020 ; Копаоник)

[Proceedings] / The 8th International Congress Biomedicine and Geosciences - Influence of Environment on human Health, Kopaonik, December 7-9, 2020 ; under the auspices of Ministry of Education, Science and Technological Development of the Republic of Serbia ; [editor Snežana Komatina]. - Belgrade : Association of Geophysicists and Environmentalists of Serbia (AGES), 2021 (Belgrade : Copy Link Studio). - 133 str. : ilustr. ; 30 cm

Radovi na engl. i srp. jeziku. - Tiraž 200. - Bibliografija uz svaki rad. - Summaries.

ISBN 978-86-80140-08-7

1. Srbija. Ministarstvo prosvete, nauke i tehnološkog razvoja 2. Asocijacija geofizičara i ekologa Srbije (Beograd)

a) Здравље - Заштита - Зборници b) Животна средина - Зборници

COBISS.SR-ID 31648521

CONTENTS

Invited Lectures	1
Aleksandra Nina <i>Detection of events and processes which affect human health by VLF/LF radio signals: solar radiation and natural disasters</i>	2
Aleksandra Kolarski <i>Monitoring intense storm activity over Balkans</i>	11
Snežana Komatina <i>Influence of Radon on Population Health in Serbia – Geological Approach</i>	17
Contributions	22
Toni Nikolić, Jasminka Nikolić <i>Mapping underground spring water with database in GIS software on sample area of Jablanica municipality, Bosnia and Herzegovina</i>	23
Mehmet Bayraktutan, Snežana Komatina <i>Kestanol Fault Zone, Turkey; Ezine-Gulpinar Fields GM and CSAMT Survey for Conceptual Modelling Geothermal System</i>	30
Vladislav Brkić <i>Disposal of gas production waste by slurry injection into deep wells</i>	35
Miomir Komatina, Snežana Komatina, Aleksandra Kolarski <i>Geology of the Sokobanja basin and genesis of radon and toron</i>	46
George A. Donoso, Magdalena Marković Juhlin <i>Promoting Geoscience using the power of Social Media</i>	51
Aleksandra Kolarski, Snežana Komatina <i>Anomalous behavior in VLF signal propagation due to possible seismo-ionospheric Effect</i>	52
Magdalena Markovic Juhlin, Snezana Komatina <i>Magnetic survey at archaeological site GROBLJISTE, Ražanj Municipalty, Serbia</i>	53

DETECTION OF EVENTS AND PROCESSES WHICH AFFECT HUMAN HEALTH BY VLF/LF RADIO SIGNALS: SOLAR RADIATION AND NATURAL DISASTERS

Aleksandra Nina*

Institute of Physics Belgrade, University of Belgrade, Pregrevica 118, 11080 Belgrade, Serbia

Abstract

There are many natural events and processes which can affect human health. In this paper we present research of the lower ionosphere disturbances induced by variations in the solar radiation and possible connected with earthquakes and tropical cyclones. To study these variations we analysed data obtained in the lower ionosphere remote sensing by very low/low frequency (VLF/LF) radio signals. We present detections of variations in the VLF signal emitted by the DHO transmitter located in Germany and received by the Belgrade receiver station located at the Institute of Physics Belgrade. We considered periodical variations due to changes in the incoming solar hydrogen $L\gamma\alpha$ radiation during a solar cycle, year and day, as well as sudden increase of the X-radiation due to solar X-ray flares. In addition, we present investigation of variations in the lower ionosphere in periods around natural disasters that can significantly affect human life and health: earthquakes and tropical cyclones.

1. Introduction

As it is well known, the solar UV radiation can provide significant problems to human health. On the other side, the solar hydrogen $L\gamma\alpha$ radiation. In addition to the constant impact of the solar radiation on human health, short-term natural disasters such are earthquakes, volcano eruptions or cyclones can cause not only numerous death but also health consequences of varying duration. For this reason, prediction of these events is of high significance and different kinds of investigations are in focus of numerous scientific investigations.

In this study we present detections of variations in the solar radiations by VLF/LF radio signals and changes in their properties in periods around earthquakes and tropical depressions before hurricanes. We show studies based on data recorded in the lower ionosphere observations by VLF/LF radio signals recorded by the Belgrade receiver station.

2. Observations

Remote sensing by VLF/LF radio signals is one of techniques for observation of the lower ionosphere which lie in altitude domain between 50 km and 90 km. This technique is based on propagation of VLF/LF radio waves several thousands kilometers in the Earth-ionosphere waveguide. Signals are emitted by transmitters located worldwide (see Fig. 1 where locations of the most important transmitters are shown on the world map) and their detection is provided by numerous, also worldwide located, receivers.

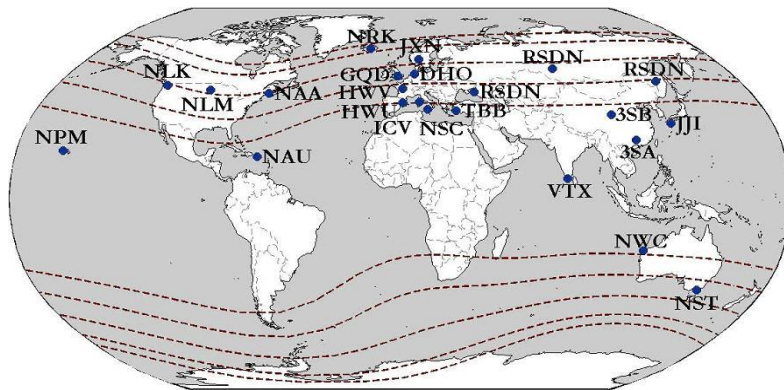


Figure 1. Locations of the most important LF/LF transmitters.

Belgrade receiver station is located at the Institute of Physics Belgrade and operates from 2003. It consists of three receiver stations: the Atmospheric Weather Electromagnetic System for Observation Modeling and Education (AWESOME) (Cohen et al., 2010), the Absolute Phase and Amplitude Logger (AbsPAL) and receiver included in the International Network for Frontier Research on Earthquake Precursors (INFREP). All of these stations have possibility of continuous and simultaneous monitoring of several signals which provide wide covering of the lower ionosphere monitoring. The most important signals which are monitored by this station are DHO, GQD, ICV, NRK, NAA and NWC. The collected databases have time resolutions of 0.02 s, 0.1 s and 1 min which allow us to investigate periodical and sudden events, and to detect disturbances lasting from a few tenths of a millisecond.

Table 1. Characteristics of some VLF/LF signals monitored by Belgrade receiver station.

Transmitter Sign	Location	Frequency (kHz)	Power (kW)
DHO	Rhauderfehn, Germany	23.4	800
GQD	Anthorn, UK	22.1	200
ICV	Isola di Tavolara, Italy	20.27	20
NRK	Grindavik, Island	37.5	800
NAA	Cutler, Maine, USA	24.0	1000
NWC	North West Cape, Australia	19.8	1000

3. Results

As we said in Introduction, this study presents analyses related to:

- Periodical variations of the VLF DHO signal amplitude due to:
 - 11-year cyclic changes in emission of the solar hydrogen $L\gamma\alpha$ radiation
 - variations in incoming this radiation in the ionospheric D-region due to Earth's revolution (i.e. seasonal variations), and

- variations in incoming $L\gamma\alpha$ radiation in the ionospheric D-region due to Earth's rotation (i.e. daily changes);
- Sudden variations of the VLF/LF signal amplitude:
 - during influence of solar X-ray flares,
 - in periods around earthquakes, and
 - in periods around beginning of tropical depressions before tropical cyclones.

These changes, described in the following text, are presented in the latest studies based on observations, signal processing and modelling.

3.1. Periodical variations

Periodical variations of the incoming solar hydrogen $L\gamma\alpha$ radiation in the D-region are consequence of variations in processes in the Sun which have period of about 11 years (solar cycles) and variations in the zenith angle of the solar radiation in the considered location. Variations in the zenith angle exists due to Earth's rotation around the Sun (seasonal variations) and around its own axis (daily variations). Analysis of these changes in the DHO signal is presented in Nina et al. (2017).

In this paper we show daily variations in signal emitted by the NAA transmitter located in the USA. As one can see in Fig. 2 which show the signal amplitude time evolution during four days on Mart 2011, there are three typical periods which describe nighttime and daytime periods and passing between them during the sunrise and sunset (solar terminator (ST) periods). The times of sunrises, noons and sunsets are indicated by the vertical lines, where the relevant left lines corresponding to conditions in Belgrade, and right ones corresponding to conditions in Cutler (Maine, USA) where the NAA transmitter is located.

- **The night-time period.** During the night-time periods, the ionosphere is not exposed to the solar radiation which allows application of this type of remote sensing in the detection of other events which induce enough week disturbances that the solar radiation mask them during the day-time periods. In this period intensity of the recorded signal i.e. its amplitude is larger than during daytime.
- **The ST period.** Keeping in mind that the NAA signal propagation path between the NAA transmitter and Belgrade is longer than 6500 km, the period when the solar terminator affects its propagation is not short. As one can see in the shadow parts, variations typical for these conditions are visible about six hours during the sunrise and approximatively the same period during the sunset.
- **The daytime period.** In the white part of Fig. 2, increase following by decrease in the amplitude is recorded for all four considered days.

The lastings of these periods, i.e. periods of the UV radiation impact in the considered area, vary during the year. During the summer day-time periods are the longest while nighttime periods are the longest during winter days. Similarly like in the case of the DHO signals, analysed in Nina et al. (2017a), values of the recorded amplitudes vary during the year, and they are affected by the changes in the emitted solar radiation during the solar cycle.

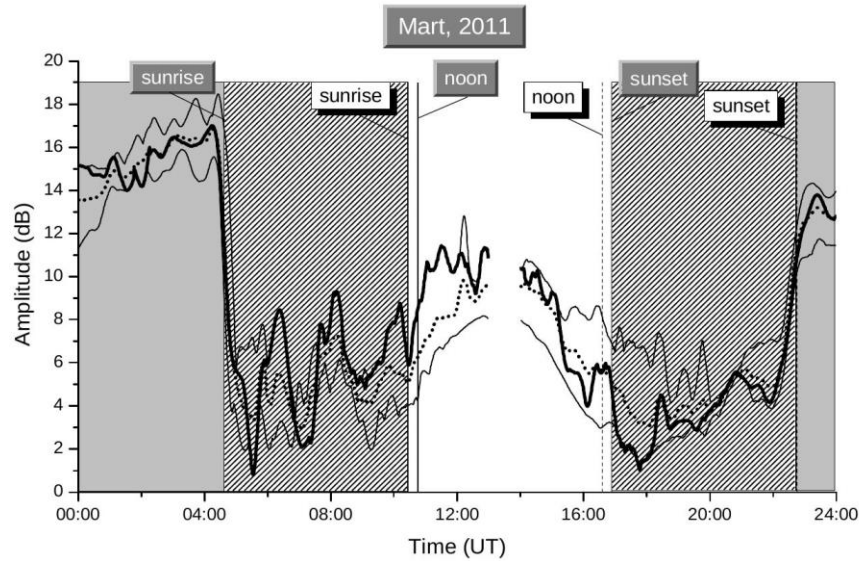


Figure 2. The amplitude time evolution during four days on Mart 2011 recorded by the AWESOME receiver station in Belgrade, Serbia for the signal emitted by the NAA transmitter located in Cutler, Maine, USA. The day-time and night-time periods are indicated by white and gray surfaces, respectively, while ST periods are indicated by shadow surfaces. The times of the sunrises, noons and sunsets are indicated by the vertical lines, where relevant left lines corresponding to conditions in Belgrade, and right ones corresponding to conditions in Cutler (Maine, USA) where the NAA transmitter is located.

3.2. Sudden variations

There are numerous events and processes in the outer space and different terrestrial layers which induce sudden disturbances in the lower ionosphere and which can be detected by the VLF/LF radio signals. A solar X-ray flare is a phenomenon which provides the most important disturbance of the considered atmospheric layer, while possible precursors of natural disasters are the most important application of the lower ionosphere monitoring.

- **Solar X-ray flares.** These astrophysical phenomena are very violent processes in the Sun following by emission of the intensive X-radiation. These events are more frequent in the maximum of the solar cycle. They are divided in A, B, C, M and X classes which domains of energy flux peaks are given in Table 2. These values relate to fluxes recorded by a GOES satellite in channel corresponding wavelength domain 0.05 nm – 0.8 nm.

A typical response of the VLF/LF signal amplitude is shown in Fig. 3. Here, we consider the NAA signal during the influence of the solar X-ray flare occurred on 5 May, 2010. Here we notice that detection of these amplitude and phase values are used in many paper for determination of the D-region electron density and other ionospheric parameters (Kolarski et al. 2011, Nina et al. 2018) using LWPC numerical program for simulation of the VLF/LF signal propagations using the Long-Wave Propagation Capability (LWPC) numerical model developed by the Space and Naval Warfare Systems Center, San Diego, USA (Ferguson, 1998). These investigations are important for practical application in telecommunication and in technologies based on satellite signals such as positioning and Earth's observations (Nina et al., 2020a).

Table 2. Energy flux domains of a solar X-ray flare of classes in A, B, C, M and X.

X-ray flare class	Energy flux peak domain (for wavelength domain 0.05 – 0.8 nm) (W/m ²)
A	$I < 10^{-7}$
B	$10^{-7} \leq I < 10^{-6}$
C	$10^{-6} \leq I < 10^{-5}$
M	$10^{-5} \leq I < 10^{-4}$
X	$I \geq 10^{-4}$

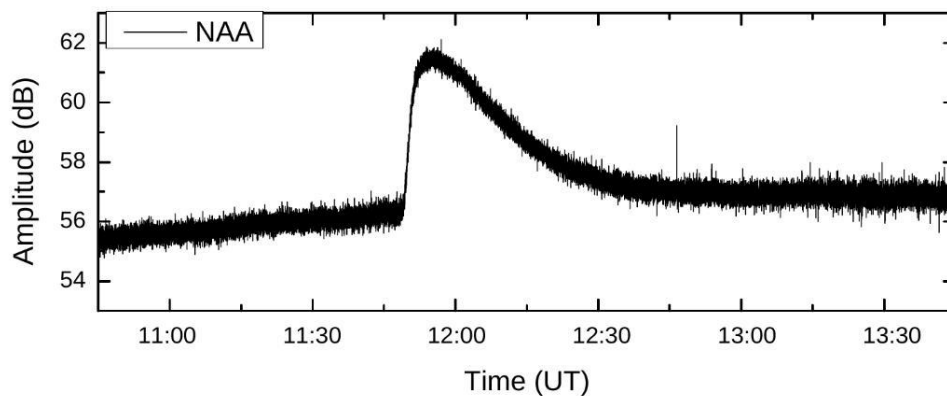


Figure 3. Time evolution of the standard deviation of differences of the recorded ICV signal amplitude from its smoothed values dA around the time (indicated by vertical dashed line) of the Kraljevo earthquake occurred on 3 November 2010. The X axis represents times of beginning of the time windows for which the considered standard deviation is calculated.

- Earthquakes. There are many studies that point out connection or possible connection between ionospheric disturbances and earthquakes (see, for example, Pulinets and Boyarchuck, 2004; Hayakawa, 2007). VLF/LF radio signal disturbances are also considered as possible precursors of these natural disasters. There are different kinds of changes in the signal amplitude which are analysed, like variations in the amplitude values a few days before earthquake events (Biagi et al., 2011), changes in the terminator time, also a few days before earthquake event (Molchanov, 1998), and the reduction of the noise amplitude less than one hour before a earthquake event (Nina et al., 2020b). The possible importance of the lower ionosphere monitoring in the EQ predictions was motivation for the integration of several receivers in the VLF/LF receiver networks like European (Biagi et al., 2011) and Pacific (Hayakawa et al., 2010) ones to search for earthquake precursors

In this paper we show an example of reduction of the noise amplitude presented as decrease of the standard deviation of differences of the recorded ICV signal amplitude from its smoothed values dA before the Kraljevo earthquake occurred on 3 November 2010 (time of its occurrence is indicated by the vertical dashed line in Fig. 4).

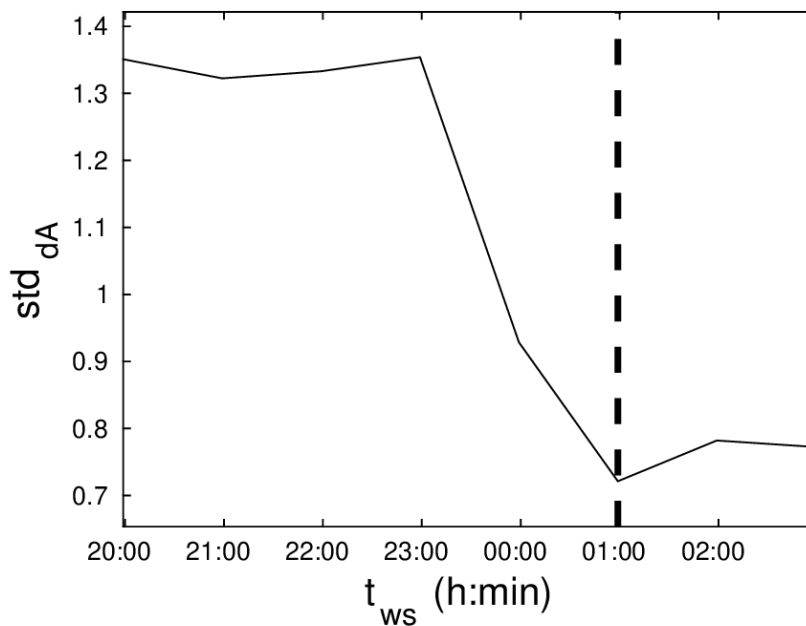


Figure 4. An example of the noise amplitude reduction presented as decrease of the standard deviation of differences of the recorded ICV signal amplitude from its smoothed values dA before the Kraljevo earthquake occurred on 3 November 2010. The time of this earthquake is indicated by the vertical dashed line.

- Tropical cyclones.** There are several studies which present variations in VLF signals before tropical cyclones. The lightning activities intensification before a tropical depression, detected as VLF signal variations, are indicated as precursors in Price et al., 2007. The lightning activity during a hurricane is analysed in some studies (Peter and Inan, 2005 and Thomas et al., 2010). In addition, connections between the perturbations of the VLF/LF signals and meteorological factors are considered in several studies (Samsury and Orville, 1994; Molinari et al., 1994; Price et al., 2009). In Nina et al. (2017), the reactions of the low ionosphere during tropical depressions (TDs) which have been detected before the hurricane appearances in the Atlantic Ocean. 41 TD events are explored using very low frequency (VLF) radio signals emitted by the NAA transmitter and recorded by the VLF receiver located in Belgrade. VLF signal deviations (caused ionospheric turbulence) are found in the case of 36 out of 41 TD events (88%). Additionally, 27 TDs which have not been developed in hurricanes are explored and similar low ionospheric reactions are found. However, in the sample of 41 TDs which are followed by hurricanes the typical low ionosphere perturbations seem to be more frequent than other TDs. In Fig. 5 we present deviation of the NAA signal amplitude in period around beginning of the tropical depression before hurricane Gordon occurred in September 2006 with respect to three other days. Vertical dashed lines represent

time when this TD is recorded. Because time sampling of these data is 6 h we cannot compare times of the TD beginning and the recorded disturbance in VLF signal amplitude.

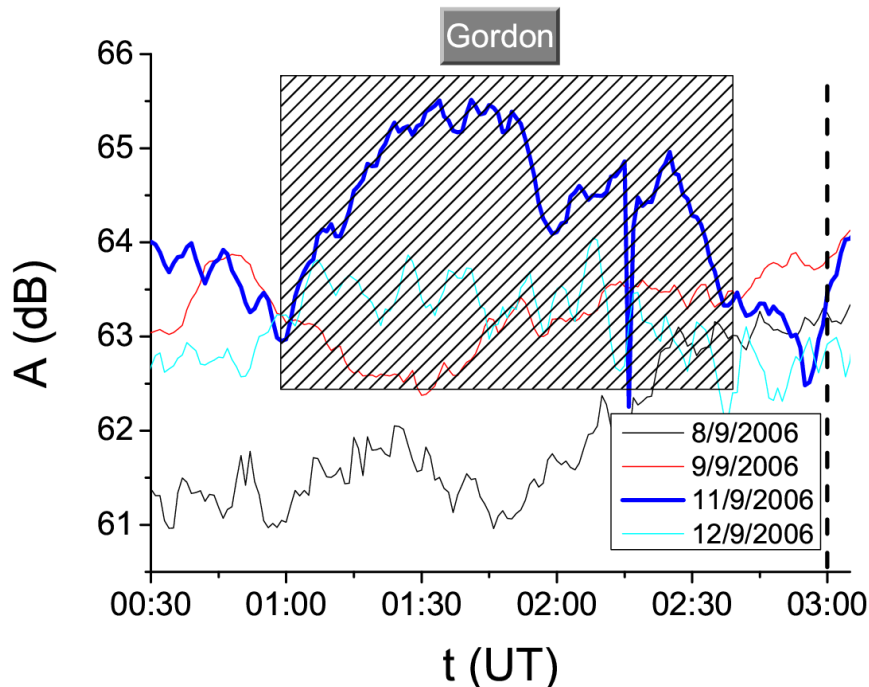


Figure 5. Deviation of the NAA signal amplitude in period around beginning of the tropical depression before hurricane Gordon occurred on September 2006 with respect to three other days. The vertical dashed line represents time when this TD is recorded.

4. Summary

In this paper we present detection of changes in the VLF/LF signal amplitudes which are consequences of the lower ionosphere disturbances induced by natural events and processes which can affect human health. We present changes in these radio signals which occurred due to variations in the solar radiation and which are (possible) connected with earthquakes and tropical cyclones. We analyse data recorded by the Belgrade receiver station located at the Institute of Physics Belgrade. We also consider periodical variations due to changes in the incoming solar hydrogen $L\gamma$ radiation during solar cycles, years and days.

Acknowledgments. The author acknowledges funding provided by the Institute of Physics Belgrade, through the grant by the Ministry of Education, Science, and Technological Development of the Republic of Serbia.

References

Biagi, P.F., Maggipinto, T., Righetti, F., Loiacono, D., Schiavulli, L., Ligonzo, T., Ermini, A., Moldovan, I.A., Moldovan, A.S., Buyuksarac, A., Silva, H.G., Bezzeghoud, M., Contadakis, M.E.,

2011. *The European VLF/LF radio network to search for earthquake precursors: setting up and natural/man-made disturbances*. Nat. Hazards Earth Syst. Sci. 11, 333–341.

Cohen, M.B., Inan, U.S., Paschal, E.W.: 2010, *Sensitive broadband ELF/VLF radio reception with the AWESOME instrument*. IEEE Trans. Geosci. Remote 48, 3.

Ferguson, J.A., 1998. *Computer programs for assessment of long-wavelength radio communications*, Version 2.0. Technical document 3030. Space and Naval Warfare Systems Center, San Diego CA.

Hayakawa, M., 2007. *VLF/LF radio sounding of ionospheric perturbations associated with earthquakes*. Sensors 7, 1141–1158.

Kolarski, A., Grubor, D., Šulić, D., 2011. *Diagnostics of the solar X-Flare impact on lower ionosphere through seasons based on VLF-NAA signal recordings*. Balt. Astron. 20, 591–595.

Molinari, J., Moore, P.K., Idone, V.P., Henderson, R.W., Saljoughy, A.B., 1994. *Cloud-to-ground lightning in Hurricane Andrew*. J. Geophys. Res. 99, 16665–16676.

Molchanov, O., Hayakawa, M., Oudoh, T., Kawai, E., 1998. *Precursory effects in the subionospheric VLF signals for the Kobe earthquake*. Phys. Earth Planet. Inter. 105, 239–248.

A. Nina, V. M. Čadež, J. Bajčetić, M. Andrić, G. Jovanović, *Responses of the ionospheric D-region to periodic and transient variations of the ionizing solar Ly α radiation*, Journal of the Geographical Institute "Jovan Cvijic" SASA, vol. 67, issue 3, (2017), 235–248

Nina, A., Radovanović, M., Milovanović, B., Kovačević, A., Bajčetić, J., Popović, L.Č., 2017b. *Low ionospheric reactions on tropical depressions prior hurricanes*. Adv. Space Res. 60, 1866–1877.

A. Nina, V. M. Čadež, J. Bajčetić, S.T. Mitrović and L. Č. Popović, *Analysis of the Relationship Between the Solar X-Ray Radiation Intensity and the D-Region Electron Density Using Satellite and Ground-Based Radio Data*, Solar Physics, vol. 293, issue 4, (2018), 64 (1-19)

Nina, A. Nico, G., Odalović, O., Čadež, V.M., Todorović Drakul, M., Radovanović, M. and Popović, LČ., *GNSS and SAR Signal Delay in Perturbed Ionospheric D-Region During Solar X-Ray Flares*, IEEE Geoscience and Remote Sensing Letters, vol. 17, no. 7, July 2020

A. Nina, S. Pulnits, P. F. Biagi, G. Nico, S. T. Mitrović, M. Radovanović, L. Č. Popović, (2020) *Variation in natural short-period ionospheric noise, and acoustic and gravity waves revealed by the amplitude analysis of a VLF radio signal on the occasion of the Kraljevo earthquake (M w = 5.4)* Sci. Total Environ. 710, 136406

Peter, W.B., Inan, U.S., 2005. *Electron precipitation events driven by lightning in hurricanes*. J. Geophys. Res. 110, A05305.

Price, C., Asfur, M., Yair, Y., 2009. *Maximum hurricane intensity preceded by increase in lightning frequency*. Nature Geosci. 2, 329–332.

Price, C., Yair, Y., Asfur, M., 2007. *East African lightning as a precursor of Atlantic hurricane activity*. Geophys. Res. Lett. 34, L09805.

Pulinets, S.A., Boyarchuk, K.A., Hegai, V.V., Kim, V.P., Lomonosov, A. M., 2000. *Quasielectrostatic model of atmosphere-thermosphere-ionosphere coupling*. Adv. Space Res. 26, 1209–1218.

Samsury, C.E., Orville, R.E., 1994. *Cloud-to-ground lightning in tropical cyclones: a study of Hurricanes Hugo (1989) and Jerry (1989)*. Mon. Weather Rev. 122, 1887–1896.

PROCEEDINGS

of the XIX Serbian Astronomical Conference

Belgrade, October 13 – 17, 2020

ЗБОРНИК РАДОВА

XIX Српске астрономске конференције

Београд, 13 – 17. октобар 2020.

Edited by Anđelka Kovačević, Jelena Kovačević Dojčinović,

Dušan Marčeta and Dušan Onić



Б Е О Г Р А Д
2021

**MONITORING OF LOWER IONOSPHERE: POSSIBLE
EARTHQUAKE PRECURSORS AND APPLICATION IN
EARTH OBSERVATIONS BY SATELLITE**

A. NINA

*Institute of Physics Belgrade, University of Belgrade,
Pregrajica 118, 11080 Belgrade, Serbia
E-mail: sandrast@ipb.ac.rs*

Abstract. Ionospheric observations can be used for indirect detection of various processes in the outer space and Earth. In addition, the ionosphere affects the propagation of electromagnetic signals used in numerous practical applications. Here, we present the latest research based on the observation of the low ionosphere by very low frequency radio signals recorded in Belgrade related to a possible new type of earthquake precursor, and the impact of the perturbed ionospheric D-region on the propagation of satellite signals used in Earth's observations.

1. INTRODUCTION

Research of the ionosphere is of great importance for both science (first of all for geosciences) and modern technologies based on the use of satellite and ground based electromagnetic signals. Practical applications of these studies are important for many contemporary area of human life including telecommunications, GPS positioning and Earth observations. Namely, disturbances of the ionosphere can strongly affect propagation of these electromagnetic waves and induce significant errors in measurements and modelling of different parameters (Nina et al., 2020b). In addition, there are many studies which indicate connections between ionospheric disturbances and natural disasters (Nina et al., 2017; Pulinets and Boyarchuk, 2004; NaitAmor et al., 2018; Kumar et al. 2016). Some of these ionospheric perturbations are recorded before events which are following by large catastrophes (Maekawa et al., 2006; Maurya et al., 2016; Molchanov et al, Yamauchi et al., 2007) and for this reason their investigation is of high priority.

The lower ionosphere can be monitored by several techniques including those based on propagation of very low/low frequency (VLF/LF) radio signals in the Earth-ionosphere waveguide. The advantages of this method in analysis of the atmospheric layer between 50 km and 90 km are (1) continuous monitoring of signals with time resolution that is usually better than 1 s, and (2) observation of large part of the lower ionosphere which is provided by numerous worldwide located transmitters and receivers.

In this paper we present recent investigation based on data collected by the Belgrade VLF/LF receiver station located at the Institute of Physics Belgrade. We pay attention to two studies related to disturbances in periods around earthquake (EQ) events (Nina et al., 2020a) and during a solar X-ray flare influence (Nina et al., 2020b). In first study attention is focused on analysis of possible connections between an earthquake and changes in electrical properties of the lower ionosphere. In the second study we analysed influence of the intensive perturbed ionospheric D-region by a solar X-ray flare on satellite signals.

2. OBSERVATIONS, DATA PROCESSING AND MODELLING

In our research we use data obtained in the lower ionosphere observation by VLF signals emitted by the ICV, GQD and DHO transmitters located in Italy, the UK and Germany (see Table 1) and recorded by Belgrade receiver station. The propagation paths of these signals are shown in map given in Fig. 1.

Table 1: Transmitter locations and frequencies for the considered VLF signals.

	Transmitter location	Frequency (kHz)
ICV	Isola di Tavolara, Italy	20.27
GQD	Rhauderfehn, Germany	22.1
DHO	Anthorn, the UK	23.4

We analyse data recorded by the Absolute Phase and Amplitude Logger (AbsPAL) and Atmospheric Weather Electromagnetic System for Observation Modeling and Education (AWESOME) receivers in the first and second analysis, respectively. We analyse data sets for all three signals with time sampling of 0.1 s and for DHO signal with time sampling of 1 s, respectively.

2. 1. NOISE AMPLITUDE REDUCTION AS POSSIBLE EARTHQUAKE PRECURSOR

There are many studies which indicate relationships between EQ events and ionospheric disturbances (see, for example, Biagi et al., 2001; Nina et al. 2020a; Pulnits and Boyarchuk, 2004). These studies are primarily based on the comparison of variations detected during different days. In Nina et al., 2020a, variations in natural short period noise amplitude are analysed for time period around the Kraljevo EQ (Mw=5.4) occurred on 3 November, 2010. We analysed data recorded by the 0.1-s time resolution in order to investigate signal changes several hours before and after the considered EQ event.

In addition, three EQs with magnitudes 4.3, 4.4 and 4.5 are analysed. One of them (Mw=4.4) occurred at location that was very close to the epicentre of the main EQ, while the epicentres of other events were at longer distance from the signal propagation paths than in the first two cases. For all of these events it is common that magnitudes were greater than 4 and that they occurred in the night-time period.

In this analysis, three signals emitted in Italy (ICV), the UK (GQD) and Germany (DHO) and recorded in Belgrade are analysed. The noise amplitude is calculated from the amplitude deviation from smoothed curve during the considered time periods.

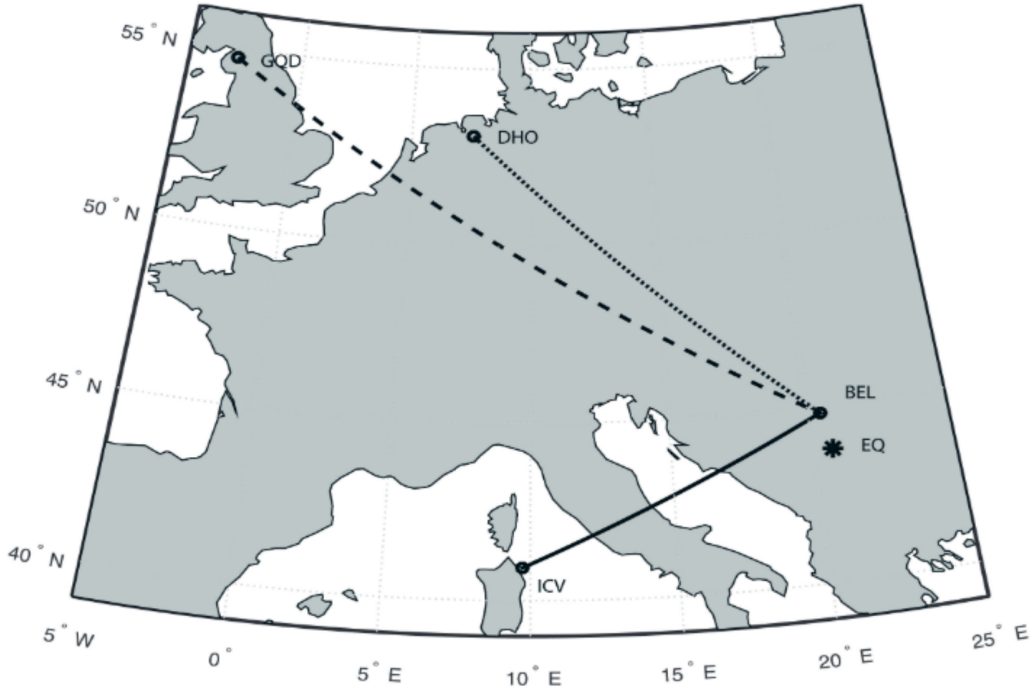


Figure 1: Propagation paths of the VLF signals recorded by the Belgrade receiver station (BEL) in Serbia and emitted by the transmitters ICV in Italy (solid line), GQD in the UK (dashed line), and DHO in Germany (dotted line). Locations of the Kraljevo earthquake is shown as stars.

2. 2. INFLUENCE OF THE D-REGION ON SATELLITE SIGNAL PROPAGATION

There are numerous models that are used in calculations of the ionospheric contribution in the signal delay, so called ionospheric delay, (Nava et al., 2008; Zhao and Zhou, 2018). Mostly, they use observational data as input and use analytical expressions for modelling of the ionospheric delay. If the observational data relates to one or more altitudes, a particular model is single or multiple layer model, respectively. In both cases these altitudes are above 100 km because upper areas has larger influences on signal propagation due to larger electron density. For this reason, calculations of the total electron content (TEC), which is required for modelling of the signal delay, are based on approximations that electron density vertical distribution can be obtained from the observational data at fixed altitudes and used expressions. Because of the fact that ionospheric parameters can be significantly changed in a localized area during some time interval, two questions should be considered: (1) Are the used expressions applicable during intensive disturbances? and (2) Can local disturbances below 100 km be important?

In Nina et al., 2020b influence of a solar X-ray flare which primarily disturbs the D-region (50 km- 90 km) on GNSS and Synthetic Aperture Radar (SAR) signal delay is considered. Error in modelling of the signal delay $P_D = C \cdot TEC_D / f^2$ if the D-region is not included in consideration depends on the total electron content in D-region, TEC_D , which is given by expression:

$$\text{TEC}_D = \delta H_D \sum_{i=1}^{N_D} N_{ei} n_i [n_i^2 - (n_0 \sin(\Theta_0))^2]^{-0.5}. \quad (1)$$

where δH_D is the thickness of horizontally uniform layers in the D-region, N_{ei} and n_i are the electron density and refractive index in layer i , respectively, and Θ_0 is the wave propagation angle in the D-region.

3. RESULTS

3. 1. NOISE AMPLITUDE REDUCTION AS POSSIBLE EARTHQUAKE PRECURSOR

Significant reduction of the noise amplitude is recorded for ICV signal emitted in Italy whose propagation path lies the closest to the EQ epicentre. The beginning of this reduction is before the EQ which indicates possibility that this type of variation can be consider as EQ precursor. Variations in the noise amplitude are also recorded for other two signals but they are not specific for the considered night and they can not be connected with EQ event.

To examine influences of the epicentre distance from the signal propagation path and to examine noise amplitude reduction recorded in the other time periods additional analyses of the ICV signal amplitude are performed. They were related to:

- Time evolution of the amplitude noise in periods around three EQs of magnitudes 4.4 (the same epicentre location like for the main EQ event), and magnitudes 4.3 and 4.5 (epicentres at larger distance than in the first two cases);
- Time evolutions of the noise amplitude during hole three days.

The noise reduction is also recorded for EQ with epicentre near the epicentre of Kraljevo EQ. In the other two cases these reductions are not recorded which indicates importance od epicentre distance from the signal propagation path.

To examine the regular daily variations in the noise amplitude (this analysis is important for the extraction of the sudden from periodic variations) the short-period noise amplitude is analysed during three whole days: 3 and 4 November when two EQs near Kraljevo occurred, and 9 November when significant reduction of the noise amplitude is also recorded in analysis of two months in periods of 1 hour around time of Kraljevo EQ ($0:56:54.4 \pm 0:30$ UT). During these day, 46 EQs (excluding 29 that occurred in a few hours after Kraljevo EQ when extraction of their influence is not possible) were detected with epicentres not far from the ICV signal propagation path (<http://www.emsc-csem.org/Earthquake/>). The most intensive were two EQs with $M_w > 5$ (near Kraljevo ($M_w = 5.4$) and in Tyrrhenian Sea ($M_w = 5.1$)) and two EQs with $M_w > 4$ (near Kraljevo ($M_w = 4.3$) and in Western Mediterranean Sea ($M_w = 4.3$)). Only 13 of these EQ events had the magnitude greater than 3. Analysis of the noise amplitude during these three days shown:

- The short-period amplitude reduction starting before the EQ event is recorded for all 4 detected EQs with magnitude greater than 4.
- 8 of 10 EQs near Kraljevo (i.e. 80%) with magnitude greater than 2.5 are connected with the noise amplitude reduction.

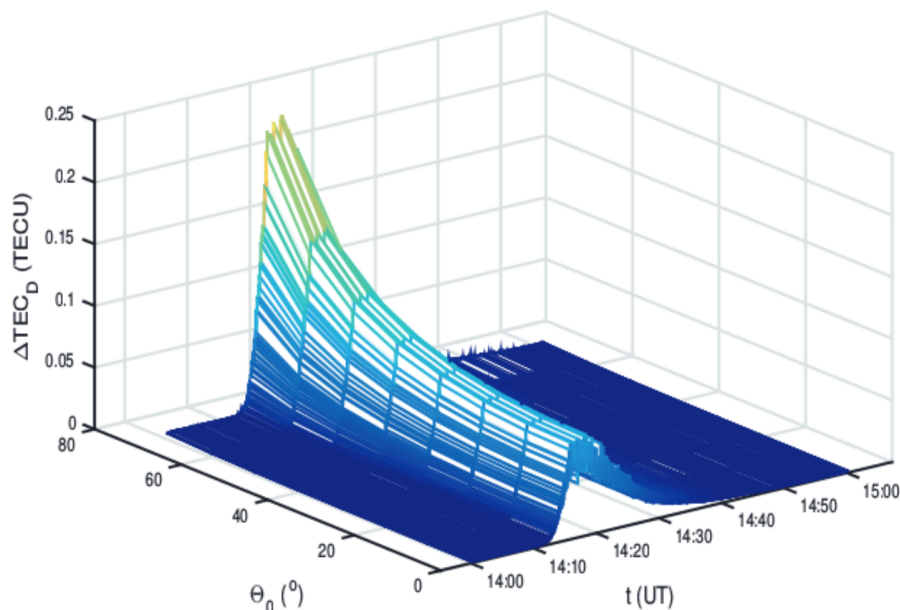


Figure 2: Time evolution of changes in the total electron density within D-region, ΔTEC_D , for different incident angles, Θ of signal in this area during influence of a solar X-ray flare occurred on 1 May 2013.

- Thirteen out of a total of 15 (or 87%) decreases of the short-period noise amplitude can be related to EQ events.

In addition, it is very important to point out that reductions of the short-period noise amplitude are recorded in all day periods.

3. 2. INFLUENCE OF THE D-REGION ON SATELLITE SIGNAL PROPAGATION

As one can see in Fig. 2, changes in TEC_D can be intensive. Results presented in Nina et al., 2020b show that, for more intensive flares, the D-region can provide the signal delay of more than 1 m for large incident angles. Keeping in mind that delays of 1 cm are included in signal propagation modelling it can be concluded that, although quiet D-region does not affect satellite signal propagations, its influence cannot be ignored in periods of intensive disturbances because errors in modelling can be important.

4. SUMMARY

In this work we present review of the recent results obtained in the lower ionosphere investigation based on data obtained by VLF/LF receiver station in Belgrade. We present analyses of (1) possible new type of earthquake precursor visualized as reduction of the signal noise amplitude before the earthquake event, and (2) influence of the ionospheric D-region which is disturbed by a solar X-ray flare on delay of satellite signals.

The main results of these studies indicate that:

- Reduction of VLF signal noise amplitude is recorded before several earthquakes and that confirmation of connection of these changes with earthquake events requires more detailed statistical analysis.
- Influence of the significantly disturbed D-region on propagation of satellite signals can be important and its contribution in signal delay should be involved in modelling.

These studies open many questions important for practical application of ionospheric research and they will be in focus forthcoming studies.

Acknowledgements

The author acknowledges funding provided by the Institute of Physics Belgrade, through the grant by the Ministry of Education, Science, and Technological Development of the Republic of Serbia.

References

- Biagi, P. F., Piccolo, R., Ermini, A., Martellucci, S., Bellecci, C., Hayakawa, M., Kingsley, S. P.: 2001, *Ann. Geophys.*, **44**, 5.
- Kumar, S., Kumar, A., Maurya, A. K., Singh, R.: 2016, *J. Geophys. Res. Space*, **121**, 5930.
- Maekawa, S., Horie, T., Yamauchi, T., Sawaya, T., Ishikawa, M., Hayakawa, M., Sasaki, H.: 2006, *Ann. Geophys.*, **24**, 2219.
- Maurya, A. K., Venkatesham, K., Tiwari, P., Vijaykumar, K., Singh, R., Singh, A. K., Ramesh, D. S.: 2016, *J. Geophys. Res. Space*, **121**, 10403.
- Molchanov, O., Hayakawa, M., Oudoh, T., Kawai, E.: 1998, *Phys. Earth Planet. Inter.*, **105**, 239.
- NaitAmor, S., Cohen, M. B., Kumar, S., Chanrion, O., Neubert, T.: 2018, *Geophys. Res. Lett.*, **45**, 10185.
- Nava, B., Cosson, P., Radicella, S.: 2008, *J. Atmos. Solar-Terr. Phy.*, **70**, 1856.
- Nina, A., Radovanović, M., Milovanović, B., Kovačević, A., Bajčetić, J., Popović, L. Č.: 2017, *Adv. Space Res.*, **60**, 1866.
- Nina, A., Pulnits, S., Biagi, P. F., Nico, G., Mitrović, S., Radovanović, M., Popović, L. Č.: 2020a, *Sci. Total Env.*, **710**, 136406.
- Nina, A., Nico, G., Ođalović, O., Čadež, V., Drakul, M. T., Radovanović, M., Popović, L. Č.: 2020b, *IEEE Geosci. Remote Sens. Lett.*, **17**(7), 1198.
- Pulnits, S., Boyarchuk, K.: 2004. *Ionospheric Precursor of Earthquakes*, Springer, Heidelberg, Germany.
- Yamauchi, T., Maekawa, S., Horie, T., Hayakawa, M., Soloviev, O.: 2007, *J. Atmos. Sol.-Terr. Phys.*, **69**, 793.
- Zhao J., Zhou, C.: 2018, *GPS Solut.*, **22**, 48.

M63

PROCEEDINGS

of the XIX Serbian Astronomical Conference
Belgrade, October 13 – 17, 2020

ЗБОРНИК РАДОВА

XIX Српске астрономске конференције
Београд, 13 – 17. октобар 2020.

Edited by Anđelka Kovačević, Jelena Kovačević Dojčinović,
Dušan Marčeta and Dušan Onić



Б Е О Г Р А Д
2021

ACTIVITIES OF THE SERBIAN EUROPLANET GROUP WITHIN EUROPLANET SOCIETY

I. MILIĆ ŽITNIK¹, A. NINA², V. A. SREĆKOVIĆ², B. P. MARINKOVIĆ², Z. MIJIĆ²
D. ŠEVIĆ², M. BUDIŠA³, D. MARČETA⁴, A. KOVAČEVIĆ⁴, J. RADOVIĆ⁵
and A. KOLARSKI⁶

¹*Astronomical Observatory, Volgina 7, 11000 Belgrade, Serbia
E-mail: ivana@aob.rs*

²*Institute of Physics Belgrade, University of Belgrade,
Pregrevica 118, 11080 Belgrade, Serbia*

³*University of Belgrade School of Electrical Engineering,
Bulevar kralja Aleksandra 73, 11000 Belgrade, Serbia*

⁴*Faculty of Mathematics, University of Belgrade, Studentski Trg 10, 11000 Belgrade, Serbia*

⁵*Department of Atmospheric Physics, Faculty of Mathematics
and Physics, Charles University, Prague, Czech Republic*

⁶*Technical Faculty Mihajlo Pupin, University of Novi Sad, 23000 Zrenjanin, Serbia*

Abstract. Europlanet society connects many different scientific institutions all over the world. The Serbian Europlanet Group (SEG) was established at 2019. It currently has 20 active scientists from 6 institutions working in Serbia in different fields of planetary science as well as related fields. Here are presented activities of SEG in 2020.

1. INTRODUCTION

The European society promotes the European planetary science as well as related fields. Its aims are to support the development of planetary science at a national and regional level, particularly in countries and areas that are currently under-represented within the community, and early career researchers who established their network within the Europlanet: the Europlanet Early Career (EPEC) network (<https://www.europlanet-society.org/early-careers-network/>). The Europlanet consists of 10 Regional Hubs. More information about organization and activities of this society can be found at the website <https://www.europlanet-society.org/>.

Serbia is one of six countries included in the Southeast European Hub that was established in 2019. The Serbian Europlanet Group (SEG) currently consists of 20 members from 6 institutions. Details of members and activities of SEG can be found at the website <https://www.europlanet-society.org/europlanet-society/regional-hubs/southeast-europe/>. In this paper are described main activities and presented scientific research of SEG members related to the Europlanet fields in 2020.

2. CONFERENCES AND WORKSHOPS OF SEG 2020

2. 1. PARTICIPATION IN THE EUROPLANET SCIENCE CONGRESSES

The Europlanet Science Congress (EPSC) is the annual meeting of the Europlanet Society. In the Europlanet Science Congress 2020, seven scientists from Serbia participated with several lectures. It was first virtual EPSC congress attended by 1168 participants from 49 countries. Here, will be mentioned two of SEG participants.

Dušan Marčeta presented research about population of interstellar asteroids and possibility that one of the observational selection effects, known as Holetschek's effect, could be used for preliminary estimation of the size-frequency distribution of this population. Aleksandra Nina presented research on new methodology for earthquake prediction which was partially realized within the Europlanet workshop in Petnica Science Center in 2019.

2. 2. PARTICIPATION IN THE XII SERBIAN–BULGARIAN ASTRONOMICAL CONFERENCE

Serbian scientists organized a Europlanet session with several lectures during the XII Serbian–Bulgarian Astronomical Conference (SBAC 12). SBAC 12 was held in Sokobanja from September 25 to 29, 2020 (Popović *et al.* 2020). SEG presented its work (Nina *et al.* 2020a) and discussed with Bulgarian colleagues and with colleagues from Europlanet Southeast HUB countries about expanding of their cooperation.

2. 3. PARTICIPATION IN THE XIX SERBIAN ASTRONOMICAL CONFERENCE

The work of SEG was presented during the XIX Serbian Astronomical Conference (19 SAC), held at the Serbian Academy of Sciences and Arts in Belgrade from October 13 to 17, 2020 (Kovačević *et al.* 2020). Aleksandra Nina participated with invited lecture about investigation of the lower ionosphere disturbances as possible earthquake precursors and application of research of the lower ionosphere influences in Earth observations by satellite during influence a solar X-ray flare. Ivana Milić Žitnik gave progress report about asteroid's motion with orbital eccentricity in the range (0, 0.2) across the 2-body mean motion resonances with Jupiter with different strengths due to the Yarkovsky effect (Milić Žitnik & Novaković 2016, Milić Žitnik 2020a).

3. RESEARCHES OF SEG MEMBERS AT 2020

SEG members are scientists in different research fields. Here are a few researches that are in the areas of Europlanet.

3. 1. ASTRONOMY

3.1.1. Model of interstellar asteroids and expected predominance of retrograde object among the discovered objects

Dušan Marčeta and Bojan Novaković examined the model of interstellar asteroids and comets and found analytical expressions for the distributions of their orbital elements (Marčeta & Novaković 2020). They payed special attention to objects which could be detectable by future LSST survey. Also, they found that majority of these objects should move along retrograde orbits resulting in asymmetry of the distribution of

their orbital inclinations. Finally, they found that this asymmetry is a result of the Holetschek effect. Since this effect is size-dependant, its influence is stronger for populations with steeper size-frequency distributions since they are comprised of larger number of smaller objects. This fact could be used for preliminary estimation of the size-frequency distribution of the underlying true population of interstellar objects once when sufficient number of objects become discovered.

3.1.2 The relationship between the 'limiting' Yarkovsky drift speed and asteroid families' Yarkovsky V -shape

Ivana Milić Žitnik examined the relationship between asteroid families' V -shapes and the 'limiting' diameters in the $(a, 1/D)$ plane. Following the recently defined 'limiting' value of the Yarkovsky drift speed at 7×10^{-5} au/Myr (Milić Žitnik 2019), she decided to investigate the relation between the asteroid family Yarkovsky V -shape and the 'limiting' Yarkovsky drift speed of asteroid's semi-major axes. She has used the known scaling formula to calculate the Yarkovsky drift speed in order to determine the inner and outer 'limiting' diameters (for the inner and outer V -shape borders) from the 'limiting' Yarkovsky drift speed. The method was applied to 11 asteroid families of different taxonomic classes, origin type and age, located throughout the Main Belt. Her main conclusion was that the 'breakpoints' in changing V -shape of the very old asteroid families, crossed by relatively strong mean motion resonances on both sides very close to the parent body, are exactly the inverse of 'limiting' diameters in the a versus $1/D$ plane. This result uncovers a novel interesting property of asteroid families' Yarkovsky V -shapes (Milić Žitnik 2020b).

3.1.3 Astrobiology-habitability of exoplanets

Balbi, Hami and Kovačević (2020) present a new investigation of the habitability of the Milky Way bulge, that expands previous studies on the Galactic Habitable Zone. This work discusses existing knowledge on the abundance of planets in the bulge, metallicity and the possible frequency of rocky planets, orbital stability and encounters, and the possibility of planets around the central supermassive black hole. Another concern for habitability is the presence of the supermassive black hole in the Galactic center, but also in nearby Active galactic nuclei, that could have resulted in a substantial flux of ionizing radiation during its past active phase, causing increased planetary atmospheric erosion and potentially harmful effects to surface life as shown by Wislocka, Kovačević, Balbi (2019). This work was featured in famous Forbes Magazine in their section Innovations. Andjelka Kovačević is a member of Working group of habitability of exoplanets of European astrobiology institute.

3. 2. GEOPHYSICS

3.2.1 Atmospheric aerosol remote sensing and modelling

The EARLINET lidar network was established with the goal of creating a quantitative, comprehensive, and statistically significant database for the horizontal, vertical, and temporal distribution of aerosols on a continental scale. Within the network Belgrade lidar station was involved in initiative for studying the changes in the atmosphere's structure, its dynamics, and its optical properties during the COVID-19 lock-down by comparison to the aerosol climatology in Europe. Near real time de-

livery of the data and fast analysis of the data products proved that aerosol lidars are useful for providing information not only for climatological purposes, but also in emergency situations like detecting airborne hazards for aviation (Papagiannopoulos *et al.* 2020). The preliminary results indicate that the lock-down did not affected the high troposphere, but for the low troposphere a certain effect can be seen. In addition, ongoing activities are related to the participation in ESA ADM-Aeolus mission (the first high-spectral resolution lidar in space) Cal/Val activity through validation of L2A products of aerosol profiles and studying the relationship between satellite AOD measurements and ground PM concentrations (Mijić & Perišić 2019).

3.2.2 Lower ionosphere

The lower ionosphere research was a continuation of research related to a possible new type of earthquake precursor in the form of signal noise amplitude reduction (Nina *et al.* 2020b) and examinations of the effects of the D-region which is disturbed by a solar X-ray flare on satellite signals (Nina *et al.* 2020c). Also, a new model for determining ionospheric parameters in the unperturbed D-region was developed.

3.2.3 Investigation of a possible lithosphere-ionosphere coupling through seismo-ionospheric effect

Possible relationship between amplitude and phase delay characteristics of the NWC/19.8 kHz signal transmitted from H. E. Holt in Australia ($\varphi = 21.8^\circ$ S, $\Lambda = 114.16^\circ$ E) towards Belgrade AbsPAL receiver ($\varphi = 44.85^\circ$ N, $\Lambda = 20.38^\circ$ E) in Serbia and seismic activity reported by Helmholtz-Zentrum Potsdam - Deutsches GeoForschungsZentrum GFZ in period from December 2005 to June 2007 was investigated with the main result presented in Kolarski and Komatina (2020).

3.2.4 Satellite radar technique for atmospheric water vapor measurement and modelling effects of the ionospheric disturbances

Satellite observation and measurements performed by the Synthetic Aperture Radar (SAR) and the Interferometric Synthetic Aperture Radar (InSAR) technique can be used for acquiring more information about the water vapor present within the atmosphere. The methodology of the SAR instrument and the InSAR technique is described in Radović (2020). Additionally, the focus is set on the four different satellites with SAR instruments working on different frequencies. Apart from that, in Radović (2020) is presented how neglecting the ionospheric perturbations which took place during the satellite measurements can influence modelling of the water vapor parameters derived from such measurements acquired by the SAR instruments carried by the mentioned satellites.

3. 3. ASTROPHYSICS

3.3.1. Atomic Molecular and Optical Physics group of researchers at the Laboratory for Atomic Collision Processes

LACP¹, Institute of Physics Belgrade, University of Belgrade, has been studying several collisional processes that involve electron scattering by atomic particles (e.g. for

¹<http://mail.ipb.ac.rs/centar3/acp.html>

helium Jureta et al. (2014)) and laser interactions with gases (Rabasović et al. 2019), nanopowders (Šević et al. 2020a,b) and single crystal phosphors (Šević et al. 2021). Electron impact cross sections are relevant parameters in modelling of processes that occur in cometary coma (Marinković et al. 2017), collisional processes in AGNs (Dimitrijević et al. 2021) or Earth's and other planets' atmospheres (Vukalović et al. 2021). Due to the immense importance of having full survey and accurate data of electron cross sections, there are several databases that maintain large sets of electron collisional data and even more, a unique portal for accessing such kind of data have been created through European framework programs (for a recent update of the Virtual Atomic and Molecular Data Centre² – VAMDC see e.g. Albert et al. (2020)).

BeamDB (Belgrade electron-atom/molecule DataBase³) is a collisional database that is maintained by the researchers of the LACP and it covers interactions of electrons with atoms and molecules in the form of differential (DCS) and integral cross sections for the processes such as elastic scattering, excitation and ionization (Jevremović et al. 2020). At present the output files that come from the search of BeamDB are present in the xml format of specific syntax developed by the International Atomic Energy Agency (IAEA)⁴. These so called “xsams” files contain full record of data sets including bibliographical entities, but the process of extracting values of cross sections is hard for researchers. That is why this group started to develop a converter which will convert xsams file into textual format file with simple columns that list values of impact energy, scattering angle, DCS and corresponding uncertainty. The next step would be adding a graphical presentation to the webpage of the BeamDB database. The graphics should present logarithm of DCS data points with error bars associated to the uncertainty versus impact energy and scattering angle in 3D graph.

Exploiting the fact that BeamDB contains large sets of DCS values obtained both experimentally and theoretically, they are in the process of developing machine learning algorithms for determining extrapolated DCS in the regions which are not accessed by experiments (Ivanović et al. 2020). The primary goal is to determine extrapolated values toward zero scattering angle as well as to large angles, usually from 150° to 180°.

It is envisaged that the BeamDB will contain electron spectroscopy data as well, beside the cross section data. At present, there is only a single threshold photoelectron spectrum of argon curated in the BeamDB, but the plans are to add energy loss spectra, presumably obtained in the LACP. This would allow them to develop tools for spectral classification and particular spectra identification based on data-mining methods. An overview of various data mining methods has been recently presented by Yang et al. (2020).

3.3.2. A&M data for stellar atmosphere modelling

Work on topics of modelling various astrophysical and laboratory plasma which are of interest for Europlanet community is continued. A&M datasets e.g. rate coefficients, Stark broadening parameters, line profiles, etc. are published during this year (see

²https://portal.vamdc.eu/vamdc_portal/

³<http://servo.aob.rs/emol>

⁴<https://www-amdis.iaea.org/xsams/documents/>

some of the papers: Srećković *et al.* 2020; Majlinger *et al.* 2020; Dimitrijević *et al.* 2020). Part of the data are hosted on SerVO at AOB⁵.

4. CONCLUSION AND FURTHER WORK

In this paper are presented activities of Serbian scientists within Europlanet society. In the first part of the paper, are described briefly conferences that occurred in 2020 which promoted work of Serbian Europlanet Group. In the second part are presented several studies of SEG important for the Europlanet research fields. Serbian scientists plan to continue work within Europlanet society in the following years and to promote the Europlanet and SEG activities, as well as to expand SEG.

Acknowledgments

This research is supported by the Europlanet. The authors acknowledge funding provided by the Institute of Physics Belgrade, Astronomical Observatory (the contract 451-03-68/2020-14/200002), Faculty of Mathematics University of Belgrade (the contract 451-03-68/2020-14/200104) through the grants by the Ministry of Education, Science, and Technological Development of the Republic of Serbia.

References

- Albert, D., Antony, B. K., Ba, Y. A. *et al.*: 2020, *Atoms*, **8(4)**, 76.
 Balbi, A., Hami, M., Kovačević, A.: 2020, *Life*, **10(8)**, 132.
 Dimitrijević, M. S., Srećković, V. A., Zalam, A. A., Miculis, K., Efimov, D. K., Bezuglov, N. N., Klyucharev, A. N.: 2020, *Contrib. Astron. Obs. Skaln. Pleso*, **50(1)**, 66.
 Dimitrijević, M. S., Srećković, V. A., Ignjatović, Lj. M., Marinković, B. P.: 2021, *New Astronomy*, **84**, 101529.
 Ivanović, S., Uskoković, N., Marinković, B. P., Mason, N. J.: 2020, *Publ. Astron. Obs. Belgrade*, **99**, 43.
 Jevremović, D., Srećković, V. A., Marinković, B. P., Vujčić, V.: 2020, *Contrib. Astron. Obs. Skalnaté Pleso*, **50(1)**, 44.
 Jureta, J. J., Milosavljević, A. R., Marinković, B. P.: 2014, *Int. J. Mass Spectrom.*, **365-366**, 114.
 Kolarski, A., Komatina, S.: 2020, *Book of Abstracts*, International Symposium GEOSCIENCE 2020, November 20 - 22 2020, Bucharest, Romania, 81.
 Kovačević, A., Kovačević Dojčinović, J., Marčeta, D., Onić, D.: 2020, *Book of Abstracts*, XIX Serbian Astronomical Conference, October 13 - 17, 2020, Belgrade, Serbia.
 Majlinger, Z., Dimitrijević, M. S., Srećković, V. A.: 2020, *Mon. Not. R. Astron. Soc.*, **496(4)**, 5584.
 Marinković, B. P., Bredehöft, J. H., Vujčić, V., Jevremović, D., Mason, N. J.: 2017, *Atoms*, **5(4)**, 46.
 Marčeta, D., Novaković, B.: 2020, *Mon. Not. R. Astron. Soc.*, **498(4)**, 5386.
 Mijić, Z., Perišić, M.: 2019, *Book of abstracts*, "Integrations of satellite and ground-based observations and multi-disciplinarity in research and prediction of different types of hazards in Solar system", Petnica Science Center, May 10-13, 2019, Geographical Institute "Jovan Cvijić" SASA, Belgrade, 51.
 Milić Žitnik, I., Novaković, B.: 2016, *Aphys. Journ. lett.*, **816**, L31.
 Milić Žitnik I.: 2019, *Mon. Not. R. Astron. Soc.*, **486**, 2435.
 Milić Žitnik I.: 2020a, *Serb. Astron. Journ.*, **200**, 25.
 Milić Žitnik I.: 2020b, *Mon. Not. R. Astron. Soc.*, **498(3)**, 4465.

⁵see e.g. <http://servo.aob.rs/mold>

- Nina, A., Radovanović, M., Popović, L. Č., Černok, A., Marinković, B., Srećković, V., Kovačević, A., Radović, J., Čelebonović, V., Milić Žitnik, I., Mijić, Z., Veselinović, N., Kolarski, A., Zdravković, A.: 2020a, *Proceedings of the XII Serbian-Bulgarian Astronomical Conference (XII SBAC)*, Sokobanja, Serbia, September 25-29, 2020, Eds: L. Č. Popović, V. A. Srećković, M. S. Dimitrijević, A. Kovačević, Publ. Astron. Soc. Rudjer Bošković, **20**, 107.
- Nina, A., Pulinets, S., Biagi, P. F., Nico, G., Mitrović, S. Dj., Radovanović, M., Popović, L. Č.: 2020b, *Science of the Total Environment*, **710**, 136406.
- Nina, A., Nico, G., Odalović, O., Čadež, V. M., Todorović, M. D., Radovanović, M., Popović, L. Č.: 2020c, *IEEE Geoscience and Remote Sensing Letters*, **17(7)**, 1198.
- Papagiannopoulos, N., D'Amico, G., Gialitaki, A., Ajtai, N., Alados-Arboledas, L., Amodeo, A., Amiridis, V., Baars, H., Balis, D., Binietoglou, I., Comerón, A., Dionisi, D., Falconieri, A., Fréville, P., Kampouri, A., Mattis, I., Mijić, Z., Molero, F., Papayannis, A., Pappalardo, G., Rodríguez-Gómez, A., Solomos, S., Mona, L.: 2020, *Atmos. Chem. Phys.*, **20**, 10775.
- Popović, L. Č., Srećković, V. A., Dimitrijević, M. S., Kovačević, A.: 2020, *Book of Abstracts, XII Serbian-Bulgarian Astronomical Conference (XII SBAC) September 25 - 29, 2020*, Sokobanja, Serbia, Astronomical Observatory, Belgrade, Serbia.
- Rabasović, M. S., Rabasović, M. D., Marinković, B. P., Šević, D.: 2019, *Atoms*, **7(1)**, 6.
- Radović, J.: 2020, Master thesis, Faculty of Physics, University of Belgrade, Serbia.
- Srećković, V. A., Dimitrijević, M. S., Ignjatović, L. M.: 2020, *Contrib. Astron. Obs. Skaln. Pleso*, **50**, 171.
- Šević, D., Rabasović, M. S., Križan, J., Savić-Šević, S., Rabasović, M. D., Marinković, B. P., Nikolić, M. G.: 2020a, *Opt. Quant. Electron.* **52**, 232.
- Šević, D., Vlasić, A., Rabasović, M. S., Savić-Šević, S., Rabasović, M. D., Nikolić, M. G., Marinković, B. P., Križan, J.: 2020b, *Tehnika*, **75(3)**, 279.
- Šević, D., Križan, J., Rabasović, M. S., Marinković, B. P.: 2021, "Temperature sensing using YAG:Dy single crystal phosphor", *Eur. Phys. J. D.*, submitted.
- Vukalović, J., Maljković, J. B., Tökési, K., Predojević, B., Marinković, B. P.: 2021, *Int. J. Molec. Sci.* **22(2)**, 647.
- Yang, P., Yang, G., Zhang, F., Jiang, B., Wang, M.: 2020, *Arch. Computat. Methods. Eng.*, accepted, <https://doi.org/10.1007/s11831-020-09401-9>.
- Wislocka, A. M., Kovačević, A. B., Balbi, A.: 2019, *Astron. Astroph.*, 624, A71.